IHEP-CEPC-DR-2015-01

IHEP-AC-2015-01

CEPC-SPPC

Preliminary Conceptual Design Report

Volume II - Accelerator

The CEPC-SPPC Study Group

March 2015

CEPC-SPPC

Preliminary Conceptual Design Report

March 2015

The CEPC-SPPC Study Group

Armen Apyan[13], Lifeng Bai[12] (白利锋), Mei Bai[45] (柏梅), Sha Bai[1] (白莎),
Paolo Bartalini [28], Sergey Belomestnykh[14] , Tianjian Bian[1] (边天剑),
Xiaojuan Bian[1] (边晓娟), Wenyong Cai[8] (蔡文勇), Yunhai Cai[15] (蔡云海),
Jianshe Cao[1] (曹建社), Weiping Chai[2] (柴伟平), Ningbo Chang[28] (畅宁波),
Fuqing Chen[1] (陈福庆), Geng Chen[4] (陈耿), Jiaxin Chen[1] (陈佳鑫),
Fusan Chen[1] (陈福三), Shiyong Chen[28] (陈时勇),Xiaonian Chen[8] (陈晓年),
Xurong Chen[2] (陈旭荣), Gang Chen[1] (陈刚), Jian Cheng[1] (程健),Yunlong Chi[1] (池云龙),
Weiren Chou[16] (周为仁), Xiaohao Cui[1] (崔小昊),Changdong Deng[1] (邓昌东),
Qingyong Deng[1] (邓庆勇), Weitian Deng[29] (邓维天), Hengtong Ding[28] (丁亨通),
Yadong Ding[1] (丁亚东), Haiyi Dong[1] (董海义), Jiajia Dong[8] (董甲甲),
Lan Dong[1] (董岚),Yuhui Dong[1] (董宇辉),Zhe Duan[1] (段哲), Jingzhou Fan[5] (范荆洲),
Junjie Fan[34] (范俊杰), Yoshihiro Funakoshi[21] (船越义裕), yonggui Gao[46] (高勇贵),
Pingping Gan[4] (甘娉娉), Jie Gao[1] (高杰), Yuanning Gao[5] (高原宁),
Huiping Geng[1] (耿会平), Dianjun Gong[1] (宫殿军), Li Gong[46] (龚丽),
Lingling Gong[1] (龚玲玲), Alfred Goshaw[26], Chen Gu[5] (顾晨), Lili Guo[8] (郭莉莉),
Yan Guo[47] (郭雁), Yuanyuan Guo[1] (郭媛媛), Ramesh Gupta[14] (古拉梅),
Tao Han[25、5] (韩涛), Yanliang Han[38] (韩艳良), Zhenghe Han[5] (韩征和),
Qingbin Hao[12] (郝清滨), Yongliang Hao[7] (郝永亮), Hongjian He[5] (何红建),
Jun He[1] (何俊), Zhenqiang He[1] (何振强), Zhiyong Hong[11] (洪智勇), Mi Hou[1] (侯汨),
Qingbo Hou[8] (侯清波), Zhilong Hou[1] (侯治龙), Yee Bob Hsiung[48] (熊怡),

Yinan Hu[39] (胡一南), Jinshu Huang[1] (黄金书), Tongming Huang[1] (黄彤明), Lihua Huo[1] (霍丽华), Qingping Ji[37] (姬清平), Junji Jia[49] (贾俊基), Xuejun Jia[1] (贾学军), Lili Jiang[1] (姜丽丽), Xingyu Jiang[37] (蒋兴雨), Dapeng Jin[1] (金大鹏), Shan Jin[1] (金山), Song Jin[1] (靳松), Ling Kang[1] (康玲), Wen Kang[1] (康文), Xiaoshen Kang[50] (康晓珅), Zhiyong Ke[1] (柯志勇), Ashutosh Kotwal[16,26], Chia Ming Kuo [51] (郭家銘), Kevin Kwok[33] (郭景炜), Ge Lei[1] (雷革), Yongbin Leng[3] (冷用斌), Bo Li[1] (李波), Chengshan Li[12] (李成山), Chunhua Li[1] (李春华), Dazhang Li[1] (李大章), Gang Li[1] (李刚), Gang Li[1] (李刚), Gang Li[1] (黎刚), Guangrui Li[5] (李光锐), Haipeng Li[4] (李海鹏), Hengne Li[41] (李衡讷), Jungang Li[1] (李俊刚), Kang Li[32] (李康), Minxian Li[1] (李敏贤), Peng Li[2] (李朋), Qi Li[1] (李琦), Qing Li[1] (李青), Quansheng Li[8] (李全胜), Shaopeng Li[1] (李少鹏), Shiyuan Li[38] (李世渊), Shu Li[26] (李数), Tianjun Li[52] (李田军), Weiguo Li[1] (李卫国), Xiaohang Li[9] (李晓航), Xiaoping Li[1] (李小平), Yijie Li[7] (李贻杰), Yijie Li[53] (李一杰), Yingying Li[33] (李英英), Yufeng Li[1] (李玉峰), Zhenghua Li[8] (李正华), Zhaohui Liang[10] (梁朝晖), Jing Liang[1] (梁静), Guoping Lin[1] (林国平), Baiqi Liu[1] (刘佰奇), Fuhu Liu[54] (刘福虎), Jing Liu[4] (刘敬), Junyu Liu[6] (刘峻宇), Hu Liu[55] (刘虎), Peng Liu[1] (刘鹏), Rong Liu[1] (刘熔), Tao Liu[33] (刘滔), Zhongxiu Liu[1] (刘钟秀), Xianghong Liu[10] (刘向宏), Yaping Liu[1] (刘亚萍), Yudong Liu[1] (刘瑜冬), Zengqiang Liu[8] (刘增强), Zhenchao Liu[1] (刘振超), Zhiquan Liu[28] (刘志权), Cheuk Yee Lo[43] (劳卓义), Fengli Long[1] (龙锋利), Xinchou Lou[1] (娄辛丑), Yanhua Lu[1](卢艳华),Yuanyong Lu[4] (陆元荣), Qing Luo[6] (罗箐), Shu Luo[44] (罗舒), Tao Luo[1] (罗涛), Xiaofeng Luo[28] (罗晓峰), Binsong Ma[1] (马斌松), Huizhou Ma[1](麻惠洲), Lianliang Ma[38] (马连良), Na Ma[1] (马娜), Qiang Ma[1] (马强), Zhongjian Ma[1] (马忠剑), Ernie Malamud[16] (马欧尼), Lijun Mao[2] (冒立军), Yanmin Mao[8] (毛艳民), Lingling Men[1] (门玲鸽), Cai Meng[1] (孟才), Zhenghui Mi[1] (米正辉), Changjun Ning[1] (宁常军), Feipeng Ning[1] (宁飞鹏), Kazuhito Ohmi[21] (大见和史), Carlo Pagani[22] (帕卡罗), Longgang Pang[28] (庞龙刚), Guoxi Pei[1] (裴国玺), Shilun Pei[1] (裴士伦), Quanling Peng[1] (彭全岭), Yuemei Peng[1] (彭月梅), Chris Prior[30] ,

Kirill Prokofiev[33] , Guangyou Qin[28] (秦广友), Qing Qin[1] (秦庆), Jianwei Qiu[14] (邱建伟), Huamin Qu[1] (屈化民), Timing Qu[5] (瞿体明), Michael Ramsey-Musolf[27] (任缪), Manqi Ruan[1] (阮曼奇), GianLuca Sabbi[17], Peng Sha[1] (沙鹏), Dmitry Shatilov[20], Yuqiao Shen[1] (沈玉乔), Renjie Shi[8] (史仁杰), Hua Shi[1] (施华), Gary Shiu[42] (萧文礼), Zongguo Si[38] (司宗国), John Skaritka[14] (司约翰), Weimin Song[1] (宋维民), Feng Su[1] (苏峰), Shufang Su[24] (苏淑芳), Akula Sujeet[36] , Yanfen Sui[1](随艳峰), Mike Sullivan[15] (沙迈克), Baogeng Sun[6] (孙葆根), Guoqiang Sun[8] (孙国强), Sichun Sun[33] (孙斯纯), Xiaguang Sun[10] (孙霞光), Yi Sun[1] (孙毅), Richard Talman[19] (陶理查), Jingyu Tang[1] (唐靖宇), Yanjun Tu[43] (屠艳珺), Bin Wang[37] (王斌), Chengtao Wang[1] (王呈涛), Dou Wang[1] (王逗), Guangyuan Wang[1] (王广源), Haijing Wang[1] (王海静), Jianli Wang[1] (王建力), Jin Wang[1] (王锦), Joseph Wang[31] (王承宇), Lian-Tao Wang[23] (王连涛), Lu Wang[8] (王陆), Meifen Wang[1] (王美芬), Na Wang[1] (王娜), Qingbin Wang[1] (王庆斌), Qun Wang[6] (王群), Tong Wang[1] (王铜), Xiangqi Wang[6] (王相綦), Xiaolong Wang[1] (王小龙), Xiaolong Wang[56] (王小龙), Xiaoping Wang[8] (王小平), Xinnian Wang[17、28](王新年), Xiongfei Wang[5] (王雄飞), Xueying Wang[8] (汪雪英), Yifang Wang[1] (王贻芳), Yiwei Wang[1] (王毅伟), Yong Wang[6] (王勇), Zhi Wang[4] (王智), Zongyuan Wang[1] (王宗源), Wenjing Wu[1] (伍文静), Uli Wienands[15] (韦乌利), Dao Xiang[7] (向导), Lei Wu[1] (吴蕾), Bowen Xiao[28] (肖博文), Ming Xiao[1] (肖铭), Yu Xiao[8] (肖豫), Qingzi Xing[5] (邢庆子), Zhizhong Xing[1] (邢志忠), Qinglei Xiu[1] (修青磊), Gang Xu[1] (徐刚), Hongliang Xu[6] (徐宏亮), Qing Xu[8] (徐庆), Qingjin Xu[1] (徐庆金), Yin Xu[37] (徐音), Fang Yan[1] (闫芳), Fen Yan[1] (鄢芬), Guo Yan[10] (闫果), Wenbiao Yan[6] (鄢文标), Yingbing Yan[3] (阎映炳), Haijun Yang[7] (杨海军), Jiancheng Yang[2] (杨建成), Liu Yang[49] (杨柳), Mei Yang[1] (杨梅), Yongliang Yang[6] (杨永良), Weichao Yao[1] (姚卫超), Chunxu Yu[37] (喻纯旭), Jiebing Yu[1] (余洁冰), Lingda Yu[1](于令达), Yongji Yu[1] (于永积), Changzheng Yuan[1] (苑长征), Li Yuan[35] (袁丽), Youjin Yuan[2] (原有进),

Junhui Yue[1] (岳军会), Teng Yue[1] (岳腾), Jian Zhai[8] (翟建), Jiyuan Zhai[1] (翟纪元), Benwei Zhang[28] (张本威), Chuang Zhang[1] (张闯), Guoqing Zhang[1] (张国庆), Hanzhong Zhang[28] (张汉中), Hui Zhang[8] (张辉), Jielei zhang[1] (张杰磊), Junsong Zhang[1] (张俊嵩), Kai Zhang[1] (张恺), Peng Zhang[1] (张鹏), Tong Zhang[1] (张铜), Xiaomei Zhang[1] (张晓梅), Yinian Zhang[9] (张沂年), Yuan Zhang[1] (张源), Yuhong Zhang[18] (张裕宏), Zhiqing Zhang[40] (张智庆), Zhuo Zhang[1] (张卓), Jingwei Zhao[1] (赵京伟), Ling Zhao[1] (赵玲), Luyang Zhao[1] (赵路阳), Tongxian Zhao[1] (赵同宪), Wei Zhao[1] (赵微), Xiaoyan Zhao[1] (赵晓岩), Ying Zhao[1] (赵颖), Zhuo Zhao[1] (赵卓), Hongjuan Zheng[1] (郑洪娟), Yong Zhong[34] (钟勇), Yuanyuan Zhong[1] (钟元元), Demin Zhou[21] (周德民), Ningchuang Zhou[1] (周宁闯), Zusheng Zhou[1] (周祖圣), Shun Zhou[1] (周顺), Siyi Zhou[33] (周思益), Dechong Zhu[1](祝德充), Hongbo Zhu[1] (朱宏博), Hongyan Zhu[1] (朱洪岩), Kun Zhu[4] (朱昆), Qianwen Zhu[57] (朱倩雯), Yingshun Zhu[1] (朱应顺), Zian Zhu[1] (朱自安), Ye Zou[1] (邹野)

[1] Institute of High Energy Physics, China (高能物理研究所)

[2] Institute of Modern Physics, China (近代物理研究所)

[3] Shanghai Institute of Applied Physics, China (上海应用物理研究所)

[4] Peking University, China (北京大学)

[5] Tsinghua University, China (清华大学)

[6] University of Science and Technology of China (中国科技大学)

[7] Shanghai Jiao Tong University, China (上海交通大学)

[8] Yellow River Engineering Consulting Co., Ltd., China (黄河勘测规划设计有限公司)

[9] Innova Superconductor Technology Co., Ltd., China (北京英纳超导技术有限公司)

[10] Western Superconductor Technologies Co., Ltd., China (西部超导材料科技股份有限公司)

[11] Shanghai Superconductor Technology Co., Ltd., China (上海超导科技股份有限公司)

[12] Northwest Institute for Non-ferrous Metal Research, China (西北有色金属研究院)

[13] Northwestern University, U.S.A.

[14] Brookhaven National Laboratory, U.S.A.

[15] SLAC National Accelerator Laboratory, U.S.A.

[16] Fermi National Accelerator Laboratory, U.S.A.

[17] Lawrence Berkeley National Laboratory, U.S.A.

[18] Thomas Jefferson National Accelerator Facility, U.S.A.

[19] Cornell University, U.S.A.

[20] Budker Institute of Nuclear Physics, Russia

[21] High Energy Accelerator Research Organization (KEK), Japan

[22] University of Milano and INFN-LASA, Italy

[23] University of Chicago, U.S.A.

[24] University of Arizona, U.S.A.

[25] University of Pittsburgh, U.S.A.

[26] Duke University, U.S.A.

[27] University of Massachusetts Amherst, U.S.A.

[28] Central China Normal University, China (华中师范大学)

[29] Huazhong University of Science and Technology, China (华中科技大学)

[30] STFC Rutherford Appleton Laboratory, U.K.

[31] Bitquant Research Laboratories, Hong Kong

[32] Hangzhou Normal University, China (杭州师范大学)

[33] Hong Kong University of Science and Technology (香港科技大学)

[34] Institute of Electronics, China (电子学研究所)

[35] Kobe University, Japan

[36] Monash University, Australia

[37] Nankai University, China (南开大学)

[38] Shandong University, China (山东大学)

[39] University of Chinese Academy of Sciences, China (中国科学院大学)

[40] Université Paris Sud - Laboratoire de l'accélérateur linéaire, France

[41] University of Virginia, U.S.A.

[42] University of Wisconsin, U.S.A.

[43] University of Hong Kong (香港大学)

[44] Xiamen University, China (厦门大学)

[45] Forschungszentrum Jülich GmbH, Germany

[46] Guangxi Normal University, China (广西师范大学)

[47] Henan Normal University, China (河南师范大学)

[48] National Taiwan University, Taiwan (国立台湾大学)

[49] Wuhan University, China (武汉大学)

[50] Nanjing University, China (南京大学)

[51] National Central University, Taiwan (国立中央大学)

[52] Institute of Theoretical Physics, China (理论物理研究所)

[53] Liaoning University, China (辽宁大学)

[54] Shanxi University, China (山西大学)

[55] Sun Yat-sen University, China (中山大学)

[56] Virginia Polytech Institute & State University, U.S.A.

[57] North China Electric Power University, China (华北电力大学)

Acknowledgements

The *CEPC-SPPC Preliminary Conceptual Design Report* (Pre-CDR) was prepared and written by the CEPC-SPPC Study Group. The study was organized and led by the Institute of High Energy Physics (IHEP) of the Chinese Academy of Sciences (CAS) in collaboration with a number of institutions from various countries. The study was partially supported by the CAS/SAFEA International Partnership Program for Creative Research Teams.

The current volume is on the accelerators. There will be a separate volume on physics and the detectors. This volume was authored by about 300 scientists and engineers from 57 institutions in 9 countries (China, US, France, UK, Germany, Italy, Russia, Japan, and Australia). It has been reviewed by an International Review Committee before its release in March 2015.

Contents

1 **INTRODUCTION 23**

2 **THE SCIENCE OF THE CEPC AND THE SPPC 28**

2.1 INTRODUCTION 28

2.2 PHYSICS WITH THE $e+e^-$ COLLIDER 28

2.3 PHYSICS WITH THE *pp* COLLIDER 30

2.4 PHYSICS WITH THE *ep* AND *eA* COLLIDER 32

2.5 PHYSICS WITH THE HEAVY ION COLLIDER 33

2.6 SUMMARY 34

2.7 REFERENCES 35

3 **MACHINE LAYOUT AND PERFORMANCE 36**

4 **CEPC – ACCELERATOR PHYSICS 41**

4.1 MAIN PARAMETERS 41

4.1.1 Design Goals 41
4.1.2 Effects Determining the Luminosity 41
4.1.2.1 *Beam-beam Effect* *41*
4.1.2.2 *Beamstrahlung* *41*
4.1.3 Beam Parameters 42
4.1.4 RF Parameters 42
4.1.5 Beam Lifetime 42
4.1.5.1 *Lifetime due to Beamstrahlung* *42*
4.1.5.2 *Radiative Bhabha Scattering* *43*
4.1.6 References 45

4.2 LATTICE 45

4.2.1 Introduction 45
4.2.2 Lattice Design of the Ring 46
4.2.3 FODO Cells 46
4.2.4 Dispersion Suppressors 47
4.2.5 Straight Sections 47
4.2.6 Dynamic Aperture 47
4.2.7 Pretzel Orbit 48
4.2.8 Saw Tooth Orbit 49
4.2.9 Discussion 50
4.2.10 References 50

4.3 INTERACTION REGION AND MACHINE-DETECTOR INTERFACE 50

4.3.1 Introduction 50
4.3.2 Interaction Region 51
4.3.2.1 *Final Focus Optics* *52*

4.3.2.2 *Dynamic Aperture* *53*
4.3.3 Machine-Detector Interface 54
4.3.3.1 *Layout of the Interaction Region* *54*
4.3.3.2 *Final Doublet* *55*
4.3.3.3 *Solenoid Field Compensation* *56*
4.3.3.4 *Synchrotron Radiation and Shielding* *56*
4.3.4 References 57

4.4 BEAM INSTABILITY 57

4.4.1 Impedance Budget 57
4.4.1.1 *RF Cavities* *57*
4.4.1.2 *Resistive Wall* *58*
4.4.1.3 *Impedance Budget* *58*
4.4.2 Single-bunch Effect 59
4.4.2.1 *Bunch Lengthening* *59*
4.4.2.2 *Microwave Instability* *59*
4.4.2.3 *Transverse Mode Coupling Instability* *59*
4.4.2.4 *Tune Shift due to Transverse Impedance* *60*
4.4.2.5 *Simulation of Transverse instability* *60*
4.4.2.6 *Beam Tilt due to Transverse Wake Fields* *61*
4.4.2.7 *Coherent Synchrotron Radiation* *62*
4.4.3 Multi-bunch Effect 62
4.4.3.1 *Transverse Resistive Wall Instability* *62*
4.4.3.2 *Coupled Bunch Instability Induced by RF HOM's* *63*
4.4.4 Electron Cloud Instability 63
4.4.5 Beam Ion Instability 64
4.4.6 References 64

4.5 BEAM-BEAM EFFECTS 65

4.5.1 Simulation Codes 65
4.5.1.1 *LIFETRAC* *65*
4.5.1.2 *BBWS/BBSS* *66*
4.5.1.3 *IBB* *66*
4.5.2 Simulation Results 66
4.5.2.1 *Choice of Working Point* *66*
4.5.2.2 *Luminosity and Lifetime* *67*
4.5.3 Dynamic Effects 69
4.5.4 Summary 70
4.5.5 References 70

4.6 SYNCHROTRON RADIATION 71

4.6.1 Introduction 71
4.6.2 Analysis of Synchrotron Radiation Source 71
4.6.3 Monte-Carlo Simulation 73
4.6.4 References 77

4.7 INJECTION AND BEAM DUMP 77

4.7.1 Introduction 77
4.7.2 Injection Time Structure 78

4.7.3 Schematic Drawing 80
4.7.4 Beam Dump 81
4.7.4.1 *Beam Dump System Design* *81*
4.7.4.2 *Beam Absorber* *82*
4.7.5 References 84

4.8 BEAM LOSS, BACKGROUND AND COLLIMATORS 84

4.8.1 Introduction 84
4.8.2 Beam Loss Mechanisms 84
4.8.2.1 *Quantum Mechanism* *84*
4.8.2.2 *Touschek Scattering* *84*
4.8.2.3 *Beam-Gas Scattering* *85*
4.8.2.4 *Radiative Bhabha Scattering* *85*
4.8.2.5 *Beamstrahlung* *86*
4.8.3 Beam Induced Background 86
4.8.3.1 *Interaction Region* *86*
4.8.3.2 *Synchrotron Radiation Background* *87*
4.8.3.3 *Lost Particle Background* *87*
4.8.3.3.1 Beamstrahlung 87
4.8.3.3.2 Radiative Bhabha Scattering 87
4.8.3.3.3 Beam-Gas Scattering 88
4.8.4 Background Shielding 88
4.8.5 References 89

4.9 POLARIZATION 89

4.9.1 Introduction 89
4.9.2 Overview of Spin Dynamics 89
4.9.3 Beam Polarization at the Z-pole 90
4.9.4 Beam Polarization at Higher Energies 91
4.9.5 References 91

5 CEPC – TECHNICAL SYSTEMS 92

5.1 SUPERCONDUCTING RF SYSTEM 92

5.1.1 Introduction 92
5.1.2 RF Cavity Design Parameters 94
5.1.3 HOM and SOM Damping 95
5.1.4 Power Coupler 98
5.1.5 Tuning and RF Control System 99
5.1.6 References 99

5.2 RF POWER SOURCE 100

5.2.1 Collider RF Power Source 100
5.2.2 Booster RF Power Source 103
5.2.3 Linac RF Power Source 104
5.2.4 Low Level RF System 107

5.3 CRYOGENIC SYSTEM 108

5.3.1 Heat Load 109

5.3.2 Refrigerator....110
5.3.3 Layout and Infrastructure....111
5.3.4 Cryogenic Plant Operation....113
5.3.5 Helium Inventory....114
5.3.6 Control System....115
5.3.7 Safety Consideration....115
5.3.8 Installed Cryogenic Power....115
5.3.9 References....116

5.4 MAGNETS....116

5.4.1 Booster Magnets....117
5.4.1.1 *Dipole Magnets*....*117*
5.4.1.2 *Quadrupole Magnets*....*118*
5.4.2 Collider Magnets....120
5.4.2.1 *Dipole Magnets*....*120*
5.4.2.2 *Quadrupole Magnets*....*122*
5.4.2.3 *Superconducting Quadrupole Magnets*....*123*
5.4.2.3.1 Overall Design Consideration....123
5.4.2.3.2 Quadrupole Coil....124
5.4.2.3.3 Anti-Solenoid Coil....126
5.4.2.4 *Sextupole Magnets*....*127*
5.4.3 References....129

5.5 MAGNET POWER SUPPLIES....129

5.5.1 Collider Power Supplies....130
5.5.2 Booster Power Supplies....132
5.5.3 Linac Power Supplies....135
5.5.4 Power Supply Electronics....135
5.5.4.1 *Introduction*....*135*
5.5.4.2 *Digital Controller*....*136*
5.5.4.3 *Special Digital Controller for Booster Power Supplies*....*136*
5.5.5 References....137

5.6 VACUUM SYSTEM....137

5.6.1 Synchrotron Radiation Power and Gas Load....138
5.6.1.1 *Synchrotron Radiation Power*....*138*
5.6.1.2 *Gas Load*....*138*
5.6.2 Vacuum Chamber....139
5.6.2.1 *Vacuum Chamber Material*....*139*
5.6.2.2 *Vacuum Chamber Shape*....*140*
5.6.3 Bellows Module with RF Shielding....141
5.6.4 Pumping System....142
5.6.4.1 *NEG Coating*....*143*
5.6.4.2 *Sputter Ion Pumps*....*144*
5.6.4.3 *Turbomolecular Pumps (TMPs).*....*144*
5.6.5 Vacuum Measurement and Control....144
5.6.6 References....145

5.7 INSTRUMENTATION....145

5.7.1 Introduction 145
5.7.2 Beam Position Measurement System 146
5.7.2.1 *Mechanical Construction* *147*
5.7.2.2 *Signal Processing* *151*
5.7.3 Beam Current Measurement 151
5.7.3.1 *DC Beam Current Transformer* *152*
5.7.3.2 *Bunch Current Measurement (BCM) System* *153*
5.7.4 Synchrotron Light Imaging System 154
5.7.4.1 *Beam Profile Monitor* *154*
5.7.4.1.1 Visible Light Beam Line 154
5.7.4.1.2 X-Ray Beam Line 155
5.7.4.2 *Bunch Length Measurement* *155*
5.7.5 Beam Loss (BLM) System 156
5.7.6 Tune Measurement System 158
5.7.7 Vacuum Chamber Displacement Measurement System 159
5.7.8 Feedback System 159
5.7.9 Other Systems 160
5.7.10 References 160

5.8 CONTROL SYSTEM 161

5.8.1 Introduction 161
5.8.2 System Architecture 161
5.8.2.1 *Control Software Platform* *162*
5.8.2.2 *Equipment Level Devices* *163*
5.8.2.3 *Network* *163*
5.8.3 Main Sub-System Level Hardware 164
5.8.3.1 *Power Supply Remote Control* *164*
5.8.3.2 *Machine Protection System (MPS)* *165*
5.8.3.3 *Vacuum Control* *166*
5.8.3.4 *Vacuum Chamber Temperature Monitoring* *166*
5.8.4 Timing System 166
5.8.5 Video Monitoring System 167
5.8.6 Data Archiving and Analysis 167
5.8.7 System Alarms 168
5.8.8 Post Mortem, Large Data Storage and Analysis 169
5.8.9 Event Log 170
5.8.10 Software Development Environment and Application 170
5.8.11 References 170

5.9 MECHANICAL SYSTEMS 170

5.9.1 Introduction 170
5.9.2 Supports in the Collider 171
5.9.3 Design Requirements 173
5.9.3.1 *Design of the Collider Dipole Support System* *173*
5.9.3.1.1 The Main Support 173
5.9.3.1.2 The Auxiliary Support 176
5.9.3.2 *Design of the Collider Quadrupole Support System* *176*
5.9.3.3 *Design of the Collider Sextupole Support System* *177*

5.9.4 Supports in the Booster 179

5.10 RADIATION SHIELDING 181

5.10.1 Introduction 181
5.10.1.1 *Workplace Classification* *181*
5.10.1.2 *Design Criteria* *181*
5.10.2 Radiation Sources and Radiation Shielding Design 183
5.10.2.1 *Interaction of High-Energy Electrons with Matter* *183*
5.10.2.2 *Radiation Sources* *183*
5.10.2.3 *Shielding Calculation Methods* *183*
5.10.2.4 *Radiation Shielding Design* *184*
5.10.3 Induced Radioactivity 185
5.10.3.1 *Specific Activity and Calculation Methods* *185*
5.10.3.2 *Estimation of the Amount of Nitrogen Oxides* *185*
5.10.4 Personnel Safety Interlock System (PSIS) 187
5.10.4.1 *System Design Criteria* *187*
5.10.4.2 *PSIS Design* *187*
5.10.5 Radiation Dose Monitoring Program 189
5.10.5.1 *Radiation Monitoring System* *189*
5.10.5.2 *Workplace Monitoring Program* *190*
5.10.5.3 *Environmental Monitoring Program* *190*
5.10.5.4 *Personnel Dose Monitoring Program* *191*
5.10.6 Management of Radioactive Components 191
5.10.7 References 191

5.11 SURVEY AND ALIGNMENT 191

5.11.1 CEPC Alignment Control Network Design 191
5.11.1.1 *Surface Control Network* *192*
5.11.1.2 *Tunnel Control Network* *193*
5.11.1.3 *CEPC Global Coordinate System* *195*
5.11.2 Component Fiducialization 196
5.11.3 Alignment Scheme for Accelerator Components in the Tunnel 196
5.11.3.1 *Alignment in the Interaction Region* *197*
5.11.3.2 *Time and Frequency of Survey and Alignment* *198*

6 CEPC – INJECTORS 199

6.1 LINAC AND e^+/e^- SOURCES 199

6.1.1 Main Linac Parameters 199
6.1.2 Electron Source 200
6.1.3 Bunching System 201
6.1.4 Positron Source 202
6.1.5 Linac 203

6.2 BOOSTER AND TRANSPORT LINES 204

6.2.1 General Description 204
6.2.2 Lattice 206
6.2.2.1 *Choice of Cell Length* *206*
6.2.2.2 *Lattice Functions* *207*

6.2.2.3 *Bypasses* ... *208*
6.2.2.4 *Dynamic Aperture* ... *209*
6.2.3 Low Injection Energy and the Low Field Issue ... 211
6.2.3.1 *Low Field Stability Test* ... *211*
6.2.3.2 *Wiggling Bend Scheme* ... *212*
6.2.3.3 *Instabilities* ... *213*
6.2.4 Beam Transfer ... 214
6.2.4.1 *Beam Transfer from the Linac to the Booster (LTB)* ... *215*
6.2.4.2 *Beam Injection to the Booster* ... *216*
6.2.4.3 *Beam Extraction from the Booster* ... *216*
6.2.4.4 *Beam Transfer from the Booster to the Collider* ... *217*
6.2.5 Summary ... 217
6.2.6 References ... 217

7 UPGRADE TO THE SPPC ... 218

7.1 INTRODUCTION ... 218

7.1.1 Science Reach at the SPPC ... 218
7.1.2 Design Goals ... 219
7.1.3 Overview of the SPPC Facility ... 220
7.1.4 References ... 222

7.2 KEY ACCELERATOR PHYSICS ISSUES ... 222

7.2.1 Main Parameters ... 222
7.2.1.1 *Collision Energy and Layout* ... *222*
7.2.1.2 *Luminosity* ... *223*
7.2.1.3 *Bunch Structure and Population* ... *224*
7.2.1.4 *Beam Size at the IPs* ... *224*
7.2.1.5 *Crossing Angle at the IPs* ... *225*
7.2.1.6 *Turnaround Time* ... *225*
7.2.1.7 *RF Parameters* ... *225*
7.2.2 Synchrotron Radiation ... 226
7.2.3 Beam-Beam Effects ... 226
7.2.3.1 *Incoherent Effects* ... *226*
7.2.3.2 *PACMAN Effects* ... *227*
7.2.3.3 *Coherent Effects* ... *227*
7.2.3.4 *Beam-Beam Tune Shift Limit* ... *228*
7.2.4 Electron Cloud Effect ... 228
7.2.5 Beam-Loss and Collimation ... 230
7.2.5.1 *Beam Loss* ... *230*
7.2.5.2 *Collimation* ... *231*
7.2.6 References ... 232

7.3 KEY TECHNICAL SYSTEMS ... 233

7.3.1 High Field Superconducting Magnets ... 233
7.3.1.1 *Requirement of the High Field Magnets for the SPPC* ... *233*
7.3.1.2 *Current Status of High Field Accelerator Magnet Technology* ... *233*
7.3.1.3 *Challenges to Meet the SPPC Requirement* ... *235*
7.3.1.4 *Preliminary Design for the SPPC Superconducting Magnets* ... *236*

7.3.2 Vacuum and Beam Screen 237
7.3.2.1 *General Vacuum Considerations* *237*
7.3.2.1.1 Vacuum Requirements 237
7.3.2.1.2 Beam Vacuum in the Low-Temperature Sections 237
7.3.2.1.3 Vacuum Instability Issues 238
7.3.2.2 *Beam Screen* *238*
7.3.3 Other Technical Challenges 239
7.3.4 References 240

7.4 RECONFIGURATION OF THE ACCELERATOR COMPLEX 240

7.4.1 Injection Chain 240
7.4.2 Integration of the CEPC and SPPC 242
7.4.2.1 *Project Uncertainty* *242*
7.4.2.2 *Geometric Constraints and Considerations* *243*
7.4.2.2.1 Construction and Commissioning Considerations 243
7.4.2.2.2 Operational Considerations 243

8 **OPTION FOR *e-p* AND *e-A* COLLIDERS 245**

8.1 INTRODUCTION 245

8.2 DESIGN CONSIDERATIONS 246

8.3 *e-p* COLLISIONS 247

8.4 *e-A* COLLISIONS 249

8.5 ADDITIONAL COMMENTS 250

8.6 SUMMARY 251

9 **CONVENTIONAL FACILITIES 252**

9.1 INTRODUCTION 252

9.2 SITE AND BUILDINGS 253

9.2.1 Preliminary Site Selection 253
9.2.2 Construction Conditions at the Preliminary Selected Site 254
9.2.2.1 *Geographical Location* *254*
9.2.2.2 *Traffic Conditions* *254*
9.2.2.3 *Hydrology and Meteorology* *254*
9.2.2.4 *Economic Profile* *254*
9.2.2.5 *Engineering Geology* *255*
9.2.3 Engineering Layout and Main Buildings/Structures 255
9.2.3.1 *General Layout of the Tunnel and Surface Buildings* *255*
9.2.3.2 *Civil Engineering Aspects of the Underground Work* *257*
9.2.3.2.1 Main Tunnel 257
9.2.3.2.2 RF Sections of the Main Tunnel 258
9.2.3.2.3 Bypass Tunnel in the Collision Areas 259
9.2.3.2.4 Auxiliary Stub Tunnels 259
9.2.3.2.5 Experimental Areas 259
9.2.3.2.6 Access Shafts 259
9.2.3.3 *Surface Areas and Buildings/Structures* *260*

9.2.4 Construction Organization 260
9.2.4.1 *Construction Conditions and Construction Options* *260*
9.2.4.1.1 Construction Conditions 260
9.2.4.1.2 Main Construction Options 261
9.2.4.2 *Construction Access and General Construction Layout* *261*
9.2.4.2.1 Construction Access 261
9.2.4.2.2 General Construction Layout 262
9.2.4.2.3 Land Use for Construction 262
9.2.4.3 *General Construction Schedule* *262*
9.2.4.3.1 General Indicators 262
9.2.4.3.2 Planned Total Period for Construction with Drill and Blast Method 263

9.3 ELECTRICAL SYSTEM 264

9.3.1 Power Supply Range and Main Load 264
9.3.2 Power Supply Scheme 264
9.3.3 Illumination System 266
9.3.4 Internal/External Communication throughout the CEPC Complex 266
9.3.4.1 *Communication* *267*
9.3.4.2 *Communication Power Supply* *267*
9.3.4.3 *Computer Network* *267*
9.3.5 Monitoring System 267
9.3.6 Video Monitoring System 267
9.3.7 Fire Detection and Alarm 267

9.4 COOLING WATER SYSTEM 268

9.4.1 Overview 268
9.4.2 Cooling Tower Water Circuits 269
9.4.3 Low Conductivity Water (LCW) Circuits 270

9.5 HVAC SYSTEM 270

9.5.1 Indoor and Outdoor Air Design Conditions 270
9.5.1.1 *Outdoor Air Design Conditions* *270*
9.5.1.2 *Indoor Air Design Conditions* *271*
9.5.2 Tunnel Air Conditioning System 271
9.5.3 Air Conditioning System of Experiment Halls 271
9.5.4 Ventilation and Smoke Exhaust System 271
9.5.5 Chilled Water System 272

9.6 FIRE PROTECTION AND WATER SUPPLY & DRAINAGE 272

9.6.1 Layout Principles 272
9.6.2 Design of Fire Protection 272
9.6.2.1 *Design of Fire Hydrants* *272*
9.6.2.2 *Distribution of Extinguishers* *272*
9.6.3 Design of Water Drainage 273

9.7 REFERENCES 273

10 ENVIRONMENT, SAFETY AND HEALTH CONSIDERATIONS 274

10.1 IONIZATION RADIATION 274
10.2 IMPACT OF CONSTRUCTION ON THE ENVIRONMENT 274
10.2.1 Impact of Blasting Vibration on the Environment and Countermeasures.274
10.2.2 Impact of Noise on the Environment and Countermeasures 275
10.2.3 Analysis of Impact on the Water Environment 275
10.2.4 Water and Soil Conservation 275
10.3 ELECTRICAL SAFETY 275
10.4 FIRE SAFETY 275
10.5 CRYOGENIC AND OXYGEN DEFICIENCY HAZARD (ODH) 276
10.6 NON-IONIZATION RADIATION 276
11 **R&D PROGRAM 277**
11.1 SUPERCONDUCTING RF 277
11.1.1 Initial SRF Technology R&D (2016-2020) 277
11.1.1.1 *Initial Technology R&D* *277*
11.1.1.2 *Infrastructure and Personnel Development* *277*
11.1.2 Pre-Production R&D (2019-2022) 278
11.1.2.1 *Pre-Production R&D* *278*
11.1.2.2 *Infrastructure and Personnel Development* *278*
11.1.3 Examples of What is Available at Other Labs 279
11.1.4 References 279
11.2 RF POWER SOURCE 280
11.2.1 650 MHz/400 kW CW Klystron 280
11.2.2 650 MHz/400 kW Solid State Amplifier (SSA) 280
11.3 CRYOGENIC SYSTEM 280
11.4 MAGNETS 281
11.5 MAGNET POWER SUPPLIES 281
11.6 VACUUM SYSTEM 281
11.7 INSTRUMENTATION 282
11.7.1 Bunch by Bunch BPM 282
11.7.2 High Vacuum Feedthroughs 282
11.7.3 Beam Loss Monitor 282
11.8 CONTROL SYSTEM 283
11.8.1 Introduction 283
11.8.2 Large Scale and High Accuracy Timing System 283
11.8.3 Machine Protection System 283
11.8.4 Control System Infrastructure 283
11.8.5 Large Size Data Handling 283
11.9 MECHANICAL SYSTEMS 284
11.9.1 Introduction 284

11.9.2 Range and Accuracy of Adjustment 284
11.9.3 Dipole Support System in the Collider 285
11.9.3.1 *Design Scheme* *285*
11.9.3.2 *Static Analysis* *286*
11.9.4 Dipole Support System in the Booster 286
11.9.4.1 *Design Scheme* *286*
11.9.4.2 *Stress Analysis* *287*
11.9.5 References 288

11.10 SURVEY AND ALIGNMENT 288

11.10.1 Geoid Refining Research 288
11.10.2 Precise Geodesy 3-D Adjustment Research 289
11.10.3 Laser Collimator System Research for the Interaction Region 290
11.10.4 Photogrammetric Survey and Alignment System 290

11.11 LINAC AND e^+/e^- SOURCES 291

11.11.1 Polarized Electron Gun 291
11.11.2 High Intensity Positron Source 291
11.11.3 S-Band Accelerator Structure Related R&D 291
11.11.4 High Stability Pulse Modulator Related R&D 291
11.11.5 High Precision Synchronization and Timing System 292

11.12 HIGH FIELD SUPERCONDUCTING MAGNET 292

12 PROJECT COST ESTIMATE AND TIMELINE 294

12.1 CONSTRUCTION COST ESTIMATE 294

12.2 OPERATIONS COST ESTIMATE 297

12.3 PROJECT TIMELINE 298

12.4 R&D BUDGET 299

12.5 REFERENCES 300

APPENDIX 1 PARAMETER LIST 301

A1.1 COLLIDER 301

A1.2 BOOSTER 307

A1.3 LINAC 311

APPENDIX 2 ALTERNATIVE DESIGNS 313

A2.1 50-KM RING VS. 100-KM RING 313

A2.2 TWO-BEAM PIPES VS. ONE-BEAM PIPE 313

A2.3 PRETZEL ORBIT VS. BUNCH TRAIN 313

APPENDIX 3 OPERATION FOR SUPER Z 315

APPENDIX 4 OPERATION FOR HIGH INTENSITY γ RAY SOURCES.....319

A4.1 THE FEATURES OF CEPC γ RAY SOURCE.....319

A4.1.1 High Flux and Brightness.....319
A4.1.1.1 From Bending Magnets.....319
A4.1.1.2 From Wiggler.....320
A4.1.1.3 From Undulator.....320
A4.1.2 Advantages.....320

A4.2 COMPARISON WITH LASER γ RAY SOURCE.....321

A4.3 APPLICATIONS OF CEPC γ RAY SOURCE.....321

A4.4 KEY TECHNOLOGIES FOR APPLICATIONS OF CEPC γ RAY SOURCE.....321

A4.4.1 Insertion Device.....321
A4.4.2 Transport and Modulation.....322
A4.4.3 Detection.....322

A4.5 SUMMARY.....322

APPENDIX 5 OPTION FOR XFEL.....323

A5.1 THE REQUIREMENTS FOR AN XFEL DRIVEN BY THE CEPC LINAC.....323

A5.2 POSSIBLE XFEL OPTIONS.....323

A5.3 R&D ISSUES.....324

APPENDIX 6 INTERNATIONAL REVIEW.....325

A6.1 EXECUTIVE SUMMARY OF THE INTERNATIONAL REVIEW COMMITTEE'S REPORT..325

A6.2 CHARGE LETTER TO THE COMMITTEE.....327

1 Introduction

The era of particle accelerators began a century ago when Ernest Rutherford made a call for "a copious supply" of particles more energetic than those from natural radioactive substances. A number of ingenious physicists responded and invented the first generation of accelerators: Rolf Wideröe built the world's first linac in an 88-cm long glass tube in 1924; Robert Van de Graaff invented a generator named after him in 1929; Ernest Lawrence demonstrated a 4-in diameter cyclotron in 1930, and John Cockcroft and Ernest Walton built an electrostatic accelerator named after them in 1932. Since then, particle accelerators have made tremendous progress and fundamentally changed the way we live, think and work. The latest example is the discovery of the Higgs boson at the gigantic 27-km circumference deep-underground *Large Hadron Collider* (LHC) at CERN in Geneva, Switzerland. This discovery was a showcase of what the LHC, the world's most powerful scientific instrument, can do to advance to the next level in this most basic frontier of science and technology.

However, there is a long standing and fundamental question in the world's high-energy physics (HEP) community – Would the LHC be the *Last Hadron Collider*? This question was raised repeatedly at HEP conferences and workshops after the demise of the SSC in the US. There were several efforts (e.g., the RLHC and VLHC) that tried to point the way forward but led nowhere for a variety of reasons.

But this situation changed dramatically in late 2012 after the Higgs discovery, which triggered renewed strategic planning in the world HEP field and renewed interest in future large circular colliders. Because the Higgs mass is low (126 GeV), a circular *e*+*e*- collider can serve as a Higgs factory. But the ring must have a large circumference in order to combat the synchrotron radiation from the high energy electron and positron beams. If such a large size ring were to exist the tunnel would be ideal for housing a *pp* collider with an energy much higher than that of the LHC.

Circular *e*+*e*- colliders have a long and glorious history. The first three such colliders – AdA in Italy, CBX in the US, and VEP-1 in the then Soviet Union – came into operation about 50 years ago in the mid-1960s. A number of other colliders followed. Table 1.1 lists the energy, luminosity and operation period of the *e*+*e*- colliders (including the sole linear collider, the SLC) that have been built and operated since 1991 [1]. The highest energy collider was LEP2 with a center-of-mass (c.m.) energy of 209 GeV, whereas the highest luminosity collider is KEKB with a luminosity of 2.1×10^{34} $cm^{-2}s^{-1}$. These numbers are close to the design goal for a Higgs factory (240 GeV, 2×10^{34} $cm^{-2}s^{-1}$). However, the difficulty is to achieve both of these parameters in the same collider. On the other hand, the design, construction and operation of a circular Higgs factory can benefit a great deal from the experience with these machines, especially LEP2 and KEKB.

Table 1.1: *e*+*e*- colliders built and operated since 1991.

Location	**Accelerator**	**Energy** (GeV x GeV)	**Luminosity** ($cm^{-2}s^{-1}$)	**Operation Period**
CERN	LEP	104.5 x 104.5	1×10^{32}	1989-2000
KEK	KEKB	8 (e-) x 3.5 (e+)	2.1×10^{34}	1998-2010
	TRISTAN	32 x 32	3.7×10^{31}	1986-1995
SLAC	PEP-II	9 (e-) x 3.1 (e+)	1.2×10^{34}	1999-2008
	SLC	46.2 x 46.2	3×10^{30}	1988-1998
DESY	DORIS	5.6 x 5.6	3.3×10^{31}	1974-1992
Cornell	CESR	1.8 x 1.8 to 5.5 x 5.5	1.3×10^{33}	1979-2008
INFN	DAFNE	0.51 x 0.51	1.5×10^{32}	1999-present
IHEP/China	BEPC & BEPC-II	1.5 x 1.5 to 2.5 x 2.5	8.5×10^{32}	1988-2005, 2008-present
BINP	VEPP-200	0.2 x 0.2 to 1 X 1	1.2×10^{32}	2010-present
	VEPP-4M	1.5 x 1.5 to 5 x 5	5×10^{30}	1984 -present

Hadron colliders also have a remarkable history. It is much more difficult and expensive to build a hadron collider than a lepton collider, and just six hadron colliders have been built in the world since 1971 when the ISR went to operation at CERN. These hadron colliders include the SPS (CERN), the Tevatron (US), HERA (Germany), RHIC (US) and the LHC. Hadron colliders are often termed "*engines of discovery*." One aims for the highest possible energy. This is called the energy frontier. From the Tevatron (c.m. energy 2 TeV) to the LHC (c.m. energy 14 TeV), the energy leap was seven-fold. It is reasonable to assume the next energy frontier collider would have another seven-fold increase to ~100 TeV. But this is much harder to accomplish than a Higgs factory. To bend these high energy protons in a ring of the same circumference contemplated for the Higgs factory requires 20 Tesla magnets. And such high field 20 Tesla superconducting magnets do not exist, without even discussing their affordability. In other words, we are not yet ready to build such a machine. We need to proceed through a well-crafted R&D plan before we can seriously consider building such a collider**.**

Based on these considerations, the Institute of High Energy Physics (IHEP) in Beijing, China, in collaboration with a number of other institutions in China as well as in many other countries, launched a study of a 50-100 km ring collider. It would first serve as an *e*+*e*- collider for a Higgs factory with the name *Circular Electron-Positron Collider* (CEPC). The facility would then be upgraded by adding a 70-100 TeV *Super Proton-Proton Collider* (SPPC) in the same tunnel. Both the CEPC and the SPPC could operate simultaneously and provide complimentary information. And there is then the intriguing opportunity to study lepton-proton collisions using the two machines together.

In early 2014, the IHEP decided to prepare and publish a Preliminary Conceptual Design Report (Pre-CDR) within a year in order for the CEPC-SPPC proposal to be considered as a line item in the Chinese government's next Five-Year Plan (2016-2020). The study was put on a fast track. This report is the product of that study.

This report is based on a 54-km ring design. The ring size was chosen mainly due to cost considerations. An alternative design of a 100-km ring is discussed in Appendix 2.

Tables 1.2 and 1.3 list the top level parameters of the CEPC and SPPC, respectively. The integrated luminosity of the CEPC is 250 fb^{-1} per interaction point (IP) per year. For two IPs and 10 years of operation, the total integrated luminosity is 5 ab^{-1}, which would generate one million Higgs particles.

The luminosity goal of the SPPC has not yet been decided. There is an ongoing discussion in the world HEP community about what the luminosity goal of a future high energy *pp* collider should be [2-5].

Table 1.2: Top Level Parameters for CEPC.

Parameter	**Design Goal**
Particles	*e+*, *e-*
Center of mass energy	240 GeV
Integrated luminosity (per IP per year)	250 fb^{-1}
No. of IPs	2

Table 1.3: Top Level Parameters for SPPC.

Parameter	**Design Goal**
Particles	*p*, *p*
Center of mass energy	70 TeV
Integrated luminosity (per IP per year)	(TBD)
No. of IPs	2

This report consists of 12 chapters and 6 appendices.

Chapter 1 is an introduction.

Chapter 2 is a brief description of the potential science reach of different collision experiments, including electron-positron collisions, proton-proton collisions, electron (or positron)-proton collisions, electron (or positron)-ion collisions, and ion-ion collisions.

Chapter 3 is an overview of the CEPC-SPPC layout and performance goals. It also discusses a staging scenario from the CEPC to the SPPC and the other collision schemes.

Chapters 4 and 5 give a detailed description of the CEPC design. Chapter 4 covers all the relevant beam physics issues of a high energy *e+e-* collider, including the lattice in both the arcs and straight sections, optics in the interaction regions (IRs), the machine-detector interface, the dynamic aperture, beam instabilities, beam-beam effects, synchrotron radiation, injection and beam dump, beam loss and background, and a brief discussion of polarization at medium (Z-pole) and high (Higgs) energies.

Chapter 5 describes the design of various technical systems for the collider, the Booster and the Linac, including the superconducting RF (SRF) system and its power source, the cryogenic system, magnets and their power supplies, vacuum, instrumentation, control, mechanical systems, radiation shielding, survey and alignment.

These chapters are followed by Chapter 6 with a description of the injectors, including the Linac and the full-energy injection Booster.

Chapter 7 discusses the upgrade of the facility with the addition of the SPPC, a high-energy proton-proton collider to be installed in the same tunnel. The SPPC, in addition to a center-of-mass energy of 70 TeV collider ring, also requires an injector chain, including a proton linac, followed by a cascade of three synchrotrons to bring the proton energy up to 2 TeV before injection into the collider.

Since the CEPC ring will remain in the tunnel when the SPPC is installed, this makes it possible to collide electrons (or positrons) with protons or heavy ions (when the SPPC operates to accelerate heavy ions). This is the subject of Chapter 8, which discusses the various options for *e-p* and *e-A* colliders.

Conventional facilities are a major part of this study, not just because the tunnel circumference is large (54.4 km), but also because the tunnel is big (6 m wide) so it will be able to accommodate three rings (the CEPC collider, the CEPC booster and the SPPC collider). In addition to the underground structure, there will be many large surface buildings and utilities. These facilities and their construction are described in Chapter 9 in the context of a possible site.

Chapter 9 is followed by a discussion of environment, safety and health considerations in Chapter 10.

Chapter 11 presents details of an extensive R&D program to be carried out prior to the construction. For the CEPC, the critical path is a successful implementation of the SRF R&D, including superconducting RF cavities, couplers, HOM dampers, tuners, and the associated RF power source and cryogenic system. A pre-production plan is also included. For the SPPC, the key technical component is the superconducting magnet. A 20-year road map is outlined.

Chapter 12 discusses a possible project timeline. A rough estimate of the construction cost as well as the operation cost (for electricity only) is given in terms of percentages for each system. The R&D budget for each system in the next five years (2016-2020) is also presented.

These 12 chapters constitute the main body of this report. In addition, there are six appendices:

Appendix 1 is a detailed parameter list for the three accelerators – the collider, the Booster and the Linac.

Appendix 2 discusses several alternative designs – building a 100-km tunnel instead of a 54-km one (which is the baseline); using two beam pipes (one for the electron beam, another for the positron beam) instead of one beam pipe (which is the baseline); and implementing a bunch train instead of a pretzel orbit (which is the baseline).

Appendix 3 discusses the potential of the CEPC to operate at lower energy and higher luminosity as a Super Z factory.

Appendix 4 is a discussion of using the CEPC as a γ-ray source, which would be unique in the synchrotron light source field.

Appendix 5 points out the possibility of utilizing the Linac beam for a free electron laser (FEL).

Appendix 6 is the Executive Summary of the report from the review of this CEPC-SPPC Pre-CDR by an International Committee chaired by Prof. Katsunobu Oide (KEK, Japan). The review took place at the IHEP in Beijing, China, from February 14 to 16, 2015.

Appendices 1-5 demonstrate the wide range of applications of the CEPC-SPPC facility when it is in place.

The CEPC-SPPC is a giant leap from the BEPC-II, the presently operating *e*+*e*- collider in China. The challenges are big and real. But the potential payoffs are enormous. It will bring China to the forefront of world high-energy physics, open up a whole new window to fundamental research, be the most powerful scientific instrument ever built, push a wide range of advanced technologies to an extent never imagined before: large volume ultrahigh vacuum; large scale super-fluid helium applications; superconducting magnets; superconducting radio frequency systems; high-power and high-efficiency microwave devices; radiation-hard materials; global control systems; advanced instrumentation and diagnostics; super-fast computing and communication networks; and giant data storage and processing systems.

The CEPC-SPPC also will educate and train a new generation of HEP and accelerator scientists and engineers, who will lead this field in future decades.

Based on the design presented in this report, if we work hard and have support from the world HEP community and from the Chinese government, we believe these goals are within our reach.

References:

1. Weiren Chou et al., "High energy physics collider table (1984-2011)", *ICFA Beam Dynamics Newsletter*, No. 57, p. 174 (April 2012).
2. Burton Richter, "High energy colliding beams: what is their future?" *Reviews of Accelerator Science and Technology*, Volume 7, p.1, World Scientific (2014),
3. Fabiola Gianotti, private communication.
4. Lian-Tao Wang, private communication.
5. Michelangelo Mangano, "Towards a definition of luminosity goals for the 100 TeV pp collider, http://indico.cern.ch/event/336571/timetable/#20150201.detailed

2 The Science of the CEPC and the SPPC

2.1 Introduction

The Standard Model (SM) of elementary particle physics has withstood extensive experimental tests and has proven to be very successful in describing the subatomic world. The Higgs boson, recently discovered at the Large Hadron Collider (LHC), is consistent with the long awaited SM Higgs. Further measurement of its properties, including its couplings to fermions, other bosons and its self-interaction, will refine this picture. Any deviations from the SM will open the door to new physics beyond the Standard Model.

While the SM has been remarkably successful in describing experimental phenomena, with the discovery of the Higgs boson completing the last missing piece, it is likely that the SM is only an effective theory at the electroweak scale. In particular, the SM does *not* predict the parameters in the Higgs potential, nor does it provide a description of the nature of the electroweak phase transition. The vast difference between the Planck scale and the weak scale still remains a mystery. The discovery of a spin zero Higgs boson, the first elementary particle of its kind, only sharpens these questions. In addition, there is no particle candidate for dark matter in the SM. It is clear that any effort to address these questions will involve new physics beyond the SM. Therefore, the Higgs discovery marks the beginning of a new era of theoretical and experimental explorations. The search for such new physics will remain the critical objectives of current and future experimental particle physics programs.

The LHC will resume operation in 2015 at a 13 TeV center-of-mass (c.m.) energy after the current shutdown for upgrades. The LHC, as well as the ALTAS and CMS detectors, are scheduled to undergo additional upgrades in 2018 and 2022, and will enter the High Luminosity LHC (HL-LHC) phase at the design c.m. energy of 14 TeV. Experiments at the LHC will maximize the physics potential which will eventually be limited by the collider c.m. energy and the large background present in the pp collision data.

On a longer time scale, lepton colliders, including the ILC, CEPC and FCC-ee, may be built and be in operation prior to the completion of the HL-LHC phase. They will provide a clean environment to study the Higgs boson. The results would be complementary to the LHC and among themselves. The envisioned high energy pp colliders FCC-hh and SPPC will extend the c.m. energies far beyond that of the LHC. The energy frontiers accessible through the LHC, HL-LHC, ILC, CEPC-SPPC and FCC will push the experimental e^+e^- and pp programs up to 1 TeV and nearly 100 TeV in c.m. energies, respectively.

2.2 Physics with the e^+e^- Collider

The CEPC e^+e^- collider is envisioned to be operated with a c.m. energy of 240 GeV where the Higgs events are produced primarily through the interaction $e^+e^- \rightarrow ZH$. With a nominal luminosity of 2×10^{34} $cm^{-2}\cdot s^{-1}$ about 1 million clean Higgs events will be produced by CEPC over a period of 10 years at each of the two interaction points.

A precision Higgs physics program will be a critical component of any roadmap for high energy physics in the coming decades. Potential new physics beyond the SM could

lead to observable deviations in the Higgs couplings from the SM expectations. Typically, such deviations can be parameterized as

$$\delta = c\frac{v^2}{M_{NP}^2} \qquad (2.2.1)$$

where v and M_{NP} are the vacuum expectation value of the Higgs field and the typical mass scale of new physics, respectively. The size of the proportionality constant, c, depends on the model, but it should not be much larger than O (1). The current and upcoming LHC runs will directly search for new physics from a few hundreds of GeV to at least a TeV. Eq. (2.2.1) implies that probing new physics beyond the LHC reach would require the measurement of the Higgs couplings at least to the percent level accuracy.

The ATLAS and CMS experiments at the LHC will continue to improve the measurement of the Higgs boson properties including couplings to gauge bosons, Yukawa couplings and self-couplings. The current level of precision in the Higgs coupling measurements are at about O (15%) in most cases. They will be significantly improved in the coming decades through the on-going LHC program, as documented in several studies [1, 2]. Precision of a few percent are achievable for some of the couplings. However, to achieve the sub-percent level of precision will need new facilities. A lepton collider operating as a Higgs factory is a natural next step.

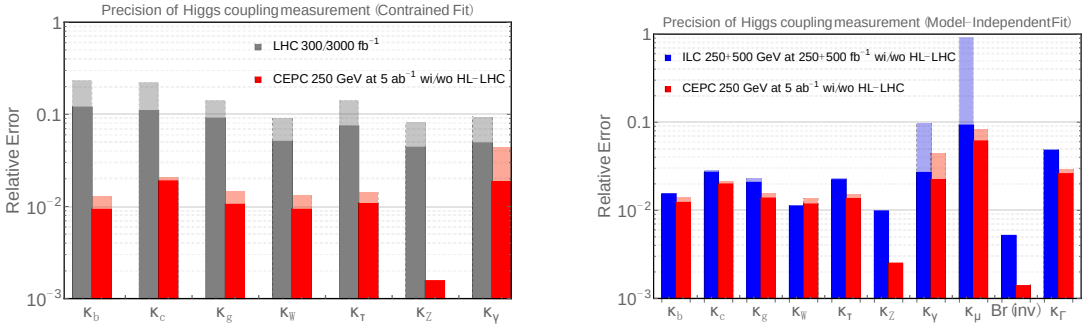

Figure 2.1: Projections of the precision of Higgs coupling measurements at CEPC. The y-axis is the percentage accuracy of the ratio between the measured size of the couplings and the Standard Model predictions. **Left**: The projections for the LHC (300 fb^{-1}, lighter grey) and HL-LHC (3 ab^{-1}, darker grey) are shown together with those for the CEPC (5 ab^{-1}, lighter red) and the combination of CEPC and HL-LHC (darker red). **Right**: The projections for the CEPC are shown together with those for the ILC (250+500 GeV with 250+500 fb^{-1}, lighter blue) and the combination of ILC and HL-LHC (darker blue).

The CEPC collider will allow the measurement of the rates of production of the Higgs boson in e^+e^- annihilations. The SM predicts those cross sections for a Standard Model Higgs. The leading production at ~240 GeV is the Higgsstrahlung process $e^+e^- \rightarrow Z^* \rightarrow ZH$, supplemented by the WW and ZZ fusions $e^+e^- \rightarrow \nu\nu\,(W^*W^*) \rightarrow \nu\nu\,H$ and $e^+e^- \rightarrow (Z^*Z^*) \rightarrow e^+e^-\,H$, respectively. Data from CEPC can help identify the nature of the Higgs boson with these measurements.

A strong advantage of the CEPC experiment over the LHC is that the Higgs can be detected through the recoil mass method by reconstructing only the Z boson without including the recoiling Higgs boson in the event reconstruction. Therefore, Higgs

production can be disentangled from its decay in a model independent way. Moreover, the cleaner environment at a lepton collider allows much better exclusive measurement of Higgs decay channels. All of these give the CEPC an impressive reach in probing Higgs properties. For example, with an integrated luminosity of 5 ab^{-1}, over one million Higgs bosons will be produced. With this sample, CEPC will be able to measure the Higgs coupling to *Z* at an accuracy level of 0.25 %, more than a factor of 10 better than the HL-LHC. Such a precise measurement gives the CEPC unprecedented reach into interesting new physics scenarios which are very difficult to probe at the LHC. The CEPC also is powerful for detecting Higgs exotic decays. For example, with 5 ab^{-1}, it can improve the accuracy of the measurement of the invisible decay branching ratio to 0.3%. It is also expected to have good sensitivity to exotic decay channels which are swamped by the backgrounds at the LHC. Also important to stress is that an e^+e^- Higgs factory can perform a model independent measurement of the Higgs width. This feature in turn allows for model independent determination of the Higgs couplings.

The CEPC can also collide e^+e^- at the Z pole and near the WW threshold to allow for precise measurement of electroweak parameters. Because of up to 4 orders of magnitude increase in luminosity at the Z pole compared to the LEP collider, the Z line shape and coupling measurement will benefit from the shorter run times with reduced systematic uncertainties. Many other electroweak parameters may also be better measured with CEPC operated at various energy points. For example, in comparison with the current precision, the oblique parameters S and T can be measured 10 times better. Further CEPC CDR work will determine in detail the potential of CEPC in improving the electroweak precision measurement.

2.3 Physics with the *pp* Collider

A high-energy pp collider, such as the SPPC, with center-of-mass energy in the 50-100 TeV range, is the natural next step after the CEPC. It represents our best opportunity for significantly extending the energy reach beyond the LHC.

The motivation for searching for new physics at the SPPC is to address the main open questions outlined in Section 2.1. In contrast to the CEPC, the SPPC will search for the signal of direct production of particles associated with new physics. With the large increase of c.m. energy, SPPC can significantly extend the sensitivity for new physics beyond that of the LHC. It will be the next milestone in the quest of pushing the energy frontier.

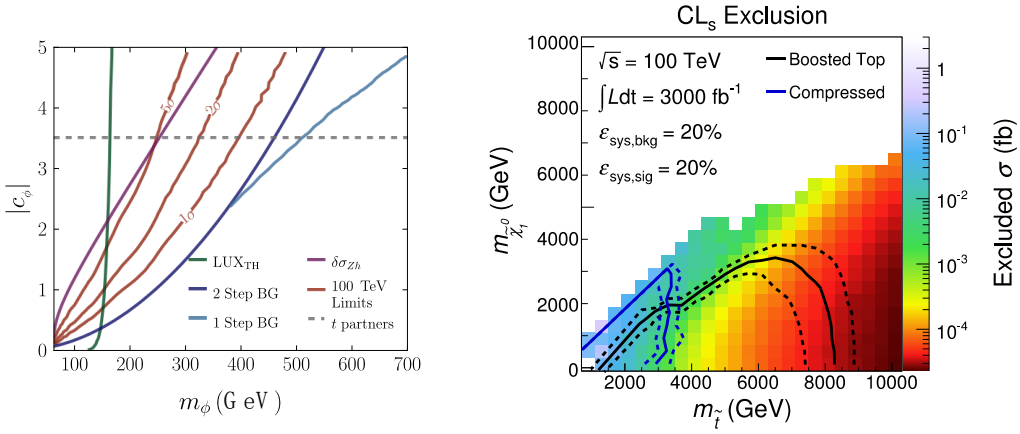

Figure 2.2: Left: The reach of singlets produced through the Higgs portal at a 100 TeV pp collider [3], with an integrated luminosity of 3 ab^{-1}. The region to the left of the green line denotes the LUX exclusion for Higgs Portal dark matter with thermal abundance. The region to the left of the dark blue line denotes estimates the possible parameter space for two-step first order phase transition, while the region between the light blue and dark blue lines denotes estimates the possible parameter space for one-step first order phase transition. **Right**: The reach for finding the stop (supersymmetric top) at a 100 TeV pp collider [4], with an integrated luminosity of 3 ab^{-1}. The two different coloured contours represent two different search strategies.

The SPPC can substantially deepen our understanding of the nature of electroweak-symmetry breaking. In particular, the SPPC can increase the precision of the measurement of the triple-Higgs coupling, which is key for probing the shape of the Higgs potential. Moreover, the new particles, which control the characteristics of the electroweak phase transition, can be directly produced and detected at the SPPC. An interesting benchmark for this scenario is the so-called "Higgs portal", wherein new particles driving the phase transition interact primarily with the Higgs. Estimates for the reach for an interesting example is shown in the left panel of Fig. 2.2, in which the signal is a pair of neutral spin-0 gauge-singlets produced through the Higgs portal. It appears that a large region of the interesting parameter space in which a first-order electroweak phase transition occurs, can be probed.

The SPPC can also help us understand the 17 orders of magnitude difference between the Planck scale and the electroweak scale, the so-called naturalness problem. The latter remains one of the central questions for particle physics, and a myriad of new-physics models have been proposed to address it. A common prediction among them is the presence of a top-quark partner. The naturalness, or the lack of fine -tuning, of any such model is proportional to the square of the top-partner's mass. The SPPC can dramatically enhance the reach for the top partner, and improve the test for naturalness by up to two orders of magnitude beyond the LHC. The example of low-energy super-symmetry (SUSY) provides a clear illustration of this opportunity. The reach for the top partner in SUSY, the stop, at a 100 TeV pp collider is shown in the right panel of Fig. 2.2. While the maximal reach for the stop at the HL-LHC is expected to be for a stop mass ~1.5 TeV, the 100 TeV pp collider can extend the reach to a stop mass of ~8 TeV.

$$M_{dark\ matter} \leq 1.8\ TeV\ \left(\frac{g_{DM}^2}{0.3}\right) \qquad (2.3.1)$$

Together with the abundance of visible matter in the universe, the presence of dark matter provides some of the strongest experimental evidence for new physics beyond the Standard Model. The weakly-interacting massive particle (WIMP), considered by many to be the most compelling dark matter candidate, is an exciting case for new physics close to the electroweak scale. However, a large region of the WIMP parameter space has MWIMP close to a TeV, as indicated in the Eq. (2.3.1) above.

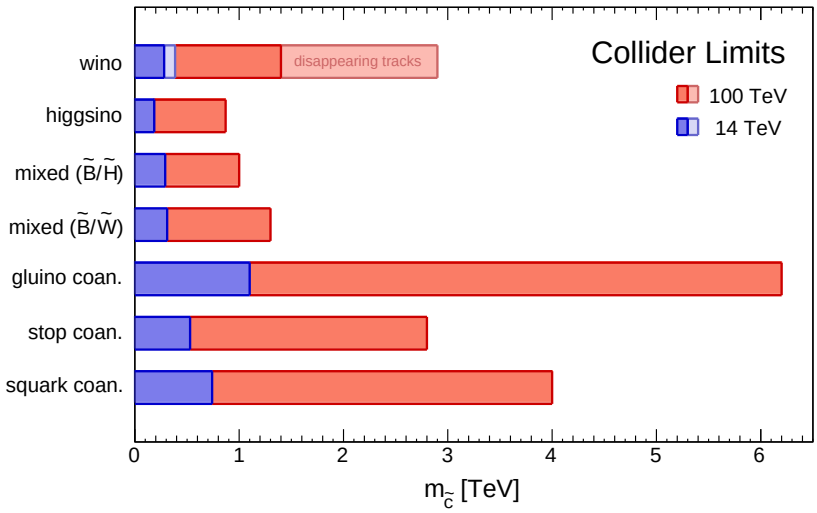

Figure 2.3: The reach of WIMP dark matter at the LHC and a 100 TeV pp collider [5], each with an integrated luminosity of 3 ab^{-1}. The projection is based on the mono-jet channel. In the case of wino dark matter, the reach from searching for a disappearing track is also included.

This mass range is largely above the reach of the dominant search channels at the LHC. A 100 TeV pp collider can significantly enhance the mass reach for WIMP dark matter, as demonstrated in Figure 2.3.

In summary, the SPPC offers a tremendous opportunity to extend the mass reach for new physics beyond that of the LHC, even with the same integrated luminosity. The results presented here (and many others not shown) demonstrate a gain of a factor of at least 5 in mass reach at a 100 TeV pp collider with 3 ab^{-1} of integrated luminosity (same as that of the HL-LHC), Since parton densities fall off rapidly at the highest mass scales, additional luminosity increases the mass reach slowly, reaching a factor of 7 with 50 times more collisions. Thus, we can state with confidence the opportunity for general gain in mass sensitivity that the SPPC would provide with the same integrated luminosity as the HL-LHC.

Of course, we have only discussed the effect of luminosity on the mass reach for new physics. We should not ignore the fact that larger luminosity offers possibilities of performing precision measurements, reducing systematics, and helps increase the reach for detection in the presence of a large SM background.

2.4 Physics with the *ep* and *eA* Collider

A high energy proton-proton collider, such as SPPC, will be the energy frontier of fundamental research in physics accessible by accelerator-based facilities in the world, while the electron-position collider, such as CEPC, will provide a clean and much needed precision tool for the study of the Higgs (referred to by some as the “God” particle), to shed light on mass generation and the mystery behind spontaneous

symmetry breaking. However, the Higgs mechanism is almost irrelevant for the mass generation of nucleons and nuclei, which make up 99% of the mass of all particles in our visible world. Nucleons and nuclei emerged from the evolution of our universe following its birth (the Big Bang), encoding all the history and secrets of the evolution and waiting for us to explore. But, neither the SPPC nor the CEPC type of accelerator facilities are natural for exploring the precise internal structure of nucleons and nuclei, and their emergence, although both facilities can create hadronic matter from the energy of the collisions.

Construction of CEPC and SPPC in a common accelerator complex provides a great opportunity to realize collisions of protons or ions with electrons or positrons (*e-p* or *e-A* where *e* stands for either e^- or e^+) in an ultra-high c.m. energy range up to 4.2 TeV, far beyond the energy of any existing and proposed future lepton-hadron colliders including the Electron-Ion Collider (EIC) in the United States and the LHeC at CERN. With precise control of the scattered lepton, such a lepton-hadron scattering facility in the ultra-deep inelastic scattering (DIS) region will provide a *clean and fully controlled* probe of the inner structure and quantum dynamical fluctuations of the dynamics of a proton down to the unprecedented distance scale of 10^{-4} fm (or one ten-thousandth of the proton size), which could be sensitive to dynamics that might restore the spontaneously broken symmetries of the Standard Model, and the quantum fluctuations caused by physics beyond the standard model. In addition, with the proposed high luminosity, lepton-hadron diffractive scattering will provide the deepest measurements of a proton with an impulse over one TeV or a resolution up to 10^{-4} fm, while keeping the proton intact, leading to the most fine tomographic images or the unprecedented spatial distributions, of quarks and gluons of momentum ranging from the one tenth to the one thousandth of the proton's momentum. This information is surely the most sensitive probe of the color confinement of QCD.

With the option of replacing protons with heavy ions with various atomic number A, the electron-ion (e-A) colliders could act as the smallest vertex detectors in the world to "map" out the dynamics of the color neutralization process and "probe" the emergence of hadrons, which is largely unknown at present. In future e-A collision experiments, some of the key questions to answer are: What is the partonic structure of nuclei in very small-x regime? What is the role of gluons and gluonic self-interactions in nuclei? What is the role of parton distributions in nuclei in the initial state for heavy ion collisions? Can one observe unambiguous signals of the gluon saturation in protons and nuclei? Can the nature of color confinement be revealed in electron-proton and electron-ion collisions at TeV scale?

2.5 Physics with the Heavy Ion Collider

Collisions at the SPPC with the proton beams replaced by heavy ion beams will produce the hottest quark-gluon plasma (QGP) ever in a laboratory setting, which could only have existed in the first few microseconds of our universe following its birth. With its unprecedented higher energy, the SPPC could access and explore the earliest history and secrets of our universe no other machine could have done.

Remarkable discoveries have been made at RHIC since its operation in 2000 with evidences pointing to the formation of a strongly coupled QGP at the center of Au+Au collisions at the highest energy at RHIC. One of the surprising discoveries is that the hot and dense QCD matter created in relativistic heavy-ion collisions displays a strong

collective flow characteristic of a strongly-coupled liquid, rather than the weakly-coupled gas of quarks and gluons as initially expected. The second discovery at RHIC is the observation of substantial jet quenching, indicating that the matter is virtually opaque to energetic quarks and gluons. Differences in the yields and flow of baryons versus mesons indicate that hadron formation at intermediate transverse momenta proceeds via coalescence of constituent quarks, providing the evidence for partonic collectivity in the final hadron spectra. The STAR experiment has also identified anti-hypertriton and anti-alpha production in Au+Au collisions, the first ever observation of an anti-hypernucleus and an anti-alpha. With more than one order of magnitude higher colliding energy, many of the proposed signals for the QGP become much stronger and easier to observe at LHC. The dense matter created in heavy-ion collisions at the LHC is much hotter and has longer lifetime during its dynamical evolution. Recent experimental data from heavy-ion collisions at LHC unambiguously confirmed the experimental evidence of QGP as first observed at RHIC.

In the future, the focus of heavy-ion collisions at RHIC and LHC will be on quantitative characterization of the strongly coupled QGP using rare probes such as large transverse momentum jets, heavy flavor particles, real and virtual photons and quarkonia states. Study of collective phenomena using detailed multiple particle correlations can also provide more precision constraints on the bulk transport coefficients of the QGP. Since existing RHIC and LHC experimental data point to interesting hints on the weakening of the interaction strength both among bulk partons and between hard probes and bulk medium, it will be extremely interesting to see whether such a trend continues at future higher collider energies and eventually reaches the weakly interacting scenario as predicted by perturbative QCD (pQCD).

One can address many important questions in future heavy-ion collision experiments in the energy range of tens or even hundreds of TeV. They include:

a) What is the effective equation of state (EoS) for strongly interacting matter at high temperatures? Can one start to see the effect of charm quarks in the EoS?
b) What is the thermalization mechanism and how does the thermalization time depend on the colliding energy?
c) What are the transport properties of strongly interacting matter at such high temperatures as probed by high-energy jets and collective phenomena? Are they approaching the weak coupling values at higher temperature as predicted by pQCD?
d) What is the nature of the initial state and its fluctuation in nuclear collisions?
e) Can we find other exotic hadrons or nuclei such as light multi-Λ hyper-nuclei, bound states of (ΛΛ) or the H di-baryon?

The answers to these important questions in strong interactions rely on both theoretical advances and experimental programs of high-energy electron-nuclei (electron-ion) and heavy-ion collisions at future collider facilities.

2.6 Summary

Future colliders offer great opportunities to study rich and exciting physics. The CEPC e^+e^- collider will bring a major leap in precision with the Higgs boson, and enable electroweak measurements with the Z and the W bosons, while the SPPC proton-proton collider will provide real discovery potential and a laboratory to address many of

the major physics issues we face today. With the CEPC and the SPPC, and the complementary *e-p* and *e-A* colliders in a common accelerator complex, we could have a unique, and possibly, the only facility in the world to be able to explore the fundamental structure of all matter, and their birth and evolution, in one facility. This would be a major step forward in the human scientific endeavour.

2.7 References

1. S. Dawson, A. Gritsan, H. Logan, J. Qian, C. Tully, et. al. arXiv: 1401.6801.
2. ATLAS collaboration, ATL-PHYS-PUB-2014-016.
3. N. Craig, H. K. Lou, M. McCullough, A. Thalapillil, arXiv:1412.0258.
4. T. Cohen, R. T. D'Agnolo, M. Hance, H. K. Lou, J. G. Wacker, arXiv:1406.4512.
5. M. Low, Lian-Tao Wang, arXiv:1404.0682.

3 Machine Layout and Performance

Figure 3.1 is a layout of the CEPC. The circumference is about 54.4 km. There are 8 arcs and 8 straight sections. Four straight sections, about 1 km each, are for the interaction regions and RF; another four, about 850 m each, are for the RF, injection, beam dump, etc. The lengths of these straight sections are determined by taking into account the future needs of large detectors and complex collimation systems of the SPPC. The total length of the 8 straight sections is about 14% of the ring circumference, similar to the LHC. Among the four IPs, IP1 and IP3 will be used for e^+e^- collisions, whereas IP2 and IP4 are reserved for *pp* collisions.

The tunnel will be underground, 50 - 100 m deep. It will accommodate three ring accelerators: the CEPC collider, the SPPC collider, and a full energy Booster for the CEPC. Therefore, the tunnel must be big, about 6 m in width as shown in Figure 3.2. (As a comparison, the LHC tunnel is 3.6 m in diameter.) This is because it is planned to keep the CEPC ring in the tunnel when the SPPC is built and operates, unlike the LHC that was installed after having removed LEP from the tunnel.

While the two colliders will be mounted on the floor, the Booster will hang from the ceiling, similar to the Recycler in the Main Injector tunnel at Fermilab.

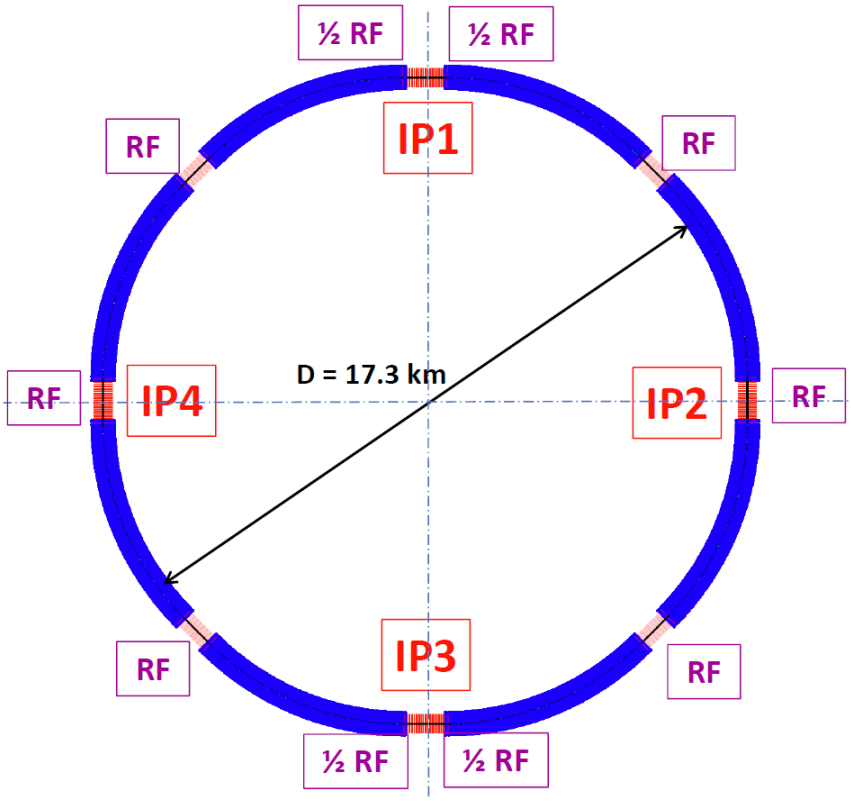

Figure 3.1: CEPC layout.

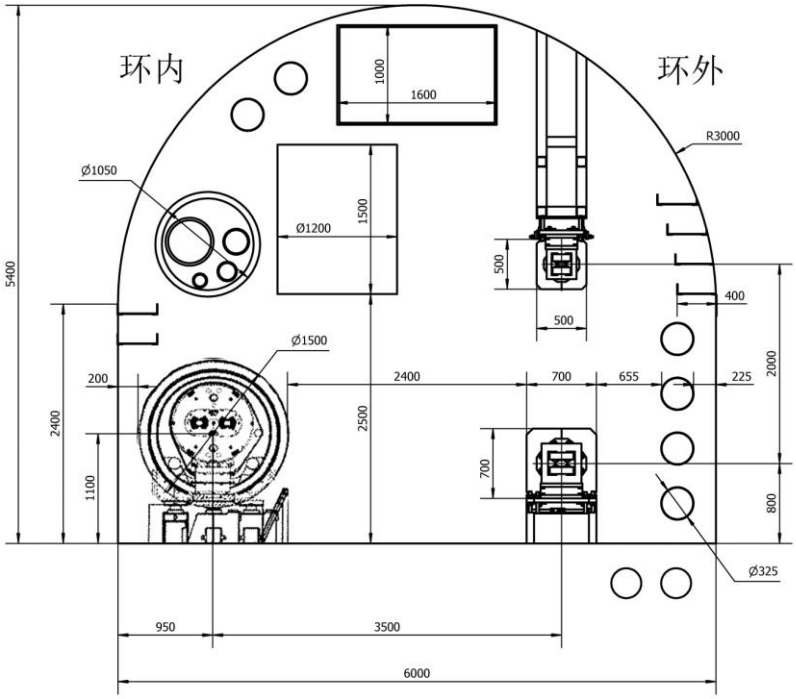

Figure 3.2: Tunnel cross section. The magnet on the left is the superconducting magnet of the SPPC, the magnets on the right are for the CEPC collider (bottom) and the Booster (top), respectively. The tunnel width is 6 m.

As shown in Table 1.1, the CEPC collider is an e^+e^- collider at center-of-mass energy 240 GeV. Both the electron and positron beams will circulate in the same beam pipe with an energy of 120 GeV each.

The decision to use a single beam pipe is a difficult one as it leads to a number of issues concerning beam physics and accelerator operation. In order to avoid parasitic collisions outside the detector, a pretzel orbit is needed, which brings the beam off center in the magnets. Because we do not allow the beam to be off center in the straight sections, where the interaction region and RF are located, the total number of bunches is limited to about 50. A pretzel orbit also makes injection and beam control more difficult. A dual beam pipe is preferable from an accelerator design and operations point of view. But it is more costly. With the constraint of cost, it was decided to use a single pipe and from this saving make the ring circumference as large as possible.

There are numerous local governments in China who have shown a strong interest in hosting this machine. Site selection is a complex process involving many factors – both technical and non-technical – that are beyond the scope of this report. As an example, Figure 3.3 shows a site candidate, Qinghuangdao, about 300 km east of Beijing. It has excellent geology.

Two different circumference rings are considered: the small ring is 54 km in circumference, the big one 100 km. Our baseline is a 54-km ring. However, if additional, non-government funds can be found, the 100-km ring will be the choice.

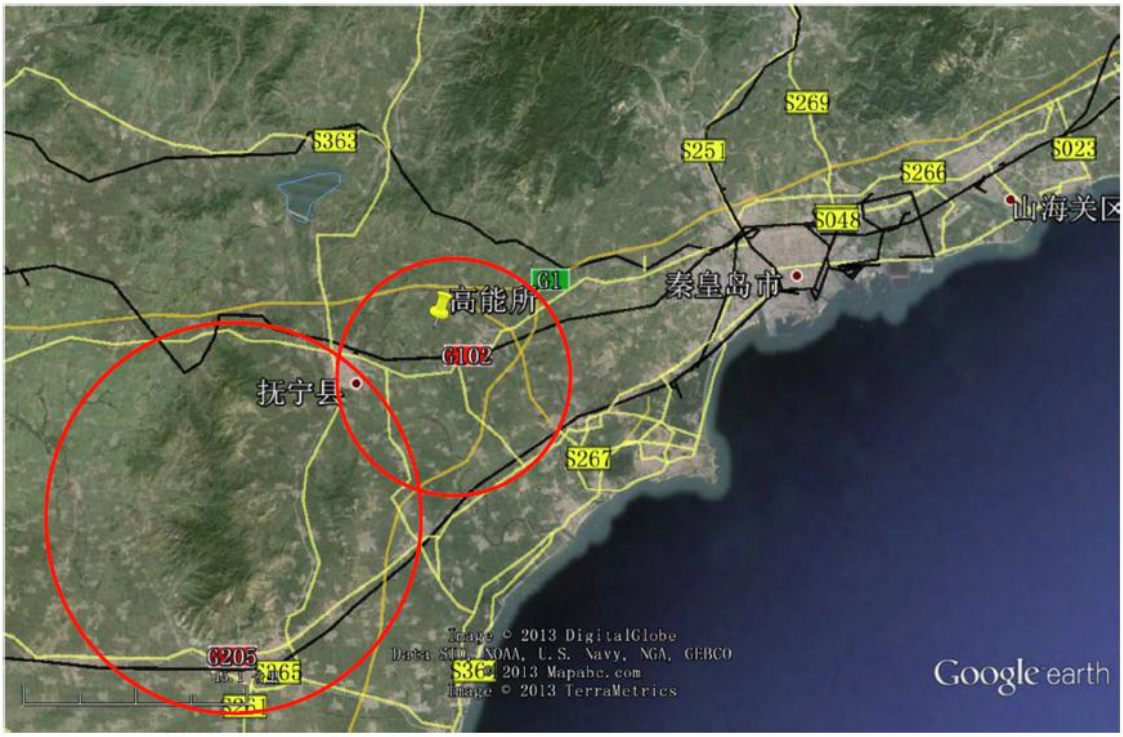

Figure 3.3: Illustration of the CEPC-SPPC ring sited in Qinghuangdao. The small circle is 50 km, and the big one 100 km. Which one will be chosen depends on the funding scenario.

Figure 3.4 shows the CEPC ring on the map of Qinghuangdao. The Yellow River Engineering Consulting Co., Ltd., has done an extensive survey and geological study in this area [1].

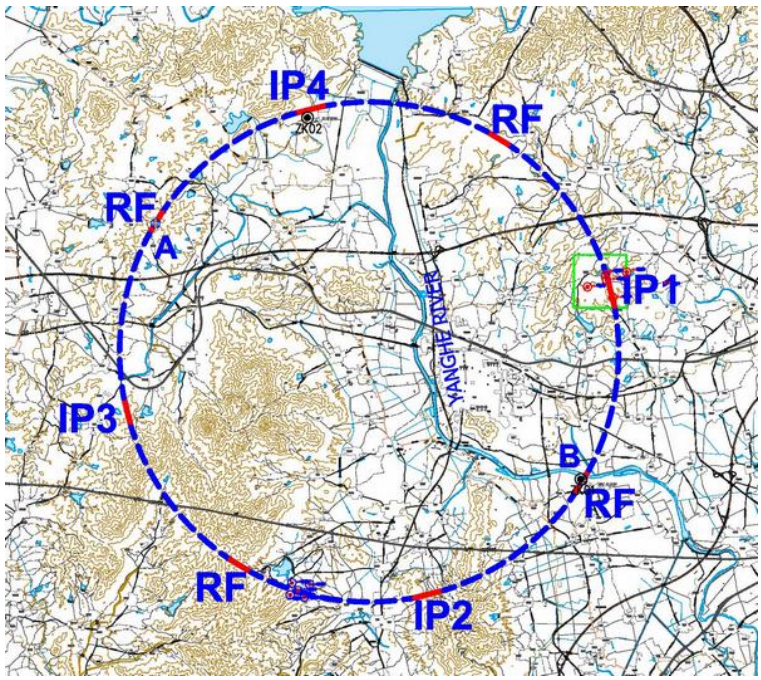

Figure 3.4: A hypothetical location of the CEPC ring on the Qinghuangdao area map.

The main parameters of CEPC are listed in Table 4.1.1 in Section 4.1. We will give a brief description of the choice of several key parameters.

Luminosity The required integrated luminosity is 250 fb^{-1} per IP per year. If the so-called "Snowmass unit" (1×10^7 sec) is used for effective operation of an accelerator in a year, one would need a peak luminosity of 2.5×10^{34} $cm^{-2}s^{-1}$. However, from the PEP-II experience, when the top-up injection method was applied, the yearly effective operation routinely reached 1.5 Snowmass units [2]. Since the CEPC will adopt this injection method by using a full-energy booster, the required peak luminosity is reduced to 1.67×10^{34} $cm^{-2}s^{-1}$. In our design, the calculated luminosity based on beam-beam simulation is 2×10^{34} $cm^{-2}s^{-1}$.

Beam current The beam current is determined by the synchrotron radiation budget, which is 50 MW per beam, or 100 MW for two beams. A 120 GeV electron circulating in a 50-km ring loses 3 GeV per turn from synchrotron radiation, which leads to the current limit of 16.6 mA per beam. Because the luminosity is proportional to the square of the bunch intensity, one should pack as many particles in a bunch as possible until the beam-beam limit is reached. For the CEPC, this gives 3.7×10^{11} particles per bunch and 50 bunches per beam.

Beam lifetime and momentum acceptance There are two principal limiting factors to the beam lifetime – radiative Bhabha scattering and beamstrahlung. The former is determined by the luminosity and there is little that can be done to offset this limit. The latter has an exponential dependence on the momentum acceptance of the machine. Our design goal of the beam lifetime is 30 minutes, which requires ±2% momentum acceptance. This is one of the most challenging goals to meet in the design.

L* and β_y* The distance between the interaction point (IP) and the first quadrupole of the final focusing doublet, L*, and the vertical beta function at the IP, β_y*, are two of the most important parameters in the interaction region (IR) optics design. In order to minimize the nonlinearity in the IR, it is preferable to have a small L* and a large β_y*. However, a small L* would make the detector design more difficult, whereas a large β_y* would reduce the luminosity. After a careful tradeoff study, it is decided to use L* = 1.5 m, and β_y* = 1.2 mm. But a β_y* as large as 3 mm is also under consideration because it would increase the dynamic aperture for off-momentum particles while its impact on the luminosity looks tolerable from the beam-beam simulation.

Injection As the beam lifetime is short, one needs full-energy top-up injection. The top energy of the Booster is 120 GeV. It is capable to inject 5% of the beam current every 10 seconds and can fill up the entire ring in 400 seconds.

RF frequencies The superconducting RF is the most demanding technical system of the CEPC. Because the Booster beam current is relatively low (0.8 mA), it is decided to use a 1.3 GHz SRF system, a mature technology that has been used in the ILC, XFEL and LCLS-II. The collider beam current is very high (33 mA) and both beams use the same RF cavity; the average RF power is bigger than in any exiting SRF system, and a large power coupler is required. Even more difficult is the HOM damper, which must

extract 99.9% of the HOM power from the cavity. Therefore, it is decided to use a 650 MHz SRF system, which is used in the IHEP ADS project and PIP-II at Fermilab.

A more detailed discussion and derivation of these and other main parameters can be found in the following section.

References:

1. Yellow River Engineering Consulting Co., Ltd., "Preliminary Conceptual Design Report for the CEPC Civil Construction and Utilities," February 2015. (in Chinese)
2. John Seeman, private communication.

4 CEPC – Accelerator Physics

4.1 Main Parameters

4.1.1 Design Goals

The goal of the CEPC is to provide e^+e^- collisions at the center-of-mass energy of 240 GeV and deliver a peak luminosity of 2×10^{34} cm^{-2}s^{-1} at each interaction point. CEPC has two IPs for e^+e^- collisions. Its circumference is 54.374 km. We limit the total synchrotron radiation losses around the machine to ~100 MW.

4.1.2 Effects Determining the Luminosity

The most important parameter of CEPC, apart from the energy of the colliding beams, is its luminosity. The luminosity determines the event rate for a given interaction process and is given by:

$$L_0 = \frac{N_e^{\,2} n_b f_0}{4\pi\sigma_x^{\,*}\sigma_y^{\,*}} FH \qquad (4.1.1)$$

Here, N_e is the bunch population, n_b is the bunch number, f_0 is the revolution frequency, σ_x and σ_y are the bunch transverse sizes at the interaction point and F is the geometric luminosity reduction factor due to the crossing angle at the IP. For the current parameters the crossing angle is zero, so F equals 1. H is the hourglass factor giving the luminosity reduction due to the change of β^* along the bunch.

4.1.2.1 *Beam-beam Effect*

The beam-beam interaction is an important effect which limits the luminosity. The beam-beam tune shift parameters ξ_x and ξ_y, defined as

$$\xi_x = \frac{r_e N_e \beta_x^{\,*}}{2\pi\gamma\sigma_x^{\,*}(\sigma_x^{\,*}+\sigma_y^{\,*})}, \xi_y = \frac{r_e N_e \beta_y^{\,*}}{2\pi\gamma\sigma_y^{\,*}\left(\sigma_x^{\,*}+\sigma_y^{\,*}\right)}, \qquad (4.1.2)$$

serve as scaling for the effects of beam-beam interactions.

In the approximation of flat beams, we can recast the expression for luminosity as a function of the tune shift:

$$L = \frac{\gamma n_b I_b}{2er_e\beta_y^{\,*}} \xi_y H \qquad (4.1.3)$$

Here we assume an upper limit of 0.1 for the beam-beam tune shift per IP.

4.1.2.2 *Beamstrahlung*

Beamstrahlung is synchrotron radiation from a particle being deflected by the collective electromagnetic field of the opposing bunch. This effect will increase the energy spread and limit the lifetime of the beams. Its importance increases considerably with energy, so beamstrahlung is an important effect in CEPC. We have used analytic formulae and computer programs to calculate and simulate the effect on the beam energy spread, bunch length and lifetime. A detailed discussion of the effect of beamstrahlung is in section 4.5.

4.1.3 **Beam Parameters**

The total beam current is defined by the synchrotron radiation power. Since the present SR power per beam is 51.7 MW (including the final focus system) and the SR loss per turn is 3.11 GeV, the maximum total beam current is 16.60 mA. CEPC is a single-ring collider, so it can't hold too many bunches. The current baseline assumes a bunch number of 50; this number could be increased when we have developed a detailed pretzel scheme. The maximum bunch intensity N_e=3.79×10^{11}.

From Eq. (4.1.3) we can see that lowering the vertical beta-function at the IP is beneficial to luminosity, but the lower limit for β_y^* comes from the final focus and chromatic corrections. A small β_y^* of 1.2 mm is set as a baseline parameter. Then we choose a large β_x^* of 0.8 m to decrease the effect of beamstrahlung.

The choice of emittance is based on the lattice design. We used a FODO cell and emittance and the momentum compaction factor can be estimated by the following formulas:

$$\varepsilon_x = \frac{C_q \gamma^2 \varphi^3 (1 - \frac{3}{4} sin^2 \frac{\mu}{2} + \frac{1}{60} sin^4 \frac{\mu}{2})}{8 J_x sin^3 \frac{\mu}{2} cos \frac{\mu}{2}}, \tag{4.1.4}$$

$$\alpha_p = (\frac{\varphi}{2})^2 (\frac{1}{sin^2 \frac{\mu}{2}} - \frac{1}{12}), \tag{4.1.5}$$

μ is phase advance per cell and φ is bending angle of the cell. J_x is the horizontal damping partition number; J_x=1 for the current CEPC parameter set. Large emittance indicates a large momentum compaction factor, and α_p is related to the bunch length and the height of the bucket. So we need to take into account the RF parameters when we choose the emittance.

4.1.4 **RF Parameters**

For the present, 650 MHz is considered as the baseline RF frequency of the collider.

From the dependencies of luminosity on the RF parameters, we see that higher luminosity needs higher RF frequency and voltage, but higher RF frequency and higher voltage result in a larger synchrotron oscillation tune which will make synchro-betatron resonances a serious problem and affect the luminosity. What's more, less α_p is good for getting less ν_s and high luminosity, but large emittance is beneficial to reduce the effect of beamstrahlung. The final choice must be a compromise between these conflicting requirements which take into account the state of modern high power RF technology. We choose an RF voltage equal to 6.87 GV and the momentum compaction factor equals 4.15×10^{-5} resulting in short bunches during collisions.

4.1.5 **Beam Lifetime**

4.1.5.1 ***Lifetime due to Beamstrahlung***

At very high energy, beamstrahlung becomes a limitation to the performance of the collider [1,2]. It increases the energy spread of the colliding beam and hence limits the

lifetime. We use the analytic formulas from [1] to calculate the beamstrahlung lifetime and we also have done simulations. These two approaches result in large differences. A detailed discussion will be deferred to section 4.5. The beamstrahlung lifetime of CEPC from simulation is about 50 minutes, as listed in Table 4.1.1.

4.1.5.2 *Radiative Bhabha Scattering*

In CEPC, lifetime due to radiative Bhabha scattering is dominant. We use the following analytic formula to calculate the cross section of the radiative Bhabha process.

$$\sigma_{ee} = \frac{16\alpha r_e^2}{3}((\ln\frac{1}{\eta} + \eta - \frac{3}{8}\eta^2 - \frac{5}{8})[\ln(\sqrt{2}\frac{a}{\lambda_p}) + \frac{\gamma_E}{2}] + \frac{1}{4}(\frac{13}{3}\ln\frac{1}{\eta} + \frac{13\eta}{3} - \frac{3}{2}\eta^2 - \frac{17}{6})),$$

$$a = \sqrt{2}\frac{\sigma_x\sigma_y}{\sigma_x + \sigma_y}. \tag{4.1.6}$$

Here, λ_p and γ_E denote the electron Compton wavelength and Euler's constant. The cross section for radiative Bhabha scattering in CEPC is 1.52×10^{-25} cm^2. We also used the simulation code BBBrem to calculate the cross section: the results are very close to the ones from the analytic formula.

The beam lifetime due to radiative Bhabha scattering is expressed by:

$$\tau_L = \frac{I}{eLn_{IP}\sigma_{ee}f_0} \tag{4.1.7}$$

From the above expression, we can see that the lifetime is inversely proportional to the luminosity. We need to strike a balance between lifetime and luminosity when we choose the parameters. Lifetime due to radiative Bhabha scattering is 55 minutes in CEPC for 2 IPs.

The total beam lifetime is about 25 minutes from the formula below:

$$\frac{1}{\tau} = \sum\frac{1}{\tau_i} \tag{4.1.8}$$

The present main parameters of CEPC are shown in Table 4.1.1.

Table 4.1.1: Main parameters of CEPC

Accelerator Parameters		
Beam energy [E]	GeV	120
Circumference [C]	km	54.374
Luminosity [L]	$cm^{-2}s^{-1}$	2.04×10^{34}
SR power/beam [P]	MW	51.7
Bending radius [ρ]	m	6094
Number of IP [N_{IP}]		2
Bunch number [n_B]		50
filling factor [κ]		0.7
Lorentz factor [γ]		234834.65
Revolution period [T_0]	s	1.83×10^{-4}
Revolution frequency [f_0]	Hz	5475.46
Magnetic rigidity [Bρ]	T ṁ	400.27
Momentum compaction factor [α_p]		3.36×10^{-5}
Energy acceptance of the ring [η]		±0.02
Cross-section for radiative Bhabha scattering [σ_{ee}]	cm^2	1.52E-25
Lifetime due to radiative Bhabha scattering [τ_L]	min	50.61
Beam Parameters		
Beam current [I]	mA	16.6
Bunch population [N_e]		3.79E+11
Emittance-horizontal [ε_x]	m ṙad	6.12E-09
Emittance-vertical [ε_y]	m ṙad	1.84E-11
Coupling factor [k]		0.003
Beam length SR [$\sigma_{s.SR}$]	mm	2.14
Beam length total [$\sigma_{s.tot}$]	mm	2.65
Interaction Point Parameters		
Betatron function at IP-vertical [β_y]	m	0.0012
Betatron function at IP-horizontal [β_x]	m	0.8
Transverse size [σ_x]	μm	69.97
Transverse size [σ_y]	μm	0.15
Beam-beam parameter [ξ_x]		0.118
Beam-beam parameter [ξ_y]		0.083
Hourglass factor [Fh]		0.68
Lifetime due to Beamstrahlung-Telnov [τ_{BS}]	min	1005
Lifetime due to Beamstrahlung [simulation]	min	47
RF Parameters		
RF voltage [V_{rf}]	GV	6.87
RF frequency [f_{rf}]	GHz	0.65

Harmonic number [h]		118800
Synchrotron oscillation tune [ν_s]		0.18
Energy acceptance of RF [η]	%	5.99
Synchrotron Radiation		
SR loss/turn [U_0]	GeV	3.11
Damping partition number [J_x]		1
Damping partition number [J_y]		1
Damping partition number [J_e]		2
Energy spread SR [$\sigma_{\delta.SR}$]	%	0.13
Energy spread BS [$\sigma_{\delta.BS}$]	%	0.09
Energy spread total [$\sigma_{\delta.tot}$]	%	0.16
Average number of photons emitted per electron during the collision [n_γ]		0.22
Transverse damping time [n_x]	turns	78
Longitudinal damping time [n_e]	turns	39

4.1.6 References

1. V.I.Telnov, “Restriction on the Energy and Luminosity of e+e- Storage Ring due to Beamstrahlung”, Phys.Rev.Letters 110,114801(2013)
2. Bogomyagkov et al., “Beam-Beam Effects Investigation and Parameters Optimization for a Circular e+e- Collider TLEP to study the Higgs Boson”,

4.2 Lattice

4.2.1 Introduction

After the discovery of a Higgs-like boson at CERN [1-3], many proposals have been made to build a Higgs factory to explicitly study the properties of this key particle. One of the most attractive proposals is the Circular Electron and Positron Collider (CEPC) project in China [4-5].

The designed beam energy for CEPC is 120 GeV. The main constraint in the design is the synchrotron radiation power, which should be limited to 50 MW per beam. The target luminosity is $2\times10^{34}\,cm^{-2}s^{-1}$.

CEPC will have arcs and straight sections between them. RF cavities compensate the energy loss in the straight section; thus one can reduce energy variations from synchrotron radiation. SPPC needs long straight sections for collimators. The compromise between the requirements of the CEPC and the SPPC are to have 8 arcs and 8 straight sections; RF cavities will be distributed in each straight section.

In this section, we show the latest design of the CEPC main ring lattice, including the pretzel scheme. Some critical issues that we encountered when designing the lattice will be discussed.

4.2.2 **Lattice Design of the Ring**

The circumference of the ring is 54.4 km with 8 arcs and 8 straight sections. The layout of the ring is shown in Figure 3.1. There are four IPs in the ring. IP1 and IP3 will be used for CEPC, while IP2 and IP4 will be used for SPPC. The RF sections are distributed in each straight section. In the IP section, the RF cavities will be symmetrically placed at the two ends of the straight section; in the other straight sections; the RF cavities can be located together at the middle of each straight section.

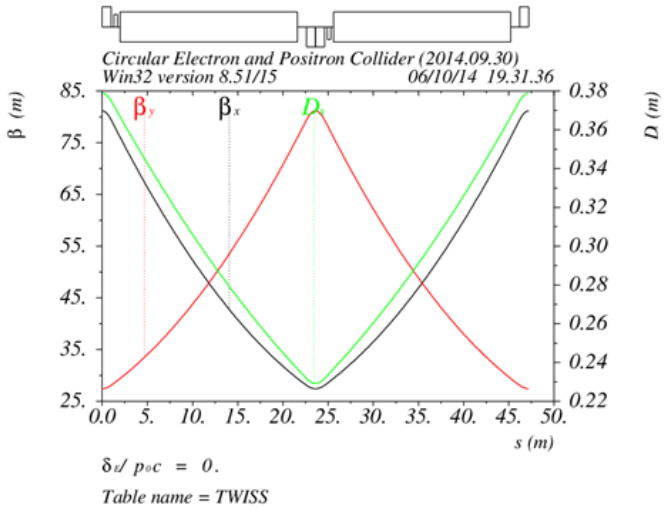

Figure 4.2.1: Beta functions and dispersion function of a standard FODO cell with 60/60 degrees phase advance in CEPC ring.

4.2.3 **FODO Cells**

The lattice for the CEPC ring has been chosen to use standard FODO cells with 60 degrees phase advances in both transverse planes. The FODO cell structure is chosen to provide a maximum filling factor. The 60 degrees phase advance is chosen for a relatively large beam emittance, resulting in a longer beamstrahlung beam lifetime, than with 90 degrees phase advance lattice cells.

A standard FODO cell with 60 degrees phase advance is shown in Fig. 4.2.1. The length of each bending magnet is 19.6 m; the length of each quadrupole is 2.0 m. There is one sextupole with length 0.4 m next to each quadrupole for chromatic corrections. The distance between the sextupole and the adjacent magnet is 0.3 m, while the distance between each quadrupole and the adjacent bending magnet is 1.0 m. The total length of each cell is 47.2 m.

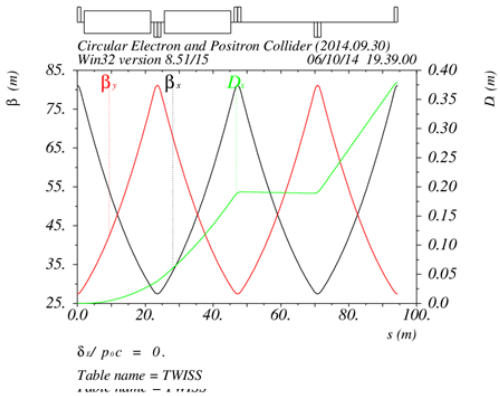

Figure 4.2.2: The beta functions and dispersion function of a dispersion suppressor in the CEPC ring.

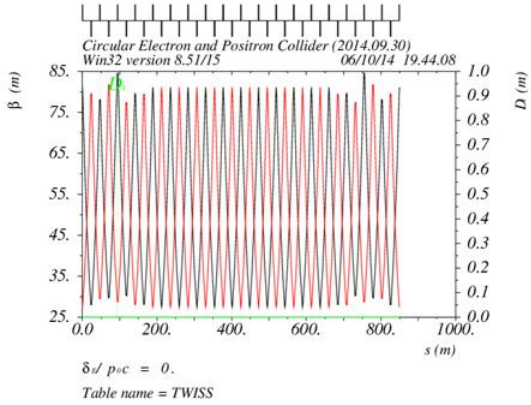

Figure 4.2.3: The beta functions and dispersion function of a short straight section in the CEPC ring.

4.2.4 **Dispersion Suppressors**

The dispersion suppressors are formed by removing the bending magnets in the second to last FODO cell on each side of every arc section in the CEPC ring. The beta functions and dispersion function of one dispersion suppressor is shown in Fig. 4.2.2.

4.2.5 **Straight Sections**

The straight sections are of two different lengths; the four straight sections containing an IP have a length of 1132.8 m, and the other straight sections have a length of 849.6 m. The first four FODO cells at each end of every straight section are used for matching and for working point adjustment. The beta functions and dispersion function of a short straight section in the CEPC ring is shown in Fig. 4.2.3.

4.2.6 **Dynamic Aperture**

We use the SAD code to track the dynamic aperture of the ring. We performed tracking with three transverse damping times to characterize the size of the dynamic aperture. Momentum spreads from +2% to -2% were tracked and the results are shown in Fig. 4.2.4. The dynamic aperture shown in the figure has been normalized to transverse beam sizes. No coupling and full coupling has been assumed to calculate the horizontal and vertical beam sizes.

From the figure we see that the dynamic aperture is ~60 times the beam sizes in both horizontal and vertical planes.

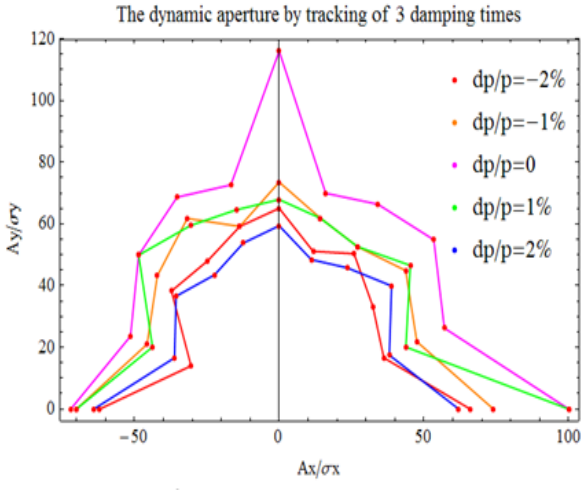

Figure 4.2.4: The dynamic aperture of the CEPC ring.

4.2.7 **Pretzel Orbit**

In order to allow both electrons and positrons to travel in the same beam pipe, the two beams have to be separated from each other at the many parasitic crossing points. This is done with a so called pretzel orbit shown in Figure 4.2.5.

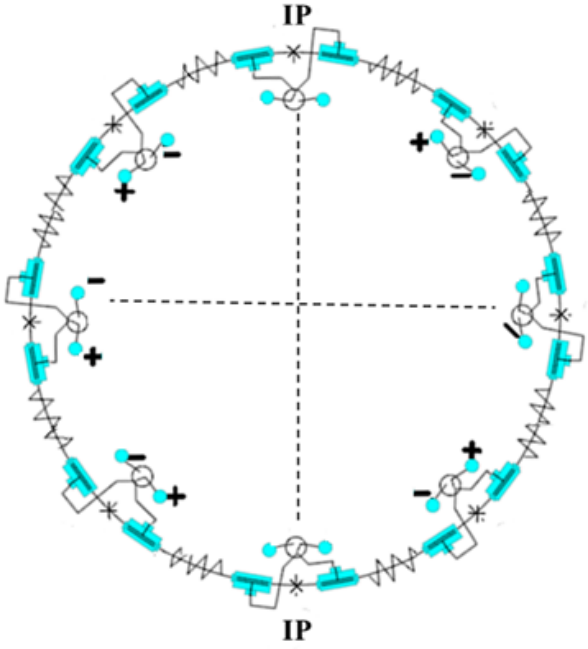

Figure 4.2.5: Pretzel scheme layout.

For CEPC, there are 50 bunches in each beam; thus there are 100 crossing or collision points. The two beams have to be separated at all the crossing points except at IP1 and IP3.

We use one pair of electrostatic separators to separate the beams in each arc section. One separator will be placed $\pi/2$ phase advance before the first crossing point in the arc section; the other separator will be placed $\pi/2$ phase advance after the last crossing point

in this arc section. With these 8 pairs of separators, all the crossing points in the arc section can be well separated. At IP2 and IP4, we need extra pairs of electrostatic separators to avoid beam collisions there. Two more pairs of separators will be placed $\pi/2$ phase advance before and after IP2 and IP4 to separate the beams at these two collision points. In total, ten pairs of electrostatic separators will be used in the CEPC ring to avoid all the parasitic collision points. The layout of the electrostatic separators and the resulting orbit is shown in Fig. 4.2.5.

Beams can be separated in either the horizontal or the vertical plane. With horizontal separation, the separation distance is larger since the beam size is larger vertically. With vertical separation, the separation distance is smaller, but separating in the vertical plane can easily induce large coupling between horizontal and vertical planes. As the coupling factor in CEPC is limited to a small value to attain high luminosity, we have chosen horizontal separation.

The maximum separation distance between the two beams has a strong effect on the beam lifetime. To allow for a reasonable beam lifetime, a maximum separation distance of $5\sigma_x$ is chosen for CEPC. The resulting pretzel orbit in one arc section is shown in Fig. 4.2.6.

4.2.8 **Saw Tooth Orbit**

The 120 GeV beam energy of CEPC is high and at this energy, synchrotron radiation is very strong. The synchrotron radiation loss per turn is 3 GeV for both beams, which means the energy difference at the entrance and exit of one arc section is ~0.3%, and at the following straight section, the energy loss will be compensated by RF cavities, and then the beam will lose energy from synchrotron radiation when entering the next arc section. Looking at the whole ring, the beam energy has a saw tooth structure. This energy saw tooth from synchrotron radiation will in turn result in a beam orbit saw tooth because of the change of the beam energy.

The saw tooth orbit has been calculated with MAD and is shown in Fig. 4.2.7. We can see that the maximum in the saw tooth orbit is ~0.6 mm, which is an order of magnitude smaller than the maximum in the pretzel orbit.

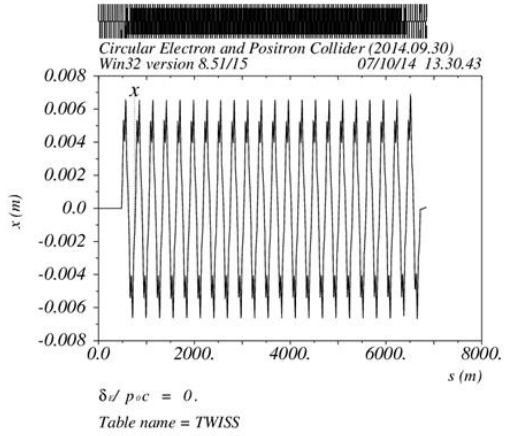

Figure 4.2.6: Pretzel orbit of the electron beam in one arc of the ring.

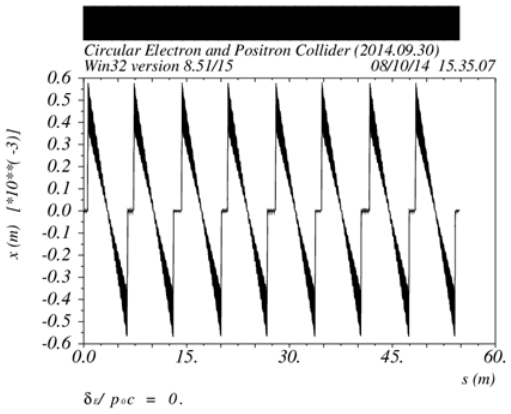

Figure 4.2.7: Saw tooth orbit in the CEPC ring.

4.2.9 **Discussion**

When designing the CEPC lattice, we came across two critical issues. First, the pretzel orbit causes a large distortion of the original beta and dispersion functions; the result is a change of tune and beam emittance. The distortion comes from the additional field seen by the beam when it is not on axis. The beam sees a dipole field in quadrupoles, where the maximum strength of that dipole field is only slightly weaker than the field in the bending magnets. In the sextupoles, the beam sees both dipole and quadrupole fields, but the strength is an order of magnitude smaller than the nominal dipole and quadrupole field in the ring. The total effect from the off axis field from the quadrupoles and sextupoles is a distortion in the periodicity of beta and dispersion functions, which can significantly reduce dynamic aperture.

Another effect from the pretzel orbit is a coupling of sextupole strength and working point.

The saw tooth orbit is common to all high-energy electron rings.

The main topics in CEPC lattice design have been investigated, but the lattice distortion from pretzel orbit and the correction scheme of saw tooth orbit has not been fully solved. More work needs to be done on the CEPC lattice design.

4.2.10 **References**

1. Adrian Cho, "Higgs Boson Makes Its Debut After Decades-Long Search," Science 337 (6091): 141–143.
2. "Observation of a New Particle with a Mass of 125 GeV," http://cms.web.cern.ch/news/observation-new-particle-mass-125-GeV.
3. CMS collaboration, "Observation of a new boson at a mass of 125 GeV with the CMS experiment at the LHC," Physics Letters B, 716(1):30-61.
4. "Accelerators for a Higgs Factory: Linear vs. Circular (HF2012)," Fermi National Laboratory, 14-16 November, 2012.
5. S. Henderson. "Accelerators for a Higgs Factory," Report at HF2012, Fermilab, 14-16 November, 2012.

4.3 Interaction Region and Machine-Detector Interface

4.3.1 **Introduction**

The interaction region (IR) of CEPC has been designed to meet the following requirements:

- Provide small beam sizes at the interaction point (IP);
- The large chromaticity generated by the final doublet (FD) must be compensated locally in order to achieve a large momentum acceptance of 2% for the whole ring;
- The solenoid field from the detector compensated to minimize its perturbation on the beam motion;
- The size of the accelerator equipment inserted into the detector should be constrained to provide the largest possible angular acceptance for the detector;
- The beam-induced background should be acceptable for the detector.

This is a preliminary design and further optimization will be carried out in future.

Table 4.3.1: Parameters of the interaction region.

Parameters	Unit	Value
Beam energy [E]	GeV	120
Bunch number / beam [n_B]	-	50
Bunch population [N_e]	-	3.79E+11
Number of IP [N_{IP}]	-	2
Emittance [$\varepsilon_x/\varepsilon_y$]	m rad	6.12E-09 / 1.84E-11
Beta function at IP [β_x^*/β_y^*]	mm	800 / 1.2
Transverse size at IP [σ_x^*/σ_y^*]	μm	69.97/0.15
Bunch length SR [$\sigma_{z,SR}$]	mm	2.15
Bunch length total [$\sigma_{z,tot}$]	mm	2.88
Beam-beam parameter / IP [ξ_x/ξ_y]	-	0.118/0.083
Energy spread SR [$\sigma_{\delta,SR}$]	%	0.132
Energy spread BS [$\sigma_{\delta,BS}$]	%	0.119
Energy spread total [$\sigma_{\delta,tot}$]	%	0.177
Average number of photons emitted per electron [n_γ]	-	0.23
Hour-glass factor [F_h]	-	0.658
Luminosity / IP [L]	$cm^2\ s^{-1}$	2.04E+34

4.3.2 **Interaction Region**

The interaction region parameters are listed in Table 4.3.1. In order to achieve a high luminosity, CEPC requires small beta functions at the IP ($\beta_x^* = 800$ mm, $\beta_y^* = 1.2$ mm). The small β_x^* and β_y^* require the final doublet to be as close to the IP as possible in order to minimize the chromaticity and keep the beta function as low as possible at the final doublet. This is shown in equations (4.3.1) and (4.3.2).

$$\xi_y \simeq \frac{L^*}{\beta_y^*} \qquad (4.3.1)$$

$$\beta_y \simeq \frac{L^{*2}}{\beta_y^*} \qquad (4.3.2)$$

ξ_y is the vertical chromaticity generated in the final quadrupole QD0, β_y is the vertical beta function at QD0 and L^* is the distance from the IP to QD0. To facilitate the design of the final focus, we chose $L^* = 1.5$ m.

The chromaticity correction scheme of the final focus system (FFS) had been well developed for the linear collider projects from the 1980s, such as SLC [1], NLC [2], and FFTB [3], and adopted by the circular collider projects such as in Super-B [4] and Super

KEKB [5]. CEPC adopts FFS optics similar to the linear colliders. Unlike the single pass feature in a linear collider, the final focus design of a circular collider has several specific issues.

4.3.2.1 *Final Focus Optics*

The final focus system is a telescopic transfer line, starting from the IP and includes: a final telescopic transformer (FT), chromaticity correction section in the vertical plane (CCY), chromaticity correction section in the horizontal plane (CCX) and matching telescopic transformer (MT). This is shown in Fig. 4.3.1.

The FT consists of two quadrupole doublets. The phase advance is π in the vertical plane and a bit less than π in the horizontal plane as the β_x^* is not very small. The first image point is at the end of the FT.

The CCY consists of four FODO cells with phase advance $\pi/2$ in both planes and begins with a half defocusing quadrupole.

Four identical dipoles make dispersion bumps. Starting from the image point, β_y is transformed from a value much smaller than the periodic solution to two large values at the end of first and third FODO cells. A pair of sextupoles is placed at these two peaks in β_y to compensate the vertical chromaticity generated by the final defocusing quadrupole. The geometric sextupole aberrations are cancelled by the $-\mathbf{I}$ transformation between the paired sextupoles. At the end of the CCY, we have the second image point, identical to the first.

The CCX is similar to the CCY and begins with a half focusing quadrupole. At the end of CCX, we have the third image point, also identical to the first one.

The MT consists of two quadrupole doublets. With MT, the Twiss functions are matched to the ARC section of the ring and make the total 6π phase advance of FFS.

We use the longitudinal cyclical symmetry of CCY and CCX to adjust the phase advances between the final doublet and the sextupoles to minimize second order chromaticity [6]. The chromatic functions along the final focus are shown in Fig. 4.3.2. The residual W functions are W_x=6.6, W_y=5.6 and second order dispersion is D'_x = -0.15 m.

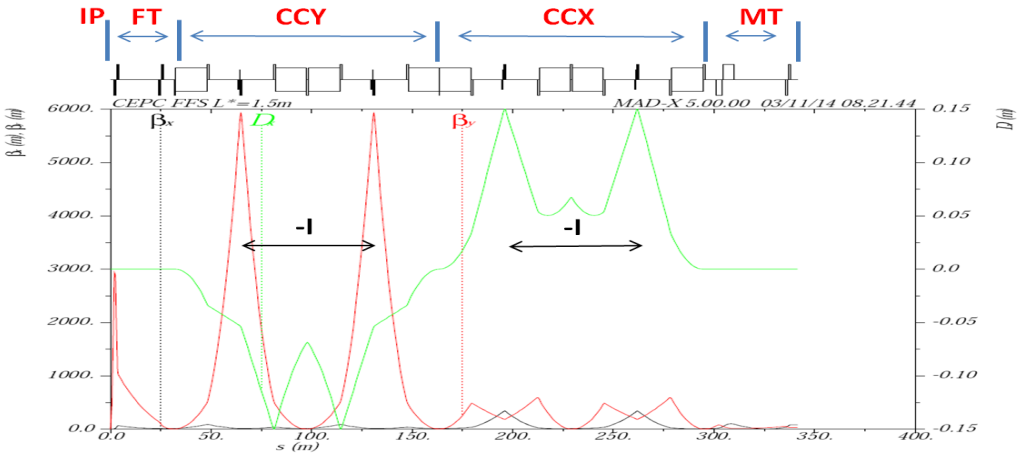

Figure 4.3.1: Lattice functions of the final focus.

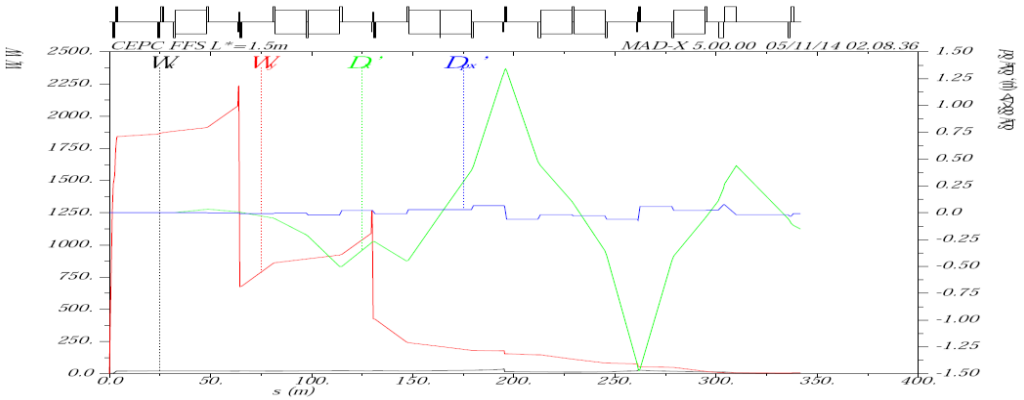

Figure 4.3.2: Chromatic functions of the final focus.

4.3.2.2 *Dynamic Aperture*

The FF was inserted into the ring by matching the Twiss functions between the FF and ARC. The Twiss functions of the whole ring are shown in Fig. 4.3.3, where the peak of β_y occurs at the two IPs. The two families of sextupoles in the ARC were re-matched to obtain as large a bandwidth as possible. The results are shown in the left hand figure of Fig. 4.3.4.

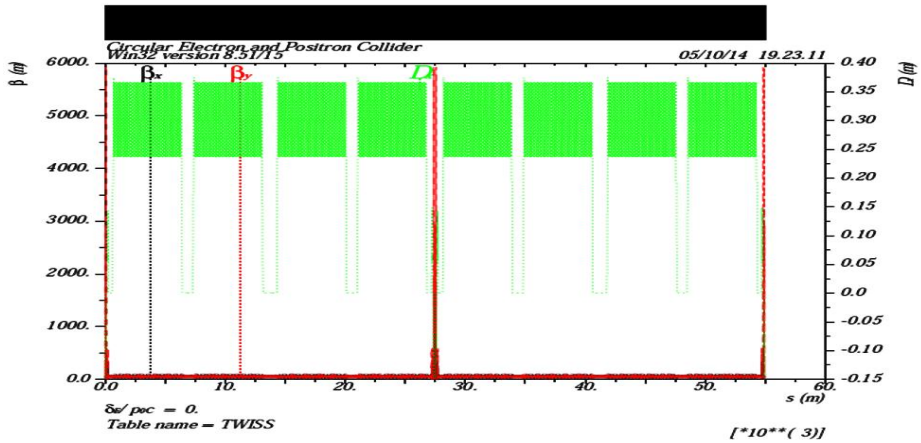

Figure 4.3.3: Lattice functions of the ring.

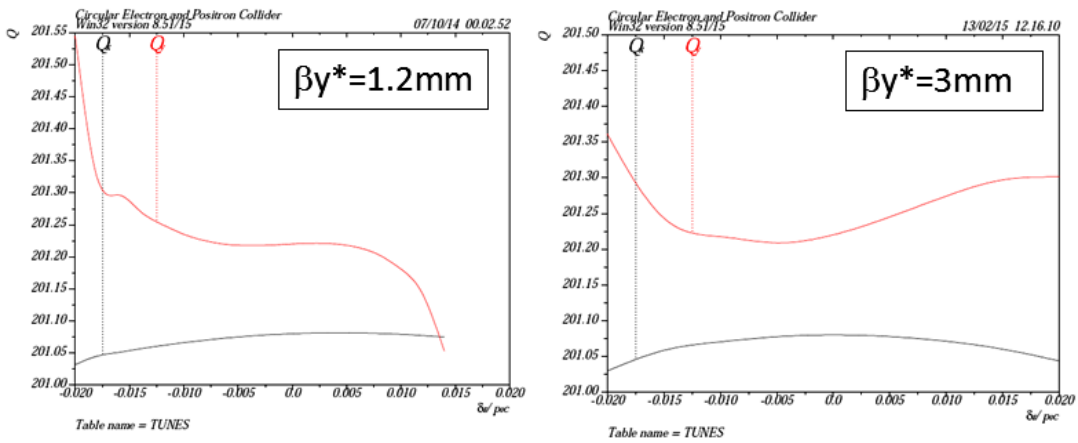

Figure 4.3.4: Tune vs. energy deviation

The dynamic aperture for the whole ring was estimated numerically with the six-dimensional tracking code SAD [8]. The particles were tracked for 240 turns corresponding to three transverse damping times. Included is synchrotron motion. Not included are radiation damping, any magnet errors, or fringe fields. The dynamic aperture is defined as the boundary between surviving and lost particles. For an on-momentum particle, the dynamic aperture is 17 σ_x (6.12 nm-rad) and 70 σ_y (0.018 nm-rad) in the horizontal and vertical planes respectively. For the off-momentum particles, the dynamic aperture decreases significantly. The results are shown in the left had figure of Fig. 4.3.5.

As shown in the beam-beam simulation [11], the luminosity will not be reduced much when β_y^* is increased from 1.2 mm to 3 mm. We also obtained a preliminary IR design for $\beta_y^* = 3$ mm by simply re-matching the final telescopic transformer and the sextupoles. The results are shown in the right hand figures of Figures 4.3.4 and 4.3.5. As expected, the dynamic aperture becomes larger though it's still small. Further optimization is underway.

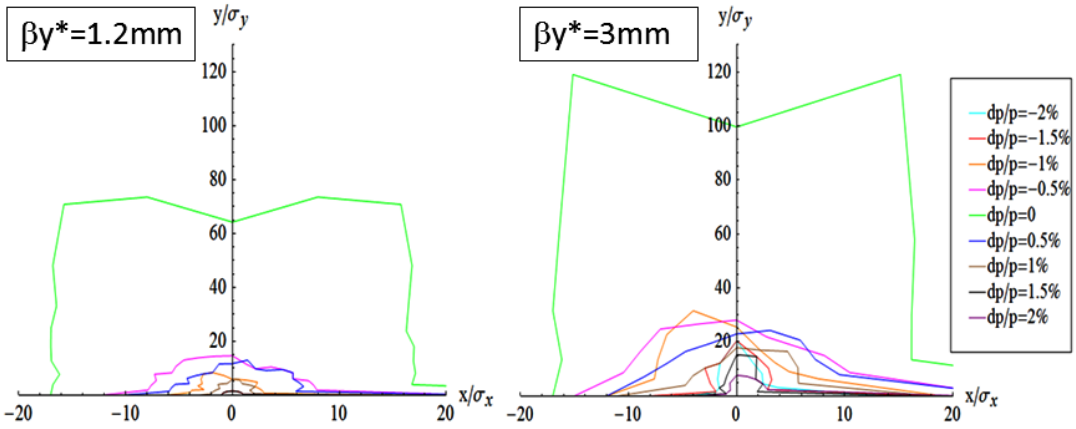

Figure 4.3.5: Dynamic aperture of the ring.

4.3.3 **Machine-Detector Interface**

4.3.3.1 ***Layout of the Interaction Region***

The interaction region of the CEPC consists of a beam pipe, surrounding silicon tracker, luminosity calorimeter and the final quadrupoles QD0 and QF1. Fig. 4.3.6 shows the preliminary layout of the interaction region.

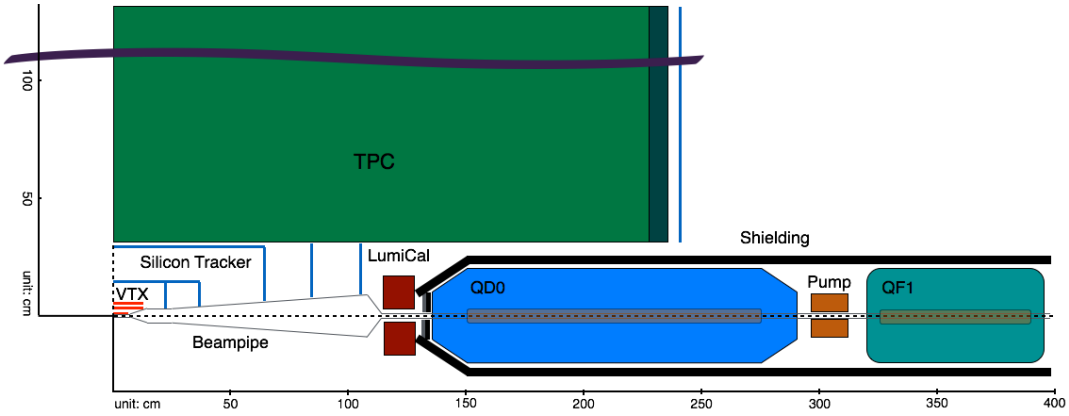

Figure 4.3.6: Interaction-region layout [9].

4.3.3.2 *Final Doublet*

The beam-stay-clear region has been determined by considering the requirements for injection [10]. It is defined as the distance between the center of the beam pipe and the outer edge of the injected beam. Vertical injection was chosen to avoid the affecting the pretzel orbit. The acceptance required for beam injection is assumed to be $2J_x = 3.5 \times 10^{-7}\text{m} \cdot \text{rad}$ for the horizontal plane and $2J_y = 7.7 \times 10^{-8}\text{m} \cdot \text{rad}$ for the vertical plane. Details of the acceptance estimate can be found in Section 4.7. With the acceptance and the Twiss functions, the beam-stay-clear region is $\sqrt{2J_x\beta_x + (D_x\sigma_E)^2}$ for the horizontal plane and $\sqrt{2J_y\beta_y}$ for the vertical plane. The beam-stay-clear region at the final doublet is shown in Fig. 4.3.7.

The inner radius of the vacuum chamber should be larger than the beam-stay-clear region. We chose 17 mm (2 mm for safety) both for QD0 and QF1. This result is 76 σ_x and 74 σ_y at QD0 and 28 σ_x and 118 σ_y at QF1, where σ denotes the dimensions of the circulating beam. The inner radius of the coil is 21 mm for the final doublet. This includes the 2 mm thickness of the vacuum chamber wall and a 2 mm installation gap between vacuum chamber and coil. The outer radius of the cryostat for the final doublet is estimated to be 200 mm which provides large enough angular acceptance for the TPC design.

Table 4.3.2 shows the parameters for the final doublet. The detailed design of these two magnets is underway

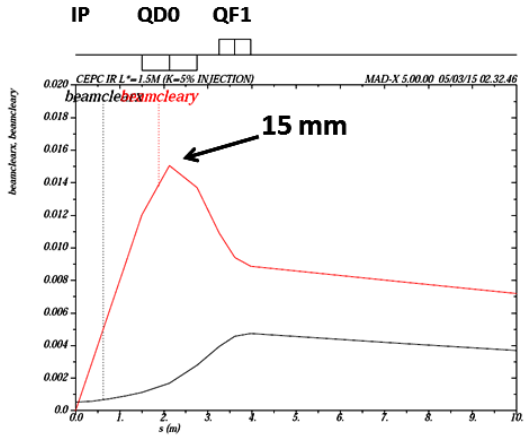

Figure 4.3.7: Beam-stay-clear region at the final doublet.

Table 4.3.2: Locations of the magnet entrance from IP, effective length, field gradients, magnet type of the final doublet, inner radius of vacuum chamber, inner radius of the coil and outer radius of the cryostat.

Magnet	z [m]	Leff [m]	Field gradient [T/m]	Type	I. R. of vac. ch. [m]	I. R. of coil [mm]	O. R. of cryostat [mm]
QD0	1.5	1.25	-300	S. C.	17	21	200
QF1	3.25	0.72	300				

4.3.3.3 *Solenoid Field Compensation*

Coupling between horizontal and vertical betatron motion will increase the vertical beam size at the IP. Coupling control is one of the key issues in high luminosity colliders. With the small vertical emittance, the coupling correction is important in the CEPC design. The solenoid field distribution along the axis is shown in Fig. 4.3.8. Work on the compensation scheme of the solenoid field is underway.

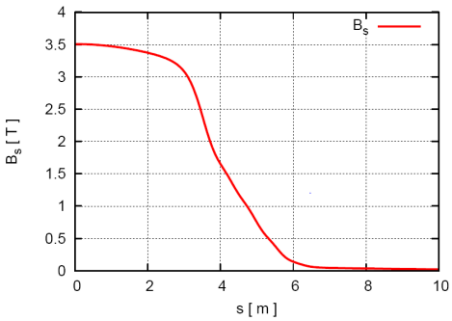

Figure 4.3.8: Solenoid field at the interaction-region.

4.3.3.4 *Synchrotron Radiation and Shielding*

The synchrotron radiation in the last bend of final focus was estimated analytically with constant beam energy and using the parameters in Table 4.3.3. The critical energy of the radiated photons is around 1 MeV and the average radiated power is 50 kW. These numbers are quite high and may make shielding difficult.

Table 4.3.3: Parameters of the last bend in the final focus.

Parameters	Value
Distance to the IP	32.5 m
Effective length	15.5 m
Bending radius	3762 m
Critical energy of the radiated photons	958 keV
Average radiation power	50 kW

4.3.4 References

1. NLC ZDR Design Group, “A Zeroth-Order Design Report for the Next Linear Collider,” SLAC Report-474, 1996.
2. J. J. Murray , K. L. Brown and T. Fieguth, “The Completed Design of the SLC Final Focus System,” SLAC-PUB-4219, Feb 1987.
3. J. Irwin, K.L. Brown, F. Bulos, D. Burke, R. Helm, G. Roy, R.D. Ruth, N. Yamamoto, K. Oide, “The optics of the Final Focus Test Beam,” Presented at the 1991 IEEE Particle Accelerator Conference, 6–9 May 1991, San Francisco, CA, USA. Publ. in Proceedings IEEE, p.2058, 1991, New York.
4. SuperB Conceptual Design Report. INFN/AE-07/2, SLAC-R-856, LAL 07-15. March, 2007.
5. Yukiyoshi Ohnishi et. al.. Accelerator design at SuperKEKB. Prog. Theor. Exp. Phys. 2013, 03A011.
6. Yunhai Cai, private communication.
7. B. W. Montague, “Linear optics for improved chromaticity correction,” CERN-LEP-NOTE-165, July 1979.
8. SAD. http://acc-physics.kek.jp/SAD/.
9. Hongbo Zhu, Detector part of CEPC pre-CDR.
10. Yukiyoshi Ohnishi, private comunication.
11. K. Ohmi, D. Shatilov, Y. Zhang. Beam-Beam Effects in the CEPC. HF2014. Oct. 9-12, 2014. Beijing, China.

4.4 Beam Instability

Interaction of an intense charged particle beam with the vacuum chamber may lead to collective instabilities. These instabilities will induce beam quality degradation or beam loss, and finally restrict the luminosity of the machine. So the study of beam instability is essential in the design of a new machine. In this section, an impedance budget is given. Based on impedance studies, beam instabilities due to single bunch and multi bunch effects are estimated. Instabilities due to interaction of the electron beam with the residual (positive) ions and instabilities from positron beam interaction with the electron cloud are also investigated.

4.4.1 Impedance Budget

The main contributions to the impedance include the RF cavities, BPMs, bellows, masks, vacuum pumps, separators, collimators, injection kickers, valves, and flanges.. Since most of the engineering design of the objects inside the vacuum are not done yet, only the RF cavities and the resistive wall impedance are considered here. A more complete impedance budget will be obtained as additional vacuum components are designed.

4.4.1.1 *RF Cavities*

A five cell superconducting RF cavity structure as shown in Figure 4.4.1 will be used in CEPC. Given a design accelerating gradient of 15.6 MV/m, 384 cavities with RF frequency of 650 MHz will be needed.

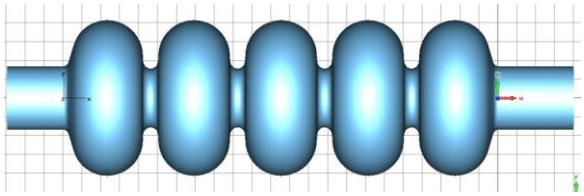

Figure 4.4.1: Five cell superconducting RF cavity model.

Since the RF cavities are cylindrically symmetric, the impedance and wake are calculated with the code ABCI [1]. The short range wake at nominal length is shown in Figure 4.4.2. We fit the bunch wake with the analytical model

$$W(s) = -Rc\lambda(s) - Lc^2\lambda'(s), \qquad (4.4.1)$$

where L and R are effective inductance and resistance, respectively. As the cavity is capacitive, the fitted L has no physical meaning. The calculated loss factor for one RF cavity is k_l = 2.328 V/pC.

4.4.1.2 *Resistive Wall*

The resistive wall wake for a Gaussian bunch in a cylindrical beam pipe is calculated analytically [2]

$$W(s) = \frac{cl}{8\sqrt{2}\pi a}\frac{1}{\sigma_z^{3/2}}\sqrt{\frac{Z_0}{\sigma_c}}f(s/c) \qquad (4.4.2)$$

where $f(x) = \sqrt{|x|^3}e^{-x^2/4}\left(I_{1/4} - I_{-3/4} \pm I_{-1/4} \mp I_{3/4}\right)\Big|_{x^2/4}$, and $I_n(x)$ is the modified Bessel function of the first kind.

Aluminum beam pipes will be used in CEPC. The beam pipe has an elliptical cross section with half heights of a_x=52 mm and a_y=28 mm. We use the vertical aperture in the calculation and obtain the longitudinal wake as shown in Fig 4.4.2.

4.4.1.3 *Impedance Budget*

The wake contributions of different impedance objects at nominal bunch length are shown in Figure 4.4.2. Table 4.4.1 lists the impedance budget of the objects considered.

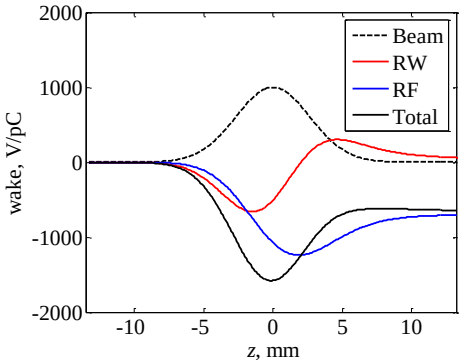

Figure 4.4.2: Longitudinal short range wake of different vacuum components.

Table 4.4.1: Summary of the impedance budget

Objects	N_{obj}	R, kΩ	L, nH	k_{loss}, V/pC	Z_{eff}, Ω
RF cavities	384	28.1	–	893.9	–
Resistive wall	–	9.5	124.4	301.3	0.0044
Total		37.6	124.4	1195.2	0.0044

4.4.2 **Single-bunch Effect**

4.4.2.1 ***Bunch Lengthening***

Interaction of the beam with broadband impedance can change the bunch length and longitudinal distribution due to potential well distortion. The longitudinal bunch density distribution is obtained by numerically solving the Haissinski equation [3,4].

The Pseudo-Green function wake with bunch length of 0.5 mm is used in the instability calculation. The wake potential and the longitudinal bunch density with the influence of the wake are shown in Figure 4.4.3. The bunch is shortened due to the capacitive property of the RF cavity. Here, only the resistive wall and RF cavity impedances are considered in the calculation.

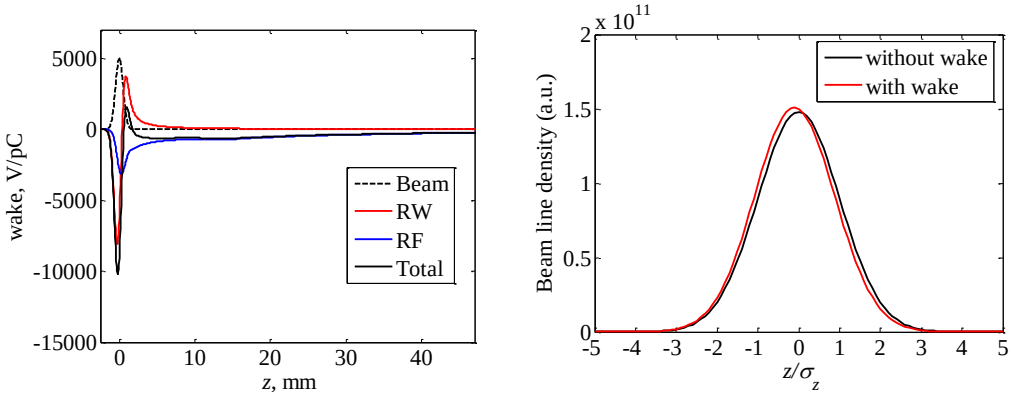

Figure 4.4.3: Pseudo-Green function wake (left) and steady-state bunch shape (right)

4.4.2.2 ***Microwave Instability***

The average threshold current for the longitudinal microwave instability is estimated according to the Boussard or Keil-Schnell criterion [5,6],

$$I_{th} = \frac{\sqrt{2\pi}\alpha_p \frac{E}{e}\sigma_\delta^{\,2}\sigma_z}{R\left|\frac{Z}{n}\right|_{eff}}, \qquad (4.4.3)$$

For the nominal design current, the threshold impedance is about 0.026 Ω.

4.4.2.3 ***Transverse Mode Coupling Instability***

The threshold bunch current for the transverse mode coupling instability is estimated using eigen mode analysis. Figure 4.4.4 shows the calculated dependence of the frequency shift of the head-tail modes with increase of beam current. It is shown that the

threshold bunch current for the TMCI is about 4 mA. Here only the resistive wall impedance is considered.

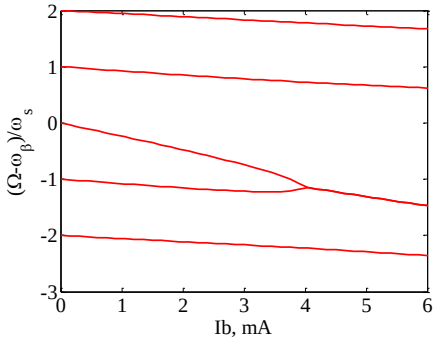

Figure 4.4.4: Dependences of the head-tail mode frequencies on the beam current.

4.4.2.4 *Tune Shift due to Transverse Impedance*

The tune operating point of the CEPC is (179.08, 179.22), which is slightly above integer in the horizontal plane. Tune shift due to transverse impedance is negative. Therefore, the beam could become unstable at lower current (or lower impedance) than that for the transverse mode coupling instability.

Tune shift is evaluated by the formula for effective impedance,

$$\Delta\nu_\beta = -i\frac{N_e r_e}{4\pi^{3/2}\gamma}\frac{L}{\nu_\beta \sigma_z}\frac{Z_{\text{eff}}}{Z_0} \tag{4.4.4}$$

$$Z_{\text{eff}} = \sum Z(\omega')h_0(\omega'-\omega_\xi)/\sum h_0\left(\omega'-\omega_\xi\right) \tag{4.4.5}$$

The tune shift is given by

$$\Delta\nu_\beta = -0.066 \times \frac{N_e}{3.77\times 10^{11}} Z_{\text{eff}}\left(\frac{M\Omega}{m}\right) \tag{4.4.6}$$

The effective impedance for $\Delta\nu_\beta = 0.08$ is $Z_{\text{eff}} = 1.2$ MΩ/m. When the tune approaches an integer, the tune variation is larger than that given by the above equation. Threshold of the effective impedance is smaller than 1.2 MΩ/m as shown in the following simulation. The effective impedance is 36 or 120 kΩ/m for KEKB or LEP, respectively, where bunch shape is taken into account. If it scales with the circumference, the effective impedance is 650 or 240 kΩ/m.

4.4.2.5 *Simulation of Transverse instability*

Simulation including the transverse impedance has been performed. The simulation can confirm the tune shift and transverse mode coupling.

First the impedance source is located at one position in the ring. The same strength impedances are put in both horizontal and vertical planes. Figure 4.4.5 shows the Fourier spectra of horizontal and vertical beam motion. Z_{eff} is scanned over the range 320-512 kΩ/m. The beam becomes unstable at 570 kΩ/m in the horizontal. The horizontal plot (left hand figure) indicates that the horizontal tune crosses the integer 179.0 at 570 kΩ/m. This instability is due to an integer resonance, but not mode

coupling. The horizontal tune shift is twice or more larger than the analytical estimate and the vertical tune shift, because the horizontal tune is close to an integer

To simulate mode-coupling instability, impedance sources are distributed at 8 positions with equal spacing. Figure 4.4.6 shows the Fourier spectra of horizontal and vertical beam motion. For both planes, betatron and synchrotron side band tunes merge at Z_{eff} = 1.5 MΩ/m, and the beam becomes unstable. The threshold agrees very well with the analytical estimate. The threshold impedance is much larger than the estimated impedance.

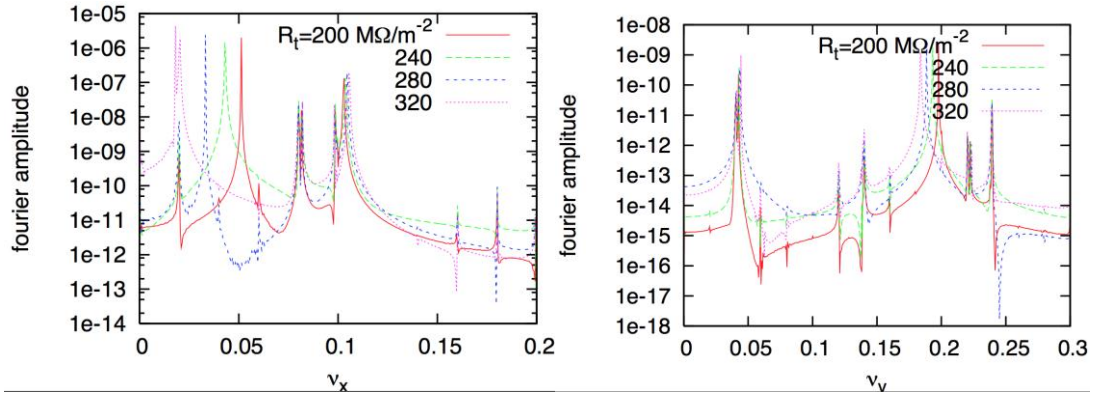

Figure 4.4.5: Beam spectra for various values of Rs. The impedance source is located at one position in the ring. Left and right plots are for horizontal and vertical.

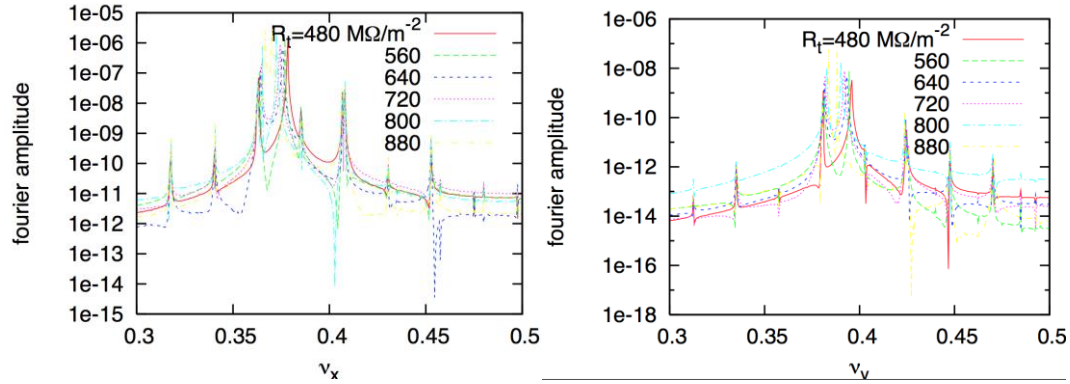

Figure 4.4.6: Beam spectra for various values of Rs. Impedance sources are located at 8 positions uniformly around the ring. Left and right plots are for horizontal and vertical.

4.4.2.6 *Beam Tilt due to Transverse Wake Fields*

When a beam passes through transverse impedance, the tail particles will receive transverse kicks and induce bunch shape distortion. The transverse kick experienced by a particle located at longitudinal position *z* is given by [3]

$$\Delta y'(z) = \frac{Ne^2}{E}\int_0^\infty dz'\rho(z'+z)W_\perp(y_b, z') \qquad (4.4.7)$$

This will lead to a transverse displacement of the bunch tail at IP [7,8]

$$\Delta y = \sqrt{0.5\beta_y^*\beta_y}\,\Delta y', \qquad (4.4.8)$$

where β_y^* and β_y are the vertical beta function at the IP and at the location of the impedance, respectively.

Considering a pretzel orbit of 5 mm and the impedance from one RF cavity, the maximum kick angle is around 1 nrad for each cavity, and the corresponding displacement at the IP is 0.19 nm. Since there are 384 cavities located in 8 positions around the ring, the displacement at the IP is $48\sqrt{8}\times0.19$ nm=25.6 nm.

4.4.2.7 *Coherent Synchrotron Radiation*

In evaluating the coherent synchrotron radiation (CSR) effect, the beam is assumed to be moving in a circle of radius ρ between two parallel plates at locations $y = \pm h$. From linear theory, the condition for the onset of coherent synchrotron radiation is given by the threshold current S_{th}, which is given as a function of shielding parameter Π [9]

$$S_{th} = 0.50 + 0.12\Pi \qquad (4.4.9)$$

where

$$S = \frac{r_e N_b \rho^{1/3}}{2\pi\nu_s\gamma\sigma_\delta\sigma_z^{4/3}}, \quad \Pi = \frac{\sigma_z\rho^{1/2}}{h^{3/2}}. \qquad (4.4.10)$$

The CEPC design parameters give Π=9.2, which means CSR is well shielded. The yield threshold bunch population is about 5.0×10^{12}, which is much higher than the designed value of 3.7×10^{11}.

4.4.3 **Multi-bunch Effect**

4.4.3.1 *Transverse Resistive Wall Instability*

One of the main origins for exciting the transverse multi-bunch instability is due to the interaction of the beam with the resistive wall impedance. Considering n_b uniformly distributed bunches, the rise time of the transverse multi-hunch instability can be estimated by [3]

$$\frac{1}{\tau_\perp} = \frac{n_b I_b c}{4\pi(E/e)\nu_{x,y}} \sum_{p=-\infty}^{\infty} e^{-(\omega_p-\xi\omega_0/\alpha_p)^2\sigma_\tau^2}\,\mathrm{Re}\,Z_\perp(\omega_p), \qquad (4.4.11)$$

where $\omega_p = (pn_b+\mu+\nu_\beta)\omega_0$. Figure 4.4.7 shows the growth rate of the transverse resistive wall instability with different mode numbers. We can see that the rise time of the most dangerous mode is about 0.3 s with mode number μ=20. The rise time is much higher than the transverse radiation damping rate.

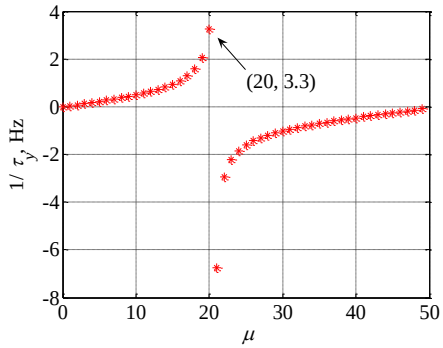

Figure 4.4.7: Resistive wall instability growth rate versus oscillation mode number.

4.4.3.2 *Coupled Bunch Instability Induced by RF HOM's*

Another dominant contribution to the coupled bunch instability is the higher order modes (HOM) of the accelerating cavities. To keep the beam stable, the radiation damping time should be less than the rise time of any of the oscillation modes. The threshold for the longitudinal impedance is estimated as shown in Figure 4.4.8. The threshold for the transverse impedance is 9.5 MΩ/m.

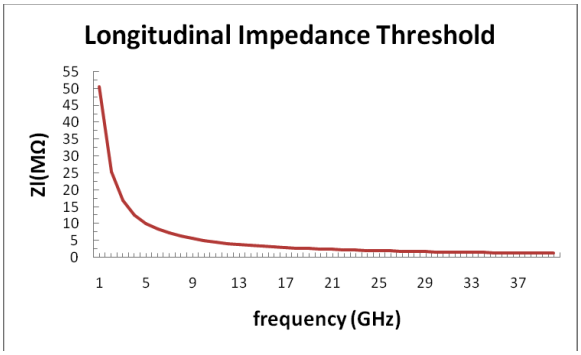

Figure 4.4.8: Longitudinal impedance threshold of the RF HOM's.

4.4.4 **Electron Cloud Instability**

The threshold value of the volume density of the electron cloud for the head-tail instability can be estimated by [10,11]:

$$\rho_{e,th} = \frac{2\gamma\nu_s\omega_e\sigma_z / c}{\sqrt{3}KQr_0\beta L} \qquad (4.4.12)$$

where $K = \omega_e\sigma_z/c$, $Q = \min(Q_{nl}, \omega_e\sigma_z/c)$, Q_{nl} depends on the nonlinear interaction, and ω_e the electron oscillation frequency.Here, we take $Q_{nl} = 7$ for analytical estimation, and obtain that the threshold density for the single bunch instability is 1.1×10^{12} m^{-3}.

For the multi-bunch instability, the electron cloud is considered as a rigid Gaussian beam with the chamber size. The characteristic frequency is expressed by

$$\omega_{G,y}^2 = \frac{2\lambda_b r_e c^2}{(\Sigma_x + \Sigma_y)\Sigma_y} \qquad (4.4.13)$$

where Σ_x and Σ_y are horizontal and vertical electron cloud sizes, and $\Sigma_{x(y)} >> \sigma_{x(y)}$.The phase angle between adjacent bunches is $\omega_G L_{sp}/c$ = 21.2, which means that the electrons will not accumulate and the multipacting effect is low due to the large bunch spacing.

4.4.5 **Beam Ion Instability**

In the electron ring, instabilities can be excited by residual gas ions accumulated in the potential well of the electron beam. With uniform filling, the ions with relative molecular mass greater than $A_{x,y}$ will be trapped

$$A_{x,y} = \frac{N_b r_p S_b}{2(\sigma_x + \sigma_y)\sigma_{x,y}}. \qquad (4.4.14).$$

Figure 4.4.9 shows the critical mass number $A_{x,y}$ along the ring. As the threshold is quite high, the ions will not be trapped by the beam.

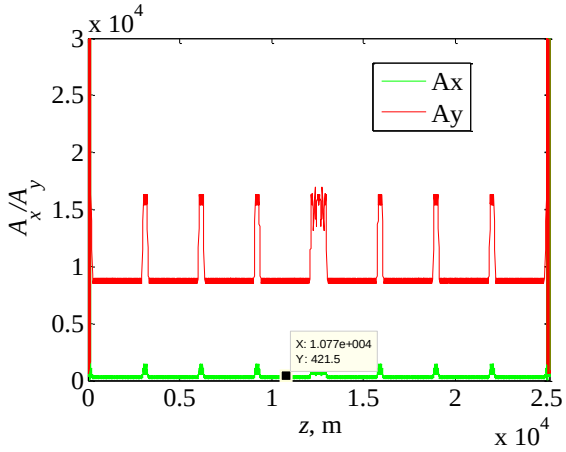

Figure 4.4.9: Critical mass number along half of the ring.

Fast beam ion instability is a transient beam instability excited by the beam generated ions accumulated in a single passage of the bunch train. The phase angle between adjacent bunches is $\omega_i L_{sep}/c$=40. So the ions will not accumulate due to the overfocus inside the bunch train.

4.4.6 **References**

1. abci.kek.jp/abci.htm.
2. A. Wu Chao, M. Tigner, “Handbook of Accelerator Physics and Engineering”, World Scientific, 1999.
3. A. Wu Chao, “Physics of Collective Beam Instabilities in High Energy Accelerators”, John Wiley & Sons, Inc., 1993.
4. J. Haissinski, Nuovo Cimento 18B, 72, 1973.
5. D. Boussard, CERN II/RF/Int. 75-2, 1975.
6. E. Keil and W. Schnell, CERN ISR-TH-RF 69/48, 1969.
7. A. W. Chao and S. Kheifets, SLAC-PUB-3052, 1983.
8. D. Zhou, K. Ohmi, A. W. Chao, IPAC2011, p.601~602, 2001.
9. K. Bane, Y. Cai and G. Stupakov, PRST-AB 13, 104402 , 2010.
10. K. Ohmi and F. Zimmermann, PRL, 85, 3821, 2000.
11. H. Fukuma, ECLOUD’12, pp.27-30, 2012.

4.5 Beam-Beam Effects

For a high energy machine such as CEPC, the power consumption due to synchrotron radiation is limited, which therefore limits the beam current. SR is also helpful since it damps oscillations and helps to weaken beam blowup. When the beam energy reaches 120 GeV, the damping time is less than 100 turns which is very helpful for suppression of instabilities, but it also means the energy change contributed by SR is about 1% per turn, which may exceed the momentum acceptance of the lattice. Also of importance is beamstrahlung, radiation excited by the beam-beam force. The radiation will blow up the energy spread, and then lengthen the bunch due to synchrotron oscillations. The other problem is that the beamstrahlung may reduce the lifetime due to the long tail of the photon spectrum.

All beam-beam simulation tools take nominal parameters as input and produce dynamical quantities as output. The only way to arrive at a specification of nominal beam parameters is to proceed by iteration. The basic strategy is to choose values for the nominal quantities to achieve a certain (nominal) luminosity, and then to verify these by simulations. If the dynamical results are substantially different from the nominal expectations, we change the nominal parameters and try again until an acceptable solution is found.

The beam-beam studies carried out to date are summarized here. Our priority is to demonstrate the feasibility of attaining or exceeding a short-time average luminosity of $2\times10^{34}\text{cm}^{-2}\text{s}^{-1}$. In this section, we present one set of parameters. This solution is not necessarily unique or optimal, but it is an existence proof that this luminosity is achievable. The short-time-average luminosity is determined by the dynamics of the beam core, while the beam lifetime is determined by the long-time dynamics of the tails of the beam. High peak luminosity is a necessary but not sufficient condition for good average luminosity. The key figure-of-merit for CEPC (or any other particle “factory”) is high integrated luminosity. This implies that a proper design must have good operational reliability and high average luminosity. This last requirement implies high peak luminosity, long beam lifetime, and the capability for rapid and frequent injection; the first two requirements are almost always in conflict, and the lifetime must be consistent with injection capability.

4.5.1 **Simulation Codes**

4.5.1.1 ***LIFETRAC***

LIFETRAC [4] developed by Dmitry Shatilov (BINP) since 1995, was used for design and performance improvements at VEPP-4 (BINP), DAFNE (INFN/LNF), VEPP-2000 (BINP), KEKB (KEK). It could determine the equilibrium distribution with radiation damping, quantum excitation and beam-beam interaction. The beamstrahlung model in the beam-beam simulation is introduced in [3]. It is noteworthy that beamstrahlung simulations are not affected by the number of slices – if the slices are large enough to correctly represent the opposite bunch. Since it is a weak-strong code, in order to be more self-consistent, a quasi-strong-strong method is used, where in repeated iterations the strong bunch’s beam parameters are assigned the geometric mean of strong and weak bunch's equilibrium value after collision. In the end, the strong bunch's parameters are the same as that of the weak bunch's equilibrium value.

4.5.1.2 *BBWS/BBSS*

These two codes were developed by Kazuhito Ohmi (KEK). BBWS is a weak strong code, and BBSS is a strong-strong code. The code was first developed as a 2-D code [5], and then extended to consider the finite bunch length effect by slicing the bunch in the longitudinal direction [6]. The codes helped make a decision to move the horizontal tune closer to half integer in the early commissioning of KEKB and increase the peak luminosity. Another big simulation success was to make it clear how the general chromaticity affects the luminosity in KEKB with a crab cavity [7].

Synchrotron radiation due to the beam-beam interaction is based on ordinary synchrotron radiation excitation with Gaussian fluctuations. However, the photon spectrum distribution is more complicated. The simulated photon spectrum is compared with CAIN and Guinea-PIG, and they agree well with each other. The beam equilibrium distribution is compared between the two models of beamstrahlung and the rms value is the same. The only difference is that there is a longer tail for the exact model. There is also no difference for the luminosity. It seems that the exact model is only required for estimates of lifetime [8].

Even the weak-strong model is not self-consistent; the bunch length is self-consistent for the beamstrahlung in the BBWS code.

Beamstrahlung causes energy spread, which results in bunch lengthening. It is assumed that the intensity of both beams is the same; thus bunch lengthening due to beamstrahlung is also the same. The bunch length of the weak beam is calculated turn-by-turn, and averaged over 100 - 1000 turns. The bunch length of the strong beam is changed every 100 - 1000 turns. The bunch length is calculated turn-by-turn in the strong-strong simulation.

The lifetime estimation method is also implemented in BBWS. One can get the equilibrium distribution with many turns of tracking data without any aperture limit. The incident flow across the aperture is evaluated by radiation damping. It is assumed the outgoing flow is the same as the incident flow; then the lifetime can be determined [8]. It has been shown that the lifetime estimated by damping flow agrees with that given by beam loss simulation.

4.5.1.3 *IBB*

The IBB code is a strong-strong code developed by Yuan Zhang at IHEP [9]. It is mainly used for BEPCII. Its model is similar to that of BBSS, but it does not take the beamstrahlung effect into account. In the beam-beam simulation for CEPC, it is only used to crosscheck the BBSS result.

4.5.2 **Simulation Results**

4.5.2.1 *Choice of Working Point*

Since the working point is very important for luminosity optimization, a tune scan is necessary and the result obtained by BBWS is shown in Figure 4.5.1, where the highest luminosity per IP is about $2 \times 10^{34} cm^{-2} s^{-1}$.

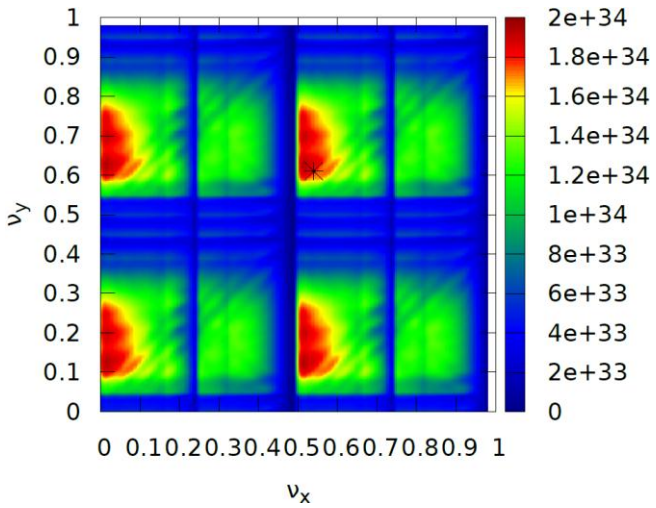

Figure 4.5.1: Luminosity per IP versus the transverse tune of half ring. The star mark is positioned at (0.54, 0.61). BBWS.

The luminosity behaviour is also checked with the strong-strong simulation (BBSS) at some working points, points (see Figure 4.5.2). It seems that (0.54, 0.61) for the half ring is a good choice, the luminosity per IP is about $1.7\times 10^{34} cm^{-2} s^{-1}$.

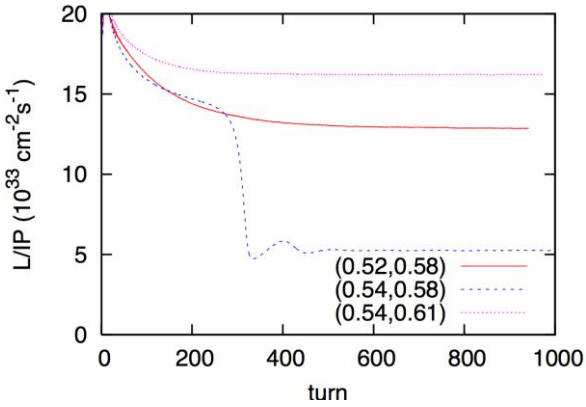

Figure 4.5.2: Luminosity behavior at different working points. BBSS.

4.5.2.2 *Luminosity and Lifetime*

How the luminosity, beam distribution and lifetime vary with the bunch current is very important and will help evaluate if the design goal are achievable.

For a flat beam, the achieved beam-beam parameter can be defined as

$$\xi_y = \frac{2 r_e \beta_y^0}{N\gamma} \frac{L}{f_0} \qquad (4.5.1)$$

where r_e is the electron classical radius, β_y^0 the nominal vertical beta function at the IP, N the bunch population, f_0 the revolution frequency, and L is the bunch luminosity. Figure 4.5.3 shows the luminosity and beam-beam parameter versus bunch current. It is shown that the luminosity with the designed bunch current is about $1.7\times 10^{34} cm^{-2} s^{-1}$. The effective beam-beam parameter is only about 0.045 with design parameters and the saturation is very clear near the design bunch current. The bunch length is nearly 3 times β_y^*, which causes a strong hourglass effect.

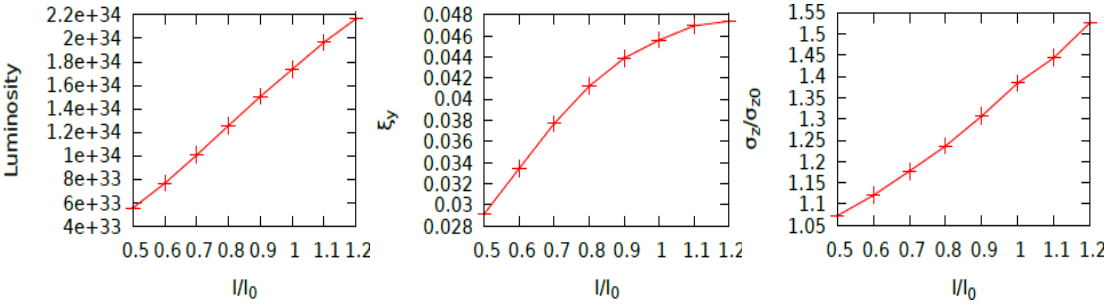

Figure 4.5.3: Luminosity/effective beam-beam parameter/bunch lengthing versus the bunch current. (LIFETRAC simulation).

Taking into account the limited momentum acceptance, the lifetime would be reduced by the larger energy spread, especially the long tail of beamstrahlung photon spectrum. The beamstrahlung lifetime is shown in Figure 4.5.4. LIFETRAC shows that it is about 85 minutes with momentum acceptance 0.02 at design bunch current. The BBWS's result is about 3 times longer.

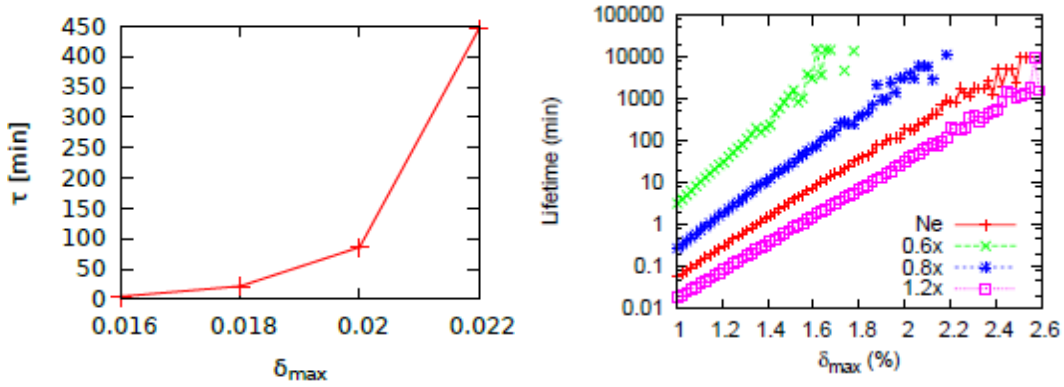

Figure 4.5.4: Beamstrahlung lifetime. The left hand figure is obtained by LIFETRAC. The right hand figure is obtained from equilibrium distribution with BBWS for different bunch populations. The horizontal axis is the momentum acceptance.

The transverse dynamic aperture also reduces the lifetime. Figure 4.5.5 shows the simulation result in the vertical direction. The lifetime is about 250/20 min for 50/40 σ_y by LIFETRAC. The BBWS result is about 6 times longer.

Figure 4.5.6 shows the beam halo distribution. There is no long tail in the horizontal direction, so we are only concerned with the vertical and longitudinal limitations. According to the LIFETRAC simulation, momentum acceptance 0.02 (85 minutes) and vertical aperture $50\sigma_y$(250 minutes) is required. The BBWS result is more optimistic for lifetime. The difference may come from:

- Statistical noise. The particle-turns $10^{10}/2$ are tracked in BBWS, and $1.5\times 10^{9}/2$ are tracked in LIFETRAC respectively.
- The algorithm for the lifetime estimation.
- Both codes use the quasi-strong-strong model in the lifetime simulation, but the details may be different.

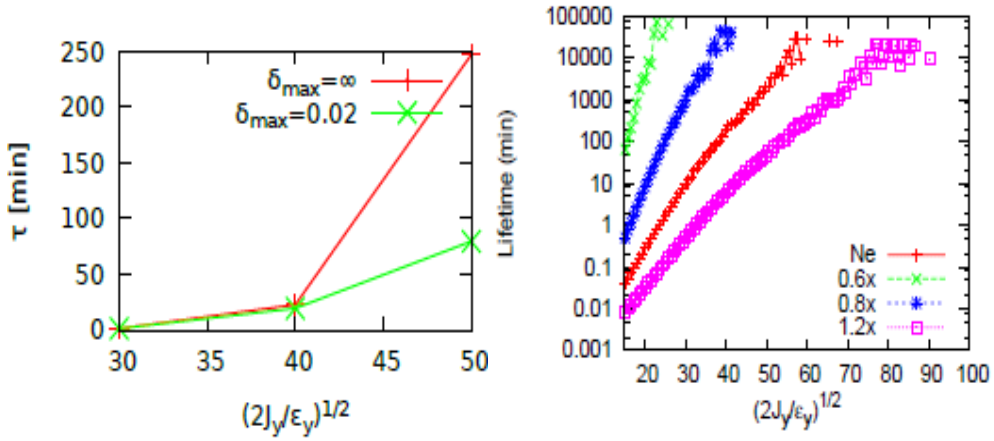

Figure 4.5.5: Lifetime limited by vertical aperture. The left hand figure is obtained by LIFETRAC for the design bunch current. The right hand figure is obtained from the equilibrium distribution with BBWS for different bunch populations.

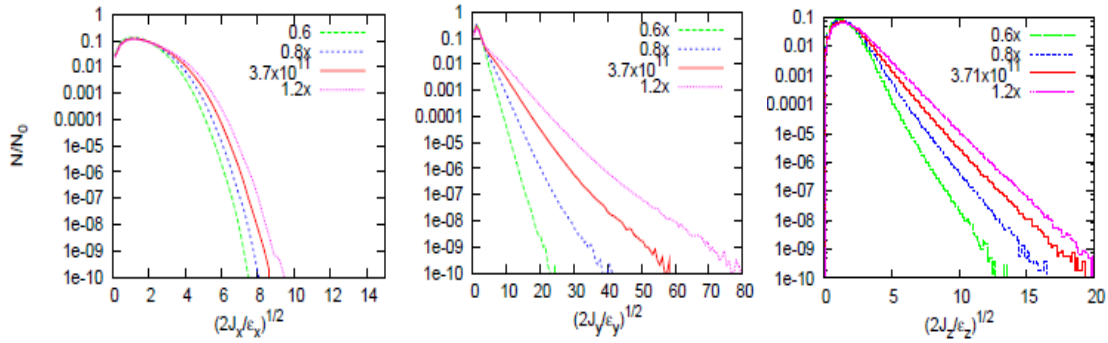

Figure 4.5.6: Beam halo distribution obtained by BBWS.

4.5.3 **Dynamic Effects**

In linear approximation, the dynamics can be treated as a 1-D system. In the weak-strong picture, the new β-function at the IP [10] is given by:

$$\beta = \frac{\beta_0}{\sqrt{1 + 4\pi\xi_0 \cot\mu_0 - 4\pi^2\xi_0^2}} \qquad (4.5.2)$$

and the dynamic emittance by:

$$\epsilon = \frac{(1 + 2\pi\xi_0 \cot\mu_0)\epsilon_0}{\sqrt{1 + 4\pi\xi_0 \cot\mu_0 - 4\pi^2\xi_0^2}} \qquad (4.5.3)$$

where ξ_0 and β_0 are the nominal values. We could estimate the strong-strong picture by iteration. It should be noted that ξ_0 would be recalculated using the dynamic beta and emittance. It is concluded that β becomes 0.28 m from 0.8 m, and ϵ becomes 12.1 nmrad from 6.79 nmrad. The equilibrium ξ_0 becomes 0.16 from 0.10.

We've obtained β just at the IP, and could continue to calculate the Twiss function just after the IP using the transfer matrix of a half beam-beam kick map

$$\begin{bmatrix} 1 & 0 \\ -\frac{2\pi\xi_0}{\beta_0} & 1 \end{bmatrix} \qquad (4.5.4)$$

It is found that $\alpha_+ = 0.84$ and $\beta_+ = 0.28$ m just after the IP. That is to say the new waist is about 0.14 m away from the IP and β is about 0.164 m at this position. One needs to be careful to check that the physical aperture is large enough at each critical position. Since L^*=1.5 m, it can be estimated that the dynamic beam size is about 2.3 times the nominal value. As we've shown there is no long tail in the horizontal direction; the aperture will be about $20\sigma_{x,0}$ at the final focus magnet.

These may be overestimates since a linear model is used and it is valid only for small oscillation particles.

When dynamic effects are included, the beam-beam simulation results shown in Figure 4.5.7 indicates the luminosity dependence on β_y^* is quite different from the geometric luminosity. When β_y^* is increased from 1.2 mm to 3 mm, the geometric luminosity (the light blue line) decreases as expected. But the luminosity from beam-beam for β_x = 0.8 m (the red line) is increased to 2×10^{34} $cm^{-2}s^{-1}$ because the actual β_x from dynamic effects is reduced significantly

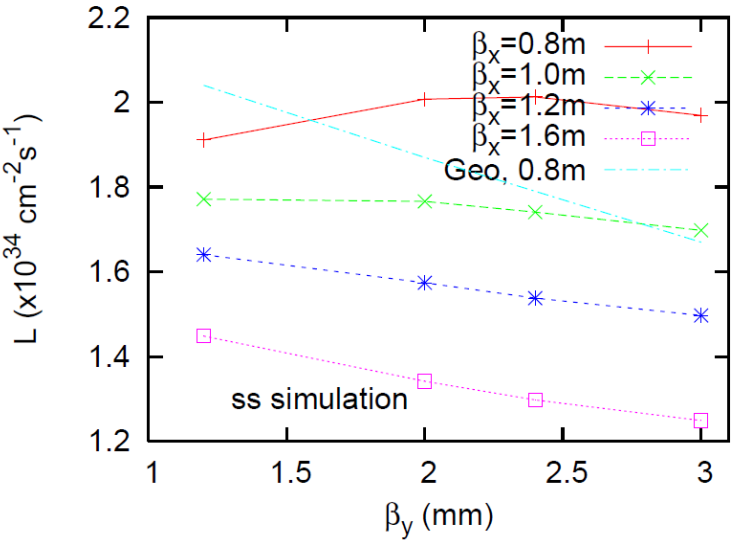

Figure 4.5.7: Luminosity dependence on β_y^* for different.values of β_x.

4.5.4 Summary

The peak luminosity can reach $2\times10^{34}cm^{-2}s^{-1}$ /IP based on beam-beam simulations. To ensure that the beam lifetime is reasonable, a dynamic aperture $20\sigma_x \times 50\sigma_y$ with δ_{max} = 0.02 is required.

4.5.5 References

1. J.E.Augustin, N.Dikansky Y.Derbenev, J.Rees, B.Richter, A.Skrinsky, M.Tigner and H.Wiedemann, "Limitations on Performance of e+ e- Storage rings and Linear Colliding Beam Systems at High Energy", 1st Workshop on Possibilities and Limitations of Accelerators and Detectors 15-21 Oct 1978. eConf C781015, (1978) 009.
2. V.I. Telnov, "Restriction on the Energy and Luminosity of e+e- Storage Rings due to

Beamstrahlung", PRL 110, 114801 (2013)
3. A. Bogomyagkov, E. Levichev, and D. Shatilov, "Beam-beam effects investigation and parameters optimization for a circular e+e− collider at very high energies", Phys. Rev. ST Accel. Beams 17, 041004 (2014)
4. D. Shatilov, "Beam-beam simulations at large amplitudes and lifetime determination", Particle Accelerators, 52, pp.65-93 (1996)
5. K. Ohmi, "Simulation of beam-beam effects in a circular e+e- collider", Phys. Rev. E, 62, pp. 7287-7294 (2000)

4.6 Synchrotron Radiation

4.6.1 **Introduction**

Synchrotron radiation (SR) is electromagnetic radiation emitted by charged particles when they move at close to the speed of light in a magnetic field. In CEPC, 120 GeV electrons and positrons pass through dipole and focusing (quadrupole) magnets and are always accompanied by the SR. The SR spectrum extends from the region of visible light through the energy range of ordinary diagnostic X-rays (hundreds of keV) up to ten MeV. The SR emitted power per unit length is huge, up to 1 kW/m. Hence, SR will cause very high radiation dose rates in many accelerator components and also in the air in the tunnel. This will cause heating of the vacuum chamber, radiation damage to machine elements, formation of ozone and nitrogen oxides in the air, and further lead to corrosion of machine components. At present, two vacuum chambers are proposed: (1) aluminum covered by lead shielding and (2) fabricated entirely of copper. Therefore, it is essential to calculate the relevant parameters for these two choices, such as energy deposition, energy spectrum in all parts of the tunnel, which can then be used to calculate heat, dose rate, and the amount of harmful gases.

4.6.2 **Analysis of Synchrotron Radiation Source**

The SR spectrum depends on the charge, the mass and energy of the particle and on the bending radius. When determining the effects of SR, there are two important parameters: the radiated power per unit beam path and the critical energy. The power of the synchrotron radiation emitted by electrons and positrons per unit length is given by the simple expression:

$$\mathrm{P(W/m)} = 14.08\frac{\mathrm{E(GeV)^4 I(mA)}}{\rho(\mathrm{m})^2} \qquad (4.6.1)$$

where P is the synchrotron power loss in W/m, E the energy of electrons and positrons in GeV, I the current of the circulating particles in mA and ρ the bending radius in meters.

The critical energy of the spectrum divides the emitted radiation power in two halves, defined by the following expression:

$$\mathrm{E_c(keV)} = 2.218\frac{\mathrm{E(GeV)^3}}{\rho(\mathrm{m})} \qquad (4.6.2)$$

where E_C is the critical energy in keV.

The energy spectrum can be calculated by the following formula:

$$S\left(\frac{\omega}{\omega_c}\right) = \frac{9\sqrt{3}}{8\pi}\frac{\omega}{\omega_c}\int_{\omega/\omega_c}^{\infty} K_{5/3}(\eta)\, d\eta \qquad (4.6.3)$$

where ω is the angular frequency of the synchrotron radiation photon in rad/s, ω_c the angular frequency of the critical energy photon in rad/s, S the relative share of spectrum at different frequencies, and K is the Bessel function.

For the 992 magnets in the CEPC main ring the bending angle is given. The radiation is emitted in a cone with half angle 1/γ, which contains 42.5% of the emitted power. γ can be expressed as:

$$\gamma = \frac{E_e}{mc^2} = 1957E_e(GeV) \qquad (4.6.4)$$

Table 4.6.1: Synchrotron radiation parameters

Synchrotron radiation parameters			values
Beam energy	E	GeV	120
Beam current	I	mA	16.60
Bending radius	ρ	m	6094
Power per unit length	P	W/m	1305.06
Critical energy	E_c	keV	628.93
Bending angle	θ	mrad	3.1669
Solid degree	φ	μrad	4.2582

According to Formula 4.6.3, if the photon energy is lower than 100 keV, the following expression will give the energy spectrum.

$$S\left(\frac{\omega}{\omega_c}\right) = 1.333\left(\frac{\omega}{\omega_c}\right)^{1/3} \qquad (4.6.5)$$

Through integration of the above formula and calculation using Formula (4.6.3), there are only a small number of photons at low energy compared to the total number of photons. These photons contribute little to the total heat and dose due to their low energy. The number of photons decreases with energy when the photon energy is lower than 100 keV and only contribute to heat in the vacuum chamber. The 1305.06 W/m power of synchrotron radiation is entirelycontributed by energy above 200 keV and is responsible for heat and dose in the air. In this situation, calculation of heat and dose which are harmful to equipment would be conservative.

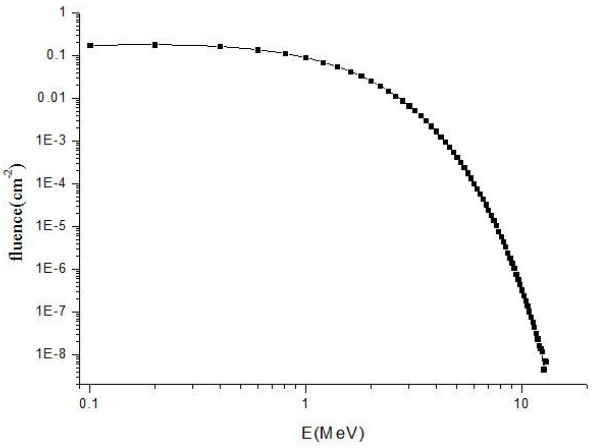

Figure 4.6.1: The photon spectrum of synchrotron radiation

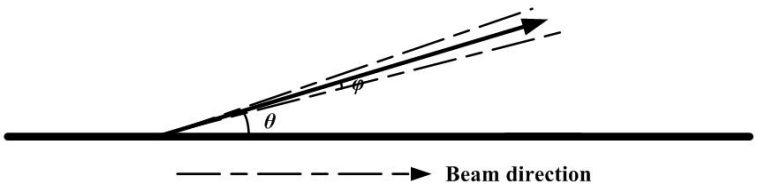

Figure 4.6.2: The direction of synchrotron radiation

The photon spectrum is calculated by Formula (4.6.3) and shown in Fig. 4.6.1.

We obtain the total number of photons in different energies. The average energy of the photons is 0.9406 MeV, and the total number of photons is $8.672\times10^{15}\,s^{-1}m^{-1}$。 The power of the photons with energy lower than 100 keV is less than 12W/m. At every point along the beam the conical light of synchrotron radiation is emitted as shown in Fig 4.6.2. Table 4.6.1 shows the relevant parameters.

4.6.3 **Monte-Carlo Simulation**

The vacuum chamber may be manufactured of aluminum (Al), lead (Pb) or copper (Cu). It is necessary to look at the effective shielding of these three different materials. In Fig 4.6.3, the mass attenuation coefficient of Cu is between Al and Pb, so the vacuum chamber could be fabricated of Cu instead of Al and Pb. In reality, however, using the mass attenuation coefficients and the simple exponential is not suitable to calculate flux, spectrum or even the dose.

Therefore, a Monte-Carlo program, MCNP, is used to study the influence of synchrotron radiation and can directly be used to calculate the energy deposition in various regions, and the photon spectrum streaming out from the vacuum chamber. The vacuum chamber is composed of a few millimeters of Al covered by 3 or 8 mm of Pb or totally composed of a few millimeters of Cu. The photons strike the vacuum chamber at a grazing angle of 3.1669 mrad. The photon energy streaming into tunnel is rather small, mainly consisting of a hardening of the energy spectrum.

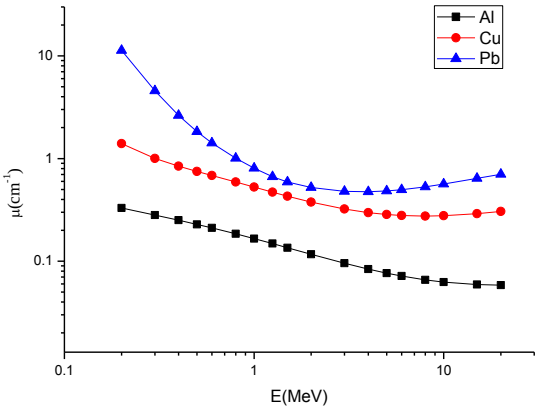

Figure 4.6.3: Mass attenuation coefficients of Al, Pb and Cu

MCNP uses a geometric model. The cross section of the vacuum chamber is shown in Fig 4.6.4. The picture on the left shows a chamber made of Al and Pb. The ends of the chamber are covered by 8 mm of Pb. The picture on the right shows a chamber totally made of Cu; the size is the same. It is difficult to describe the complete chamber with its arc in 3 dimensions, but fortunately the radius of curvature of the main ring is 6000 m, and the chamber can be represented by a straight line over tens of meters distance. Hence, the vacuum chamber is designated as 80 meters long, the same as the photon source. The cross section is an ellipse in the xy plane, with origin in the ellipse center and the z axis is along the light of sight. Then the photon direction is in the xz plane, at 3.1669 mrad to the z axis.

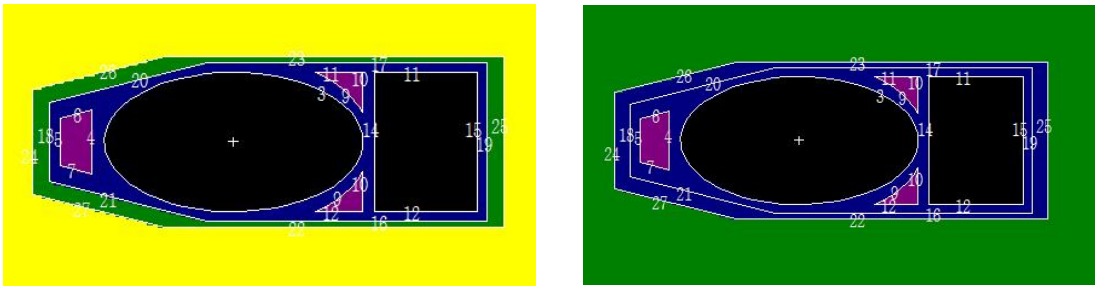

Figure 4.6.4: Vacuum chamber cross section (Al + Pb, or Cu)

In the input to MCNP, the 80-meter long tunnel is divided into eight sections, each 10 meters long. The goal is to accurately record the energy deposition and spectrum. The source is linear, 80 meters long. Every point on this linear source emits a light cone at an angle to the linear source. The spectrum is shown in Fig 4.6.1. The F6 card is used to record the energy deposition of an equivalent photon. The energy deposition of an equivalent photon and the energy deposition in air for a radius of 2.25 m from the tunnel center are recorded.

Table 4.6.2: Energy deposition of an equivalent photon (in MeV/g), dose rate (Gy/h) and heat (W/m) in different areas. The first two lines in the tables refer to water in cooling channels.

Al + Pb			
Materials	Energy deposition (MeV/g)	Dose rate (Gy/h)	Heat (W/m)
Left H_2O	3.38×10^{-7}	1.3426×10^{5}	------
Right H_2O	4.42×10^{-8}	1.7795×10^{4}	------
Al	5.35×10^{-7}	2.125×10^{5}	7.159×10^{2}
Pb	8.46×10^{-8}	3.3603×10^{4}	3.373×10^{2}
Air	2.276×10^{-10}	0.904×10^{2}	------
Cu			
Materials	Energy deposition (MeV/g)	Dose rate (Gy/h)	Heat (W/m)
Left H_2O	1.85×10^{-7}	7.3482×10^{4}	------
Right H_2O	2.56×10^{-8}	1.0168×10^{4}	------
Inner Cu	2.20×10^{-7}	8.7388×10^{4}	9.762×10^{2}
Outer Cu	2.26×10^{-8}	8.9363×10^{3}	7.117×10^{1}
Air	2.58×10^{-10}	1.0248×10^{2}	------

The energy deposition of an equivalent photon and the dose rate and power in different areas are given in Table 4.6.2. In this model, there is only a vacuum chamber in the tunnel without magnets and other components, so the dose rate in the air is large. Most of the power is converted into heat deposited in the metal.

The spectrum in air (Al + Pb, Cu) is shown in Fig 4.6.5. The energy of most of photons is between 100 keV and 300 keV; the vertical axis represents the flux of photons produced by an equivalent photon. The flux out of Cu is obviously lower than for the Al + Pb case.

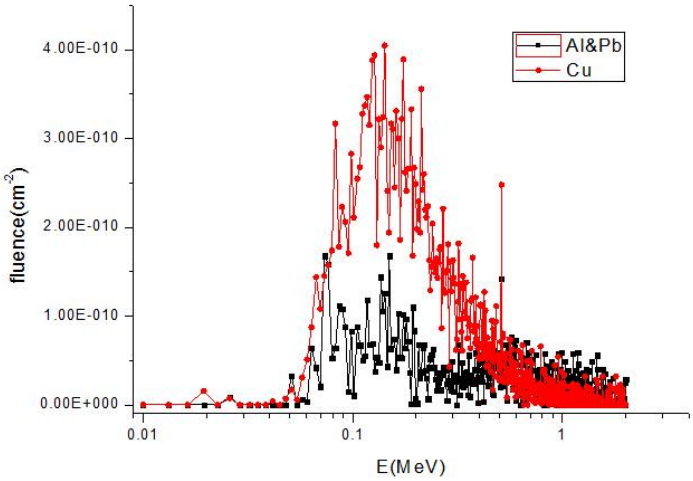

Figure 4.6.5: The spectrum of photons in the air (Al + Pb, Cu)

Another design for the CEPC vacuum chamber is copper, with a simple elliptical cross section, 100 mm×50 mm, and thickness 6 mm, shown in Fig 4.6.6. The energy deposition of an equivalent photon, dose rate, and heat in copper and air are shown in Table 4.6.3. The heat deposited in the vacuum chamber is 65.8%, which is smaller than the 80.7% in Al + Pb and 80.3% in the copper of the LEP structure. Meanwhile, the dose rate deposited in the air increases by an order of magnitude. The photon spectrum in air is shown in Fig 4.6.7.

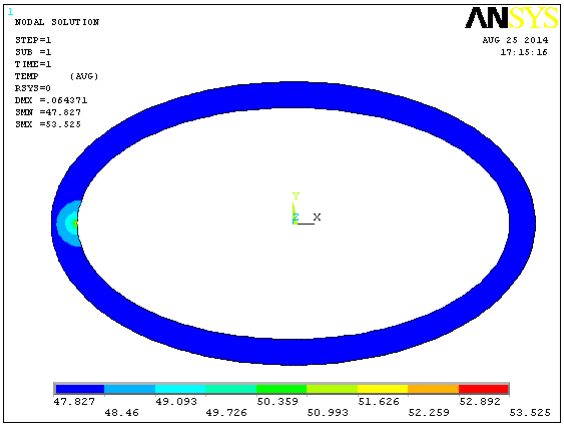

Figure 4.6.6: Cross section of the copper vacuum chamber

Table 4.6.3: Energy deposition of an equivalent photon (in MeV/g), dose rate (Gy/h) and heat (W/m) in different areas

Cu			
Materials	Energy deposition (MeV/g)	Dose rate (Gy/h)	Heat (W/m)
Cu	5.5226×10^{-7}	2.1936×10^{5}	8.593×10^{2}
Air	1.859×10^{-9}	7.384×10^{2}	------

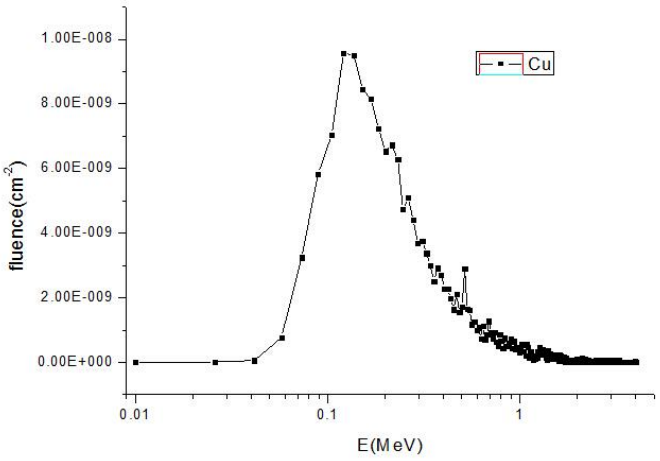

Figure 4.6.7: The spectrum of photons in air (6 mm Cu)

4.6.4 References

1. Fasso, G.R.Stevenson and R.Tartaglia. "Monte-Carlo simulation of synchrotron radiation transport and dose calculation to the components of a high-energy accelerator," CERN/TIS-RP/90-11/CF (1990)
2. K.Burn, A.Fasso, K.Goebel and et al. "Dose estimations for the LEP main ring," HS divisional report and LEP note 348 (1981)
3. A.Fasso, K.Goebel and M.Hoefert. "Lead shielding around the LEP vacuum chamber," HS divisional report and LEP note 421 (1982)
4. A.Fasso, K.Goebel and M.Hoefert. "Radiation problems in the design of the large electron- positron collider (LEP)," CERN 84-02 Technical Inspection and Safety Commission (1984)

4.7 Injection and Beam Dump

4.7.1 Introduction

The injection system design for CEPC is determined by the beam lifetime in the e+e- collider, and the particle production rate of the beam source. To reduce the cost of the whole system, the length of the Linac is chosen to be as short as possible, and a Booster ring is used to ramp the beams from the Linac energy to the full injection energy of the main collider. Therefore, the whole CEPC system is composed of three parts: the Linac, the Booster, and the main collider, as shown in Figure 4.7.1. The Linac is 6 GeV, and the Booster ramps the electron and positron beams from 6 GeV to 120 GeV.

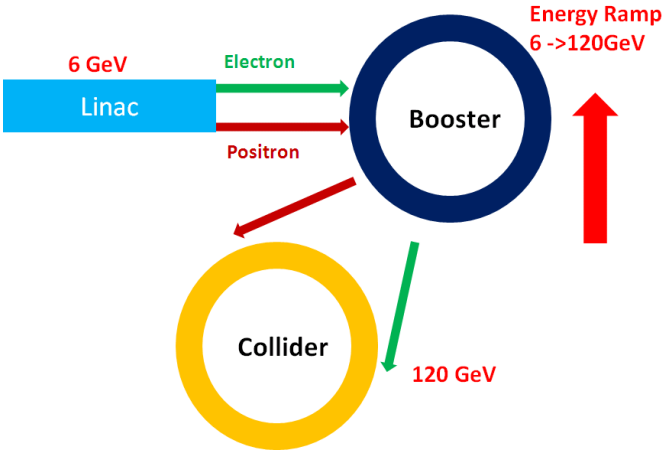

Figure 4.7.1: Schematic of the CEPC system configuration.

The injection system should fulfill the following requirements: the filling time of the main collider ring should be much smaller than the beam colliding time; the bunch charge in the Linac and Booster should be smaller than the largest charge production rate in the positron source; the efficiency of the injection system should be higher than 90%. Some of the main parameters of the injection system are shown in Table 4.7.1.

Table 4.7.1: Main Parameters of the injection system.

Linac Energy	6 GeV
Booster Energy	6-120 GeV
Bunch number in the booster	50
Injection Period	90 sec
Injection time length	10 sec
Luminosity drop in top-up mode	10%
Bunch charge in Booster	2.8 nC
Kicker field strength	500 Gauss
Septum field strength	400 Gauss
Thickness of septum	2 mm

4.7.2 **Injection Time Structure**

The injection time structure is mainly affected by the beam lifetime. Beam lifetime in a storage ring is a parameter describing the particle loss and is defined by [1]:

$$\frac{1}{\tau} = -\frac{1}{N}\frac{dN}{dt}. \qquad (4.7.1)$$

Many different effects reduce the beam intensity, so the beam life time includes many components. The total lifetime and the lifetime due to a single beam loss mechanism are related by:

$$\frac{1}{\tau_{total}} = \sum \frac{1}{\tau_i} \qquad (4.7.2)$$

For the CEPC lifetime these effects are taken into account [2]:

- Beam-Gas scattering

- Quantum fluctuation of radiation
- Touschek effects
- Radiative Bhabha
- Beamstrahlung effect

The beam lifetime is shown in Table 4.7.2; in the calculation a gas consisting of 80% H_2 and 20% CO at pressure of 1E-8 Torr, and a 1.5 cm vacuum chamber radius is assumed.

Table 4.7.2: Lifetime of CEPC due to different effects.

	Lifetime	Unit
Elastic H2 scattering	189	Hours
Elastic CO scattering	15	Hours
Inelastic H2 scattering	149	Hours
Inelastic CO scattering	14	Hours
Transverse quantum	2218	Hours
Longitudinal quantum	Infinity	Hours
Touschek	530	Hours
Radiative Bhabha	51	Minutes
Beamstrahlung	80	Minutes
Total lifetime	30	Minutes

From these lifetime values, injection into the main collider has to be done in a top-up mode due to the short total lifetime. To reduce the injection time, 50 bunches are injected from the Booster in one ramping cycle. The bunches in the Booster are designed to have the same time structure as the main collider, and the kickers in the Booster and collider are turned on before a bunch arrives and turned off afterwards; thus 50 bunches are injected into the main collider one by one. Assuming a 30 minute total lifetime, and a 10% luminosity drop, we should inject every 90 seconds and the required bunch charge in the Booster should be 2.8 nC. Since the damping time of the Booster at low energy is more than 100 seconds, the positron production rate at the source must be higher than 2.8 nC/bunch. The injection time length is mainly determined by the ramping time of the Booster; we assumed this number to be 10 seconds. When the collider is empty, the injection rate should be larger than that in the top-up mode to fill the main ring in a reasonable time interval. By reducing the injection period from 90 seconds to 60 seconds, we can fill the ring to its peak current in 30 minutes, as shown in Figure 4.7.2.

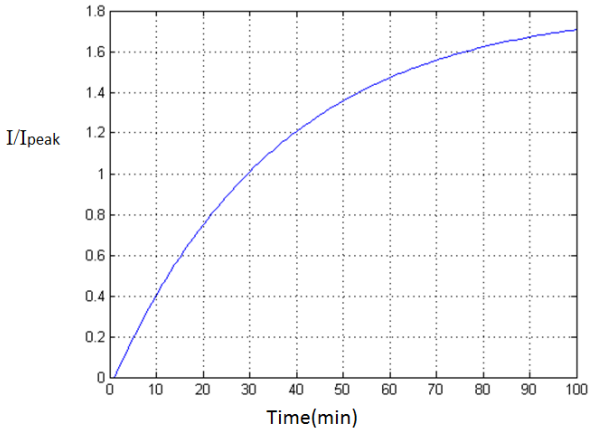

Figure 4.7.2: The current in the main collider with a 60 second injection period.

4.7.3 **Schematic Drawing**

The main collider (Fig. 4.7.3) shows that straight sections IP1 and IP2 are used for the CEPC interaction point and detectors. Straight sections IP3 and IP4 are preserved for the interaction regions of SPPC; thus injection into the main ring has to be done in the remaining straight sections. In our design, the injection of electrons and positrons take place in the straight sections right next to IP1. The Booster is installed in the same tunnel as the main colliders. It has the same circumference and is above the collider as shown in Fig. 4.7.4. Thus the beams have to be transported vertically from the Booster to the main collider.

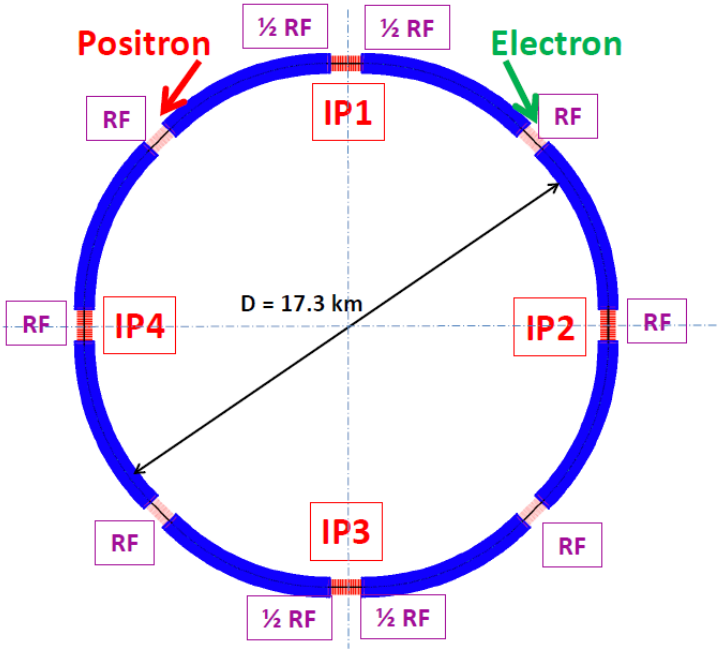

Figure 4.7.3: A schematic drawing of the injection points in the main ring.

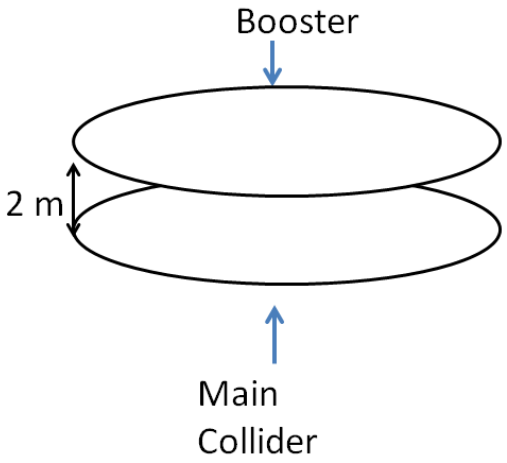

Figure 4.7.4: The geometrical structure of the Booster and main collider.

Betatron injection is chosen as a baseline mode. The injection septa give a vertical bend to the injected beams, and three kickers bump the circulating beam near the injected beam vertically.

The bump height and the machine acceptance is determined from the injection phase space [3]:

$$\text{Acceptance length} > 5\sigma_c + 10\,\sigma_i + S \qquad (4.7.3)$$

$$\text{Bump height} > 10\,\sigma_i + S \qquad (4.7.4)$$

where σ_c is the beam size of the circulating beam, σ_i is the beam size of the injected beam, S is the thickness of the septum board. For our design, the kicker gives a 20 mm bump and the acceptance should be larger than 15 mm.

4.7.4 **Beam Dump**

4.7.4.1 ***Beam Dump System Design***

It is important to be able to dump the electron and positron beams in a controlled way in the main collider. The function of the beam dump system is to reliably absorb the power from the electron and positron beams. For safe, long-term operation, the dump must be able to withstand the thermal stress and possible fatigue stress.

The concept of the beam dump system has been adapted from LEP [4] as a baseline for our system. We must have the capability to absorb an energy of 0.4 MJ/beam.

The beam dump consists of a fast kicker and two beam absorbers, as shown in Figure 4.7.5. These systems are all installed in the straight section between IP3 and IP4. The kicker magnet is located adjacent to a defocusing quadrupole, and the two absorbers are symmetrically placed on the two sides of the kicker, and about 50 m from the kicker. The kicker deflects both the electron and positron beams in the vertical direction, and deflection angle can change during the dumping process. A vertical deflection can also be provided by off-axis passage in the horizontal focusing quadrupoles next to the kicker.

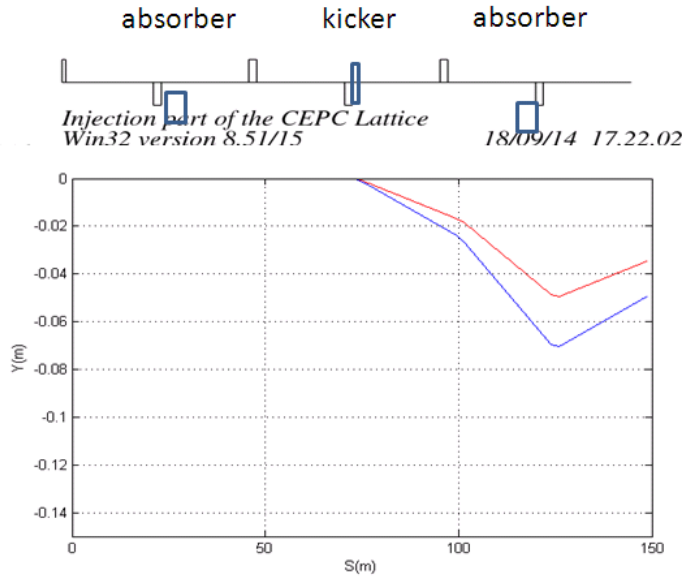

Figure 4.7.5: Schematic plot of the beam dump system and beam orbits for different deflecting angles.

To make the dump system work well, the rise time and fall time of the kicker must be chosen to satisfy certain conditions. The rise time should be fast enough so that the kicker can rise to its full strength between two bunches, about 1.7 μs for operation with 50 bunches/beam. To avoid all of the beam energy deposition at a single point, the fall time of the kicker should be long enough so that different bunches experience a gradually decreasing deflection angle during the 160 μs revolution time. The main kicker parameters are given in table 4.7.3.

Table 4.7.3: Main parameters of the dump kicker.

Parameters		Unit
Maximum deflecting angle	1	mrad
Minimum deflecting angle	0.7	mrad
Kick strength	400	mT.m
Magnet length	2	m
Magnet rise time	1.5	μs

4.7.4.2 *Beam Absorber*

The critical components of the dump are the absorbers. We have investigated several materials (aluminum, copper, graphite) for the absorbers taking into account the properties of thermal conductivity, melting temperature etc. For an absorber of high energy electrons and positrons we chose aluminum. The aluminum should be chemically, thermally and mechanically processed and forged. A water cooling system is incorporated to prevent excess heating.

Monte Carlo simulations were done to find the optimal absorber dimensions. The energy deposition by the primary beam was calculated using the GEANT4 Monte Carlo simulation code [5]. The beam parameters used in the GEANT4 simulations are given in Table 4.1.1. Preliminary dimensions of the absorber were chosen to be 200 cm x 200 cm x 350 cm. A beam of 15000 electrons with energy 120 GeV initiates a shower inside the

aluminum absorber. Fig. 4.7.6 shows the deposited energy density contours for a slice of the aluminum dump when struck by a 120 GeV electron beam. Figures 4.7.7 and 4.7.8 show the penetration depth and the projected transverse spread respectively of the deposited energy. The maximum energy deposition density by the beam (50 bunches) in the absorber is 450 J/cm^3. This is equivalent to 170 J/g. The temperature rise will be 210^o C (the aluminum melting point is 1220^o C).

From the figures it is clear that the optimum dimensions for the aluminum absorber should be 100 cm x 100 cm x 250 cm. The dump will be positioned 50 m from the beam line and have concrete shielding.

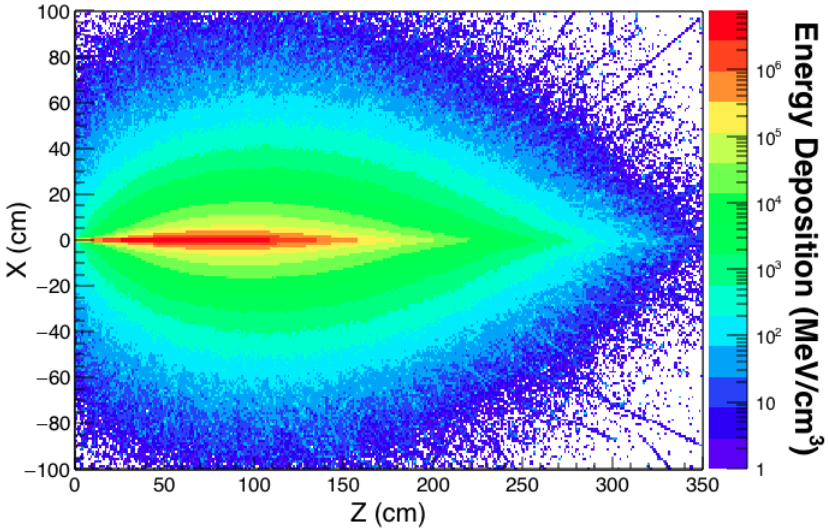

Figure 4.7.6: Deposited energy density in the aluminum absorber.

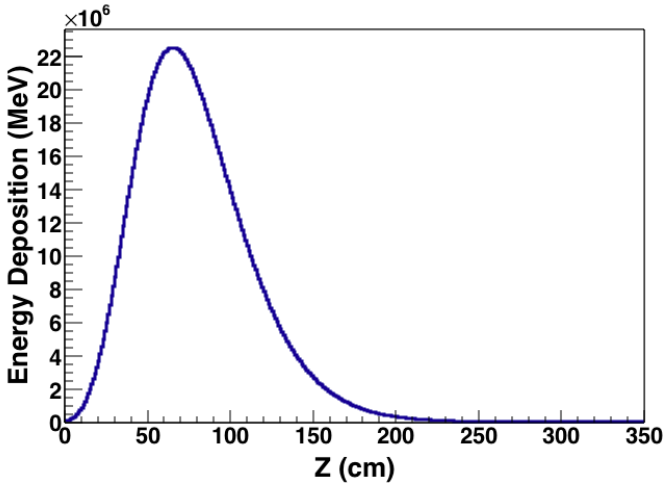

Figure 4.7.7: Longitudinal distribution of the deposited energy in the aluminum absorber.

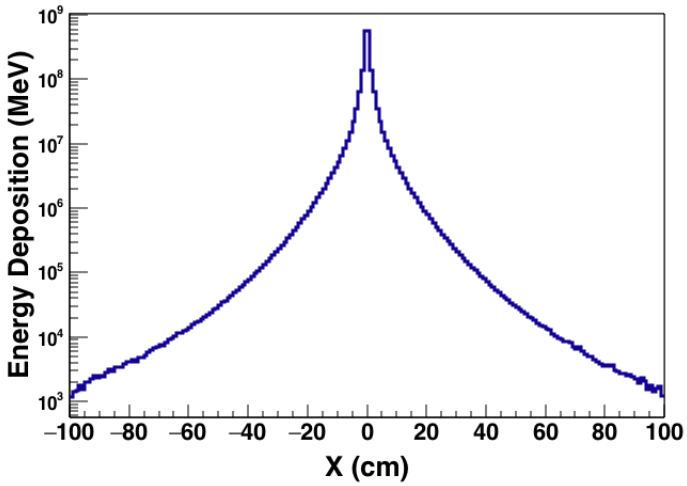

Figure 4.7.8: Transverse distribution of of the deposited energy in the aluminum absorber.

4.7.5 References

1. S.Y. Lee, Accelerator Physics, (World Scientific Publishing, 2004), 456
2. A. Hofmann, Proceedings, General accelerator physics, vol. 1. CERN Geneva CERN-94-01
3. J.T. Seeman, Injection Issues of Electron-Positron Storage Rings, SLAC-PUB-5933
4. LEP Design Report, Vol. II, CERN-LEP/84-01.
5. GEANT4-a simulation toolkit, NIMA, vol. 506, p. 250, (2003).

4.8 Beam Loss, Background and Collimators

4.8.1 Introduction

In this section, we describe beam loss mechanisms that result in particles lost in the interaction region and the protection system required for shielding.

4.8.2 Beam Loss Mechanisms

4.8.2.1 *Quantum Mechanism*

Particle losses occur for Guassian particle distributions in 6-dimensional phase space due to the finite transverse aperture or energy acceptance. The lifetime caused by these effects is given by

$$\tau_q = \frac{1}{2}\tau_u \frac{e^{\zeta}}{\zeta}, \text{ with } \zeta = \frac{A_u^2}{2\sigma_u^2} \qquad (4.8.1)$$

Substituting the CEPC design parameters, we calculate that the quantum lifetime is larger than 1000 hours.

4.8.2.2 *Touschek Scattering*

Particles in a circulating bunch execute transverse betatron oscillations around the equilibrium orbit. Since the transverse velocities are statistically distributed, these

particles can be scattered by collisions changing transverse momenta into longitudinal momentum and lead to a strong energy variations. If the energy variation exceeds the energy acceptance of the machine, the particle will be lost.

The rate of the Touschek effect per bunch which causes particles to exceed the energy aperture and the resulting Touschek lifetime can be calculated with the following formula:

$$\frac{1}{\tau_{tou}} = \frac{Nr_e^2 c\lambda^3 D(\varepsilon)}{8\pi\sigma_x\sigma_y\sigma_z\gamma^3}, \qquad (4.8.2)$$

The Touschek lifetime is inversely proportional to the third power of γ. So, in large energy machines such as CEPC, the Touschek effect doesn't reduce beam lifetime significantly. We substitute the design parameters of CEPC and obtain the Touschek lifetime is larger than 1000 hours..

4.8.2.3 *Beam-Gas Scattering*

Although the pressure of the beam pipe can be made very low, there still are many residual gas molecules. When particles are scattered by residual gas molecules, their direction will be changed (Coulomb scattering), or their energy may be decreased with emission of a photon (bremsstrahlung).

The Coulomb scattering and bremsstrahlung cross sections can be represented by the following formulas:

$$\sigma_1 = \frac{2\pi Z^2 r_e^2 \langle\beta\rangle}{\gamma^2 a}, \qquad (4.8.3)$$

$$\sigma_2 = 4\alpha r_e^2 Z^2 \left\{\frac{4}{3}\ln\frac{183}{Z^{1/3}}\left(\ln\frac{1}{\varepsilon_{rf}} - \frac{5}{8}\right) + \frac{1}{9}\left(\ln\frac{1}{\varepsilon_{rd}} - 1\right)\right\}, \qquad (4.8.4)$$

Then we can calculate the beam lifetime due to beam-gas scattering by the following formula.

$$\frac{1}{\tau} = \frac{1}{N}\frac{dN}{dt} = \sigma c N g, \qquad (4.8.5)$$

where c is the speed of light and Ng represents the density of the residual gas molecules.

If the residual gas molecule is CO and the pressure is 10^{-7} Pa. then substituting the CEPC design parameters, we calculate the beam-gas lifetime is about 150 hours for Coulomb scattering and 14.5 hours for bremsstrahlung.

4.8.2.4 *Radiative Bhabha Scattering*

The process of radiative Bhabha scattering can be summarized as follows. The electron and positron that collide can emit a photon. If the energy of the emitted photon is large enough, the final electron and positron may be outside the energy acceptance of the machine and result in beam loss.

Radiative Bhabha scattering has a large cross-section at small scattering angles. The cross-section and lifetime of radiative Bhabha scattering can be calculated by formulas 4.8.6 and 4.8.7 below or by the simulation code BBBREM.

$$\sigma_{ee} = \frac{16\alpha r_e^2}{3}((\ln\frac{1}{\eta} + \eta - \frac{3}{8}\eta^2 - \frac{5}{8})[\ln(\sqrt{2}\frac{a}{\lambda_p}) + \frac{\gamma_E}{2}] + \frac{1}{4}(\frac{13}{3}\ln\frac{1}{\eta} + \frac{13\eta}{3} - \frac{3}{2}\eta^2 - \frac{17}{6})),$$

$$a = \sqrt{2}\frac{\sigma_x\sigma_y}{\sigma_x + \sigma_y}.$$

The radiative Bhabha scattering lifetime obtained from BBBREM is about 52 minutes, very close to the result calculated with the formulas.

4.8.2.5 *Beamstrahlung*

Beamstrahlung is the synchrotron radiation from a particle being deflected by the collective electromagnetic field of the opposing bunch. This effect will increase the energy spread and limit the lifetime of the beams. Referring back to 4.5 the lifetime caused by beamstrahlung obtained by simulation is about 47 minutes.

The lifetimes caused by different effects are summarized in the following table.

Table 4.8.1: Lifetime caused by different effects in CEPC

Loss mechanisms	**Lifetime**	**Comment**
Quantum effect	Larger than 1000 hrs	
Touschek effect	Larger than 1000 hrs	
Beam-gas scattering Coulomb)	About 150 hrs	The residual gas is CO and the pressure is about 10^{-7} Pa.
Beam-gas scattering (bremsstrahlung)	About 14.5 hrs	
Radiative Bhabha scattering	About 50 minutes	simulated
Beamstrahlung	About 47 minutes	simulated

4.8.3 Beam Induced Background

All of these mechanisms can result in particles that strike the beam pipe. This is not serious if the lost particle hits the region beyond the interaction region. On the contrary, if the particle is lost in the interaction region, it will cause background events in the detector. Furthermore, if the number of background events is large, the lost particles will damage the detector and reduce its lifetime. So we need to make detailed simulations to evaluate this background and find methods to reduce it to a low level. As calculated in the last section, the beam lifetime is primarily affected by beam-gas scattering, radiative Bhabha scattering and beamstrahlung. So the simulation of background is focused on these aspects.

In addition, synchrotron radiation photons which are emitted when the beam goes through the last bending or quadrupole magnet in the final focus region may also hit the beam pipe and penetrate the detectors. In particular, CEPC's high energy will produce photons with high momentum which may lead to serious detector damage.

The background expected at CEPC can be divided into the two categories mentioned above: synchrotron radiation photons and lost particles.

4.8.3.1 *Interaction Region*

The interaction region of CEPC consists of the beam pipe, the surrounding silicon detectors, the luminosity calorimeter and the interface to the final focus quadrupoles, namely QD0 and QF1. The preliminary layout outlined in Fig. 4.3.6 in Section 4.3

features a short focal length of L*=1.5 m, the distance between QD0 and the interaction point.

4.8.3.2 *Synchrotron Radiation Background*

The synchrotron radiation photons passing through the beam pipe consist of two sources: the last bending magnet and the quadrupole magnets in the interaction region.

Since the last bending magnet will bend the beam from the original orientation to orientation along the z axis in the IR, the synchrotron radiation emitted from the last bending magnet will pass through the IR and may penetrate the detectors.

Table 4.8.2 Parameters of the last bending magnet

Beam current	Distance from IP	Length	Bending angle	Critical energy	Power
16.6 mA	32.5 m	15.5 m	4.1 mrad	958 keV	50 kW

For the synchrotron radiation from the quadrupoles in the final focus region, we use the code provided by M. Sullivan to do the simulation. We assume the aperture in the region with a distance less than 8.2 cm as 1.5 cm and the aperture in other region as 4 cm. The simulation results are shown in the following table.

Table 4.8.3: The number and power of photons striking at different regions

Region	Distance from IP (m)	Number of photons	power
1	-5~ -2.75	0	0
2	-2.75~ -1	3.842E4	1.691E-3
3	-1~ -0.5	0	0
4	-0.5~0	1.241E+6	4.089E-1
5	0~1	1.335E+7	3.674
6	1~2.75	5.092E+7	11.686
7	2.75~4	1.029E+7	21.139

4.8.3.3 *Lost Particle Background*

4.8.3.3.1 Beamstrahlung

Due to the pinch effect in the beam-beam interaction, the trajectories of the particles are bent and they emit radiation called "beamstrahlung". This process potentially has a large impact on the beam energy spread and the luminosity spectrum.

However, given their low energy and small production angle relative to the beam axis they create negligible backgrounds in the detector.

4.8.3.3.2 Radiative Bhabha Scattering

To simulate the radiative Bhabha scattering, we use BBBREM as the generator to get the initial beam coordinates after the scattering and then input those initial beam coordinates into SAD [1] to track the particles until they hit the beam pipe.

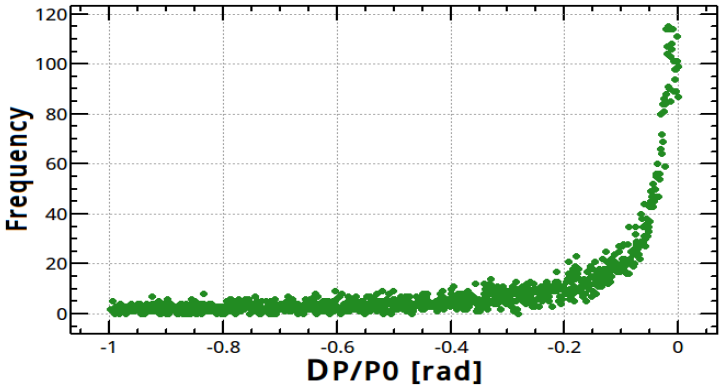

Figure 4.8.1. The energy spread of particles generated by BBBREM (larger than the design acceptance)

Of about 100,000 particles generated by BBBREM [2] (energy spread larger than the designed acceptance) about 3.8% of them will be lost in the interaction region. The loss distribution is illustrated in Fig. 4.8.2.

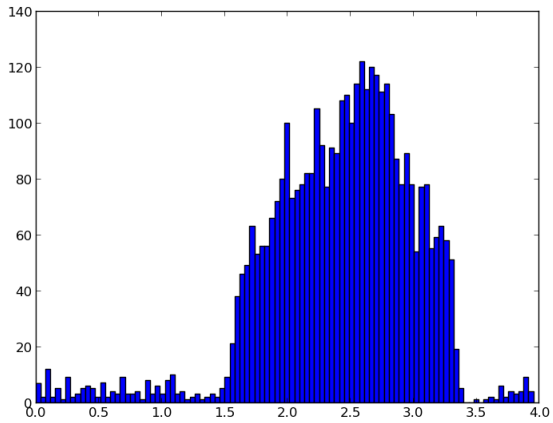

Figure 4.8.2. Distribution of the particles lost in the IR (generated byBBBREM)

4.8.3.3.3 Beam-Gas Scattering

A Monte Carlo algorithm will be developed to generate the bremsstrahlung process based on the formulas for beam-gas scattering and the algorithm embedded in the code SAD [1].

Then particles will be tracked and information about them recorded if they are lost in the IR. This detailed simulation will be finished in the future.

4.8.4 **Background Shielding**

Detectors are shielded from lost particles by the following methods.

1. Maintaining low pressure to reduce beam-gas scattering at its source, where the source for most of this effect extends from the IP to 30 – 60 m upstream (based on B-factories experience [3]). Details to reduce the pressure in this region are described in section 5.6, vacuum.

2. Close to the IR beam pipe and vertex detector should be shielding with high-Z material. The inner part of the detector is designed with the SR shielding requirement in mind.
3. Collimators should be placed upstream of the IP to remove scattered beam particles. In cases where lost particle trajectories pass outside of the beam-stay-clear envelope it may be possible to significantly reduce the flux by placement of a collimator at points of high dispersion and high beta.

4.8.5 References

1. SAD. http://acc-physics.kek.jp/SAD/.
2. R.Kleiss and H.Burthardt, "BBBREM-Monte Carlo simulation of radiative Bhabha scattering in the very forward direction," NIKHEF-H/94-01 and CERN SL/94-03 (OP)
3. KEKB B-Factory Design Report, KEK Report 95-7.

4.9 Polarization

4.9.1 Introduction

Particle spins are an important experimental tool in modern high-energy physics studies. From the experience at LEP and other high energy lepton accelerators, transversely polarized beams are essential to the beam energy calibration, via the resonant depolarization technique [1] while colliding experiments between longitudinally polarized electron and positron beams are also of great interest to the high-energy physics community. Therefore, the provision of polarized lepton beams in CEPC is an important topic in this design study.

4.9.2 Overview of Spin Dynamics

The spin vector precesses about the magnetic field lines in any magnetic element. In a flat storage ring like CEPC, the field is dominated by the vertical field in the bending magnets so the spin appears to precess about an axis close to the vertical direction, most of the time.

In an ideal electron (positron) storage ring, transverse polarization in the vertical direction will spontaneously build up to an asymptotic level of 92.4%, due to the Sokolov-Ternov effect [2]. However, the spin precession axis is not vertical everywhere and can vary with energy. As a result, stochastic emission of synchrotron radiation will cause spin diffusion and lead to depolarization near spin resonances,

$$\nu_s = k + l \cdot \nu_x + m \cdot \nu_y + n \cdot \nu_z, \;\; k, l, m, n \in \text{integer}, \qquad (4.9.1)$$

where ν_s is the spin tune (number of 2π precessions per turn), and ν_x, ν_y and ν_z are the orbital tunes, respectively. The balance between these two effects leads to an asymptotic polarization P_{eq} over a polarization time τ_{dk} [3],

$$P_{eq} \approx \frac{92.4\%}{1 + \tau_{st}/\tau_{dep}}, \quad \frac{1}{\tau_{dk}} = \frac{1}{\tau_{st}} + \frac{1}{\tau_{dep}}, \qquad (4.9.2)$$

where τ_{st} and τ_{dep} are the time constants of the Sokolov-Ternov effect and the depolarization effect, respectively.

For a planar ring, $\nu_s \approx E_{beam}[\text{GeV}]/0.4406486$. The major challenge to maximize beam polarization at high energies is to minimize orbital imperfections. In LEP, a wise choice of the spin tune close to half integer, a precise control over the vertical closed orbit, and optimization of the accelerator lattices created a good starting point for application of Harmonic Spin Matching [4], which was essential for optimization . Moreover, the synchrotron sidebands of the first order spin resonances will become important, if the beam spin tune spread is comparable to the spacing of these base resonances, and the depolarization will be greatly enhanced [5]. This prevents beam polarization at ultra-high beam energy, since the spin tune spread scales as

$$\Delta \nu_s \propto \frac{E_{\text{beam}}^2}{\sqrt{\rho}} \qquad (4.9.3)$$

where ρ is the ring bending radius.

Beam polarization above 5% to 10% was observed in LEP up to 61 GeV [4], which is sufficient for beam energy calibration, with the upper limit set by the large spin tune spread. A simple scaling from LEP following Eq. (4.9.3), which assumes the same level of orbital imperfections, does not give a usable transverse polarization for beam energy calibration at the WW threshold (81 GeV beam energy) for CEPC, in contrast with the case of TLEP. However, a better control over the machine orbit can be expected for a new machine and this energy limit might possibly be increased.

To evaluate the equilibrium beam polarization in CEPC, a simulation framework [6] has been set up based on the Polymorphic Tracking Code (PTC) [7]. It includes a normal form analysis of linearized orbital and spin motions to obtain the spin orbit coupling function, and deals with only first order spin resonances. Moreover, it also includes a Monte Carlo simulation [8] of the spin diffusion effects, which can treat higher order spin resonances as well. In addition, modeling and correction of machine imperfections can be implemented in MADX [9] and passed to PTC afterwards to check the effects on the equilibrium beam polarization.

4.9.3 **Beam Polarization at the Z-pole**

The Sokolov-Ternov polarization time τ_{st} is 44 hours at 45.5 GeV for CEPC, in contrast with 5 hours in LEP, and 150 hours in FCC-ee [10] It will take around 5 hours to achieve a 10% transverse polarization. Asymmetric polarization wigglers [11] as used in LEP can also be used in CEPC to boost the rate of polarization build-up. The choice of the wiggler parameters needs to take into account their effects on the beam parameters, and ensure the spin tune spread is within the safe range. In addition, polarizing wigglers generate a non-trivial amount of synchrotron radiation.

Colliding beam experiments with longitudinally polarized electron and positron beams have more stringent requirements compared to beam energy calibration. A beam polarization near at least 50% is desired for both beams. At LEP this was achieved (although without spin rotators). There is concern that the beam-beam interaction might cause depolarization, and at LEP, transverse polarization of 40% was observed for colliding beams, for a beam-beam tune shift of 0.04, and the polarization difference between colliding and non-colliding bunches was within a few percent [4]. A

quantitative prediction for CEPC will be made when the parameter set for operation at the Z-pole is available. Spin rotators are also necessary to rotate the polarization vector to the longitudinal direction at IPs, and the movable spin rotators [12] developed at HERA are a good candidate. More study is also needed to take into account the adverse effects of the beamstrahlung and the pretzel orbit.

4.9.4 **Beam Polarization at Higher Energies**

As mentioned above, the maximum polarization decreases rapidly with increasing beam energy and spin tune spread. It is natural to consider reducing the dependence of the spin tune spread on the beam energy spread. Several possible approaches using Siberian snakes have been proposed. One approach [13] proposes to build a polarizer ring or utilize a polarized electron gun before the Booster to generate polarized beams or only a polarized electron beam, and the beams are then accelerated in the Booster with a suitable number of snakes, and finally injected into the main ring also equipped with snakes to render the spin tune independent of beam energy. Another approach [14, 15] utilizes a combination of snakes and asymmetric wigglers to allow radiative polarization build-up in the ring with an acceptable spin tune spread. Detailed studies of these schemes are required to demonstrate the feasibility of implementing transverse or longitudinal polarization for higher energies in CEPC.

4.9.5 **References**

1. L. Arnaudon et al, Z. Phys. C 66(1995)45.
2. A. A. Sokolov and I. M. Ternov, Sov. Phys. Dokl 8(1964)1203.
3. Ya. S. Derbenev, A. M. Kondratenko, Sov. Phys. JETP. 37(1973) 968.
4. R. Assmann et al, AIP Conference Proceedings 570(2001)169.
5. Ya. S. Derbenev, A. M. Kondratenko and A.N. Skrinsky, Part. Accel. 9(1979)247.
6. Z. Duan, Private notes (2015).
7. E. Forest, F. Schmidt, and E. McIntosh, KEK Report 2002-3 (2002) and CERN-SL-2002-044(AP).
8. J. Kewisch, DESY Report 83-032 (1983).
9. Methodical Accelerator Design (MAD) program, CERN, http://cern.ch/mad/.
10. See the FCC-ee parameter list, http://tlep.web.cern.ch.
11. A. Blondel and J. M. Jowett, LEP Note 606 (1988).
12. J. Buon and K. Steffen, Nucl. Inst. Meth. A 245(1986) 248.
13. M. Bai et al, “Possible approach for reaching high energy polarized electron-positron beams,” EUCARD workshop “Spin optimization at Lepton accelerators,” Mainz, Germany, 2014.
14. U. Wienands, “Is polarization possible in TLEP?,” 4th TLEP workshop (2013).
15. S. Mane, “Polarization at TLEP/FCC-ee: ideas and estimates,” arxiv:1406.0561.

5 CEPC – Technical Systems

5.1 Superconducting RF system

5.1.1 Introduction

The RF system accelerates the electron and positron beams, compensates for synchrotron radiation loss and provides sufficient RF voltage for energy acceptance and the required bunch length in the CEPC Booster and collider ring. Superconducting radio frequency (SRF) cavities are used because they have much higher continuous wave (CW) gradient and energy efficiency as well as larger beam aperture compared to normal conducting cavities. These substantial advantages result in fewer cavities, low impedance and thereby less disruption to the beam; also the AC power consumption is less. To deliver the target integrated luminosity, high-availability SRF components as well as rapid commissioning and efficient operation with minimal downtime are required. The SRF system is one of the most important technical systems of CEPC and is a key for achieving its design energy and luminosity. It will dominate, with the associated RF power source and cryogenic system, the overall machine cost, efficiency and performance.

The CEPC SRF system will be one of the largest and most powerful SRF accelerator installations in the world. Eight RF stations are placed in eight straight sections of the tunnel, and two of them split into two half stations at the interaction points IP1 and IP3. The total RF station length is approximately 1.4 km with 12 GeV of RF voltage. Table 5.1.1 shows the main parameters of the SRF system.

CEPC will use 384 five-cell 650 MHz cavities for the collider (main ring) and 256 nine-cell 1.3 GHz cavities for the Booster. The collider cavities operate in CW. The Booster cavities operate in quasi-CW mode with the following time sequence: first, stay at 1 MV/m for one second of electron injection from the Linac, followed then by a ramp up to 20 MV/m in four seconds, followed by one-second extraction to the collider and then the RF is turned off. After a four-second magnet ramp down, the same ten-second cycle begins for positrons. The RF and cryogenic duty factor of the Booster, with respect to a purely CW operating mode, is about 20 % for continuous alternative injection and extraction of electrons and positrons.

Each of the 10 m-long collider cryomodules contains four 650 MHz cavities, and the 12 m-long Booster cryomodule contains eight 1.3 GHz cavities. A Euro-XFEL/ILC-type cryomodule structure slightly modified for CW or quasi-CW operation will be used. Modifications envisioned are enlargement of the two-phase pipe and helium vessel chimney diameters, removal of a portion of the 5 K shield while keeping the intercepts, and without superconducting quadrupoles inside. The collider cryomodule will have one beamline HOM ferrite damper on each side at room temperature. An RF station consists of 12 collider cryomodules and 4 Booster cryomodules. The collider module will be mounted on the tunnel floor and the Booster module hung from the ceiling in series with the collider module string at a different beamline height.

During the conceptual design phase, significant effort is needed to identify high-risk challenges that require R&D. The highest priority items are efficient and economical damping of the huge HOM power with minimum dynamic cryogenic heat load, achieving the cavity gradient with high quality factor in the vertical test and real

accelerator environment, robust 300 kW high power input couplers that are design compatible with the cavity clean assembly and low heat load.

The RF system parameters are listed in Table 5.1.1.

Table 5.1.1: CEPC superconducting RF system parameters

Parameter	Unit	Main Ring	Booster (120 GeV)
Synchrotron radiation power	MW	103.42	2.46
Bunch charge	nC	60.64	3.2
Bunch length	mm	2.65	2.66
Bunch number	-	100	50
Beam current I	mA	33.2	0.87
RF frequency f_{RF}	MHz	650	1300
RF voltage V_{RF}	GV	6.87	5.12
Number of cavity	-	384	256
Cavity operating voltage V_c	MV	17.9	20
Cavity operating gradient E_{acc}	MV/m	15.5	19.3
Operating temperature	K	2	2
Q_0 at operating gradient	-	4E+10	2E+10
Q_{ext} of input coupler	-	2.2E+06	1E+07
Cavity bandwidth	Hz	295	130
RF power / cavity	kW	280	20
Number of RF power source / cavity	-	1	1
Number of cavity / module	-	4	8
Cryomodule length	m	10	12
Number of cryomodule	-	96	32
Cryomodules / RF section	-	12	4
RF section length	m	120	48
Total RF length	m	960	384

In parallel with design and key R&D, extensive development of SRF personnel, infrastructure and industrialization is essential for the successful realization of CEPC. The world's largest SRF infrastructure and talent pool should be built. Chinese industry should participate in the R&D and pre-production work as early as possible. A more detailed SRF R&D and pre-production plan is described in Chapter 11.

5.1.2 **RF Cavity Design Parameters**

The preliminary cavity RF design parameters are shown in Table 5.1.2. The choice of RF frequency of the cavity accelerating mode is determined by several factors. Lower frequency is preferred for energy acceptance, beam stability and low parasitic loss. Higher frequency is better for bunch length, and especially the size, cost and quality control of the cavity. Since the Booster has 2.6 % of the beam current of the collider and 20 % duty cycle, we chose the frequency of 1.3 GHz, a frequency which has been developed worldwide since the early 1990s. The CEPC collider will use 650 MHz, the second sub-harmonic of the Booster frequency. These frequencies minimize the construction and operating cost, fulfill the beam dynamics and luminosity requirements and allow CEPC to use the mature technology developed by TESLA and adopted for XFEL and ILC. These frequencies have the most synergy with other ongoing SRF projects in China and abroad.

Table 5.1.2: CEPC cavity RF design parameters

Parameter	Unit	Main Ring	Booster
Cavity frequency	MHz	650	1300
Number of cells	-	5	9
Cavity effective length	m	1.154	1.038
Cavity iris diameter	mm	156	70
Beam tube diameter	mm	170	78
Cell-to-cell coupling	-	3 %	1.87 %
R/Q	Ω	514	1036
Geometry factor	Ω	268	270
E_{peak}/E_{acc}	-	2.4	2
B_{peak}/E_{acc}	mT/(MV/m)	4.23	4.26
Cavity longitudinal loss factor $k_{/\!/\,HOM}$ *	V/pC	1.8	3.34
Cavity transverse loss factor $k_{\perp}$*	V/pC/m	2.4	35.3
Acceptance gradient	MV/m	20	23
Acceptance Q_0	-	4E10	2E10

* collider bunch length 2.65 mm, booster bunch length 2.66 mm.

Given the total synchrotron radiation power, parasitic loss and RF voltage, the main ring cavity numbers and voltages are mainly determined by the input coupler power handling capability, taking into account that the acceleration should be divided equally between the eight straight sections and other details such as cryomodule size optimization. The main ring input coupler operating power has been chosen to be 280 kW, nearly double the BEPCII power level. This is a balance between SRF system capital cost, coupler operational risk, and cavity gradient and impedance.

The matched Booster cavity bandwidth is 33 Hz, which is hard for transient LLRF control during voltage ramping and beam extraction. Therefore, the Booster cavity is over coupled and needs 20 kW input power assuming 50 Hz detuning. If both amplitude

and phase control (e.g. para-phasing) of the cavities are used for the energy ramp, the assumptions for microphonics and transient control could be relaxed with more analysis.

The cavity gradient is determined by the cell numbers when the cavity RF voltage and frequency are fixed. More cells is better for low gradient, but will increase the cavity HOM power and impedance and lower the coupling of the HOMs. We chose 5-cell and 15.5 MV/m for the collider cavity. 4-cell (19.4 MV/m) is also an option. Because of the low current and duty cycle of the Booster, the TESLA 9-cell cavity at 19 MV/m is chosen.

The 650 MHz cavity baseline is bulk niobium operating at 2 K with Q_0 = 4E10 at 15.5 MV/m, and Q_0 = 4E10 at 20 MV/m for the acceptance vertical test. The 1.3 GHz cavity baseline is bulk niobium operating at 2 K with Q_0 = 2E10 at 19.3 MV/m, and Q_0 = 2E10 at 23 MV/m for the acceptance vertical test. New nitrogen-doping [1] and flux expulsion [2] technology for the high quality factor SRF cavity could be used to reach these targets. Thin film technology (such as Nb_3Sn [3]) will be studied as an alternative. To avoid field emission, very clean cavity surface processing and string assembly is required. Electro-polishing is also needed.

5.1.3 **HOM and SOM Damping**

Higher-order-modes (HOMs) excited by the intense beam bunches must be damped to avoid additional cryogenic loss and multi-bunch instabilities. This is accomplished by extracting the stored energy via HOM couplers mounted on both sides of the cavity beam pipe and the HOM absorbers inside the cryomodule (for the Booster) or outside the cryomodule (for the main ring).

The large bunch spacing of CEPC results in very small beam spectral line spacing (main ring 0.55 MHz, Booster 0.275 MHz). Therefore it is impossible to detune the HOM modes away from the beam spectral lines with the large HOM frequency scattering from cavity to cavity caused by fabrication tolerances and RF tuning of the fundamental mode. The average power losses can be calculated as single pass excitation. As shown in Table 5.1.3, HOM power damping of 3.5 kW for each 650 MHz 5-cell cavity and 21 kW for each cryomodule is required for the CEPC main ring. Resonant excitation should be considered especially for the low frequency modes below cut-off.

Table 5.1.3: CEPC SRF cavity HOM power and heat load.

	Main Ring	Booster
HOM power / cavity	3.5 kW	5.3 W
HOM power / module	21 kW	56 W
HOM 2K heat load / module	13 W	5.9 W
HOM 5K heat load / module	39 W	3 W
HOM 80K heat load / module	390 W	43.8 W
Percent of total cryogenic load	22 %	11 %

About 80 % of the HOM power is above the cut-off frequency of the cavity beam pipe and will propagate through the cavities and finally be absorbed by the two HOM absorbers at room temperature outside the cryomodule. Each absorber has to damp about 10 kW of HOM power; thus the absorber can't be placed in the cryogenic region.

Ferrite HOM absorbers developed for KEKB and SuperKEKB have achieved much higher power levels [4] and can be used for the CEPC main ring. The ferrite damper for the BEPCII spare cavity developed by IHEP can handle up to 4.5 kW. A ceramic HOM absorber at 70 K in the cryomodule beam line will be used for the Booster [5]. A LEP/LHC-type HOM coupler [6, 7] will be used for kW level power handling capability. BNL is also developing kW class coaxial HOM couplers. Waveguides at the cavity beam pipes [8] are also suitable for the main ring cavity HOM power extraction, but with large size waveguides, more complicated structure and interfaces of the cryomodule, and large heat load. Another possible solution to damp the HOM power is to put two cavities in one cryomodule or a hybrid cryomodule with water cooled HOM absorber inside the cryomodule.

Cryogenic heat loads in different temperature regions of the main ring and Booster cryomodule are given in Table 5.1.3. The Booster heat loads are scaled from ILC TDR [9] data. The duty factor of the Booster HOM power is 50 % for continuous injection, which will be much lower for longer beam lifetime. The XFEL/ILC type HOM coupler and absorber can easily handle the Booster HOM power.

HOM power dissipation in the main ring cryomodule is the main concern. Table 5.1.3 gives the preliminary upper limit estimate, which is also the design goal for the HOM heat load. The main ring cryomodule will use RF shielded bellows (copper plated) and gate valves, and flanged connections with gap-free gaskets to reduce the HOM power generation and dissipation. Assume 10 kW HOM power propagating through the beam tubes and bellows (thin copper film RRR=30, in the abnormal skin effect regime), the power dissipation is less than 2 W/m. The heat load at 5 K and in the 80 K region is dominated by HOM coupler cable heating. We will make careful calculation and engineering design to reduce the power dissipation.

The beam instability calculation gives the upper limit of the external quality factor of the HOMs with high R/Q of the main ring 650 MHz cavity, as shown in Table 5.1.4. Large HOM frequency spread from cavity to cavity (assume σ_f = 0.5 MHz and 5 MHz) will relax the Q_{ext} requirement. It is easy to reach these Q_{ext} values with the LEP/LHC HOM coupler for the modes below cut-off frequency and with the beam pipes for the modes above cut-off. Although the beam current is 1/40 of the main ring, the Booster has much weaker radiation damping especially during the low energy part of the ramp. The measured Q_{ext} and the calculated growth time of the dominant modes of the TESLA 1.3 GHz 9-cell cavity are shown in Table 5.1.5. The instability growth times are much shorter than the radiation damping time in the low energy region of the Booster. Both transverse and longitudinal feedback systems will be needed to mitigate the multi-bunch instabilities. Another concern of the HOMs is that some modes far above cut-off frequency may become trapped among cavities in the cryomodule due to the large frequency spread [10].

Table 5.1.4: Damping requirements of prominent HOMs of 650 MHz 5-cell cavity.

Monopole Mode	f (GHz)	R/Q (Ω) *	Q_{limit} σ_f = 0 MHz	Q_{limit} σ_f = 0.5 MHz	Q_{limit} σ_f = 5 MHz
TM011	1.173	84.8	5.1E+5	2.9E7	5.8E7
TM020	1.350	5.5	6.8E+6	3.7E7	7.5E7
Dipole Mode	f (GHz)	R/Q (Ω/m)**	Q_{limit} σ_f = 0 MHz	Q_{limit} σ_f = 0.5 MHz	Q_{limit} σ_f = 5 MHz
TE111	0.824	832.2	2.3E+4	1.2E6	2.4E6
TM110	0.930	681.2	2.8E+4	1.5E6	3.0E6
TE112	1.225	36.2	5.2E+5	1.9E6	3.7E6
TM111	1.440	101.5	1.9E+5	1.0E7	2.0E7

* Longitudinal R/Q with the accelerator definition and $k_{/\!/\,\text{mode}} = 2\pi f \cdot (R/Q) / 4$ [V/pC]

** Transverse R/Q: $k_{\perp\,\text{mode}} = 2\pi f \cdot (R/Q) / 4$ [V/(pC·m)]

Table 5.1.5: Damping of prominent HOMs with two couplers per 1.3 GHz 9-cell cavity.

Monopole Mode	f (GHz)	R/Q (Ω)	Q_{measured}*	σ_f (MHz) *	τ (ms)
TM011	2.450	156	5.9E4	9	1500
TM012	3.845	44	2.4E5	1	472
Dipole Mode	f (GHz)	R/Q (Ω/m)	Q_{measured}*	σ_f (MHz) *	τ (ms)
TE111	1.739	4283	3.4E3	5	218
TM110	1.874	2293	5.0E4	1	44
TM111	2.577	4336	5.0E4	1	22
TE121	3.087	196	4.4E4	1	497

* TESLA cavity measurement data

Further design optimization of HOM properties of the main ring cavity is needed. For example, enlarge the iris diameter to decrease loss factors while keeping relatively high R/Q and low surface field of the fundamental mode, identify trapped modes within the cavity and cryomodule, and reduce the cavity cell number or design asymmetry end cells to avoid trapped modes.

The other four pass-band modes of the operating mode of the multi-cell cavity (hereby we call them the Same Order Modes, SOMs) may also drive instabilities or extract significant RF power from the beam. SOM parameters of the Collider 650 MHz 5-cell cavity are given in Table 5.1-6, including the Q limit of the coupled bunch instability.

Since the SOMs are so close in frequency to the operating mode, they can't be damped in the same way as HOMs using HOM couplers or beam tubes. The SOMs' external Q of the HOM coupler is estimated to be around 1E10, similar with the cavity Q_0. While the input coupler can be used as the SOM coupler, the calculated external Q values are listed in the table, which are enough to damp the beam instability.

The SOM frequencies are nearly fixed and have very small spread between cavities when the operating mode is tuned to near 650 MHz during operation. The total SOM power is quite small when we consider the real cavity passband modes frequencies and the bunch time spacing of the collider. Even assuming resonant excitation (beam spectral lines coincide with all the SOM frequencies), the total SOM power is about 1

kW and with the input coupler damping, the power dissipated on the cavity wall is negligible (~ 0.1 W).

Table 5.1.6: SOMs damping of the 650 MHz 5-cell cavity by the input coupler.

Mode	f (MHz)	R/Q (Ω)	Q_{limit}	$Q_{\text{input coupler}}$	P_{SOM} (W)	$P_{\text{SOM-res}}$ (W)
π/5	632.322	0.02	4.5E+9	1.2E+07	1.3E-5	268.9
2π/5	637.099	0.00017	5.4E+11	3.3E+06	8.7E-7	0.6
3π/5	643.139	0.341	2.6E+8	1.7E+06	9.31E-3	638.9
4π/5	648.146	0.078	1.1E+9	1.2E+06	2.92E-4	105.8

5.1.4 **Power Coupler**

For CEPC, one of the key technologies is the very high power handling capability of the input power coupler for the main ring SRF cavity. Both the Q_0 and the accelerating gradient for CEPC SRF cavities are high, which requires that the coupler can be assembled with the cavity in a Class 10 cleanroom. In addition, considering the large number of couplers, heat load (both dynamic and static) is another important issue to be solved. The main challenges of the input power couplers are as follows: very high power handling capability (CW 300 kW), two windows for vacuum safety and cavity clean assembly, very small heat load, simple structure for cost saving, high yield and high reliability.

Considering the excellent performance, close frequency and IHEP experiences, the BEPCII 500 MHz SCC coupler design is taken as the baseline. Several modifications are considered for the CEPC main ring SRF cavity: reduce the distance between the window and the coupling port, putting the window into the cryostat profile and thus having the window and cavity assembled in a Class 10 cleanroom, add one waveguide or cylindrical type warm window for vacuum safety, redesign the mechanical structure for higher power capacity and lower heat load.

For the Booster 1.3 GHz cavity, since the average input power is less than 4.4 kW, the KEK STF1-type coupler developed by IHEP can be used. A high power conditioning test went up to 800 kW with a 0.75% duty factor, i.e. an average power of 6 kW. If higher input power and/or variable coupling is needed, a KEK cERL main linac coupler [11] can be the reference. Table 5.1.7 lists the main parameters of the input power couplers for the main ring and the Booster SRF cavities.

Table 5.1.7: Parameters of the input power couplers for CEPC SRF cavities.

Parameters	Main ring	Booster
Frequency	650 MHz	1.3 GHz
Maximum power	CW, 300 kW	Average < 4.4 kW (20 kW peak)
Q_{ext}	2E6	1E7
Coupling type	Antenna	Antenna
Coupler type	Coaxial	Coaxial
Number of windows	2	2
Window type	One waveguide or cylindrical warm window; One coaxial Tristan type warm window	Two same size coaxial Tristan type windows: one warm, one cold

5.1.5 **Tuning and RF Control System**

The total number of tuners for CEPC is 640 (384 for the main ring cavities, 256 for the Booster cavities). Highly reliable and maintainable tuners are required. The parameters of the tuning system is listed in Table 5.1.8. The lever-end tuner [12] is chosen to be the baseline design for the main ring 650 MHz 5-cell cavity and Booster 1.3 GHz 9-cell cavity.

Table 5.1.8: Main parameters of tuner

Parameters	650 MHz cavity tuner	1.3 GHz cavity tuner
Coarse tuning range	500 kHz	900 kHz
Coarse tuning resolution	1 Hz	1 Hz
Fine tuning range	200 Hz	1 kHz
Fine tuning resolution	0.1 Hz	0.1 Hz
Motor / tuner	1	1
Piezo / tuner	2	2

5.1.6 **References**

1. A. Grassellino, et al., "Nitrogen and argon doping of niobium for superconducting radio frequency cavities: a pathway to highly efficient accelerating structures," Supercond. Sci. Technol. 26 102001 (2013).
2. A. Romanenko, et al., "Dependence of the residual surface resistance of superconducting radio frequency cavities on the cooling dynamics around T_c," J. Appl. Phys. 115, 184903 (2014).
3. S. Posen, et al., "Recent progress in Nb_3Sn SRF cavity development at Cornell," Proceedings of IPAC2014, Dresden, Germany.
4. M. Nishiwaki, et al., "Developments of HOM dampers for SuperKEKB superconducting cavity," Proceedings of SRF2013, Paris, France.
5. XFEL Technical Design Report, 2006.
6. A. Butterworth, et al., "The LEP2 superconducting RF system," Nuclear Instruments and Methods in Physics Research A, 587 (2008): 151‑177.
7. E. Haebel, et al, "The higher-order mode dampers of the 400 MHz SC LHC cavities, 8th Workshop on RF superconductivity," Padova (Italy), 1997.
8. R.A. Rimmer, et al., "The JLAB ampere-class cryomodule conceptual design," Proceedings of EPAC 2006, Edinburgh, Scotland.
9. ILC Technical Design Report: Volume 3, Part II: 46.
10. J. Sekutowicz. "Multicell superconducting structures for high energy e+e- colliders and free electron laser linacs," EuCARD Editorial Series on Accelerator Science and Technology, Vol.01 (2007).
11. H. Sakai, et al., "Development of input coupler for compact ERL main linac," Proceedings of ERL2011, Tsukuba, Japan.
12. I. Gonin, et al., "New Helium Vessel and Lever Tuner for the 650 MHz Cavities for Project X," Proceedings of PAC2013, Pasadena, CA USA.

5.2 RF Power Source

5.2.1 **Collider RF Power Source**

Accelerators used for high-energy physics experiments require high power radio frequency sources to provide the energy needed to accelerate the particles. The RF power needs to be stable and predictable such that any variation in the supplied RF power has a limited and acceptable impact on the accelerated beam quality.

The RF power source delivers energy to the electrons to compensate for the energy loss from synchrotron radiation and from interactions with the beam chamber impedance. The RF power source also delivers energy to the beam when ramping to higher energy and captures and focuses the electrons into bunches. The beam and the RF station are two dynamic systems which strongly interact; this complicates stability considerations for the combined system.

The CEPC collider beam power is about 100 MW, so if the amplifier efficiency of amplifier is low, the AC input power will exceed our CEPC primary power limit of 300 MW. The high power klystron is the more attractive option because of its potential for higher efficiency, higher than the other option of a solid state amplifier. Table 5.2.1 shows power demand comparisons between klystron and solid state amplifier (SSA).

Table 5.2.1: Comparison of power demands between klystron and SSA

Parameters	Klystron	Solid state amplifier
Overall efficiency (%)	50	40
Beam power (MW)	100	100
DC input power (MW)	200	250
RF overhead factor	1.3	1.3
AC input power (MW)	260	325

The CEPC SRF system consists of 384 RF stations per beam. Each RF station includes a 5-cell 650 MHz accelerating superconducting cavity. In addition to the energy losses due to radiation in dipoles, damping wigglers, and undulators, the RF power transmitter must provide for the HOM losses excited by the beam. A minimum transmitter power of 280 kW is required to meet the sum of the radiated, HOM, and reflected power demands. With one klystron for two cavities, the specified saturation power of the klystron should be in the range of 600 to 700 kW. This takes into account linear operation of the klystron, and circulator and waveguide losses. The choice of one klystron for two cavities is justified technically by better control of microphonic noise and minimum perturbation in the case of a klystron trip. Table 5.2.2 shows the RF power demands for the CEPC collider SRF system. The CEPC collider RF power source configuration is shown in Figure 5.2.1.

Table 5.2.2: CEPC collider SRF system parameters

Parameters	Value
Operation frequency	650 MHz +/- 0.5 MHz
Cavity Type	650 MHz 5-cell
Cavity number	384
RF input power (kW)	280 CW
RF source number	192
Klystron output power (kW)	800 CW

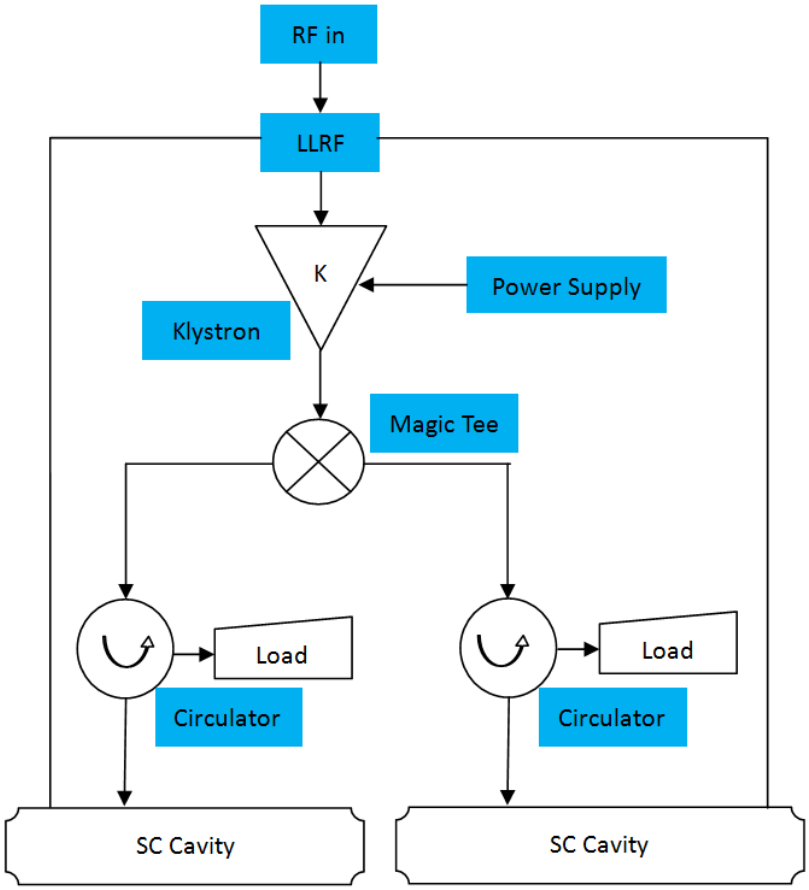

Figure 5.2.1: RF power source configuration

Considering the klystron operation lifetime and power redundancy, each cavity will be individually powered with a CW klystron amplifier capable of delivering more than 400 kW. A single 800 kW klystron amplifier will drive two of the main ring cavities through a magic tee and two rated circulators and loads. The klystron characteristics and performance are summarized in Table 5.2.3. Klystrons that meet or exceed this power level are not available from the three vendors specializing in thyratrons: CPI, Toshiba, and Thales. The klystron, with gun and collector, would be about 4 m in length and could be manufactured in industry after initial R&D and could be developed from existing 500 MHz or 700 MHz CW klystrons by a partnership between IHEP and an industrial company. Computer simulation tools will be used to design the klystron including the electron gun, electromagnet, cavities and RF output structure.

Table 5.2.3: Klystron key design parameters

Parameters	Value
Center frequency (MHz)	650
Bandwidth (-1dB) (MHz)	0.5
Output power (kW)	800
Beam voltage (kV)	90
Beam current (A)	18
Efficiency (%)	65
Gain (dB)	40

The klystron DC supplies for the cathode and auxiliaries (anode modulation, cathode heating, focal coils, and ion pump) will be provided by a Chinese company. The power supplies and the control system are housed in three different cabinets which together belong to a single mechanical unit.

The DC power supply for the cathode is a Pulse Step Modulator (PSM) currently used for broadcast transmitters. The PSM switching power supplies have the benefit of low stored energy, and fast turn-off capability of the IGBTs, eliminating the need for a crowbar circuit to protect the klystron. The power supply will have redundant built in switching cards, and will operate at full capacity even with several card failures. Designed for 90 kV/18 A, this PSM essentially consists of 140 power modules which are connected in series and supplied through their own secondary winding from two transformers. The two transformers are shifted in phase, resulting in 12-pulse loading of the mains with a 6-pulse rectification in the module chain. Each one of the 140 modules represents an autonomous voltage source which may be switched on/off individually by means of fast IGBT switches operating at 5 kHz. The switching sequence and pulse duration is generated and monitored by the PSM control system such that the thermal loading of all modules is distributed equally. The switching frequency can be suppressed at the output of the module chain, by means of a low pass filter.

The RF transmitter will have local control via a PLC, with system parameters and control available to the main control system via an Ethernet link. The PLC will also monitor the PSM switch modules, so that failed modules are logged and transmitter repairs can be scheduled for the next maintenance period.

The main PSM features are efficiency, regulation speed and accuracy, and compatibility with large variation of the load impedance. These fit well with the performance specifications listed in Table 5.2.4. Moreover, the modular concept with high redundancy (up to four defective modules without performance degradation) makes it very reliable, easy to maintain and there is no need for HV crowbars.

Table 5.2.4: PSM performance specification

Parameters	Value
High voltage (kV)	90
Current (A)	18
Voltage stability (%)	< 2
Efficiency (%)	>90
Turn-off time (us)	<5
Stored energy (J)	<15

The RF power delivered by the klystron will be fed into the cavity input coupler via a WR1500 waveguide line including monitoring directional couplers as well as a circulator to isolate the klystron from the variable (beam-loaded) cavity impedance. All these waveguide components are commercially available.

5.2.2 **Booster RF Power Source**

The CEPC Booster RF system consists of 1300 MHz superconducting RF cavities. There are 32 cryomodules, each containing eight 9-cell superconducting cavities. These need 256 sets of 1300 MHz power sources. and will have reasonable efficiency (~50%) high reliability and also no requirement for a solenoid, HV PS, filament PS or vacuum pump. 256 solid state amplifiers comprise the required 1300 MHz CW power source. The Booster SRF system parameters are in Table 5.2.5.

Table 5.2.5: CEPC Booster SRF system parameters

Parameters	Value
Operation frequency	1300 MHz +/- 0.5 MHz
Cavity Type	1.3 GHz 9-cell
Cavity number	256
RF input power (kW)	20 peak/cavity
RF source number	256 (25 kW SSA)

Different possible alternatives for the CEPC Booster power sources were considered in terms of modularity and technology: vacuum tubes (Klystron, IOT – Inductive Output Tube, Diacrode) and solid state. Most current vacuum tube production is for the market of television (TV) broadcast transmitters (50 kW in the ultrahigh frequency band), an area where the IOT is progressively replacing the klystron. This tendency is accelerated by the advent of digital TV, which requires lower power (< 10 kW), and is better suited for the IOT or solid state technology. For accelerator applications, which require higher average power (several 100 kW), klystrons have generally been used. However, the use in accelerators represents a small part of the market, not sufficient to assure the survival of klystron production.

The solid state amplifier (SSA) is another alternative; SSAs are being considered for an increasing number of accelerators, both circular and linear. Their capabilities extend from a few kW to several hundred kW, and from less than 100 MHz to above 1 GHz. SSAs are based on transistors instead of vacuum tubes. Reasonable efficiency (~ 50%), high gain, and modular design provide high reliability. High power amplifiers are usually built with multiple power modules for easier power upgrades to meet the needs of different experiments.

The SSA solution presents significant advantages compared to vacuum tubes: (1) high modularity with associated redundancy and flexibility, (2) elimination of high voltage handling and the high power circulator, (3) simpler start-up procedures and operation control, (4) no need for periodic replacement, (5) lower operation costs (no costly spare parts) and easier maintenance.

In the Booster each cavity could be powered with a 25 kW SSA consisting of a combination of 650 W elementary modules (about 50 modules per amplifier). The amplifier modules, based on a technology developed in house, with MOSFET transistors, integrated circulator and individual power supply, could then be fabricated in

industry. A circulator with a 1200 W 50 Ω RF termination is integrated in each module in order to protect the transistors from excess reflected power; moreover, this component is essential for ensuring stable conditions. The input and output circuits are matched to two pairs of adjustable capacitors. The basic topology for a 25 kW amplifier is shown Figure 5.2.2.

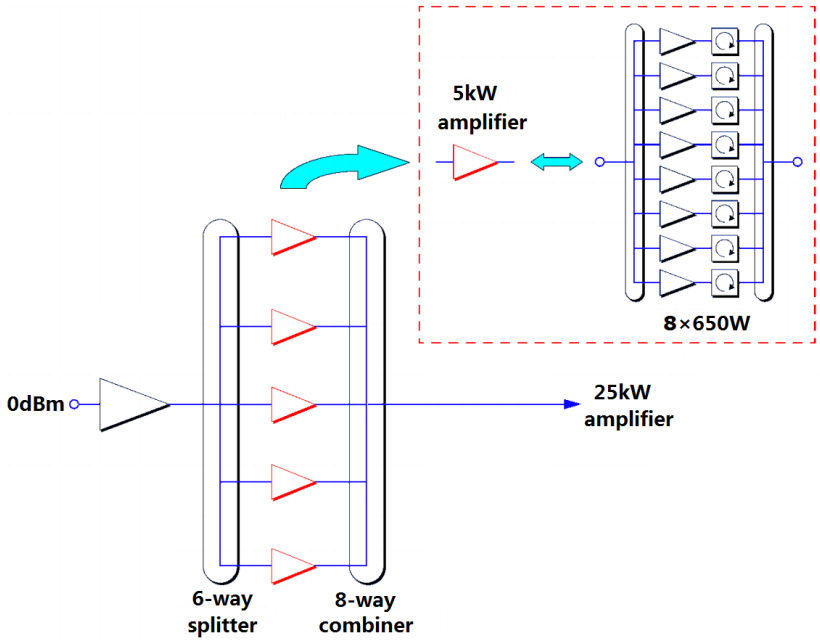

Figure 5.2.2: 25 kW amplifier basic topology

The output of the each module drives a common WR650 waveguide into a superconducting cavity. The amplifier specifications are listed in Table 5.2.6.

Table 5.2.6: Specifications of the Amplifier

Parameters	Value
Operating Frequency	1300 MHz +/- 0.5 MHz
Gain	67 dB
Efficiency	40% at 25 kW

5.2.3 **Linac RF Power Source**

The injector for the CEPC is a 500 m-long S-band Linac with maximum electron and positron energy of 6 GeV. In order to maintain a reasonable over-all length at high center-of-mass energy, the main linac of an electron-positron linear collider must operate at a high accelerating gradient. For copper (non-superconducting) accelerator structures, this implies a high peak power per unit length and a high peak power per RF source, assuming that a limited number of discrete sources are used. To enhance the peak power produced by an RF source, the SLED RF pulse compression scheme in use on existing linacs, and new compression methods that produce a flatter output pulse are being considered for CEPC.

The main high power RF components of the CEPC Linac are composed of 35 units of 80 MW S-band klystron tubes and conventional pulse modulators. Figure 5.2.3 is a simplified schematic of the RF power source.

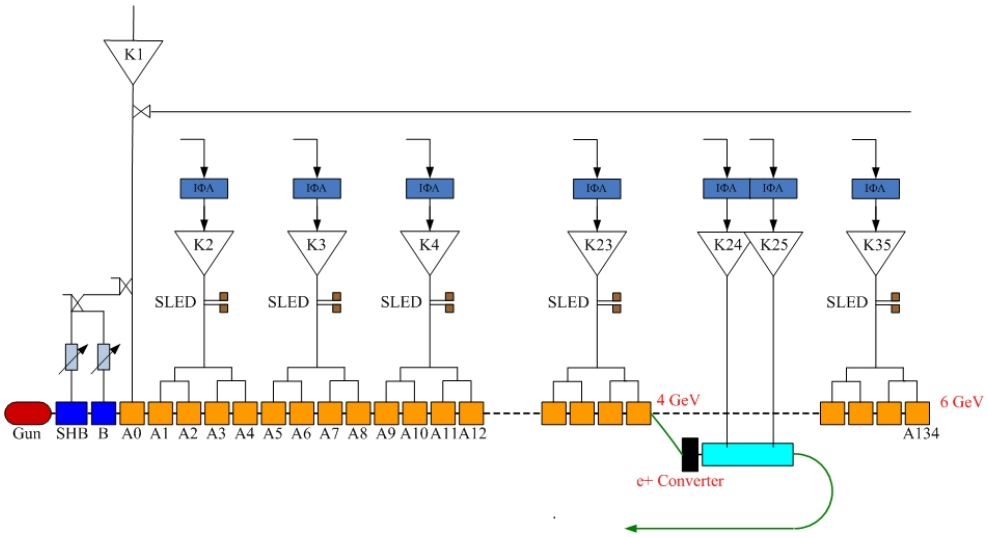

Figure 5.2.3: Simplified schematic of the Linac RF power source

In general, the klystrons are designed to produce a minimum of 80 MW peak power with extremely stringent phase and amplitude stability performance requirements. They are focused by magnets and operate up to 400 kV beam voltage with a micro-perveance of 2. The basic design has been simplified by using a fixed-frequency tuned five-cavity klystron for fixed-frequency operation. Initially, the output was to be divided between two output waveguides, but improvements in window design and performance have allowed us to change the output to a single output window structure.

The klystron tube is designed to meet the basic requirements of 80 MW peak power output with a minimum gain of 50 dB at 2856 MHz. To achieve these objectives the tube was designed as a five-cavity amplifier with the major design parameters listed in Table 5.2.7. Pulsed 2856 MHz high-power klystrons are a mature technology and several manufacturers can meet or exceed these power requirement.

Table 5.2.7: Parameters of 80 MW klystron

Parameters	Value
Frequency (MHz)	2856
Output power (MW)	80
Efficiency (%)	42
Gain (dB)	53
Pulse length (us)	4
Pulse rate (pps)	100
Beam voltage (kV)	400
Beam current (A)	488
Drive power (W)	350

The klystrons are powered by pulsed modulators, a line type pulser with well-established technology and reliability. The traditional approach is to use pulse forming networks with hard-tube (thyratron) switches to produce RF pulses. Table 5.2.8 lists the

main specifications of the modulator. The 80 MW klystron tube requires about 400 kV on its cathode voltage and the thyratron anode voltage should be less than 50 kV, so a pulse transformer with a turns ratio of 1:17 was selected. The modulator generates pulses with peak voltage of more than 23.5 kV and peak current of more than 8160 A. In order to accelerate an electron beam with a pulse width of 1 μsec, the flat-top of klystron beam voltage is required to be more than 2 μsec long. The long-term regulation and the pulse flatness of the klystron beam voltage is to be less than ±0.15% to prevent RF phase modulation and microwave power fluctuations.

Table 5.2.8: Main specifications of the modulator

Parameters	Value
Peak output power (MW)	200
Average output power (kW)	80
PFN charging voltage (kV)	50
PFN impedance (Ω)	2.85
Pulse width (us)	＞4 μs (flat top)
Pulse flatness (%)	±0.15
Pulse rate (pps)	100
Pulse transformer turns ratio	1:17

The modulator can be divided into four major sections: a charging section, a discharging section, a pulse transformer tank, and a klystron load. In the charging section, a SCR AC-AC voltage regulator controls the primary 3-phase 380 V AC power. The voltage regulator receives feedback signals from the primary AC voltage and the high voltage DC (HVDC) detector. Fig.5.2.4 is a simplified modulator circuit diagram.

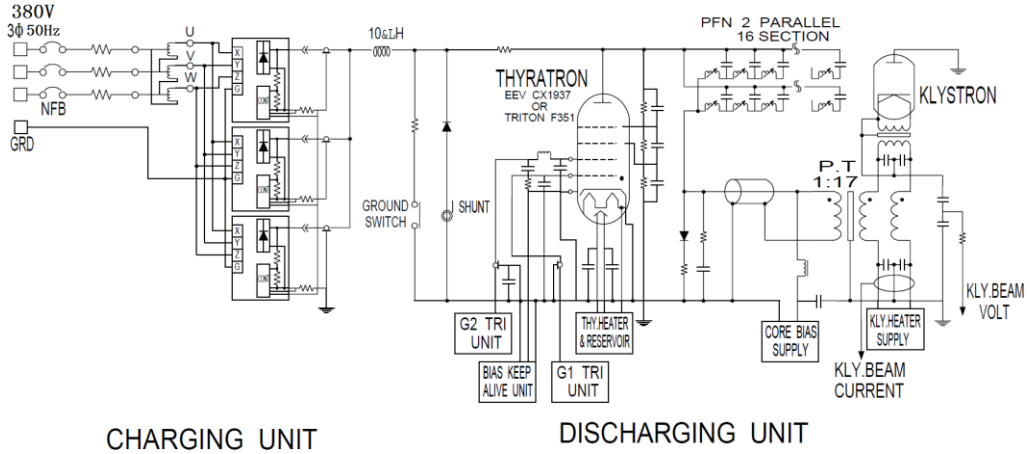

Figure 5.2.4: Simplified modulator circuit diagram.

The closed loop control of the AC-AC voltage regulator ensures stable HVDC output. The maximum HVDC is 25 kV. For system and personnel safety, the interlock has static and the dynamic modes. The static mode includes door interlocks, ground hooks, heater PS trips, cooling water flow and temperature status, and over voltage and current trips. The dynamic mode uses an analog signal from the vacuum system and a digital signal of for SCR AC over current. The pulse-forming network (PFN) is

resonantly charged from a HVDC filter capacitor through the charging inductor and diode. Pulse-to-pulse beam voltage regulation is better than $\pm 0.5\%$ by using closed loop control of the SCR AC-AC voltage regulator. Two parallel, fourteen section, type-E Guillemin networks are used for the PFN. The PFN impedance is about $2.8\,\Omega$. Each PFN capacitor has a fixed capacitance of 50 nF, and each PFN inductor can be varied manually up to 4.5 μH. By adjusting the inductance of each PFN section, we can precisely tune the flattop of the modulator output voltage pulse. The end of line clipper (EOLC) shown in Fig. 5.2.1 removes excessive negative voltage developed after discharge of the PFN capacitors as well as the thyratron. Two triaxial cables in parallel are used to make electrical connections between the PFN and the pulse transformer. The pulse transformer has a 1:17 turn ratio. Components in the pulse transformer tank are immersed in high voltage insulating mineral oil.

The klystron is mounted on the pulse tank top cover and is connected to the high voltage output of the pulse transformer. The klystron impedance at the primary of the pulse transformer is 2.8 Ω, which matches the PFN impedance. During fine-tuning of the PFN impedance, we intentionally produce about 5% positive mismatch to extend switch lifetime by reducing anode dissipation in the thyratron.

5.2.4 **Low Level RF System**

There are altogether three different RF power source systems with different frequencies, normal or superconducting structures and cavities, pulsed or CW operation mode. All must be phase-coherent. The frequency generation (2856MHz / 650MHz / 1.3 GHz), the phase reference system, and independent control of each site should be integral part of the whole accelerator complex. These criteria are basic to design of the low-level RF system. The parameters for this system are shown in Table 5.2.9.

Table 5.2.9: Low level RF system parameters

Subsystem		Technical specification or parameters	
Frequency generation		Accuracy	2x10e-6/year
		Stability	10 ppm
Phase reference system		Additional Phase Noise	10 dBm
		Phase stability	10 ppm
		Sub-sites	675+
		Distance	~
		Optical fiber or electrical distribution	O/E,E/O
Control for sub-sites	Linac	Quantity	35
		Operating Frequency	2856 MHz
		Work mode	Pulse,4 us/10 ms
		Amplitude stability requirements	0.1 °
		Phase stability requirements	0.1%
	Booster	Quantity	256
		Operating Frequency	1.3 GHz
		Work mode	CW
		Amplitude stability requirements	0.1 °
		Phase stability requirements	0.1%
	Ring	Quantity	384
		Operating Frequency	650 MHz
		Work mode	CW
		Amplitude stability requirements	0.1 °
		Phase stability requirements	0.1%
Interface to Accelerator control system		To Timing system	
		To MPS /Interlock system	
		To Operator	
		EPICS interface	
		others	

5.3 Cryogenic System

The CEPC has 640 superconducting cavities. In the Booster, there are 256 ILC type 1.3 GHz 9-cell superconducting cavities; eight of them will be packaged in one 12-m-long module. There are 32 such modules. In the collider ring, there are 384 650-MHz 5-cell cavities; four of them will be packaged into one 10-m long module. There are 96 of these.

All the cavities will be cooled in a liquid-helium bath at a temperature of 2 K to achieve a good cavity quality factor. The cooling benefits from helium II's thermophysical properties of large effective thermal conductivity and heat capacity as well as low viscosity. It is a technically safe and economically reasonable choice. The 2 K cryostat will be protected against heat radiation by means of two thermal shields cooled to temperatures from 5 - 8 K and from 40 - 80 K.

The cryogenic system is designed for fully automatic operation during extended periods. Reliability and stability are what concerns us most.

5.3.1 **Heat Load**

For CEPC, the heat load is mainly from the superconducting cavities. Two types of superconducting cavities provide the energy for the Booster and the collider. The quality factor is more than 2×10^{10} at 19.3 MV/m for Booster cavities and 4×10^{10} at 15.5 MV/m for collider cavities. Table 5.3.1 shows the detailed parameters for the two cavity types and the total dynamic heat load from the cavity wall.

Table 5.3.1: Parameters of the Booster and collider ring cavities

	Unit	Booster	Collider
Frequency	MHz	1300	650
Voltage	MV	20	17.9
duty factor		20%	CW
cells number per cavity		9	5
Cavity number		256	384
module number		32	96
R/Q		1036	514
Q		2E10	4E10
Operation temperature	K	2	2
Cavity dynamic heat load	W	3.86	15.6
Total dynamic heat load	KW	0.99	5.99

From the table we can see that of the total 128 SCRF cryomodules in the CEPC, the 96 Main Ring 5-cell 650 MHz SCRF cryomodules comprise the largest cryogenic cooling load and therefore dominate the design of the cryogenic system.

Table 5.3.2 summarizes the static and dynamic heat loads of CEPC Booster and collider cryomodules at the nominal operating conditions at different temperature levels. The total equivalent entropic capacity is 78.6 kW at 4.5 K.

Table 5.3.2: CEPC heat load

	Unit	BOOSTER			COLLIDER		
		40-80K	5-8K	2K	40-80K	5-8K	2K
Module static heat load	W	140	20	3	200	40	8
Module dynamic heat load	W	140	10	30.88	200	40	62.4
HOM loss per module	W	52.8	3.2	7.2	390	39	13
Connection boxes	W	50	10	10	50	10	10
Total heat load	KW	11.45	1.22	1.47	78.2	11.9	8.48
Overall net cryogenic capacity multiplier		1.54	1.54	1.54	1.54	1.54	1.54
4.5 K equivalent heat load with multiplier	KW	1.34	1.74	7.3	9.12	16.97	42.13
Total 4.5 K equivalent heat load with multiplier	KW	10.38			68.22		
Total heat load of Booster and collider	KW	78.6					

The figures in Table 5.3.2 include an “overall net cryogenic capacity multiplier,” a multiplier of the estimated heat loads, in general use in the cryogenic community. This factor includes a margin for plant regulation, a buffer for transient operating conditions, a buffer for performance decreases during operation and a buffer for general design risks. We use the multiplier parameter from the ILC Design report [1].

5.3.2 **Refrigerator**

The CEPC heat loads shown in Table 5.3.2 require the helium refrigerator plants to have a total capacity over 78.6 kW at 4.5 K. Eight individual refrigerators will be employed for the CEPC cryogenic system. The cryogenic plant capacities are equivalent to 12 kW at 4.5 K for each cryogenic station.

Many aspects must be taken into account during refrigerator design, including cost, reliability, efficiency, maintenance, appearance, flexibility, and convenience of use. The initial capital cost of the cryogenic system as well as the high energy costs of its operation over the life of the facility represent a significant fraction of the total project budget, so reducing these costs has been the primary focus of our design. Reliability is also a major concern, as the experimental schedule is intolerant of unscheduled down time.

The refrigerator main components include compressors, oil removal equipment, and the vacuum-insulated cold box containing the aluminum plate-fin heat exchangers and several stages of turbo-expanders.

The fundamental cooling process - expanding compressed helium gas to do work against low-temperature expansion engines, then recycling the lower pressure exhaust gas through a series of heat exchangers and subsequent compression - is a variant of the Carnot process that has been in use for many decades.

Helium is compressed at ambient temperature by a two-stage screw compressor group to a pressure in the 20 bar range. After re-cooling to ambient temperature and careful oil removal and drying residual water vapor, the high pressure helium is cooled in a cascade of counter-flow heat exchangers and expansion turbines. At the 40-K and 5-K levels helium flows are directed to the thermal shields of the cryomodules. The corresponding return flows are fed back to the refrigerator at suitable temperature levels. Inside the refrigerator cold-box the helium is purified from residual air, neon and hydrogen by switchable adsorbers at the 80-K and 20-K temperature levels.

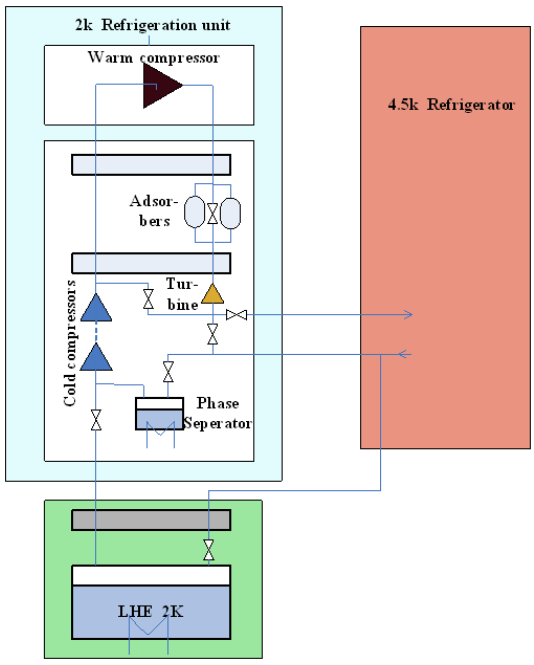

Figure 5.3.1: 2-K refrigerator flow diagram

The cryoplant will supply 4.5 K helium to the cryomodules. At each cryomodule the helium goes through a phase separator and a counter-flow heat exchanger to recover the cooling power, then expanded to 31 mbar via a JT-valve, resulting in helium II liquid at 2 K. The low pressure helium vapor from the 2-K saturated baths surrounding the cavities returns to the refrigerator through the gas return tube. The vapor is then pumped away and returned to the cryoplant.

There are two options for such a pumping system. One relies solely on cold compressors; the other employs a set of cold compressors followed by a final stage of warm compression. After superheating in the counter flow heat exchanger, the gas is compressed in the multiple-stage cold compressors to a pressure in the 0.5 to 0.9 bar range. This stream is separately warmed up to ambient temperature in exchangers and goes back to the warm compressors. The choice of a warm vacuum compressor makes it easier to adjust for heat load variations. This approach, which CERN uses in the LHC plants [2], also allows for an easier restart of the 2-K system after a system stoppage.

5.3.3 **Layout and Infrastructure**

The CEPC ring is separated into 8 sections by 8 straight sections. The superconducting RF and cryogenic systems are installed at these straight sections. In each RF station, there are four 12-m-long 1.3 GHz cryomodule strings and twelve 10-m-long 650 MHz cryomdule strings. Every two cryomodules share one valve box.

The 2-K cryogenic system consists of oil lubricated screw compressors, a liquid-helium storage vessel, a 2 K refrigerator cold box, cryomodules, a helium-gas pumping system and high-performance transfer lines. The cryogenic station is situated alongside the RF station. The cooling power required at each RF station will be produced by a 12 kW, 4.5 K refrigerator. These are installed at eight cryogenic stations, and distribute helium to the adjacent superconducting cavities.

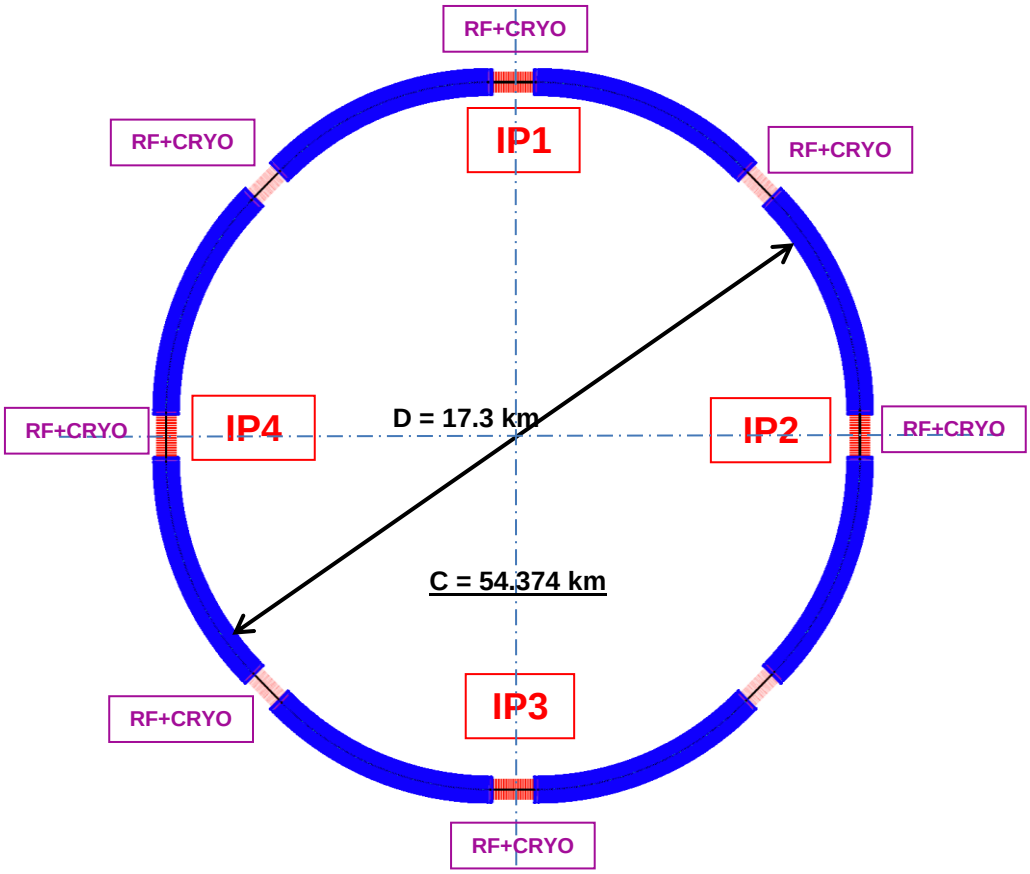

Figure 5.3.2: Distribution of the components of the CEPC cryogenic system

For reasons of simplicity, reliability and maintenance, the number of active cryogenic components distributed around the ring is minimized and the equipment locations chosen following these principles:

1) Equipment is installed as much as possible above ground to avoid the need for excavation of additional large underground caverns. Normal temperature equipment should be installed on ground level.
2) For safety reason, nitrogen is not allowed in the tunnel.
3) To decrease heat loss, the equipment working at temperatures below liquid nitrogen temperatures shall be installed near the cryomodules [3].

Equipment at ground level includes the electrical substation, the warm compressor station, storage tanks (helium and liquid nitrogen), cooling towers, and upper cold-boxes with liquid nitrogen precooling. Underground are the lower cold-boxes, 2-K cryomodules, multiple transfer lines, and distribution valve boxes. Fig. 5.3.3 shows the general architecture of the cryogenic system.

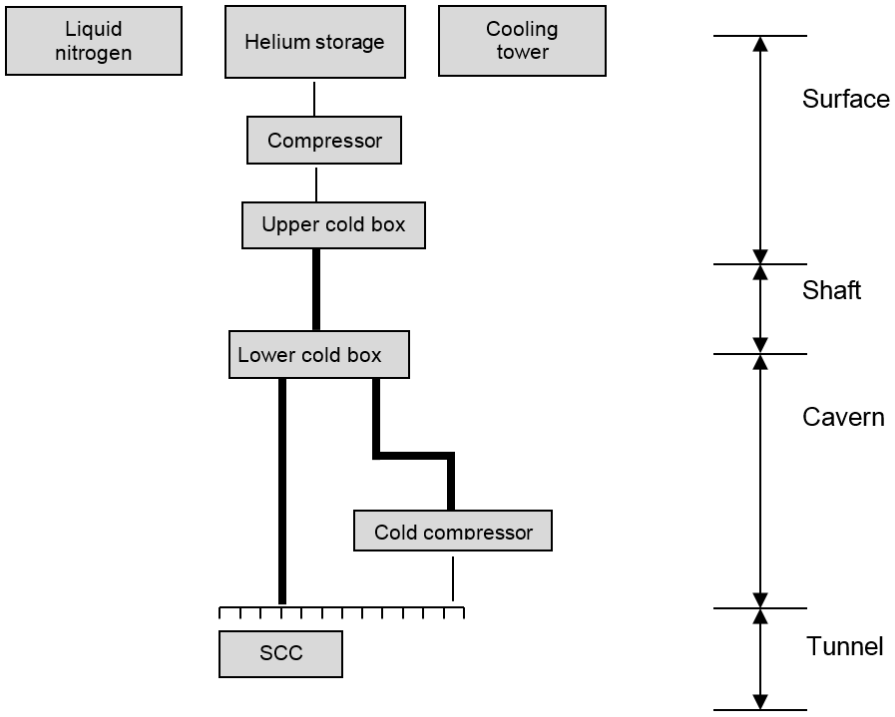

Figure 5.3.3: General architecture of the CEPC cryogenic system

5.3.4 **Cryogenic Plant Operation**

Saturated He II cools the RF cavities at 2 K. In view of the high thermodynamic cost of 2 K refrigeration, the thermal design of the components aims at intercepting heat loads at as high a temperature as possible. Hence, helium gas-cooled shields intercept radiation and conduction at 40 – 80 K and also at 5 – 8 K. The 40 – 80 K thermal shield is the first major heat intercept, shielding the cold mass from the bulk of the heat leaks at ambient temperature. This is followed by the 5 – 8 K shield for lower temperature heat interception.

A two-phase line (liquid-helium supply and vapor return) connects each helium vessel and connected once per module to the major gas return header. A small diameter warm-up/cool-down line connects the bottoms of the helium vessels. The cavities are immersed in baths of saturated superfluid helium, gravity filled from a 2-K two-phase header. Saturated superfluid helium flows along the two-phase header, which has phase separators located at one or both ends; the two-phase header is connected to the pumping return line. Fig 5.3.4 illustrates the flow.

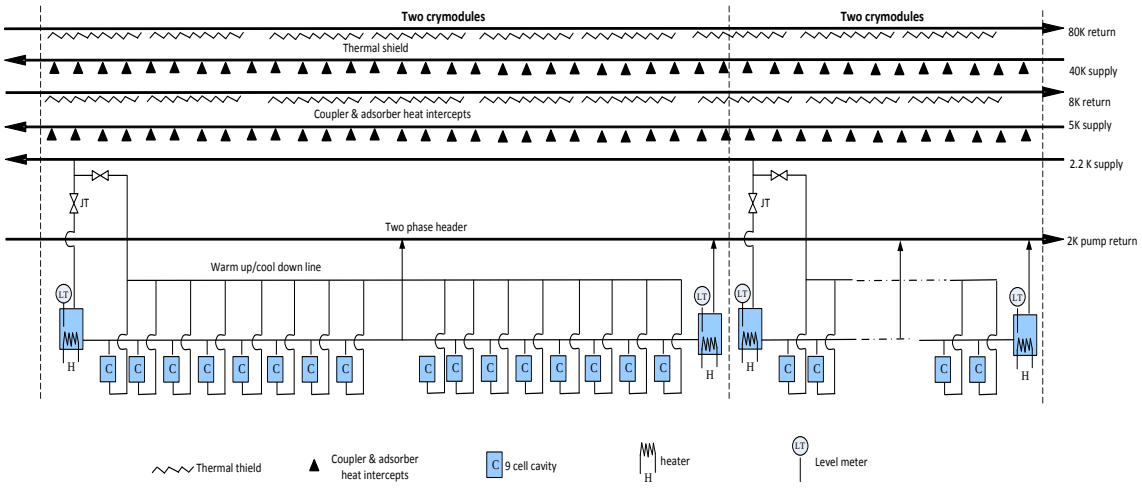

(a) The cooling scheme for Booster 9-cell cavities

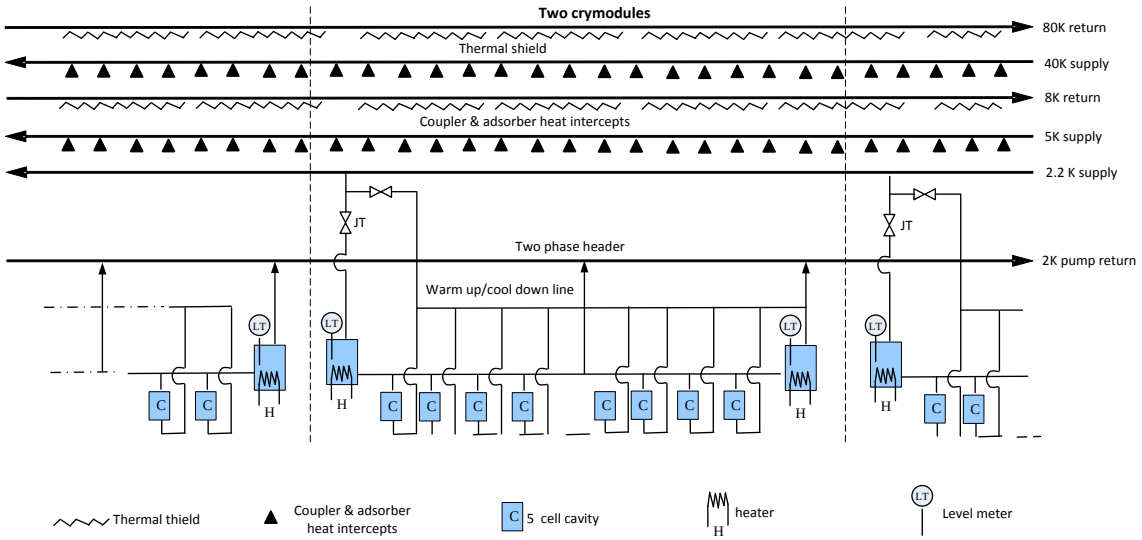

(b) The cooling scheme for Collider ring 5 cell cavities

Figure 5.3.4: Flow cooling scheme of CEPC

5.3.5 **Helium Inventory**

Most of the helium inventory consists of the liquid helium which bathes the RF cavities in the helium vessels and is roughly 70% of the entire system inventory. The volume of one 1.3 GHz and one 650 MHz module is about 320 liters and 346 liters, respectively. The total liquid helium volume in the system is 41,792 liters.

Accounting for the liquid in the Dewar, transfer lines, etc., and using the 70% factor mentioned above, the liquid volume in the system is 59,702 liters, or 8,657 kilograms [4].

Assuming that all the helium is returned to the helium tanks after machine shutdown, the inventory will be 5.3E4 cubic meters. To safely operate the cryogenic system, a coefficient factor of 60% is added, so CEPC needs a standard 8.8E4 cubic meter helium inventory system. The total helium inventory of the entire machine is about 14,000 kg.

5.3.6 **Control System**

A process control system is required for the widely distributed cryogenic components and for continuous cryogenic plant operation. A high degree of automation of the cryogenic processes will contribute to the overall system reliability [5].

The control system has to integrate local PLC controls of the screw compressors, cold boxes, the cold compressors and other sub-systems as well as state-of-the-art micro-processor controlled valve actuators and transmitters.

Standard industrial components will be used as much as possible and the control system follows an industrial approach.

5.3.7 **Safety Consideration**

For safety no nitrogen is used in the tunnel. There are two other importantsafety issues that need to be carefully considered. One is when the heat load increases unexpectedly; there should be enough discharge capacity available by means of safety valves or rupture disks to protect the equipment from damage. The other issue is to have oxygen detectors and venting equipment in case of helium leakage in the tunnel to protect personnel from injury.

There are other specific concerns about personnel safety including:

- Oxygen deficiency hazard. Because of the large quantities of compressed or liquefied gases of trapped cryogenic fluids, pressure relief systems must be appropriately designed and incorporated;
- High voltage distribution for compressor motors. For compactness and efficiency large motors are designed to run at several kilovolts;
- Hearing loss. Ear protection must be strictly adhered to in the high acoustic levels in and near the compressor room.

All of these items are generic to large cryogenic systems around the world and there are effective safeguards that must be carefully applied.

5.3.8 **Installed Cryogenic Power**

For Carrot circulation, the system efficiency is given by

$$COP_{ideal} = \frac{Q}{W} = \frac{T_0}{T_{amb} - T_0} \qquad (5.3.1)$$

For example, the efficiency from 300 K to 4.5 K is 0.015, or 66 W/W. But in fact although it is not possible to reach this value, one can come infinitely close to it. The refrigerator efficiency ɳ should be included:

$$COP_{real} = COP_{ideal} * ɳ. \qquad (5.3.2)$$

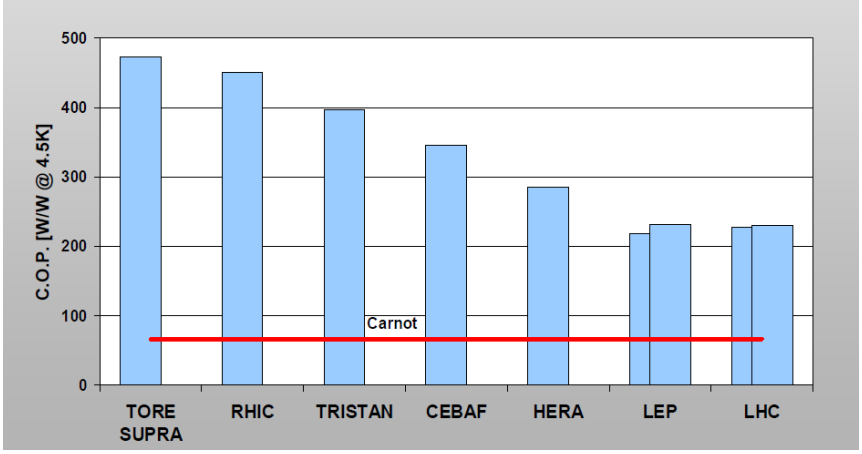

Figure 5.3.5: Refrigerator COP at 4.5 K

Fig 5.3.5, a survey of existing cryogenic plants at major accelerator facilities, shows that the best real COP today is about 230 W/W at 4.5 K in LHC [6].

In the ILC design, the real COP at 40 - 80 K, 5 - 8 K and 2 K are 16.4, 197.9 and 703.0 respectively. With our installed power estimate shown in Table 5.3.3, the total installed power for both Booster and collider rings is about 17.63 MW.

Table 5.3.3: Cryogenic system installed power requirements

	40-80 K	5-8 K	2 K
Booster heat load（kW）	17.63	1.88	2.26
Collider heat load（kW）	120.43	18.33	13.06
CEPC TOTAL（kW）	138.06	20.21	15.32
COP（W/W)	16.4	197.9	703.0
Installed power（MW）	2.26	4.00	10.77
Total installed power（MW）	17.63		

5.3.9 References

1. ILC Technical Design Report: Volume 3, Part II, p 54.
2. P. Lebrun. “Large cryogenic helium refrigeration system for the LHC.” in Proceedings of the 3rd International Conference on Cryogenics & Refrigeration, ICCR2003, pages 11-13. 2003.
3. LHC design report, volume 1, chapter 11, cryogenic system.
4. ILC Technical Design Report, volume III, part II, p 54.
5. XFEL TDR p. 514.
6. P. Lebrun, “Cryogenic refrigeration for the LHC (2009).” http://www-fusion-magnetique.cea.fr/matefu/school_2/Tuesday/lebrun-LHCcryogenicrefrigeration.pdf.

5.4 Magnets

This section describes the magnets required for the three accelerators: Linac, Booster and the Collider. Also included are the magnets for beam transport lines and

injection and extraction.

The total length of the Linac is 500 m; there are 35 triplet quadrupole lenses and 35 correctors in it. The circumference of the Booster and the Collider is nearly similar, about 54.4 km. The Booster has 5,120 dipoles, 1,528 quadrupoles and 1,248 sextupoles. The Collider has 1,984 dipoles, 2,304 quadrupoles and 1,984 sextupoles. The length of the dipole magnets for the Booster and Collider are 8 m and 18 m respectively. This means that more than 65% of the Booster and Collider circumference will consist of dipole magnets. Therefore, cost becomes an important issue in the magnet design, especially the dipoles. Since the dipole field is very low, as in LEP's dipole magnets, steel-concrete cores will be used to make the yokes. There are two advantages to steel-concrete cores. One is cost reduction of the steel since 80% of the steel is substituted by concrete if a filling factor of 0.2 is used as in the detailed descriptions below. Another advantage is an increase in the working magnetic induction in the iron. Thus the magnets are less sensitive to differences in iron quality and in particular to the coercive force. To further reduce the dipole magnet cost, aluminum instead of copper will be used for the coils.

5.4.1 **Booster Magnets**

5.4.1.1 ***Dipole Magnets***

There are 5,120 dipole magnets in the Booster. Each magnet is 8 m long; it has two C-shaped steel-concrete cores of about 4 m length, which are installed end to end in groups. The field in the magnet gap will change from 32 Gauss to 614 Gauss during acceleration from injection energy to extraction energy, as shown in Fig. 5.4.1. Due to this very low field, the cores are composed of stacks of low carbon steel laminations, 1.5 mm thick, spaced 6 mm apart. The gaps are filled with a cement mortar. The filling factor of 0.2 gives a small drop of ampere turns at the maximum field.

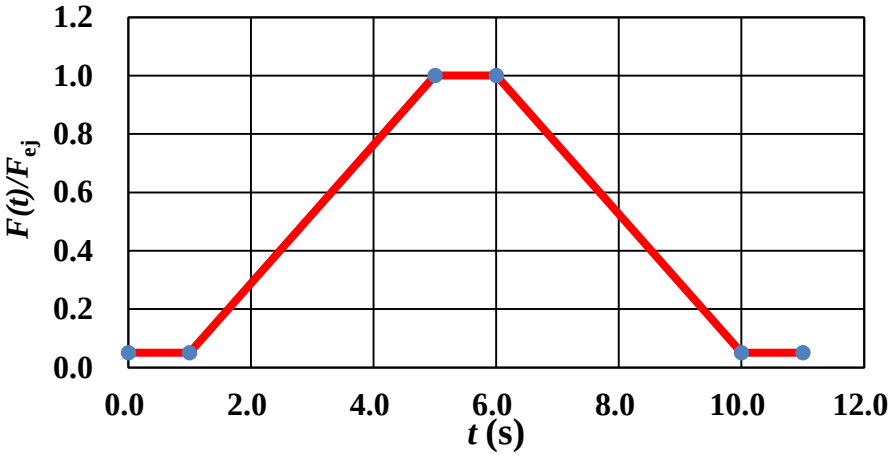

Figure 5.4.1: The magnetic field cycle of the Booster

For conductors are made from 99.5% pure aluminum of cross section 40×40 mm^2. Since the Joule heating is low, the Booster dipole magnets can be air cooled.

The uniformity of the integral field of the 4-m-long dipole cores can be optimized within 3×10^{-4} by pole shimming in 2D or end chamfering in 3D. The cross section and magnetic flux of the dipole magnet is shown in Fig. 5.4.2, and its main parameters are listed in Table 5.4.1.

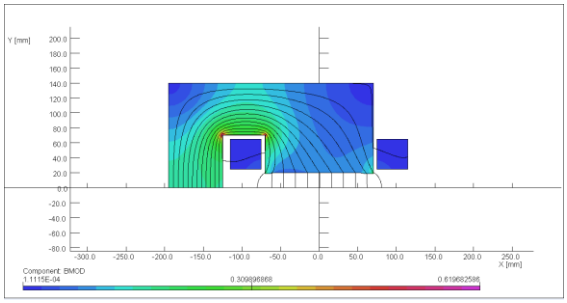

Figure 5.4.2: Magnetic flux distribution

Table 5.4.1: The main parameters of the Booster dipole magnet.

Quantity	5120
Minimum field strength (Gauss)	32
Maximum field strength (Gauss)	614
Magnetic gap (mm)	40
Bending angle (mrad)	2.584
Magnetic Length (m)	8
Bending radius (m)	6519
Good field region (mm)	52
Current (A)	1000
Conductor cross section (mm)	40×40
Turns per pole	1
Resistance of the magnet (mΩ)	0.624
Current density in Aluminum(A/mm^2)	0.65
Operating voltage (V)	0.634
Power per magnet (kW)	0.624
Induction per magnet (mH)	0.164
Core cross section (W×H)（mm）	236×260
Core length (m)	8
Core mass (t)	1.6
Aluminum Mass (t)	0.153

5.4.1.2 *Quadrupole Magnets*

Because of the large number of quadrupole magnets in the Booster, reducing the cost is important. Hollow aluminum conductor is selected for the coil instead of conventional copper, because of the much lower price and reduced weight. The iron core is made of 1.5 mm thick laminated low carbon silicon steel sheets. The pole has parallel sides so that simple racetrack shaped coils can be used. The whole magnet will be assembled from four identical quadrants, and can also be split into two halves for installation of the vacuum chamber.

Due to the long length, 2D magnetic field analysis is sufficient at this stage in the conceptual design. The pole profiles are designed to introduce positive 12-pole and 20-pole multipole fields to compensate for end field effects.

The cross section for the quadrupole magnet has been designed and optimized using OPERA-2D [3]. In the simulation, only one quarter of the magnet is modelled. The magnetic flux lines and magnetic flux density distribution are show in Fig. 5.4.3 and Fig. 5.4.4, respectively.

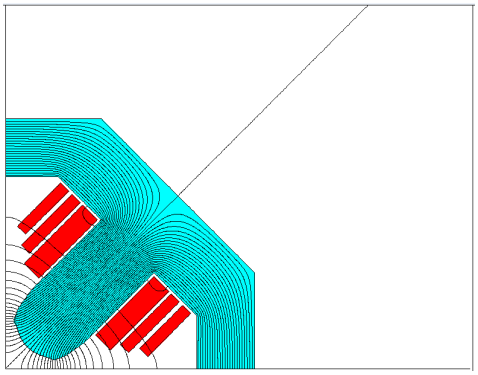

Figure 5.4.3: 2D flux lines of QF (One quarter cross section)

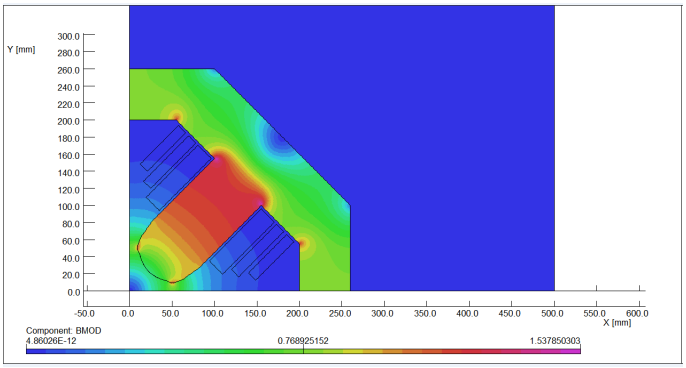

Figure 5.4.4: Magnetic flux density distribution of QF

The calculated multipole field contents normalized to the quadrupole field are listed in Table 5.4.2.

Table 5.4.2: 2D field harmonics （unit, 1×10^{-4}）

n	B_n/B_2 at R=26.5 mm	B_n/B_2 at R=17.5 mm
2	10000	10000
6	4.42	3.50
10	1.48	0.47
14	0.19	0.09

The main design parameters are listed in Table 5.4.3.

Table 5.4.3: Main design parameters of Booster quadrupole magnets

Magnet name	QF	QD
Quantity	764	764
Bore diameter（mm）	64	48
Field gradient（T/m）	14.3	14.3
Magnetic length（m）	1.0	1.0
Ampere-turns per pole（AT）	6050	3402
Coil turns per pole	25	21
Excitation current（A）	242	162
Conductor size（mm）	11×11, ∅6, r1(Hollow Aluminum conductor)	9×9, ∅4.5, r1(Hollow Aluminum conductor)
Current density（A/mm^2）	2.6	2.5
Resistance（Ω）@35°	0.082	0.095
Inductance（H）	0.038	0.027
Voltage drop（V）	19.8	15.3
Joule loss（kW）	4.8	2.5
Water pressure（kg/cm^2）	6	6
Cooling circuits	4	4
Water flow velocity（m/s）	1.85	1.7
Total water flow（l/s）	0.21	0.11
Temperature increase（℃）	6.5	6.4
Core width and height（mm）	520×520	400×400
Core length（mm）	978	984
Net core weight（t）	1.2	0.7
Net conductor weight（t）	0.07	0.04

5.4.2 **Collider Magnets**

5.4.2.1 ***Dipole Magnets***

Due to the low field level of 700 Gauss, design of the dipole magnets is similar to LEP dipole magnets. Each magnet has four C-shaped steel-concrete cores of about 4.5 m length, installed end to end in groups. The cores are composed of stacks of low carbon steel laminations, 1.5 mm thick, spaced by 6 mm gaps filled with cement mortar. The filling factor of 0.2 gives a small drop of ampere turns at the maximum field. Because of large quantity of 1,984 magnets and their long length of 18 m, the scheme of steel-concrete core not only increases the working field in the yokes of the dipole magnets but also reduces their cost significantly.

For economic reasons, the excitation bars are made from 99.5% pure aluminum of cross section 60×40 mm^2 with a cooling hole of 9 mm in diameter. The bars are bent and interconnected at the ends of the magnets.

By using the OPERA-2D and 3D programs, the pole size and pole shape of the magnet is optimized. The distribution of the vertical component B_y is shown in Fig. 5.4.5. The design parameters are listed in Table 5.4.4.

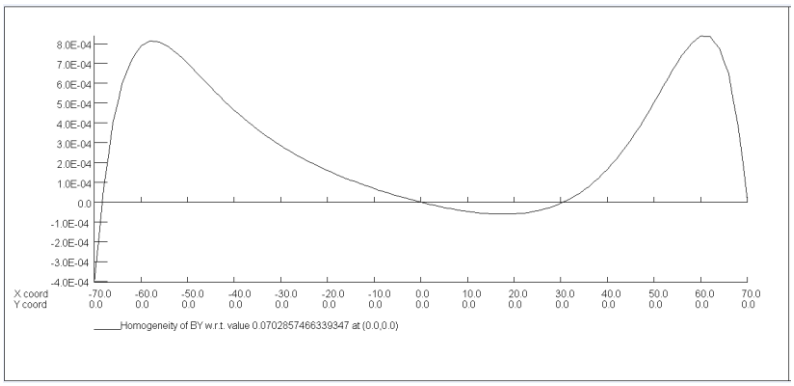

Figure 5.4.5: Distribution of the field By

Table 5.4.4: The main parameters of dipole magnets for the Collider

Quantity	1984
Maximum field strength (T)	0.07
Magnetic gap (mm)	80
Bending angle (mrad)	3.17
Magnetic Length (m)	18
Bending radius (m)	6094
Good field region (mm)	100
Current (A)	2250
Conductor cross section (mm)	60×40, ∅9,r2
Turns per pole	1
Resistance of the magnet (mΩ)	0.963
Current density (A/mm^2)	1.0
Operating voltage (V)	2.25
Power per magnet (kW)	5.1
Induction per magnet (mH)	0.33
Number of water circuits per magnet	2
Water pressure (kg/cm^2)	6
Flow velocity(m/s)	3.14
Water flux (l/s)	0.4
Temperature rise(℃)	4
Core cross section (W×H)（mm）	450*400
Core center length (m)	18
Core mass (t)	9.4
Aluminum Mass (t)	0.5

5.4.2.2 *Quadrupole Magnets*

Because of the large number of quadrupole magnets in the Collider, reducing the cost is of great concern in the design, while at the same time meeting the physical requirements. The design is similar to that of quadrupole magnets in LEP. Hollow aluminum conductor is used for the coils. The iron core is made of laminated low carbon silicon steel sheet with a thickness of 1.5 mm. The pole has parallel sides so that simple racetrack shaped coils can be used. The magnet will be assembled from four identical quadrants, and can also be split into two halves for the installation of the vacuum chamber.

Since they are long 2D magnetic field analysis is used. The good field region is assumed to be 86% of the magnet bore diameter, and the harmonic field is less than 5×10^{-4}. The pole profiles are designed to introduce positive 12-pole and 20-pole multipole fields to compensate for end field effects.

The cross section of the quadrupole magnet is designed and optimized using OPERA-2D [3]. In the simulation, only one quarter of the magnet is modelled. The magnetic flux lines and magnetic flux density distribution are show in Figures 5.4.6 and 5.4.7 respectively.

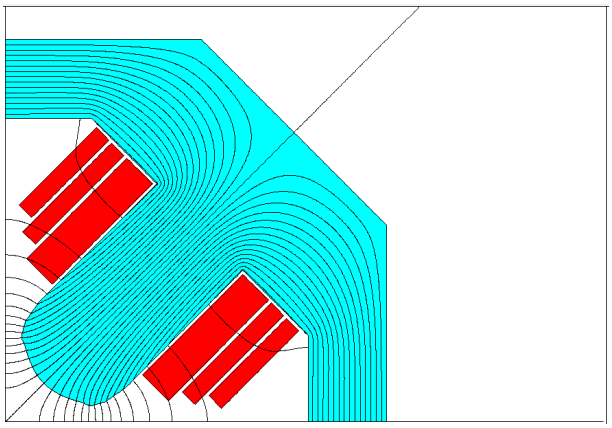

Figure 5.4.6: 2D flux lines (One quarter cross section)

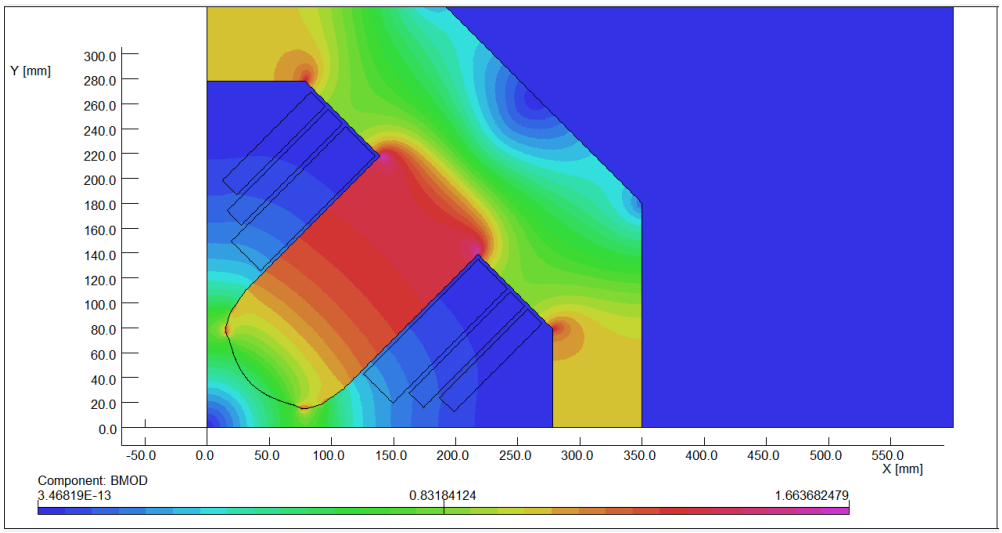

Figure 5.4.7: Magnetic flux density distribution

The calculated multipole field contents normalized to the quadrupole field are listed in Table 5.4.5.

Table 5.4.5: 2D field harmonics（unit, 1×10^{-4}）

n	B_n/B_2 at R=43mm
2	10000
6	4.59
10	1.85
14	0.30

The main design parameters are listed in Table 5.4.6.

Table 5.4.6: Main design parameters of the collider quadrupole magnet

Magnet name	CEPC MQ
Quantity	2304
Bore diameter（mm）	100
Field gradient（T/m）	10
Magnetic length（m）	2.0
Ampere-turns per pole（AT）	10382
Coil turns per pole	29
Excitation current（A）	358
Conductor size（mm）	15×15, ∅9, r1(Hollow Al conductor)
Current density（A/mm^2）	2.2
Resistance（Ω）@35°	0.1
Inductance（H）	0.095
Voltage drop（V）	35.7
Joule loss（kW）	12.8
Water pressure（kg/cm^2）	6
Cooling circuits	4
Water flow velocity（m/s）	1.6
Total water flow（l/s）	0.41
Temperature increase of coolant（℃）	8.5
Core width and height（mm）	700×700
Core length（mm）	1960
Net core weight（t）	4.5
Net conductor weight（t）	0.24

5.4.2.3 *Superconducting Quadrupole Magnets*

5.4.2.3.1 Overall Design Consideration

The requirements of the CEPC Interaction Region superconducting quadrupole magnets are listed in Table 5.4.7.

Table 5.4.7: Requirements of CEPC Interaction Region quadrupole magnets

Name	Magnetic length (m)	Field gradient (T/m)	Coil inner radius (mm)
QD	1.25	304	20
QF	0.72	309	20

There are two types of high gradient quadrupole magnets in the interaction region. The magnetic field at the pole exceeds 7T and the design and construction of these quadrupoles is very challenging. These two magnets are inside the detector solenoid magnet which has a field of about 3.5T. So these quadrupole magnets are iron-free magnets, and Nb_3Sn technology must be used to meet the requirements. The coils are made of Rutherford type Nb_3Sn cables, and are clamped by stainless steel collars.

For long quadrupole magnets, 2D magnetic field analysis is sufficient in the conceptual design phase. The radius of the good field region is assumed to be 14 mm, and the harmonic field content smaller than 3×10^{-4}. To achieve this field quality, the position precision of the coil needs to be better than 0.02 mm.

To minimize the effect of the longitudinal detector solenoid field on the accelerator beam, anti-solenoid coils are used. Their magnetic field direction is opposite to the detector solenoid field, and the combined total integral longitudinal field generated by the detector solenoid and anti-solenoid coils is nearly zero.

5.4.2.3.2 Quadrupole Coil

Conceptual design is based on a typical quadrupole block coil. The two type quadrupole coils have the same cross section, but different lengths. The magnetic field calculation is performed using OPERA-2D [3]. Only one quarter of the magnet is modelled, and the magnetic flux lines and magnetic flux density distribution are shown in Fig. 5.4.8 and Fig. 5.4.9, respectively.

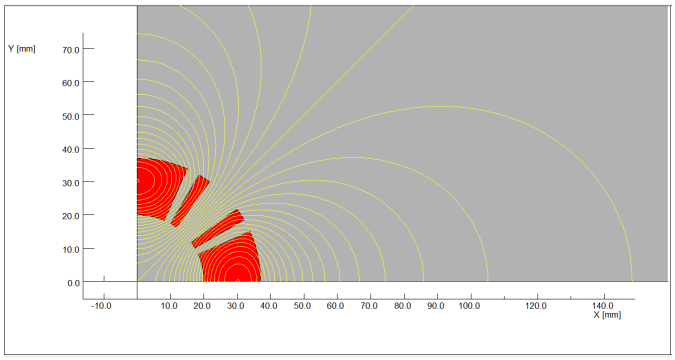

Figure 5.4.8: 2D flux lines (One quarter cross section)

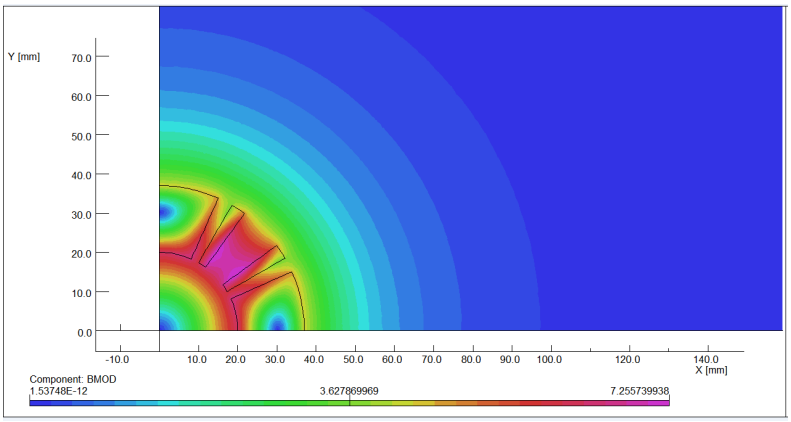

Figure 5.4.9: Magnetic flux density distribution

The calculated relative multipole field contents are listed in Table 5.4.8.

Table 5.4.8: 2D field harmonics（unit, 1×10^{-4}）

n	B_n/B_2@R=14 mm
2	10000
6	0.07
10	-0.02
14	-2.2

The main design parameters of the quadrupole magnets are listed in Table 5.4.9.

Table 5.4.9: Main design parameters of the interaction region quadrupole magnets

Magnet name	QD	QF
Field gradient (T/m)	304	309
Magnetic length (m)	1.25	0.72
Cable Type	Rutherford Type Nb_3Sn Cable	
Coil turns per pole	24	24
Excitation current (kA)	8.15	8.25
Coil layers	2	2
Cable Width (mm)	8	8
Stored energy (KJ)	70.2	41.4
Inductance (mH)	2.1	1.2
Peak field in coil (T)	7.2	7.1
Coil inner diameter (mm)	40	40
Coil out diameter (mm)	74	74
Cable weight (kg)	26	17
Cold mass weight (kg)	190	125
Cryostat diameter (mm)*	400	400
Coil mechanical length (mm)	1500	950

* Including quadrupole magnet and anti-solenoid for compensating the detector solenoid.

5.4.2.3.3 Anti-Solenoid Coil

Two types of anti-solenoid coils (Anti-QD and Anti-QF) are placed within QD and QF respectively. Each pair of quadrupole and anti-solenoid coils is at the same longitudinal position (along the beam line) and in the same cryostat. The two types of anti-solenoid coils have the same cross section, but with different lengths.

The magnetic field calculation is performed with OPERA-2D [3], using an axial-symmetric model. The total integrated longitudinal field of Anti-QD and Anti-QF is about 14.1 T-m. The magnetic flux lines and longitudinal field distribution, B_z of Anti-QD are shown in Fig. 5.4.10 and Fig. 5.4.11, respectively.

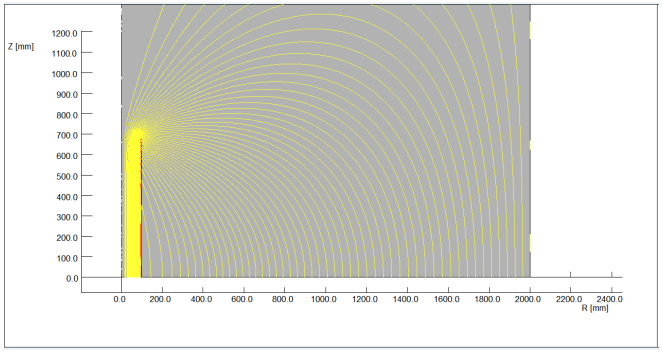

Figure 5.4.10: 2D flux lines of Anti-QD (half cross section)

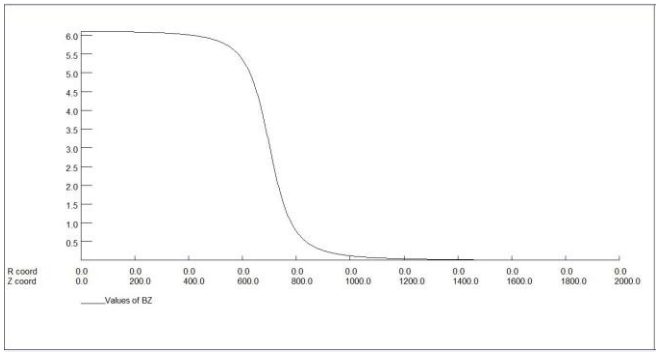

Figure 5.4.11: Longitudinal field distribution of Anti-QD

The main design parameters of the anti-solenoids are summarized in Table 5.4.10.

Table 5.4.10: Main design parameters of the interaction region anti-solenoids

Magnet name	Anti-QD	Anti-QF
Central field（T）	6.1	6.1
Magnetic length（m）	1.4	0.9
Conductor Type	NbTi-Cu Conductor, 4×2mm	
Coil layers	10	10
Coil turns	3500	2250
Excitation current（kA）	1.96	1.98
Stored energy (KJ)	472	301
Inductance（mH）	246	155
Peak field in coil (T)	6.2	6.2
Coil inner diameter (mm)	160	160
Coil out diameter (mm)	200	200
Cable weight (kg)	145	95
Cold mass weight (kg)	230	150
Coil mechanical length (mm)	1460	950

The cross section of the QD and QD coil is shown in Fig. 5.4.12 (inner quadrupole coil; outer anti-solenoid coil).

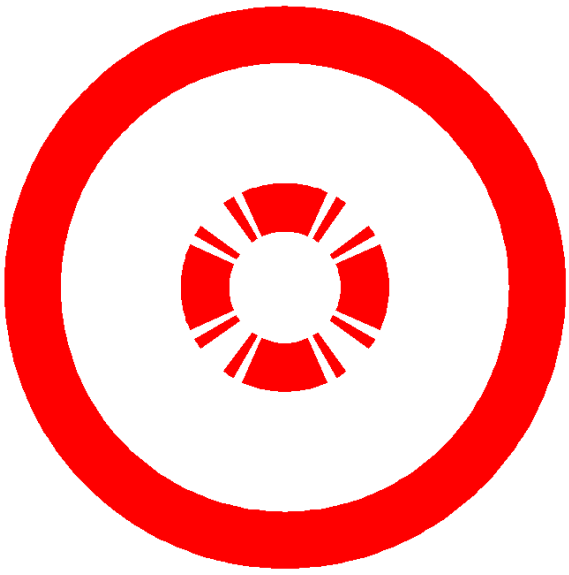

Figure 5.4.12: Cross section showing the quadrupole and anti-solenoid coils

5.4.2.4 *Sextupole Magnets*

There are two types of sextupole magnets in the Main Ring, with the same aperture and cross section but of different lengths. The cores of the sextupole magnets are made from 1.5 mm thick low carbon steel laminations. To reduce cost, the coils will be wound from hollow aluminium conductors. A 3D model of the sextupole is shown in figure 5.4.13. By optimizing the pole face shape, all the high harmonic errors can be reduced to less than 5.0×10^{-4}.

The magnets are composed of six parts, three of them are welded together to form the upper and lower halves, which are then bolted together. This makes vacuum chamber installation convenient. The main parameters of the two type of sextupole magnets are listed in Table 5.4.11.

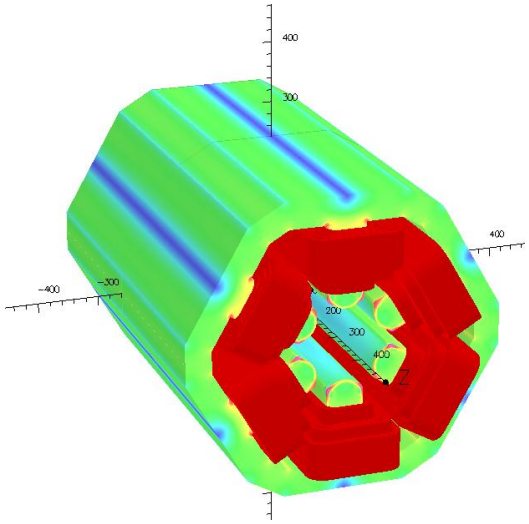

Fig. 5.4.13: 3D model of the sextupole magnet

Table 5.4.11: The main parameters of the sextupole magnets for the Collider

	SD	SF
Quantity	992	992
Magnetic Length (mm)	700	400
Strength of sextupole field (T/m^2)	180	180
Aperture diameter(mm)	120	120
Good field region, GFR radius (mm)	100	100
Harmonic field errors across GFR	0.10%	0.10%
Excitation amp-turns（At）	5156.620	5156.620
Size of conductor（mm）	20*10D5	20*10D5
Area of conductor（mm^2)	130.00	130
Coils turns on each pole	16	16
Current（A）	322.29	322.29
Current density（A/mm^2)	2.48	2.48
Ampere factor	1.02	1.02
Average turn length (mm)	1792.2	1174.2
Total conductor length in each coil (m)	28.68	18.79
Weight of conductor (kg)	60.43	39.60
Resistance (Ohm）	0.03745	0.02454
Voltage drop on resistance (V)	12.07	7.91
Power loss (kW)	3.890	2.549
Inductance (H)	0.01480	0.00854
Width/Height of iron core (mm)	520	520
Length of iron core (mm)	670	370
Weight of iron core (kg)	586.85	300
Total weight of each magnet (ton)	0.680	0.357

Number of parallel circuits	6	6
Water pressure drop (kg/cm^2)	6	6
Inner diameter of cooling water pipe (mm)	5	5
Length of each parallel circuit (m)	31.54	20.67
Velocity of water flow (m/s)	2.53	3.22
Water flow（l/s）	0.2982	0.3797
Temperature rise (degrees)	3.11	1.60

5.4.3 References

1. LEP design report, CERN-LEP-84-01, CERN, Geneva, 1984.
2. K. Tsuchiya, et al., "Superconducting Magnets for the Interaction Region of KEKB," *IEEE TRANSACTIONS ON APPLIED SUPERCONDUCIIVITY*, 9 (2), pp: 1045-1048, June 1999.
3. OPERA, "Vector Fields Software," Cobham Technical Services, http://www.vectorfields.com.

5.5 Magnet Power Supplies

A large number of power supplies are required for powering the magnets of the CEPC Collider, Booster, low energy beam transport (LEBT) and the Linac.

The Collider power supplies are d.c. supplies. All the power supplies are rated for 120 Gev operation with 10 ~ 15% safety margins in both current and voltage. All the dipole, quadrupole and sextuple power supplies are unipolar, and all correction power supplies are 4-quadrant to allow reversal of the current through the load as needed.

In the Booster, the particles are accelerated from 6 GeV to 120 GeV. The power supplies for the Booster operate at a repetition frequency of 0.1 Hz.

The following shows the basic design criteria for the power supplies.

- Meet the accelerator physics design requirements.
- Work in close collaboration and communication with the magnet designers to choose the most suitable circuits.
- Modular design for most power supplies.
- High reliability, better EMC and convenient electrical and mechanical features for easy maintenance and replacement.
- Fully digital design for all supplies.
- Switching mode provided in all systems.

The parameters are set as follow:

- Magnet parameters and connection modes (including cable losses) determine current and voltage ratings.
- Cable current density less than $2A/mm^2$
- Water cooling for power supplies with power greater than 10 kW, and forced air cooling for the others.
- Power factor of the mains network: $\cos\phi = 0.9$.
- Efficiency of power supplies: $\eta = 0.87$.

- Computation of cable resistance: $R = \rho \times \frac{l}{s}(1 + \Delta T \alpha)$

where ρ is the resistivity of copper (0.0182 at 20°C), α is the temperature coefficient (0.00393/°C), l is the cable length and s is the total cross section of the cable in mm^2.

5.5.1 **Collider Power Supplies**

Fig. 3.1 in Chapter 3 shows the layout of the Collider. Power supply buildings will be built at ground level and located between two ARCs. In order to save on the length of power cables, two adjacent half-arcs will use one or two or four power supplies. There are 8 power supply halls corresponding to the 8 arcs in the tunnel as in Figures 5.5.1a and 5.5.1b..

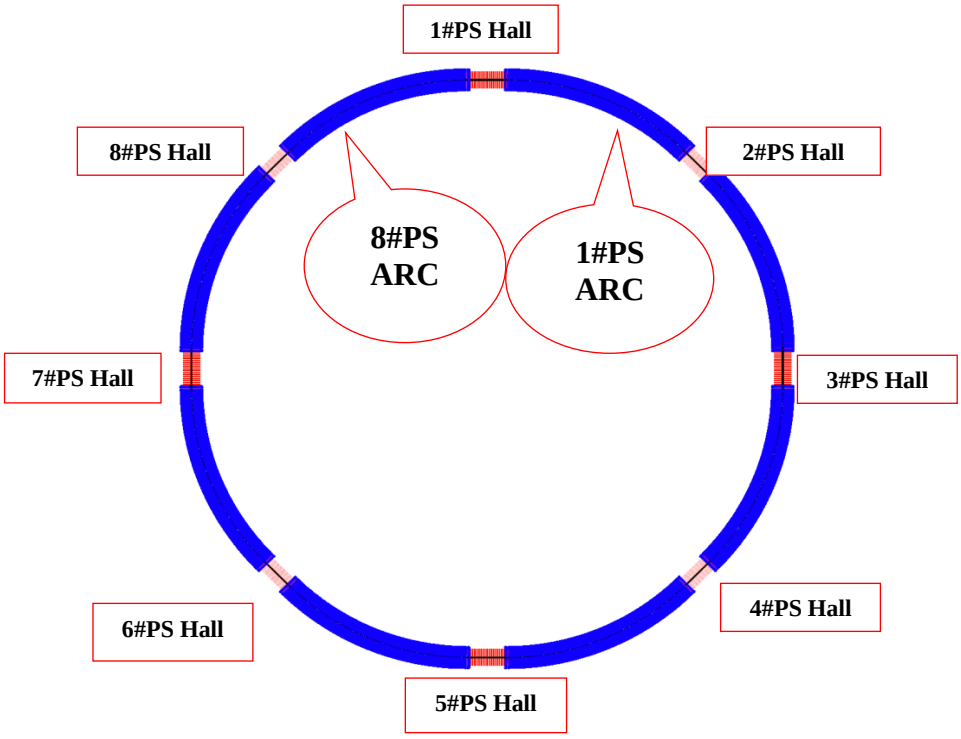

Figure 5.5.1a PS Hall layout

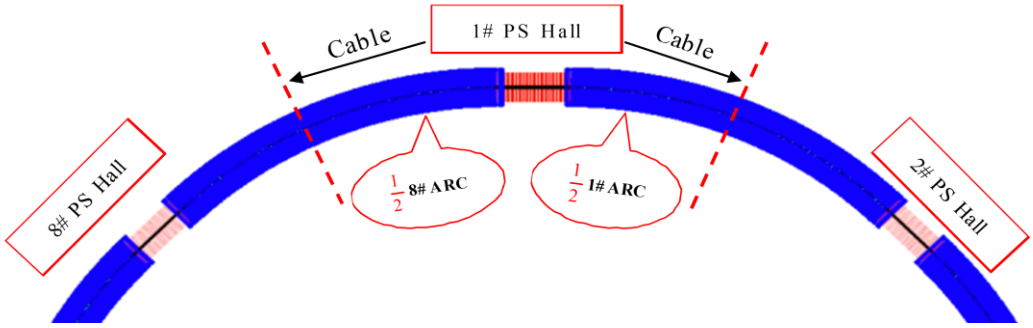

Figure 5.5.1b PS Hall layout

System reliability is required to be very high and the system should operate with a mean-time-between-failures (MTBF) of several months. The power supply is designed with built-in redundancy by using a modular approach. The power part is divided into n + 1 modules, n supplying nominal current, and one module in reserve in case of a trip. Automatic 'hot' switching between modules will be designed to realize 'hot' maintenance and repair. Efficient monitoring and diagnosis methods will be adopted to anticipate faults. Correction devices will compensate for mains voltage sags and there will be a UPS.

The Collider consists of 1,984 dipole magnets. Dipoles in each ARC are connected in series and powered by one power supply. Thus there are 8 dipole magnet power supplies, each 1.26 MW (including an allowance for cable losses). The ratings for the manufacturers include 10 ~ 15% safety margins in both current and voltage.

Each power supply has a load of 248 dipole magnets.

The quadrupoles are divided into 16 focusing families and 16 defocusing families, each family corresponding to one-half of an arc. Each family consists of 72 series-connected magnets and is powered by one separate power supply. The current in each quadrupole can be separately adjusted with a shunt up to +/- 2%.

The sextupoles are divided into 32 focusing families and 32 defocusing families. For each ARC, there are four families of focusing sextupoles and four families of defocusing sextupoles. Each family consists of 31 series-connected magnets and is powered by one separate supply.

The total number of correction BH and BV magnets is about 1,500, and each one is powered by a separate supply. For convenient maintenance and repair, the ratings for all correction power supplies is the same. They are a module-based design.

Table 5.5.1: Main magnets parameters and required ratings

Type	magnets parameters	Required Ratings	Number
Dipole	0.33 mH/1 mΩ	2250 A/2.25 V	1984
Quad.	95 mH/100 mΩ	358 A/35.7 V	2304
Sext.D	37 mΩ	322.3 A /12.1 V	992
Sext.F	25 mΩ	322.3 A /7.9 V	992

Table 5.5.2: Power supplies for the Collider

Power Supply	**Load parameters**	Required Ratings	Designed Ratings for manufacturers
Dipole	82 mH /0.248 Ω	2250 A/558 V	2500 A/710 V
Quad.	6.84 H/7.2 Ω	358 A/2577.6 V	394 A/3073 V
Sext.D	1.15 Ω	322.3 A/375 V	355 A/600 V
Sext.F	0.78 Ω	322.3A/244.9 V	355 A/470 V
Correction			40 A/10 V

Table 5.5.3: Power supply requirements

Power Supply	**Number**	Stability 8hours	Power (kW)/set Ratings
Dipole	8	100 ppm	1600 2250 A/700 V
Quad.	32	100 ppm	985 358 A /2750 V
Sext.D	32	300 ppm	181 323 A/560 V
Sext.F	32	300 ppm	139 323 A/430 V
Correction	1500	500 ppm	0.4 40 A/10 V
Total power for the Collider supply system			55 MW

5.5.2 **Booster Power Supplies**

For the Booster the design criteria are the same as for the main ring power supplies. There is a small difference from the DC power supplies of the main ring because the current for the Booster supplies is dynamic with a repetition rate of 0.1 Hz. Fig. 5.5.2 shows the Booster magnetic field cycle.

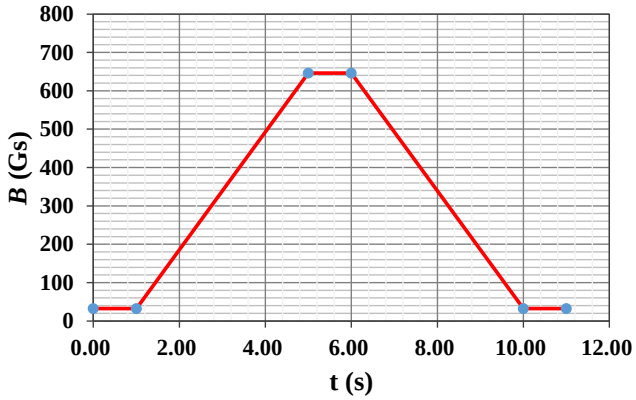

Figure 5.5.2: The magnetic field cycle of the Booster

There are 8 ARC units for the Booster, the same as for the main ring. The Booster consists of 5120 dipole magnets. For each ARC, all dipoles are connected in series and powered by one power supply. There are a total of 8 dipole magnet power supplies, each of 582 kW (including an allowance for cable losses). The manfacturer's ratings add a 10 ~ 15% safety margins for both current and voltage. For each power supply, 640 dipole magnets are the load.

The quadrupoles are divided into 16 focusing families and 16 defocusing families, and each family corresponds to one half of an arc. Each family consists of 40 series-connected magnets and is powered by one separate power supply.

The sextupoles are divided into 32 focusing families and 32 defocusing families. For each ARC, there are four families of focusing sextupoles and four families of defocusing sextupoles. Each family consists of 20 series-connected magnets and is powered by one separate power supply.

The total number of correction BH and BV magnets is 1,436, and each magnet is powered by one separate power supply. For convenient maintenance and repair, the rating for all correction power supplies is the same and has a module-based design.

Table 5.5.4: Booster magnets parameters and ratings

Type	magnets parameters	Required Ratings	Number
Dipole	0.43 mH/0.125 mΩ	1000 A/1.3 V	5120
Quad.F	38 mH/82 mΩ	251 A/19.8 V	764
Quad.D	27 mH/95 mΩ	168 A/15.3 V	764
Sext.D	40.4 mΩ	100 A/4.0 V	624
Sext.F	63 mΩ	95 A /6.0 V	624
Corr.BH	2.85 mH/51.2 mΩ	28.41 A/1.46 V	764
Corr.BV	5.34 mH/75.8 mΩ	24.5 A/ 1.86 V	764

Table 5.5.5: Power supplies for Booster magnets

Power Supply	**Load parameters**	Required Ratings	DesignedRatings for manufacturers
Dipole	131 mH /0.38 Ω	1000 A/395.2 V	1100 A/610 V
Quad.F	1.52 H/3.28 Ω	251 A/794 V	270 A/1150 V
Quad.D	1.1 H/3.8 Ω	168 A/615.6 V	178 A/900 V
Sext.D	3.64 Ω	100 A/27.2 V	110 A/165 V
Sext.F	5.56 Ω	95 A/43.2 V	110 A/190 V
Corr.BH	2.85 mH/51.2 mΩ	28.41 A/1.46 V	40 A/10 V
Corr.BV	5.34 mH/75.8 mΩ	24.5 A/1.86 V	40 A/10 V

Table 5.5.6: Booster Power supplies requirements

Power Supply	**Number**	Stability 8hours	Power (kW) Ratings
Dipole	8	500 ppm	560 1000 A/560 V
Quad.F	16	500 ppm	264 251 A/1050 V
Quad.D	16	500 ppm	138 168 A/820 V
Sext.D	32	1000 ppm	15 100 A/150 V
Sext.F	32	1000 ppm	16.2 95 A/170 V
Corr.BH	718	1000 ppm	6.2 29 A/214 V Above ground
			0.4 40 A/10 V Underground
Corr.BV	718	1000 ppm	4.8 26 A/186 V
			0.4 40A/10V Underground
Total power for the Booster power supply system			20 MW above ground 13 MW underground

5.5.3 **Linac Power Supplies**

The design of the Linac (400 m) power supply system is based on data from operation of the BEPCII Linac (200 m) power supply system.

Quadrupole power supplies:

Number: 200

Power: 5 kW (100 A/50 V)

Correction power supplies:

Number: 120

Power: 1.6 kW

Total power for Linac power supply system: 1.2 MW.

The total power of the CEPC power supply system is 68 MW (if all correction power supplies were installed in the tunnel). If one also includes the power supplies for the IR, and spectrometer, the total power is about 80 MW.

5.5.4 **Power Supply Electronics**

5.5.4.1 ***Introduction***

The control system of the early accelerator power converters was analog. Following is a brief summary of some of the features of these analog systems.

- Mature technology, used for many years and extensively developed;
- For any changes of the PID controller (proportional-integral-derivative controller) parameters, a manual hardware modification had to be done; if any major changes were needed in the control system, the regulation hardware had to be redesigned;
- The performance of the regulation was mainly dependent on the DAC (digital to analog converter) and the DCCT (direct current current transducer);
- Not convenient for diagnostics.

For a long period, the introduction of a variety of digital signal processors, such as MCU, DSP and FPGA, has made it possible to replace analog regulation functions like PID controllers with digital algorithms implemented in intelligent processors.

The advantages of digital control over analog include:

- Complex though fast control algorithms can be implemented and remain stable in relation to the process dynamics;
- Flexible for different projects;
- No extra offset or drift and better noise immunity;
- Parameter optimization and changes of the control system can be done by software; hardware redesign is not required;
- Friendly for debugging and diagnostics;
- Easy to extend functionality.

For the CEPC power supplies, digital control based design will be implemented.

5.5.4.2 *Digital Controller*

Fig. 5.5.3 shows the digital controller. For a digital control system, the performance of the converter is mainly determined by the ADC (analog to digital converter) and the DCCT. Based on the digital controller there is only one DCCT used for both feedback and display, compared to the analog system where two DCCTs are necessary for separate feedback and display.

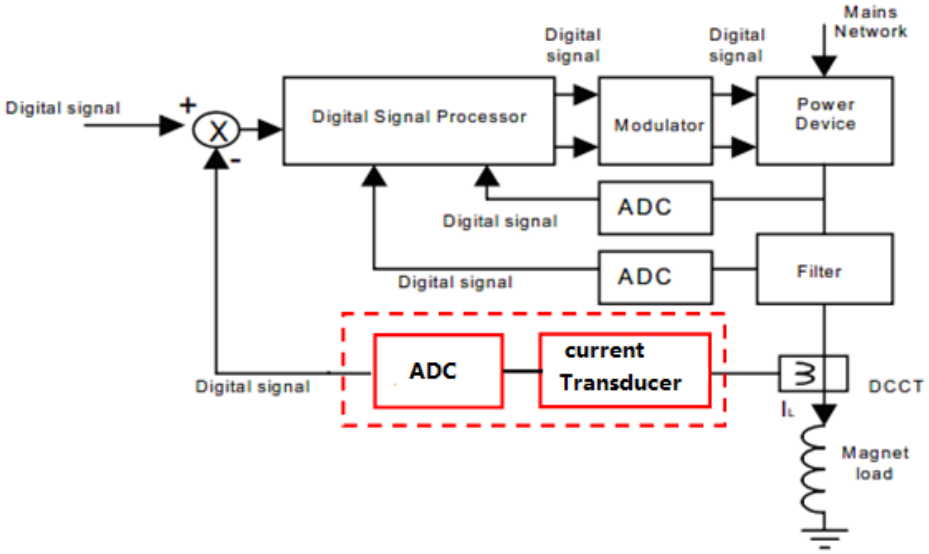

Figure 5.5.3: Digital controller for CEPC magnet power supplies.

5.5.4.3 *Special Digital Controller for Booster Power Supplies*

For the Booster supplies, the output cycles with a repetition rate of 0.1 Hz. In order to reduce the tracking error, the digital controller is specially designed as shown in Figure 5.5.4. Modern control algorithms will be implemented for decreasing the current tracking error to improve performance.

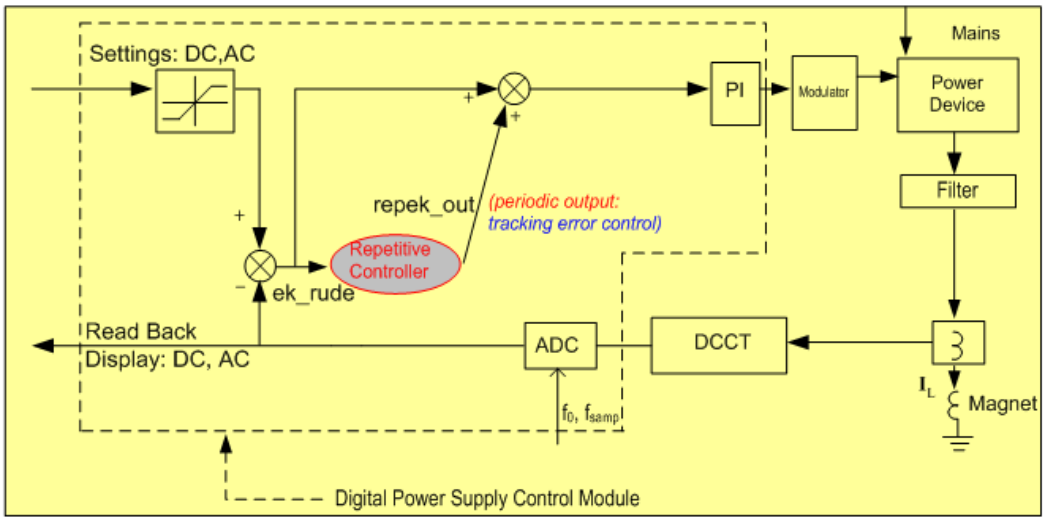

Figure 5.5.4: Digital controller for the Booster power supplies

5.5.5 References

1. J. Cheng, Preliminary Design Report of Power Supply System for BEPCII, 2002..
2. Conceptual Design Report of POWER SUPLLIES for the project SESAME..
3. Conceptual Design Report of POWER SUPLLIES for the project LEP.

5.6 Vacuum System

Beam lifetime and stability are of major importance in any storage ring. The interaction of the stored particles with the molecules of the residual gas leads to particle losses and gives rise to background in the detectors. Calculating the expected pressure is an essential part of the vacuum system design. The gas load is determined by thermal desorption and also from the dynamical gas load produced by synchrotron radiation.

There are two 120 GeV circulating beams, each 16.6 mA.These beams emit intense synchrotron radiation (SR) in a forward-directed narrow cone. This energetic photon flux produces strong outgassing from the vacuum chamber and a large dynamic pressure increase, which limits the beam lifetime and may cause increased background in the experiments. Therefore, the pumping must maintain the specified operating pressure under the condition of a large dynamic photodesorption gas load.

The dominant loss mechanism is energy loss through the emission of photons due to bremsstrahlung on the nucleus and electrons of the residual-gas molecules. The rate of energy loss for an electron of energy E is given by

$$-dE/dt = c\rho E/Xo\ , \qquad (5.6.1)$$

where c is the velocity of light, ρ is the density of the residual gas and Xo is its radiation length. Particles are lost from the circulating beam only if their energy is outside the acceptance of machine: E±dE. This is accounted for by the factor $W \approx \ln(E/\delta E)$. The resulting time constant for beam decay is

$$1/\tau = cW\rho/Xo\ . \qquad (5.6.2)$$

The only machine-dependent parameter is the energy acceptance. W is typically in the range 6 to 10. For nitrogen Xo = 386 kg/m2 and converting from density to partial pressure P, the beam lifetime can be expressed approximately as

$$\tau(h) = 3\times10^{-8}/P_{N2}\ (\text{Torr}). \qquad (5.6.3)$$

To estimate the beam-gas lifetime, knowledge of the residual gas composition is required. Generally, the dynamic pressure is dominated by desorbed H_2 (>60％) and $CO+CO_2$ (<40％). Heavy molecules such as Ar are particularly bad whereas light molecules such as H_2 are not critical.

The basic requirements for the UHV system are:

- A vacuum lower than 3×10^{-9} Torr. It can be shown that the beam lifetime would exceed 20 h if there only beam gas interactions.
- Good lifetime must be achieved soon after the initial startup with a stored beam.
- The system must be capable of quick recovery after sections are let up to air for maintenance or repairs.

- The chamber wall must be as smooth as possible to minimize electromagnetic fields induced by the beam.
- Very low pressure must be achieved in the interaction regions to minimize detector backgrounds from beam-gas scattering. We would like a pressure of 3×10^{-10} Torr or lower outside of the Q1 magnet.
- Sufficient cooling is required to safely dissipate the heat load associated with both synchrotron radiation and higher-order-mode (HOM) losses.
- Capability to shield outer ring components from synchrotron radiation.

5.6.1 **Synchrotron Radiation Power and Gas Load**

In the design of the vacuum system, two issues produced by the synchrotron radiation must be considered. One is the heating of the vacuum chamber walls owing to the high thermal flux and another is the strong gas desorption (both photon-desorption and thermal desorption). The dynamic pressure induced by synchrotron radiation can rise by several orders of magnitude once a beam begins to circulate. In this section, we quantify the effects and evaluate their impact.

5.6.1.1 ***Synchrotron Radiation Power***

To estimate the heat load, we start from the well-known expression [Sands, 1970] for the synchrotron radiation power (in kW) emitted by an electron beam in uniform circular motion:

$$P_{SR} = \frac{88.5E^4 I}{\rho} \tag{5.6.4}$$

where E is the beam energy (in GeV), I is the total beam current (in A), and ρ is the bending radius of the dipole (in meters). The linear power density (in kW/m) along the circumference is given by

$$P_L = \frac{P_{SR}}{2\pi\rho} = \frac{88.5E^4 I}{2\pi\rho^2} \tag{5.6.5}$$

For CEPC, E = 120 GeV, I = 2 × 0.0166 A, ρ = 6094 m, we find from Eqs. (5.6.4) and (5.6.5) the total synchrotron radiation power P_{SR}=100 MW and a linear power density of P_L =2.62 kW/m.

5.6.1.2 ***Gas Load***

The gas load arises from two processes: thermal outgassing and synchrotron-radiation-induced photodesorption. Thermal outgassing is common to all vacuum systems and occurs in the absence of synchrotron radiation; that is, it contributes mainly to the base pressure of a ring in the absence of circulating beam. With good clean assembly procedures and the proper choice of materials, thermal outgassing is a minor load on the system. The gas load due to synchrotron radiation actually determines the operating pressure of the ring.

To estimate the desorption rate, we follow the approach of Grobner et al. [1983]. The effective gas load due to photodesorption is found to be

$$Q_{gas} = 24.2EI\eta \text{ [Torr·L/s]}, \tag{5.6.6}$$

where E is the beam energy in GeV, I the beam current in A, and η the photo-desor ption coefficient in molecules/photon. The photodesorption coefficient η is a proper ty of the chamber that depends on several factors:

- Chamber material
- Material fabrication and preparation
- Amount of prior exposure to radiation
- Photon angle of incidence
- Photon energy

Experimental measurements indicate that a copper (or aluminum) chamber may eventually develop an effective $\eta \approx 10^{-6}$. For a vacuum chamber with desorption coefficient $\eta = 2\times10^{-6}$, the dynamic gas load is

$$Q_{gas} = 4.84\times10^{-5} EI \quad [\text{Torr}\cdot\text{L/s}], \qquad (5.6.7)$$

And the linear gas load is

$$Q_L = \frac{Q_{gas}}{2\pi\rho} \quad [\text{Torr}\cdot\text{L/s}\cdot\text{m}]. \qquad (5.6.8)$$

We obtain the total dynamic gas load of Q gas = 1.93×10^{-4} Torr·L/s, and a linear SR gas load of $Q_L = 5.04\times10^{-9}$ Torr·L/s/m.

5.6.2 **Vacuum Chamber**

5.6.2.1 ***Vacuum Chamber Material***

The SR power deposited calls for a water-cooled high electrical conductivity chamber (aluminum or copper). Extruded aluminum chambers have been used in the LEP storage ring; they were water-cooled and covered with a lead cladding to prevent other components from being damaged by radiation. The LEP dipole chamber, shown in Fig. 5.6.1, consists of

- the elliptical beam channel (1) in the figure
- the pumping channel which carries the NEG strip (2) in the figure
- the cooling channels (3) in the figure.

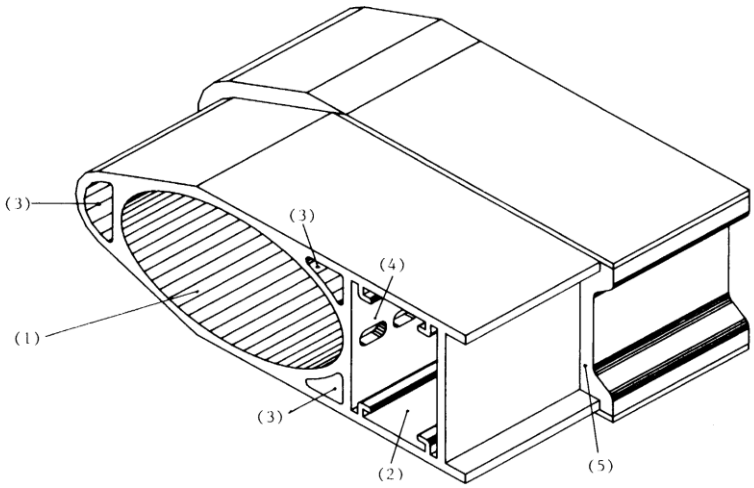

Fig. 8.4 LEP dipole vacuum chamber, with: 1) the elliptic beam channel (131 mm × 70 mm); 2) the rectangular pumping channel where the NEG strip is mounted; 3) three cooling channels; and 4) the pumping slots. The lead shielding (5) varies between 3 and 8 mm in thickness.

Figure 5.6.1: LEP dipole vacuum chamber.

Copper is preferred in CEPC because of its naturally lower molecular yields, lower electrical resistance, and its lower radiation, giving more efficiency in preventing photons from escaping through the vacuum chamber wall, damaging the magnets and other components. And since the chamber walls in the ARC sections are subjected to very high thermal loads, copper with its excellent thermal conductivity is preferred. Vacuum chambers in the straight sections will be fabricated from stainless steel.

Copper has been extensively used for B-factory vacuum chambers, and it has been found that its initial molecular yields were lower than aluminum by nearly 1~2 orders of magnitude. The PSD (Photon Stimulated Desorption) tests on copper at DCI have shown that a photodesorption coefficient of 10^{-6} can be achieved in a reasonable time at high current. [1] Such a low photodesorption coefficient allows us to design the CEPC vacuum chamber with a conventional elliptical or octagonal shape, instead of being driven to adopt an antechamber design that is more difficult and expensive to fabricate. The apparent cost disadvantage of copper is offset by the relative simplicity of the copper shape, by the reduction in the amount of pumping needed, and by the shortening of the vacuum commissioning time.

Copper also has the considerable advantage of being self-shielding and thus can protect the magnets and other hardware from radiation damage caused by the hard component of the synchrotron radiation. The need for lead shielding, which would be required to accompany an aluminum chamber, is eliminated.

5.6.2.2 *Vacuum Chamber Shape*

The cross-section of the dipole vacuum chamber is elliptical, 100 mm wide by 55 mm high (Fig. 5.6.2). The standard length of this dipole chamber is 8 m, and the chamber wall thickness is 6 mm. The expected radiation dose outside the vacuum chamber is lower than 1×10^{-8} rad/year. A cooling channel attached to the outer wall of the beam duct carries away the heat produced by synchrotron radiation hitting the chamber wall. The beam duct will be fabricated from UNS C10100, high-purity,

oxygen-free, high-conductivity copper, and the cooling channel will be fabricated from USN C10300, an oxygen-free copper alloy. The vacuum flanges are made of stainless steel.

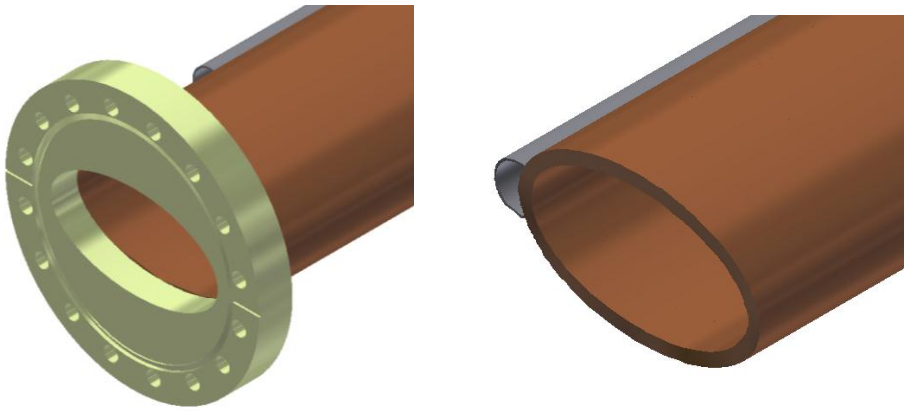

Figure 5.6.2: CEPC copper dipole vacuum chamber.

One of the main challenges in designing the vacuum chamber is to adequately handle the high thermal synchrotron radiation power incident on the vacuum chamber wall. The linear power density in the CEPC storage ring reaches 2.62 kW/m. Finite-element analysis of a dipole chamber subjected to this power shows that the highest temperature reaches 72°C, the maximum stress is 141 MPa, and the maximum deformation is 1.2×10^{-3} mm, which is in the safety range.

The chamber consists of an extruded copper chamber and cooling channel with two conflate-type end flanges. The chamber will be extruded in full lengths from UNS C10100 copper, while the cooling channel will be extruded from UNS C10300 copper. These are both drawn to achieve their final shape and to produce a minimum half-hard temper. The pieces are then cleaned and joined by electron-beam welding. After welding, the subassembly is stretch-formed to its correct radius, then the ends are machined and the part cleaned. Finally, the end flanges are TIG-brazed onto the ends of the chamber. A one-piece chamber extrusion eliminates all longitudinal vacuum welds, which affords a more accurate and dependable chamber.

An oxide layer on the chamber inner surface contains a large amount of carbon released as CO and CO_2 in photodesorption. To remove this first oxide layer and to produce a new oxide layer that is free of carbon, a commercially available chemical cleaner containing H_2O_2 and H_2SO_4 will be used, or a standard acid etch with H_2SO_4, HNO_3, HCI and water will be applied.

5.6.3 **Bellows Module with RF Shielding**

The primary function of the bellows module is to allow for thermal expansion of the chambers and for lateral, longitudinal and angular offsets due to tolerances and alignment, while providing a uniform chamber cross section to reduce the impedance seen by beam. Figure 5.6.3 shows the schematic drawing of the RF shielding bellows module.

The usual RF shield has many narrow Be-Cu fingers that slide along the inside of the beam passage as the bellows is compressed. One of the key issues for this finger-

type RF shield is the strength of the contact force. Each contact finger should touch a beam tube with an appropriate contact force to keep a sufficient electrical contact against a high frequency current. The larger the force, of course, the better the electrical contact, but the more the abrasion (dust generation) during mechanical flexing. It is important to have a minimum contact force to avoid excess heating and arcing at the contact point. The leakage of HOM RF from the slits between contact fingers into the inside of bellows is another important problem.

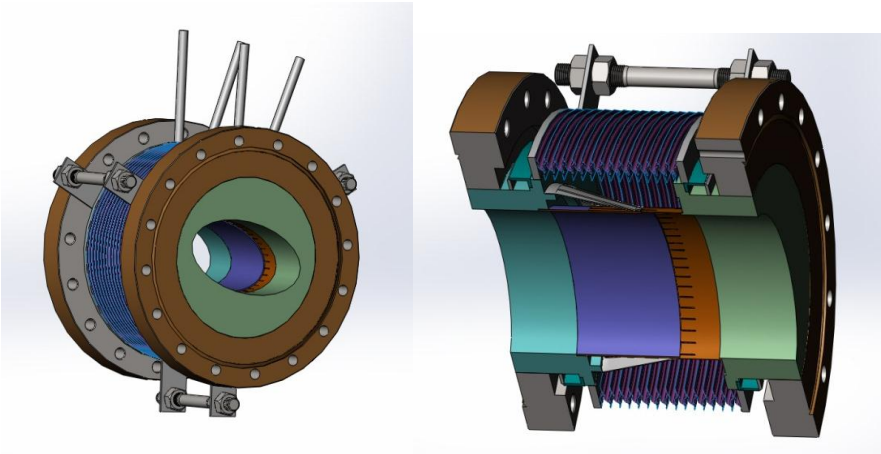

Figure 5.6.3: RF shielding bellows module.

The fingers maintain a relatively high contact pressure of 110±10 g/finger, and the slit length between fingers is 20 mm. The RF-shield can accommodate a maximum expansion of 10 mm and contraction of 20 mm, allowing for a 2 mm offset. The step at the contact point is limited to less than 1 mm. The cooling water channel takes care of synchrotron radiation power, Joule loss and HOM heat load on the inner surface, and leaked HOM power inside the bellows.

5.6.4 **Pumping System**

The 54.4 km circumference of the ring will be subdivided into 260 sectors by all metal gate valves. These allow pumping down from atmospheric pressure, leak detecting, bakeout, and vacuum interlock protection to be done in sections of manageable length and volume. Considering that the superconducting RF cavities may require being moved out of position for servicing, two gate valves will be installed near each RF cavity. to avoid other sectors from being exposed to atmosphere. Each sector has several roughing valves and an intake gas valve. Roughing down to approximately 10^{-7} Torr will be achieved by an oil free turbo-molecular pump group. The major portion of the pumping is achieved with Non Evaporable Getter (NEG)-coated copper chambers in the ARC sections. Sputter ion pumps will be used to maintain pressure and pump CH_4 and noble gases that can't be pumped by the NEG. For the pumping system in the interaction regions where the detectors are located, depending on the space available, NEG pumps, sublimation pumps and sputter ion pumps will be used.

5.6.4.1 *NEG Coating*

NEG coating has been used for several years in various accelerators. NEG coating suppresses electron multipacting and beam-induced pressure rises, as well as provides extra linear pumping. In initial applications, NEG-coated chambers were mounted in small amounts in specific locations, covering a minor fraction of the vacuum surfaces. Recently, NEG-coated chambers have been adopted to a larger extent. LHC has used 6 km of coated pipes, being to date the largest machine to use NEG-coated technology. NEG coating is a cost effective technology to improve vacuum performance in high energy accelerators.

The NEG coating is a titanium, zirconium, vanadium alloy, deposited on the inner surface of the chamber through sputtering. The NEG-coated chamber is first inspected for gross contamination or surface defects, which could cause poor film adhesion. Each dipole chamber will be fitted with three cathodes made by twisting together Ti, Zr and V metal wires. These twisted wires are mounted along the chamber axis to achieve uniform thickness distribution along the perimeter. Each TiZrV cathode is made of three 0.5 mm wires and to keep the cathode close to the chamber's axis, several ceramic spacers are placed along the chamber length, plus two adaptors at the extremities.

Chambers are then evacuated to the 10^{-9} mbar range by the turbomolecular pump group and before coating baked overnight and leak tested with helium. A Residual Gas Analyzer (RGA) is also used to monitor partial pressure. During this process gas and pressure were krypton at ~0.1 mbar, and the chamber temperature around 110 °C.

Even though well known in principle, the sputtering process for thin getter film deposition needs to be optimized to avoid instability and lack of reproducibility which can significantly change the gas sorption and surface properties (e.g. secondary electron yield, ion-induced gas desorption). During coating, all related parameters (plasma gas pressure, substrate temperature, plasma current, and magnetic field value) will be recorded and suitably adjusted to ensure the stability of the deposition process. After coating, the chambers will be cooled down to room temperature, exposed to air and left to age for a couple of days before being visually inspected again. Aging is a recommended procedure, since it helps identify areas where the film adhesion is poor.

The vacuum in a NEG-coated chamber is improved by both reduced desorption yield and direct pumping by the NEG alloy. The NEG-coated dipole vacuum chamber has no additional pumps. When exposed to air, the NEG surface is saturated and loses its pumping activity. An essential operation is activation, which produces diffusion of the saturated surface layer into the bulk of NEG material by heating the NEG-coated chamber. NEG films can be fully activated at relatively low temperature, like 250°C for 2 hrs. Even lower activation temperature for longer times (e.g. 180°C for 24 hrs.) has been successfully applied in the case of aluminum chambers which cannot withstand high temperature bake-out. After activation, the pumping action depends on the amounts and molecular species of the gases which have been pumped and on the temperature of the NEG film. An investigation of pumping for various combinations of different gases has shown that the pumping of CO and CO_2 is not affected by the presence of H_2, while the pumping speed of H_2 is reduced by the presence of CO and/or CO_2 on the NEG surface, but the pumping speed of H_2 is always higher than that of CO/CO_2..

5.6.4.2 *Sputter Ion Pumps*

Sputter ion pumps are required to pump Ar, He and CH_4, which are not absorbed by the NEG. During the period of beam cleaning, CH_4 will be an important component of the residual gas, and this determined the number of sputter ion pumps to be installed. A sputter ion pump will be mounted every 20 m; the number of pumps can easily be doubled if necessary. The sputter ion pumps are started only after the NEG has been activated, i.e. at a pressure of 10^{-7} Torr or lower. This allows several pumps to be connected in parallel to one common power supply.

Sputter ion pumps have high reliability, no moving parts, long life and high radiation resistance. In addition, the ion pump current is proportional to vacuum pressure and the array of pumps can provide a detailed pressure profile around the ring. The power supplies of ion pumps will trip to protect the ion pumps from damage if the ion current rises above a pre-set value. The leakage current of the pumps is less than 10% of the current drawn at 1×10^{-9} Torr, which make the pump suitable for use as a pressure monitor. Ion pump currents can be stored in a databank, enabling the operators to conveniently find problems

5.6.4.3 *Turbomolecular Pumps (TMPs).*

Mobile turbomolecular pump groups are used for pump down and bake-out. These groups consist of a 4 L/s dry fore pump and a 200 L/s TMP. Several mobile TMP groups connected to a sector will pump the sector down to 10^{-7} Torr. The same mobile groups will also serve for rough pumping of other vacuum tanks such as RF cavities, electrostatic separators, wiggler tanks, etc.

Vacuum gauges (Penning, Pirani) are integrated into the mobile groups, while leak detectors can be connected to the high-pressure end of the TMP.

The advantage of a mobile TMP group lies not only in their reduced number and cost, but also in the fact that no special radiation-resistant equipment is required. Standard pumps and gauges will be used and the group will be removed from the tunnel during machine operation.

5.6.5 **Vacuum Measurement and Control**

The size of CEPC excludes the installation of closely spaced vacuum gauges. Only some special sections such as the injection regions, RF cavities and interaction regions are equipped with cold cathode gauges and residual gas analyzers. For the remainder of the ring only the current of the sputter ion pumps will be monitored continuously and should provide adequate pressure measurements down to 10^{-9} Torr. Some mobile diagnosis equipment can be brought to places of interest during pump down, leak detection and bake-out when the machine is accessible. All metal corner valves (manually operated) will be provided every 80 m. High pressure gauges will be installed in each sector in order to protect the NEG against damage during activation.

The control of the vacuum system will be part of the general computer control systems and includes the control of the sputter ion pumps, vacuum gauges, sector valves, and the monitoring of the water cooling of the vacuum chambers. Vital interlocks (sector isolation valves, RF cavities, water cooling) will be hard-wired. Other controls will only be needed locally and temporarily, and therefore will be handled by mobile terminals.

Due to the high radiation levels in the tunnel, all the vacuum electronic devices will be located at the service buildings.

5.6.6 References

1. "An Asymmetric B Factory (based on PEP) Conceptual Design Report," SLAC, June, 1993.
2. LEP design report, June 1984.
3. KEK B Design Report, June, 1995.
4. CAS (CERN Accelerator School) VACUUM TECHNOLOGY, 1999.
5. A.Poncet, Vacuum System of A Tau-Charm Factory, 1993.
6. O. Grobner, J.Vac.Technol. A9 (3), May/Jun 1991.
7. Anders Hansson, et al., "Test of a NEG-coated copper dipole vacuum chamber," Proceedings of EPAC08, Genoa, Italy, 3693-3695.
8. A. Conte, et al., "NEG coating of pipes for RHIC: an example of industrialization process," Proceedings of PAC07, Albuquerque, New Mexico, USA, 212-214.
9. Brad Mountford, et al., "First experience on NEG coated chamber at the Australian Synchrotron Light Source," Proceedings of EPAC08, Genoa, Italy, 3690-3692.

5.7 Instrumentation

5.7.1 Introduction

The beam instrumentation system, consisting of various beam monitors and signal processing electronics must provide precise and sufficient information so that accelerator physicists and machine operators can improve the injection efficiency, optimize the lattice parameters, monitor the beam behavior and increase the luminosity. Good instrumentation is also essential for efficient commissioning.

For CEPC, there are unique problems specific to the large size of the ring. Considering the long distances, it is not a good choice to use copper cables to send signals; we should digitize the analog signals in the tunnel and use optical fibers to send data from electronics near the monitors to the local stations in an auxiliary tunnel. The positrons and electrons pass through the same monitor, and we should distinguish them by polarity. We summarize our design philosophy:

- Satisfy the requirements for long-term stable operation;
- Appropriate precision and speed for parameter measurements;
- Large dynamic range under different conditions;
- Coupling impedance of the devices must be as small as possible;
- In house construction of components should be used as much as possible to save money.

There are also some requirements of the CEPC beam instrumentation system that are different from two-ring colliders since the same instrumentation sees both circulating beams**.**

We need to monitor beam status quickly and accurately, measure and control the bunch current efficiently, and cure beam instabilities. The beam orbit measurement is important, especially in the interaction region. It can help us know the beam position, offset and crossing angle and it is advantageous for increasing the luminosity. There are several subsystems, including BPMs for beam position, the DCCT for average beam

current measurement, the tune measurement system, the photon monitoring system which includes a CCD camera for monitoring the beam profile, and a streak camera for measurement of bunch length. These systems are described below in detail.

Table 5.7.1 summarizes the main technical parameters of the storage ring beam instrumentation systems.

Table 5.7.1 Main technical parameters of CEPC Beam Instrumentation Systems

Subsystems		**Parameters**	**Quantity**
BPM	Bunch by Bunch	Measurement area (x × y)： ±40 mm×±20 mm Accuracy：1 mm Resolution：0.1 mm	2324
	Closed orbit	Measurement area (x × y)： ±20 mm×±10 mm Accuracy：0.1 mm Resolution：<0.001 mm Measurement time of COD：< 4 s	
BLM		Dynamic range:10^6-10^8 Counting rates: ≤10 MHz Radiation environment: <10^8 Rad Response time: ~ns	2400
Tune		Resolution：0.0001 (0.1kHz) Accuracy：0.0005 (0.5kHz)	2
DCCT		Dynamic measurement range：0.0~1.5 A Linearity：0.1 % Zero drift: <0.05 mA Remarks: shielding needed	2
BCM		Measurement range：10 mA / per bunch Relative precision：1/4095 Smallest bunch spacing：0.5 m	2
Feedback system	Transverse	Damping rate > 20 ms^{-1} Oscillation amplitude < 1 mm	2
	Longitudinal	Damping rate > 0.5 s^{-1} Energy error < 0.6%	2
Synchrotron light monitor	Beam size measurement	Resolution：10% beam size	1
	Bunch length measurement	Resolution：0.5 ps (using streak camera) Measurement time：1s	1

5.7.2 **Beam Position Measurement System**

Beam position measurement is basic. According to the principle that one BPM should be placed near each quadruple, there will be 2,324 BPMs. This also includes some additional ones at specific locations. Because the entire circumference is 54.4 km,

we will set up 32 local stations for BPMs and other instruments in the auxiliary tunnel. Thus there will be a local station every 1.7 km and each will control and monitor about 72 BPMs. Front end electronics and digital electronics of the BPMs should be put in the tunnel. Considering the limited space in the tunnel, it is a good option to place the electronics under the magnet girder. But radiation shielding of the electronics needs to be carefully considered.

The data from the digital electronics will be sent by optical fiber to local stations where there will be a multiplex system for communicating with other local stations and the central control room.

High resolution is necessary for the BPMs at the special regions near the IP or near the local chromaticity correction sextupoles. Non-linear mapping will be used for the off-axis position of the beams due to the pretzel. An orbit slow feedback system and an IP point orbit feedback system using the BPM information is being carefully considered.

5.7.2.1 *Mechanical Construction*

The design criteria for CEPC BPM system are the following:

- Short length to save space;
- Skewed sensor positions to avoid direct impacts of synchrotron radiation;
- Minimum RF loading and higher modes coupling to the beam;
- High precision for interchangeability;
- Flanges for replacement in case of a leak;
- Resistance to corrosion and to baking up to 300°C.

The best solution is a capacitive monitor with a button-like electrode, as used in most other electron machines. In order to attain the required geometrical accuracy, the four buttons will be mounted on a machined block of aluminum welded into the copper vacuum chamber. A matched feedthrough needs to be designed in order to avoid reflections and endure high temperatures of up to 200℃. The feedthrough is made of titanium and the outer conductor as well as the flange with its plug is made of stainless steel.

The pickup output voltage can be expressed by

$$V_{\text{pickup}}(t)=I_{\text{image}}(t) \times Z_t \qquad (5.7.1)$$

In the time domain, where $I_{\text{image}}(t)$ is proportional to the bunch current $I_{\text{bunch}}(t)$, Z_t is the longitudinal transfer impedance [1-3]. The transfer impedance depends on the capacitance C of the electrodes and the input resistor, R, in the external circuitry. Figure 5.7.1(a) shows the absolute value and phase of the transfer impedance for an l = 10 cm long cylindrical pick-up with capacitance C = 100 pF and an ion velocity of β_i= 50% for high (1 MΩ) and low (50 Ω) input impedance of the amplifier [2].

Figure 5.7.1(b) shows the frequency spectrum of the pickup electrode voltage, which is high-pass, the same as the transfer impedance. A Gaussian function in the time domain of width σ_t has a Fourier transform described by a Gaussian function of width $\sigma_f = 1/(2\pi\sigma_t)$ centered at $f = 0$. The σ_f of the beam is 16 GHz. The cut-off frequency of the BPM $f_{cut} = \omega_{cut}/2\pi = (2\pi RC)^{-1}$ is 3 GHz, where σ_t is the bunch length, and R and C are the input impedance and capacitance of the electrode.

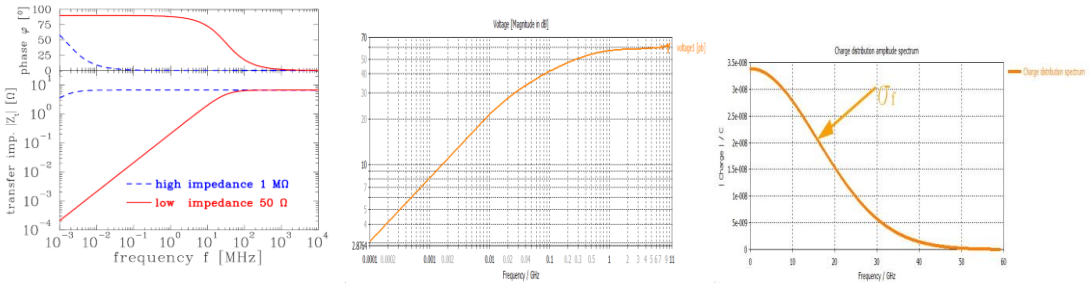

Figure 5.7.1: (a) Absolute value and phase of the transfer impedance (b) the frequency spectrum of the pickup electrode voltage signal obtain by CST simulation (c) the frequency spectrum of a Gaussian bunch.

In order to study the pickup electrode response to the beam, the CST (Computer Simulation Technology) particle wake-field simulations [4] are done based on the specific beam parameters and vacuum pipe dimensions of our accelerator. The CST transient solver cannot deal with the situation when the connection port is not aligned with the Cartesian coordinate planes. Figure 5.7.2 shows the ideal button BPM design and the approximate version, respectively. Others also suggest using this same approximation [5]. As shown in figure 5.7.2, the radius and height of the electrode is 4 mm and the center of the pickup electrode is located in α= 45 º.

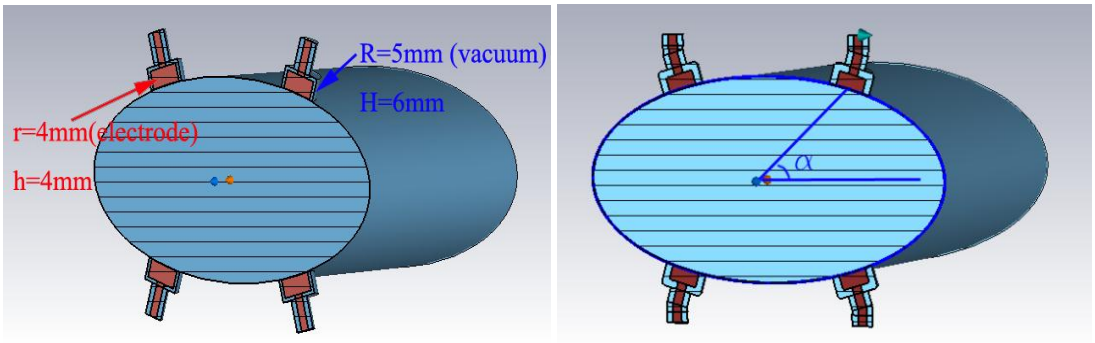

Figure 5.7.2: (a) the ideal button BPM (b) the approximate model with a connection port aligned to the Cartesian coordinate planes.

Figure 5.7.3 (a) shows a pickup signal in such an approximate model. The simulation and design parameters are shown in table 5.7.2. In order to reduce the simulation time, suppress higher frequencies and match the low-pass filter properties of the cable, the bunch length is adjusted to 10 mm [6, 7]. The test results [6] show that there is no strong difference between the simulation and the measurements. I_{bunch} is over 2000 A as shown in Figure 5.7.3 (b), which means that a transfer impedance of 0.1 Ω can induce a voltage over 100 volts. As shown in Figure 5.7.3 (a), the amplitude of signal is hundreds of volts even with the small size electrode with a radius of 4 mm. Figure 5.7.3 (c) is the sensitivity mapping of the simulation in the range of 60 mm × 40 mm. The scan range is shown in the inset figure of 5.7.3 (c), where U= △x/Σ, V=△y/Σ. The transverse response of the signal is non-linear for large amplitudes; the horizontal and vertical sensitivities near the center of the pipe are 4.17%/mm and 2.99 %/mm as shown in Figure 5.7.3 (d).

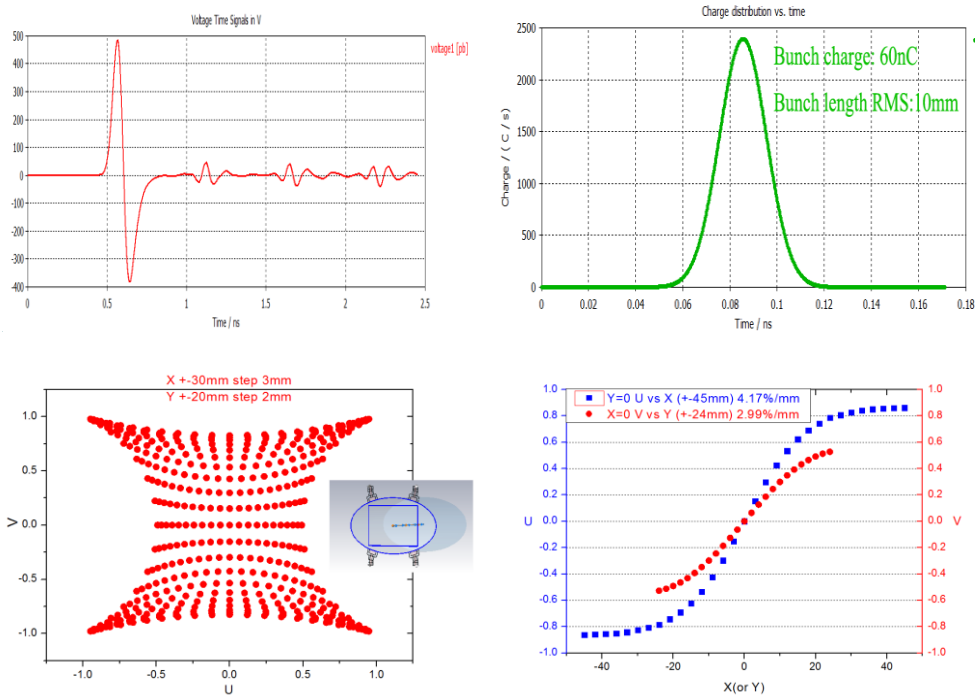

Figure 5.7.3: (a) the signal of an electrode (b) bunch charge distribution in the time domain (c) sensitivity mapping of the button BPMs on elliptical pipes (d) sensitivity near the center of the pipe.

Table 5.7.2: Main parameters used for CST simulation.

Parameters		Design report	CST simulation
Bunch	Length (mm)	2.58	10
	Population	3.7×10^{11}	
Vacuum pipe	Elliptic cylinder a/b (mm)	Elliptic cylinder 52/28	

As shown in Figure 5.7.3 (d), the horizontal sensitivity is greater than the vertical when the electrode is located at the 45° . The sensitivity is determined by the azimuthal angle in an elliptical pipe or by the distance to the x and y axes. Table 5.7.3 is the sensitivity at different angles, α. In order to get a more accurate determination of the BPM sensitivity, the simulation model is adjusted in some detail, so the sensitivity changes by a small amount at 45° . At an azimuthal angle of 56° horizontal and vertical sensitivities are equal

Table 5.7.3: Sensitivity at different azimuthal angles.

	Horizontal (%/mm)	Vertical (%/mm)
35°	5.96	2.34
45°	5.29	3.36
55°	4.54	4.30
60°	4.08	4.61
56°	4.43	4.40

We define the coupling factor between the beam and the pickups as the voltage at the middle of the vacuum pipe when applying one volt at one of the pickups [8]. This definition is also suitable for the coupling factor between the electrodes. We can also obtain the electrode-to-ground capacity [7, 8] using the CST electrostatic solver. The capacity of one button electrode C=Q/U=0.86 pF, where Q is the charge on the electrode of when a one volt potential is applied to it. Because of the small size of the pickups and long distance between pickups, the coupling factor between the beam and pickups is 4%, whereas the coupling factor between the pickups is much smaller. Figure 5.7.4 (a) is the potential isoline when a one volt potential is applied to the top right electrode.

The thermal properties of the BPMs in the cold modules are important to investigate. Thermal analysis has been done using the CST multi-physics studio because of the very high peak power. The peak power of the pickups is $P_{\text{peak}}=(U_{\text{peak}})^2/R$=4.6 kW and the average power $P_{average}=\frac{c\int\frac{V^2}{R}}{\Delta s}=\frac{\sqrt{\pi}\sigma_s P_{peak}}{2\Delta s}$=0.04 w, where σ_s=10 mm and Δs=1.07 km is the pickup length and the interval between bunches. The pipe and pickups are aluminum; the loss factor of the beam in a 1000 mm distance is 68.6 V/nC. Figure 5.7.4 (b) shows the wake potential

There are three steps to obtaining the temperature distribution of the BPM: (1) use the wake field solver to get the loss factor; (2) use eigenmode of the setup get the loss field distribution; (3) get the temperature distribution using the thermal solver [6, 9]. A 1000 mm pipe is chosen for this eigenmode simulation. Figure 5.7.4 (c) is the simulated temperature distribution. The highest temperature near the pickups is 303 K.

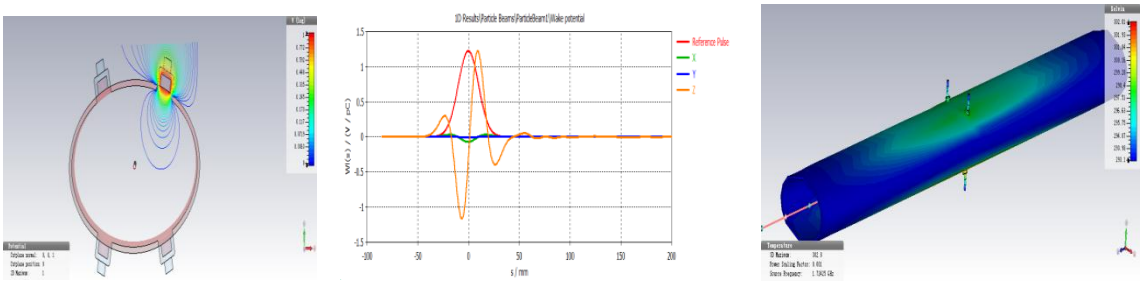

Figure 5.7.4: (a) the isoline of potential when 1V applied to right up electrode (b) wake potential of the beam (c) temperature distribution of the BPM using CST multi-physics studio thermal solver.

5.7.2.2 *Signal Processing*

Because of the size of the ring, we should install electronics in the tunnel and shield sensitive electronics from radiation. Since two beams pass through the BPMs, timing signals distinguish the positrons from the electrons.

With high speed ADCs and high resolution we can acquire bunch by bunch positions. The entire system will use microTCA.4 standard structure. This includes RFFE (radio frequency front-end electronics), high speed 8 channel ADCs, digital electronics and clock signals. Four channels are used for positrons and the other four channels for electrons. Precision timing can help to accomplish peak sampling. The schematic diagram of the bunch by bunch BPM electronics is shown in Fig. 5.7.5.

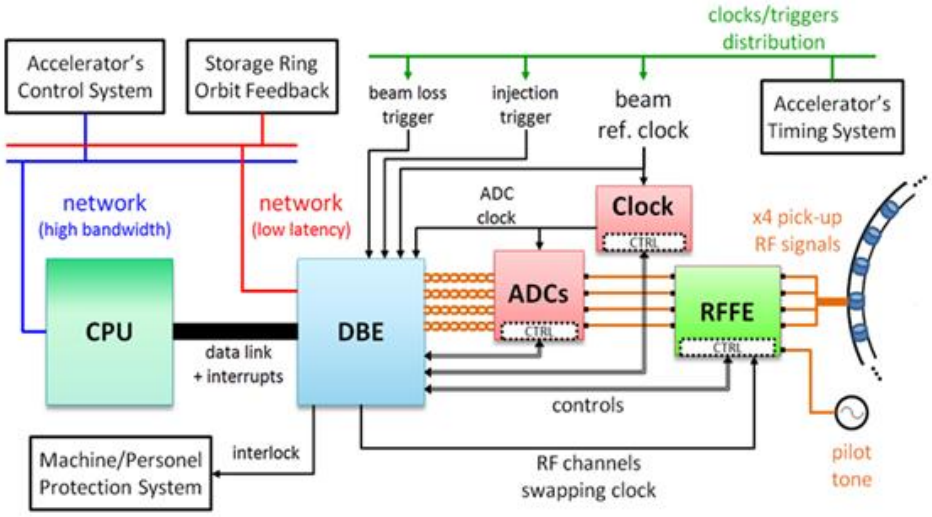

Figure 5.7.5: Schematic of the bunch by bunch BPM system

BPM electronics will be installed under the magnet girder in the tunnel with two layers of shielding material, polyethylene and lead as shown in Fig. 5.7.6.

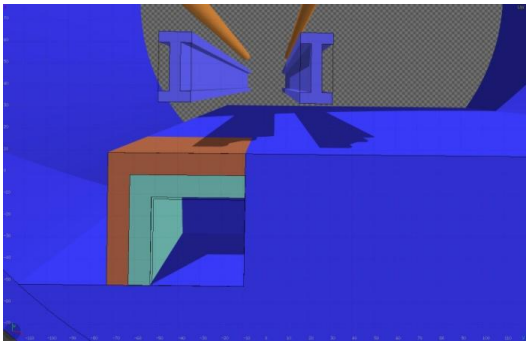

Figure 5.7.6: BPM ectronics shielding

5.7.3 **Beam Current Measurement**

Beam current measurements include average current measurements (DCCT) and the bunch current monitoring system (BCM).

5.7.3.1 *DC Beam Current Transformer*

The average current and life time are important parameters. The DCCT (Direct-current current transformer) measures average beam current. DCCTs are essential for commissioning, machine tuning, operation and machine/personnel safety. They have large dynamic range, wide bandwidth and high resolution and often are the only truly calibrated beam instrument in an accelerator and serve as a reference for the calibration of other beam diagnostics.

The DCCT includes three parts: magnetic coils, control electronics and a data acquisition system. The DCCT needs to be shielded from stray electromagnetic fields in order to have sufficient resolution. The ceramic pipe must be carefully designed to avoid a discontinuous structure and thus decrease beam impedance. The DCCT is always installed in a straight section but must be placed at a distance from superconducting cavities, quadrupole and corrector magnets and power supply cables. The design of the magnetic coils is the key technology of the DCCT. There are three magnetic coils; one is a fast response transformer, and the other two are second harmonic magnetic modulators. The fast response transformer senses rapid beam changes for coarse adjustments; the magnetic modulator senses slow beam drifts for precision adjustments.

We will select amorphous and nanocrystalline materials to construct the DCCT because of their high permeability. We could select a mature commercial product like the Bergoz NPCT shown is in Figure 5.7.7. The modulator, second harmonic detection, PI adjustment, signal amplifier and I/V converting circuits need to be designed.

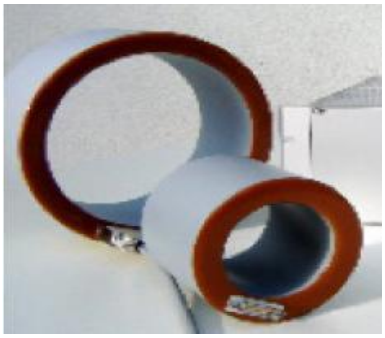

Fig. 5.7.7: Bergoz DCCT

Depending on the development of new materials, a new type of DCCT can be made using Tunneling Magneto Resistance (MR) effects. The air gap structure can permit this type of DCCT to be easily installed without breaking the vacuum.

GSI (Germany) has proposed a new design for the DCCT using the MR effect. But this new type of DCCT cannot be developed further because of its lower sensitivity and resolution.

What is needed is a breakthrough in discovering a much larger MR. The resolution of the newest TMR chip can reach a sensitivity to nano-tesla fields and make a new type of DCCT achievable.

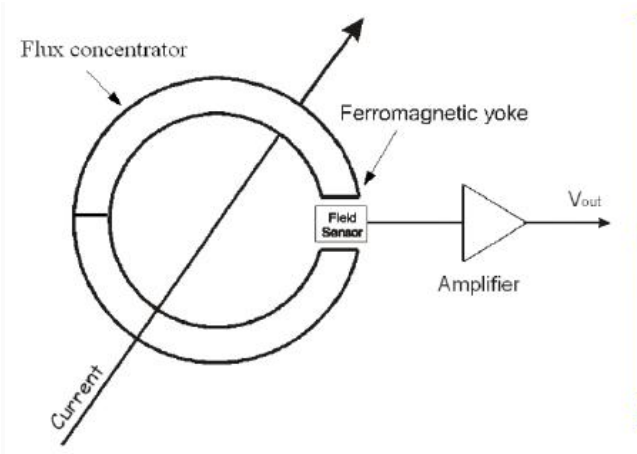

Figure 5.7.8: The principle of a new type of DCCT

5.7.3.2 *Bunch Current Measurement (BCM) System*

The BCM needs to measure the relative charge distribution among the 100 bunches ($50e^+$ and $50e^-$) circulating in the ring. Through absolute calibration of the DCCT these BCM measurements will be continuously transformed into individual bunch intensities, the results stored in the accelerator's database for display and control of the current of individual bunches

The bunch current measurement system includes picking up the signal from the FCT, high speed digital signal acquisition and processing locally at the beam instrumentation station, and the bucket selection control. To achieve feedback time less than the Booster injection period, the signal processing will occupy a very short time and be synchronous with the injection frequency. The signal will be transmitted by fiber. The schematic of the system is shown in Fig. 5.7.9. The hardware of this system will be purchased commercially and the software developed in house..

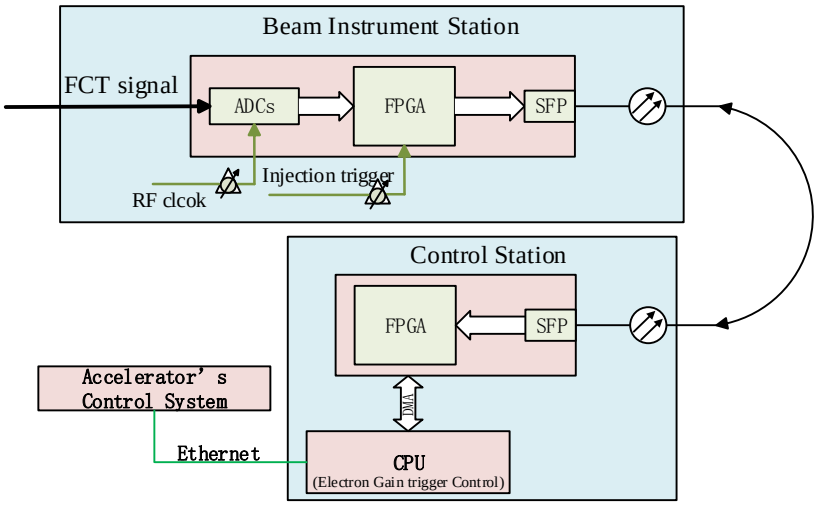

Figure 5.7.9: Schematic diagram of bunch current measurement system

5.7.4 Synchrotron Light Imaging System

5.7.4.1 *Beam Profile Monitor*

The emitted synchrotron light, visible, uv and X-rays, is a powerful non-destructive diagnostic tool. The emitted light is divided into two parts by a water-cooled Be mirror. The reflected visible light can be used in a direct imaging system and double slit interferometer, and beam sizes measured. Transmission X-rays pass through the device front end, a shielding wall, an Al window, and then come to an X-ray optical laboratory where an X-ray pinhole imaging system will be set up and a CCD camera used to record the transverse size.

5.7.4.1.1 Visible Light Beam Line

The light emitted by the bending magnet is extracted by a Be mirror, and then reflected so it arrives in the visible light laboratory outside the tunnel. There are a light table and streak camera in the laboratory for measuring the beam size using a double slit interferometer.

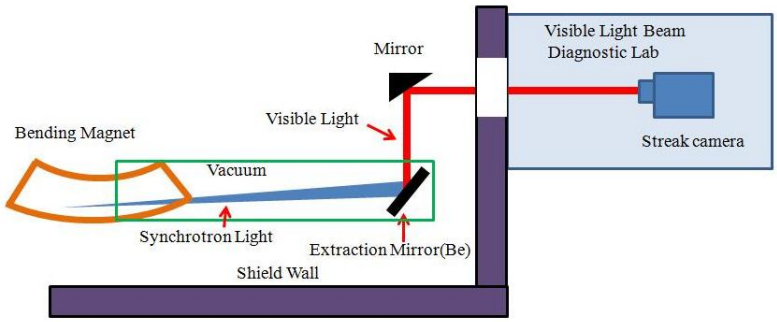

Figure 5.6.10: Schematic of visible light diagnostic beam line

The visible light is extracted by a Be mirror which needs to be specifically designed like the one at KEK (see Fig.5.7.11). The mirror can reflect visible light and X-rays can penetrate it. However, some X-rays will be absorbed and cause the mirror to deform. So the middle of mirror is thin to let X-rays to pass through. Both ends of the mirror have a water-cooled hole to decrease the temperature.

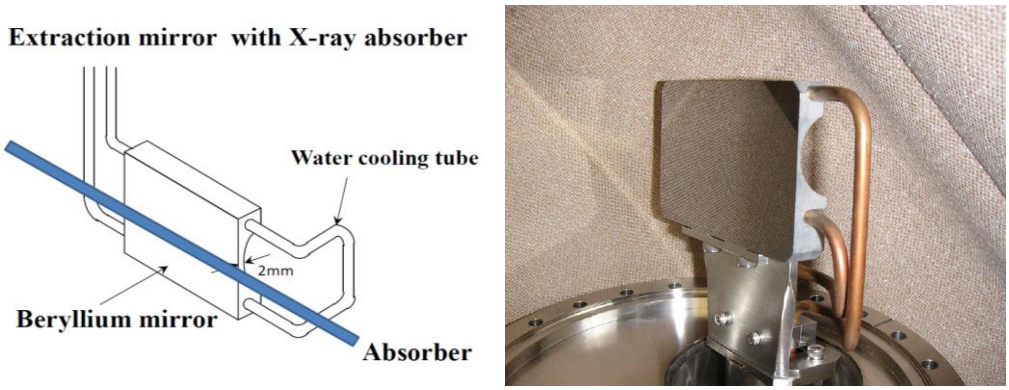

Figure5.7.11: Design of extracted Be mirror at KEK

5.7.4.1.2 X-Ray Beam Line

The resolution of an X-ray pinhole can be as small as 2 μm. The beam size is about 40 μm × 1000 μm, so an X-ray pinhole is an appropriate choice, as shown in Fig. 5.7.12

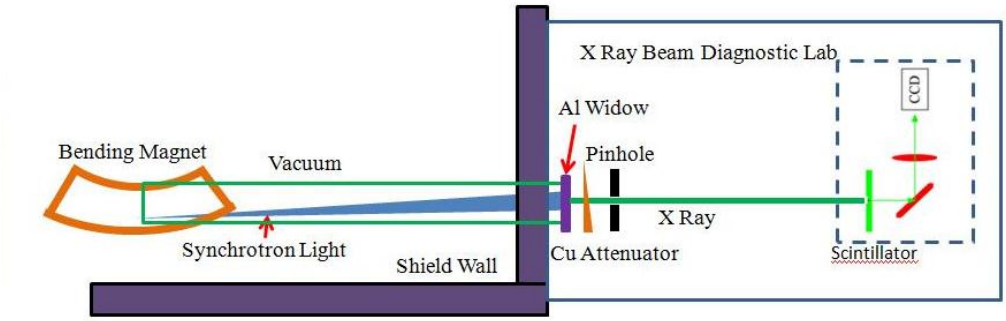

Figure 5.7.12: X-ray beam line

The synchrotron light is extracted to the X-ray beam diagnostic laboratory. Part of the X-rays are absorbed by the Al window; the rest pass through the micron level diameter hole and make an image of the beam on a scintillator, in which X-rays are transformed into visible light to make an image on a CCD camera. The beam size can be obtained by calculating the amplifying coefficient and folding in the system error.

5.7.4.2 *Bunch Length Measurement*

Synchrotron radiation can also provide bunch length measurements using a streak camera. Hamamatsu and Optronis both manufacture precision streak cameras with resolution that can reach sub-picoseconds.

On the other hand, a two photon intensity interferometer can be used to measure the very short beam length. Fig.5.7.13 shows calculations and the experimental results at KEK PF [10].

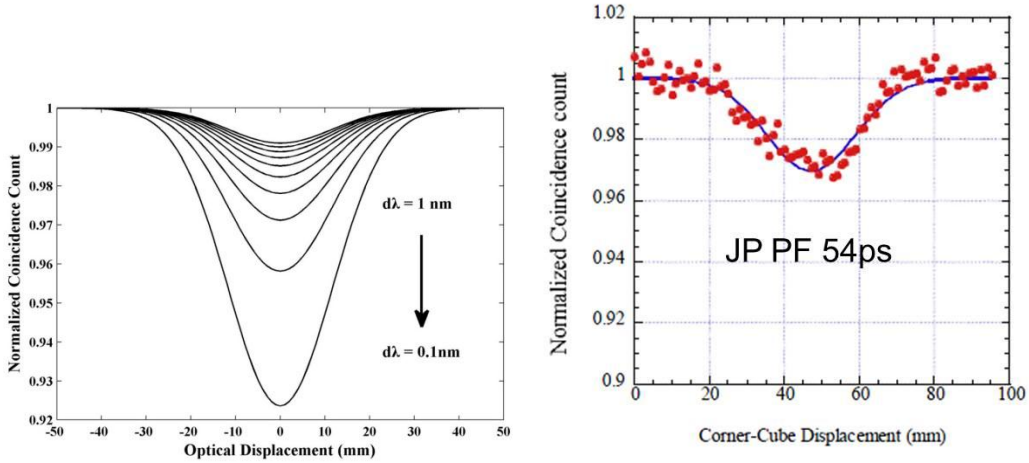

Figure 5.7.13: From KEK: calculations and experimental results

5.7.5 **Beam Loss (BLM) System**

Radiation losses can be monitored with the aid of Beam Loss Monitors (BLM). These are commercially available radiation detectors, mounted onto the outside of the vacuum chambers to indicate whether, when and where the beam is lost. BLM monitors can be ionization chambers, Cherenkov counters, or PIN-photodiode and scintillators with photomultiplier tubes (PMT).

The important factors to consider for selecting the right type of BLM for CEPC are intrinsic sensitivity, dynamic range, radiation hardness, response time and sensitivity to synchrotron radiation (SR). Table 13.4 summarizes the performance parameters of the four type BLMs.

Table 5.7.4: performance parameters of four BLM types

Type of BLM	Dynamic range	Response time	Sensitivity (for MIPs)	Radiation resistance	Sensitivity to SR
Ionization chamber	10^8	89 μs	600 ($Elec_{gain}$) (1L)	>100 Mrad	Sensitive
PIN-photodiode	10^8	5 ns[11]	100 ($Elec_{gain}$) (1 cm^2)	>100 Mrad	Insensitive
Cherenkov counters	10^5~10^6	10 ns	270 (PMT_{gain})(1L)	100 Mrad	Insensitive
Scintillators+PMT	10^6	20 ns	≈$18 \cdot 10^3$ (PMT_{Gain})	≈20 Mrad	Sensitive

Ionization chambers are used as BLMs in many accelerators. An ionization chamber in its simplest form consists of two parallel metal electrodes separated by a gap. The gap is filled with compressed air; argon and helium can be used to improve linearity and dynamic range. Whereas ionization chambers have wide dynamic range and high irradiation capability, they have the disadvantage of being slower and being sensitive to synchrotron radiation [12]. So for that reason they are not suitable for our machine.

Scintillators (with PMT) are very fast and bunch to bunch measurements can be achieved. The main drawback comes from the scintillator darkening when used in a high dose environment. The gain of PMTs varies within a factor 10, so a careful intercalibration of their sensitivities is necessary. Lastly this detector is expensive and also sensitive to synchrotron radiation.

Cherenkov based fibers are much more radiation hard but much less sensitive to beam losses than scintillators. However, with the additional gain of a PMT their sensitivity exceeds the ionization chamber. Cherenkov light is emitted when a charged particle's velocity βc is greater than the light velocity c/n in a medium with an index of refraction n>l. Cherenkov light is instantaneous, unlike scintillators, and the threshold for light output is several hundred keV, making Cerenkov detectors insensitive to the background radiation from synchrotron radiation. For example, electrons below about 150 keV will not produce any light, while 1 GeV protons or 0.5 MeV electrons produce about 169 photons/cm [13]. But the energy of synchrotron radiation photons strongly depends on beam energy. In CEPC, the critical energy Ee of synchrotron radiation photons is calculated for CEPC beam energy E=120 GeV, bending radius ρ=6094 m:

$$E_c(keV) = 2.2\frac{E(GeV)^3}{\rho(m)} \approx 628 \text{ keV} \qquad (5.7.2)$$

The synchrotron radiation photons of 628 keV undergo a photo effect. The emitted electrons (E≈628 keV) can produce more than 169 photons/cm in Cherenkov fibers. Therefore, we conclude that the Cherenkov fibers cannot be shielded against synchrotron radiation photons in CEPC.

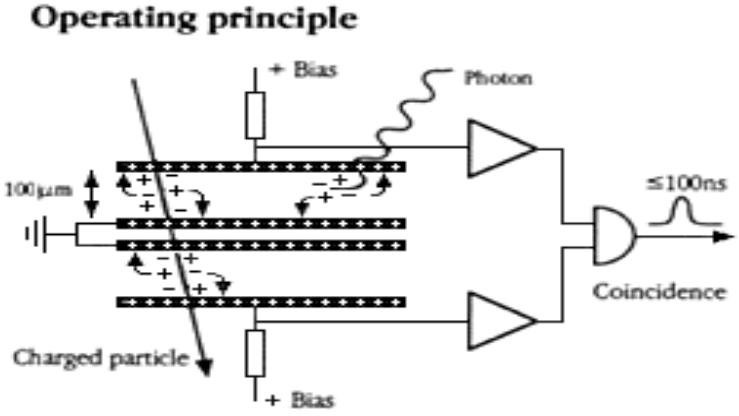

Figure 5.7.14: Principle of the PIN-photodiode beam loss monitor

PIN-photodiode are very fast, not very expensive, and have good radiation resistance. They have a large dynamic range and a high sensitivity but they exist only in small sizes. As shown in Fig.5.7.14, the Pin-photodiodes detector consists of two PIN-photodiodes mounted face-to-face. High energy charged particles produce signals in both diodes whereas a photon interacts in one diode only. Although the PIN-photodiode is relatively insensitive to synchrotron radiation background, at electron beam energy greater than 45 GeV, the synchrotron radiation photon undergoes mainly a photo effect or a Compton effect; the emitted electron may reach the second diode, resulting in coincidence signals [14]. However, this problem was resolved elegantly at HERA [15] and at LEP [16]. As shown in the Fig. 5.7.15, a thin copper (or lead) layer between the two diodes can reduce the probability for the emitted electron to reach the second diode. In this way the background due to synchrotron radiation can be reduced. In LEP (electron beam energy E = 80 GeV), the copper layer further reduces the background rate by a factor of 10 [15]. The optimal thickness of the layer can be calculated from the range of electrons in matter. The penetration depth R in which 90~95% of the incident electrons are stopped is given by (for Al) [16],

$$\mathrm{R(Al)} = \mathrm{A}\cdot\mathrm{E}\cdot[1-\frac{B}{(1+C\cdot E)}]mg/cm^{-2} \qquad (5.7.3)$$

with A = 0.55 • 10^{-3}gcm^{-2}keV^{-1}, B = 0.984, C = 3 • 10^{-3}keV^{-1}, E = energy of the electron.

For energies above 100 keV and for materials with higher Z (e.g. copper) the range is approximately:

$$0.6 \leqslant \mathrm{R/R(Al)} \leqslant 1 \qquad (5.7.4)$$

In our machine, synchrotron radiation photons can produce electrons (628 keV) by the photo effect. The range of the emitted electrons in copper (ρ_{Cu} =8.96 g/cm^3) is ≈ 0.26 mm.

Therefore, a thin layer of about 300 μm of copper between the diodes is sufficient to stop most of the Compton and photo electrons. This layer will not influence MIPs produced by beam losses. So, the detection efficiency of the BLM from beam losses is unchanged.

A thin layer of a high Z material like lead or copper between the two photodiodes inside the BLM leads to a decrease of background counts due to SR. but a fraction of the coincidence rate at high dose rates comes from multiple photons which interact at the same time in the two diodes. To reduce this coincidence rate, additional lead shielding will be needed around the BLMs [15, 16]. The optimum thickness of the lead shield should be tested.

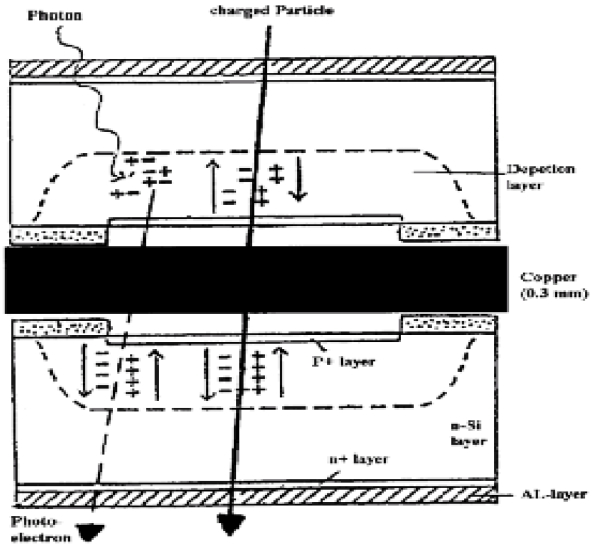

Figure 5.7.15: Two PIN-photodiodes with a copper layer between them

From the comparison between the four types of BLMs and the experience with the BLM systems in HERA and LEP, the pin-photodiodes detector is recommended to be installed in the CEPC storage ring. The detectors will be placed around the machine, at locations where the betatron amplitude functions reach a maximum i.e. in the arcs near each quadrupole. The efficiency of a BLM will be highest if it is located at the maximum of the shower. Monte Carlo simulations are needed to find the exact optimum locations for the monitors, as well as to calibrate the BLMs in terms of lost particles/signal.

5.7.6 **Tune Measurement System**

The system to measure betatron tunes must be flexible enough to cope with various requirements. For example, betatron tunes may differ for positrons and electrons because of the large orbit separation resulting from the momentum saw tooth. Individual bunch measurement is useful to identify intensity related tune shifts. Furthermore, beam-beam effects result in various coherent oscillation modes.

The system foreseen will consist of a magnetic shaker and an electrostatic pick-up for each plane. The H and V systems will both be installed in a straight section, at a sufficient distance from the IP so that gating on individual bunches is possible.

Apart from the traditional swept-frequency excitation for the tune measurement, some newer technology like direct diode detection will be investigated.

Direct Diode Detection（3D）is a technique developed at CERN initially for the LHC tune measurement system [17] and more recently for observing beam motions of very small amplitude [18]. The basic idea is to time stretch the beam pulse from the pickup in order to increase the betatron frequency content in the baseband. This can be accomplished by a simple diode detector followed by an RC low pass filter [19].

The 3D method has many advantages: simplicity and low cost, revolution frequency suppression, robustness against saturation, flattening out the beam dynamic range, independently of the fill pattern. At the same time, it also has disadvantages: it operates in the low frequency range, its response is dominated by the largest bunches, and it cannot measure bunch by bunch tunes [19].

5.7.7 **Vacuum Chamber Displacement Measurement System**

Due to heat effects caused by synchrotron radiation and beam loss, the vacuum chamber will suffer random displacements. This can degrade the BPM resolution. So in order to calibrate the BPMs, this displacement must be measured.

The system for doing this includes a Linear Variable Differential Transformer (LVDT), a signal processing unit, a computer and network.

The displacement monitor is mounted near the BPM. The signal is sent by a 600 m cable to the local station. The electronics can be purchased from a company like NI (National Instruments) or designed in house along with the data sampling electronics and the A to D converter.

5.7.8 **Feedback System**

There are 50 bunches in the Booster, the bunch current is 0.01 mA, and due to HOMs and the resistive wall instability, multi-bunch instabilities may occur. There is almost no synchrotron radiation damping. In order to cure these instabilities, feedback systems in all three dimensions are necessary. The feedback system must sense bunch motion and deliver either deflection or acceleration independently to each bunch in order to damp all of the possible multi-bunch instabilities.

The transverse feedback system consists of front end electronics, digital electronics, amplifier and kicker. Front end electronics convert the BPM oscillation signal to basic quantities. Then follows processing in the digital electronics, putting in a 90 degree phase shift, removing the closed orbit component and a single turn delay. The analog signal then is sent to the amplifier and kicker to give a beam angular kick. A power amplifier drives a 50 **Ω** strip line kicker shorted at one end [20, 21]. The plates of the kicker are powered differentially using a hybrid power divider driven by the combined amplifier output.

The longitudinal feedback system is more difficult than the transverse feedback system. Apart from the three parts mentioned above, there is back end electronics. The digital signal processing needs to add in the carrier frequency. For the longitudinal feedback system, a pillbox cavity kicker is necessary. We will evaluate existing and well-tested feedback systems at other laboratories and also consider developing a more modern system.

5.7.9 **Other Systems**

A beam polarization measurement system and energy and energy spread measurement systems should be studied and prototypes set up for CEPC.

Transverse beam polarization could be measured by a laser Compton polarimeter which is based on spin-dependent Compton scattering of circularly polarized photons from polarized electrons and positrons.

Beam energy and energy spread measurements need to be thoroughly investigated

5.7.10 **References**

1. Beam Instrumentation, LEP design report Vol. II, 1984.
2. Peter Forck, "Pick-ups for bunched beams," Lecture Notes on Beam Instrumentation and Diagnostics JUAS 2012 Lecture, 2012.
3. P. Forck, P.Kowina, D. Liakin, "Beam position monitors," CERN Accelerator School Beam Diagnostics, Dourdan, France, 2008.
4. www.cst.com. The "Studio Suite" of CST (Computer Simulation Techology) is a set of applications for simulating various electromagnetic configurations and properties.
5. D. Lipka, DESY Hamburg, Private communication, 2015.
6. D. Lipka, B. Lorbeer, D. Nolle, M. Siemens, S. Vilcins, "Button BPM Development for the European XFEL," Germany, DIPAC,2011.
7. Y. Cenger, N. Baboi, "Characterization of Button and strip line beam positon monitors at FLASH," DESY 2007
8. N. Baboi, "Electromagnetic Simulations for the PETRA III BPMs," DESY, Hamburg, 2006.
9. D. Lipka, "Heating of a DCCT and a FCT due to wake losses in PETRAIII," 2013.
10. T. Mitsuhashi, M. Tadano, "Measurement of Bunch Length Using Intensity Interferometry," Proceedings of EPAC 2002, Paris, France.1936-1938.
11. A. Zhukov, "Beam loss monitors (BLMS): physics, simulations and applications in accelerators," Proceedings of BIW10, Santa Fe, New Mexico, USA.
12. K. Wittenburg. "Beam loss monitors."
13. R.E. Shafer, "A tutorial on beam loss monitoring," (TechSource, Santa Fe). 2003. AIP Conf.Proc. 648 (2003).
14. I. Reichel, "The Loss Monitors At High Energy."
15. T. Spickermann and K. Wittenburg,"Improvements in the useful dynamic range of the LEP Beam Loss Monitors," CERN SL-Note 97-05.
16. K. Wittenburg, "Reduction of the sensitivity of the pin diode beam loss monitors to synchrotron radiation by use of a copper inlay," DESY HERA 96-06.
17. LHC Design Report vol.1, chapter 13.7 "Tune, chromaticity and betatron coupling," CERN,2004.
18. A. Gasior et al., "Sub-nm beam motion analysis using a standard BPM with high resolution electronics," BIW10, La Fonda Hotel, Santa Fe, New Mexico, USA.
19. M. Gasior, R. Jones, "The principle and first results of betatron tune measurement by direct diode detection," LHC-Project-Report 853.
20. G. Codner, M. Billing, et al., "CESR Feedback System Using a Constant Amplitude Pulser," Proceedings of the 8th Beam Instrumentation workshop. pp 552-59.
21. Rogers, "Coupling of a Shorted Stripline Kicker to an Ultrarelativistic Beam,"Cornell CBN, 95-04, April 21, 1995.

5.8 Control System

5.8.1 **Introduction**

The CEPC control system covers the entire 54.4 km Collider, the Linac and its injection system, about 2 km long, as well as the Booster.

The system controls and monitors all the equipment with OPIs (Operator Interface), robust and efficient communications, beam tuning and application tools to achieve the desired beam acceleration and accumulation goals and high peak and integrated luminosity.

To build such a large control system, better quality is achieved by using as much as possible commercial and industrial products and techniques. The collection and distribution of large volumes of control messages and monitoring data, together with the different level system alarms and data archiving are a major challenge in the design.

The time relationship among these widely distributed devices related to beam source, injection, accumulation, acceleration, extraction, circulation, diagnostics and post-mortem analysis must be adequately recorded. For the Booster, a synchronization accuracy of several microseconds among the hundreds of related power supplies is required.

As electronic techniques have evolved, hardware prices have decreased rapidly, while at the same time better performance has been achieved. It is anticipated that this trend will continue. This indicates that the purchase and final component mass production should be done as late as possible. On the other hand, technical studies and interface design between different systems should be made as early as possible to ease system development, integration and commissioning. A full-scale prototype system should be set up for development and tests.

5.8.2 **System Architecture**

The control system will be divided into 3 layers, as illustrated in Fig. 5.8.1, with the possible addition of access from world wide websites. Ethernet will be the control system backbone. Now 40 Gb/s components are in wide use and soon 100 Gb/s components will become available. With this increasing higher performance of network switches, direct connection to the Ethernet at 1 to 10 Gb/s is a good choice. For those systems with high intensity real-time computing, FPGA [1] plus MTCA/XTCA [2] will be better choices for the ease of scalability. For most of the slow-speed applications, PLC (Programmable Logic Controller) based systems should be used as much as possible to improve overall reliability.

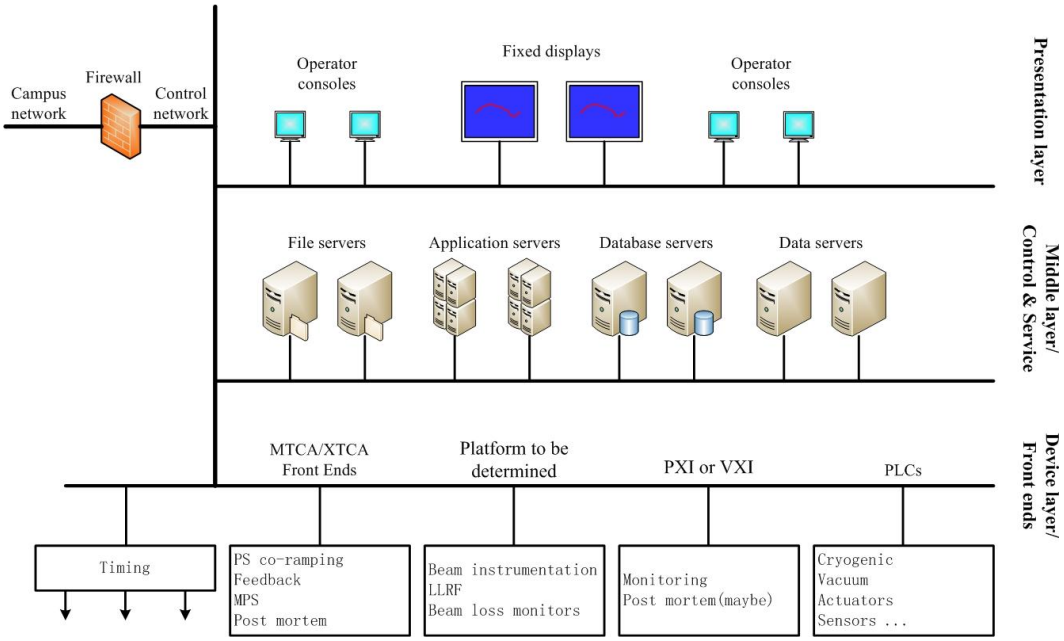

Figure 5.8.1: Control system architecture

5.8.2.1 *Control Software Platform*

A good control software platform should be chosen or developed to build the control system. It should have good reliability to contribute to high operation efficiency, good scalability to ease upgrades, and good maintainability to ease maintenance. Data exchange, such as control commands and monitoring information among thousands of devices, should be handled effectively. The whole control system should have rich drivers to access to the front end devices, rich tools to store and retrieve the useful data, rich tools to provide friendly operator interfaces, and rich application interfaces for further development. Also, it should integrate the most modern techniques.

Computer, control and software techniques have been developing very fast since their birth. As a base design, EPICS [3] (Experimental Physics and Industrial Control System) is chosen as the global control platform; other tools and the latest technology trends will be investigated and followed.

EPICS has been widely applied in large experimental facilities around the world. It was originally developed by Los Alamos National Laboratory and Argonne National Laboratory and has been continuously improved over the years by different laboratories. There are many application tools and device drivers that have been implemented, which eases overall system integration. Here in China EPICS has been applied successfully in the accelerator control systems of the BEPCII [4] (Beijing Electron Positron Collider II) and CSNS [5] (China Spallation Neutron Source).

EPICS is based on a client-server model with communications through Ethernet. Its main components are OPI, IOC (Input Output Controller) and CA (Channel Access). OPI is the client side module for operators, IOC is the server side input output control module and CA is the communication module. Fig. 5.8.2 shows the structure of EPICS.

The OPI layer provides IOC database management, graphical user interface and other control and monitoring software, such as system alarms, data archiving, real-time and historical curves. IOC runs on the server computer to manage the real-time database

and communication with the front-end devices equipped with suitable drivers. CA supports the TCP/IP protocol for the clients to transparently access data in the real-time database of the IOCs.

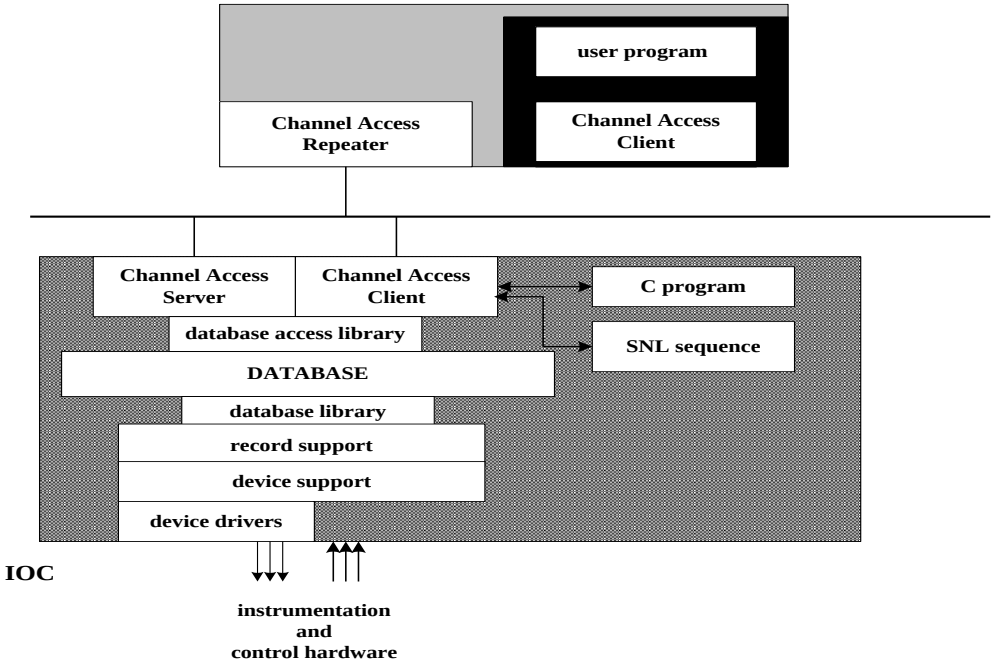

Figure 5.8.2: Structure of EPICS

5.8.2.2 *Equipment Level Devices*

MTCA crates will probably be used for the LLRF (Low Level Radio Frequency) control for high bandwidth real-time data exchange between different RF cavities. Modules designed in house will be used for the approximately 4000 power supplies. A co-ramping function will be designed for all the power supply control modules. PLCs will be used to control the cryogenic and vacuum systems, the adjustable collimators, the machine protection system and the vacuum chamber temperature monitoring system. Beam instrumentation devices will be integrated into the whole system directly via Ethernet.

Commercial PXI [6] crates and modules or self-designed modules will be used for post-mortem data acquisition and analysis. Industrial computers will be used as IOC for some of the device level controls.

5.8.2.3 *Network*

The control system network will be a core redundant design with 40 Gb/s interface to the different aggregation switches. Edge switches are connected to the aggregation switches to provide communication to the devices. Links of 10 Gb/s will be provided to the different devices by the aggregation switches. Links of 1 Gb/s and 100 Mb/s will be provided to the different devices by the edge switches.

A 40 Gb/s backbone is selected due to current technical capabilities and the potential large data rate both in the average and in sudden events. A higher bandwidth helps to decrease packet transmission latency, and thus improve system stability.

Aggregation and edge switches will be provided at each local control station and the CCR (Central Control Room). A three-layer structure is preferred for cost-saving considerations.

A total of about 5000 IPs are foreseen, so about 130 edge switches will be used.

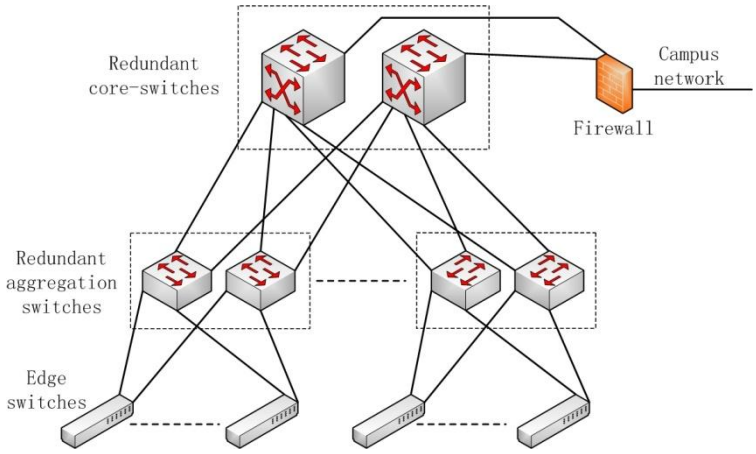

Fig. 5.8.3: The accelerator control network

5.8.3 **Main Sub-System Level Hardware**

5.8.3.1 ***Power Supply Remote Control***

There are about 4000 power supplies in total, of which more than 3000 are for correctors. Power supplies in the Booster ring need to be co-ramped during beam acceleration, while the others only need to be set to the correct currents. The power supply remote control is designed to fulfill both requirements to ease maintenance so the only difference is in the physical connection and software configuration.

Since CEPC is so large it is not easy to repair or replace a broken device within a short time. Therefore redundant design will be considered wherever possible. Two redundant controllers will be installed in a control crate designed here at IHEP. Each interface card has two completely isolated connectors. All the connections will be done through a passive backplane. Two isolated crate power supplies will provide power to the two control routes. Global redundancy will be done through network packets exchange or heart-beat cable connections between the two controllers. Fig. 5.8.4 shows the redundant connections of the power supply remote control. Fig. 5.8.5 shows the preliminary remote control crate arrangement.

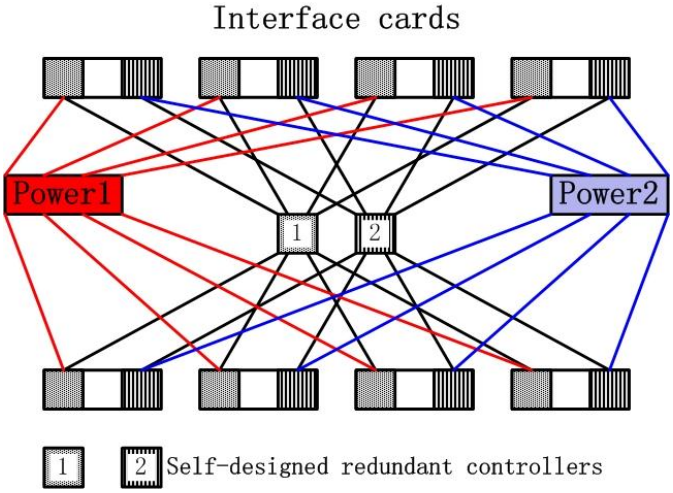

Figure 5.8.4: Redundant design of the power supply remote control

Figure 5.8.5: Preliminary power supply remote control crate arrangement

5.8.3.2 *Machine Protection System (MPS)*

The energy stored in the collider ring is about 690 kJ for both beams, and the energy injected into the collider from the Booster is about 34.5 kJ per pulse train. When necessary to prevent damage to the equipment, beam in the collider should be aborted into the beam dump and injection should be stopped when there are component problems or the dose rates due from lost particles are too high. The MPS will provide this global protection with interface to the related systems.

Power supplies, RF cavities, beam-loss monitors, pulsed power supplies for kickers, cryogenic system, vacuum system, beam-pipe temperature monitoring system and timing system, and perhaps other systems should all be connected to the MPS.

Redundant controllers will be used to ease maintenance and increase reliability. IO connections will *not* be redundant to save the total cost.

The beam revolution time is about 0.17 ms. The protection system response time must be compatible with this, so a low level FPS (Fast Protection System) may need to be designed as a part of the MPS.

Fig. 5.8.6 shows the architecture of the MPS at one station.

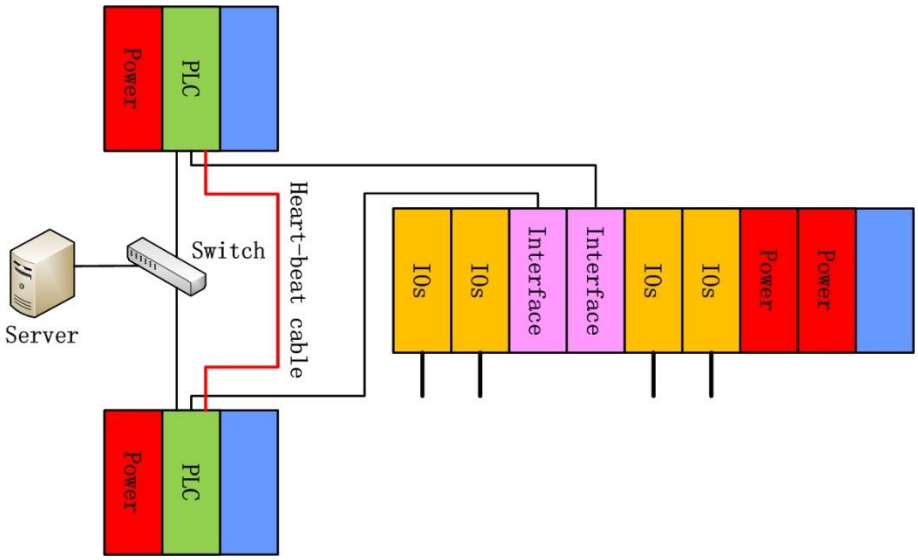

Figure 5.8.6: Structure of the MPS at one station

5.8.3.3 *Vacuum Control*

Interface to vacuum devices are relay contacts and RS232/485 ports. Relay contacts are for on/off control and protection and the RS232/485 ports are for monitoring. Similar to the MPS design, redundant PLCs will be used for relay contacts with similar structure as shown in Fig. 5.8.6. Devices for RS232/485 integration will be determined later.

There are a total of about 520 vacuum valves and 2160 gauges distributed around the collider and Booster rings. Complicated interlocks with the other systems, such as RF cavities and kickers need to be designed and a prototype system built.

5.8.3.4 *Vacuum Chamber Temperature Monitoring*

Synchrotron photons from beam missteering can cause vacuum chamber heating. Too much heat can raise the temperature, worsen the vacuum and possibly damage the chambers. So temperature monitoring of the vacuum chambers is essential, especially for the bending parts of the collider ring where SR is generated. There will be two temperature sensors at each dipole for a total of about 8000 sensors.

The relationship between the vacuum chamber temperature monitoring system and the MPS need to be clarified, since there are so many sensors.

5.8.4 Timing System

The timing system of CEPC will accomplish the following tasks:

- Send signals for precise timing in the acceleration sequence:
  - e-gun triggered, positrons generated
  - electrons and positrons accelerated, injected into the Booster, ramped up, extracted to the storage ring
- Provide synchronizing clocks to equipment such as the data acquisition systems.

- Send post mortem events to the data acquisition devices for the RF, cryogenics, power supplies, and beam instrumentation and other systems when receiving predefined signals from the MPS.
- Provide precise timestamps to most of the hardware systems.

An event-based digital timing system will be designed for CEPC, including encoding, transmitting, receiving and decoding. Single-mode fiber cables will be used for timing distribution. A prototype will be set up.

5.8.5 **Video Monitoring System**

Video monitoring is necessary for operators to learn about the environment status at different stations. To save cost, switches of this system are connected in series. Fig. 5.8.7 shows the overall structure of the video monitoring system.

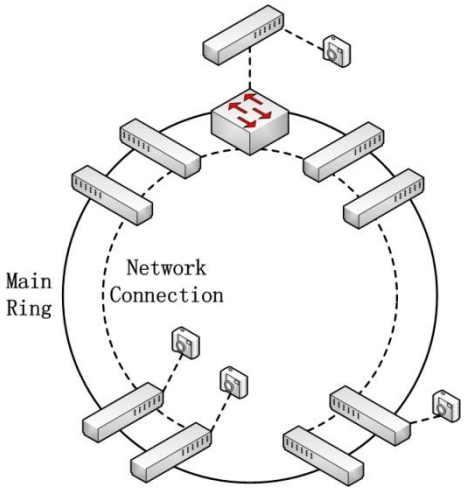

Figure 5.8.7: Overall structure of the video monitoring system

5.8.6 **Data Archiving and Analysis**

The number of signals that need to be archived is in the tens of thousands. Several data archives will be needed to improve overall efficiency.

Redundant storage servers are used for safe data storage and to provide high data availability. A special server is used for fast data retrieval. The analysis server and the OPIs can also be deployed in the campus network to lessen the burden on the control network.

The overall system will be developed with JAVA and a relational database.

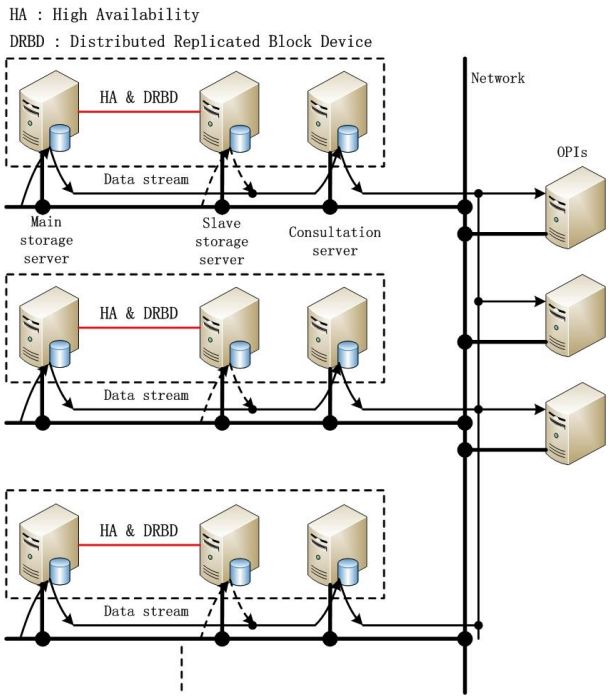

Figure 5.8.8: Hardware configuration and data flow of data archiving

5.8.7 **System Alarms**

Abnormal situations should be collected, stored and reported. Thousands of alarm signals are expected from different systems. To deal properly with the many alarms, and to provide as meaningful information as possible to the operators, the alarm system should be designed with several levels. The fundamental level will be the equipment level. These are the alarm sources. Data with an accurate timestamp should be recorded at this level and overall alarm signals provided to the network for server level storage and treatment. Alarm servers will collect and store the alarm signals from the different equipment on the control network. Alarm servers will provide the relevant information whenever an abnormal situation occurs. OPIs should provide the operators with the right information for them to deal with abnormal situations.

Fig. 5.8.9 shows the architecture of the alarm system.

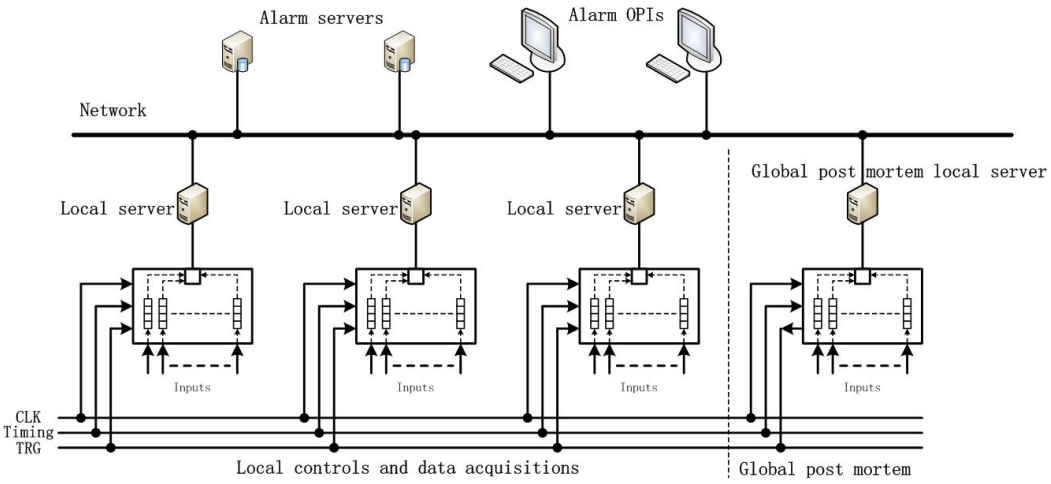

Figure 5.8.9: Alarm system architecture

5.8.8 **Post Mortem, Large Data Storage and Analysis**

All the control and data acquisition systems should have the ability and necessary interface to record a period of data with an accurate timestamp whenever there is problem. The time accuracy required and the time window for recording the data are defined differently for different systems. Some of the smaller systems can provide analog and/or digital signals directly to the global post mortem system.

Fig. 5.8.10 shows the structure of the post mortem system. Local controls and data acquisition are the same as in the alarm system. The triggered window data in the local devices will be transmitted into the post mortem servers whenever there is a problem. A software analysis interface should be defined and provided by the post mortem servers. Post mortem OPIs will analyze the data through the analysis interface.

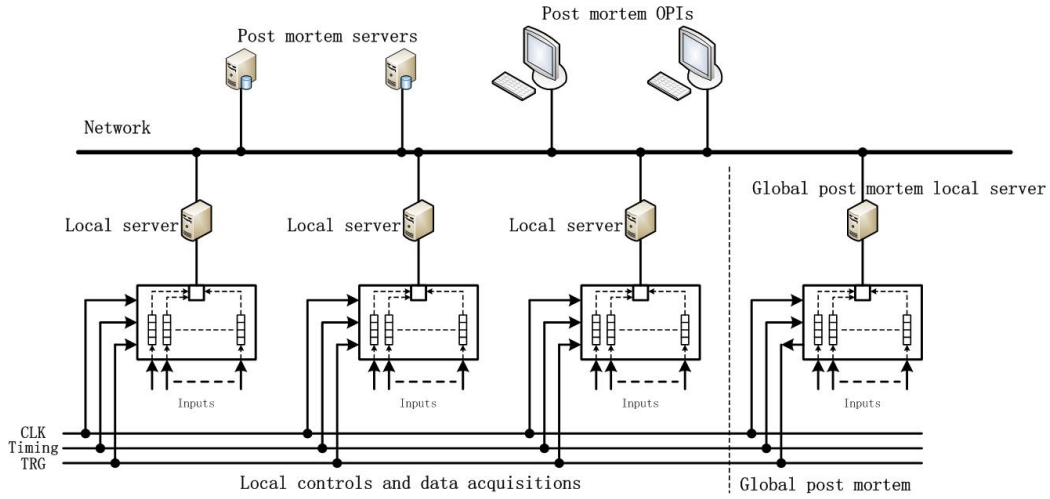

Figure 5.8.10: Post mortem system architecture

5.8.9 Event Log

An automatic way to store equipment status and prepare an operations report should be developed. This provides the operators and accelerator experts the tools they need to study the machine and also to learn of minor problems and implement timely improvements. A tree structure is considered for distinguishing the information from different systems and at different levels. Also provided will be electronic logbooks for each item and for the accelerator complex as a whole.

5.8.10 Software Development Environment and Application

The software development environment should be defined early to facilitate future compatibility during system integration and to ease maintenance. This includes the operating systems, the development tools, the software upgrade strategy and the hardware platform. Standardization should be done first and the strict control of software versions is a must. Also, a global software and hardware platform should be provided for simultaneous development work.

Upgradability must be considered early during the setup of the programming environment and software development. Careful study is needed and protocols established as early as possible.

Some rack servers will be used for the data archiving/analysis, accelerator physics software, alarm service and post mortem service. Blade servers [7] and raid disks [8] will be provided for high reliability software IOCs and other applications.

5.8.11 References

1. http://www.xilinx.com; http://www.altera.com
2. http://www.picmg.com
3. http://www.aps.anl.gov/epics/index.php
4. IHEP, Design Report of BEPCII, May, 2002.
5. IHEP, Design Report of CSNS, April, 2011.
6. http://www.pxisa.org
7. A blade server is a thin, modular electronic circuit board containing one, two, or more microprocessors and memory that is intended for a single, dedicated application and can be easily inserted into a space-saving rack.
8. RAID or “redundant array of independent disks” is a data storage virtualization technology that combines multiple disk drive components into a logical unit for the purposes of data redundancy or performance improvement.

5.9 Mechanical Systems

5.9.1 Introduction

The Booster is mounted above the Collider (Main Ring, or MR). To reduce cost, each magnet is supported and adjusted separately.

- Supports in the Collider: the pedestal is made either of concrete poured during tunnel construction or else is made of prefabricated concrete sections. The support between magnet and adjusting mechanism increases the contact

area and thus reduces stress and magnet displacement. The adjusting mechanism has 6 DOFs. (degrees of freedom)

- Supports in the Booster: the pedestal is made of steel frames attached to the tunnel. Several different schemes for doing this are described below. The adjusting mechanism and magnet support are similar to those in the MR.

5.9.2 **Supports in the Collider**

Dipole, quadrupole, and sextupole magnets and correctors are all supported separately. Each support contains the pedestal, magnet support and adjusting mechanism.

- Dipole support system: four magnet modules of length 4500 mm each are connected to form a unit of total length 18000 mm, as shown in Figure 5.9.1. To avoid deformation, the support system of each module contains two main supports and two supplementary supports, as shown in Figure 5.9.2. The main support is for support and adjustment (6 DOFs), while the supplementary supports are only for support (1 DOF).

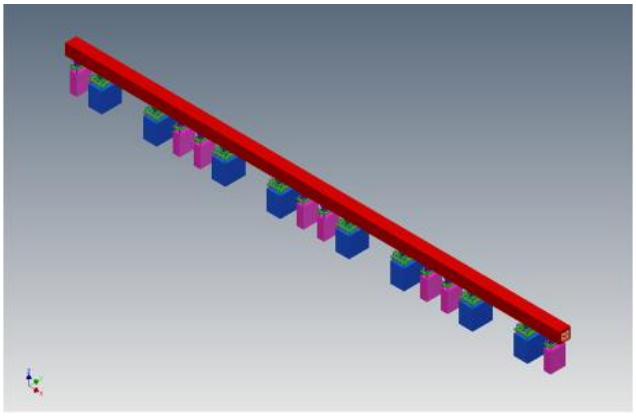

Figure 5.9.1: Dipole magnet and its supports

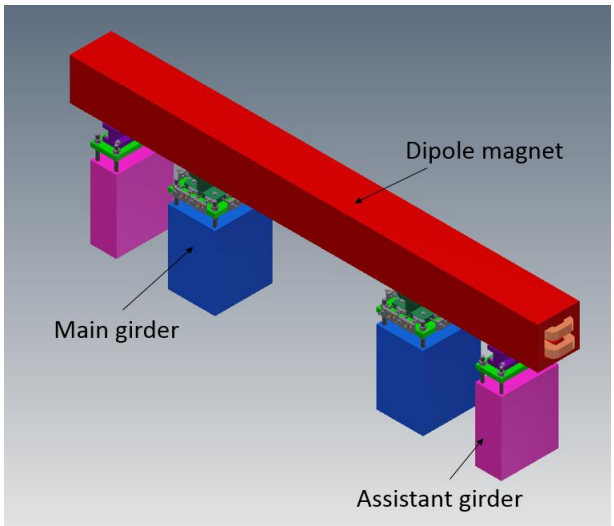

Figure 5.9.2: Dipole magnet and its supports for each module (supports are called girders in the figure)

- Quadrupole support system: The quadrupole magnet is 2000 mm long; it has two supports, like the dipole supports described above. Figure 5.9.3 shows the scheme.

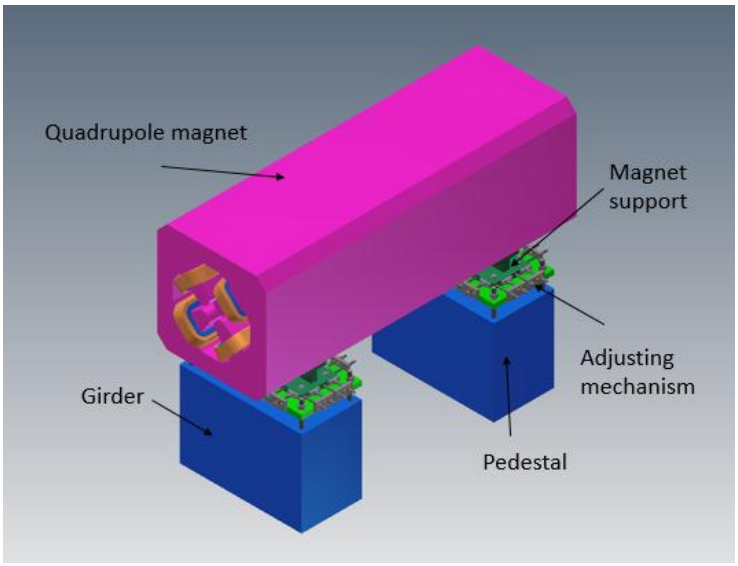

Figure 5.9.3: Quadrupole magnet and its supports

- Sextupole support system: There are two kinds of sextupole magnets, of length 670 mm and 370 mm. Each sextupole magnet has one support, shown in Figure 5.9.4, also similar to the dipole and quadrupole supports.

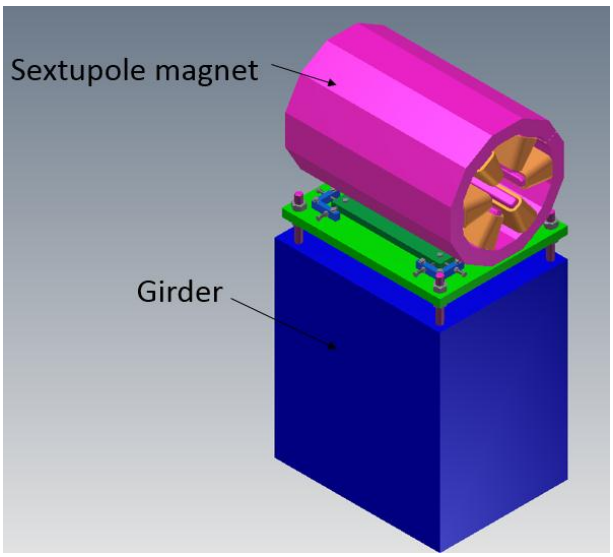

Figure 5.9.4: Sextupole magnet and its support

5.9.3 **Design Requirements**

Suppose the +Z axis of the support coordinate system is along the beam, the +Y axis upward and the coordinate system is a right-hand one.

- Range and accuracy of adjustment are shown in Table 5.9.1.

Table 5.9.1: Range and accuracy of adjustment

	Range of adjustment	Accuracy of adjustment
X	$\geq \pm 20mm$	$\leq \pm 0.02mm$
Y	$\geq \pm 30mm$	$\leq \pm 0.02mm$
Z	$\geq \pm 20mm$	$\leq \pm 0.02mm$
$\Delta\theta x$	$\geq \pm 10$mrad	$\leq \pm 0.05mrad$
$\Delta\theta y$	$\geq \pm 10$mrad	$\leq \pm 0.05mrad$
$\Delta\theta z$	$\geq \pm 10$mrad	$\leq \pm 0.05mrad$

- Stability with large time constants, avoiding creep and fatigue deformation.
- Simple and reliable mechanics for safe mounting and easy alignment.

5.9.3.1 ***Design of the Collider Dipole Support System***

To reduce cost, the dipole support system for each module (4500 mm) contains two main supports and two shorter auxiliary supports.

5.9.3.1.1 The Main Support

The main support is shown in Figure 5.9.5, including the pedestal, magnet support and adjusting mechanism. To avoid coupling of horizontal and vertical adjustments, the adjusting mechanism is a separated type and consists of 2 layers – a top layer and a bottom layer. The magnet is supported by the top layer. When horizontal alignment is done, the magnet support is fixed to the bottom layer with bolts. The magnet support and bottom layer are shown separately in Figures 5.9.6 and 5.9.7.

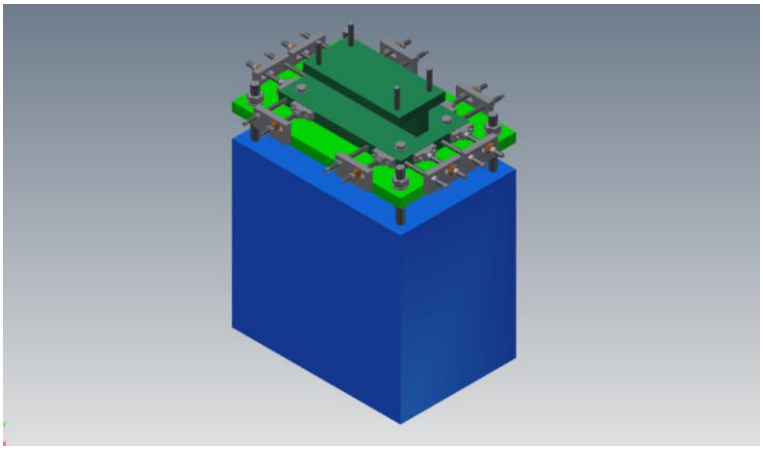

Figure 5.9.5: The main support

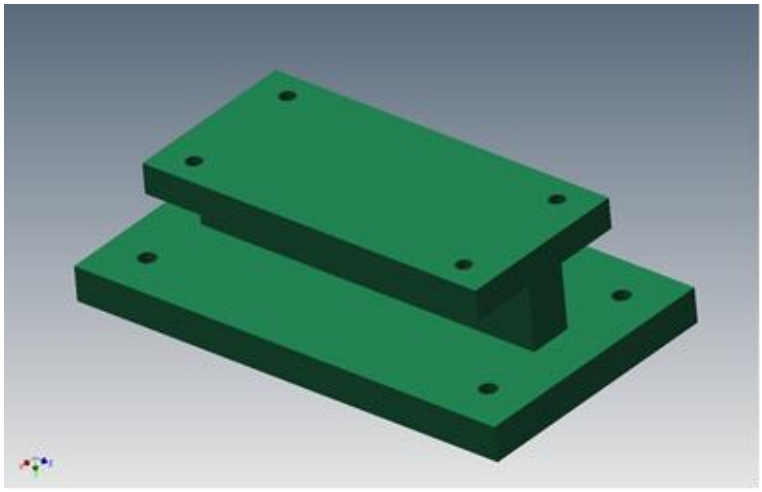

Figure 5.9.6: The magnet support showing two layers: top (up) and bottom (down)

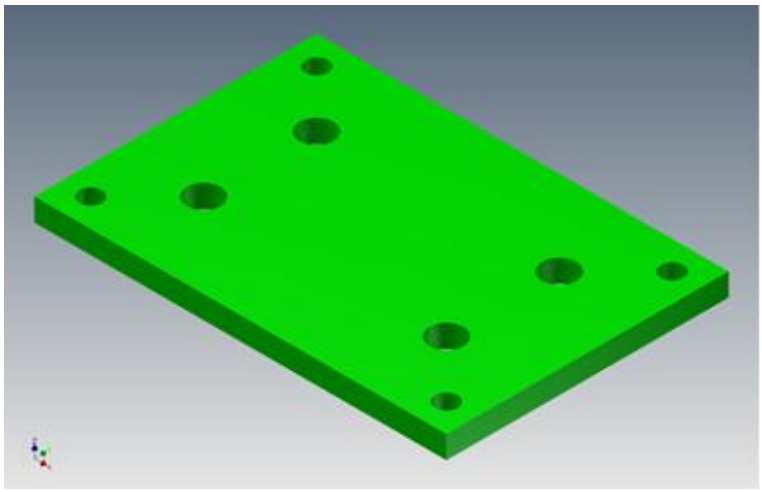

Figure 5.9.7: The down-layer

There are four M42 screw bolts for each main support, supporting the magnet, as shown in Figure 5.9.8. The vertical position is adjusted by screw nuts. The weight of each magnet module is 4000 kg, and each adjustment mechanism is 250 kg. Then the force on each screw bolt is:

$$\left(\frac{4000}{2}+250\right)\times\frac{1}{4}\times 9.8=5500(N) \qquad (5.9.1)$$

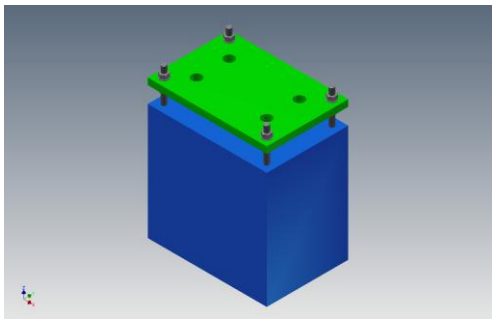

Figure 5.9.8: Vertical adjustment mechanism

The compressive stress of the screw bolt is about 4.8 MPa, satisfying the static stress requirement.

The horizontal position is adjusted by push-pull bolts shown in Figure 5.9.9. The coefficient of friction of steel on steel is 0.17, so the force on the active bolt is:

$$\left(\frac{4000}{2}+250\right)\times 9.8\times 0.17 = 3750(N) \qquad (5.9.2)$$

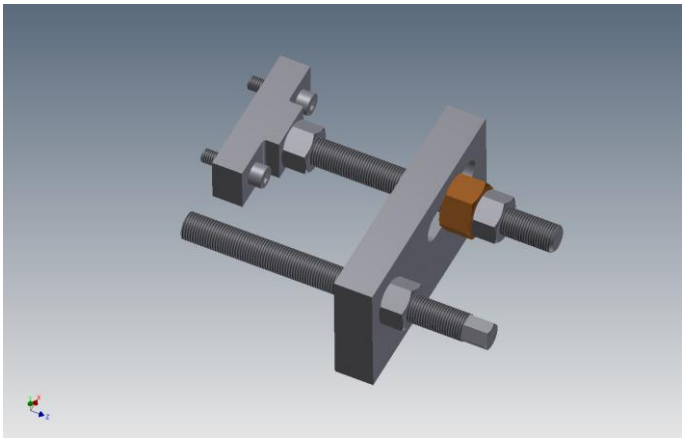

Figure 5.9.9: The push-poll bolts

The main loads are the weights of the magnet and main support itself, all of which are static loads. The contact area between pedestal and ground is fully constrained. Displacement analysis is in Table 5.9.2.

Table 5.9.2: Displacement analysis of the main support

Parameters	Results	Remarks
Software	Inventor 2011	
Elastic modulus	200 GPa	
Poisson's ratio	0.3	
Max. displacement	0.03934 *mm*	Figure 5.9.10
Max. Y-axial displacement	0.03934 *mm*	Figure 5.9.11

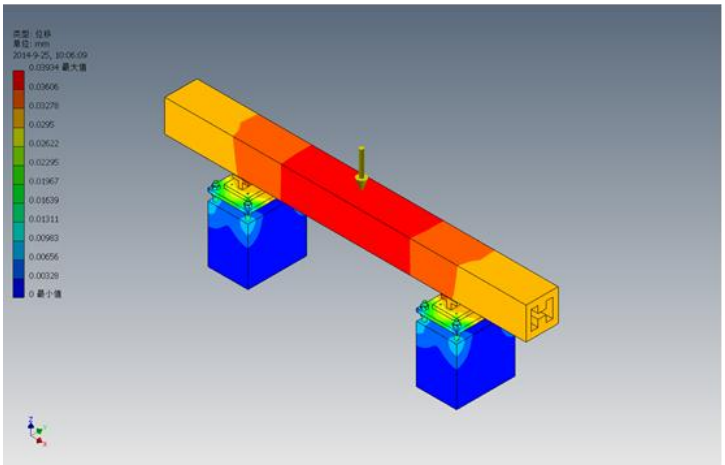

Figure 5.9.10: Displacement distribution by gravity

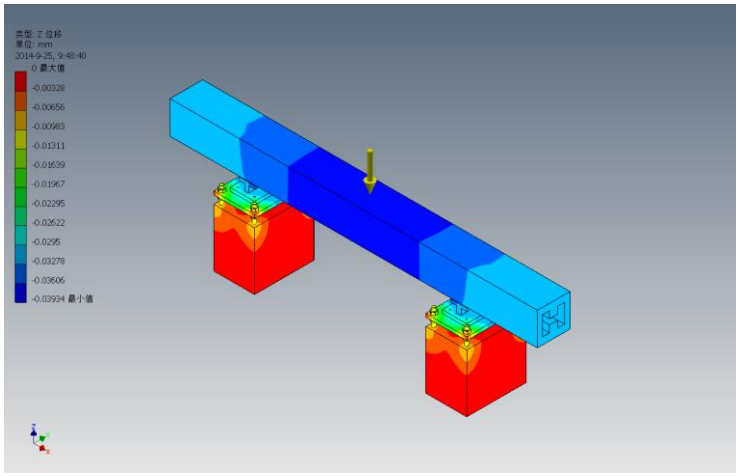

Figure 5.9.11: Y-axis displacement distribution by gravity

5.9.3.1.2 The Auxiliary Support

The auxiliary support has only a Y-axis DOF. Together with the main supports, they support the magnet module and avoid deformation. Similar to the vertical adjustment mechanism of the main support, the adjusting mechanism is a screw bolt. The auxiliary support is showed as Figure 5.9.12.

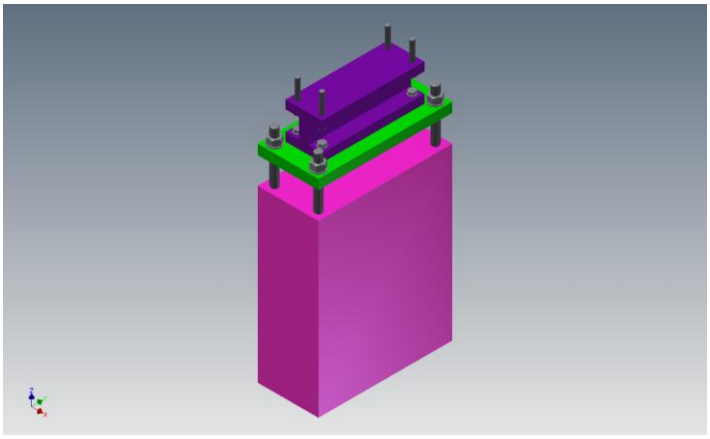

Figure 5.9.12: The auxiliary support

5.9.3.2 *Design of the Collider Quadrupole Support System*

The quadrupole magnet is 2000 mm long, supported by two supports, shown in Figure 5.9.3. These supports are similar to the main supports of the dipole magnet.

The weight of each quadrupole magnet is 6400 kg, and each adjustment mechanism is 250 kg. The magnet is supported by eight M42 screw bolts. Then the compressive stress on each screw bolt is calculated to be 6.7MPa, satisfying the static stress requirement.

The displacement analysis is showed as Table 5.9.3.

Table 5.9.3: Displacement analysis of the quadrupole supports

Parameters	Results	Remarks
Software	Inventor 2011	
Elastic modulus	200 GPa	
Poisson's ratio	0.3	
Max. displacement	0.037 *mm*	Figure 5.9.13
Max. Y-axial displacement	0.037 *mm*	Figure 5.9.14

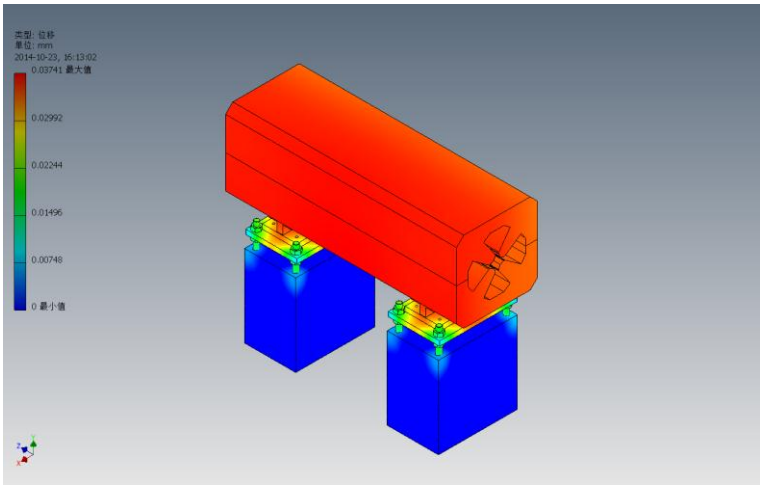

Figure 5.9.13: Quadrupole displacement distribution by gravity

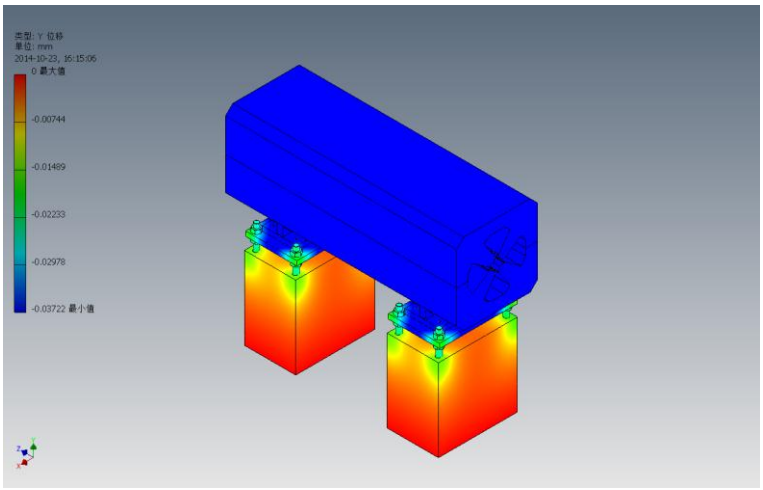

Figure 5.9.14: Quadrupole Y-axis displacement distribution by gravity

5.9.3.3 *Design of the Collider Sextupole Support System*

There are two types of sextupole magnets of lengths 670 mm and 370 mm. A common support is adopted for both lengths. The adjustment mechanism contains four vertical screw bolts and four push-pull bolts, as shown in Figure 5.9.15.

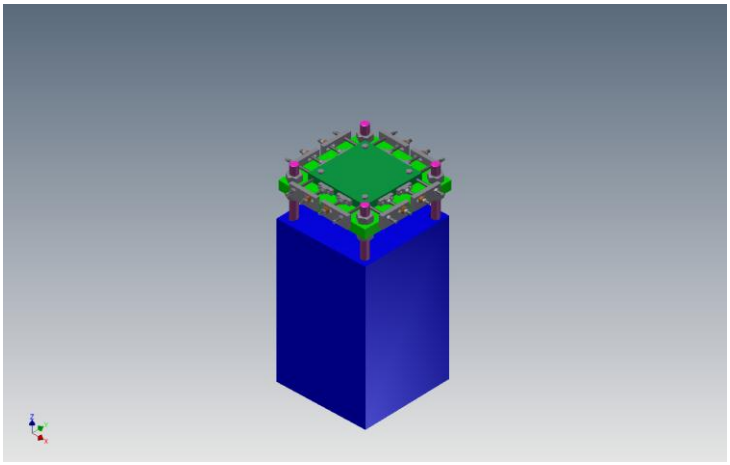

Figure 5.9.15: Support for sextupole magnet

The displacement and stress are analyzed. For the 670 mm long magnet, the weight is 666 kg, and each adjustment mechanism is 250 kg. The magnet is supported by four M42 screw bolts. The compressive stress on each screw bolt is 1.8 MPa, satisfying the static stress requirement.

The displacement analysis is shown in Table 5.9.4.

Table 5.9.4: Displacement analysis of the sextupole supports

Parameters	**Results**	**Remarks**
Software	Inventor 2011	
Elastic modulus	200 GPa	
Poisson's ratio	0.3	
Max. displacement	0.0418 *mm*	Figure 5.9.16
Max. Y-axial displacement	0.0418 *mm*	Figure 5.9.17

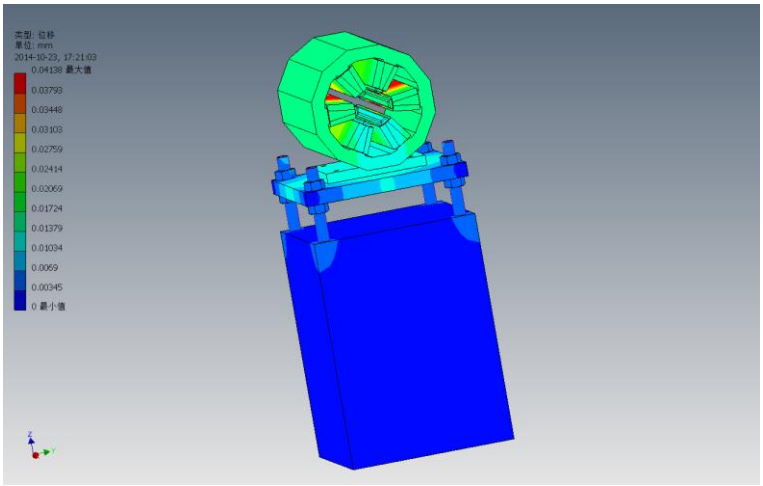

Figure 5.9.16: Sextupole displacement distribution by gravity

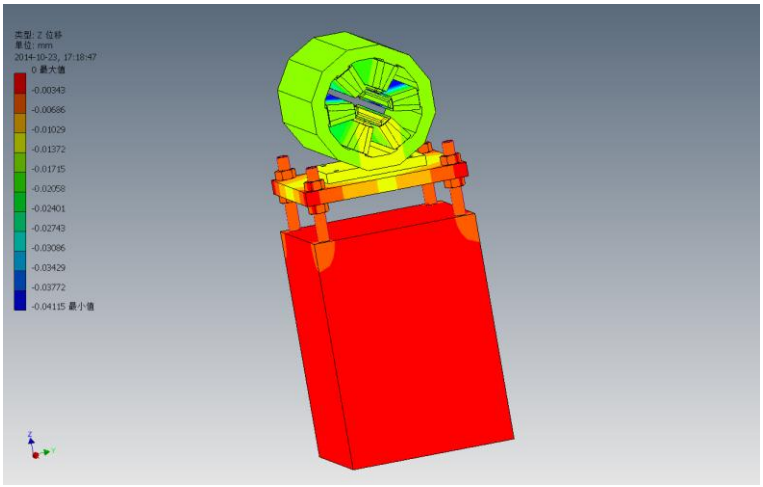

Figure 5.9.17: Sextupole Y-axis displacement distribution by gravity

5.9.4 **Supports in the Booster**

The Booster is above the Collider. For the Booster support system, three schemes have been considered.

- Scheme 1: the supports are hung from the top of the tunnel; the magnets then hang from the bottom of the support as shown in Figure 5.9.18.
- Scheme 2: the supports are fastened to the wall on one side of the tunnel; the magnets are mounted on the top of the support as shown in Figure 5.9.19.
- Scheme 3: the supports are integrated into a single unit, supporting magnets for both the MR and Booster as shown in Figure 5.9.20.

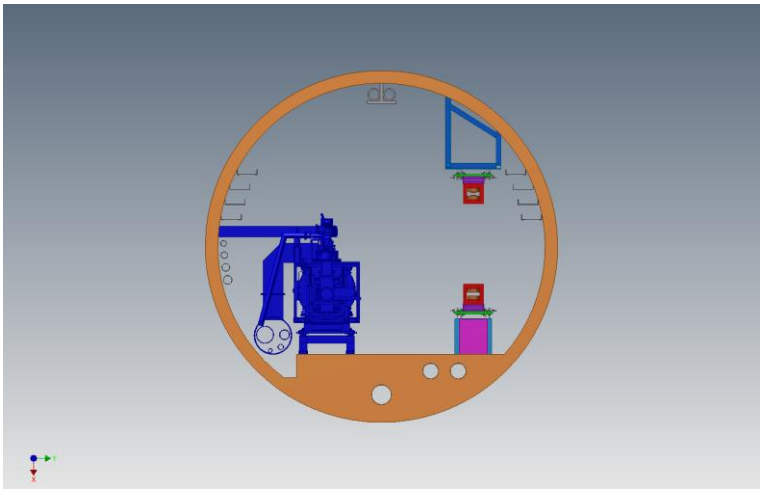

Figure 5.9.18: Scheme 1 of Booster supports

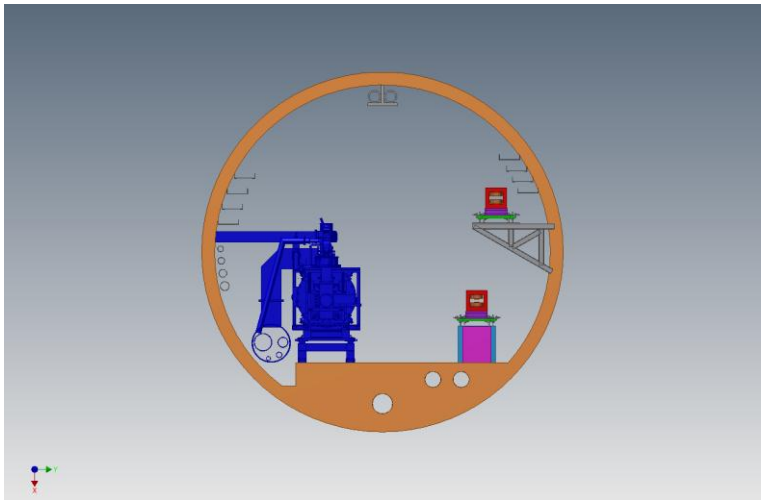

Figure 5.9.19: Scheme 2 of Booster supports

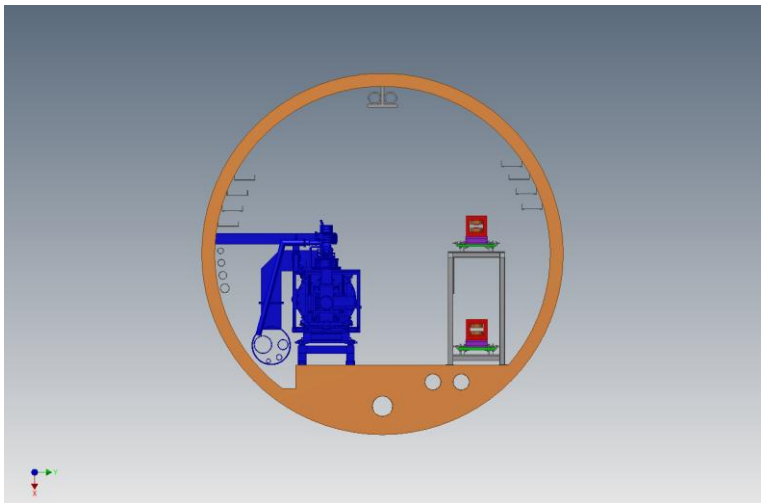

Figure 5.9.20: Scheme 3 of Booster supports

After a comprehensive review Scheme 1 has been selected. Similar to the dipole magnet in the Collider, four magnet modules (1/4 dipole iron core) of length 4000 mm each are connected to become a magnet unit of total length 16000 mm. The support design is for each module of 4000 mm. For Scheme 1, the supports are shown in Figure 5.9.21. To reduce cost, each module has four supports, including two main supports and two auxiliary supports. The main support has 6 DOFs, for support and adjustment. The auxiliary support has only a Y-axis DOF to avoid large deformations. Similarity, each support includes pedestal, adjusting mechanism and magnet support. The pedestal is made of a steel frame, and the adjusting mechanism and support are similar to that of the main supports in the Collider. The remaining challenge is how to hang, align and replace the 16-m long dipole magnet in the Booster.

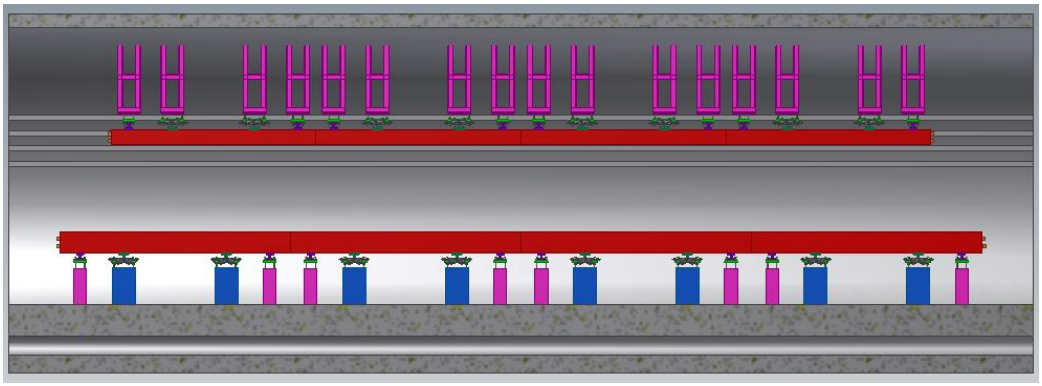

Figure 5.9.21: Longitudinal cross section of Scheme 1

5.10 Radiation Shielding

This section describes the radiation protection aspects of the CEPC-SPPC Project. It gives an account of the expected radiological situation and the provisions made to minimize the radiological consequences for those working on the project, or living in its vicinity. These precautions include adequate shielding where necessary and a state-of-the-art radiation monitoring and alarm system as well as a rigorous access control system to protect personnel.

5.10.1 **Introduction**

5.10.1.1 ***Workplace Classification***

For administrative convenience, radiation areas are classified as follows:

a) **Radiation monitored area**. Registered radiation workers can enter freely at any time. This includes facilities, halls and areas and surfaces outside concrete shielding;
b) **Radiation controlled area**. Access to this area is limited and permission and access procedures are required. An example is the auxiliary tunnel;
c) **Forbidden area**. Access to this area is forbidden. An example is the tunnel while the beam is on.

Occupancy factors for each area should be clearly defined after all the functional structures and modes of operation are defined.

5.10.1.2 ***Design Criteria***

Standards and rules for this project while designing the radiation protection system are as follows. Table 5.10.1 lists the dose limits from the national standards.

1. The national standard of the People's Republic of China, "Basic standards for protection against ionizing radiation and for the safety of radiation sources", GB 18871-2002.
2. The national standard of the People's Republic of China, "The rule for radiation protection of particle accelerators", GB 5172-1985.
3. ICRP publication 103 "The 2007 Recommendations of the International Commission on Radiological Protection".

Table 5.10.1: Dose limits in the national standards GB18871-2002.

Item		Worker	Public
Effective Dose	Average in 5 years	20 mSv/year	1 mSv/year
	Max. in a single year of the 5 year period	50 mSv/year	5 mSv/year
Equivalent Dose	Lens of the eye	150 mSv/year	15 mSv/year
	Skin	500 mSv/year	50 mSv/year

According to these standards, the maximum occupational exposure limit is 50 mSv per year. However, in applying the ALARA ("as low as reasonably achievable") philosophy, the goal is to maintain exposures well below this limit. The dose limits for shielding design are listed below:

1. Prompt dose rate limit for different areas are listed in Table 5.10.2.

Table 5.10.2: Prompt dose rate limits for different areas.

Area	Design Value	Example
Radiation monitored area	< 2.5 μSv/h	Outside the tunnels, where a worker can stay longer
Radiation controlled area	< 25 μSv/h	Outside the tunnels, where a worker can stay occasionally
Forbidden area	>>1 mSv/h	Inside the tunnels; worker cannot access during accelerator operation
Site boundary	0.08 mSv/year	

2. Residual dose rate limit for workers to enter the tunnel: < 1 mSv/h (30 cm, 4 h down) [1].
3. Dose limits for soil, ground water and air activation:
   Design criteria: The exempt value for activation is according to GB18871-2002: "if there is more than one kind of radionuclide, only if the ratio of activity (or specific activity) to its exempt value of each kind of the radionuclide was less than 1, it is exemptible." This is expressed as Formula (5.10.1).

$$\sum_{i=1}^{n} \frac{S_{i\_saturation}}{S_{i\_exempt}} < 1 \qquad (5.10.1)$$

   This is a convenient method to evaluate soil and ground water activation: The prompt dose rate is ~5.5 mSv/h in a thickness of 1 m of soil to ensure it is below the exempt value shown above.

5.10.2 **Radiation Sources and Radiation Shielding Design**

5.10.2.1 ***Interaction of High-Energy Electrons with Matter***

The particles of a high energy electron beam interact with matter via various processes such as beam-gas, beam-collimator, beam-target or beam-dump interactions. Electromagnetic cascades and nuclear reactions dominate and result in:

- The production of ionizing radiation fields (prompt, mixed radiation fields);
- The production of radioactive nuclei inside the target material (induced activity).

5.10.2.2 ***Radiation Sources***

In a high energy accelerator, there are two main radiation sources: the prompt and the residual radiation fields. Figure 5.10.1 depicts the radiation sources around an accelerator.

The so-called prompt, mixed radiation fields are mainly composed of neutrons and photons, and also some charged hadrons (protons, pions, kaons, etc.) and leptons (e.g. muons). The composition of the fields at a given point in or outside the tunnel strongly depends on its position with respect to the beam loss and the kind of shielding in between.

Radioactive isotopes are produced in the accelerator components and the accelerator tunnel structure during nuclear reactions between a high energy primary or secondary particle with the nucleus of target atoms. The radioactive ("unstable") isotopes decay, mainly by emitting betas and gammas, until they reach the "Valley of Stability". Since the half-lives of the radioactive isotopes range from fractions of seconds to years and more, radiation fields will always be present in the machine once it becomes operational and are the source of the remnant dose rates.

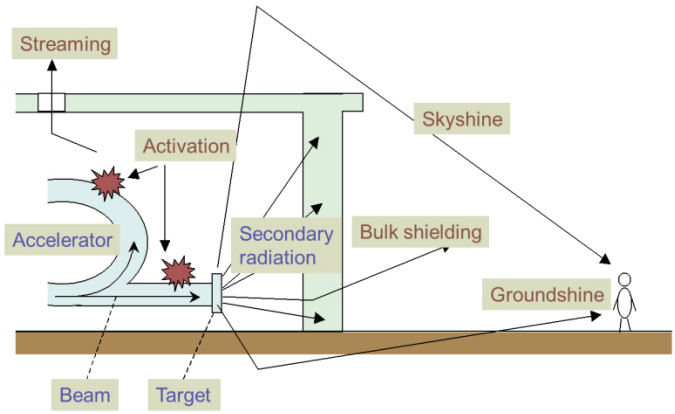

Figure 5.10.1: Sketch of the radiation sources around an accelerator.

5.10.2.3 ***Shielding Calculation Methods***

All the radiation shielding design will be based on Monte-Carlo (MC) simulations using the FLUKA and MCNP codes. After simulation, the results are checked by comparison with empirical formulas.

FLUKA is a general purpose tool for calculations of particle transport and interactions with matter. It covers an extended range of applications spanning proton

and electron accelerator shielding to target design, calorimetry, activation, dosimetry, detector design, accelerator driven systems, cosmic rays, neutrino physics, and radiotherapy.

MCNP (Monte Carlo N-Particle) is a general-purpose code that can be used for neutron, photon, electron, or coupled neutron/photon/electron transport. Specific areas of application include, but are not limited to, radiation protection and dosimetry, radiation shielding, radiography, medical physics, nuclear criticality safety, detector design and analysis, nuclear oil well logging, accelerator target design, fission and fusion reactor design, decontamination and decommissioning.

5.10.2.4 *Radiation Shielding Design*

The radiation shielding design philosophy adopted is that the shielding thickness of the main tunnel be determined by the radiation level caused by both the average beam loss along the tunnel, and at hot spots, such as the locations for collisions, injection, collimation and beam dump. The latter needs to have additional local shielding to reduce the radiation level to be the same as for the main tunnel.

Because nearly all the beam loss parameters in different locations are not specified, we use for the simulations the prompt and residual dose rate caused by an average 1 W/m beam loss and the beam energy of CEPC and SPPC. The radiation levels for other beam loss parameters can be calculated using appropriate conversion coefficients. With those results, shielding for additional hot spots can be designed.

Simulation results for the shielding thickness of the main tunnel are shown in Figure 5.10.2 with beam loss parameters of 1 W/m for 120 GeV electrons and 45 TeV protons. The material assumed is a 1 cm thick Fe beam pipe.

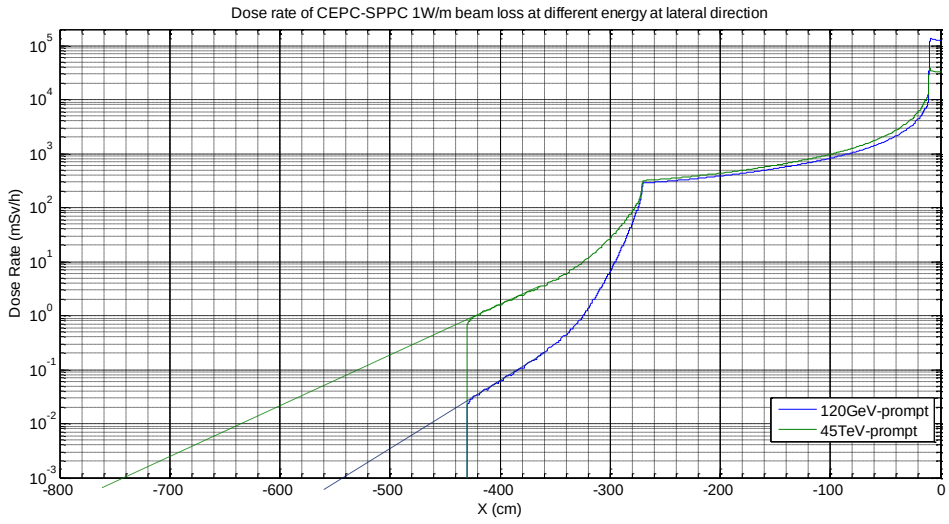

Figure 5.10.2: Distribution of the prompt radiation dose rate (270 cm~330 cm is concrete and outside 330 cm is soil).

Figure 5.10.3 shows the residual dose rate as a function of distance. From the figure, we see that after 100 days of continuous operation followed by a 4-hour shutdown, the residual dose rate satisfied the handbook maintenance condition [1].

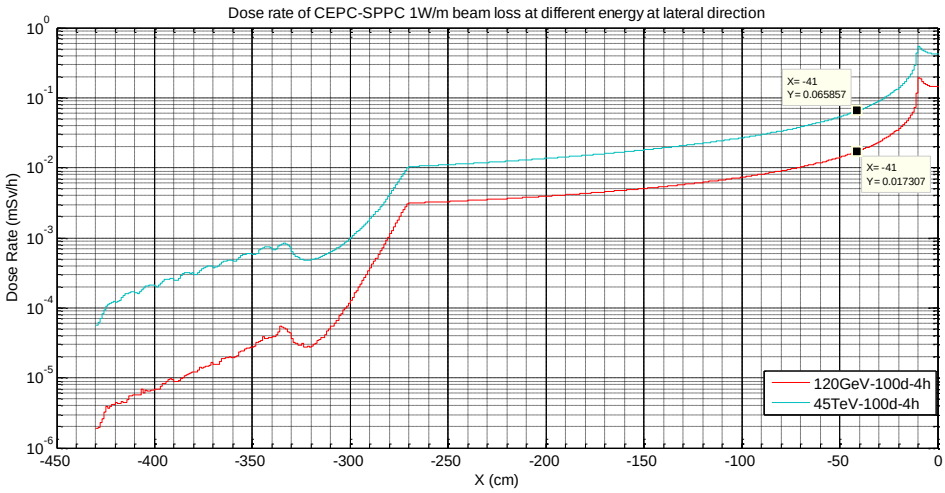

Figure 5.10.3: Distribution of the residual radiation dose rate (270 cm~330 cm is concrete and outside330 cm is soil).

5.10.3 **Induced Radioactivity**

5.10.3.1 ***Specific Activity and Calculation Methods***

The lost beam interacts with surrounding components and produces radionuclides. In addition, the air absorbs the secondary γ–rays and O_3 (ozone) and NO_X (nitrogen oxides) and other harmful gases will be generated.

The main activation yields in different places include:

- The concrete shielding: ^{24}Na
- Air activation:^{11}C ,^{13}N,^{15}O
- Cooling water activation: ^{11}C,^{13}N,^{15}O,^{7}Be,^{3}H
- Soil activation: ^{7}Be,^{3}H

Direct calculation of isotope production with FLUKA is used for the calculation of the specific activity induced by electron interactions in the beam line, shielding components and in the environment (air, rock, water, etc.).

Also the traditional method of folding particle fluence with energy-dependent cross sections for the production of certain isotopes can be used in some situations.

5.10.3.2 ***Estimation of the Amount of Nitrogen Oxides***

From γ rays, the oxygen in the air is decomposed into free radicals. Free radicals of oxygen combine with O_2 to form O_3. O_3 combines with NO in the air to form NOx, NO_2 combines with H_2O in the air to form HNO_3. (nitric acid) In this process, the production (defined as the number of molecules produced per absorption of 100 eV energy of the γ ray) of O_3, NO_X, HNO3 is 10, 4.8, 1.5 respectively. For simplicity, we only calculate the amount of O_3. The amount of NO_X can be obtained using the proportions above.

The methods and results of the calculation are as follows:

In an irradiation space of volume V, chemical decomposition and ventilation for the removal of ozone are calculated. If the disposition from chemical decomposition of ozone is not considered conservatively, then the number of ozone molecules, N, is obtained with the following equation:

$$\frac{dN}{dt} = PG - \left(\alpha' + \frac{KF}{V}\right)N \qquad (5.10.2)$$

Solving this equation, gives the following:

$$\mathrm{N} = \frac{\mathrm{PG}}{\alpha' + \frac{\mathrm{KF}}{\mathrm{V}}}\left[1 - \mathrm{e}^{-(\alpha' + \frac{\mathrm{KF}}{\mathrm{V}})\mathrm{t}}\right] \qquad (5.10.3)$$

In this formula:

P – the power absorbed by the air in eV/s;

G – the production of O_3, usually the G value is between 0.03 to 0.09 molecules per eV; G = 0.06 molecules per eV is used in the calculation;

F – the ventilation rate of the irradiated area in cm^3/s;

V – the volume of the irradiated area in cm^3;

K – the mixing uniformity coefficient, K=1/3;

α' – chemical decay constant of O3, chemical half-life of O3 is about 50;

t – the irradiation time in seconds.

One ppm O_3 concentration in the air is equivalent to 2.463×10^{13} O_3 molecules in 1 cm^3 of air. The formula uses ppm to represent O_3 concentration in the irradiation volume:

$$\mathrm{C_p} = \frac{\mathrm{N}}{2.463 \times 10^{13}\mathrm{V}} \qquad (5.10.4)$$

It is easy to deduce the power absorbed by the air with the following formula:

$$\mathrm{P} = 6.25 \times 10^{18} \sum_{\mathrm{i}} \left[\mathrm{E_{\gamma i}}\Psi_{\gamma \mathrm{i}}(\mathrm{K}/\Phi)_{\mathrm{i}}\right]\rho_{\mathrm{air}}\mathrm{V_{air}} \qquad (5.10.5)$$

In this formula:

$E_{\gamma i}$ – energy interval of γ ray, eV;

$\Psi_{\gamma i}$ – average flux in energy interval of γ ray, $cm^{-2}s^{-1}eV^{-1}$

$(K/\Phi)_I$ – the conversion coefficients from mono-energetic photon flux to air kerma, Gy•cm^2

ρ_{air} – air density in standard condition, kg/m^3

V_{air} – the volume of air, m^3

6.25×10^{18} – conversion coefficient from Joules to electron volts, eV/J

The physical meaning of $E_{\gamma i}\Psi_{\gamma i}$ is the fluence rate of specific energy photons. The physical meaning of $\rho_{air}V_{air}$ is the mass of air. $E_{\gamma i}$ and $\Psi_{\gamma i}$ could be simulated by Monte-Carlo, $(K/\Phi)_i$ could be referred and interpolated from the ICRU74 or ICRP74 reports.

Hence, the O_3 concentration is given by:

$$C_p = \frac{PG}{2.463 \times 10^{13} V(\alpha' + \frac{KF}{V})}\left[1 - e^{-(\alpha' + \frac{KF}{V})t}\right] \qquad (5.10.6)$$

The density of O_3 is 1.964×10^{-3} g/cm^3, so the concentration of O_3 in the air in g/cm^3 is given by:

$$C_g(t) = 7.97 \times 10^{-17} \frac{PG}{V(\alpha' + \frac{KF}{V})}\left[1 - e^{-(\alpha' + \frac{KF}{V})t}\right] \qquad (5.10.7)$$

Because the chemical half-life of O_3 is only 50 minutes, the concentration of O_3 in the tunnel could become easily saturated. The saturated concentration is Cg (g/cm^3) and calculated with Formula (5.10.8):

$$C_g(t) = 7.97 \times 10^{-17} \frac{PG}{V(\alpha' + \frac{KF}{V})} \qquad (5.10.8)$$

5.10.4 **Personnel Safety Interlock System (PSIS)**

5.10.4.1 ***System Design Criteria***

The PSIS is designed following these criteria:

1. Hardware is the most reliable component in the system so all critical device interlock signals are given by hardware.
2. At the highest interlock level the PSIS has top priority to shut off the beam in the Central Control System.
3. **Fail safe:** the beam will be shut off when a critical device in the PSIS breaks down.
4. **Redundancy:** redundancy is used in the design to ensure reliability, reduce fault time and to preserve upgrade possibilities.
5. **Multilayer protection:** interlock key, emergency shut-off button, emergency door-open button, acousto-optic alarm, search and secure (patrol) before beam start-up, camera, etc., will ensure multiple layers of personnel safety.
6. **People oriented:** the primary purpose of PSIS is personnel safety, but in addition it should be convenient to operate and maintain with a good human-computer interface.

5.10.4.2 ***PSIS Design***

The PSIS consists of a Programmable Logic Controller (PLC) system and Access Control System (ACS), PLC monitor interlocking equipment, and ACS administrative interlocking information. The access conditions for the interlock areas stipulate that the names and identification numbers of all persons who enter must be known/shown and recorded. Figure 5.10.4 shows the layout of the PSIS.

The PLC system consists of the access controller, interlock key, emergency/patrol button，emergency door open button, acousto-optic alarm and interlock equipment. Multilayer personnel protection is guaranteed by interlock signals from this equipment. Meanwhile, host double backup and double lines for signal transmission will guarantee reliability.

The ACS includes a camera, LED display, data server, etc. So in this way the PSIS can monitor the interlock areas, and display and store the interlock information.

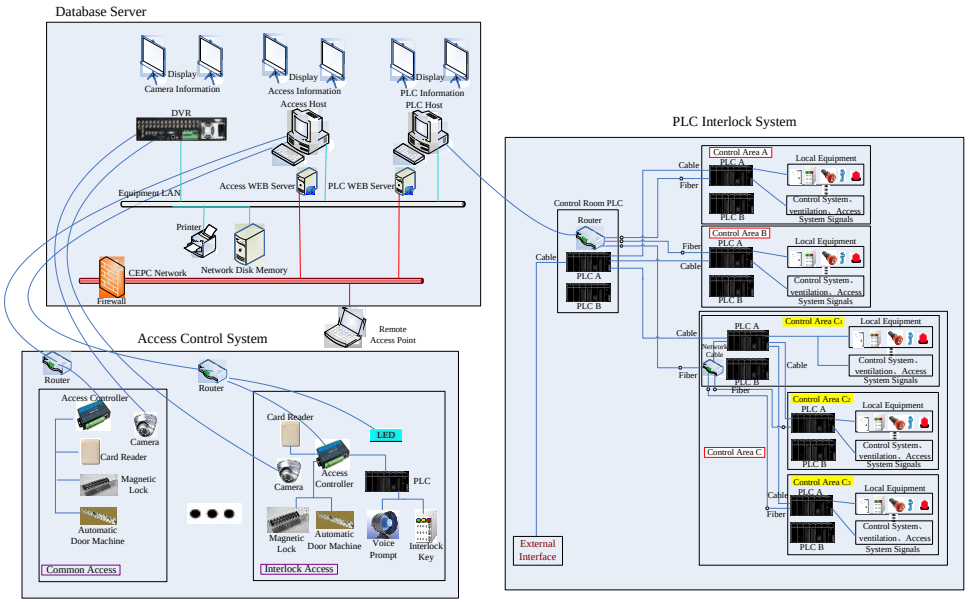

Figure 5.10.4: Layout of the PSIS.

A patrol (search and secure) must be done without fail in every interlock area before CEPC startup to make sure that no person is left in that area. An acousto-optic alarm will signal startup from the “ready” signal from Central Control System (CCS) and warn anyone in the area to leave immediately and rapidly. The access control system will still be working in a “shutdown” phase. The beam will be shut off immediately by an emergency button in case of accident. Figure 5.10.5 shows the operation flow chart of the PSIS.

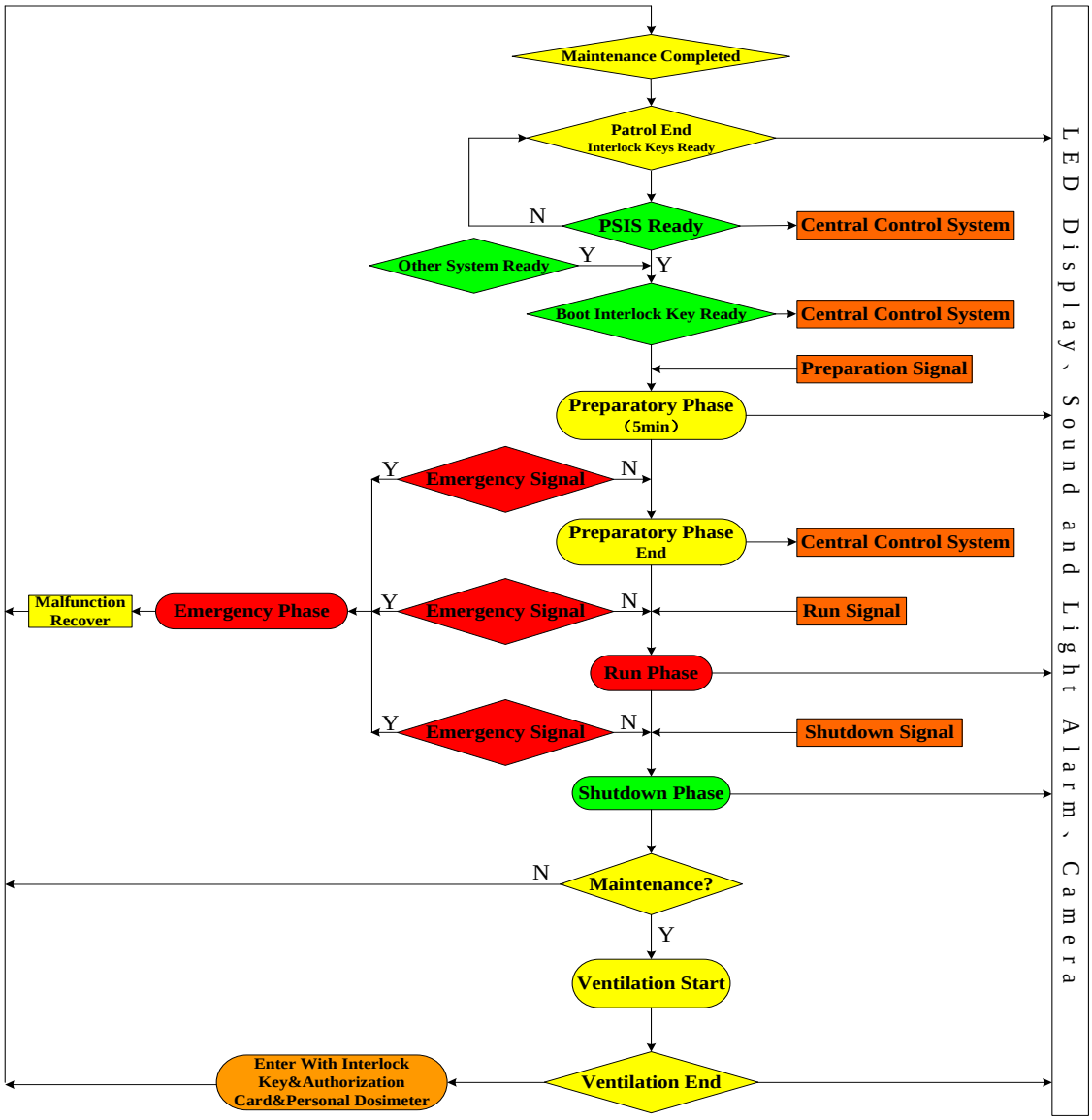

Figure 5.10.5: Operation flow chart of the PSIS.

5.10.5 **Radiation Dose Monitoring Program**

5.10.5.1 ***Radiation Monitoring System***

The radiation monitoring system for the workplace/environment safety of the project will be a new, state of the art system. It will take into account the latest legal requirements, international standards, the results of a preliminary hazard analysis, the latest technical developments and in particular the specific requirements such as the operation phase time structure or special composition of the radiation fields.

PSIS will provide continuous measurements of the ambient dose equivalent and the ambient dose rate equivalent in the underground areas together with the surface areas inside and outside the project perimeter. If preset radiation levels are exceeded within radiation controlled areas, an alarm will be triggered and transmitted. Remote alarms will also sound in the control rooms. PSIS will permanently monitor the level of radioactivity in water and air released from the facility installations. For radiation

protection purposes it will also include hand-foot monitors, site gate monitors, monitors of tools and materials that have been in radiation areas.

The radiation monitoring system provides remote supervision, long term database storage and off-line data analysis. A typical frame diagram is given in Figure 5.10.6. As others might be interested in the data, the system is open and the data will be accessible for clients via the WEB.

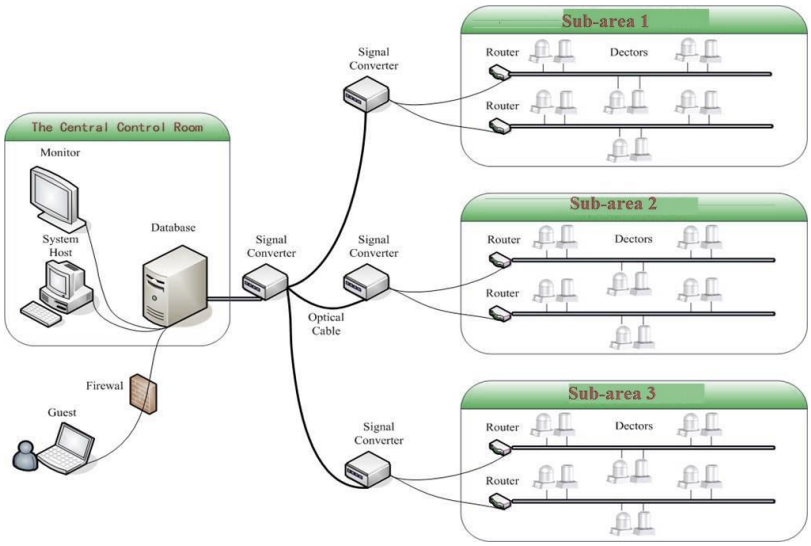

Figure 5.10.6: Frame diagram of the radiation monitoring system.

To achieve control and data communication in different conditions, the communication system contains 4 communicating paths: Ethernet network, wireless sets, GPRS sets and offline records.

5.10.5.2 *Workplace Monitoring Program*

The workplace monitoring program is built to guarantee that the radiation level of the workplace complies with relevant regulations, through establishing monitoring sites at all the main entrances to high radiation level areas and in the workplaces near the accelerator or radioactive sources. Once a radiation level exceeds the set critical value, monitors would sound the alarm to inform people to evacuate. Each site has one gamma detector and one neutron detector.

5.10.5.3 *Environmental Monitoring Program*

The objective of the environmental monitoring program is to prove that the facility complies with the regulatory limits in force and to provide early warning if violation of these limits is imminent. The program includes: monitoring and measurements of dose rate levels in the environment, monitoring of radioactivity in released fluids (air, water), monitoring and measurement of activity densities in various environmental matrices (plants, soil), environment radiation background survey. Among them, in order to evaluate the impact on the environment and establish a base line, a radiation background survey should begin 2 or 3 years before the equipment is constructed, and continue 3-5 years after the formal operation begins.

The dose rate and doses in the environment will be monitored and measured with environmental radiation monitoring stations, located at critical or representative places.

Each station will consist of a pressurized ionization chamber for gamma monitoring and a rem-counter for neutrons. These work on-line and generate alarms when dose-rate thresholds are exceeded.

Each fluid or gas extraction duct likely to contain radioactivity produced in the facility will be equipped with a monitoring station. Each station consists of an on-line real-time monitor for short-lived radioactive substances together with a sampler. Whilst the readings of the monitor will be stored in a database, the filters will be replaced periodically and analyzed in an off-line laboratory for longer-lived beta and gamma activity. The measurements will be carried out especially after upgrades to the facility.

5.10.5.4 *Personnel Dose Monitoring Program*

All staff will participate in the personal dose monitoring program. OSL (Optically Stimulated Luminescence) was chosen for γ cumulative dose monitoring, and the CR-39 solid track dosimeter was chosen for neutron cumulative dose monitoring.

An electronic personal dose alarm should be used by persons entering the tunnel for maintenance.

5.10.6 **Management of Radioactive Components**

Radioactive accelerator components as well as radioactive items from general services will be a byproduct of the operation of the accelerators. As a result of the interaction of particle beams with matter, various nuclear processes will occur and as a consequence, parts of the accelerator structure and its surroundings will become radioactive. The specific activity of the radioactive components depends on the material composition, the location of the material with respect to beam losses, the irradiation history and on the elapsed decay time. All the radioactive components no longer in use should be initially transferred to temporary storage and then sent to long-term repositories or disposed of according to legal requirements.

5.10.7 **References**

1. CSNS radiation shielding design report (the 4th draft).
2. The national standard of the People's Republic of China, Basic standards for protection against ionizing radiation and for the safety of radiation source", GB 18871 2002.

5.11 Survey and Alignment

5.11.1 **CEPC Alignment Control Network Design**

The CEPC alignment control network is designed following the layout of the site complex and requirements for locating and adjusting the accelerator components. It can also be used to monitor the deformation of the accelerator alignment in time.

CEPC consists of a Linac about 500 m in length, a Linac to storage ring beam transport line (BT) about 230 m in length and a Collider (sometimes termed SR in this section) about 54 km in circumference. The Booster is between the Linac and the Collider. Fig. 5.11.1 is the layout of CEPC.

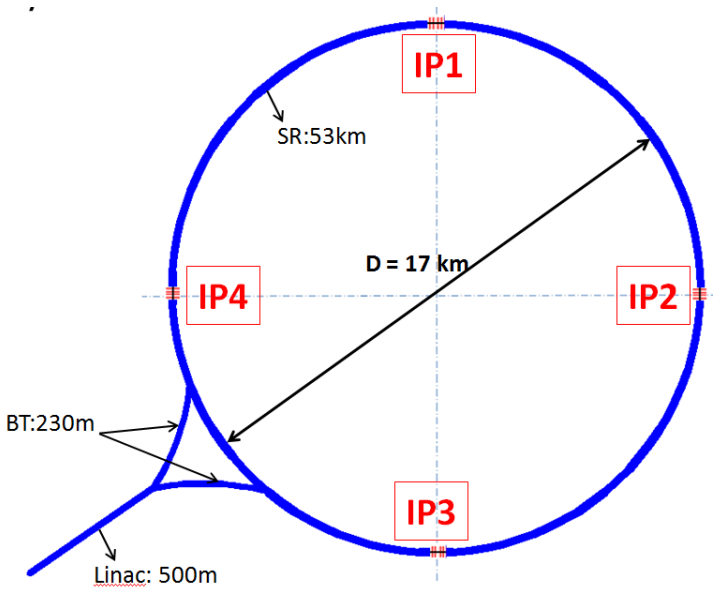

Figure 5.11.1: Layout of CEPC.

The alignment control network consists of a surface control network and a tunnel control network. The tunnel control network further consists of a backbone control network and a densification control network. This densification control network is divided into a Linac-BT control network and a SR control network. Fig. 5.11.2 shows this alignment control network structure.

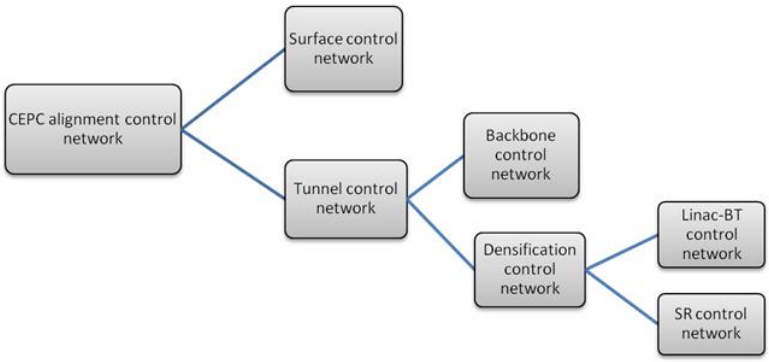

Figure 5.11.2: CEPC alignment control network structure.

5.11.1.1 *Surface Control Network*

The surface control network is used to control the location of buildings and components and to provide high precision reference data for the tunnel networks. It is comprised of 15 monuments located in the tunnel and based on bed rock, with 2 of them located in the Linac enclosure, 13 of them located in the Collider enclosure.

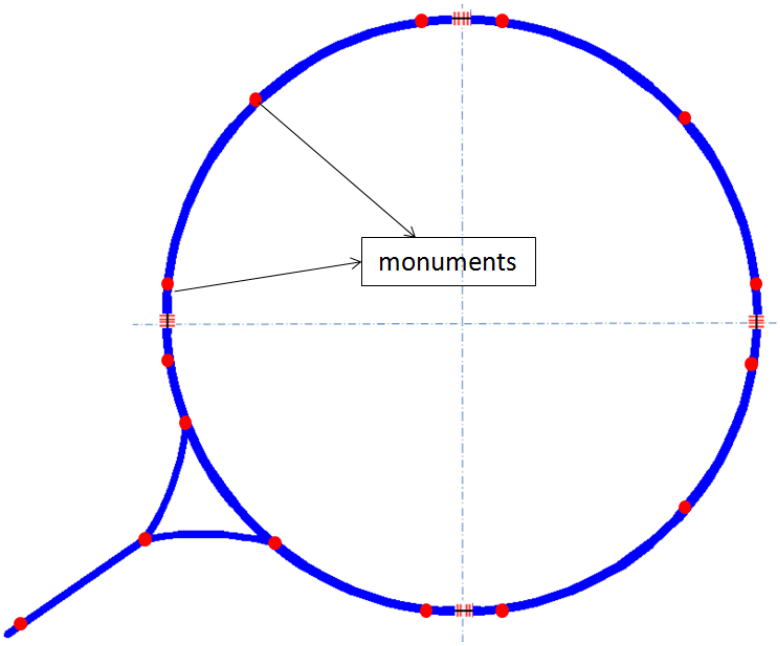

Figure 5.11.3: Surface control network.

These 15 monuments not only belong to the surface control network, but also are the monuments of the tunnel control network, and therefore connect the two networks. There are intervisible holes above these monuments, through which we can measure the monuments from the ground.

We use the GPS to carry out the surface control network survey. The 15 monuments will be projected onto the ground by using the wildNL. The GPS receivers will be stationed on the ground and centered on the local projective monument. The GPS are used to measure the distances between these projective monuments and the GPS observations will be processed by using the Trimble Total Control software. After the software processing we will obtain the position relationship between these projective monuments. The height difference between the monument and its projective monument can be measured by the laser tracker. Using the projective monumentpositions and the height differences we can calculate the coordinates of all the monuments in the surface control network.

5.11.1.2 *Tunnel Control Network*

The tunnel control network consists of a backbone control network and a densification control network. Considering the capability of measurement instruments and the precision requirement of the survey network, we plan to set the control point sections along the tunnel at intervals of 300 m for the backbone control network and 6 m for the densification control network.

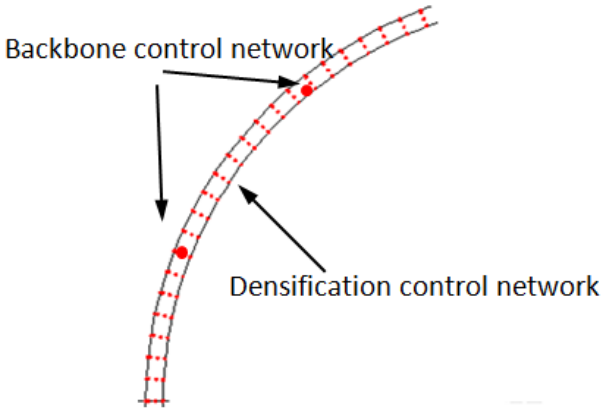

Figure 5.11.4: Backbone control network and densification control network.

As shown in Fig. 5.11.5 in each section, there are four monuments, two on the floor, one on the outer wall and one on the ceiling.

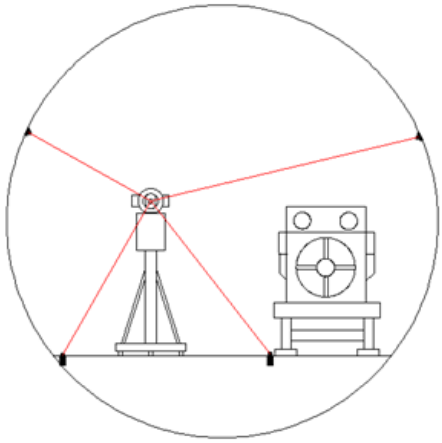

Figure 5.11.5: Monuments layout in a section.

There are 183 backbone control point sections along the Linac, the BT and the SR tunnel. We plan to carry out the transverse survey for the backbone control network by the free station method. The apparatus station is set between every two neighboring backbone sections and measures the points in these two sections.

There are 8994 densification control point sections along the Linac tunnel, the BT tunnel and the SR tunnel .We use laser trackers to carry out the horizontal and network surves together by free station method. The apparatus station is set between every two neighboring sections. At each station the laser tracker should measure 30 points. The number of common control points between neighboring stations is 25.

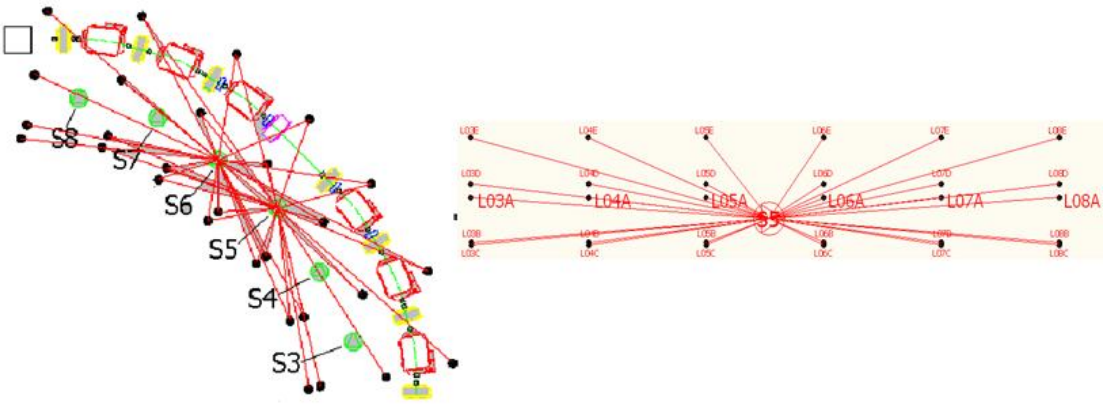

Figure 5.11.6: Densification control network survey

In order to obtain the horizontal and vertical coordinates at each station we need to establish a horizontal frame for the laser tracker.

We plan to use a Leica digital level to carry out the level network survey along the tunnel. In each section there are four control points; we only measure the points on the floor.

5.11.1.3 *CEPC Global Coordinate System*

The origin is located in the storage ring center, the Y points to the IP1, the X is perpendicular to the Y and points to the IP2, and the Z is perpendicular to the origin level plane and points up.

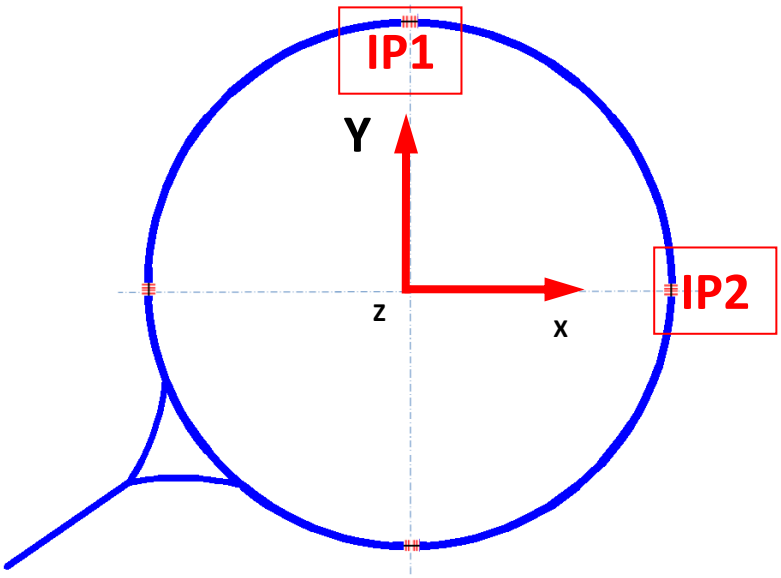

Figure 5.11.7: CEPC global coordinate system

After the control network survey and the data processing we can obtain all the control point coordinates in the global coordinate system. Using these control points as references we can do alignment for all the accelerator components.

5.11.2 **Component Fiducialization**

We mainly use a laser tracker to carry out the component fiducialization. Other instruments such as measuring arms, levels, transit squares, all kinds of fiducial apparatus and work tools are also necessary. As an example for the dipole, through measuring the fiducial planes and fiducial points of the magnet, we can establish a coordinate frame for the magnet. In this frame we can obtain the position relationship between the fiducial points and the center line of the magnet. The errors in the components' fiducialization in X, Y, Z directions are about 0.04-0.10 mm.

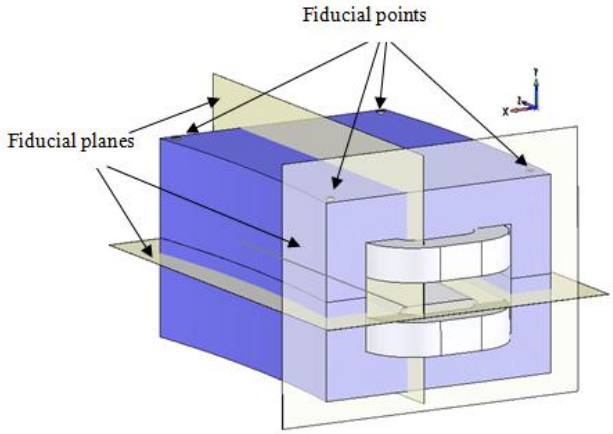

Figure 5.11.8: Dipole fiducialization.

After the fiducialization we can calculate their nominal coordinates in the global coordinate system.

5.11.3 **Alignment Scheme for Accelerator Components in the Tunnel**

We can choose one of the two surfaces as the alignment datum plane for all the accelerator components in the tunnel. One is the horizontal plane of the ring center. If the accelerator components are installed based on it, there will be a roll angle 'a' with each instrument station horizontal plane; a≈4.6″. The other surface is the Earth spherop. If the accelerator components are installed based on it, there will has a roll angle 'a' with the storage ring center horizontal plane; a≈4.6″.

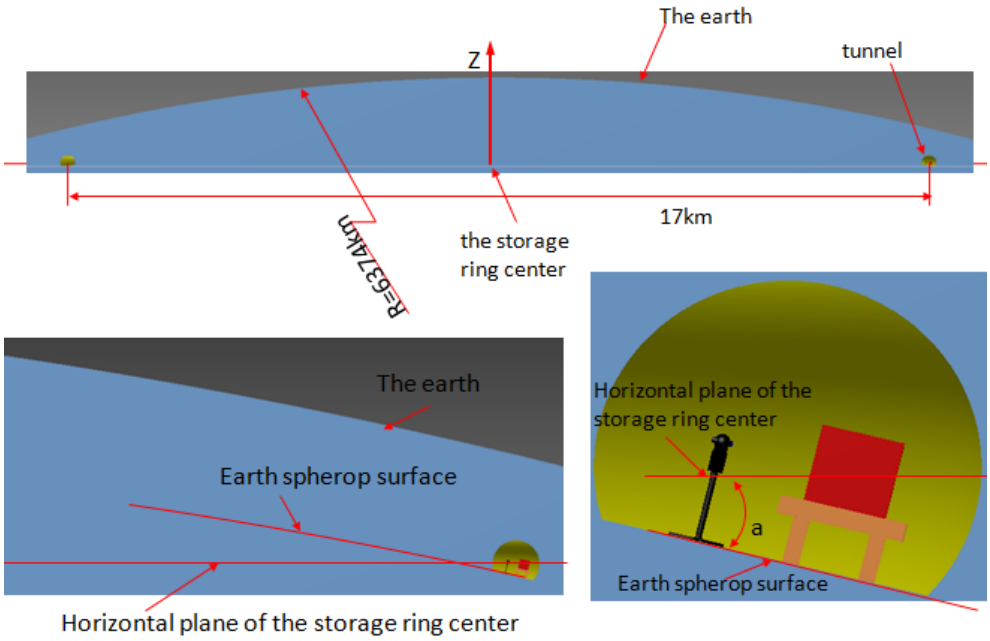

Figure 5.11.9: Two alignment datum planes.

We use the tunnel control network and laser trackers to align accelerator components in the tunnel. We set a laser tracker station near the component to be aligned and measure the points in the control network. Through best fit we can determine the position of the laser tracker relative to the control network. Using the laser tracker to measure the fiducial points located on the component, we can obtain the position of the component relative to the network and adjust the offset of the component to the required tolerance.

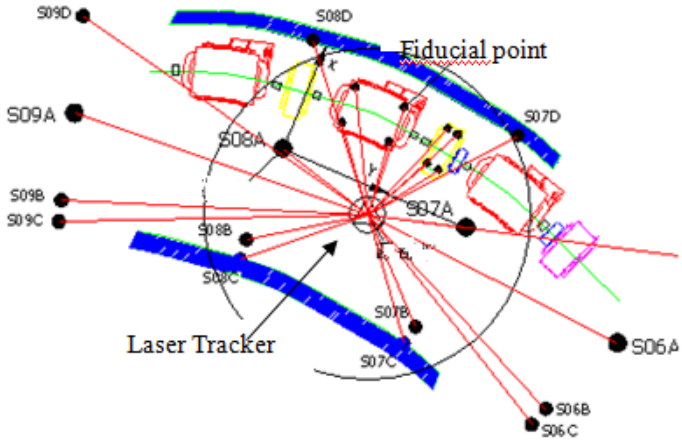

Figure 5.11.10: Component alignment in the tunnel.

The required component alignment tolerances are still being researched.

5.11.3.1 *Alignment in the Interaction Region*

Many components are located in the interaction region and the alignment work there is very difficult. The detector is too big to achieve the intervisiblity between the two

sides. Using laser trackers is the most convenient method but an auxiliary tunnel which connects both sides will be needed.

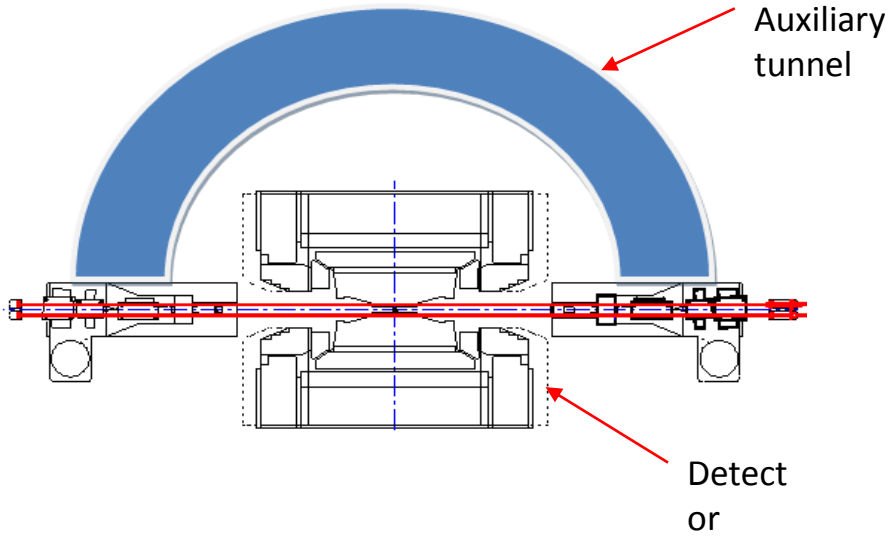

Figure 5.11.11: Auxiliary tunnel in the interaction region.

Alignment in the interaction region will be much more demanding than in the ARCs due to the extremely low values for the β-functions there. We plan to use laser trackers to do a rough alignment first, then use a laser collimator system to carry out a high-precision refined alignment.

Indoor GPS can be another efficient method for the interaction region alignment especially after all the components are installed and the laser collimator system is not suitable to use.

Nikon's iSpace is a kind of indoor GPS used for large volume metrology, tracking and positioning. The accuracy of an iSpace system can reach 0.05 mm. This accuracy is uniform across the entire measurement volume, regardless of the size of the metrology enabled area. It has inherent robustness, can carry out continuous monitoring including on-line compensation in the case of transmitter displacement and drift. It guarantees optimum system performance without user intervention. The standard setup includes 8 transmitters and with additional transmitters can achieve even better accuracy.

The iSpace is more convenient for the interaction region alignment and achieves better accuracy than using laser trackers. We will install the transmitters on the ceiling of the tunnel. Then we can survey the detector and the IP components directly on both sides.

5.11.3.2 *Time and Frequency of Survey and Alignment*

We plan to utilize the machine shutdown periods to carry out complete surveys, probably every three years. We would organize 10 teams, each able to measure 8 stations per day, and thus complete a complete survey in 70 days.

We can install a hydrostatic levelling system (HLS) along the tunnel to monitor foundation settlement. Then subsequently in every year we can only survey those areas where there is uneven settlement that exceeds 1 mm in 100 m, and also areas where the beam is abnormal. This can greatly reduce the alignment burden

6 CEPC – Injectors

6.1 Linac and e^+/e^- sources

6.1.1 Main Linac Parameters

The first part of the injector is a normal conducting S-band Linac and provides electrons and positrons at an energy up to 6 GeV. There are a number of subsystems as shown in Figure 6.1.1.

- 150 kV-200 kV thermionic triode gun with a 50 Hz modulation at the gun grid and high-voltage deck for the baseline design
- 100 kV-150 kV photocathode dc gun with a super-lattice structure GaAs cathode as a component requiring further
- 142.8375 MHz sub-harmonic bunching cavity
- 571.35 MHz sub-harmonic bunching cavity
- 2856.75 MHz bunching cavity
- positron converter and capture section
- positron beam return transport line (200 MeV)
- a positron damping ring
- 2856.75 MHz traveling wave-accelerating structures operating in the 2π/3 mode and with a length of 3.05 m (135 tubes)
- 2856.75 MHz 65 MW klystrons and their modulators (35 sets)
- low-level RF controls
- magnets and power supplies
- vacuum system
- beam diagnostics

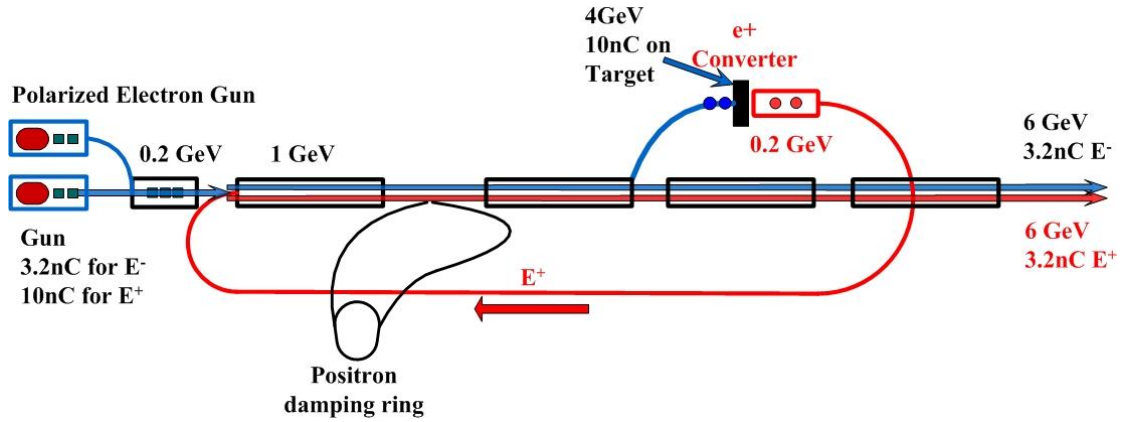

Figure 6.1.1: CEPC Linac

The main parameters of the Linac are listed in Table 6.1.1.

Table 6.1.1: Main Parameters of the CEPC Linac

Parameter	Symbol	Unit	Value
e^- beam energy	E_{e-}	GeV	6
e^+ beam energy	E_{e+}	GeV	6
Repetition rate	f_{rep}	Hz	50
e^- bunch population	N_{e-}		2×10^{10}
e^+ bunch population	N_{e+}		2×10^{10}
Energy spread (E^+/E^-)	σ_E		$<1\times10^{-3}$
Emittance (e^-)			0.3 mm· mrad
Emittance (e^+)			0.3 mm· mrad

6.1.2 **Electron Source**

The electron source consists of two electron guns: one is a thermionic gridded cathode driven by high voltage pulser for the baseline design, and the other is a polarized GaAs photoemitter excited by a laser which is an item for future R&D. After leaving one of these guns, the bunches pass through a "Y" bend and into two sub-harmonic bunching cavities operating at 142.8375 MHz and 571.35 MHz and an S-band buncher at 2856.75 MHz, as shown in Figure 6.1.2.

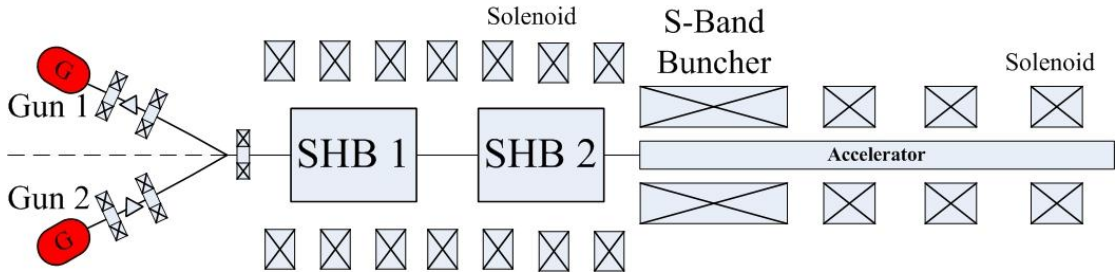

Figure 6.1.2: Linac electron source

The thermionic gun is a triode-type gun, consisting of an anode, a cathode, a grid, a high voltage power supply, a high voltage deck, a pulser and a control unit. The main parameters of the thermionic electron gun are shown in Table 6.1.2. In our design, the charge of electrons and positrons for injection is 3.2 nC. Two operation modes are required. One is to provide a 3.2 nC bunch charge for electron injection, and the other is to provide an 11 nC bunch charge as the primary electron beam for positron production. These different intensity electron beams for the two modes are generated from the cathode by changing grid bias and grid pulser voltages.

Table 6.1.2: The main parameters of the thermionic electron gun

Gun type	Thermionic Triode Gun		
Cathode	Y824 (Eimac) Dispenser		
Beam Current (max.)		A	15
High Voltage of Anode		kV	150-200
Bias Voltage of Grid		V	0 ~ -200
Pulse duration （FWHM）		ns	1.0
Repetition Rate		Hz	50
Electron operation	Bunch charge	nC	3.2
Positron operation	Bunch charge	nC	11nC

To achieve the maximum beam pulse current required for positron injection (11A, 11 nC/1.0 ns), a Barium-impregnated tungsten cathode will be used in the thermionic gun, as shown in Figure 6.1.3. A 200 kV (maximum) GLASSMAN high-voltage deck is used with a fast pulser cathode driver to extract the electron beam.

Figure 6.1.3: The cathode grid assembly

For a future development to have collisions between a polarized electron beam and an unpolarized positron beam, a photocathode DC-gun type electron source using a specially prepared GaAs/GaAsP superlattice can be added. This will enable the Linac to produce a high-intensity and low-emittance beam with high polarization. The proposed polarized electron beam routinely yields at least 85% polarization with a maximum QE of ~1%. The high voltage between cathode and anode is 100 - 150 kV.

6.1.3 **Bunching System**

After leaving the electron guns, the electron bunches go into the bunching system, which consists of the following components:

- The first sub-harmonic buncher operating at 142.8375 MHz (20th subharmonic)
- The second sub-harmonic buncher operating at 571.35 MHz (5th subharmonic)
- A constant-impedance travelling-wave S-band buncher operating in $2\pi/3$ mode at 2856 MHz.

The two sub-harmonic pre-bunchers and the one S-band buncher act to velocity modulate the non-relativistic electron beam emerging from the gun, and compress the pulse before it passes into the buncher. A beam pulse of 1.0 ns FWHM length from the gun is compressed into a single bunch of 10 ps (FWHM) by an RF bunching section with two sub-harmonic bunchers of 142.8375 MHz and 571.35 MHz and an S-band (2856.75 MHz) buncher cavity. The main parameters of the sub-harmonic pre-bunchers and S-band buncher are shown in Table 6.1.3.

Table 6.1.3: The main parameters of the sub-harmonic pre-buncher and S-band buncher

First sub-harmonic pre-buncher		
Type	Re-entrant	
Frequency	MHz	142.8375
Unloaded Q		8175
Shunt impedance	MΩ	1.4
$E_{surface,\ max}/E_{gap,\ max}$		2.53
Second sub-harmonic pre-buncher		
Frequency	MHz	571.35
Unloaded Q		13000
Shunt impedance	MΩ	3.7
$E_{surface,\ max}/E_{gap,\ max}$		2.44
S-Band Buncher		
Type	Constant impedance ,TW, 2π/3-mode	
Frequency	MHz	2856.75
Operating temperature	^{o}C	40±0.1
Input and output VSWR		≤1.2
Bandwidth (VSWR ≤ 1.2)	MHz	≥4.0
Peak RF input power	MW	3
Phase velocity (V_p/c)/group velocity (V_g/c)		0.75 / 0.0119
Shunt impedance	MΩ/m	36
Unloaded Q		11000
RF attenuation parameter	Neper/m	0.228
Number of cavities		4＋2×0.5

6.1.4 **Positron Source**

Positrons are generated using a multi-GeV electron beam impinging on a high-Z, high density target. The positron yield per incident electron is approximately proportional to the electron energy so that the positron current is proportional to the incident power of electron beam. To achieve a 3.2 nC per bunch positron beam, a 4 GeV primary electron beam with an intensity of 10 nC/bunch is required. The average beam power is 2 kW at a repetition rate of 50 Hz.

Figure 6.1.4 is a schematic of the positron source. The beam is extracted from the Linac, and passes through an extraction transport line, and strikes a tungsten target. Emerging from the target is a wide spectrum of low energy electrons, positrons, and

photons. The large transverse emittance of the positron beam emerging from the target is transformed to match the capture section aperture with a pseudo-adiabatically changing solenoidal field consisting of a 6-T pulsed field from a flux concentrator superimposed on a DC solenoidal field.

Immediately following the target is a 1.5-m length high-gradient (designed for 40 MeV/m) constant-impedance S-Band (2856.75 MHz) RF-capture section with a large aperture. This section is powered with a dedicated klystron source. The high-gradient capture section is followed by three conventional SLAC 3-m constant-gradient accelerator sections which are powered by a common klystron to boost the energy of the captured positrons to 200 MeV. The capture section and the first 3-m structure uses a uniform solenoid for focusing. Downstream are two 3-m structures using focusing by large aperture quadrupoles. After the first 3-m structure, a momentum selection chicane consisting of four identical rectangular bending magnets and a collimator will be used to select positrons in the desired energy range.

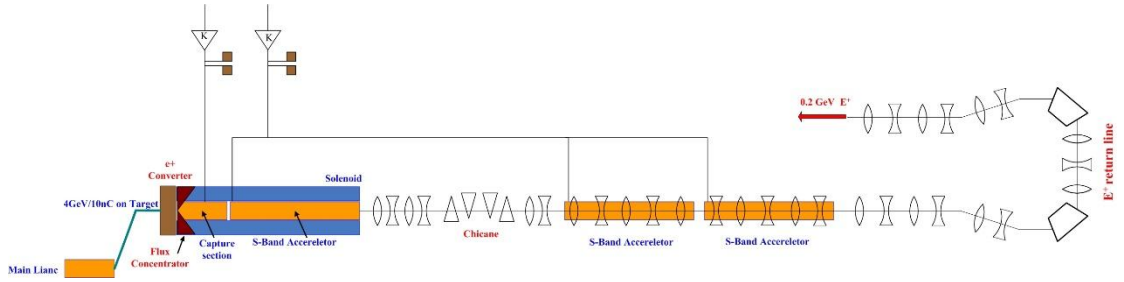

Figure 6.1.4: Positron source scheme.

The 200 MeV positrons are then transported back to the beginning of Linac through a quadrupole lattice and reinjected into the Linac where they are accelerated to 6 GeV. Table 6.1.4 shows the main parameters of positron source.

Table 6.1.4: The main parameters of the positron source

Positron source			
E^- beam energy on the target		GeV	4
E^- bunch charge on the target		nC	10
Target material		W	
Target thickness		mm	14
Focus device	Flux Concentrator		6 T
E^+ bunch charge after capture		nC	3.2
E^+ Energy after capture section		MeV	200

6.1.5 **Linac**

The 6 GeV Linac operates at 50 Hz, is approximately 500 m long and is powered by 35 klystrons. The accelerating gradient is about 20 MeV/m. A strong focusing lattice consisting of several tens of quadrupoles maintains the transverse beam size. A pair of x-y correction dipoles and a stripline beam position monitor are associated with each quadrupole for trajectory correction. High resolution profile monitors are located along the Linac. Monitors for the energy, energy spectrum, and emittance growth are placed

near the end of the Linac to allow either automatic or operator correction during operations.

The klystrons and their associated modulators are the key to acceleration. Each produces 65 MW at 2856.75 MHz. The power is then evenly divided among four 3-m constant gradient accelerating sections on a support girder. At 20 MeV/m, each klystron is thus capable of providing 250 MeV acceleration to each particle at a repetition rate of 50 Hz. The phase and amplitude of each klystron are monitored and adjusted using a new control system that maintains the phase and power tolerances at 0.1 degrees and 0.1% respectively.

Table 6.1.5: Accelerating structure parameters

Parameters		Unit
Operation frequency	2856.75	MHz
Operation temperature	40.0 ± 0.1	^{o}C
Number of cells	84 +2 coupler cells	
Section length	3048	mm
Phase advance per cell	2π/3 - mode	
Cell length	35.0012	mm
Disk thickness (t)	5.84	mm
Iris diameter (2a)	26.231～19.243	mm
Cell diameter (2b)	83.460～81.781	mm
Shunt impedance (r_0)	54.6～63.9	MΩ/m
Q factor	13990～13836	
Group velocity (v_g/c)	0.0208～0.0070	
Filling time	830	ns
Attenuation factor	0.57	Neper

S-Band SLAC type constant-gradient copper accelerating structures operating in 2π/3 mode at 2856 MHz will be used to accelerate the bunched electron and positron beams up to the final energy. The accelerating structure parameters are shown in Table 6.1.5. There are a total of 134 accelerating structures. The operation temperature is 40°C, which is maintained within 0.1˚ so that the phase shift along the entire length of an accelerator section is kept within 2˚.

6.2 Booster and Transport Lines

6.2.1 General Description

The Booster provides 120 GeV electron and positron beams to the CEPC collider for top-up injection at 0.1 Hz. The Booster is in the same tunnel as the collider, placed above the collider ring and has about same circumference. Bypasses are arranged to avoid the detectors at IP1 and IP3. Electron and positron beams are injected from the Linac through the LTB transfer line (Linac to Booster) into the Booster in one of the 850-m long straight sections. Beam extraction at maximum energy takes place in the other two straight sections. Electron and positron beams are injected to the collider through two BTC (Booster to Collider) transfer lines. Figure 6.2.1 illustrates the layout.

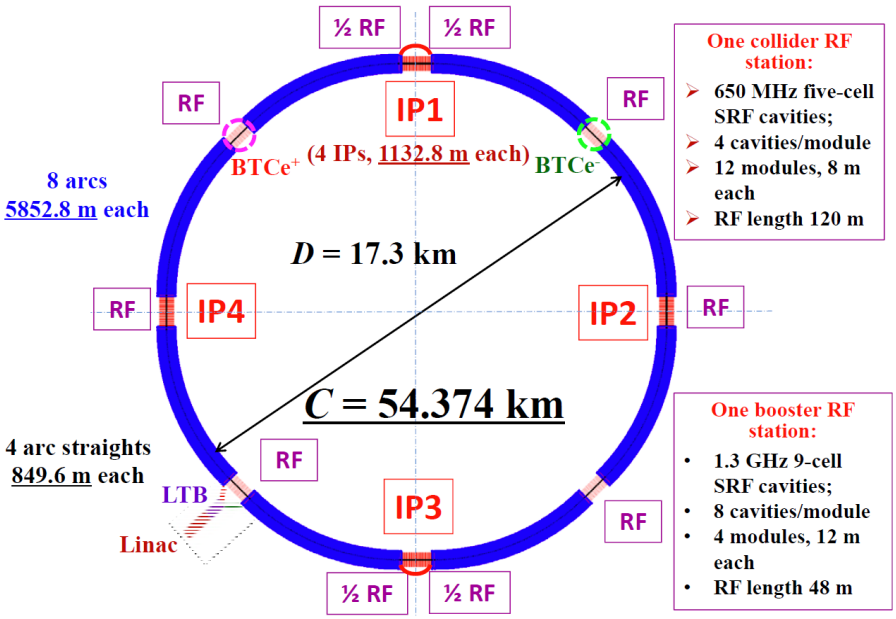

Figure 6.2.1: Layout of the CEPC Booster

As shown in Fig.6.2.1, the CEPC collider is designed with four interaction points, where IP1 and IP3 are for e+e- collisions, while the other two IP's are reserved for the future pp collider, SPPC. The collider circumference is 54.374 km, including 8 arcs of 5852.8 m, 4 arc straight sections of 849.6 m each and 4 interaction region straights of 1132.8 m each. The RF frequency of the Booster is 1.3 GHz, a factor of two higher than the collider. There are eight RF stations in the Booster, providing a total RF voltage of 5.12 GV. One RF station consists of 4 cryo-modules, 12 m long; each of them contains eight 9-cell super-conducting cavities. Table 6.2.1 lists the Booster parameters.

The bunch number in the Booster is the same as in the collider. The bunch population is based on the assumption of 5% current decay in the collider between two top-ups. The synchrotron radiation power density of 45 W/m at 120 GeV is much lower than in BEPCII of 415 W/m [1].

Because of the very low synchrotron radiation damping rate, a scheme of single bunch injection from Linac to Booster is adopted. In this scheme, electron and positron beams with bunch population of 2×10^{10} and emittance of 0.3 mm-mrad are injected onto the central orbit of the Booster. Overall transfer efficiency from the Linac to collider is assumed to be 90 %.

Table 6.2.1: Main Parameters of the CEPC Booster

Parameter		Symbol	Unit	Value
Injection energy		E_{inj}	GeV	6
Ejection energy		E_{ej}	GeV	120
Circumference		C	km	54.4
Revolution frequency		f_0	kHz	5.4755
Bending radius		ρ	km	6.519
Bending field	E = 6 GeV	B_{inj}	T	0.0614
	E = 120 GeV	B_{ej}		0.00307
SR loss/turn		U_0	GeV	2.814
Bunch number		k_b		50
Bunch population		N_e	10^{10}	2.0
Beam current		I_b	mA	0.87
RF frequency		f_{rf}	GHz	1.3
Total RF voltage		V_{rf}	GV	5.12
SR power @ 120GeV		P_{sr}	MW	2.46
SR power density @120GeV		p_{sr}	W/m	45

The Booster operates at 0.1 Hz as shown in Fig. 6.2.2. Beam injection from the Linac to Booster takes 1 second; the energy ramp takes 4 seconds, 1 second flat top is for beam extraction to the collider, and 4 seconds for the magnets to ramp down.

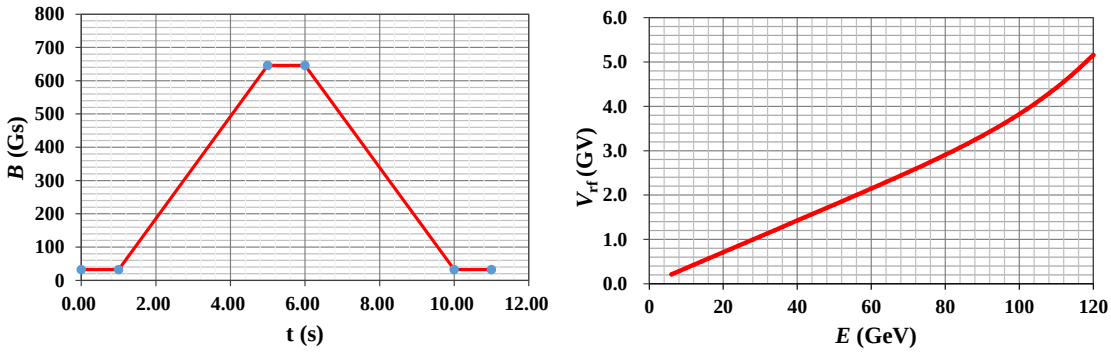

Figure 6.2.2: Magnetic cycle and RF voltage during the Booster ramp.

6.2.2 **Lattice**

6.2.2.1 ***Choice of Cell Length***

A separated function FODO-cell-based lattice is selected for the Booster for its flexibility. It is easy to achieve dispersion suppression by omitting bending magnets. Also this lattice choice is good for the bypass design.

Since the Booster is installed in the same tunnel as the collider, its ARC arrangement is similar. However, the length of the cells and other parameters can be optimized to

satisfy the required beam properties and to optimize cost. Lattice parameters for three different cell lengths are presented in Table 6.2.2.

Table 6.2.2: Lattice parameters scaling to the cell length

FODO cell Length L_c	Relation	47.2	71.7	94.4	m
Quadrupole strength	$\|k_Q l_Q\| \propto L_c^{-1}$	0.044	0.029	0.022	m^{-1}
Max. beta function in a cell	$\beta_{max} \propto L_c$	81.2	123.3	162.3	m
Max. dispersion in a cell	$D_x \propto L_c^2$	0.38	0.87	1.52	m
Betatron tune	$\nu_{x,y} \propto L_c^{-1}$	189.2	124.6	94.6	
Momentum compaction factor	$\alpha_p \propto L_c^2$	3.43	7.91	13.72	10^{-5}
Chromaticity	$\xi \propto L_c^{-1}$	86.4	56.9	43.2	
Sextupole strength SF/SD	$\|k_s l_s\| \propto L_c^{-3}$	0.15/0.24	0.043/0.07	0.019/0.03	m^{-2}
Natural emittance	$\varepsilon_{x0} \propto L_c^3$	6.8	23.8	54.4	nm
Synchrotron tune (V_{RF}=5GV)	$\nu_s \propto L_c$	0.204	0.31	0.41	
Max. betatron beam size *x/y*	$\sigma_\beta \propto L_c^2$	0.74/0.53	1.71/1.21	2.97/2.10	mm
Max. beam orbit spread	$\sigma_{xE} \propto L_c^2$	0.49	1.14	1.97	mm
Max. horizontal beam size	$\sigma_x \propto L_c^2$	0.89	2.06	3.57	mm
Bunch length (V_{RF}=5.12 GV)	$\sigma_z \propto L_c$	1.82	2.76	3.64	mm

As can be seem from Table 6.2.2 the longer the cell, the larger the beta functions, dispersion, emittance and beam size, and also the smaller the chromaticity, weaker sextuples, and, more importantly, the less cells and machine components. The Booster cell length is chosen as 71.7 m (about 1.5 times the collider cell length of 47.2 m) as the baseline design. The total number of FODO cells in the Booster is 764. The cell length will be further optimized in the conceptual design stage, taking into account both performance and cost. Having equal cell length to the collider remains a straightforward option for the Booster lattice.

6.2.2.2 *Lattice Functions*

The Booster lattice is based on FODO cells with length of 71.7 m. The structure of two types of super-periods in the booster is indicated in Fig. 6.2.3.

Arc straight	-DIS	78 FODO cells	DIS	IR straight

Arc straight	-DIS	78 FODO cells	DIS	Bypass

Figure 6.2.3: Two types of super-periods in the Booster.

There are 8 arcs in the Booster; each of them consists of 78 FODO cells and two dispersion suppressors (each contains one regular FODO cell and one straight section FODO cell). There are two quadrupoles of 1 m each, 8 dipoles of 8 m each, two sextupoles of 0.2 m each in a regular FODO cell of 71.7 m. Total length of an arc is

5846.6 m. There are 12 FODO cells in the arc straight section and 15 FODO cells in the IR straight section (for IR2 and IR4). In IR1 and IR3, two bypasses are designed to keep the beam clear of the detectors. The computer code MAD [2] is used for the optics design. The lattice functions in the Booster are shown in Fig. 6.2.4.

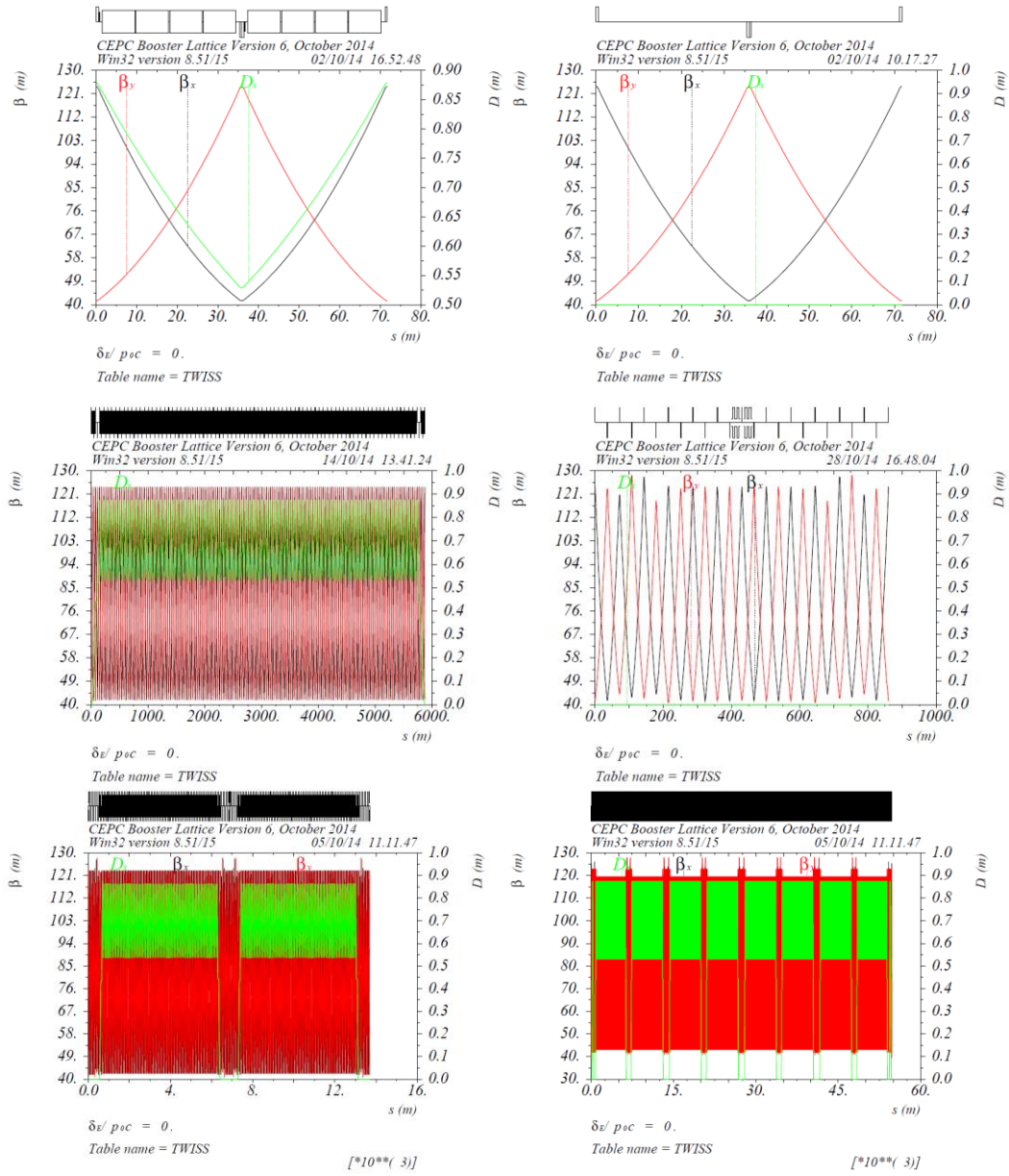

Figure 6.2.4: Booster lattice functions. Upper left: regular FODO cell; upper right: straight section FODO cell; middle left: arc; middle right: arc straight section; bottom left: super-period; bottom right: full ring.

6.2.2.3 *Bypasses*

Two bypasses re arranged to skirt the detectors at IP1 and IP3 of the collider. The structure of a half bypass is shown in Fig. 6.2.5.

-3*FODO -3*Lc	-DIS 2*Lc	BPI1 4f_1·Lc	-DIS 2*Lc	FODO 2*Lc	DIS 2*Lc	BPI2 1.5f_2·Lc

Figure 6.2.5: Structure of half bypass

Seen in Fig. 6.2.5 are the bypasses based on FODO cells. The bypass design removes 3 regular FODO cells in the arcs to the bypasses and keeps the straight sections BPI1 and BPI2 dispersion free. The advantage of this design is that no additional bending magnets are required. The length of a bypass is $L=2\times(6+4f_1+1.5f_2)\cdot L_c$ and the width of the bypass is $W=(9.5+9f_1)\cdot\theta_c L_c$. By changing f_1 and f_2, both length and width of the bypass can be adjusted to meet the Final Focusing System (FFS) length and detector width. In the present design, we take f_1=1.0 and f_2=1.0 making a bypass width of 13.0 m and total length of 2×820 m, and circumference about the same as the collider.

Lattice functions in long straights in IP2 and IP4 and half bypass in IP1 and IP3 are shown in Fig. 6.2.6.

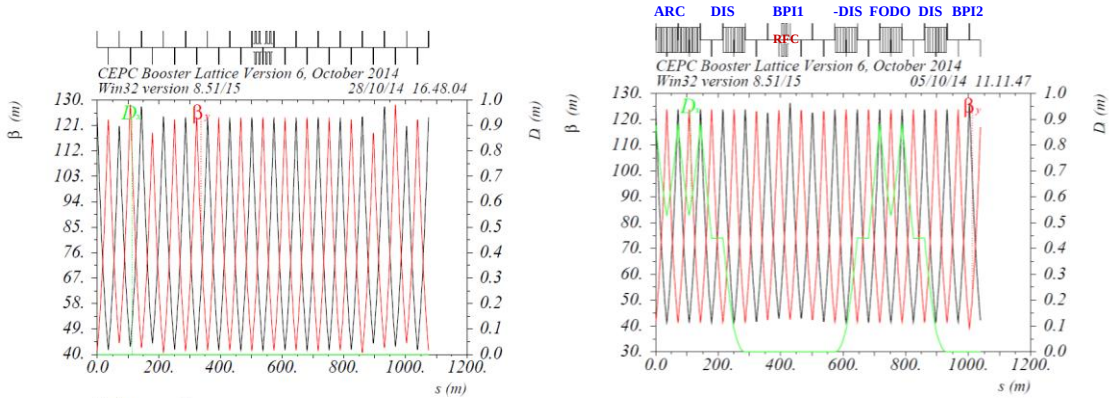

Fig. 6.2.6: Lattice functions in long straights in IP2 and IP4 and half bypass in IP1 and IP3

6.2.2.4 *Dynamic Aperture*

The dynamic aperture of the Booster is studied with the optics computing code SAD [3]. Two families of sextupoles, SF and SD, are near quadrupoles QF and QD in FODO cells and are used for chromaticity correction, $\xi_x = \xi_y = 0.5$. Figure 6.2.7 plots the dynamic aperture for particles of $\Delta p/p = 0, \pm1\%, \pm2\%$ obtained from tracking with 3 different damping times and assuming the transverse coupling $r = \varepsilon_y/\varepsilon_x = 0.01$.

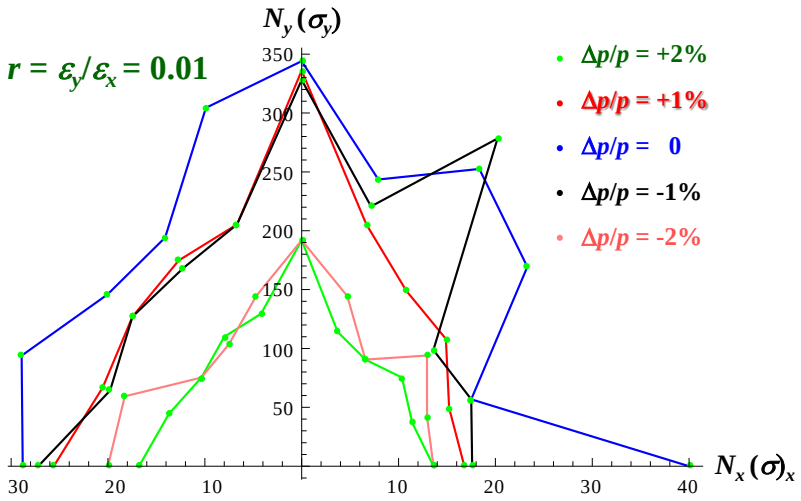

Figure 6.2.7: Dynamic aperture plots for on and off momentum particles

The Booster lattice-related parameters are summarized in Table 6.2.3.

Table 6.2.3: Booster lattice parameters

Parameter	Symbol	Unit	Value
FODO cell length	L_c	M	71.665
Total number of FODO cells	N_c		764
Phase advance in a cell (H/V)	μ_x/μ_y		60 °/60 °
Dipole length	L_B	M	8.0
Defection angle of dipole	θ_B	mrad	1.2272
Quadrupole length	L_Q	M	1.0
Quadupole strength (QF/QD)	k_Q		0.02817/-0.02817
Sextupole length	L_S	M	0.2
Sextupole strength (SF/SD)	k_S	m-3	0.2018/ -0.3338
Maximum β function (H/V)	β_{max}	M	123.84/122.97
Transverse betatron tune (H/V)	ν_x/ν_y		127.18/127.28
Maximum dispersion function	D_{max}	M	0.879
Length of bypass	L_{bp}	M	1640
Width of bypass	W_{bp}	M	13.0
Transverse beam emittance (H/V)	$\varepsilon_x/\varepsilon_y$	nm·rad	20.5/0.205
Transverse damping time @ E_{inj}/E_{ej}	τ_x/τ_y	Ms	124578/15.6
Longitudinal damping time	τ_s	Ms	62318/7.8
Momentum compaction factor	α_p	10^{-5}	7.69
Beam energy spread	σ_e	%	0.127
Synchrotron oscillation tune	ν_s		0.32076
Bunch length (V_{rf}=5.12 GV)	σ_z	Mm	2.66
Maximum beam size (H/V)	$(\sigma_x/\sigma_y)_{max}$	Mm	1.948/0.159

6.2.3 **Low Injection Energy and the Low Field Issue**

As seen in Table 6.2.1, the bending field of the CEPC booster is 614 G at 120 GeV. To reduce the cost of the Linac injector, the injection energy into the Booster is chosen as 6 GeV with an injection magnetic field of 30.7 G, about 1/7 of the injection field of LEP [4]. The issue: is the magnetic field stable enough at such a low field compared to the earth's field of 0.5-0.6 G and its variations? To mitigate the low field problem, an effort is made to increase the bending field at injection.

6.2.3.1 ***Low Field Stability Test***

The existing BEPC bending magnet and ADS power supply are used to test low magnetic field stability; the stability of the power supply is better than 1×10^{-4}. A Hall probe system with accuracy of 0.1G or $\Delta B/B$ of 3×10^{-3} is used in these field measurements. The setup is shown in Figure 6.2.8.

Figure 6.2.8: Magnetic field test setup

A test was performed by the IHEP magnet group [5]. The magnetic field outside and inside the magnet with zero excitation current was measured first. As shown in Figure 6.2.9, the earth's field (outside the magnet) is about 0.8 G , with B_x=0.55 G (south-to-north) ; B_y=0.45 G (vertical) and B_z=0.25G (east-west); while the field inside the magnet is dominated by its residual field.

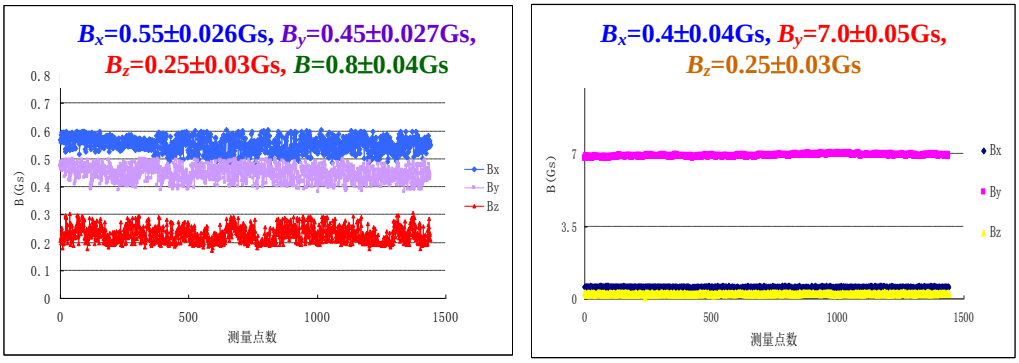

Figure 6.2.9: Measured field outside and inside of the magnet

The 24-hour magnetic field stability was measured for different excitation currents, the results are given in Figure 6.2.10.

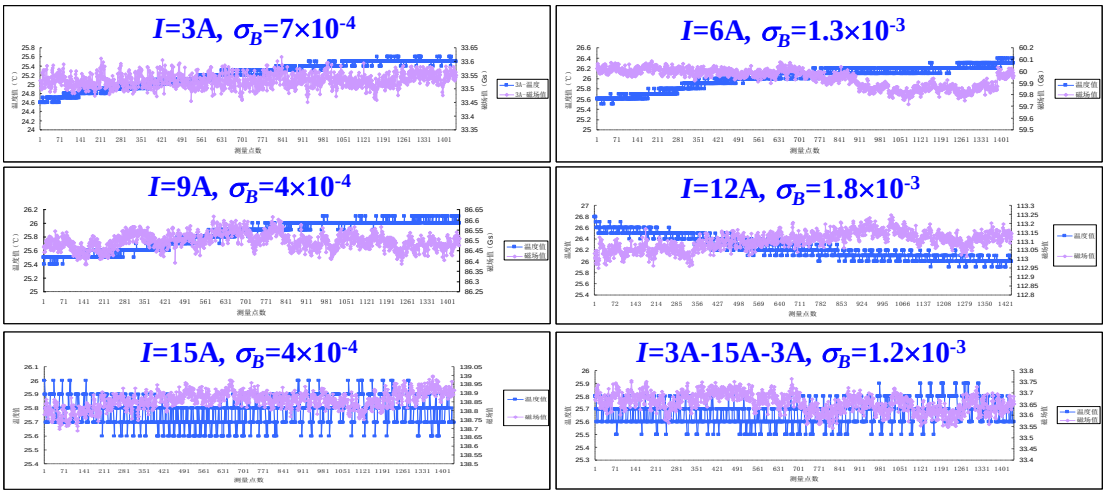

Figure 6.2.10: 24-hour magnetic field stability test for different excitation currents

The test shows that the magnetic field stability around 30 G is around 1×10^{-3}, which indicates the injected beam energy for the Booster of 6 GeV is feasible in view of magnetic field stability.

In the meantime, simulation studies of the earth's magnetic field effects on the beam behavior is being carried out and the tests of earth-field shielding by using this set-up is also planned.

6.2.3.2 *Wiggling Bend Scheme*

The idea of the wiggling bend scheme, shown in Figure 6.2.11, comes from combining higher field and lower field magnets whose bends partially cancel each other and together create the desired integrated field. Operating the magnets at higher currents makes for more stable operation. There are four bending magnets in a Booster half-cell. Two outside bends are excited by a bipolar power supply.

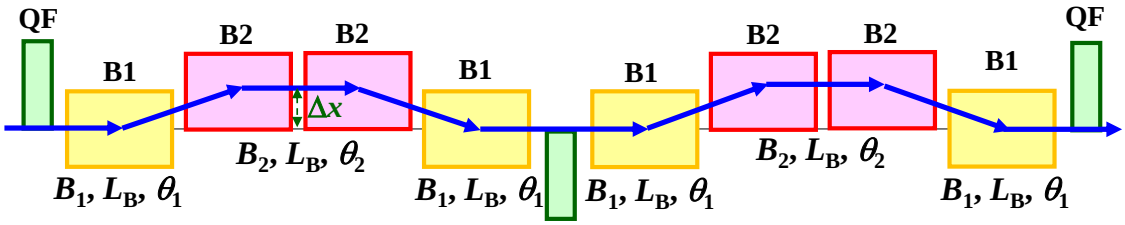

Figure 6.2.11: The wiggling bend scheme

The magnetic field of the bends is set during the ramp, keeping the total bending angle constant, i.e. $\theta_{B2}+\theta_{B1}=2\theta_B$. In principle, B_1 can be as low as $-0.9B_{ej}$ at injection for $B_2=B_{ej}$. However, then the orbit offset $\Delta x = \theta_1\times (L_B+L_D)$ may become too large. Here we take $B_1 = -0.1B_{ej}=60$ G, and $B_2=0.2\ B_{ej}$, i.e. double the field of the baseline design with $\Delta x = 20$ mm. Magnetic field and energy ramping curves are shown in Fig.6.2.12.

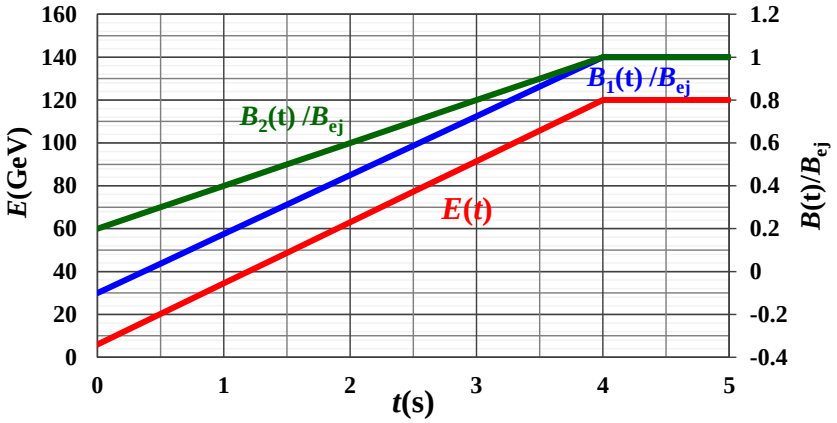

Figure 6.2.12: Magnetic field and energy ramping curves in wiggling bend scheme

6.2.3.3 *Instabilities*

The beam instability due to single bunch and multi-bunch effects are estimated at injection energy. The beam is expected to be more stable at high energy.

The low injection energy not only results in a low magnetic field, but also beam instability. The beam energy in the Booster at injection is 1/20 of that in the collider, while the beam intensity in the Booster is also 1/20 of the collider. However, beams may become unstable for there is almost no synchrotron radiation damping in the Booster.

According to preliminary studies, the single bunch instability is dominated by the transverse mode coupling instability (TMCI). Considering the impedance generated from the resistive wall and the RF cavities, we obtain the single bunch threshold current of 27 μA, shown in Fig. 6.2.13. This is higher than the design bunch current of 18 μA, but doesn't leave much margin.

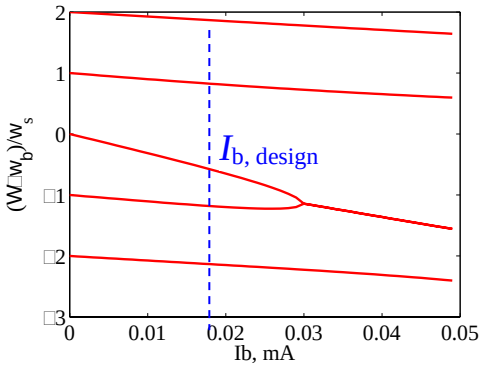

Fig 6.2.13: The transverse mode coupling instability

For TMCI, the transverse resistive wall instability has a growth time for the most dangerous mode of 34 ms in the vertical plane. The dependence of the instability growth rate on the oscillation mode number is shown in Fig.6.2.14. Since the growth rate is much shorter than the transverse radiation damping time, a transverse feedback system is needed to stabilize the beams.

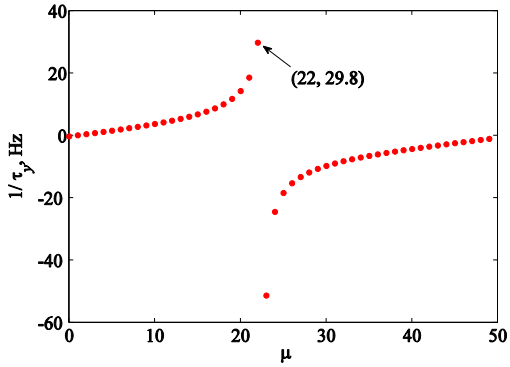

Fig 6.2.14: The instability growth rate vs. oscillation mode number.

Another important cause for exciting TMCI is the interaction of the beam with the higher order modes (HOM) of the accelerating cavities. Since there are 256 cavities in the ring, a frequency spread σ_f in the resonant frequency of the HOM's is considered in calculating the effect of the whole RF system. The growth rates of the HOM's are shown in Table 6.2.4. We see that the most dangerous longitudinal mode gives a growth rate of 472 ms. So a longitudinal feedback system is needed. The most dangerous transverse mode gives a growth rate of 22 ms. Since the growth rates are based on using a Gaussian random number generator, adequate safety margins should be taken when choosing the feedback systems.

Table 6.2.4: The parameters and growth rate of the first few HOM's

Monopole Mode	f (GHz)	R/Q (Ω)*	Q	σ_f (MHz)	τ (s)
TM011	2.450	156	58600	9	1.5
TM012	3.845	44	240000	1	0.5
Dipole Mode	f (GHz)	R/Q (Ω/m)**	Q		τ (ms)
TE111	1.739	4283	3400	5	218
TM110	1.874	2293	50200	1	44
TM111	2.577	4336	50000	1	22
TE121	3.087	196	43700	1	497

* $k_{\parallel}$ mode$= 2\pi f\ (R/Q)/4$ [V/pC]

** $k_{\perp}$ mode $= 2\pi f\ (R/Q)/4$ [V/(pC m)]

6.2.4 **Beam Transfer**

6 GeV electron and positron beams are injected into the Booster ring through the LTB transfer line, accelerated to 120 GeV, and then extracted and transported to the collider through the BTC transfer line.

6.2.4.1 *Beam Transfer from the Linac to the Booster (LTB)*

The LTB brings electron and positron beams from the Linac to the Booster and matches phase space functions. The LTB layout is illustrated in Fig. 6.2.15.

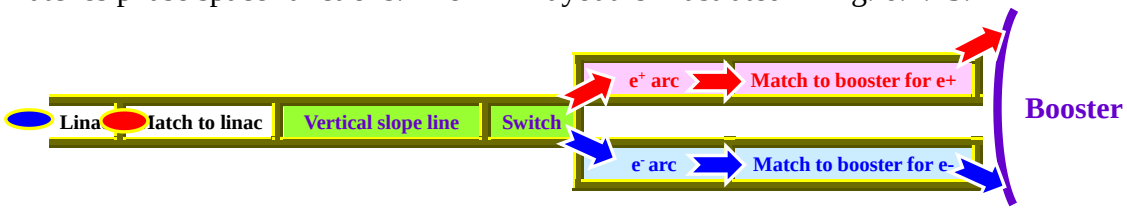

Figure 6.2.15 : Layout of LTB

As shown in Fig. 6.2.15, LTB is comprised of a vertical sloping line (VSL), a switch yard and e^+e^- branch lines. The vertical slope line connects the Linac at ground level to the Booster 50 m deep. It consists of a bend-down section making a 1:10 slope, successive 15 straight 90° FODO cells and a bend-down section making it dispersion free at the end of VSL. The switch yard matches the Twiss parameters with the VSL and delivers electron and positron beams to their individual branch lines. In the e^+ and e^- branch lines, beams are transferred into two arcs and then matched to the Booster through the final matching sections. Each arc contains 2 dispersion suppressors and 6 regular 90° FODO cells. The dispersion suppressors are carefully arranged to avoid conflict of the magnets in two branches. The lattice functions in the transfer line LTB are shown in Fig. 6.2.16.

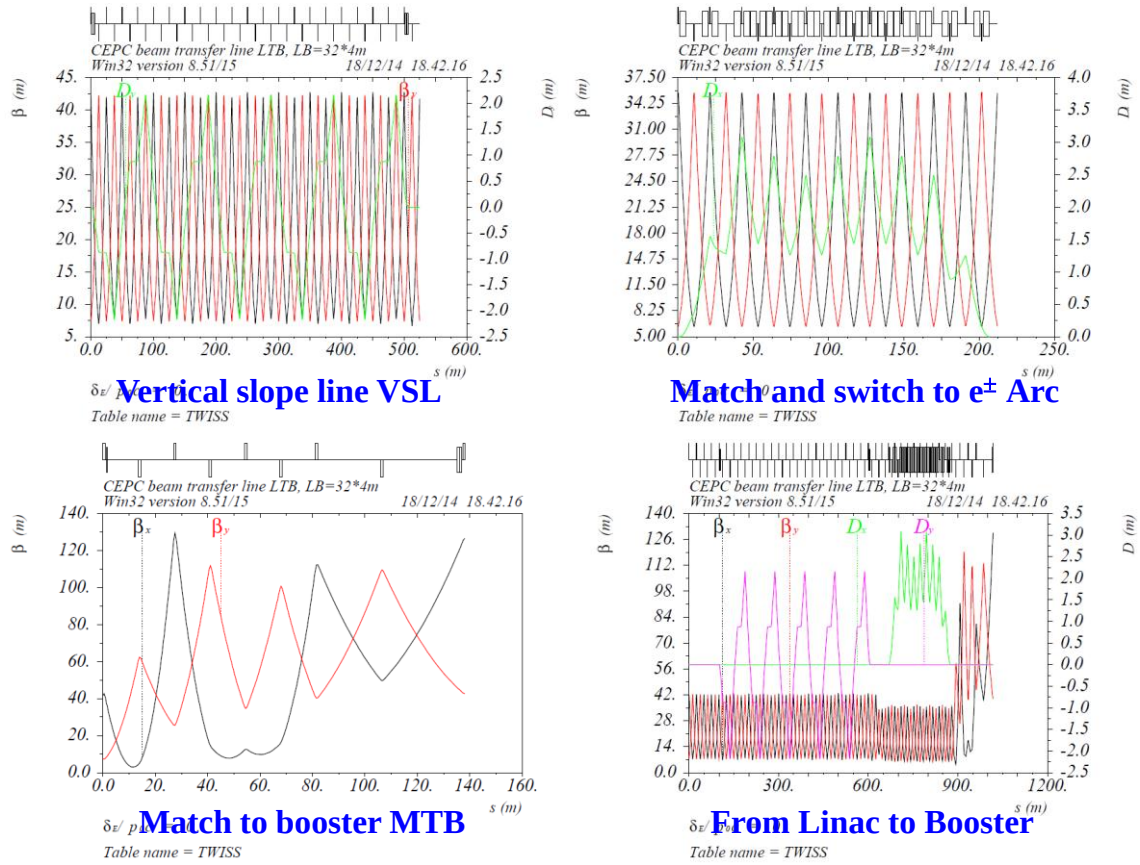

Figure 6.2.16: The lattice functions in the transfer line LTB

6.2.4.2 *Beam Injection to the Booster*

A horizontal septum is used to bend beams into the Booster, and a single kicker downstream of the injected beams kicks the beams onto the Booster orbit at a maximum injection rate of 100 Hz. Figure 6.2.17 pictures the injected bunches in the septum and Booster. The kicker needs to deflect the beam with displacement of $x_k=12\sigma_{x,ej}+3\sigma_{x,inj}+d$ at the entrance of the septum in order to avoid particle loss of both bunches.

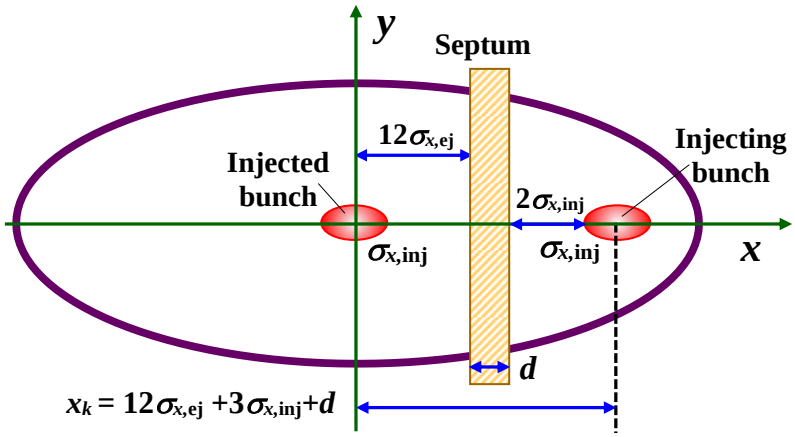

Figure 6.2.17: Beam injection into the Booster

The main parameters of the injection septum and kicker are listed in Table 6.2.5. The strength of the septum and kickers corresponds to 12 GeV for a future upgrade.

Table 6.2.5: Main parameters of the injection septum and kickers

Component	Length (m)	Waveform	Deflection angle(mrad)	Field (T)	Beam-stay-clear	
					H (mm)	V (mm)
Septum	2.0	DC	9.1	0.18	41.4	13.4
Kicker	0.5	1.5 μs half-sine wave	0.40	0.032	41.4	13.4

6.2.4.3 *Beam Extraction from the Booster*

A single kicker and 4 orbit bumps are used for beam extraction horizontally from the Booster at a maximum extraction rate of 100 Hz. Lambertson magnets bend beams vertically into the BTC transfer line. The main parameters of the extraction septum and kicker are listed in Table 6.2.6.

Table 6.2.6: Main parameters of the extraction septum and kickers

Component	Length (m)	Waveform	Deflection angle(mrad)	Field (T)	Beam-stay-clear	
					H (mm)	V (mm)
Lambertson	10.0	DC	9.1	0.41	41.4	18.6
Kicker	2.0	1.5 μs half-sine wave	0.33	0.046	41.4	13.6

6.2.4.4 *Beam Transfer from the Booster to the Collider*

The Booster is placed in the CEPC tunnel 2 m above the collider. The Lambertson septum bends beams down to the BTC transfer line and matches Twiss parameters to the collider. A detailed BTC design needs to be carried out together with collider injection. The lattice functions in BTC are shown in Fig. 6.2.18.

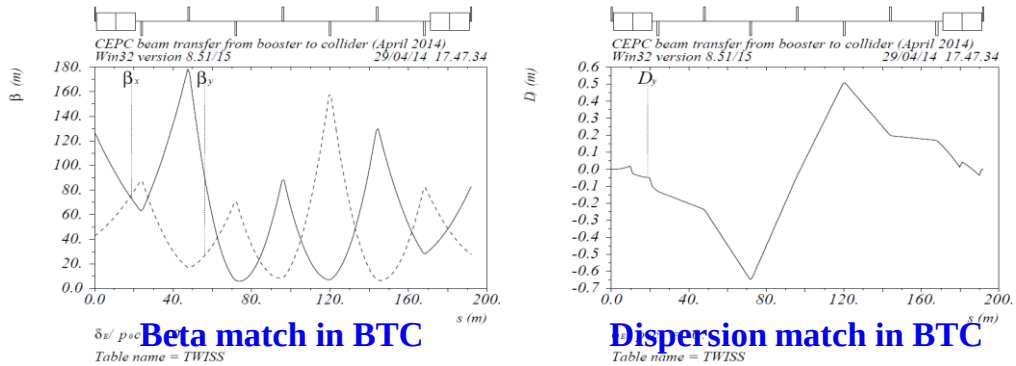

Figure 6.2.18: The lattice functions in the transfer line BTC

6.2.5 **Summary**

This design study finds no showstoppers in the lattice, bypasses, dynamic aperture, beam transfer and requirements of the technical systems. The issues related to low energy injection, including performance at low magnetic field and beam instabilities, remain a central concern in the design. The wiggling bend scheme is proposed to mitigate this problem, while schemes of extending the Linac injector with damping rings and adding a pre-Booster are being considered. There are some other technical challenges as well: the low HOM 1.3 GHz SC cavities, the supports and alignment, as well as lowering the cost of some components.

6.2.6 **References**

1. BEPCII Team, “Performance and Prospects of BEPCII,” Proc. IPAC2012, 1030-1034, May 2012.
2. H. Grote, C. Iselin, “The MAD Program (Methodical Accelerator Design) User's Reference Manual,” CERN/SL/90-13(AP).
3. SAD Home Page, “Strategic Accelerator Design,” http://acc-physics.kek.jp/SAD/.
4. LEP Design Report, CERN-LEP/TH/83-29, June 1983.
5. Z. Zhang, “Low field stability test of the BEPC dipole,” IHEP Internal Report, June, 2014.

7 Upgrade to the SPPC

7.1 Introduction

7.1.1 Science Reach at the SPPC

SPPC is an extremely powerful machine far beyond the scope of the LHC, with the center of mass energy nearly 100 TeV, a peak luminosity of 1.2 x 10^{35} cm^{-2} s^{-1} (and an integrated luminosity of 30 ab^{-1} assuming 2 interaction points and ten years of running). SPPC will dramatically broaden the physics reach. Together the CEPC and SPPC will have the capability to precisely probe Higgs physics. In addition, SPPC will explore directly a much larger region of the landscape of new physics models, and make a huge leap in our understanding of the physical world. There are many issues in energy-frontier physics that SPPC will explore, including the mechanism of Electroweak Symmetry Breaking (EWSB) and the nature of the electroweak phase transition, the naturalness problem, and the understanding of dark matter. These three questions are correlated and point to different exploration directions leading to more fundamental physics principles. SPPC will break new grounds and have great potential of making profound breakthroughs in answering all these questions.

As a "Higgs factory", the CEPC can measure with high precision the properties of the Higgs boson. With the benchmark integrated luminosity of 5 ab^{-1}, a sample of one million Higgs can be obtained and the total Higgs width measured to a relative precision of 2.9%. Using the recoil mass method, CEPC can precisely measure the absolute Higgs couplings to the Z bosons g(HZZ) and the invisible decay branching fraction at the sub percent level, to gluons, W bosons and heavy fermions [g(Hgg), g(HWW), g(Hbb), g(Hcc), and g(H$\tau\tau$)] at percentage level. In addition, it can measure the rare decay couplings [g(H$\gamma\gamma$) and g(H$\mu\mu$)] to the 10% level. However, limited by its center of mass energy, CEPC cannot directly measure g(Htt) and g(HHH). These two couplings are extremely important for understanding EWSB and naturalness [1].

Extending the Higgs factory program, billions of Higgs bosons will be produced at the SPPC. This huge yield will provide important physics opportunities, especially for the rare but relatively clean channels. For example, SPPC can improve the measurement of the Higgs-photon coupling, observe the coupling g(H$\mu\mu$), and test the other rare decays such as H $\rightarrow$ tc, $\mu\tau$. Reaching a higher energy threshold, SPPC could measure g(HHH) to 10% level [3], and directly determine the coupling g(Htt) to the sub-percentage level [2]. The Higgs self-coupling is regarded as the holy grail of experimental particle physics, not only because of the experimental challenges, but also because this coupling is a key probe to the form of the Higgs potential. By measuring g(HHH), SPPC can help answer the question whether electroweak phase transition is of the 1st order or 2nd order. This question is crucially connected to the idea of electroweak baryogenesis.

As an energy frontier machine, the SPPC could discover an entirely new set of particles in the *O* (10 TeV) regime, and unveil new fundamental physics principles. One of the most exciting opportunities is to address the naturalness problem. The naturalness problem stems from the vast difference between two energy scales: the currently probed electroweak scale and a fundamental scale, such as the Planck scale. Solutions to the naturalness problem inevitably predict the existence of a plethora of new physics

particles not far from the electroweak scale. Discovery of such new particles will be a stunning success. Searching for them at the LHC can probe the level of fine-tuning down to 10^{-2}, while SPPC would push this down to the unprecedented level of 10^{-4}, beyond the common understanding of the naturalness principle.

Dark matter remains one of most puzzling issues in particle physics and cosmology. Weakly interacting massive particles (WIMPs) are still the most compelling dark matter candidates. If the dark matter interacts with the Standard Model particles with coupling strength similar to that of the weak interaction, the mass of a WIMP particle could easily be in the TeV range, likely to be discovered at SPPC. Combining the relevant bounds on the mass and coupling with results from the direct (underground) and the indirect (astro-particle) dark matter searches, SPPC would allow us to substantially extend the coverage of the WIMP parameter space in large classes of models.

At the SPPC energy regime, all the SM particles are essentially "massless", and electroweak symmetry and flavor symmetry will be restored. The top quark and electroweak gauge bosons may behave like partons in the initial state, and like narrow jets in the final state. Thus understanding SM processes in such unprecedented environments poses new challenges and offers unique opportunities of sharpening our tools in searching for new physics at higher energy scales.

SPPC is a complex accelerator facility and will be able to support research in different fields of physics. Similar to the multiuse of the accelerator complex at CERN, besides the energy frontier physics program in the collider, the beams from each of the four accelerators in the injector chain can also support their own physics programs. The four stages are a proton linac (p-Linac), a rapid cycling synchrotron (p-RCS), a medium-stage synchrotron (MSS) and the final stage synchrotron (SS). This can occur during periods when beam is not required by the next-stage accelerator. For example, the high-power proton beam of about 0.7 MW from the p-Linac can be used for production of intense beams of neutrons, muons and rare isotopes for a wide range of research areas. The high-power beams of 10 GeV from the p-RCS and 180 GeV from the MSS can be used to produce very powerful neutrino beams for neutrino oscillation experiments and the high energy beam from the SS can be used for research on hadron physics. The option of heavy ion collisions also expands the SPPC program into a deeper level of nuclear matter studies.

In summary, SPPC will play a central role in experimental particle physics in this post-Higgs discovery world. It is the natural next stage of the circular collider physics program after CEPC. Combining these two world class machines, we will certainly arrive at a new milestone in our pursuit of the fundamental laws of nature.

7.1.2 **Design Goals**

SPPC is a proton-proton collider, a discovery machine at the energy frontier. Given the 54.4 km circumference tunnel predefined by CEPC, we will try to achieve the highest possible collision energy in p-p collisions with the anticipated accelerator technology in the 2030's. This, of course, depends on the magnetic field that bends the protons around the ring.. Taking into account the expected evolution in detector technology we can expect that the peak luminosity of 1.2×10^{35} $cm^{-2}s^{-1}$ will be usable. At least two IPs will be available.

This pre-CDR report describes what the SPPC will look like, basic design parameters, and its major challenges in accelerator physics and technology. It also

explores compatibility in the same tunnel with the previously built CEPC and different operating modes such as electron-proton, proton-ion, and electron-ion.

Table 7.1.1: Key SPPC parameters

Parameter	Value	Unit
Collision energy (cm)	71.2	TeV
Peak luminosity	1.2×10^{35}	$cm^{-2}s^{-1}$
Number of IPs	2	
Circumference	54.4	km
Injection energy	2.1	TeV
Overall cycle time	~15	Hours
Dipole field	20	T

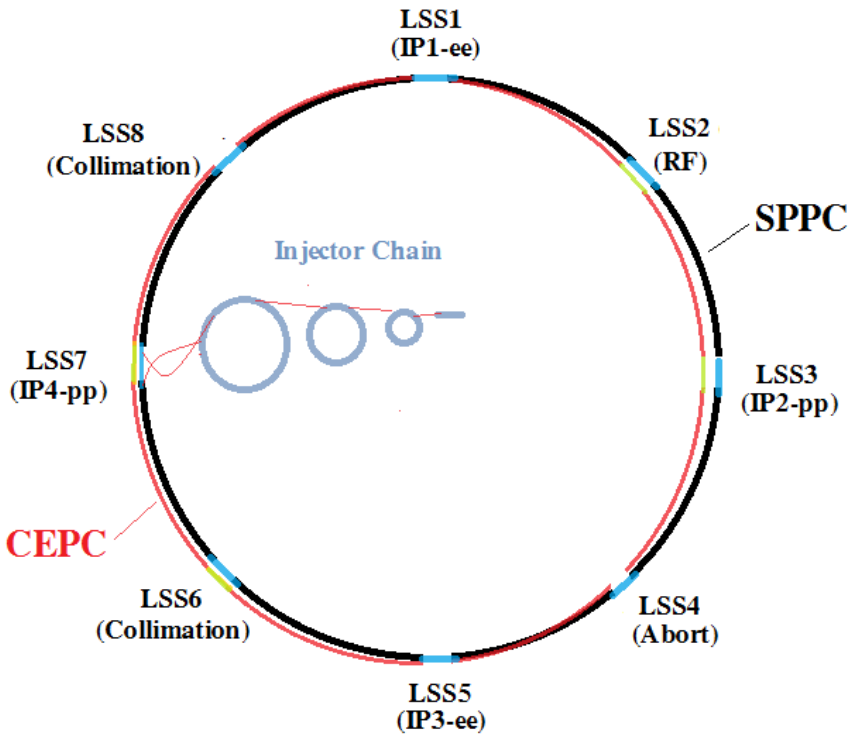

Figure 7.1.1: SPPC accelerator complex

7.1.3 **Overview of the SPPC Facility**

The collider will coexist with the previously built CEPC, housed in the same tunnel, of circumference 54.4 km. The shape and symmetry of the tunnel is a compromise between the two colliders. The SPPC requires relatively longer straight sections which will be described later. This means eight identical arcs, and eight long straight sections of equal length for two large detectors, injection and extraction, RF stations and a complicated collimator system. Based on expected progress in high-field magnet technology in the next 15-20 years, we expect that a field of 20 T will be attainable for the main dipole magnets. A hybrid structure of Nb_3Sn and high-temperature superconducting (HTS) conductors with two beam apertures is foreseen. Assume a

filling factor of 79% in the arcs (similar to LHC) SPPC will potentially provide beams at a collision energy (c.m.) of about 71 TeV.

With a circulation beam current of about 1 A and small beta functions (β*) of 0.75 m at the collision points, the peak luminosity can reach 1.2×10^{35} $cm^{-2}s^{-1}$. The high beam energy, high beam current and high magnetic field will produce very large synchrotron radiation power which will impose critical problems to the vacuum system which is based on cryogenic pumping. We expect that this technical challenge will be solved in the next two decades by developing efficient beam screens to guide out the heavy heat load from the synchrotron radiation and reduce the electron cloud density within the beam apertures. In the case of being forced to lower the synchrotron radiation power, we will have to reduce the bunch population or the number of bunches and try to regain the luminosity by achieving a smaller β*.

Similar to other proton colliders using superconducting magnets, the injection energy is mainly defined by the field quality of the magnets at the bottom of their range. The persistent current in the coils distorts the field distribution at injection energy. Other factors favoring relatively higher injection energy are the coupling impedance which is important to collective beam instabilities, smaller emittance to reduce apertures of beam screen and magnet and relax the requirement on the good-field-region of the magnets. If our design is similar to LHC, we would have a ratio of 15 in top to bottom fields, and therefore an injection energy of 2.37 TeV. A larger energy gain of up to 20 can also be considered, which means an injection energy of 1.78 TeV. This will also make the injector chain cheaper. In this report, we have adopted a modest design with the injection energy of 2.1 TeV.

The injector chain pre-accelerates the beam to injection energy with the required beam properties such as bunch current, bunch structure, and emittance. The injection chain determines the beam fill period. To reach 2.1 TeV, we have designed a four-stage injector chain: a linac (p-Linac) to 1.2 GeV, a rapid cycling synchrotron (p-RCS) to 10 GeV, a medium-stage synchrotron (MSS) to 180 GeV, and finally the super synchrotron (SS) to 2.1 TeV. High repetition rates for the lower energy stages help reduce the SS cycling period. This is important because the SS uses superconducting magnets and also to reduce the beam fill period of the SPPC. The beams can also be used for other applications or research purposes when the accelerators are not preparing beam for injection into the SPPC.

As luminosity decays exponentially from its peak with a lifetime of about 10 hours, to have a large integrated luminosity, the turn-around time from end of collisions to reinjection into the SPPC will be made reasonably short, perhaps as short as 1 hour. However, in practice the turnaround time will be 4-6 hours and this means the average cycle time is about 15 hours. The constant luminosity mode during collision, very helpful to the detectors, will be studied by allowing a higher beam-beam tune shift or reducing the beta functions at the collision points.

There are a number of technical challenges in designing and building the collider including its injector chain. The two most difficult are the development and production of high-field magnets as high as 20 T and the vacuum - beam screen associated with very strong synchrotron radiation. Significant R&D efforts in the coming decade are needed to solve these problems.

7.1.4 References

1. Nima Arkani-Hamed's talk at CFHEP, Aug 2014; also refer to the physics case Pre-CDR Vol. 1.
2. M. Mangano, Event's structure at 100 TeV: a first look, presentation at International Workshop on Future High Energy Circular Colliders, Beijing Dec 16-17 2013.
3. A. J. Barr, et.al, Higgs Self-Coupling Measurements at a 100 TeV Hadron Collider, arXiv 1412.7154.

7.2 Key Accelerator Physics Issues

7.2.1 Main Parameters

7.2.1.1 *Collision Energy and Layout*

To reach the design goal for the c.m. energy of $\geq$ 70 TeV in this relatively small circumference of 54.4 km, very high-field magnets of about 20 T have to be used. A hybrid structure of Nb_3Sn and high-temperature superconducting conductors will be used to reach this field level. In addition, the ring should be designed to be as compact as possible. This means that both the arcs and long straight sections will use space efficiently. Although the lattice has not been designed, it is supposed it will be a traditional FODO in the arcs and other parts of the insertions except at the IPs where triplets are used to produce very small β*s. One can make a very preliminary outline design for the SPPC without a real lattice. The arcs represent most of the circumference, and the arc filling factor is taken as 0.79, similar to LHC. A key issue here is to define the number of long straight sections and their lengths. They are needed for producing very small beta functions where the large physics detectors are placed, and for the beam injection and extraction systems (abort), collimation systems and RF stations. Some compromises have to be made to have a relatively compact design of the long straight sections. Our design is more compact than LHC. Being compatible with the CEPC layout, a total length of about 6.4 km is reserved for the long straight sections, with eight long straight sections of which 4 are 1100 m long and the 4 others are 850 m long. With this configuration, the top beam energy is 35.6 TeV which provides 71.2 TeV in collision energy. The main parameters are listed in Table 7.2.1.

Table 7.2.1: Main SPPC parameters

Parameter	Value	Unit
Main parameters		
Circumference	54.4	km
Beam energy	35.6	TeV
Lorentz gamma	37918	
Dipole field	20	T
Dipole curvature radius	5928	m
Arc filling factor	0.79	
Total dipole magnet length	37246	m
Arc length	47146	m
Total straight section length	7554	m
Energy gain factor in collider rings	17.0	

Injection energy	2.1	TeV
Number of IPs	2	
Revolution frequency	5.48	kHz
Physics performance and beam parameters		
Peak luminosity per IP	1.2E+35	$cm^{-2}s^{-1}$
Beta function at collision	0.75	m
Circulating beam current	1.0	A
Nominal beam-beam tune shift limit per IP	0.006	
Bunch separation	25	ns
Number of bunches	5835	
Bunch population	2.0E+11	
Accumulated particles per beam	1.2E+15	
Normalized rms transverse emittance	4.1	μm
Beam life time due to burn-off	9.5	hour
Total / inelastic cross section	140	mb
Reduction factor in luminosity	0.96	
Full crossing angle	73	μrad
rms bunch length	75.5	mm
rms IP spot size	9.0	μm
Beta at the 1st parasitic encounter	19.5	m
rms spot size at the 1st parasitic encounter	45.7	μm
Stored energy per beam	6.6	GJ
SR power per beam	2.1	MW
SR heat load at arc dipoles	57.8	W/m
Energy loss per turn	2.10	MeV

7.2.1.2 *Luminosity*

The luminosity is designed to be as high as possible, though present day detectors cannot handle such high event rates. It is believed that ongoing R&D efforts on detectors and general technical evolution will be able to solve the problem of handling a very high event rate at SPPC. The peak luminosity level of 1.2×10^{35} $cm^{-2}s^{-1}$ is considered extremely high for a proton machine as compared to previously built machines such as the Tevatron [3] and LHC [2] and also in designs such as SSC [4], VLHC [5], HE-LHC, HL-LHC and FCC-hh. In order to achieve this high luminosity, a large number of bunches and high bunch population are needed. This will be supported by a powerful injector chain. Besides the challenges in the detectors, very high synchrotron radiation and very strict beam loss control associated with a high circulation current of 1 A are major challenges to the vacuum system and the machine protection system.

Another important parameter is the integrated luminosity. One needs to account for the intensity decay of the stored protons during the collision, the cycle turnaround time and the shrinking of the transverse emittance due to synchrotron radiation. Beam decay and turnaround time reduce the integrated luminosity. It is still under discussion if emittance shrinkage from synchrotron radiation can increase peak luminosity after the

collision start. The adverse side is that we have to accept a larger beam-beam tune shift which is usually limited to 0.010-0.015. An emittance blow-up system is required to counteract the emittance shrinkage. Another method to increase the integrated luminosity is to adjust β* during the collision by taking advantage of emittance shrinking while keeping the beam-beam tune shift constant.

7.2.1.3 *Bunch Structure and Population*

More bunches with relatively small bunch spacing are very important for achieving high luminosity. However, the bunch spacing is limited both by parasitic collisions in the proximity of the IPs and the electron cloud instability. Furthermore one needs to consider the ability of the detector trigger systems to cope with short bunch spacing. Although the bunch gap of 25 ns was designed as a baseline for LHC, the machine has been operating to date with 50 ns bunch spacing. It was found that there are problems in operation mainly due to the electron cloud effect. It is believed that the problems related to 25 ns at LHC will be overcome in the near future. Therefore, we have chosen 25 ns for the nominal bunch spacing at SPPC. The bunch spacing of 25 ns is set by the RF system in the MSS of the injector chain and preserved from there on. The possibility of using shorter bunch spacing will be investigated in the future.

Different time gaps among bunch trains are needed for beam injection and beam extraction in both SPPC and the injector chain. They depend on the practical designs of the injection and extraction (abort) systems. For example, the rise time of the kickers for beam extraction from SPPC is considered to be the longest required gap, about a few microseconds. Altogether, the bunch filling is about 80% of the ring circumference, similar to LHC.

These gaps in the bunch structure have a significant impact on the beam dynamics during collision. On one hand, the gaps between bunch trains are useful in suppressing collective beam instabilities; on the other hand, there are different average numbers of collisions per revolution for different bunches, and this will produce different beam-beam effects.

Bunch population is first defined in the p-RCS of the injector chain, where the beam from the p-Linac is filled into the RF buckets by both transverse and longitudinal paintings. Similar to the SPL linac for LHC, with a relatively high-energy linac beam, one can obtain a higher bunch population in the presence of space charge effects in the p-RCS. Longer bunch from the p-RCS will be split evenly into many smaller bunches in MSS by a special RF system, and it is there where the nominal bunch population and bunch spacing are formed. The bunch population will decay once collisions begin. With the nominal bunch number and bunch population, one will have a large circulating current of about one A in the collider rings, similar to the future HL-LHC.

7.2.1.4 *Beam Size at the IPs*

The transverse and longitudinal beam sizes are critical parameters for the luminosity. On the one hand, smaller beam sizes are very demanding, and superconducting quadrupole triplets are used to make a very strong transverse focusing system near the IPs; on the other hand, too small beam sizes will result in large beam-beam effects and other collective beam instabilities.

The beam sizes are determined by the insertion lattice and the beam emittance. The normalized emittance is predefined in the p-RCS of the injector chain and preserved

with a slight increase in the course of reaching the top energy of the SPPC due to many different factors such as nonlinear resonance crossings. However, at the maximum energy of 37.6 TeV or even earlier in the later part of the acceleration, synchrotron radiation will take effect. At the maximum energy of 37.6 TeV the damping times are about 1.6 hours and 0.8 hours for the transverse and longitudinal emittances, respectively. We may exploit this feature to reduce beam sizes at the IPs to enhance the integrated luminosity. However, a fallback solution is a stochastic emittance heating system to counteract the synchrotron radiation effect or control the emittance during the collision process.

7.2.1.5 *Crossing Angle at the IPs*

To avoid parasitic collisions near the IPs which produce background for experiments, it is important to separate the two beams except at the IPs. There will be a crossing angle between the two beams. The method is to avoid the beam overlapping at the first parasitic encounters, 7.5 m from the IPs when the bunch spacing is 25 ns. The magnitude of the crossing angle can be estimated by assuming a separation no less than two times the full beam size or 12 times the rms beam size at those locations. At the SPPC, the crossing angle at the collision energy is about 75 μrad and may be increased later in a more realistic design. Compared with head-on collisions, this bunch crossing angle will result in a few percent luminosity reduction. The crossing angle is usually different at injection due to different lattice settings and larger emittance.

Since the two beams at the superconducting quadrupole triplets close to the IP are not well separated from each other by the crossing angle, the apertures of the quadrupoles will be increased significantly.

7.2.1.6 *Turnaround Time*

Turnaround time is the total time period when the beams are out of collision, including the programmed count down checking time before injection, the final check with a pilot shot, the beam filling time with SS beam pulses, the ramping up (or acceleration) time and the ramping down time. Filling one SPPC ring requires 6 SS beam pulses. This means a filling time of about 10 minutes including pilot pulses. The ramping up and down times are each about 18 minutes. Altogether, the minimum turnaround time is about 1.1 hours. However, the experience at LHC and other proton colliders shows that about only one third of the operation sequence from injection to the top energy are successful and the average turnaround time is closer to 5.5 hours. It is considered acceptable to have a total cycle time of about 15 hours, during which the beams are in collision and the detectors can take date for about 10 hours.

7.2.1.7 *RF Parameters*

The main acceleration system at SPPC is by superconducting cavities at 400 MHz. However, an additional RF system at 200 MHz is considered helpful for longitudinal matching from SS to SPPC during injection. Although the ramping-up time is mainly defined by the superconducting magnets, the RF system should provide sufficient acceleration voltage during the process to maintain the acceleration rate with a large longitudinal acceptance. When nearing the final stage of acceleration, synchrotron radiation will play a significant role. About 10 MV in RF voltage is needed to compensate the synchrotron radiation, and the situation is similar during the collisions

(and the preparation phase bringing the beams into collision). Therefore, a total RF voltage of either 24 or 32 MV per beam will be provided by the 400 MHz system.

7.2.2 **Synchrotron Radiation**

Synchrotron radiation power is proportional to the fourth power of the Lorentz factor and the inverse of the radius of curvature in the dipoles and is an important effect at the few TeV level and in superconducting dipoles. At the SPPC synchrotron radiation becomes so important that it imposes technical challenges to the vacuum system and a limit on the circulating current. The heat load from synchrotron radiation is very difficult to guide out of the machine because the vacuum chamber itself is at liquid helium temperature. The radiation produces a great many secondary electrons which are the most important source of the electron cloud. A sophisticated beam screen situated between the beam and the vacuum chamber is needed, though the inner apertures of the magnets are already very limiting. The working temperature at the beam screen is a key parameter in the design. The beam screen is also important in controlling the coupling impedance and reducing the electron cloud effect. With a beam current of 1 A and a 20 T magnetic field, the synchrotron radiation power reaches about 58 W/m per aperture in the arc sections, more than two orders higher than that at LHC. The average critical photo energy is about 2.1 keV. There is also a synchrotron radiation effect in the high-gradient superconducting quadrupole magnets. The technical challenges of the vacuum system and beam screen are described in Section 7.3.2.

As mentioned earlier, the synchrotron radiation effect also has an important impact on beam dynamics. Both longitudinal and transverse emittances will shrink with lifetimes of one hour or so at the top energy. The short damping time helps to eliminate collective beam instabilities. One may try to exploit this feature to enhance the machine performance such as implementing luminosity levelling.

7.2.3 **Beam-Beam Effects**

Beam-beam effects, which could lead to emittance growth, lifetime decrease and instabilities, have a very important effect on the luminosity of a collider. There are several different types of beam-beam effects affecting the performance of a proton-proton collider, namely the incoherent beam-beam effects which influence beam lifetime and dynamic aperture, the PACMAN effects which will cause bunch to bunch variation, and coherent effects which will lead to beam oscillations and instabilities.

The nominal parameters given in Table 7.2.1 are used for a preliminary study of beam-beam effects. By using the beam-beam theory [1] one obtains an estimate for the beam-beam limit $\xi_{y,\max} = 0.0064$ per IP. As LHC has already reached a value of ΔQ_{tot}~0.02 with 3 interaction points, it is reasonable to choose the nominal beam-beam parameter as 0.006.

7.2.3.1 ***Incoherent Effects***

Each particle in a beam will feel a strong nonlinear force when the beam encounters the counter rotating beam. This has deleterious effects on the dynamic behavior of the particle. This nonlinear interaction will lead to an amplitude dependent tune spread for the particles in both transverse planes. This should be studied to keep the tunes away

from crossing dangerous resonance lines. According to experience at both the Tevatron and LHC, the total tune spread from all IP crossings should be kept to no more than 0.015. As an example, a beam-beam tune footprint [6] with 2 head-on interactions at SPPC (using the LHC tunes) is shown in Fig 7.2.1. From the plot one can see that the footprint at small amplitudes is crossed by 10th order and 11th order resonances and at higher amplitudes by 13th order resonances. Thus, dynamic aperture is reduced by the beam-beam interaction at the IP, which may lead to beam loss. Therefore, tunes slightly above the LHC values would seem to be a better choice.

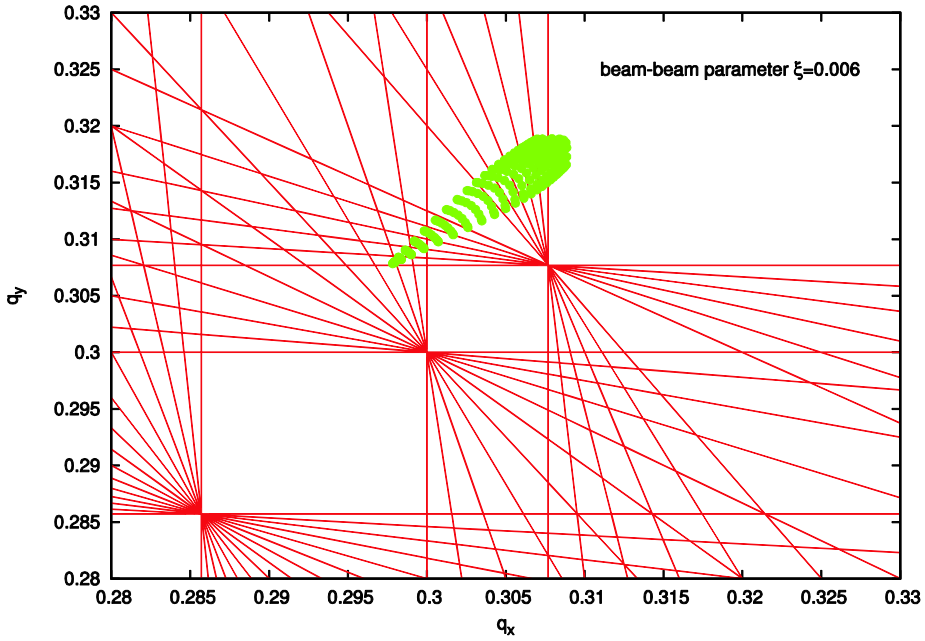

Fig 7.2.1: Two dimensional tune distribution versus amplitude (footprint)

7.2.3.2 *PACMAN Effects*

The circumference and bunch number at SPPC are both about twice those at LHC. With a similar bunch spacing of 25 ns it is expected that the PACMAN effects may have a similar influence to that seen at CERN, that is to say that only about half of the whole bunches at SPPC would be regular bunches. The identification of regular bunches is important since the measurements such as tune, orbit or chromaticity should be selectively performed on those bunches. We have to choose a proper fill pattern and crossing scheme to reduce these effects.

7.2.3.3 *Coherent Effects*

Coherent beam-beam effects would be expected in SPPC, because the two colliding beams are equally strong. Coherent modes of oscillations of the two counter rotating beams are coupled by the beam-beam interaction and the coherent dipole mode is the most dangerous mode where a bunch oscillates as a rigid object around its nominal orbit. According to LHC experience, it might be an option to use asymmetric collisions (different bunch intensities) at SPPC to suppress the excitation of the coherent mode due to the beam-beam effect.

7.2.3.4 *Beam-Beam Tune Shift Limit*

In order to achieve a higher luminosity, new ideas and technologies are under study, such as the crab waist collision scheme, beam feedback and so on. They look effective for increasing collider luminosity. New theory and simulation work could guide the study for a luminosity upgrade in the future. The beam-beam simulations by Ohmi predict that the beam-beam limit at LHC might be larger than 0.03 by including SR emittance shrinkage and proton burn off and it is hopeful to achieve a much higher integrated luminosity with the method.

7.2.4 **Electron Cloud Effect**

Beam instability is caused by the electron cloud (EC). The buildup of accumulated photon electrons and secondary electrons has proved to be one of the most serious restrictions on collider luminosity in PEP II, KEKB, LHC, and BEPC. The EC links together the motion of subsequent bunches and induces coupled bunch instability. It also leads to emittance blow-up and luminosity degradation. For next-generation super proton colliders such as SPPC, a bunch population higher than 10^{11} and a bunch spacing less than or equal to 25 ns, the EC effect will be more critical for reaching the luminosity goal of 1×10^{35} $cm^{-2}s^{-1}$.

There are three sources for the electron cloud, photon electrons, residual gas ionization and secondary electron emission. At a vacuum of about 1.0 nTorr, the residual gas density is about 2×10^{13} $1/m^3$. With an ionization cross section of 2.0 Mb, the electrons produced by gas ionization can be ignored. The necessary condition for electron amplification is that the average secondary electron emission yield (SEY) exceeds one. Electron multipacting occurs if the electrons emitted from the wall reach the opposite side wall just prior to the arrival of the next bunch. The criterion $n = \frac{r^2}{n_b r_e L_{sep}}$ can be used to estimate which kind of electrons are the dominant component in the electron cloud. In the formula, r is the radius of the vacuum pipe, n_b the number of particles in the bunch, L_{sep} is the bunch spacing and r_e=2.8×10^{-15} m, the classical electron radius. If n<1, part of the primary electrons are lost before the next bunch arrives and secondary electrons dominate the electron cloud; if n>1, the primary electrons interact with more than one bunch and photon electrons compose most of the electron cloud. The estimated parameter n for different pp colliders are listed in Table 7.2.4-1. The EC build-up saturates when the attractive beam field at the chamber wall is compensated on the average by the electron space charge field. The line density of the electron cloud in the vacuum chamber is $\lambda_e = n_b/L_{sep}$, which corresponds to the volume density $\rho_{e,neutr} \approx \frac{\lambda_e}{\pi ab}$, where a and b are half sizes of the elliptical vacuum pipe. According to the estimated neutralization density shown in Table 7.2.2, the EC density in the SPPC rings will be comparable to those at LHC and FCC-hh.

The EC links oscillation between subsequent bunches and may lead to coupled bunch instability. The action propagated by the EC between subsequent bunches can be presented as a wake field expressed as $W_{ec,x,y}/L = 4\pi\rho_{e,neutr}/N_b$, which gives the dipole component per unit length of the wake field. Based on the wake field, the growth rate for the coupled bunch instability is shown as $\frac{1}{\tau_{e,CB}} = \frac{2r_p N_b c^2}{\gamma\omega_\beta ab L_{sep}}$. The coupled bunch instability can be damped by a feedback system. The EC also drives transverse

emittance blow-up, which is very important at lower energy when the synchrotron radiation damping is very weak. The single bunch instability caused by the short-range wake field can be analyzed with the two particle model where head and tail particles each carry a charge of $n_b e/2$. The head particles disturb the EC distribution and the oscillation in the bunch head will be transferred to the bunch tail. For sufficiently long bunches, $\omega_e \sigma_z > c\pi/2$, the wake field felt by the tail particle is $W_{0,SB} \approx 8\pi\rho_e C/N_b$. C is the circumference of the ring and ρ_e is the volume density of the accumulated electron cloud. The single bunch instability manifests itself as a strong-tail or transverse mode coupling instability (TMCI). With the strong head-tail model, the dimensionless parameter $\Gamma = \frac{N_b r_p W_{0,SB} \bar{\beta}}{16\gamma\nu_s} < 1$, is used to give the threshold of the wake field. The EC threshold density for the instability is expressed as $\rho_{e,threhold} < \frac{2\gamma\nu_s}{r_p \pi C \bar{\beta}}$. Rough estimates on TMCI and the density threshold for SPPC are summarized in Table 7.2.2. Some measures such as solenoid magnetic fields, clearing electrodes, or pipe coating should be taken to diminish the electron cloud.

Table 7.2.2: Estimates on electron cloud instability for some super pp colliders

	LHC	FCC-hh	SPPC
Bunch particles (10^{11})	1.15	1.0	2.0
Bunch spacing (ns)	25	25	12.5/25/50
Beam energy (TeV)	7	50	31.7
Pipe radius (mm)	20	13	20
Parameter *n*	0.165	0.189	0.19/0.095/0.048
Neutralization line density (10^{10}/m)	1.53	1.33	5.32/2.66/1.33
Neutralization volume density (10^{13}/m^3)	1.22	2.51	4.24/2.12/1.06
Wake field *W/L* (10^3/m^2)	1.33	3.15	2.66/1.33/0.67
Betatron tune	43.3	-	60.3
Synchrotron tune	0.006	0.002	0.005
Growth time (ms)	4.31	-	2.07/4.15/8.3
Circumference (km)	26.7	100	50
Threshold electron density (10^{13}/m^3)	0.66	0.147	0.468

The accumulated electron cloud as a focusing force on the proton beam will cause an incoherent tune shift as the counterpart to space charge. Assuming the EC is transversely uniform around the beam, the tune shift is given by the formula $\Delta\nu = \frac{r_p}{\gamma}\bar{\beta}\rho_{ec}C$. A larger tune shift can lead to a severe drop in luminosity. For SPPC, with an average betatron function of about 100 m, the tune shift is estimated to be about 0.00225 which cannot be ignored when the EC density is about 1.0×10^{13} m^{-3}. Therefore, in future lattice designs, it is necessary to consider the tune shift caused by the EC.

Because of very high synchrotron radiation power and low-temperature beam pipes for the superconducting magnets at SPPC, the deposited power on the beam screen from the secondary electron multipacting may be a serious issue. The measured deposited power in the dipole magnets of LHC has proved to increase exponentially to about 10 W/m, when SEY is larger than 1.4. Therefore, SEY at SPPC should be controlled to stay below 1.4 or even 1.2 by coating TiN or NEG on the internal walls of the vacuum chamber and devices inside the vacuum.

7.2.5 **Beam-Loss and Collimation**

7.2.5.1 ***Beam Loss***

Beam losses are extremely important for safe operation in a machine like SPPC where the stored energy in the beam can be as high as 6.6 GJ per beam. Beam losses can be divided into two classes, namely irregular losses and regular losses. Irregular beam losses are avoidable losses and are often the result of a misaligned beam or of a fault in one of the accelerator elements. A typical example is a trip of the RF which causes the loss of synchronization during acceleration and collisions. Vacuum problems also fall into this category. These losses may be distributed around the machine. A well designed collimator system might collect most of the lost particles, but even a fraction of the lost particles may cause problems at other locations. Regular losses are those that are typically non-avoidable and localized in the collimator system or on other aperture limits. They might occur continuously during operation and correspond to the lifetime/transport efficiency of the beam in the accelerator. The lowest possible loss rate is defined by the theoretical beam lifetime limitation due to various effects, e.g. Touschek effect, beam-beam interactions, collisions, transverse and longitudinal diffusion, residual gas scattering, halo scraping and instabilities.

1) **Touschek effect:** The Touschek effect describes the scattering and loss of charged particles in a storage ring, and is also referred to as intrabeam scattering. It is determined by the average of the scattering rate around the ring.
2) **Beam-beam interactions:** Beam-beam interactions at the IPs will of course produce collisions to study but also elastic and inelastic scattering and will lead to emittance blow-up or beam loss.
3) **Transverse and longitudinal diffusion:** A number of physical processes cause beam particles to leave their trajectories and strike the machine aperture. One example is resonance crossings or unstable motion caused by unavoidable field errors and higher order multipoles. Particles inside the dynamic aperture may also diffuse out from the core of the beam and into the unstable region, e.g. through intrabeam scattering, beam-gas scattering and beam-gas bremsstrahlung.
4) **Residual gas scattering:** This includes inelastic beam-gas nuclear inelastic (including quasi-elastic and diffractive) interactions and elastic beam-gas nuclear elastic interactions (both coherent and incoherent) of the incoming beam with the residual gas, as well as Coulomb scattering on residual gas around the ring. The scattering degrades the beam quality and also causes immediate beam loss.
5) **Collimator tails:** This term denotes the protons escaping from the betatron and momentum cleaning insertions and then being intercepted by the tertiary or quaternary collimators. Also called “tails from collimators” or “tertiary/ quaternary beam halo”, they are related to the inefficiency of the main collimation system.
6) **Instabilities:** A beam becomes unstable when the moments of its distribution exhibit exponential growth (e.g. barycenters and standard deviations in different coordinates) which result in beam loss or emittance growth. There are a wide variety of mechanisms which may produce collective beam instabilities with the most important one being the electron cloud effect as described above.

7.2.5.2 *Collimation*

For high-power proton accelerators, halo particles might potentially impinge on the vacuum chambers and get lost. The radiation from the lost particles will trigger quenching of the superconducting magnets, damage many radiation-sensitive devices, and cause residual radioactivity that prevents hands-on maintenance. The problem can be solved largely by introducing collimation systems which confine the particle losses to specified locations where one can provide better shielding and heat-load transfer. For the SPPC with large stored energy in the beams and high beam energy, the situation is even more complicated, mainly because extremely high collimation efficiency is required. In addition, it is very difficult to collimate very high energy protons efficiently. For example, LHC which has lower beam energy and stored energy, presently uses 98 two-sided and 2 one-sided movable collimators, for a total of 396 degrees of freedom, which provide a four-stage collimation system to collimate 100 MJ of stored energy per beam [7]. LHC is upgrading the collimation system for future operation at their design energy of 14 TeV (c.m.) and will do more for their high-luminosity upgrade (HL-LHC). Two warm interaction regions (IRs) or long straight sections are used to provide betatron collimation and momentum collimation. Both betatron and momentum collimations have been designed using the sophisticated multi-stage collimation method. The main difference is that a modest dispersion function in the long straight is required for momentum collimation but there is no such need for the betatron collimations.

With the multi-stage collimation method, the primary collimators of small thickness are the closest to the beam in transverse phase space and will scatter the primary halo particles. They must be located at large β value to maximize the impact parameters and reduce the scattering out probability. The secondary and sometime even tertiary collimators will intercept and stop part of the scattered particles; however, they also produce scattered out particles, which are called secondary and tertiary beam halos. The absorbers will stop the showers from upstream collimators and the additional tertiary or quaternary collimators are used to protect the superconducting quadrupole triplets at the colliding interaction regions directly [8]. The introduction of the collimation system not only uses up precious space in the rings, but also increases the coupling impedance, important for collective beam instabilities.

For SPPC, the stored energy in the beam is as high as 6.6 GJ per beam which is about 16 times that of the LHC at design energy. Therefore, if the same beam loss power is allowed, then to prevent frequent SC magnet quenching, the cleaning inefficiency at SPPC should be about 1/16 of the one at LHC. This means a cleaning inefficiency of 4.3×10^{-6}. Five-stage collimation systems for both betatron and momentum collimations are foreseen. Figure 7.2.2 shows the schematic for a five-stage collimation system. Two long straight sections of about 850 m are needed to provide the required space for hosting the collimation systems. The one for momentum collimation should be designed for a location with modest dispersion functions.

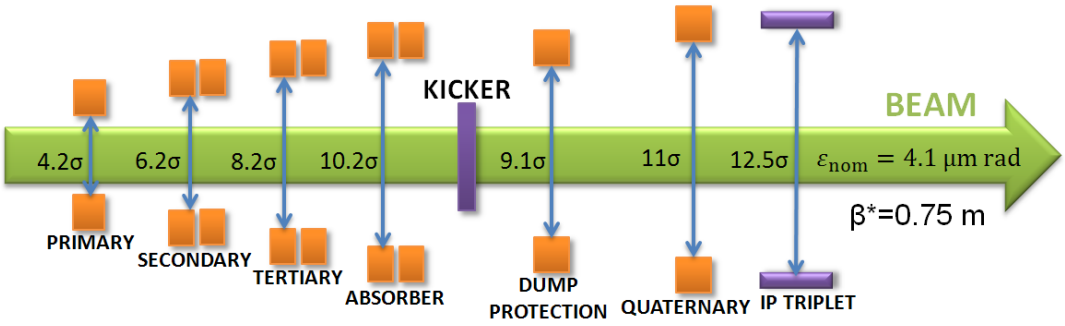

Figure 7.2.2: Schematic for the multi-stage collimation system at SPPC

Besides the method used at LHC, other methods will be studied, including the one studied in CERN and FNAL which uses bent crystal [11-12] and the one by employing nonlinear magnets to enhance the collimation efficiency [13-14].

7.2.6 References

1. J. Gao, Private note to be published.
2. LHC Design Report, Main Ring-CERN-2004-003-V1.
3. Tevatron Design Report, fermilab-design-1983-01.
4. SSC Design Report.
5. "Design Study for a Staged Very Large Hadron Collider," Fermilab TM-2149, June 2001.
6. T. Sen, Private Communication.
7. S. Redaelli, et.al., "Operational performance of the LHC collimation," proceedings of HB2010, Morschach, Switzerland, (2010), p. 395.
8. B. Salvachua, et.al., "Cleaning performance of the LHC collimation system up to 4 TeV," proceedings of IPAC2013, Shanghai, China, (2013), p. 1002.
9. N. Catalan-Lasheras, "Transverse and Longitudinal Beam Collimation in a High-Energy Proton Collider (LHC)," Zaragoza, November 1998 p. 51.
10. M. Serluca, et.al., "Hi-lumi LHC collimation studies with MERLIN code," Proceedings of IPAC2014, Dresden, Germany, (2014), p. 784.
11. W. Scandale et al., "First results on the SPS beam collimation with bent crystals," Physics Letters B, Volume 692, (2010) p. 78–82.
12. V. Zvoda et al., "Advanced bent crystal collimation studies at the Tevatron (T-980)," Proc. of PAC2011, New York, USA (2011) 73-75.
13. Z. Guo, J.Y. Tang et.al., "A novel structure of multipole field magnets and their applications in uniformizing beam spot at target," NIM-A, 691(2012), p. 97-108.
14. Y. Zou, J.Y. Tang, J.Q. Yang, "Resonant slow extraction in synchrotrons by using anti-symmetric sextupole fields," Proceedings of IPAC2014, Dresden, Germany, (2014), p. 827.

7.3 Key Technical Systems

7.3.1 **High Field Superconducting Magnets**

7.3.1.1 ***Requirement of the High Field Magnets for the SPPC***

To bend and focus the high energy proton beams, SPPC needs thousands of high-field dipoles and quadrupoles installed around a tunnel 54.4 km in circumference. The nominal apertures in these magnets is 40 to 50 mm. The field strength of the main dipoles is 20 T. A field uniformity of 10^{-4} is needed within 2/3 of the aperture radius. The magnets are designed to have two beam apertures of opposite magnetic polarity to save space and cost. The distance between the two apertures of the main dipole is 330 mm; however, that is subject to change based on detailed design optimization to control the cross-talk between the two apertures within a reasonable magnet size. The outer diameter of the main dipole and quadrupole magnets should not be larger than 900 mm, so that they can be placed inside cryostats having an outer diameter of 1500 mm. The total magnetic length of the main dipole magnets is about 39 km out of the total circumference of 54.4 km. Assuming the length of each dipole magnet is 15 m, in total there about 2600 dipole magnets to be installed. High gradient quadrupoles for SPPC are divided into the following three groups: 1) for those at the IPs, single-aperture magnets with D = 60 mm, B_{pole} = 20 T; 2) for those in the matching section, D = 60 mm, B_{pole} = 16 T; 3) for those at arcs, D = 45 mm, B_{pole}=16 T. The ones in the matching sections and arcs are two-in-one or yoke-sharing magnets.

7.3.1.2 ***Current Status of High Field Accelerator Magnet Technology***

One of the most challenging technologies for SPPC is the development of the high field superconducting magnets. All the superconducting magnets used in present accelerators are made with NbTi. These magnets work at significantly lower field than the required 20 T (23.5 T is really required to have an operating margin), e.g., 3.5 T at 4.2 K at RHIC and 8.3 T at 1.8 K at LHC. As shown in Fig. 7.3.1, the critical current density J_c of most superconductors falls rapidly with the magnetic field. A reasonable design of accelerator magnets requires that the average J_c of the cable should be above 500 A/mm^2 at the desired field. For example, it is possible to develop a 15-T dipole with Nb_3Sn; however, for well beyond that one has to look for alternate superconductors. Fortunately, the advent of high critical temperature superconductors (HTS) allows us to develop magnets with much higher magnetic field as required for SPPC. Apart from high critical temperature, a remarkable property of HTS superconductors is that unlike NbTi or Nb_3Sn, their current carrying capacity does not decrease substantially with field in the range of interest for SPPC (see Fig. 7.3.1). For this reason they are also sometimes called High Field Superconductors (HFS). To obtain a dipole with a field of 20 T, a realistic approach based on the current J_c level of superconductors is to use combined coils in a hybrid magnet design: NbTi and Nb_3Sn or only Nb_3Sn coils provide a field of 15 T, and the other 5 T is provided by HTS (Bi-2212 or YBCO) insert coils.

Development of superconducting dipole magnets started more than thirty years ago in US laboratories, as shown in Fig. 7.3.2. At BNL the Sampson magnet obtained a 5-T main field in the late 1970's, which was followed by LBNL-D10 and CERN-Asner that reached 8-9 T in the late 1980's. The Twente-MSUT magnet is the first dipole magnet which obtained a dipole field beyond the limitation of NbTi. LBNL holds the Nb_3Sn

dipole magnet records over the past fifteen years: Their D20 dipole reached 13.5 T in a 50-mm aperture in 1997; HD2 dipole reached 13.84 T in an aperture of about 40 mm in 2007. The HD1a dipole reached a peak field of 15.4 T in the coil but without an accelerator aperture of appropriate field quality. The RD3C dipole reached 10 T in a 35-mm twin aperture with a common coil configuration. All these magnets were fabricated based on "Wind and React" technology and tested at 4.5 K. A similar common coil magnet was developed using "React and Wind" technology at BNL and reached over 10.2 T in a 31-mm aperture, which is the record for "React and Wind" technology. All of these magnets are R&D magnets. The current maximum dipole field for real accelerator magnets is a nominal 8.3 T for the LHC main dipoles. To raise it to 20 T in 15 years or about by the year 2030 would require significant R&D in developing both the superconductor technology and the magnet technology.

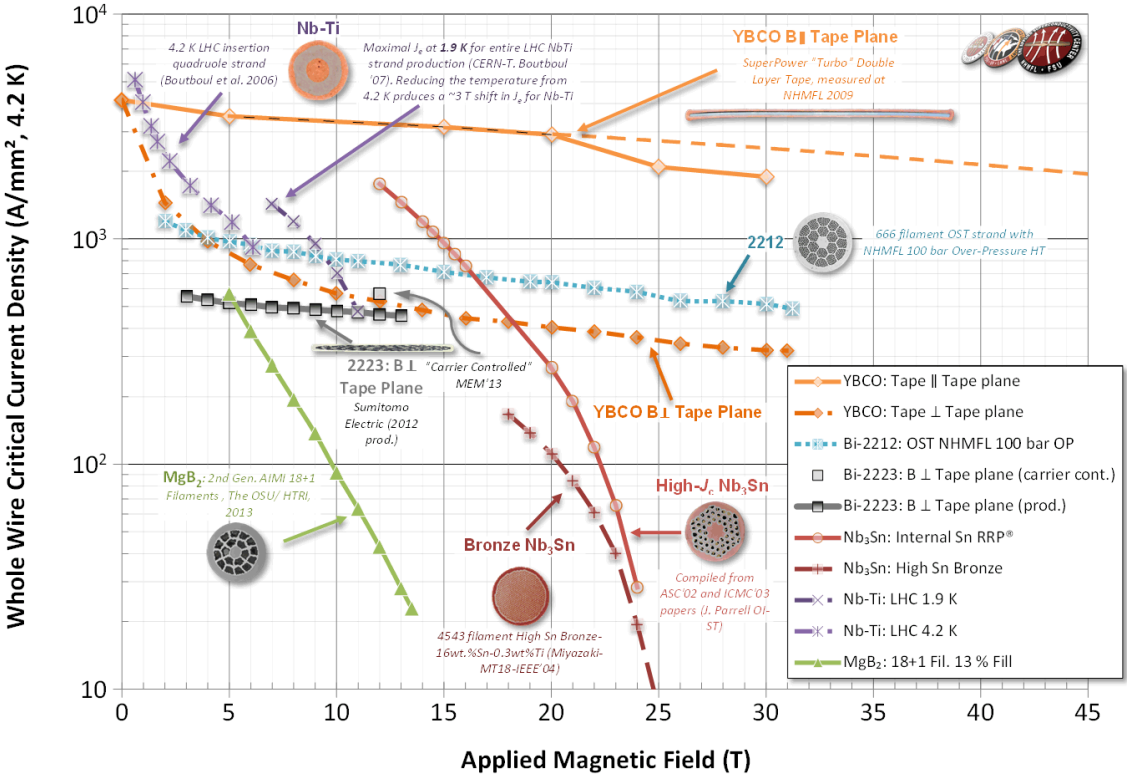

Fig. 7.3.1: Whole wire critical current density of main superconductors at 4.2 K [1]

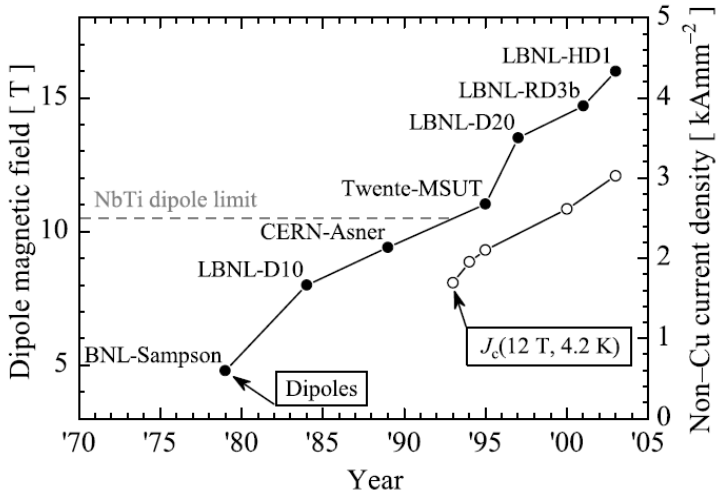

Fig 7.3.2: Evolution in the highest field in Nb_3Sn dipoles [2]

7.3.1.3 *Challenges to Meet the SPPC Requirement*

1) **Performance, volume, and cost:** Performance, volume, and cost of superconductors: based on the present critical current performance of superconductors, thousands of tons of Nb_3Sn and HTS superconductors will be needed to fabricate the SPPC 20-T dipole and quadrupole magnets. The cost for the superconductor materials will be very high and a major cost driver. However, there is significant potential for the further increase of J_c in both Nb_3Sn and Bi-2212 [3-4] and this is expected to reduce the required quantity of superconducting materials and the cost of the SPPC project. It will be a major challenge for superconductor manufacturing industries to improve the performance, reduce the cost and scale up for the volume of superconductors required for the project.
2) **High-level magnetic force at 20 T:** The magnetic force in superconducting coils increases as the square of the field. With a 20-T level main field, the stress in Nb_3Sn or HTS coils are higher than 200 MPa. As both Nb_3Sn and Bi-2212 superconducting materials are strain sensitive, the J_c goes down quickly with increasing strain. An innovative method [5] to manage the strain level in coils is expected to be developed in the future. YBCO, on the other hand, can tolerate much higher stress and strain (a factor of three more) without showing any degradation.
3) **Field quality of HTS coils wound with tape conductors:** The current distribution in HTS tape conductors is not as uniform as LTS (Low temperature superconductor) conductors such as NbTi and Nb_3Sn, which are made up of thousands of small filaments of only a few microns in diameter. The magnetization effect in tape conductors is also more serious because of the much larger size of conducting elements. Both effects make it difficult for the magnets with the HTS coils to reach the field quality uniformity level of 10^{-4} with the present designs. Future detailed study and innovative solutions are expected to produce designs with the required field quality.
4) **Quench protection of HTS coils:** The quench propagation speed in HTS coils is hundreds of times lower than with LTS coils, which makes the present quench

detection and protection methods unsuitable for HTS coils. Future study and innovative solutions are expected in the future.

5) **Crosstalk:** Twin aperture 20-T magnets must achieve a field quality of 10^{-4} and an outer diameter of 900 mm. So the magnetic cross-talk between the two apertures should be controlled without increasing the size of the magnet. Moreover, the iron saturation effect should be carefully studied and field errors must be balanced between the field levels at injection (low current) and collision (high current).

A preliminary R&D plan for the 20-T magnets is in Section 11.12.

7.3.1.4 *Preliminary Design for the SPPC Superconducting Magnets*

A preliminary conceptual design of a 50-mm aperture 20-T 2-in-1 common coil dipole is shown in Fig. 7.3.3. The design is based on the current J_c level of the superconductors. The large bend radius allows the use of "React and Wind" technology for coil fabrication. The short sample dipole field of the magnet is 22 T at 4.2 K (the figure shows 20-T dipole field at 91% load line ratio). The outer diameter of the iron yoke is 720 mm. In total six racetrack coils are needed to reach a short sample field of 22 T. Two inner coils are made with Bi-2212 and four outer coils with Nb_3Sn. All the coils have simple racetrack geometry except a small one with a few turns at the pole. The Bi-2212 coils are wound with 20-mm wide cables. The cable is fabricated with fifty Bi-2212 round wires of 0.8 mm in diameter. The outer four Nb_3Sn coils are wound with two types of cables: 22-mm width wider cable fabricated with fifty-five Nb_3Sn wires and 15-mm width narrow cable fabricated with thirty-seven Nb_3Sn wires. The operating current is 14.5 kA at 20 T. The critical current density of the Nb_3Sn and Bi-2212 superconductors is calculated with the data in [1, 2] respectively (Bi-2212 with 100 bar overpressure heat treatment). For such a 20-T common coil dipole of 1 m length, the required length for the 0.8-mm diameter Nb_3Sn wire is 39 km (about 166 kg) and for the 0.8-mm diameter Bi-2212 wire is 13.8 km (about 60 kg). We will also consider the use of YBCO tape in future design studies.

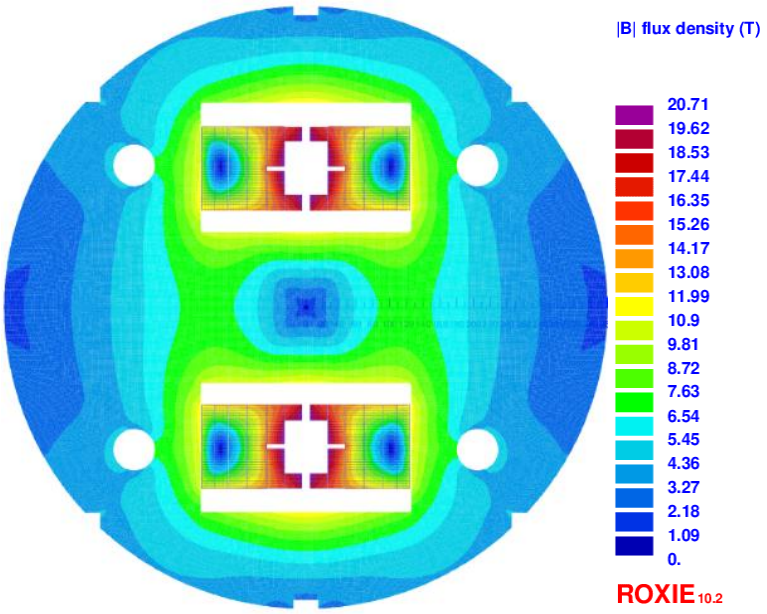

Fig. 7.3.3: Conceptual design of the 20-T dipole for SPPC

7.3.2 **Vacuum and Beam Screen**

7.3.2.1 ***General Vacuum Considerations***

7.3.2.1.1 Vacuum Requirements

SPPC has three vacuum systems: beam vacuum for the chambers in the low-temperature sections, beam vacuum for the chambers in the room-temperature section, and insulation vacuum for the cryogenic system.

Insulation vacuum of the cryogenic system which aims to avoid convective heat transfer does not need high vacuum; the room-temperature pressure in the cryostat before cool-down does not have to be better than 10 Pa, and at cryogenic temperature, without any significant leak, the pressure will stabilize around 10^{-4} Pa. As a huge volume of insulation vacuum is needed at SPPC, careful design is needed to reduce the cost.

The requirement for beam vacuum is much more stringent because of the beam lifetime requirement which depends on the nuclear scattering of protons on the residual gas. To ensure about 100 hours beam lifetime, the equivalent hydrogen gas density should be below 10^{15} H_2 per m^3, and should be below 10^{13} H_2 per m^3 in the interaction regions around the experiments to meet the requirement of a low background. Correspondingly, the equivalent pressure at room temperature will stabilize in the range from 10^{-8} to 10^{-9} Pa.

7.3.2.1.2 Beam Vacuum in the Low-Temperature Sections

In the design of the vacuum chamber in the cryogenic system two aspects need to be simultaneously considered: the vacuum pumping strategy and the thermal absorbing circuit. First, the cold surface in the chamber will condense the gas to its saturated vapor pressure as a cryopump; second, the heat leak into the cryogenic system would be amplified 1000 times at room temperature.

The vacuum pumping strategy should be designed to correspond to the working temperature of the superconductor. For SPPC, the working temperature of the superconductor is always below 20K, where the residual gas is only H_2 whose saturated vapor pressure is larger than 1.33×10^{-9} Pa. Actually, the saturated vapor pressure of H_2 is 9071.7 Pa at 20K, and 1.33×10^{-9} Pa at 3K. This means to pump H_2 another method must be used. A Non Evaporable Getter (NEG) coating on the chamber is a good choice. For the cryogenic system working above 3K, and for the one working below 3K, the H_2 could also be pumped by the wall of the chamber. The beam screen is a key issue here and is discussed in the next subsection.

7.3.2.1.3 Vacuum Instability Issues

Vacuum instability issues are currently under investigation.

7.3.2.2 *Beam Screen*

The main function of a beam screen is to shield the cold bore of the superconducting magnets from SR. At SPPC SR is especially critical because of the very high beam energy and very high magnetic field in the arc dipoles. The estimated SR power is about 64 W/m per aperture in the arc dipoles, which is much higher than the 0.22 W/m at LHC. This greatly increases the difficulty of the beam screen design.

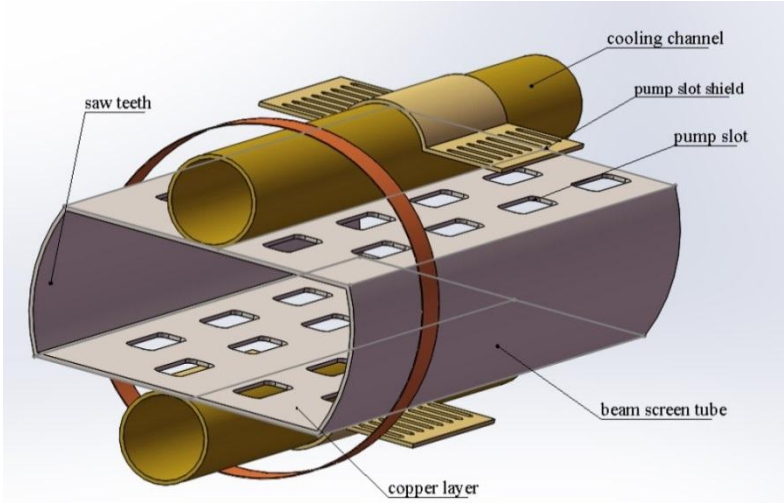

Figure 7.3.4: Schematic diagram for a beam screen under consideration for SPPC

The design of the beam screen should take into account different aspects in the SPPC ring, such as vacuum stability, mechanical support, influence on beam dynamics and refrigeration power. Figure 7.3.4 shows a schematic under consideration for the beam screen at SPPC. The main problems are as follows:

1) The SR power deposition in the SPPC main dipoles is two orders of magnitude higher than that at LHC. Therefore, how to bring the high power out of the cold bores of the superconducting magnets is a critical issue. If liquid helium is chosen as the refrigerant, it is hard to keep the temperature below the 4.2 K and the cost will be very expensive. The operating temperature of the beam screen must be increased for economic reasons and to decrease technical difficulty. However, the operation temperature of the beam screen is limited by several factors. The resistive wall impedance is increased with the increase of operating

temperature, and this may cause collective beam instability. The operating temperature is also limited by heat leakage to the cold bore which is dependent on the temperature difference between the two bodies. Thus the operating temperature should be chosen carefully. Different refrigerants can be considered, such as liquid neon or liquid oxygen.

2) Vacuum in the beam screen is a difficult problem. Several factors can impact the vacuum in the beam pipe, for example, the beam structure, the beam energy, the beam population, the critical photon energy and synchrotron radiation power. Beam structure has an important effect on the buildup of the electron and ion clouds which may lead to vacuum instability. Proper beam screen structure may restrain the generation of the electron cloud. The inner wall is coated by a thin film of low secondary electron yield to reduce electron production. As the pressure increase stimulated by SR photons is much more serious than in LHC, the reduction in the desorption yield of the inner wall is very important here. The pumping speed is the dominant factor for vacuum stability. The beam screen must be designed with sufficient transparency to retain an effective pumping speed. However, good transparency obtained by adding more slots will increase the resistive impedance which may cause beam instabilities. The beam screen design has to solve all these problems.
3) The beam screen should have sufficient strength to resist the instant huge electromagnetic force generated by superconducting magnet quenches. Stainless steel can also be used as the base structure material at SPPC, and a thick copper film of 75 μm coated on the base to decrease the wall impedance. On the other hand, the thinner the film is, the smaller the electromagnetic force.
4) The beam screen structure shape and size needs to be optimized in order to decrease the transverse wall impedance.

In order to solve the design and technical problems for the beam screen, R&D efforts are to be carried out as follows:

1) Based on the thermal analysis of the beam screen operating at high temperatures (40 - 60K), one should study different structures and refrigerants. A test bench will be set up to check the simulation results. This test bench will include the heat source, beam screen, cold bore, super conductor and refrigerator.
2) Different coatings on the stainless steel base will be studied to reduce the wall impedance and secondary electron yield at 40-60 K.

7.3.3 **Other Technical Challenges**

Besides the two most critical technologies described above, high-field magnets and vacuum/beam screens, there are also other important technologies requiring development in the coming decade in order to build SPPC. Among them, the machine protection system requires an extremely highly efficient collimation system and a very reliable beam abort system. The latter is very important for damping the huge energy stored in the circulating beams when the magnet quenches or other abnormal operating conditions occur. If the extraction system has to be installed in a relatively short straight section, one has to develop a new technology for more powerful kickers. A complicated feedback system is required to maintain beam stability. The beam control system also controls emittance blow-up in the main ring which is important for controlling beam-

beam induced instabilities and leveling the luminosity. Beam loss control and collimation in the high-power accelerators of the injector chain pose additional challenges. A proton RCS of 10 GeV and about 4 MW is still new to the community and needs special care. The gigantic cryogenic system for magnets, beam screens and RF cavities also needs special consideration.

7.3.4 References

1. Peter Lee, "A Comparison of Superconductor Critical Currents," online available: http://www.magnet.fsu.edu/magnettechnology/research/asc/plots.html.
2. D.R. Dietderich, A. Godeke, Cryogenics 48, (2008) p. 331–340.
3. X. Xu, M. Sumption, X. Peng, and E. W. Collings, "Refinement of Nb3Sn grain size by the generation of ZrO2 precipitates in Nb3Sn wires," Appl. Phys. Lett. 104, 082602 (2014).
4. D. C. Larbalestier, J. Jiang, U. P. Trociewitz, F. Kametani, C. Scheuerlein, M. Dalban-Canassy, M. Matras, P. Chen, N. C. Craig, P. J. Lee, and E. E. Hellstrom, "Isotropic round-wire multifilament cuprate superconductor for generation of magnetic fields above 30 T," Nature Materials, Vol. 13, (2014) pp. 375-381.
5. N. Diaczenko et al., "Stress management in high-field dipoles," Proc. of PAC1997, Vancouver, (1997) p. 3443-3445

7.4 Reconfiguration of the Accelerator Complex

7.4.1 Injection Chain

The injector chain by itself is an extremely large accelerator complex. To reach the beam energy of 2.1 TeV required for injection into the SPPC, we require a multi-stage acceleration system, with a general accelerator design rule of 10-20 times in energy gain in each stage, with the exception of p-RCS where the energy gain is lower than 10. Here, a design of a four-stage injector chain has been outlined. It not only accelerates the beam to the energy for injection into the SPPC, but also prepares the beam with the required beam properties such as the bunch current, bunch structure, and emittance, and as well the beam fill period. As shown in Figure 7.4.1, the present design of the injector chain includes a superconducting linac (p-Linac) of 1.2 GeV in energy and 0.7 mA in average current, a rapid cycling synchrotron (p-RCS) with a repetition rate of 25 Hz which boosts energy to 10 GeV, a medium-stage synchrotron (MSS) to 180 GeV which has the relatively lower repetition rate of 0.5 Hz, and the Super Synchrotron (SS) to 2.1 TeV which is a synchrotron based on superconducting magnets with maximum dipole field of about 8 Tesla. Higher repetition rates for the lower energy stages help reduce the SS cycling period and the SPPC beam fill period. The high-power beams in the complex can also be used for other applications or research purposes when the accelerators are not preparing beam for the injection into SPPC. As the bunch population is determined by the SPPC, the accelerators of the injector chain have the potential to load more accumulated particles or deliver higher beam power for their own diverse applications.

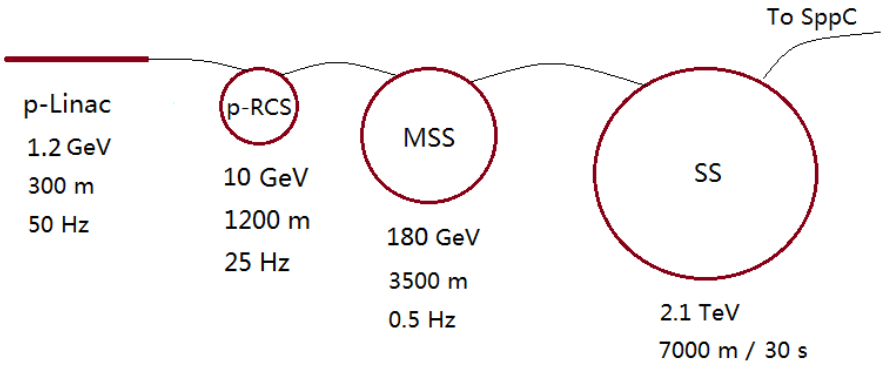

Figure 7.4.1: Injector chain for the SPPC

A dedicated heavy-ion linac (I-Linac) together with a new heavy-ion synchrotron (I-RCS), in parallel to the proton linac, is needed to provide heavy-ion beams at the injection energy of the MSS, with a beam rigidity of about 36 Tm which is the same as the 10 GeV proton beam. The main parameters for the proton injector chain are shown in Table 7.4.1.

Superconducting linacs have undergone tremendous development and will make even more progress in the next decade. A pulsed linac of 1.2 GeV or so will be much less expensive than some years ago. Hence we have chosen 1.2 GeV in energy and a 50 Hz repetition rate for the p-Linac. The total beam power of 0.84 MW can be partially used for other applications, as only half of the beam is fed to the next-stage of acceleration in the p-RCS.

The p-RCS is a really powerful machine in beam power. Around the world there are no examples of beams of this power and energy combined. Only one of the proton driver schemes or studies for the future Neutrino Factory has performance close to this. The high repetition rate of 25 Hz will shorten the beam filling time in the MSS. The MSS is a medium cycling rate synchrotron which takes a small fraction of the beam pulses available from the p-RCS. This means that most of the beam pulses from the p-RCS can be used for other physics programs. The MSS will use mature accelerator technology but be on a larger scale than existing proton rapid cycling synchrotrons.

The MSS has a beam power similar to the p-RCS but with much higher beam energy. The SPS at CERN and the Main Injector at Fermilab are two good examples for its design. However, due to higher beam power the beam loss rate should be controlled more strictly. A bunch splitting technique by using a multiple harmonic RF system is used here and in the SS to prepare the bunch gap of 25 ns required by the SPPC. Certainly, the beam from the MSS will find additional physics programs in addition to being the injector for the SS.

The SS will be a special machine, as it will use superconducting magnets similar to those used at LHC, perhaps with a higher ramping rate. However, we do not need to consider synchrotron radiation here. Therefore, there are no apparent critical technical risks in building the SS. It is unclear if the beam from the SS can find its own physics programs besides being the SPPC injector.

Table 7.4.1: Main parameters for the injector chain at SPPC

	Value	Unit		**Value**	**Unit**
p-Linac			**MSS**		
Energy	1.2	GeV	Energy	180	GeV
Average current	0.7	mA	Average current	21	uA
Length	~300	m	Circumference	3507	m
Repetition rate	50	Hz	Repetition rate	0.5	Hz
Beam power	0.84	MW	Beam power	3.8	MW
p-RCS			**SS**		
Energy	10	GeV	Energy	2.1	TeV
Average current	0.35	mA	Total protons	5.3E14	
Circumference	900	m	Circumference	7000	m
Repetition rate	25	Hz	Repetition period	30	s
Beam power	3.5	MW	Protons per bunch	2.0E11	
			Dipole field	8	T

7.4.2 **Integration of the CEPC and SPPC**

The present proposal calls for continuing the CEPC *e*+*e*- program after the SPPC is brought into operation. Housing both CEPC and SPPC, the two largest and most complex particle accelerators in the world, in a common underground tunnel and operating them alternatively and optionally simultaneously are unprecedented. Thus there is no prior experience we can learn from. While in principle it is plausible, there are high technical and operational risks associated to such a plan in addition to the complications of machine operation and maintenance. Therefore we must apply careful consideration and planning at an early stage of the CEPC-SPPC project. In this section, we first present a brief discussion on the anticipated risk factors and suggestions for mitigating these risks. We then address several special issues for achieving good integration of the CEPC and SPPC facilities.

7.4.2.1 ***Project Uncertainty***

While it is necessary and also advantageous to start the basic planning and preliminary conceptual design studies for SPPC at the present time, nevertheless, there are many intrinsic uncertainties which could prevent us reaching a perfect solution. The first and perhaps the biggest risk factor is the challenge in anticipating a long term science program, considering that the project life cycle of CEPC-SPPC could easily exceed 40 years. The development of science may change the research goals and direction in the future which could significantly deviate from what we are planning now. The progress of accelerator technology development in several key areas (such as ultra-high-field superconducting magnets) is also difficult to predict over a long time span. There are well known cases of projects that failed to reach important science goals due to various limits or constraints posed in the beginning phase of the projects. Therefore,

to mitigate these risk factors and improve the chance of success of SPPC, it is advisable to leave a sufficiently large margin in the technical aspects of the facility within the foreseeable budget scenario. This includes maximally expanding the SPPC performance range (primarily the energy range and luminosity target), and to take the least optimistic forecast of technology developments

7.4.2.2 *Geometric Constraints and Considerations*

Considerable study and planning have been carried out for fitting these two independent super colliders into the same underground tunnel. One aspect of this study is to satisfy the geometric constraints. Presently, three collider rings, two for the proton beams and one shared by electron and positron beams, plus a full-energy lepton booster ring, will be housed in the tunnel, thus requiring a sufficiently large tunnel cross section. This also needs to take into account the large space between the rings for machine maintenance and repair. Detectors for the two colliders occupy different straight sections of the rings; however, by-passing of the detectors of the other collider is needed and also not trivial, due to the extremely high beam energies for both colliders. At other locations that large machine elements such as SRF modules are installed, the beam lines of the other collider also may need a special design.

7.4.2.2.1 Construction and Commissioning Considerations

Installation of SPPC may pose one of the biggest challenges. It will most likely require a long (multi-year) shutdown of CEPC, affecting its physics program. As a matter of the fact, in the design studies of LHeC, a Large Hadron-electron Collider envisioned at CERN, a linac-ring collider scenario was chosen as the baseline primarily to avoid a long shutdown of LHC. The SPPC design should be optimized to enable rapid installation and commissioning to shorten the CEPC shutdown. Protection of the CEPC machine during the construction and commissioning of the SPPC is also challenging.

7.4.2.2.2 Operational Considerations

Placing the CEPC and SPPC collider rings side-by-side may provide an opportunity for sharing resources and equipment such as the liquid helium supply line and power supply line and network communication lines, leading to a cost reduction for SPPC. Radiation protection may also be shared, requiring less or no upgrade for operating the SPPC, particularly under the operational mode of alternative running of the two colliders. The central control system and machine control center staffing may also be shared. By having these two installations at the same site other cost savings will be the shared campus with its infrastructure such as administration, on-site computers, user amenities and library.

There are also restrictions caused by two super colliders in the same complex. If the two colliders are indeed operated simultaneously, there will be considerable load variation in the power grid, at the time the CEPC enters the top-off mode, or the SPPC hadron injector complex (including the linac and three booster rings) prepares and injects a proton beam into the collider storage ring. Engineering studies should be carried out and if it proves this is a serious issue, the CEPC-SPPC infrastructure must be proper designed and constructed to handle such a load variation.

On the engineering side, there are several technical problems that are further amplified by the “two colliders in one tunnel” arrangement. For example, removing the heat generated from the machine elements of the two colliders must be addressed in

order to maintain a uniform and stable temperature inside the tunnel, since a large temperature variation may affect proper functioning of some electronic systems. Though it will likely not be a problem, one also needs to evaluate the effect of heat generated by the CEPC warm magnets on the SPPC cold magnets and cryogenic system.

Machine protection is another challenge for the CEPC-SPPC joint facility. An event or even worse a major accident of one collider could affect the other, causing tremendous damage of the equipment and monetary loss.

It is foreseen that simultaneous operation of two colliders will introduce an overhead and reduce the duty factors of an individual collider. . Maintenance and repair of one collider may force suspension of operation and data-taking of the other collider.

8 Option for *e-p* and *e-A* Colliders

8.1 Introduction

High energy proton-proton colliders, such as the SPPC, will be the energy frontier of fundamental research in physics accessible by accelerator-based facilities, while the electron-positron collider, such as CEPC, will provide a clean and much needed precision for the study of the Higgs, to shed light on the mass generation and the mystery behind spontaneous symmetry breaking. However, the Higgs mechanism is almost irrelevant for mass generation of nucleons and nuclei, which make up 99% of the mass of all particles in our visible world. Nucleons and nuclei emerged from the evolution of our universe following its birth (the Big Bang), encoding all the history of evolution. But, neither the SPPC nor the CEPC type of accelerator facility is natural for exploring the precise internal structure of nucleons and nuclei, and their emergence, although both facilities can create hadronic matter from the energy of the collisions.

Construction of CEPC and SPPC in a common accelerator complex provides a great opportunity to realize collisions of protons or ions with electrons or positrons (e-p or e-A where e stands for either e- or e+) in an ultrahigh center-of-mass (c.m.) energy range up to 4.1 TeV, far beyond the energy of any existing and proposed future lepton-hadron colliders including the Electron-Ion Collider (EIC) in the United States and the LHeC at CERN. With precise control of the scattered lepton, such a lepton-hadron scattering facility in the ultra-deep inelastic scattering (DIS) region will provide a clean and fully controlled probe of the inner structure and quantum fluctuations of the dynamics of a proton down to the unprecedented distance scale of 10^{-4} fm (or one ten-thousandth of the proton size). This could be sensitive to the dynamics that might restore the spontaneously broken symmetries of the standard model, and the quantum fluctuations caused by physics beyond the standard model. These measurements of a proton with a momentum transfer of over one TeV while keeping the proton intact, lead to the finest tomographic images or the unprecedented spatial distributions, of quarks and gluons of momentum ranging from the one tenth to the one thousandth of proton's momentum. This information is sensitive to the color confinement of QCD.

The SPPC with proton beams replaced by heavy ion beams will produce the hottest quark-gluon plasma ever in a laboratory setting. Such extreme conditions could only have existed in the first few microseconds of our universe With the option of colliding leptons with heavy ions in an *e-A* collider, the heavy ions with various atomic weight A could act as the smallest vertex detectors in the world to “map” out the dynamics of color neutralization and “probe” the emergence of hadrons, a necessary phase in the evolution of our universe from its birth, which is largely unknown. With the CEPC and the SPPC in a common accelerator complex, we could have a unique, and possibly, the only facility in the world able to explore the fundamental structure matter, and its birth and evolution in one place.

It is relatively straight forward to bring a beam from CEPC and a beam from SPPC into collision at one or multiple interaction points (IP). The estimated luminosity in the *e-p* collisions can reach several times $10^{33}/cm^2/s$ at each detector. The challenge is to design an interaction region (IR) to optimize performance of this collider, and to bypass the non-colliding beams near this detector if the *e-p* or *e-A* collisions are to be run simultaneously with the SPPC or CEPC programs.

In this chapter, we summarize a preliminary design study of an *e-p* or *e-A* collider. We begin with a presentation of general design considerations, followed by nominal parameters for *e-p* and *e-A* collisions. We conclude this chapter with some additional comments and a brief summary.

It should be understood that the positron beam can also be used and there is virtually no change of the design parameters for positron-proton or positron-ion collisions.

8.2 Design Considerations

The basic assumption of this design study is that no major and costly upgrade will be required in either CEPC or SPPC for realizing *e-p* or *e-A* collisions. Thus the *e-p*/*A* collider performance will depend entirely on the beams envisioned for the future *e*+*e*- and *pp* colliders. The conceptual design also takes into account the operational limits of CEPC and SPPC such as their maximum energies and currents, the synchrotron radiation power budget, the final focusing of the colliding beams as well as fundamental beam physics effects such as instabilities, particle scattering phenomena and beam-beam interactions. Within these limits, nevertheless, we are free to alter some of the beam or machine parameters such as the bunch charge and repetition rate, beam emittance aspect ratio or crab crossing angles, for achieving an optimized collider performance.

Since *e-p* or *e-A* collisions are an additional capability of the facility, naturally there is a question about whether simultaneous operation with *e*+*e*- or *pp* collisions or even both is feasible while still being able to deliver performance acceptable to the physics program. Non-dedicated operation may introduce additional constraints on the electron or proton/ion beam parameters in order to maintain good performance of the *e*+*e*- or *pp* program.

The two biggest differences between the CEPC and SPPC machines are the bunch structure and emittance. The electron beam has very few bunches (current design up to 50). On the other hand, the proton or ion beams in SPPC have a very large number of bunches, varying from 3000 to 6000, depending on the operational bunch repetition rate. Clearly it would be very inefficient to preserve the original bunch structures since the majority of the proton or ion bunches will not collide with any electron or positron bunches. This plus an extreme asymmetry of the beam emittance aspect ratio of the lepton and hadron beams (see below) effectively excludes the option of simultaneous operations of *e*+*e*- and *e-p*/*A* collisions in the complex.

Without the constraint of running *e*+*e*- and *e-p/A* collisions simultaneously, the electron beam is no longer limited to 50 bunches; thus it can be altered to match the bunch numbers of a proton beam from SPPC. In addition, since only one lepton beam is required in the CEPC ring in this scenario, the electron beam current can be doubled under the same limit (50 MW per beam) of synchrotron radiation power, an advantage which will double the *e-p* or *e-A* luminosities.

Selection of the beam focusing parameters is also driven by the usual interaction region design considerations. For example, the spot sizes of the two colliding beams should be matched at a collision point for reducing beam-beam effects. However, the emittances are very different. The lepton beam is extremely flat (the aspect ratio can be as large as 333) while the proton beam is basically round. Matching of the two beams requires a very large β^* for the electron beam in the vertical direction; this blows-up the beam-beam parameters. The operational scenario where *e-p* and *e*+*e*- are not run simultaneously allows us to change the electron beam to round by utilizing transverse

coupling. This should greatly simplify matching of the beam spot sizes, therefore resulting in a significant increase in *e-p* luminosity.

In the SPPC energy regime, synchrotron radiation and its effect on the proton or ion beam are no longer negligible. The damping time of a proton or heavy ion beam is similar or even shorter than the time of a beam store. As a consequence, the proton or ion beam emittance will approach an equilibrium value (a balance of synchrotron radiation damping and quantum excitation, and intra-beam scattering) during the store. This will affect the peak luminosity as well as the integrated luminosity. This will be discussed further in section 8.4.

This *e-p*/*A* collider is a highly asymmetric one, with an energy ratio over 370, higher than any other e-p/A colliders ever built, designed or studied. Simple kinematics shows that the particles from collisions will go dominantly in the forward direction of the proton or ion beam, and are further highly concentrated around zero scattering angle. While the science program and detector design are still under development for *e-p* or *e-A* collisions based on CEPC-SPPC, it is expected that the forward detection of particles with extremely small scattering angles will be a critical requirement or feature of the detector design. Designing an interaction region to support such extremely forward detection will be very challenging. In section 8.5 we present a straw-man design.

The science program utilizing deep inelastic scattering as a probe usually requires experimental data collected over an energy scan, namely, collecting data at varying energies of the colliding electron and/or proton (ion) beams. Such an energy scan requires the collider design to be optimized over a broad center-of-mass energy range. The future CEPC-SPPC *e-p* and *e-A* design studies will take this into account. In this report, we present a preliminary conceptual design with nominal parameters at just one representative energy point, namely, 120 GeV electron energy and 35.6 TeV proton energy (or 14 TeV per nucleon for all-stripped lead ions), the highest energies that CEPC and SPPC can provide.

8.3 *e-p* Collisions

Table 8.3.1 presents nominal design parameters for *e-p* collisions for the case with only one beam in the CEPC ring. The electron beam current is 33.8 mA and one is still under the operational limit of 100 MW total SR power. The electron beam could have thousands of bunches to match the bunch pattern of the proton beam when the electrostatic separators of the pretzel orbital scheme are turned off. For achieving luminosity optimization and also a better interaction region design, we not only make the electron beam round by using transverse coupling, but also obtain a factor of 6.3 reduction of the electron beam equilibrium emittance by changing to different optics for the electron ring, namely, changing the betatron phase advance of an arc FODO cell from 60 °to 135 °.

There are two sets of *e-p* collision parameters in Table 8.3.1 which correspond to two possible scenarios. The first set is a dual-program operation mode such that *e-p* collisions are run simultaneously with *pp* collisions at other IPs and detectors. In this case, the proton beam parameters such as the bunch length and transverse emittance are identical to these of the SPPC design presented in other chapters. However, the proton beam current is reduced to 0.86 A from the 1 A nominal value in order to keep the electron beam-beam parameter below 0.15. This will reduce the luminosity of the *pp* collisions by 14%. The bunch numbers for both electron and proton beams are nearly

6000, maintaining a 40 MHz repetition rate (thus 25 ns bunch spacing) as well as a gap (or multiple gaps) of 5.2 km long in the beam bunch trains. The final focusing of the proton beam is also identical to that for *pp* collisions; however, the electron β* is increased to 7.2 cm in order to match the beam spot size at the collision point. As a comparison, the CEPC *e+e-* vertical β* is only 1.2 mm. The luminosity without geometric corrections is 3.49×10^{33} /cm^2/s.

In the second operational scenario, the *e-p* collisions are run in a dedicated mode, namely, without *pp* collisions at other detectors. This permits further adjustment of the proton beam parameters to enhance performance, nearly doubling the *e-p* luminosity to 6.04×10^{33} /cm^2/s. The proton emittance is reduced to 2.35 mm mrad, which is achievable using present accelerator technologies and, of course, a new ion injector complex. This emittance reduction can be maintained by synchrotron radiation damping. There are also less bunches in both colliding beams thus requiring half of the proton beam current without loss of luminosity.

Table 8.3.1: Nominal parameters for *e-p* collisions in the CEPC-SPPC facility

Operational scenario		***e-p* and *pp***		***e-p* only**	
Particle		proton	Electron	Proton	Electron
Beam energy	GeV	37,400	120	37,400	120
Center-of-mass energy	GeV	4240		4240	
Beam current	mA	860	33.8	430	33.8
Particles per bunch	10^{10}	16.8	0.66	16.7	1.31
Number of bunch		5973	5973	3000	3000
Bunch spacing	Ns	25	25	50	50
Bunch repetition rate	MHz	40	40	20	20
Normalized emittance, (x/y)	μm rad	4.1	250	2.35	250
Geometric emittance, h. / v.	nm rad	0.1	1.07	0.059	1.07
Bunch length, RMS	cm	7.55	0.242	7.55	0.242
Beta-star (x/y)	cm	75	7.5	75	4.15
Beam size at IP, (x/y)	μm	8.78	8.78	6.65	6.65
Beam-beam parameter per IP(x/y)		0.0002	0.15	0.00068	0.15
Luminosity per IP without reduction	10^{33}/cm^2/s	3.67		6.34	
Crossing angle	mrad	0.8		0.8	
Crossing angle reduction with crabbing		1		1	
Hour glass reduction factor		0.898		0.783	
Luminosity per IP, with reduction	10^{33}/cm^2/s	3.3		5.0	

The two geometric correction factors to the *e-p* collision luminosity are the crab crossing and hour-glass effects. Due to the very short bunch spacing and high energies of the colliding beams, a finite crossing angle is introduced to enable rapid beam separation near an interaction point, thus alleviating the parasitic beam-beam effect. The minimum crossing angle is 0.8 mrad which provides a horizontal separation of $5(\sigma_e+\sigma_p) \approx 3$ mm. σ_e and σ_p are the rms bunch sizes of the electrons and protons at the first parasitic collision point which is 3.75 m or 7.5 m from a collision point for 25 ns or 50 ns bunch spacing respectively. We propose to utilize SRF crab cavities on both sides of a collision point (the so-called local crabbing compensation scheme) to restore head-on collisions; otherwise the luminosity loss due to a crossing angle is enormous. The required transverse kick voltages are estimated to be ≈ 63 MV and ≈ 1 MV for the proton and electron beams respectively, assuming a 650 MHz RF frequency and modest values for the betatron functions (400 m and 200 m) at the location of the crab cavities. We assume there is no luminosity reduction with crabbing.

It can be shown that due to a significant relaxation increase of the electron β*, the luminosity reduction factors due to the hour-glass effect are 90% and 79% for the two parameter sets in Table 8.3.1.

The *e-p* luminosities at other beam energies can be estimated following a similar design approach as well as similar parameter limits. Table 8.3.2 shows the *e-p* luminosities at several representative electron energies (*Z* and *W* factories). At the lower energies, the electron beam emittance is decreased and its current can be increased while still observing the same operational limit of radiation power, leading to higher luminosities.

Table 8.3.2: e-p collisions with different electron energies at the CEPC-SPPC facility running in a dedicated operation mode

Particle		Proton	Electron	Proton	Electron	Proton	Electron
Beam energy	GeV	37,400	45 (***Z***)	37,400	80 (***W***)	37,400	175 (***t***)
Center-of-mass energy	GeV	2597		3462		5120	
Beam current	mA	45.5	1480	256	171	643	7.5
Particles per bunch	10^{10}	0.89	28.9	5.0	3.34	25	0.29
Number of bunch		5973		5973		3000	
Bunch spacing	ns	25		25		50	
Normalized emit., (x/y)	μm rad	2.35	13.2	2.35	74.1	2.35	775
β* (x/y)	cm	75	29.5	75	9.25	75	1.95
Beam-beam parameter / IP		0.015	0.15	0.0017	0.15	0.0005	0.058
Hour glass reduction		0.991		0.931		0.556	
Luminosity per IP (with hour-glass reduction)	10^{33} /cm^2/s	14.6		9.31		1.17	

8.4 *e-A* Collisions

The conceptual design of *e-A* collisions at the CEPC-SPPC facility follows the same design principles as for *e-p* collisions; nevertheless, the synchrotron radiation damping effect on the high energy heavy ion beams is surprisingly much stronger than that on the proton beams, thus requiring some additional considerations and beam parameter adjustments.

It can be shown by simple scaling that the synchrotron radiation damping time of an ion beam is a factor of A^4/Z^5 shorter than that of a proton beam in a storage ring. Both beams have the same magnetic rigidity. *A* is the atomic number and *Z* is the number of stripped electrons from the ion. Taking a fully stripped lead ion ($^{208}Pb^{82+}$) as an example, the above damping time reduction factor is about 0.5. Thus damping of the lead ion beam is twice as fast as that of a proton beam. The equilibrium emittance of an ion beam has an even higher reduction factor, Z^3/A^4, which equals 0.0003 for the fully stripped lead ion. This means the lead ion beam equilibrium emittance (in a balance of synchrotron radiation damping and quantum excitations) is four orders of magnitude smaller than that of the proton beam. This is clearly a non-physical result since intra-beam scattering which can cause rapid emittance growth has not been taken into account. These small beam emittances lead to a very high particle density which increases the probability of intra-beam scattering, thus resulting in a growth of the beam emittance. After one to two damping times, the ion beam emittance will reach an equilibrium value (in a balance of the radiation damping, quantum excitation and intra-beam scattering induced heating). It has been estimated this true equilibrium emittance of a fully stripped lead ion beam is about 0.22 μm rad in the SPPC collider ring, approximately 10

times smaller than the proton emittance. We use this value to estimate the luminosity of *e-A* collisions shown in Table 8.4.1. It should be noted that an accurate estimate of the ion beam emittance depends on the lattice design of the SPPC ring. Other parameters in Table 8.4.1, such as the bunch length and number and final focusing, are identical to the *e-p* collision design shown in Table 8.3.1. The luminosity reaches $1.1 \times 10^{32}/cm^2/s$ per nuclei per interaction point. Multiplying the number of nucleons inside a lead ion, the luminosity reaches $2.25 \times 10^{34}/cm^2/s$ per nucleon per detector.

Table 8.4.1: Nominal parameters for *e-A* collisions based on the CEPC-SPPC facility

Particle		**Lead ($^{208}Pb^{82+}$)**	**Electron**
Energy	GeV/u	14,744	120
Beam current	mA	425	33.8
Particles per bunch	10^{10}	0.2	1.31
Number of bunch		3000	3000
Bunch spacing	ns	50	50
Bunch repetition rate	MHz	40	40
Normalized emittance, (x/y)	μm rad	0.22	250
Geometric emittance, h. / v.	nm rad	0.14	1.07
Bunch length, rms	cm	7.55	0.242
β* (x / y)	cm	75	1
Beam size at IP, (x/y)	μm	3.25	3.25
Beam-beam parameter per IP(x/y)		0.0028	0.15
Luminosity per nuclei per IP without reduction	$10^{33}/cm^2/s$	0.032	
Crossing angle	mrad	0.8	
Crossing angle reduction (with full crabbing)		1	
Hour glass reduction factor		0.355	
Luminosity per nuclei per IP, with reduction	$10^{33}/cm^2/s$	0.011	
Luminosity per nucleon per IP, with reduction	$10^{33}/cm^2/s$	23.6	

8.5 Additional Comments

It is likely that the highest cost item for adding this *e-p* or *e-A* capability to the facility is the detector. It is anticipated that design of an adequate interaction region will likely be the most critical R&D item for studies of an *e-p* or *e-A* collider. Forward particle detection will likely be a critical requirement for the detector and the interaction region.

Usually, a large detector space between the collision point and the first focusing magnet are required for the both the lepton and hadron beams. In the case of the proton or ion beams, this requirement will be similar to that of SPPC. On the other hand, the CEPC detector space, like at all other lepton-lepton colliders, is very small in order to enable an extremely small (~1.2 mm) vertical β* for high luminosity. Making it significantly larger will be one of the challenges and further detector and interaction region design studies will help to determine this important parameter. A relaxed electron β* as shown in Table 8.1.3 should greatly help to achieve chromatic compensation and a good dynamic aperture.

Another critical R&D issue in the design of the interaction region is to provide sufficient separation of the colliding beams at the locations of the final focusing magnets. The separation due to the crab crossing angle is merely a few cm if the detector space is 25 m and smaller than the physical size of warm or superconducting magnets. Additional schemes must be implemented to avoid interference between the beam transport and these magnets.

Estimating beam and luminosity lifetime, and evaluating and mitigating various sources and beam effects that limit these lifetimes is critical R&D yet to be carried out. Nonlinear and collective beam dynamics, particularly the beam-beam effect, must be thoroughly studied.

Design optimization for achieving better performance of a collider is the focus in the next stage of design studies. There are indications that several machine and beam parameters can be further adjusted to gain even higher luminosities. One example is decreasing the proton β* to 55 cm which should result in an increase in the *e-p* luminosity by 21%.

8.6 Summary

In the chapter, we summarized the main results of a preliminary conceptual design study of an *e-p* or *e-A* collider based on the CEPC-SPPC facility. This collider can be run simultaneously with *pp* collisions in SPPC, and possibly share its physics detectors. The luminosity in these *e-p* collisions could exceed a few 10^{33} /cm^2/s.

9 Conventional Facilities

9.1 Introduction

The CEPC conventional facilities are designed to accommodate a 120-GeV Collider, a Booster, two detectors, a gamma-ray source, a linear accelerator, and space reserved for the SPPC. The layout of the components and spaces and the construction systems selected need precisely defined geometric relationships, specific environmental conditions, and appropriate safety and shielding measures. The design of the conventional facilities addresses the usability, flexibility and operational efficiency of the overall project.

The principles for the general layout of the CEPC are:

1) The length and depth of the tunnel must meet the accelerator and detector requirements.
2) The general layout should meet the requirements for safe operation and convenient access.
3) The tectonic stability conditions at the preliminary project site chosen are good. There is a simple geological structure, relatively intact rock mass, overlying strata with proper thickness, and favorable hydrogeological conditions along the tunnel route, all of which can facilitate construction.
4) Convenient access to water and power is important.
5) Access shafts or adits should be selected based on the topographical and geological conditions for entering the underground tunnel.
6) The access shafts should avoid densely populated areas, and auxiliary facilities such as cooling towers and substations should be close to the access shafts.
7) The transportation requirements by road and/or rail for shipment of accelerator components and experimental equipment to the site should be met.
8) The number and length of construction adits should be determined based on the topographical and geological conditions, construction methods and site access conditions along the tunnel, and they should be favorable for balancing the quantities of material used during contruction as well as the and construction periods of all the tunnel sections.
9) The impact on the local environment should be reduced as much as possible and impact of surface facilities on existing buildings/structures shall be avoided as much as possible.
10) The requirements of relevant current national codes and specifications must be met.

A detailed description of the conventional facilities can be found in Ref. [1]. A preliminary 3D layout drawing is shown in Figure 9.1.1.

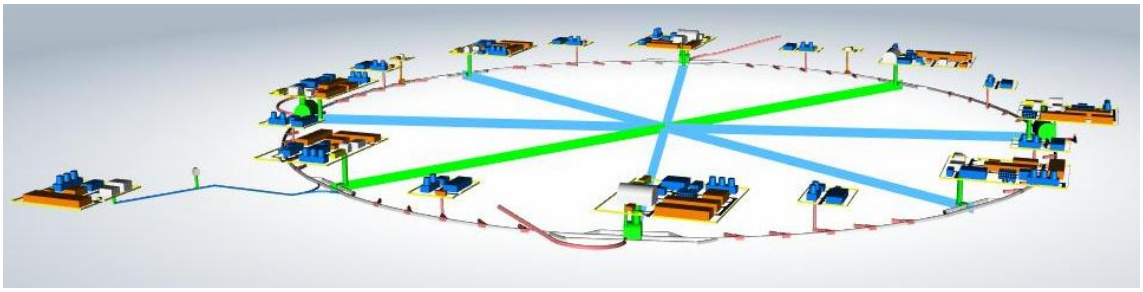

Figure 9.1.1: Preliminary 3D layout drawing of the CEPC.

9.2 Site and Buildings

9.2.1 **Preliminary Site Selection**

Basic principles for site selection:

1) The tectonic stability conditions are good, avoiding deep fractures and neotectonic activity regions, and with ground motion peak acceleration generally less than 0.10 g.
2) Rock conditions are relatively good; preferably there is a large area of hard rock with stable lithology and favorable for tunneling.
3) The terrain elevation variations are small, and preferably in low mountains and hilly areas.
4) The Quaternary overburden is not very thick.
5) The water permeability of the rock is relatively low.
6) Exogenic geological phenomena are relatively undeveloped.

At the current project stage, several areas for the site have been selected from Hebei, Guangdong and Shaanxi Provinces, and a site survey has been conducted in these three provinces. A comparison among the geological conditions of these preliminary selected areas has been made according to the characteristics and site selection requirements of the project and in consideration of the site survey results. Geologically, in Hebei Province, Funing County and the area from Shanghai Pass to Suizhong are favorable sites for underground engineering, because they have good conditions for tunneling in rock and there are no engineering restrictions. In Guangdong Province, the area from north of the Huadu District of Guangzhou City to the east of Qingyuan, the area around Tai Mountain and Gudou Mountain and the area to the east of Xinxing are favorable sites for large-scale underground construction, because there are no engineering restrictions and possible problems may be dealt with by taking necessary engineering measures. In Shaanxi Province, the eastern part of Hanzhong City is a favorable site for underground construction in terms of topographical and rock conditions, while the southern part of Huangling County is a favorable site for underground construction in terms of rock and hydrogeological conditions.

Since the project is an important international scientific and technological facility, further comparison needs to be made among these possible sites and with the additional consideration of such factors as the social environment, the ecological environment, engineering design and project investment and nearby cultural resources and educational institutions. Particularly, for an economically developed region like Guangdong,

environmental factors, such as social development, economy and ecology, would play a greater role in site selection.

The Funing site is a preliminary and temporary selection at the current stage of planning and for implementation of further work.

9.2.2 **Construction Conditions at the Preliminary Selected Site**

9.2.2.1 ***Geographical Location***

Funing County is located in northeast Hebei Province and to the northwest of Qinhuangdao City. The country town is 453 km from the provincial capital, Shijiazhuang, 240 km east of Beijing, and 30.5 km west of Qinhuangdao.

9.2.2.2 ***Traffic Conditions***

Transportation in Funing County is convenient. There are five railways: Beijing-Harbin, Tianjin-Shanghai Pass, Qinhuangdao-Shenyang Passenger Dedicated High-speed Railway, Datong-Qinhuangdao, and Qinhuangdao-Qingdao. Roads and highways in the area are No. 102 and No. 205 National Highways, 5 provincial roads, and the Beijing-Shenyang, Coastal and Beijing-Harbin (G1) Expressways. The Qinhuangdao-Chengde Expressway runs through the county, so it acts as an important transportation hub in the Qinhuangdao Region. The county town is 35 km away from the port of Qinhuangdao, 45 km away from the Shanghai Pass airport and 25 km away from the new Qinhuangdao airport.

9.2.2.3 ***Hydrology and Meteorology***

The preliminary selected site, Funing County, enjoys the semi-humid continental monsoon climate of the warm temperate zone. At the same time, it is also affected by the maritime climate, so that it has four distinct seasons, sufficient sunshine and abundant rainfall. The area has an annual average temperature of 10 - 11 ℃, an annual average frost-free period of 170 - 190 days, annual average sunshine of 2700 - 2800 hours, and annual average precipitation of 640 - 740 mm.

The main rivers within the area include the Luanhe, the Yinma, the Yanghe, the Daihe and the Tanghe Rivers, all of which are perennial rivers flowing from north to south and finally into the Bohai Sea. The large Yanghe River Reservoir has a total storage capacity of 3.86×109 m3, and there are also many smaller reservoirs in the area.

9.2.2.4 ***Economic Profile***

Funing County covers an area of 1,646 km. As of 2012, the total population of this county was 495,898.

In 2012, the County achieved a gross national product of RMB 14,917,660,000, with a yearly growth rate of 5.3%.

Funing County is a suburban county near Qinhuangdao City which is one of the 14 coastal port cities open to the outside world as approved by the State in 1984. Qinhuangdao City had a population of nearly 3,000,000 in 2010. Funing is also one of the counties in the first group of nationwide coastal counties with a greater opening to the outside world as listed by the State Council of China in 1988.

9.2.2.5 *Engineering Geology*

Generally the selected site is in a low mountain and hilly area. Topographically, it is high in the west and low in the east. The water systems in the site include the Yanghe River water system and the Yinma River water system. The formation lithology mainly includes Archean metamorphic rocks dominated by gneiss and schist, Mesozoic magmatic rocks dominated by granite, and Mesozoic volcanic rocks dominated by tuff. These are mainly hard rocks. The surface overburden is not very thick and the thickness of fluvial alluvium is 15 - 20 m. In the selected site area. There is no distribution of deep regional fractures. Ground motion peak acceleration is 0.10 - 0.15 g and basic seismic intensity of Degree VII, so it is basically stable in terms of regional stability. There are two types of groundwater in the area: pore water in loose rock and fissure water in the weathered bedrock zone, with the poor water yield property of the latter. Within the selected site area, exogenic geological phenomena are not developed, the thickness of the weathered zone is 20 ~- 30 m. There are no major engineering geological problems restricting construction. Therefore, it is a suitable site for this large-scale underground project.

Main engineering geological problems:

1) Water burst in the tunnel. The zones with a possible water burst problem include the section passing through the Yanghe River in the lower reaches of the Yanghe River Reservoir and the section passing through the Yanghe River in the southeastern part of Yanghe River Reservoir and their alluvial plains. A water gushing-out problem may also be found near the partial fault fracture zone, especially in the area with a thick partially-weathered zone.
2) Stability of surrounding rocks. Most of the tunnel sections are composed of slightly-weathered to fresh rock mass, so the surrounding rocks are relatively stable. At the depth at which the tunnel will be constructed, a small part of the tunnel section is composed of moderately-weathered rock mass, so the problem of stability of surrounding rocks may exist. When the tunnel passes through the fault fracture zone, the stability of surrounding rocks is poor and appropriate measures should be taken. The inlet section of an access shaft is composed of highly-weathered to moderately weathered rock mass, which has poor stability, so there also there are measures that should be taken. The experiment halls are designed with a large span and high side wall. Block stability problems of side walls always exist no matter what excavation method is used. If the open excavation method is adopted, the stability of surrounding rocks above the upper moderately-weathered zone is poor.

9.2.3 **Engineering Layout and Main Buildings/Structures**

9.2.3.1 *General Layout of the Tunnel and Surface Buildings*

The underground system mainly consists of a 54.4 km long tunnel (refer to Fig. 9.2.1). Considering that the overburden layer of the alluvial plain of the Yanghe River in the southeast of the site is thick, Point B, through which the tunnel passes the Yanghe River, is designated as the lowest tunnel point, and Point A, one diameter across from Point B, is designed as the highest tunnel point. The longitudinal slope of the tunnel is 0.3% according to the topographical conditions, as well as the drainage requirements during the construction and operation periods.

The surrounding rocks of the tunnel consist of granite, gneiss, schist and tuff, and they are mainly Class II to III rocks.

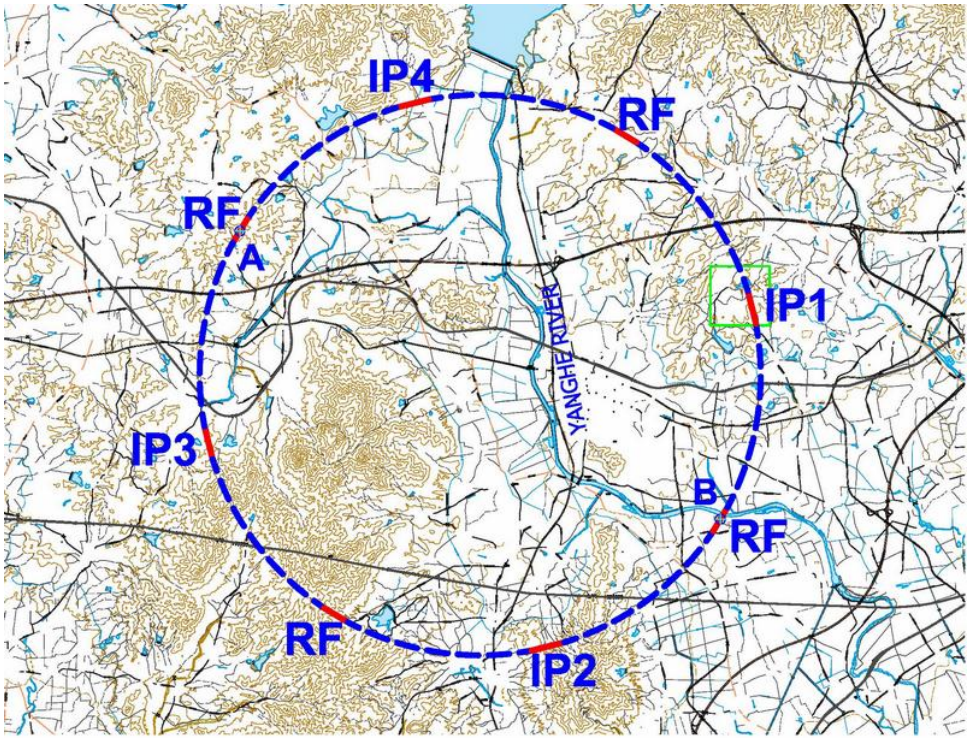

Fig.9.2.1: Layout of the CEPC Tunnel

The underground construction consists of the following:

- Main ring tunnel
- Experiment halls located at IP1 and IP3 for CEPC. IP2 and IP4 are reserved for SPPC.
- Linac and BT tunnel including a 500 m long Linac tunnel and a 600 m long beam transfer tunnel;
- Auxiliary tunnels including RF auxiliary tunnels, bypass tunnels in collision areas and several auxiliary stub tunnels;
- Access shafts: located in the experiment halls and RF areas, used for transporting staff and equipment into the tunnels and halls.
- Gamma source line: this consists of two pairs of front end tunnels connected to two different straight sections of the main ring tunnel, and also includes experimental halls and shafts at each end of the pairs of line tunnels.

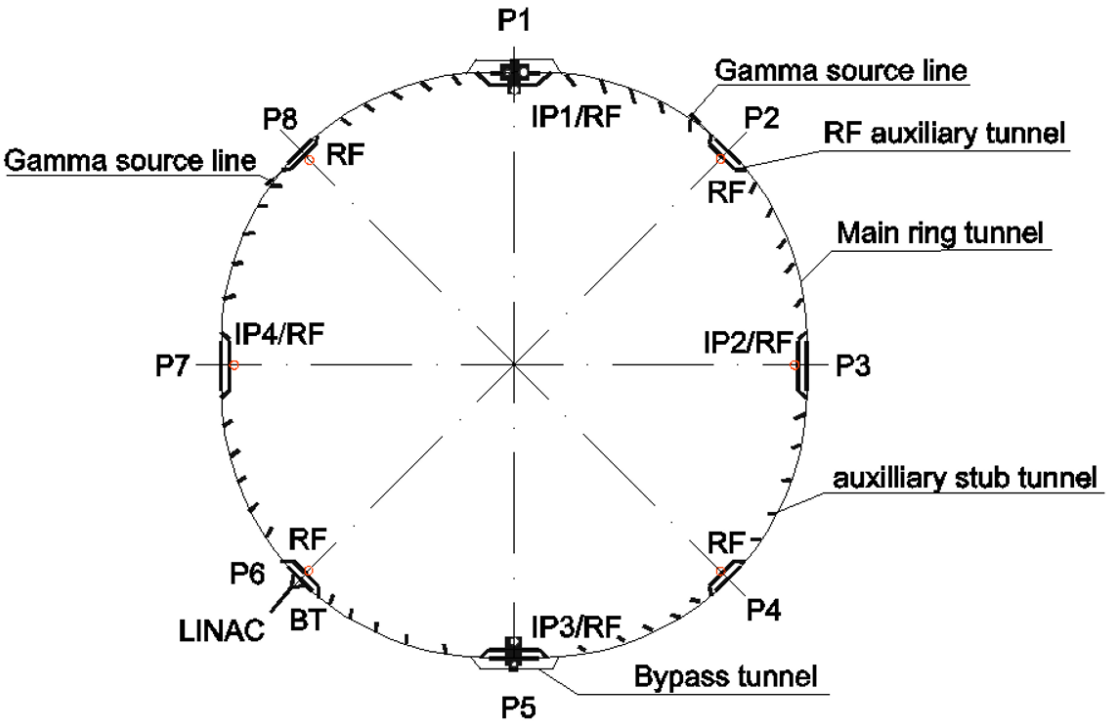

Fig 9.2.2: General Layout of the Underground Areas

The locations of surface buildings/structures within the scope of the main ring area, such as machine service buildings, cooling towers, electrical substations and ventilation systems are close to the access shafts, through which these surface buildings/structures can be connected with the underground equipment networks.

9.2.3.2 *Civil Engineering Aspects of the Underground Work*

9.2.3.2.1 Main Tunnel

The total length of the main tunnel will be 54.4 km with a longitudinal slope of 0.3%. It will consist of eight arcs each 5852.8 m long, four straight sections for the IPs each 1038.4 m long, and four straight sections for RF sections, each 849.6 m long. The normal tunnel cross-section is divided into three parts.

- The outer side, where the CEPC machine components and services will be installed.
- The inner side, reserved for the SPPC.
- The middle area of the tunnel, which will be reserved for handling and transport equipment.

Selection of tunnel cross section: Circular, portal-shaped and horseshoe-shaped sections are all possibilities. If the Tunnel Boring Machine (TBM) construction method is adopted, a circular section will be selected. If the drill and blast method is used, all of these types of cross-section are possibilities. The choice will be made and dimensions defined by construction transportation requirements during the construction period, as well as the equipment layout and access requirements during operation. The shape and dimensions will be determined based on a comprehensive technical and economic comparison. The portal-shaped cross-section shown in Fig 9.2.3 is the current design.

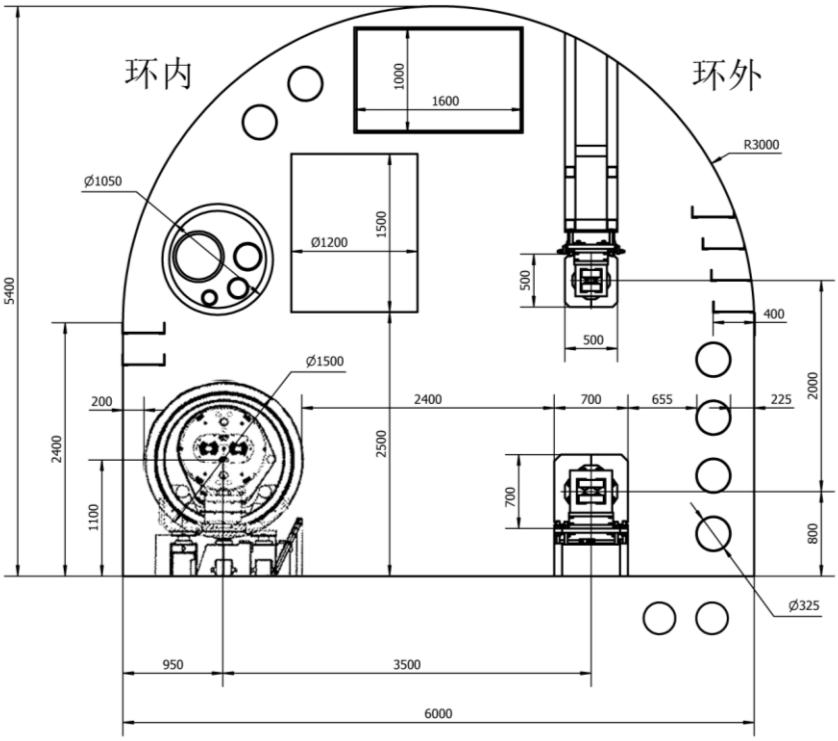

Fig 9.2.3 Cross section of the main ring tunnel over most of the circumference.

Lining structure and waterproof material: The underground tunnels and caverns of the project are Grade I waterproof. Besides meeting the structural requirements, support and lining structures should also comply with the waterproof requirements. The types of possible lining include shotcrete-anchorage support, reinforced concrete lining, steel fiber reinforced concrete lining, and steel structure lining. Waterproof materials include waterproof coils, waterproof paint, and rigid waterproof material. Since the selection of lining structure and waterproof material has a significant impact on project cost, the types of lining structure and waterproof material will be determined based on a comprehensive technical and economic comparison. The application of new processes, technologies and materials will also be considered. Currently it is proposed to use drainage and profiled steel sheet on the arch of the tunnel in rock class II, drainage, profiled steel sheet and damp-proof decorative wall in rock class III, 25~50 cm-thick reinforced concrete as the lining structure and waterproof sheet in rock class IV~V.

9.2.3.2.2 RF Sections of the Main Tunnel

There are four RF sections, each 849.6 m long. In the collision areas, each has a total length of 1,038.4 m and includes two 1/2 RF sections. In total there are 8 RF sections with an enlarged width of 7.2 m as shown in Fig 9.2.4. Running parallel to the RF section tunnel is the RF auxiliary tunnel with a width of 5.5 m. It is designed to accommodate klystrons, cryogenic equipment, cooling water, and local controls.

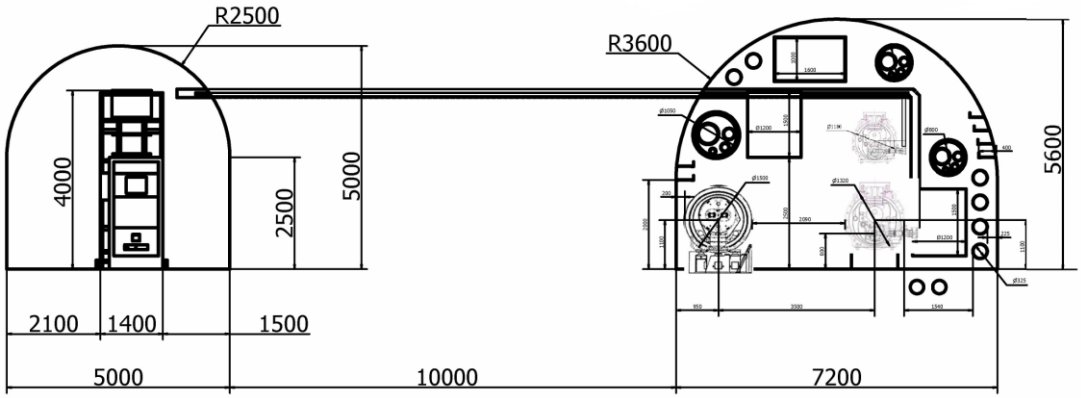

Fig 9.2.4: Cross section of the main ring tunnel at the RF sections

9.2.3.2.3 Bypass Tunnel in the Collision Areas

Each collision area is provided with a 1200 m long auxiliary tunnel with width of 4.5 m (Fig. 9.2.5), which is used for bypassing the Booster beamline.

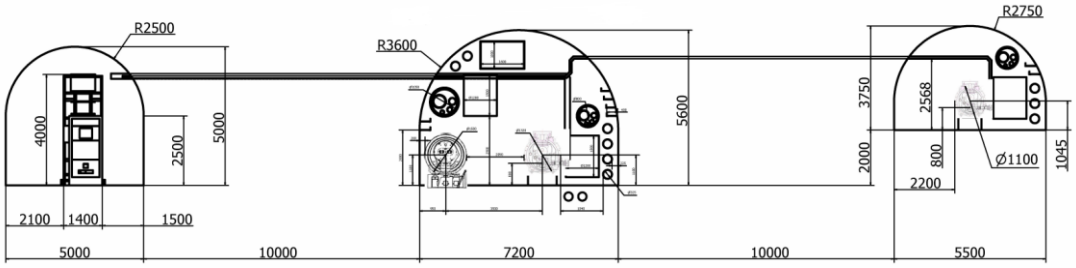

Fig 9.2.5: Cross section of the main ring tunnel in the collision area.Left: RF auxillary tunnel; Middle: Main tunnel; Right: Bypass tunnel.

9.2.3.2.4 Auxiliary Stub Tunnels

Spaced at regular intervals around the main tunnel, 48 stub tunnels will house the electrical substations and other service and electronic equipment. Each stub will have a finished width of 7 m and a length of 30 m.

9.2.3.2.5 Experimental Areas

In total, four experimental halls are planned. The halls at IP1 and IP3 will be 30×30×30 (length × width × height in meters) for CEPC and those at IP2 and IP4 are reserved for SPPC and those dimensions specified later.

9.2.3.2.6 Access Shafts

- Each experiment hall includes an access shaft, 15 m in diameter for equipment installation, a shaft of 5 m diameter for emergency escape, and access shafts with 10 m diameter for the bypass tunnel.
- Each RF section is provided with an access shaft with a diameter of 10 m.

9.2.3.3 *Surface Areas and Buildings/Structures*

Various services buildings will be erected adjacent to each access shaft to house power converters, helium compressors, assembly areas, and utilities in order to reduce the length of feeders. Complete building dimensions will be specified later. For now, the floor area sizes of CEPC surface buildings/structures can be listed and are shown in the table below.

Table 9.2.1: Floor area sizes of CEPC surface buildings/structures.

Purpose	location and floor area size of building										Total
	P1	P2	P3	P4	P5	P6	P7	P8	Linac	BT	
	IP/RF	RF	IP/RF	RF	IP/RF	RF	IP/RF	RF			
Control / duty rooms	1200	200	200	200	600	200	200	200	400		3400
Power converter for magnets	1500	1200	1200	1200	1500	1200	1200	1200	500	200	10900
HV power converter	2500	2500	2500	2500	2500	2500	2500	2500	3500		23500
110 kV electric substation	1500	1500	1500	1500	1500	1500	1500	1500			12000
10 kV electric substation	600	500	500	500	600	500	500	500	350		4550
HVAC	800	600	600	600	800	600	600	600	600	60	5860
Cryogenic (helium compressor)	1500	1500	1500	1500	1500	1500	1500	1500			12000
Cooling pump station	800	800	800	800	800	800	800	800	500	80	6980
Cooling towers	800	800	800	800	800	800	800	800			6400
Experimental assembly work	1500				1500						3000
Magnet assembly and calibration		3000									3000
Unloading equipment	200	200	200	200	200	200	200	200	200	150	1950
Compressed air	200	200	200	200	200	200	200	200			1600
Chilled water plant	1200	1200	1200	1200	1200	1200	1200	1200	400		10000
Electronics room	600	600	600	600	600	600	600	600	450	80	5330
Other	500	500	500	500	500	500	500	500			4000
Total	15400	15300	12300	12300	14800	12300	12300	12300	6900	570	114470

9.2.4 **Construction Organization**

9.2.4.1 *Construction Conditions and Construction Options*

9.2.4.1.1 Construction Conditions

The Project is located in Funing County under the administration of Qinhuangdao City, with a straight-line distance of 30.5 km from Qinhuangdao City. The project area has well-developed transportation, e.g. the Beijing-Harbin (G1) Expressway, No. 261 Provincial Road, No. 102 National Highway, and the Beijing-Shenyang Railway. In

addition, there are village-to-village roads or simple roads leading to the construction sites of experiment halls and access shafts. The fields along the route of the project are wide and open and favorable for a distributed arrangement of construction sites.

The project site is close to an urban area, so electrical power is ample and convenient. The project area passes through the Yanghe River twice. Since there is water in the river throughout the year, the water supply conditions are also good.

9.2.4.1.2 Main Construction Options

The current preliminary plan is to use the drill and blast method for construction of experiment halls and access shafts. The TBM method will be used for construction of the main ring tunnel. The exact details will be based on the underground enclosure layout, the engineering geological conditions, site construction conditions (such as site topography, construction access, construction power supply) and construction schedule requirements.

Four experiment halls are arranged at regular intervals around the main ring tunnel. Based on the topography and tunnel depth, open excavation is used for the shallowly buried locations while tunnel excavation is applied at deeply buried locations. The halls and caverns built with the open excavation method are excavated from top to bottom in layers. The double-beam gantry crane or tower crane is selected for lifting equipment. For the halls and caverns built by the tunnel excavation method, it is planned to provide some construction adits to be used as construction mucking and transportation passages.

Around the main ring tunnel are arranged 16 access shafts with the diameters of 15 m, 10 m and 5 m. These access shafts have an average depth of about 70 m. The maximum is about 240 m and the minimum about 40 m. Mining methods are adopted to excavate these access shafts from top to bottom.

At regular intervals around the main tunnel, 8 underground buildings/structures are arranged to divide the main ring tunnel into 8 equal sections, each of which is about 6.8 km long. To reduce the quantities of material required for building temporary structures, both in the drill and blast and TBM methods, the access shafts are used as the construction accesses to the main ring tunnel, and the access tunnels are used as the construction accesses to the experiment halls by tunnel excavation. These will have a cross-section of 5×6.5 m, an average length about 1,000 m and a slope of 10%.

For construction by drill and blast, the permanent shafts and temporary construction shafts are used as construction access, and evenly spaced along the tunnel axis. There are a total of 16 construction accesses and 32 working faces. The control length of a single working face is 1.7 km. For construction by TBM, 4 TBMs will be used with working face control length of 13.6 km. Full-face steel formwork jumbo is adopted for tunnel lining, with working face control length of 1.7 km.

9.2.4.2 *Construction Access and General Construction Layout*

9.2.4.2.1 Construction Access

The project area is 30.5 km from Qinhuangdao City, with some already existing site access. Most zones along the project route are connected by simple roads. These can be reconstructed and expanded if needed to be used as on-site construction accesses. As for the experiment halls, in order to meet the requirements for transportation of construction equipment and experiment components, the road will be considered as Mining Level 2, with pavement of concrete or asphalt concrete and 7 m wide. As for the other

construction shafts, which will be considered as Mining Level 3, the pavement will be clay bound macadam and the road 6 m wide.

9.2.4.2.2 General Construction Layout

Taking into account the layout of engineering buildings/structures, natural conditions along the route, as well as the construction requirements, the construction sections along the route are arranged in 16 dispersed construction areas at every 3.4 km. These construction areas include 4 TBM construction areas and 4 access shaft construction areas. The layout of a construction area shall be combined with land use for ground buildings as much as possible, so as to reduce temporary land use.

Temporary facilities for construction should take full advantage of existing local resources, including roads, bridges, production and living facilities, drainage facilities, and power transmission and communication lines.

The spoil disposal area should be selected taking into consideration the comprehensive land-use planning of local cities and towns. Planned spoil disposal areas should be used as much as possible. Construction accesses should be combined with the traffic along local trunk roads as much as possible. The accesses to construction adits should be combined with local village roads. Construction accesses to the halls should be combined with permanent roads, and construction of new roads should be considered.

9.2.4.2.3 Land Use for Construction

The land use for construction includes permanent and temporary land use. This project mainly focuses on underground work, and its permanent land use is mainly for ground buildings and permanent access. This totals 580,000 m^2. Temporary land use consists of borrow pits, spoil disposal area(s), temporary access and construction sites, etc., totaling 1,825,000 m^2, of which the temporary land use for the spoil disposal area is about 1,361,000 m^2.

9.2.4.3 *General Construction Schedule*

9.2.4.3.1 General Indicators

The work during the total construction period includes preparation (construction roads, temporary construction adits, air, water and electricity for construction, etc.), experiment halls, access shafts, excavation and lining work in the ring tunnel.

Construction preparation work includes land acquisition and relocation, supplies for access, water, electricity, communications and air and site leveling. This construction preparation period generally lasts 6 - 8 months based on a comprehensive consideration of topographical conditions and other construction conditions.

Access shaft work: The construction of access shafts includes excavation, support and lining. For an access shaft with diameter less than 10 m, the advance is generally about 20 - 40 m/month for the upper overburden section and about 60 - 70 m/month for the rock section. For an extra-large access shaft with a diameter of 15 m, a top-to-bottom shaft sinking method is used and the advance depth is generally 50 - 60 m/month.

For excavation of the ring tunnel by drill and blast, the excavation progress is related to the length of the working face and the classification of surrounding rock. With the working face control length of 1.7 km and the average advance of 60 - 80 m/month, the tunnel excavation period is about 28 months. For tunnel excavation by TBM, the

average advance is 500 - 700 m/month. Therefore with the working face control length of 13.6 km, the tunnel excavation period is about 23 months.

Lining of one bay (12 m each) of the ring tunnel is finished every 3~4 days. If the working face control length is 3.4 km, and the waterproof structure construction and lining done simultaneously, then the period of time for tunnel lining and waterproofing is about 12 months.

Construction of experiment halls. For a shallowly buried hall built using the open excavation method, construction progress is mainly controlled by mucking capacity. For a 30×30×30 hall, the excavation period is considered to be 2 months for the upper overburden and about 4 months for the other layers. The total construction period is planned to be 6 - 8 months due to the additonal time to install support and lining. For a deeply buried hall built by the tunnel excavation method, the construction adit is used for mucking and the total construction period for excavation and support is about 8 - 10 months.

9.2.4.3.2 Planned Total Period for Construction with Drill and Blast Method

The total construction period is 55 months, including 8 months for construction preparation, 45 months for construction of the main portions and 2 months for completion.

The critical path is the construction preparation period (8 months) → construction of construction access shafts (5 months) → tunnel excavation period (28 months) → tunnel lining and waterproof period (12 months) → completion period (2 months). The construction of ground buildings will be conducted gradually as the project progresses, and the underground work will be done at the same time, so as not to extend the total project construction time.

The total period for construction with the TBM method (using 4 sets of open-type TBMs) is planned as follows:

- The TBM launching and arriving shafts should be combined with the shafts of permanent buildings/structures. The design and manufacture of the TBM is planned to be completed during the construction preparation period. For a TBM, design and manufacture takes 10 months, transportation takes 2 – 3 months and then there are 3 months for installation and commissioning.
- The total construction period by TBM is 57 months, including 8 months for construction preparation, 47 months for the main part of the construction and 2 months for completion.
- The critical path is construction preparation period (8 months) → construction of construction access shafts (6 months) → TBM assembling period (3 months) → tunnel excavation with TBM (26 months) → tunnel lining and waterproof period (12 months) → completion period (2 months). The construction of ground buildings will be done gradually and the underground work will be done at the same time, so as to not extend the total construction period.

9.3 Electrical System

9.3.1 Power Supply Range and Main Load

The power supply for the CEPC mainly is for detectors, the accelerator itself, and general facility utilities such as illumination and elevators. Power for the CEPC campus as it develops in the future shall also be included in this initial design and planning.

A high level of reliability of electrical services to CEPC is essential. The electrical demand loads of CEPC during operation are shown in Table 9.3.1. The connected equipment shall be in compliance with national codes.

Table 9.3.1: CEPC Electrical Loads (operational demand)

system	location and electrical loads(MW)					Total
	ring	Booster	Linac	BT	IP	
power source	230	15	2.1			247.1
cryogenics	16	2			1	19
power converter for magnets	60.5	13.2	1.2	1	1	76.9
experimental devices					14	14
dedicated services	15	5	1	1	2	24
utilities	55	10	2.5	1	2	70.5
general services	15		1	1	1	18
campus						30
Total	391.5	45.2	7.8	4	21	499.5

9.3.2 Power Supply Scheme

It is planned to use a 220 kV level for power to the project. The initial plan is to take 220 kV power from the 500 kV Tianma Substation. Stand-by power may be taken from other substations nearby. The specific connection mode is to be defined upon the completion of the connection system design.

It is planned to have a 220 kV central substation (220kV/110kV/10kV) with four 240 MVA transformers located within the project area. The 220 kV central substation has 4 incoming lines (2 for the main power and 2 for stand-by power). Sixteen 110 kV outgoing lines will provide power to CEPC and several 10 kV outgoing lines will provide power to the campus laboratories and buildings.

Eight 110 kV/10 kV step-down substations are placed at each point of the ring, each with two 63 MVA transformers, two 110 kV incoming lines and twenty-four 10 kV outgoing lines mainly for power to the equipment in the surface buildings and that section of the underground tunnel. The layout of the CEPC 110 kV electrical networks is shown in Fig. 9.3.1.

10 kV/0.4 kV power distribution systems are in the vicinity of various load points.10 kV cables lead from the 110 kV/10 kV step-down substation to the underground tunnel and form a 10 kV looped network. A schematic diagram of the CEPC power distribution is shown in Fig. 9.3.2.

For loads of critical importance, a diesel generator (or EPS, UPS or DC power supply system) is installed for emergency power.

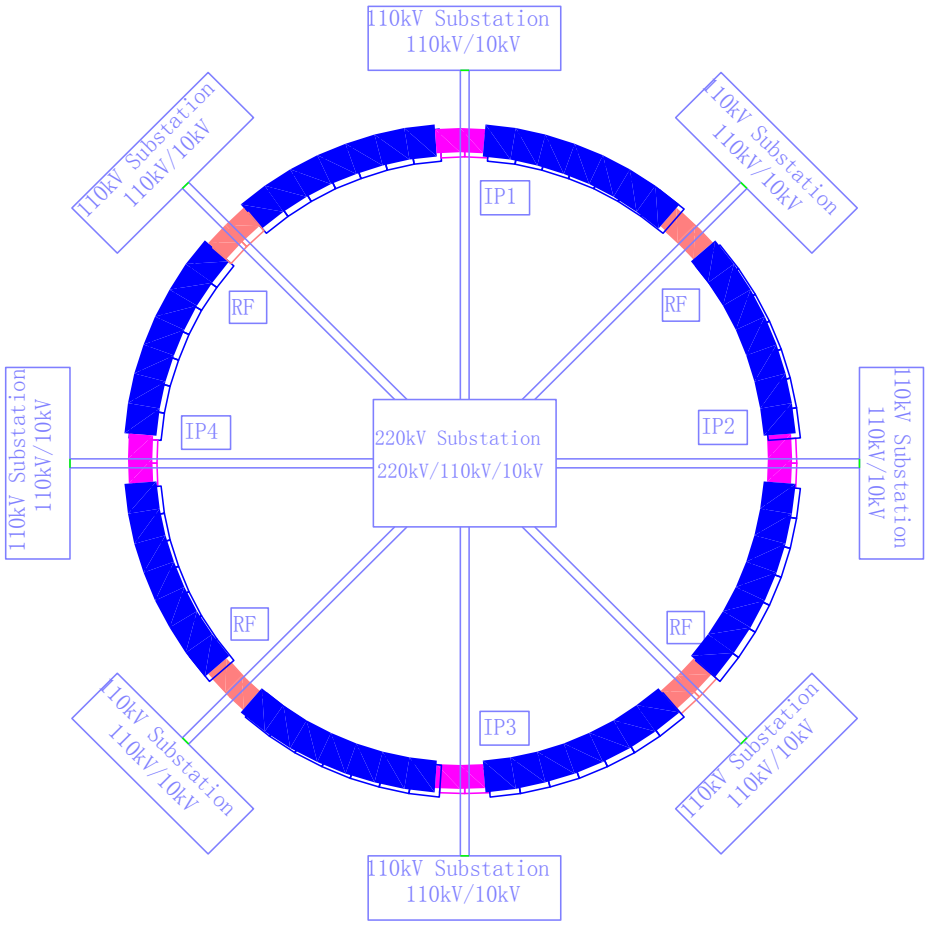

Fig. 9.3.1: Layout of CEPC 110 kV electrical networks

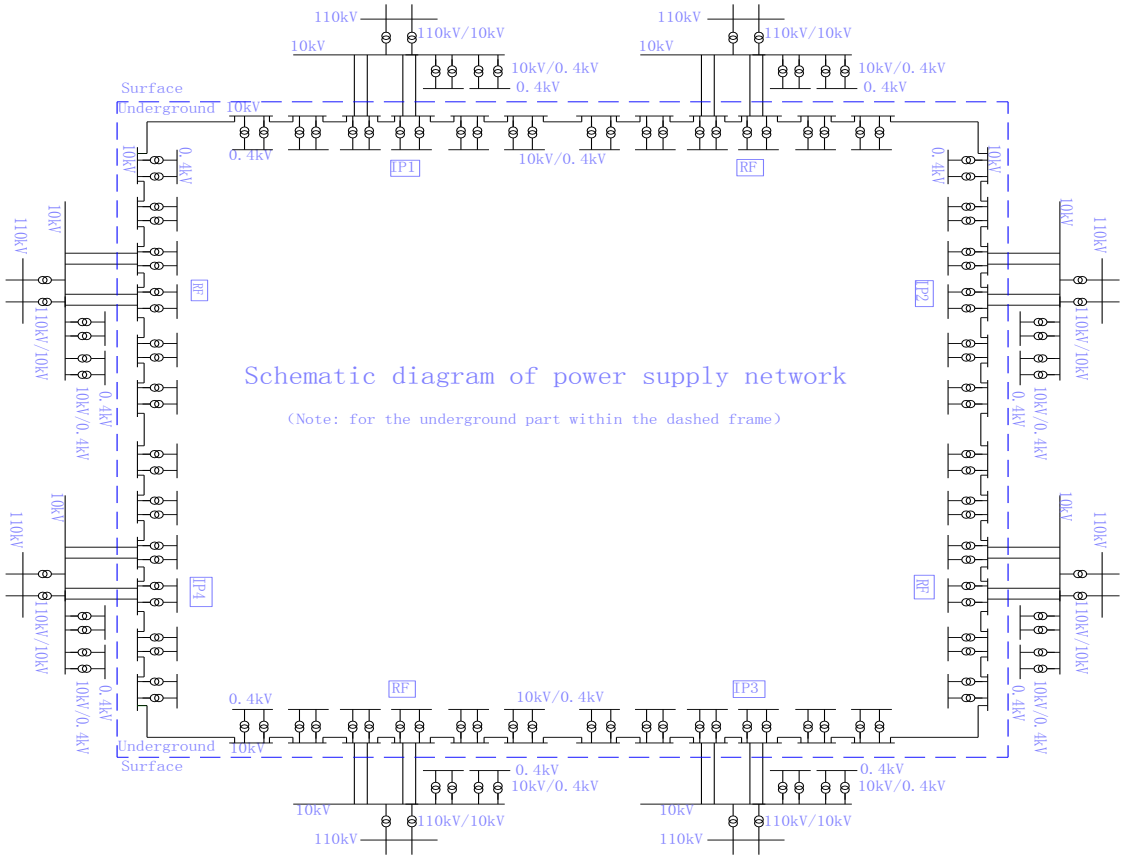

Fig. 9.3.2: Schematic diagram of CEPC power distribution network

9.3.3 **Illumination System**

1) Scope of the illumination system: Two systems for normal illumination and emergency illumination are provided for surface facilities and underground enclosures. In case of a power loss to the normal illumination system, the emergency illumination system can still provide illumination at important areas required for evacuation or continuous operation. Emergency power can be obtained from a diesel generator or EPS.
2) All lamps are of the energy-saving type. Energy-saving fluorescent lamps or LEDs are adopted in general purpose areas. Moisture-proof lamps shall be used in the tunnels.

9.3.4 **Internal/External Communication throughout the CEPC Complex**

Internal communication includes speech and network communication at shafts, various experimental halls, in underground enclosures, as well as in rooms housing machine equipment and components. (Note: communications between surface buildings/structures and internal communications are excluded in this category.)

9.3.4.1 *Communication*

Communication is by optical fiber. Optical cables are to be laid in the cable tray in shafts and underground tunnel, and optical communication equipment is to be provided in each machine room. A bandwidth of 10 Gb/s is considered as standard.

A soft switching system is provided in the machine room of the communication center, offering services to users via communication and computer networks. Telephone communication is available among users and between users and the outside world via the soft switching system.

9.3.4.2 *Communication Power Supply*

A high-frequency switching power supply (with 2 sets of batteries) is in each machine room and used to power communications equipment. Batteries shall be able to provide continuous power for at least 3 hours.

9.3.4.3 *Computer Network*

A LAN composed of an Ethernet switch, router, etc. is in the experimental halls. Networks are connected to each other via communication systems or optical cables, as well as connected to the external internet. Network security equipment and software are set up for network security. Power to the computer network is ensured with an UPS that shall last for at least 3 hours.

9.3.5 **Monitoring System**

Object that require monitoring mainly involve utilities, such as power supplies, ventilation and air-conditioning and inside shafts and underground tunnels.

The monitoring system consists of a monitoring center and a host system consisting of a data server, operator workstation, printer, network equipment and UPS system. Local control units are placed in the vicinity of various monitored systems. A loop Ethernet is between the host computer and local control units via optical cables.

9.3.6 **Video Monitoring System**

Video monitoring systems are placed in shafts, underground tunnels and experiment halls. A video monitoring system consists of a live camera transmission network and monitoring center equipment. Storage devices like DVR, video servers, big-screen video monitoring equipment are provided in the monitoring center.

9.3.7 **Fire Detection and Alarm**

Fire detection and alarm systems consist of heat and smoke detectors, thermometric cables, alarm buttons, audible and visual alarms and alarm controller. They are located at shafts, underground tunnels, and experimental halls. The fire detection and alarm systems are to be powered by a fire supply source and be provided with independent UPS.

9.4 Cooling Water System

9.4.1 **Overview**

There are many electronic devices in CEPC. Most of the electrical power consumed by those components is eventually absorbed by the cooling water as heat energy. In addition to its cooling function, it is quite critical for some subsystems where the operating temperature must be held constant.

The cooling water system consists of a low-conductivity water (LCW) closed-loop circuit, a cooling tower water (CTW) circuit, and a deionized water make-up system. The LCW system absorbs heat from the various devices in CEPC, and this heat is transferred through plate heat exchangers to the cooling tower water circuits (CTW) and finally rejected into the atmosphere by cooling towers. A flow diagram of a typical cooling water system is shown in Fig. 9.4.1.

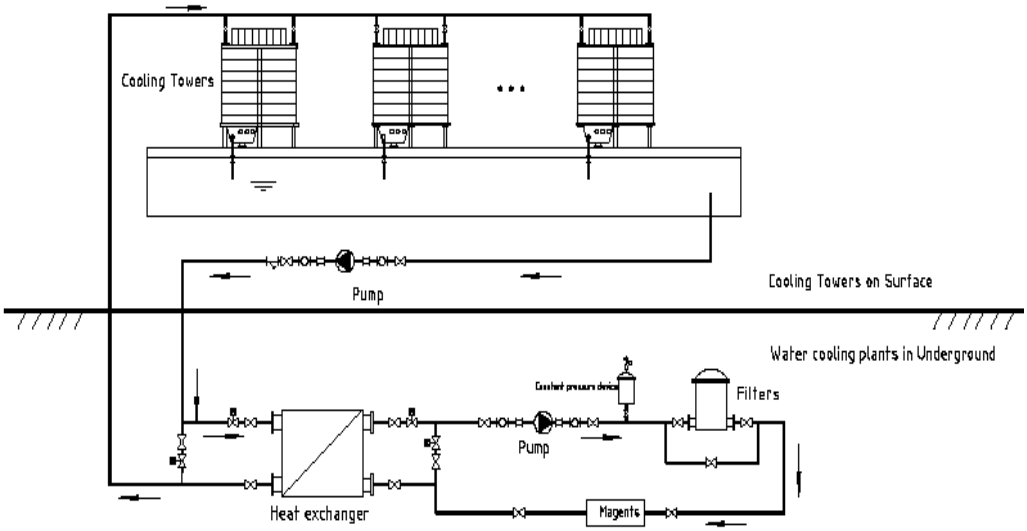

Fig. 9.4.1: Flow diagram of a typical cooling water system

The major heat sources of the entire facility are RF power sources, magnets, vacuum chambers, cryogenic compressors, power converters, etc. The total heat load dissipated by CEPC is about 306 MW, and the estimated heat loads are summarized in Table 9.4.1.

Table 9.4.1: Estimated cooling water heat loads

System	Location and heat loads(MW)					
	ring	Booster	Linac	BT	IP	Total
Power source	130	10	1.0			141.6
Cryogenics	16	2			1	19
Power converter for magnets	5.5	1.1	0.11	0.1	0.1	6.91
Experimental devices					8	8
Magnets	42	8	1	1	1	53
Vacuum chamber of ring	60	3				63
Pump	13.5	1.11	0.26	0.06	0.36	15.29
Total	267	25..21	2.37	1.16	10.46	306.2

There are 8 CTW pump stations at each point of the ring and an additional CTW system for the Linac. The CTW equipment will be installed close to access shafts of these areas, and its LCW circuits will be located underground at machine level in order to reduce pipe pressure. There will be a deionized water plant at each point of the ring and at the Linac. These plants will supply low-conductivity makeup water for each of the LCW circuits in the area. The layout of cooling water circuits in the main ring is shown in Fig. 9.4.2.

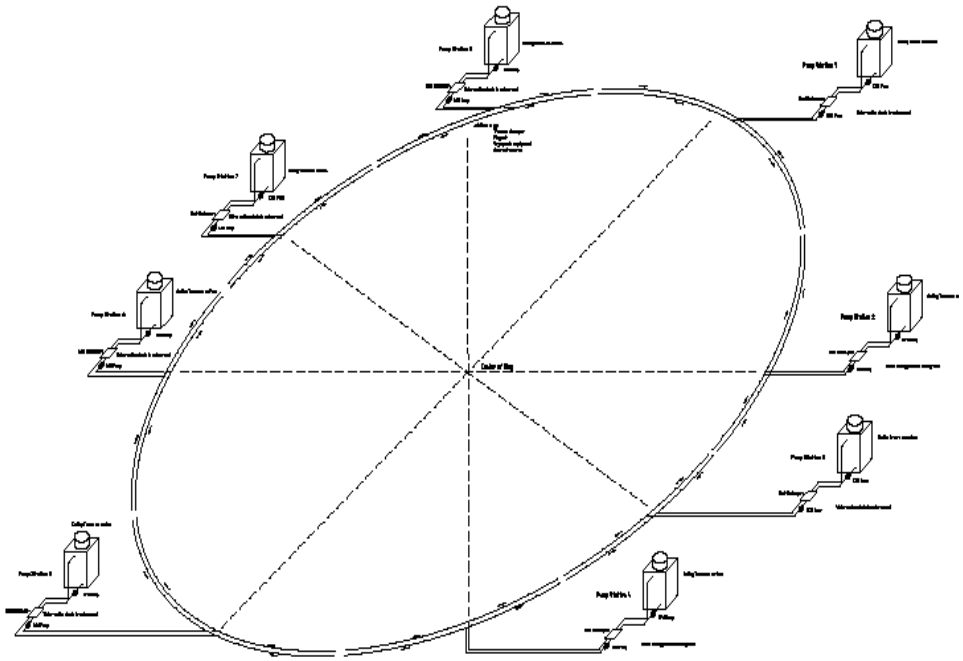

Fig. 9.4.2: Layout of cooling water circuits in the ring

9.4.2 **Cooling Tower Water Circuits**

The cooling tower water system provides coolant for the plate heat exchangers in the LCW circuits. They will be installed at each point of ring and Linac area where service buildings will house its pumps and filters, etc. Supply water temperature will be 29℃ based on a wet-bulb air temperature of 26℃ ambient. The main parameters of those circuits are shown in Table 9.4.2. Make-up water is introduced through an automatic valve which is connected to the raw water pipeline.

Table 9.4.2: Parameters of the cooling tower water system

Parameters	ring	Booster	Linac	BT	IP	Total
heat load (MW)	276.9	26.13	2.48	1.2	10.46	317.04
supply water temperature	29℃					
temperature rise	5℃					
flow rate (m^3/h)	47596	4494	426	206	1800	54522

9.4.3 **Low Conductivity Water (LCW) Circuits**

There are several closed-loop LCW subsystems in the Linac, main ring, and experimental area. They are defined by equipment characteristics, operational requirements, and location. They are:

- Linac area: accelerating tube, waveguide circuit, klystron circuit, and the beam transfer line circuit.
- Main ring area: magnet circuits, vacuum circuits, RF circuits, and converter circuits at each point. Each of magnet and vacuum circuits will serve two half adjacent octants of ring.
- Experimental area circuits.

The main parameters of those circuits are shown in Table 9.4.3. Supply water temperature for the ring will be 31℃ based on the outlet temperature of the cooling tower which may, however, be exceeded in the summer months. This relatively high temperature has been chosen in order to avoid the use of expensive refrigerators.

Table 9.4.3: Parameters of low-conductivity circuits

System	Location	Heat loads	Flow rate
		MW	M3/h
Accelerating tube, waveguide circuit	Linac	0.8	400
Klystron circuit		1.56	268
BT magnet circuit	BT	1.16	160
Ring magnet circuit	Ring	6.86*8	736*8
Vacuum chamber circuit		8.4*8	902*8
RF circuit		18.19*8	1560*8
Power converter circuit		0.9*8	129*8
Circuit for experiment area	IP	4.18*2	450*2
Total		286.68	28344

9.5 HVAC System

9.5.1 **Indoor and Outdoor Air Design Conditions**

9.5.1.1 ***Outdoor Air Design Conditions***

The CEPC project may be located near Qinhuangdao City in Hebei Province, and outdoor air design conditions at this site are as follows:

- Outdoor design dry-bulb temperature for summer air conditioning: 30.6 ℃
- Outdoor design wet-bulb temperature for summer air conditioning: 25.9 ℃
- Outdoor design temperature for summer ventilation: 27.5 ℃
- Outdoor design relative humidity for summer ventilation: 55%
- Outdoor wind speed in summer: 2.3 m/s
- Outdoor design temperature for heating: -9.6 ℃
- Outdoor design temperature for winter ventilation: -4.8 ℃
- Outdoor wind speed in winter: 2.5 m/s

9.5.1.2 *Indoor Air Design Conditions*

For the interior of the 54.4 km ring tunnel, the temperature is 30 ~ 34 ℃, and shall be lower than 35 ℃; the relative humidity is 50% ~ 60%, and shall be lower than 65%.

For the 4 experimental halls, temperature is about 26 ℃; the relative humidity is 50% ~ 60%, and shall be lower than 65%.

9.5.2 **Tunnel Air Conditioning System**

Based on the current design, the air conditioning cooling load in the underground tunnel is about 60 MW. It is divided into 8 subsystems, with an air conditioning cooling load for each subsystem of about 7.5 MW.

48 groups of modular air conditioning units are arranged in stub tunnels around the ring with the units spaced 1130 m apart. Each group of air conditioning units performs air conditioning within a range of 550m in both directions, and supplies cool air to the tunnel by air conditioning ducts. There are independent air-conditioning systems for the RF auxiliary tunnels, with temperature to be less than 25℃ during shutdown period and less than 30°C when operating.

9.5.3 **Air Conditioning System of Experiment Halls**

Ten sets of modular air conditioning units are installed at the IP1 and IP3 experiment halls. For each modular air conditioning unit, the air volume is 20,000 m^3/h and excess pressure is 250 Pa. No air conditioning system is installed at this point in the project in the IP2 and IP4 experimental halls reserved for SPPC.

9.5.4 **Ventilation and Smoke Exhaust System**

It will be of great importance to arrange the emergency smoke control facilities to ensure fire safety for underground personnel. The normal air and smoke exhaust system is used to exhaust smoke to the outside in a timely way to ensure safe evacuation of relevant personnel. For the underground caverns, it is planned to integrate the smoke control system with the mechanical air exhaust system. Emergency smoke control is adopted for the ring tunnel and experiment halls.

In the tunnel, the majority of heat generated by the machine is removed by LCW. Ventilation of the tunnel is performed during shutdown, and temperature and humidity in the tunnel are maintained by the air conditioning system during machine operation.

For ventilation, in addition to the thermal load the following functions must be considered:

- Supply fresh air to personnel;
- Maintain suitable temperature for the equipment;
- Dehumidify to prevent condensation;
- Allow for smoke exhaust;
- Exhaust air from the tunnel before access;
- Filter the exhausted air.

It is planned to make shafts with odd numbers as air supply and shafts with even numbers as air exhaust for the 8 shafts. A fan room is placed at the floor of each shaft, and two reversible smoke exhaust fans (1 for service and 1 for standby) are arranged in

the fan room. During the exhaust of smoke from the tunnel, the two fans can be operated simultaneously. In addition, 1 mixed flow fan is arranged at the floor of the stairway hall of the emergency exit in the collision area to use as a positive pressure fan.

The experiment hall covers an area of 900 m2, and has a height of 30 m, Because of its size it is difficult subdivide it up into separate "smoke bays." According to provisions of the Code of Design on Building Fire Protection and Prevention, the required smoke exhaust rate is 54,000 m^3/h. Therefore, the smoke control system is integrated with the ventilation system in the experiment hall, and 2 smoke exhaust fans (1 for service and 1 for standby) are arranged nearby in the experiment hall. One is used as an exhaust fan under normal operation, and both fans are used as smoke exhaust fans simultaneously in case of a fire. The exhaust duct is led to the ground outside by a shaft.

9.5.5 **Chilled Water System**

There are chilled water plants at each point of ring and Linac area to supply chilled water for air-conditioning units. The cooling tower water system for the chilled water system will be integrated with the one for the accelerator itself.

9.6 Fire Protection and Water Supply & Drainage

9.6.1 **Layout Principles**

The underground ring tunnel and experiment hall contain the collider and other electromagnetic equipment. Fire protection is designed with fire hydrants and extinguishers, and the leakage drainage pumps shall be specified following the experience at similar projects and the preliminarily estimate for volume of water leakage.

9.6.2 **Design of Fire Protection**

9.6.2.1 ***Design of Fire Hydrants***

According to relevant provisions of the Code for Fire Protection Design of Buildings (GB50016-2006), the underground tunnel and experiment hall shall be provided with fire hydrants with a spacing of not more than 30 m, and 1820 pieces of SNJ65 pressure reducing and stabilizing fire hydrants shall be provided in total.

DN100 fire pipes shall be connected from the underground cooling water pipes.

9.6.2.2 ***Distribution of Extinguishers***

According to relevant provisions of the Code for Design of Extinguisher Distribution in Buildings (GB50140-2005), the hazard classes are for a Class D fire and a Class E electrical fire. The whole underground tunnel is considered as a fire compartment, and 2173 distribution points are arranged in total, with each distribution point being arranged with two MF/ABC6 ammonium phosphate salt dry powder extinguishers. There are 4346 extinguishers in total.

There are 4 experiment halls in total, with an area of 900 m2. Each hall shall be provided with 4 wheeled extinguishers, namely, 16 extinguishers total.

9.6.3 **Design of Water Drainage**

Currently, the water leakage volume of the underground tunnel shall be similar to other projects. Three 200RJC60-20×6 long-shaft deep-well pumps (1 for service and 2 for standby) have the following pump parameters: Q=60 m3/h, H=120 m and N=37 kW. In addition, corresponding valves and drainage pipelines shall be provided.

9.7 References

1. Yellow River Engineering Consulting Co., Ltd., “Preliminary Conceptual Design Report for the CEPC Civil Construction and Utilities,” February 2015. (in Chinese)

10 Environment, Safety and Health Considerations

Environmental, safety and health aspects should be integrated into the design, construction and operation of CEPC at all levels to most efficiently avoid negative consequences. Operation of existing accelerators gives us the opportunity to identify the principal hazards and associated risks. The main hazards and risks are: ionizing radiation, electrical safety, non-ionizing radiation, fire safety (including emergency preparedness), construction activities, cryogenic and oxygen deficiency hazards, seismic safety issues, hazardous material issues, environmental, waste, noise, confined space, pressure, ozone, material handling, and experimental operation.

The preparation of environmental impact and occupational hygiene assessment documents for this project will be carried out during the design and development phases. Specific requirements for implementation of safety-related codes and standards will be defined and detailed in the next design phase. In addition, surveys of sites of historic and prehistoric periods and preservation and mitigation of project impact on them will be conducted and coordinated with the national historic preservation law.

10.1 Ionization Radiation

Radiation safety is addressed in Section 5.10.

10.2 Impact of Construction on the Environment

The main buildings/structures of this Project include underground buildings/structures (main ring tunnel, experimental halls, Linac and access shafts) and surface buildings/structures. A potential site is located in Funing County, which is far from major cities There are a few villages nearby the buildings/structures, and no large-sized buildings/structures. There are local underground pipeline networks that need to be identified and avoided during excavation.. Impacts of construction on the environment mainly include the impact of blasting vibration and noise generated by underground construction (main ring tunnel, hall and shaft) and the impact on water quality of domestic sewage and wastewater generated by construction.

The key environmental protection issues during construction are water and noise protection. Optimization of the sewage treatment process and noise protection measures is to protect the eco-environment and the health of area population.

10.2.1 Impact of Blasting Vibration on the Environment and Countermeasures

There are only a few civilian houses and residents in the construction area. The impact is mainly possible damage to houses caused by blast shock waves and the tolerance of residents towards vibration frequency and intensity.. Impact on the ground environment is small as the working face of buildings/structures construction is mainly deep underground. Blasting can be controlled by proper selection of blasting parameters during construction.

10.2.2 **Impact of Noise on the Environment and Countermeasures**

The impact on the sound environment is mainly from excavation blasting, crushing of sand and gravel, mixing of concrete, construction transport and the operation of heavy machinery. As most of work is underground, the scope and time duration of impact on ambient noise are limited. Considering that the impact is mainly on construction personnel and the residents near the tunnel, low noise equipment and necessary work force protection need to be adopted during construction.

10.2.3 **Analysis of Impact on the Water Environment**

Sewage and wastewater generated in the project construction area include construction wastewater and domestic sewage. Sewage being discharged directly into the watercourse nearby without treatment may have a large impact on water quality. Treatment of construction wastewater and domestic sewage must be carried out and discharges brought up to standard or recycling needs to be implemented.

10.2.4 **Water and Soil Conservation**

Water loss and soil erosion may be generated by inadequate design of living quarters, construction roads and disposal areas. Due to the thick overburden, if inadequately designed, have a large impact on the surrounding surface water. Therefore, engineering and biological measures need to be taken to prevent scouring of rainfall runoff to the construction site and disposal area, so as to reduce water loss and soil erosion.

10.3 Electrical Safety

There are many high voltage or high current pieces of equipment on the site, which can present an electrical hazard to personnel if not properly secured. The design, installation and operation of electrical equipment will be in compliance with the national electrical codes and standards. Primary mitigation of the hazard will be by deenergizing equipment, placement of barriers and effective administrative procedures and formal personnel training.

10.4 Fire Safety

Based on previous accelerator experience, the predominant sources of fire have come either from electrical malfunctions or abnormal heat loads/overheating in components. These can cause break down of the electrical insulation and subsequent arcing. Accelerator components in the tunnel are primarily fabricated out of non-flammable materials. Combustible materials in general are kept to a minimum. VESDA (Very Early Smoke Detector Apparatus) warning system and cable temperature alarm system will be installed in all underground tunnels and halls. Sprinklers, hydrants and water curtains have not been specified to avoid possible water damage to the machines. Because there are no existing codes and standards for a facility like CEPC, the fire safety measures will be specified and detailed in the next design phase and subject to the approval of authorities.

10.5 Cryogenic and Oxygen Deficiency Hazard (ODH)

Some failure modes of the cryogenic system may be followed by a helium and or nitrogen release into the underground tunnel and oxygen deficiency could occur. Personnel working in the tunnel shall be warned and evacuate safely. There is need to provide an oxygen deficiency monitoring system, ventilation, escape routes and sufficient personnel training .

10.6 Non-Ionization Radiation

Non-ionizing radiation hazards on the site include: RF radiation and magnetic fields.

11 R&D Program

11.1 Superconducting RF

CEPC will require two large SRF systems: 384 cavities operating at 650 MHz in 96 cryomodules for the main ring and 256 cavities operating at 1300 MHz in 32 cryomodules for the Booster. This would be one of the largest SRF installations in the world. To succeed with designing, fabricating, commissioning and installation of such a system, a very significant investment in R&D, infrastructure and personnel is absolutely necessary.

11.1.1 **Initial SRF Technology R&D (2016-2020)**

The initial R&D goals would be to develop with industry the prototypes of all components and demonstrate the required performance.

11.1.1.1 ***Initial Technology R&D***

1. Develop an SRF cavity of each type; order several prototypes from industry; perform a series of tests to optimize the cavity surface treatment; build vertical test set ups and perform tests to demonstrate the cavity performance goals. Weld helium jackets on the cavities, re-test and demonstrate the performance goals.
2. Design fundamental RF power couplers (FPCs a.k.a. RF input couplers); order at least two couplers of each type from industry; build FPC test stands; test the FPCs and demonstrate that their performance meets the CEPC requirements.
3. Design HOM dampers; fabricate one or two prototypes of each design; design and build test set ups; test the HOM dampers.
4. Design and fabricate frequency tuners and a LLRF control system.
5. Design and build a short (two-cavity) horizontal cryomodule for each cavity type; build a test stand; demonstrate performance of all components integrated together into a cryomodule.

11.1.1.2 ***Infrastructure and Personnel Development***

For the initial R&D, most of the infrastructure (clean rooms, HPR system, vertical and horizontal test stands) is available on-site or can be accommodated on-site. Some existing facilities will have to be upgraded; additional project-specific equipment will be purchased and some additional space is needed. This can be estimated as soon as a detailed R&D plan is developed.

At this stage, it is very important to begin the hiring and development of personnel. The core project personnel must be in place by the middle of this phase of the project. It will take at least 4 years with two teams working in parallel: one working on the main ring SRF and the other on the Booster SRF. Each core team should consist of about 10 people (physicists, engineers, technicians). Support from other technical groups will be required when necessary. Collaboration with other laboratories (BNL, DESY, Fermilab, JLab, KEK, …) will help to shorten this stage of the project.

11.1.2 **Pre-Production R&D (2019-2022)**

The goal during this pre-production phase is to demonstrate robustness of fabrication and assembly processes of the cryomodule and its components. It will establish procedures, quality control steps, test set ups, assembly sequences, etc. for the production run.

11.1.2.1 ***Pre-Production R&D***

During the pre-production phase, it is suggested to build and test two Booster cryomodules and three main ring cryomodules. To accomplish this, the following will be necessary:

1. Build and test thirty 1.3 GHz Booster cavities and forty 650 MHz main ring cavities. This will allow pre-qualification of vendors for cavity mass production, establish treatment processes and debug all procedures, demonstrate that the cavity fabrication and treatment approaches are adequately robust to produce cavities meeting requirements with high yield (~ 90 %). Several cavities of each type should be chosen for horizontal testing. Two to three cavity fabrication and treatment vendors should be pre-qualified by the end of this step.
2. Build and test twenty FPCs for the Booster cavities and sixteen FPCs for the main ring cavities.
3. Build and test a sufficient number of tuners and other ancillary components.
4. Build and test cryomodules and demonstrate cryomodule performance. A cryomodule beam test is recommended especially for the HOM damping and heat load performance of the main ring cryomodule.

11.1.2.2 ***Infrastructure and Personnel Development***

A large scale SRF R&D and production facility will have to be built before 2019 on the CEPC site. A superconducting RF (and Magnet) Laboratory (Hall) of at least 10,000 m^2 is needed to accommodate facilities and assembly lines necessary for the production run, but it will be populated initially only with facilities and assembly lines sufficient for pre-production. The CEPC SRF team should make site visits at the beginning of the initial R&D phase (2016) and study facilities used at JLab and XFEL as well as industries for SRF system production and scale them as appropriate to the size of the CEPC SRF system. If a large scale SRF lab can't be built before 2019 on the CEPC site, as an intermediate step, a similar but smaller lab should be built (mainly to use existing experimental halls or workshops) during 2017-2018.

The facility (on the CEPC site and in industry) should include: cavity inspection and local repair facilities, RF laboratory and tuning set ups, BCP and EP treatment facilities, annealing furnaces, 4 vertical test stands, clean rooms, HPR systems, FPC preparation and conditioning facilities, cryomodule assembly lines, 4 cryomodule horizontal test stations, high power RF equipment and a cryogenic plant.

To build and install the Booster SRF system in three years (2023-2025), the production facility should have the capacity to assemble about 1 cryomodule per month. To build and install the main ring SRF system in four years (2023-2026), the assembly lines should manufacture about 2 cryomodules per month as well. To sustain this rate, the vertical test stands should be able to test 2 Booster cavities per week and 2 main ring cavities per week.

Commissioning and operation of the pre-production facility should begin during the last two years of the initial R&D phase (2018-2019). The pre-production stage will take 4 years, two of which will be for equipment installation and commissioning. The pre-production capacity of the off-site facility should be one fifth to one quarter of the eventual production facility.

Starting in the last year of the initial R&D (2019), the core SRF teams should begin hiring and training more personnel (~ 200 FTEs, mostly engineers and technicians), who will then work first in the pre-production and then in the production facility.

11.1.3 **Examples of What is Available at Other Labs**

JLab

JLab has recently completed a production run for the CEBAF 12 GeV Upgrade, which included building ten 8-cavity 1500 MHz cryomodules. The SRF infrastructure at Jlab was recently upgraded [1]. This is a good example of a contemporary SRF facility. It has the capacity of: i) testing 4 cavities per week; ii) assembling 2 cryomodules per month; iii) performing 1 cryomodule test per 6 weeks. CEPC will need to have double JLab's capacity for i) and ii) and 6 times higher for iii).

LCLS-II

LCLS-II will rely on facilities at JLab and Fermilab for the SRF cryomodule production. CEPC's facility will be approximately equal to the combined JLab's and Fermilab's facilities.

Europe

A good summary of SRF infrastructure available in Europe is given in [2]. There are several tables in an annex to this paper, listing SRF related equipment available in different European laboratories.

European XFEL

The European XFEL production rate is one 8-cavity cryomodule per week, which requires an average cavity production and vertical acceptance testing rate of at least eight per week [3]. This is comparable with the required CEPC production rate. In ref. [4] one can find a description of the XFEL cryomodule assembly facility at CEA in France. The cryomodule test facility at DESY can test 3 cryomodules at once.

11.1.4 **References**

1. C. E. Reece, P. Denny, A. V. Reilly. Performance characteristics of Jefferson lab's new SRF infrastructure. Proc. SRF 2013, p. 216
2. W. Weingarten. Strategy/result for RF test infrastructures. Report EuCARD-MIS-2011-003
3. D. Reschke, et al. Analysis of the RF test results from the on-going cavity production for the European XFEL. Proc. LINAC 2014
4. C. Madec, et al. The challenges to assemble 100 cryomodules for EXFEL. Proc. SRF 2013, p. 816

11.2 RF Power Source

11.2.1 650 MHz/400 kW CW Klystron

Because the CEPC collider RF cavity frequency is 650 MHz, the power source is also the same frequency. The cavities will be powered with a CW power source capable of delivering more than 560 kW. Taking into account the klystron operation lifetime and power redundancy, each cavity will be individually powered with a CW klystron amplifier capable of delivering more than 800 kW.

There are no 650 MHz CW klystrons available from the major klystron vendors, CPI, THALES and TOSHIBA. Table 11.2.1 summarizes the current status of available klystrons near 650 MHz frequency range.

Table 11.2.1: Present status of klystrons near 650 MHz frequency range

Frequency (MHz) / Vendor	CPI (kW)	THALES (kW)	TOSHIBA (kW)
400		180/250/300/800	
476	1200		
499	800		
500	70/100/800	180/250/300/800	165
500.08			180
508.6			1200
700	1000		
704	1000		
805		180/250/300/800	

The klystron could be manufactured by industry after initial R&D. The klystron could be developed from existing 500 MHz or 700 MHz CW klystrons jointly by IHEP and an industrial company.

In addition, the new depressed collector klystron will be considered as a possibility. It will be studied, and discussed with an appropriate company that could be a partner with IHEP.

11.2.2 650 MHz/400 kW Solid State Amplifier (SSA)

Because of the lower efficiency in solid state amplifiers, the base line power source for CEPC collider is the klystron. A 650 MHz/150 kW SSA has been developed by two different Chinese companies: Beijing BBEF Science & Technology Co., Ltd. and Chengdu Kaiteng Sifang Digital Radio & TV Equipment Co., Ltd., Their efforts are to develop a 400 kW SSA with increased efficiency and lower cost. This will provide more options for the CEPC collider RF power source.

11.3 Cryogenic System

The refrigerator is the key component of the cryogenic system, which includes the oil lubricated screw compressor, the oil separator, the turbine expander, the high efficiency heat exchanger, the cold compressors, cryogenic valves, and the insulation vacuum cold box and control system. The ancillary facilities include helium storage

tanks, liquid nitrogen storage tank, distribution valve boxes, LHe storage Dewar, and the cooling water system.

A CEPC cryogenic system will be constructed along with the SRF cavity test station. This will include one refrigerator and its ancillary facilities to accommodate the amount of vertical and horizontal testing required for superconducting cavities in the first 5 years.

11.4 Magnets

In the R & D stage of CEPC project, three prototype magnets will be developed to study the key technical issues of magnet design and production.

First, is the prototype dipole magnet for the Booster; the following key technical issues will be carefully studied. 1) Magnetic and mechanical design of the dipole magnet at very low field. 2) The method of earth field shielding. 3) The eddy current effect induced by ramping. 4) The fabrication procedures of 4-5 m long steel-concrete cores with small cross section. 5) The in-situ assembly of 16 m long magnets and in situ welding of hollow aluminum conductors.

Second, is the prototype quadrupole magnet for the Main Ring. Issues: 1) The magnetic and mechanical design of the quadrupole magnet with economical cross section and size. 2) Development and mass production of high quality hollow aluminum conductors. 3) The fabrication procedures of coils wound from hollow aluminum conductors. 4) The magnetic field measurement of the 2 m long quadrupole magnet with small aperture.

Third, is the prototype superconducting quadrupole magnet for the Interaction Region in the Main Ring. Issues: 1) The magnetic and mechanical design of the superconducting quadrupole magnet with very high gradient. 2) Development of Ni_3Sn Rutherford cable. 3) The fabrication procedures of coils wound by Ni_3Sn Rutherford cable. 4) The design and development of the cryomodule. 5) Magnet assembly and test.

The total cost evaluation of the three prototype magnets is about 8.15 M RMB.

11.5 Magnet Power Supplies

All magnet power supplies will be produced domestically. R&D is needed for some critical equipment or sub systems.

- Full digital control system for digital power supplies.
- Automatic data acquisition system for current stability of power supplies and automatic coefficient-correction system to promise the precision of load currents.
- Stability research on the power supply based on the redundant design of N+1 module.
- Radioaction tolerance design and tests for power supplies which are needed to be installed under tunnel.
- EMC research

11.6 Vacuum System

There are two types of dipole chambers that can be considered. One is an aluminum chamber similar to the LEP vacuum chamber. It has a beam channel, three cooling water channels, a pumping channel used to install NEG strips, and lead shielding

covering the dipole chamber with thickness 3 to 5 mm. The other choice is a copper chamber with a beam channel and a cooling water channel, coated with a NEG film inside the dipole chamber. Prototypes of these two types of dipole chambers will be fabricated and tested. The final choice will be decided based on the R & D results.

The aluminum chamber manufacturing procedure follows these steps:

- Extrusion of the chambers,
- Machining of the pumping slots,
- Machining of the components to be welded,
- Chemical cleaning,
- Welding of the side ports,
- Mounting of the NEG strips,
- Welding of the covers of the pumping channel, water connections and flanges,
- Leak detection,
- Lead coating the outside of the chamber.

The copper chamber manufacturing procedure is:

- Extrusion of the beam pipe and cooling channel,
- Machining of the components to be welded,
- Chemical cleaning,
- Electron-beam welding,
- Welding of the end flanges and water connections,
- Leak checks,
- NEG coating of the inside of the chamber.

11.7 Instrumentation

11.7.1 **Bunch by Bunch BPM**

Depending on the distance to the IP point, the time between the positron and electron passing through the BPMs differ by 4.0 ns to 1.67 μs. So we want different type electronics to acquire the BPM position. Since we put the electronics in the tunnel, radiation protection for the electronics is important.

11.7.2 **High Vacuum Feedthroughs**

High vacuum feed throughs are an important part of BPMs and kickers. Two points to consider: ceramic welding can maintain high vacuum and 50 ohm matching can avoid signal reflection.

11.7.3 **Beam Loss Monitor**

Pin diode beam loss monitors are useful because of their advantages. But for CEPC, due to the high energy and therefore the high counting rate, gas ionization chamber type monitors will be adopted and developed.

An ionization chamber consists of two parallel metallic electrodes (anode and cathode) separated by a gap. The gap is filled with gas (compressed air, argon, xenon). Ionization chamber response times can reach to 0.3 μs and by adopting special signal

processing, the dynamic range can reach 10^6-10^8. Ionization chambers can be built from radiation-hard materials like ceramic, glass and metal with no radiation damage or aging. With the progress in electronics technology response time of gas ionization chamber BLMs can reach the microsecond level, and the problem of large noise can be eliminated by appropriate setting of the threshold.

11.8 Control System

11.8.1 **Introduction**

Because of the large scale of CEPC, both in geographical extent and large energy stored, there are significant and difficult challenges to develop a precise timing system and the required machine protection. Also, the number of signals to be controlled and monitored will be very large. Therefore, the infrastructure of the control system needs to be studied carefully, and techniques for handling the large amount of data developed.

11.8.2 **Large Scale and High Accuracy Timing System**

High accuracy timing signals are needed since the bunches are short and the RF frequencies high. Fiber optics will be used to transmit signals. Therefore time drift in the fibers due to temperature variations will be a big problem due to the large distance between stations. To achieve the high accuracy needed, a demonstration system should be set up to study the temperature caused time drift effect and to solve this problem.

11.8.3 **Machine Protection System**

A fast and reliable machine protection system is needed to protect hardware from damage in case of machine malfunction and the large amount of stored energy in the beams. Reliable and radiation hard connections, redundant techniques, fast response algorithms, real time self-monitoring techniques, need to be studied, and prototypes built, tested and evaluated.

11.8.4 **Control System Infrastructure**

A highly distributed control system with a high performance network will be the backbone initially. Infrastructure of the control system should be studied carefully to make sure that it can fully fulfill the requirements and furthermore has the possibility for upgrades.

11.8.5 **Large Size Data Handling**

Data rates and data size will be large due to the large number of signals to be controlled and monitored. How to store, retrieve, analyse and visualize the data will be a big problem. Efforts should be made as early as possible to study the related techniques and set up a demonstration system.

11.9 Mechanical Systems

11.9.1 Introduction

The key technologies and difficulties requiring additional R&D are the magnet support systems in both the Collider and the Booster rings. Mechanical system R&D goals:

- Develop simple and reliable mechanics for safe mounting and easy alignment;
- Design the installation and replacement method for Booster dipole magnets;
- Design the alignment method for dipole magnets in both rings and design a system for experimental verification of the alignment;
- The systems must be stable with large time constants, avoiding creep and fatigue deformation;
- Reduce the cost through structural optimization and experiment.

11.9.2 Range and Accuracy of Adjustment

Suppose the +Z axis of the girder coordinate system is along the beam, the +Y axis upward and the coordinate system is a right-hand one as seen in Figure 11.9.1. The range and accuracy of adjustment is listed in Table 11.9.1.

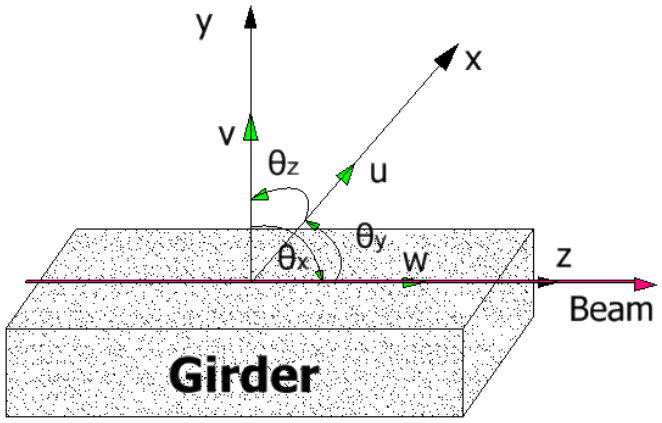

Figure 11.9.1: Coordinate system of the magnet support (called girder in this figure)

Table 11.9.1: Range and accuracy of adjustment.

	Range of adjustment	Accuracy of adjustment
u	≥±20 *mm*	≤±0.02 *mm*
v	≥±30 *mm*	≤±0.02 *mm*
w	≥±20 *mm*	≤±0.02 *mm*
θx	≥±10 mrad	≤±0.05 *mrad*
θy	≥±10 mrad	≤±0.05 *mrad*
θz	≥±10 mrad	≤±0.05 *mrad*

11.9.3 **Dipole Support System in the Collider**

11.9.3.1 ***Design Scheme***

The design scheme for the Collider dipole support is shown in Figure 11.9.2 and the supports of one module (1/4 of dipole iron core) is shown in Figure 11.9.3. Each module needs to be aligned separately. As the module is long, 4500 mm, two main supports and two auxiliary supports compose one support system, avoiding dipole magnet deformation. The main supports have 6 DOFs for supporting and adjusting the magnet module. The auxiliary supports have only a Y-axis DOF, placed at the locations with large deformation, to reduce stress and deformation. Each support consists of a pedestal, adjusting mechanism and magnet support layers. The pedestal is either poured during construction or made of prefabricated concrete forms.. The magnet support layers between the magnet and adjusting mechanism enlarges the contact area to reduce stress and displacement of the magnet. The adjusting mechanism for adjusting and fixing the magnet has 6 DOFs. The detailed structure is presented in Section 5.9.2.

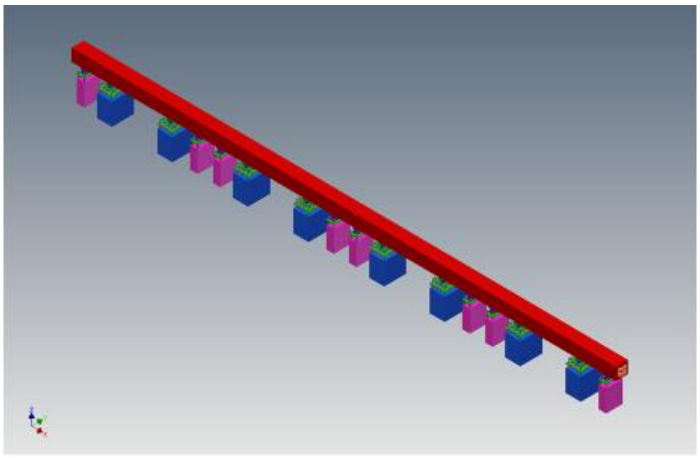

Figure 11.9.2: Dipole magnet and its supports for each unit

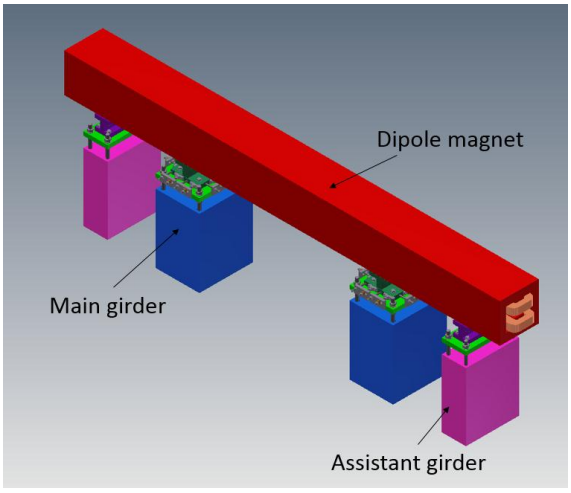

Figure 11.9.3: Dipole magnet and its supports for each module. (Note: Support is called girder and auxiliary support is called assistant girder in this figure.)

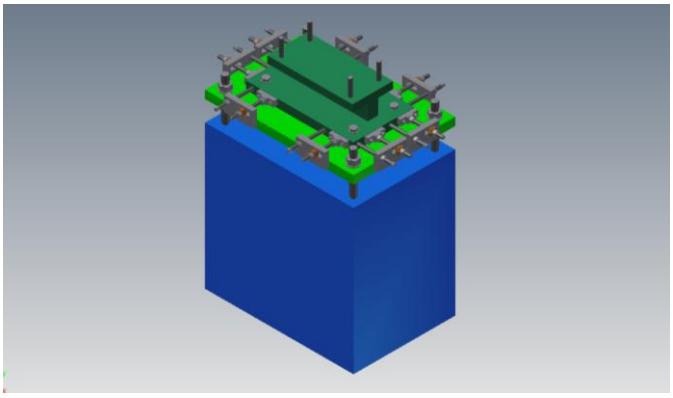

Figure 11.9.4: The main support

11.9.3.2 *Static Analysis*

The static analyses details are discussed in Section 5.9.2.

11.9.4 Dipole Support System in the Booster

11.9.4.1 *Design Scheme*

Figure 11.9.5 shows the Booster spatially above the Collider. The Booster dipole magnet unit is 16 m long, and composed of four 4000 mm magnet modules (1/4 of dipole iron core). Each module needs to be aligned separately. As the module is long, two main supports and two auxiliary supports comprise one support system to avoid deformation. The main supports have 6 DOFs for supporting and adjusting the magnet module. The auxiliary supports have only a Y-axis DOF, placed at the locations with large deformation, to reduce the stress and deformation. The difficulties are how to hang and align and replace the 16 m long dipole magnet in the Booster.

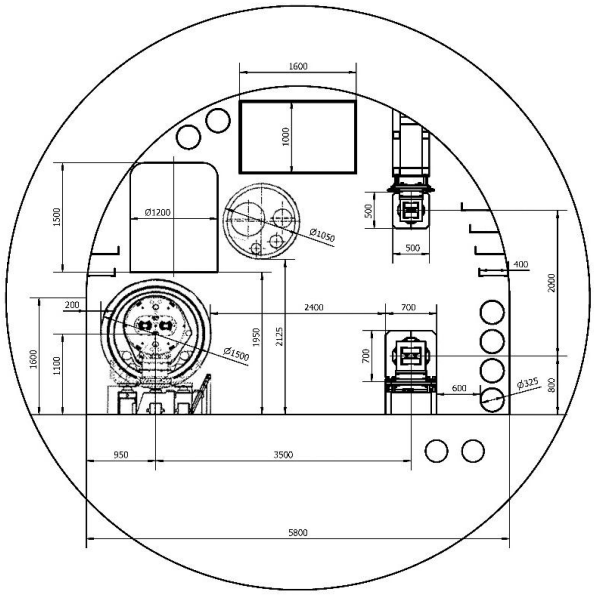

Figure 11.9.5: The cross section of the tunnel

For hanging supports in the Booster, three schemes are considered. For Scheme 1, the supports are hung from the top of the tunnel. In Scheme 2, the supports are fixed to one side of the tunnel. And in Scheme 3, the supports are integral for both rings. The detailed structure and layout are discussed in Section 5.9.3.

Each support includes pedestal, adjusting mechanism and magnet support layers. The pedestal is made of a steel frame; the other two components are similar to those of the main supports in the Collider. The structure of the main support is shown in Figure 11.9.6.

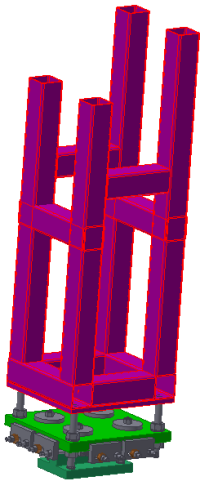

Figure 11.9.6: The main support of dipole magnet in the Booster

11.9.4.2 *Stress Analysis*

Scheme 3 must have enough height to contain the magnets for both rings. The instability is bad and the quantity of steel required is large. Considering these points, Scheme 3 is placed as a reserve. Schemes 1 and 2 both have successful experience in other accelerators [1,2]. The weight of each dipole magnet module is 2422 kg. The stress analysis is presented as follows. Follow-up work includes vibration analyses, and consideration of installation, replacement and alignment methods to select which scheme is better.

- Scheme 1
  The weakest point of Scheme 1 is at the support bolts. Suppose there are 8 M42 screw bolts for hanging the magnet and each bolt experiences the same force. Then the elastic stress on each bolt is 2.4 MPa, satisfying the static stress requirements.
- Scheme 2
  Figure 11.9.7 shows a magnet module and its supports. According to the analyses mentioned above, the compressive stress on each support bolt is 2.4 MPa, satisfying the static stress requirement. Suppose the weight is supported equally by each tri-frame, and the stress on the contact area is uniform, then the analysis of the tri-frame is shown in Figure 11.9.8. The stress at the supporting point is about 19 MPa, and the stress at the fixed point is 8.7 MPa, both satisfy the static stress requirements. The maximum stress is 43 MPa, at a one specific point, which can be removed or reduced by structure optimization.

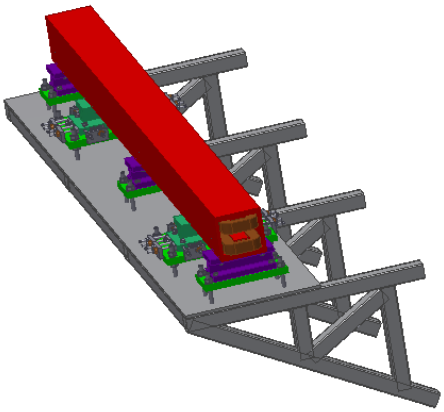

Figure 11.9.7: Booster supports in Scheme 2.

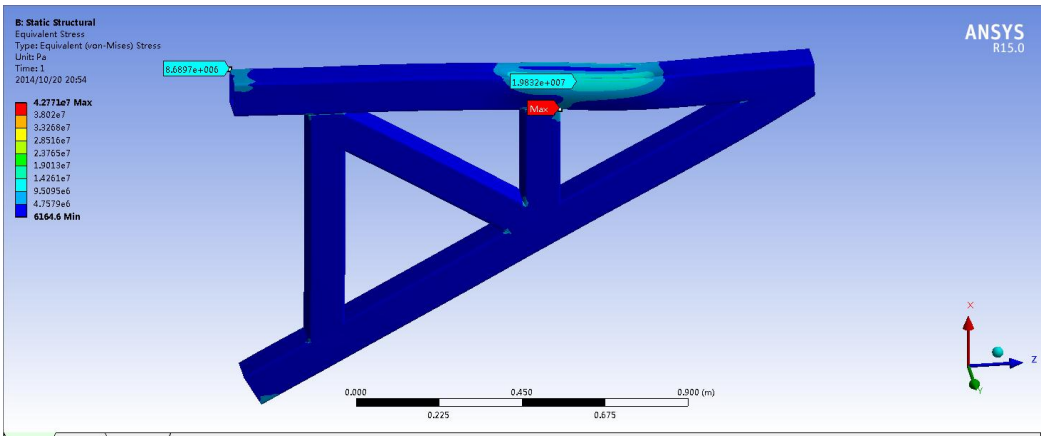

Figure 11.9.8: Stress analysis of supports in Scheme 2

11.9.5 **References**

1. Euro-XFEL tunnel TDR, pp. 458-460.
2. TPS Booster Magnet Girder Design and Installation, technical report.

11.10 Survey and Alignment

11.10.1 **Geoid Refining Research**

The accelerator complex is designed to be built in a plane. To determine the coordinates of every component in the accelerator complex we use a Cartesian coordinate system built by laying out a series of control networks. Through the control networks, survey and survey result adjustments, we can obtain the position relationship of these control network monuments. Based on these monuments we can determine the plane on which the accelerator complex will be built and build the Cartesian coordinate system.

A traditional control network survey is within a small area, such as 300 m×300 m, and the survey is divided into a horizontal survey and a level survey. In this way we can

avoid accumulation of errors. By the moving station method, we use our survey instruments to measure many stations to complete the control network survey. At each station we can measure the horizontal and level coordinates of the monuments by measuring the geoid orientation. For a small area we hypothesize that the geoids we measured in every station are in the same plane, so we can do datum adjustments in horizontal and in level separately. But for a large area geoid undulation must be taken into account. If we use the traditional method to do datum processing the error will become very large. So we need to do a geoid refining survey, and find out the change of gravitational potential and deviations from the vertical.

We plan to carry out geoid refining research. To do this research we need to measure a series of points along a 34 km (ring diameter) length with 100 m interval spacing between points. We will calculate the equipotential geoid curve. For an object within 17 km the geoid refining accuracy should be better than 5 mm.

This geoid refining achievement can significantly improve the survey and location precision in large engineering projects such as CEPC-SPPC.

11.10.2 **Precise Geodesy 3-D Adjustment Research**

Based on geoid refining, we can correct all the control network monument coordinates to the earth ellipsoid and use the earth ellipsoid as a reference to do datum processing. As shown in Figure 11.10.1 the CEPC survey range is very large; the Z axis of each instrument station coordinate system is not parallel to the Z axis of accelerator global coordinate system.

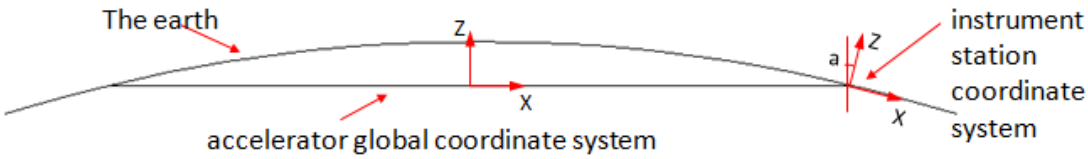

Figure 11.10.1: accelerator global coordinate system and instrument station coordinate system.

The angle ‘a’ increases with the size of the ring. Assume the earth radius R = 6374 km and the ring diameter D = 17 km. Then if the horizontal and vertical distances L = h = 5 m, we calculate that the differences between L and L’, h and h’ are both 6.6 mm. This is illustrated by Figure 11.10.2.

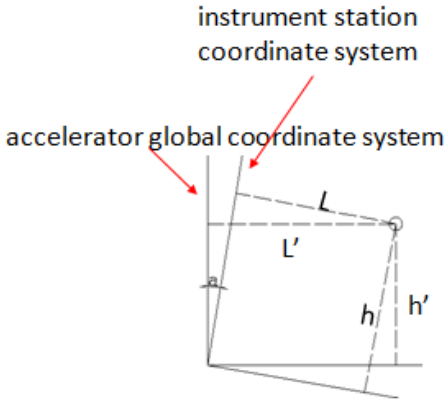

Figure 11.10.2: Differences in horizontal and vertical.

So the traditional 2D+1D network adjust method is not suitable and we must do research to develop a 3-D adjustment method. The new method should use the earth ellipsoid as a reference and in order to avoid error accumulation, the Z axis of each instrument station should be fixed during adjustment calculations.

This research will include establishment of the adjustment model, software programming and survey test verification.

Precise geodesy 3-D adjustment can be applied to land surveying, city planning, expressway construction, high-speed railway construction, and water conservation projects. It can significantly improve survey precision and increase productivity.

11.10.3 **Laser Collimator System Research for the Interaction Region**

A lot of components are located in the interaction region, but the intervisiblity is poor or unavailable there. We plan to use a laser collimator system to carry out alignment in this region. This can be quite precise and suitable for linear alignment.

We will install two laser collimators on one side of an IP and two targets on the other side. Using laser trackers and levels to align the laser collimators and targets to the nominal position we then can use this system to align all the components between them relative to the beam orbit. The accuracy we want to achieve is 0.1 mm in 100 m.

.

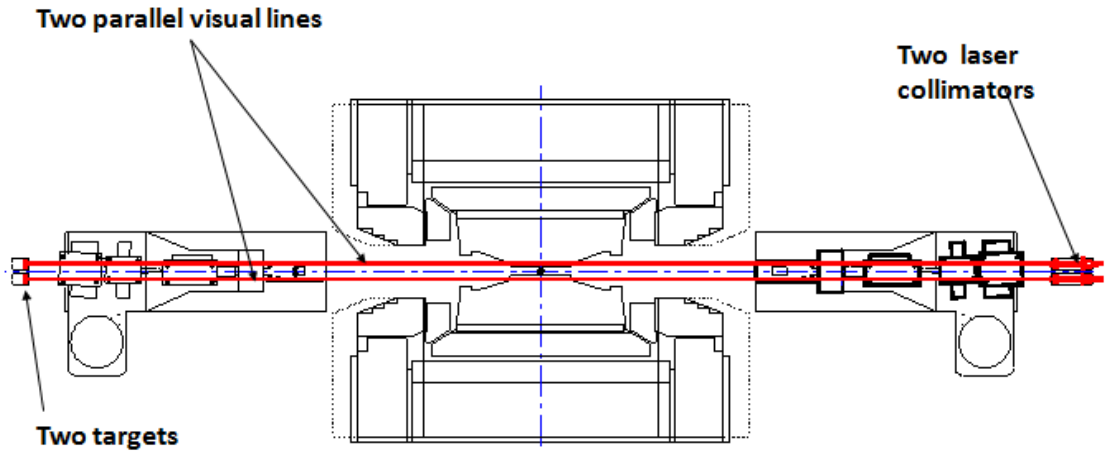

Figure 11.10.3: Interaction region alignment.

11.10.4 **Photogrammetric Survey and Alignment System**

In order to improve the efficiency of the CEPC survey and alignment we will carry out R&D on a high precision photogrammetric survey and alignment system. We have done some preliminary photogrammetry R&D based on BEPCII, including algorithm development, software programming and survey experiments.

To apply the photogrammetry technology to accelerator alignment we still have some problems to be solved. For the complicated environment of the accelerator tunnel, it is very difficult for the program to identify the features from the image. (An example of a feature would be a fiducial mark inscribed on the outside of a magnet based on magnetic measurements.) We need to design special targets and develop effective methods to enhance the identification rate. We need to do calibration calculations to decrease the camera lens distortion. We need to improve our program algorithm to increase the feature extraction accuracy. We need to develop the adjust algorithm used

for photogrammetry which can process the joint survey result of several measurement stations. We should also build the hardware platform that can take enough high accuracy photos of the fiducial points. Many experiments need to be done to verify effectiveness and accuracy..

11.11 Linac and e^+/e^- sources

11.11.1 **Polarized Electron Gun**

A photocathode dc-gun type electron source using a specially prepared GaAs/GaAsP super-lattice photocathode is one of the most critical electron source components, and for IHEP, this is a rather new technology. So this requires further study.

The R&D for the polarized electron source will be focused on five aspects: first, studies of the basic physical properties of the semiconductor photo-cathode itself; second, to build a prototype of 100-150 kV photocathode DC gun system; third, R&D on the electron gun itself, the goal being to achieve a high gun voltage while maintaining a low dark current to ensure a long cathode lifetime; fourth, collaborative research on high polarization photocathodes; fifth, to develop a polarization measurement device for electron beam.

11.11.2 **High Intensity Positron Source**

Although the technology of conventional positron sources is mature and can satisfy the requirements for the CEPC Linac, some components, in particular the target and the flux concentrator, would benefit from further optimization.

The R&D for high intensity positron source will be focused on the following aspects: a simulation study on positron yield by optimizing target material, thickness and capture efficiency; and the optimization of the flux concentrator design with high performance. This work will be a collaboration on high intensity positron production on the Super-KEKB Linac.

11.11.3 **S-Band Accelerator Structure Related R&D**

S-Band SLAC type accelerator is a mature technology. But the RF power feed is through a single coupling-hole which results in a field asymmetry. The time dependent multipole fields in the coupler induce a transverse kick along the bunch and cause an increase of beam emittance. An S-Band accelerator structure adopting a dual-feed racetrack design instead of the single-feed couplers will be developed to minimize the multipole field effects and improve beam quality.

11.11.4 **High Stability Pulse Modulator Related R&D**

A future option for the CEPC Linac is to construct a FEL. The Linac for a FEL requires very tight control of the klystron RF phase jitter which is directly related to modulator output pulse amplitude stability. To improve the pulse stability of the Linac modulator, attention was focused on PFN charging voltage stability which directly affects the modulator output pulse stability.

A prototype of a high performance pulse modulator with a 10 ppm stability charging systems will be considered. The goal is modulator pulse amplitude stability of 30 ppm rms. The following power electronic technology and advanced measurement and controlling technology will be adopted: SPRC (series-parallel resonant converter) power electronic, high voltage technology, fast timing control system, modern electronic measuring technology.

11.11.5 **High Precision Synchronization and Timing System**

The high beam stability for FEL generation requires RF phase and amplitude to be within a tight tolerance. An advanced LLRF system is essential for a high performance electron beam for the FEL application. This requires R&D on RF power source control, high precision timing system and beam feedback.

11.12 High Field Superconducting Magnet

A preliminary plan for the R&D at IHEP on 20 T accelerator magnets is as follows:

- **2016-2020**. Development of magnets with field in the 10 to 12 T range. The magnets will use Nb_3Sn and be twin-aperture dipoles with field quality of 10^{-4}. Also an activity projected during this time period will be the fabrication and test of 2 to 3 T Bi-2212 coils and 4 to 6 T YBCO HTS coils in a 10 to 12 T background field. Basic research will be performed on tape superconductors suitable for accelerator magnets and explorations made of field quality, fabrication method and quench protection.
- **2021-2025**. Development of 15 T Nb_3Sn twin-aperture dipoles and quadrupoles with field uniformity of 10^{-4}. Also anticipated is the fabrication and test of 4 to 5 T Bi-2212 and 6 to 8 T YBCO HTS coils in 12 to 15 T a background field.
- **2026-2030**. During this period 15 T Nb_3Sn coils will be combined with HTS coils to achieve the 20 T field required by SPPC. Actually, 23.5 T would provide an operating margin. But some other possibilities still exist e.g.by using very high J_c Nb_3Sn (*X. Xu et al, Appl. Phys. Lett. 104 082602*) only or HTS only to reach the 20 T field. The goal is for these prototype dipoles and quadrupoles to have field uniformity of 10^{-4}. These will be the SPPC prototype dipoles and quadrupoles. Infrastructure build-up will continue.

For the first five years from 2016 to 2020, our work will focus on the development of the 12 T operational field twin-aperture Nb_3Sn dipole with field quality of 10^{-4} and related infrastructure. These activities include:

a) Magnetic design: coil geometry study (common coil, block type, cos-theta type, CCT type), field quality control (iron saturation, filament magnetization), mechanical structure (shell-based structure, collar structure), management of strain in the coils.
b) Magnet construction and test: manufacture and test of several Nb_3Sn 10 to 12 T operational field dipoles. The work will be carried out mainly at IHEP. However, there will be parallel collaborative activities and related infrastructure build-up in other institutes and industries. The magnets will be manufactured in such a way that they will allow HTS insert coil testing. In-house test facilities will be developed at IHEP.

c) R&D and production for high J_c Nb_3Sn has the goal of further increasing J_c and the production of long wires.
d) Development of a Rutherford cabling machine in China will also occur as a collaboration with related institutes or companies.
e) R&D done on advanced insulation materials for high-field magnets will be carried out collaboratively with related institutes or companies.
f) Fabrication equipment will be built and procedures established for producing high-field Nb_3Sn coils. This includes coil winding, heat reaction, conductor joint and epoxy impregnation.
g) The test facility for high-field accelerator magnets will be constructed for carrying out field measurements, and experimentally developing the quench protection system. The test facility includes a power supply and cryostat.

For HTS materials, we will carry out the R&D on Bi-2212 and YBCO conductors and coils in parallel. At this stage, significantly more work is needed to choose between Bi-2212 and YBCO. This program includes:

a) Fabrication and testing of 2 to 3 T Bi-2212 coils in a 12 T background field.
    - R&D and production of Bi-2212 conductor to further increase J_c, optimization of the reaction process; the production of long lengths of wire will be done in collaboration with industry.
    - Establishment of the fabrication equipment and procedures such as heat reaction and conductor joints, for high-field Bi-2212 coils.
    - Production and testing of Bi-2212 coils: a total of 10 to 20 coils will be wound and tested at 4 K with 12 T background field.
    - Quench protection study of Bi-2212 high-field coils.
b) Fundamental research on YBCO superconductor for accelerator magnets, fabrication and testing of YBCO coils with 12 T background field.
    - R&D and production of YBCO conductor: study the angular dependence of J_c and develop equipment and methods for the production of long wires and cost reduction. As with Bi-2212, the YBCO work will also be based on collaboration with related institutes or companies. Establishment of the fabrication equipment and procedures for making high-field YBCO coils to optimize field quality, and to learn how do cabling and joints.
    - Production and testing of YBCO coils: a total of 10 to 20 coils will be wound and tested at 77 K and those that pass the tests at 77 K will then be tested at 4 K with a 12 T background field.
    - Quench protection study of YBCO high-field coils.

12 Project Cost Estimate and Timeline

12.1 Construction Cost Estimate

The most expensive technical systems of the CEPC are the "big three": (1) the superconducting RF (SRF) system; (2) the RF power source; and (3) the cryogenic system.

The synchrotron radiation power of the e^+ and e^- beams is 50 MW each, which must be replenished by the SRF systems.

There are two SRF systems:

- 1.3 GHz 9-cell cavities for the booster, similar to the ILC, XFEL and LCLS-II
- 650 MHz 5-cell cavities for the CEPC collider, similar to the ADS and PIP-II

This synergy makes it possible to make a reliable cost estimate based on the experience of the other accelerators,

Two cost references were particularly useful: the actual cost of LEP1 and LEP2, and the cost estimate of the LCLS-II 4 GeV SRF linac.

The LEP1 cost was well documented [1, 2]. The total in 1986 prices was 1.3 billion Swiss francs (BCHF). LEP2 added 288 SRF systems in the 1990s for about 0.5 BCHF [3]. Taking into account inflation, the construction of LEP1 and LEP2 would cost roughly 2.6 BCHF today. As the CEPC is twice as large as LEP, plus having a full-energy booster in the same tunnel and a new linac, the cost would be about 7 BCHF were it to be built in Switzerland. The cost in China is lower, especially the civil construction. Our goal is to reduce this by half to about 3.5 BCHF, or 20 billion Chinese Yuan.

But, of course, a simple cost scaling will not work accurately. For example, while the civil construction in China can be much cheaper than in Switzerland, the klystron price is the same worldwide as only a few vendors can manufacture them.

Two cost estimate exercises were carried out at the IHEP: one by the magnet group, another by the vacuum group. Each group was given the LEP design and was asked to estimate the cost if the identical magnet or vacuum system was built in China. The result showed that the LEP magnet would cost 30% less if fabricated in China. But the saving on the vacuum system was smaller because China does not have the advanced aluminium extrusion technology.

The LCLS-II is another useful reference. Its 4 GeV linac uses 1.3 GHz 9-cell ILC type cavities and cryomodules. The cost is 2.7 million US dollars (USD) per module, or a total of 105 million USD for 38 modules. But this cost does not include non-superconducting RF components (klystron, modulator, RF distribution, etc.) [4]. The CEPC booster needs 32 cryomodules (1.3 GHz), and the collider 96 cryomodules (650 MHz). The LCLS-II figure was used as a cross check for the cost estimate of the CEPC cryomodules.

There are several measures taken for reducing the cost:

- When there are several different technology options, the cheaper one is chosen for the baseline.
- Two beams (e^+ and e^-) will share the same beam pipe as in LEP and CESR.
- As the CEPC has smaller beam emittance than LEP, the magnet aperture is reduced by 20% from the LEP magnet aperture. This saves construction as well as the operation costs.

- Although the solid state RF power source is more reliable and easier to maintain than the klystron, the latter is cheaper and has higher efficiency. So klystrons are chosen for the baseline.
- For tunnel construction, the tunnel boring machine (TBM) method is faster than the drill and blast method. But the latter can save 20-30% and thus is chosen. Moreover, this method can make a gate-shaped tunnel (like in a subway system) as in Figure 3.2, which provides more usable space than a circular shape.

The actual cost estimate of the CEPC was done by using a Work Breakdown Structure (WBS). Table 12.1 shows the WBS at Level 2. When this Pre-CDR was written, the WBS of most systems reached Level 4. In a follow-up Technical Design Report (TDR), the WBS will reach Level 7. A 10% contingency has been added.

Table 12.1: Work Breakdown Structure (WBS) of the CEPC

CEPC Work Breakdown Structure (WBS) at Level 2	
1	**Total**
2	**Accelerators**
2.1	Accelerator physics
2.2	Superconducting RF system
2.3	Cryogenic system
2.4	Magnets
2.5	Power supplies
2.6	Mechanical Systems
2.7	Vacuum
2.8	Instrumentation
2.9	Survey and alignment
2.10	Control
2.11	Radiation shielding
2.12	Linac
2.13	RF power source
2.14	Booster
2.15	Superconducting magnet R&D
2.16	Contingency
3	**Detector**
3.1	TPC
3.2	VTX
3.3	Calorimetry
3.4	Muon detector
3.5	Magnet
3.6	Computing, simulation and software
3.7	Trigger and data acquisition
3.8	Contingency
4	**Light sources**
4.1	γ ray source station
4.2	FEL
5	**Civil construction**
5.1	Tunnel and experimental hall construction
5.2	Mechanical and electrical installation

	5.3	Metallic structure installation
	5.4	Temporary engineering
	5.5	Independent costs
	5.6	Contingency
	5.7	Other costs
6	**Utilities**	

The accelerators are the most expensive part of the project, representing 63% of the total construction cost. Civil construction is about 26% of the total.

For the accelerators, the "big three" systems – SRF, RF power source and cryogenics – account for almost half of the cost. Figure 12.1 shows the relative cost of each accelerator system.

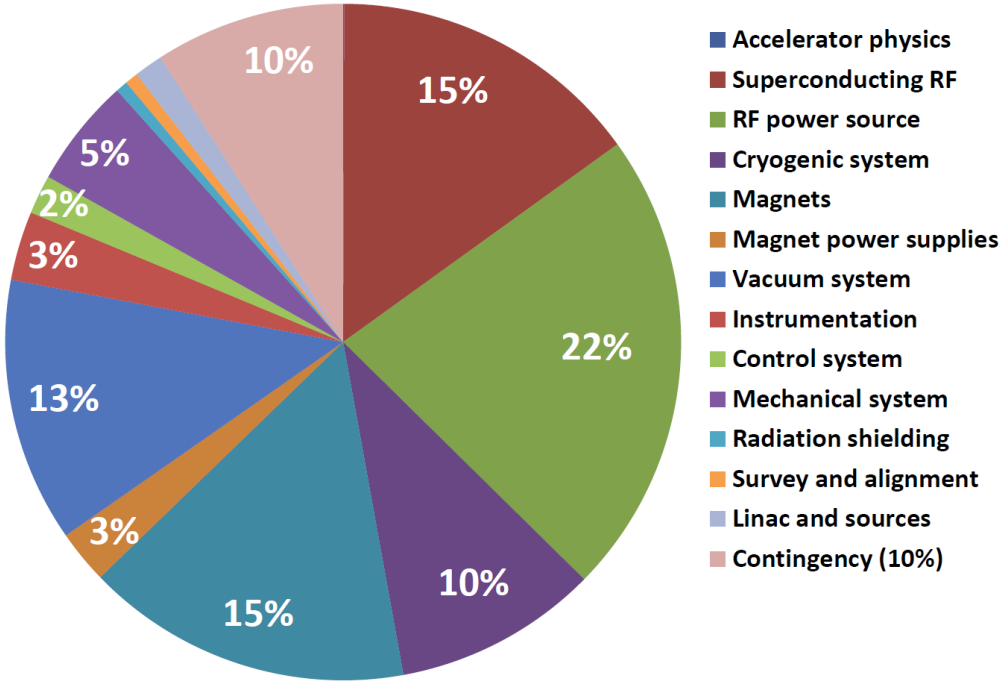

Figure 12.1: Relative cost of the CEPC accelerator technical systems.

It should be pointed out that the cost of the cryogenic system in this plot (10%) is based on a high efficiency HOM damper, which needs to be developed. Both the 1.3 GHz and 650 MHz SRF systems will operate at 2° K. The Carnot efficiency from the ILS study is listed in Table 12.2. Because the average beam current in the CEPC is high (16.6 mA for each beam), HOM loss in the cavity is significant (2.3 kW per beam in each cavity). Most of the HOM power must be taken out and dissipated at higher temperatures. Table 12.3 is the required efficiency of the HOM damper, a figure which is very demanding. How to design and implement such a damper is a critical R&D item for the CEPC.

Table 12.2: Carnot efficiency for CEPC SRF.

	40 K to 80 K	5 K to 8 K	2K
Efficiency in W/W	16.4	197.9	703.0

Table 12.3: Required efficiency of the HOM damper.

	40 k to 80 k	5 k to 8 k	2k
HOM heat load distribution	3%	0.3%	0.1%

12.2 Operations Cost Estimate

In addition to the capital construction cost, the operations cost is another major issue. It is mainly determined by the power consumption to operate the CEPC. When the Tevatron was running, the average total power usage at Fermilab was 58 MW. When the LHC was running, CERN used 183 MW (average over 2012). The consensus for a operating a future circular Higgs factory is that the power should not exceed 300 MW, in which 100 MW is for the synchrotron radiation. In other words, the wall plug efficiency (the ratio between the beam power and the wall power) should be 33%. This is a tall order as today's most efficient accelerator, the PSI cyclotron in Switzerland, has an efficiency of only 18%. The design efficiency for the ILC is just 9.6%. In order to have a highly efficient CEPC, one needs a highly efficient SRF system. The recent development of a new type of klystron (Collector Potential Depression, or CPD) is of particular interest as its claimed efficiency can be as high as 80%. Reuse and recycle of waste power from the accelerator is part of a general study nicknamed "green accelerators."

When this report was written, the estimated total power consumption of the CEPC was about 500 MW based on today's technology. Figure 12.2 shows the relative power consumption of each system in the CEPC. We will continue to investigate new technologies (e.g., the CPD klystron) to reduce these figures.

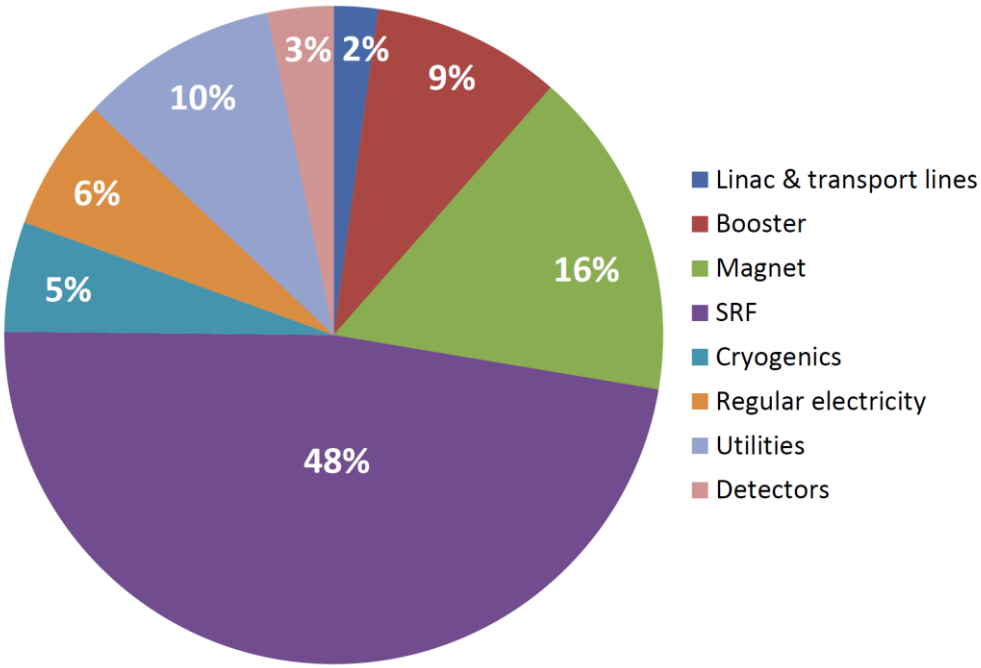

Figure 12.2: Relative power consumption of each system in the CEPC.

12.3 Project Timeline

Figure 12.3 shows our current conception of a timeline for the CEPC and SPPC facility. It consists of the following stages:

- The first milestone is to complete a Preliminary Conceptual Design Report (Pre-CDR) early in 2015. This goal was accomplished as the readers are reading this report.
- This report will be submitted to the Chinese government for inclusion in the government's 13th Five-Year Plan, which starts in 2016. If the CEPC gets approval, the R&D will take place from 2016 to 2020.
- Construction will start in 2021 in the government's 14th Five-Year Plan and will take about 7 years.
- Experiments can begin as early as 2028 during the 15th Five-Year Plan.
- For the SPPC, the focus will be to develop cost effective high-field superconducting magnets (16 – 20 Tesla) using a combination of Nb_3Sn and HTS superconductors. This will take about 15 years. The engineering design of the SPPC will start in 2030 and construction begin around 2035.

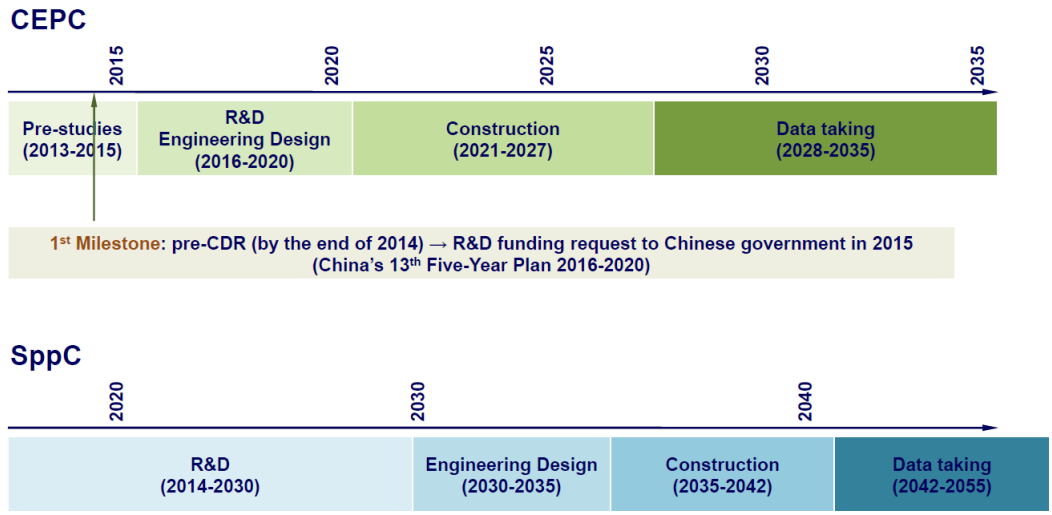

Figure 12.3: A possible timeline.

Of course the realization of such a "fast track" timeline depends on many factors. Some are under our control, some are not. After completion of this Pre-CDR, the focus turns to the R&D.

A critical path of the CEPC timeline is to achieve successful R&D for the two SRF systems:

- Collider: 650 MHz, 384 cavities in 96 cryomodules;
- Booster: 1.3 GHz, 256 cavities in 32 cryomodules.

This would be the largest SRF installation in the world. To succeed with designing, fabricating, commissioning and installation of such a system, a significant investment in R&D, infrastructure and personnel is necessary. The R&D has two parts:

- Prototyping as well as technology development for several critical components, in particular, the power coupler and the HOM damper.

- Pre-series production:
  - To fabricate and test 15-20 1.3 GHz cavities and 30-35 650 MHz cavities.
  - To establish a large RF facility similar to that at JLab, Fermilab and DESY for cavity inspection and tuning set ups, RF laboratory, several vertical test stands, clean rooms, HPR systems, FPC preparation and conditioning facility, cryomodule assembly lines, horizontal test stations, high power RF equipment, a cryogenic plant, etc.
  - To acquire the capability of assembling one Booster module and two Collider modules each month.
  - To have at least two vendors for each type of RF cavity.
  - Personnel development.

This R&D plan will need large resources and require several years. If the construction starts in 2021, the tunnel will take 4-5 years to complete. So there should be enough time for the pre-series production before the mass production of cavities.

12.4 R&D Budget

To carry out a successful R&D plan, an R&D budget was estimated for each system. (Details of the R&D plan are in Chapter 11). The total R&D budget is RMB one billion in five years (2016-2020), or about USD 160 million.

The breakdown for each system is shown in Figure 12.4. The majority of the R&D budget (58%) will be invested in the "big three" systems – SRF, RF power source and cryogenics – in order to establish a large RF facility as described above. The superconducting magnet represents another large portion (18%) of the R&D budget.

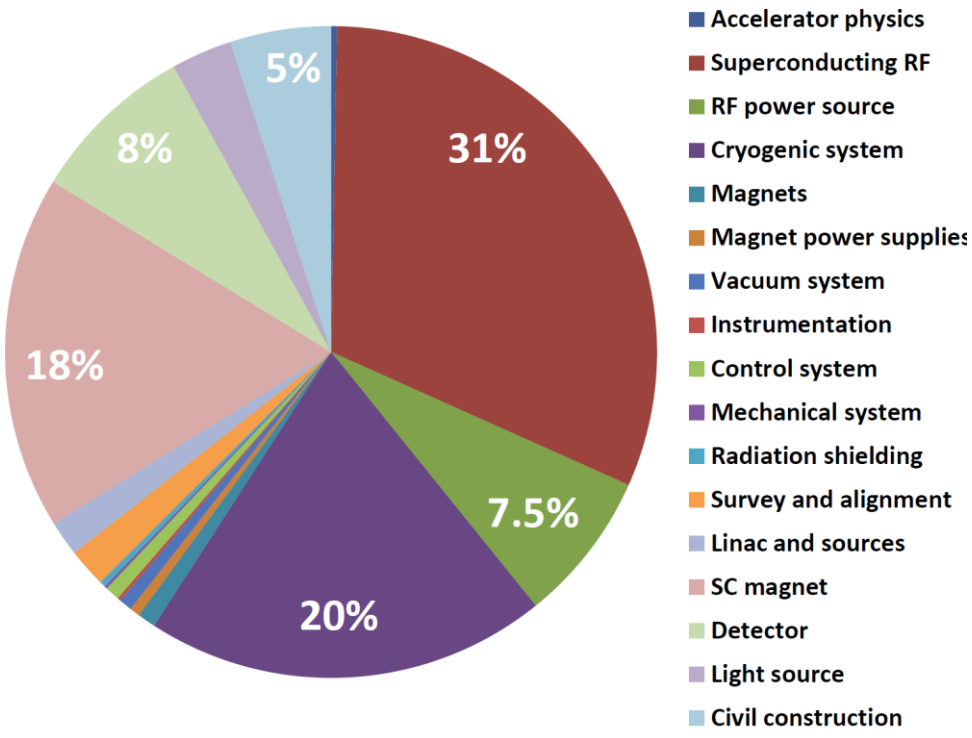

Figure 12.4: Breakdown of the R&D budget of each system.

12.5 References

1. “Financial Position of the LEP Project – Final Report,” CERN/FC/3313, May 30, 1990.
2. Herwig Schopper, “LEP – The Lord of the Collider Rings at CERN 1980-2000,” Springer (2009).
3. Steve Myers, private communication.
4. Marc Ross, private communication

Appendix 1 Parameter List

A1.1 Collider

Fundamental constants		
electronic charge	C	1.60E-19
speed of light	m/s	3.00E+08
C_q		3.83E-13
fine structure constance	α	0.0073
classical radius of electron [r_e]	m	2.82E-15
Euler's constant[γ_E]		0.577
electron Compton wavelength [λ_e]	m	3.86E-13
rest mass energy of electron	MeV	5.11E-01
Accelerator Parameters		
Beam energy [E]	GeV	120
Circumference [C]	km	54.374
Luminosity [L]	$cm^{-2}s^{-1}$	2.04E+34
SR power/beam [P]	MW	51.71
Bending radius [ρ]	m	6094
N_{IP}		2
n_B		50
filling factor [κ]		0.70
Lorentz factor [γ]		234834.66
Revolution period [T_0]	s	1.83E-04
Revolution frequency [f_0]	Hz	5475.46
Magnetic rigidity [$B\rho$]	T·m	400.27
momentum compaction factor [α_p]		3.36E-05
Energy acceptance Ring[η]		0.02
cross-section for radiative Bhabha scattering [σ_{ee}]	cm^2	1.52E-25
lifetime due to radiative Bhabha scattering [τ_L]	min	50.61

build-up time of polarization [τ_p]	min	21
Beam Parameters		
Beam current [I]	mA	16.60
Bunch population [N_e]		3.785E+11
emittance-horizontal [ε_x]	m·rad	6.12E-09
emittance-vertical [ε_y]	m·rad	1.84E-11
coupling factor [κ]		0.003
Beam length SR [$\sigma_{s.SR}$]	m	0.00214
Beam length total [$\sigma_{s.tot}$]	m	0.00265
Interation Point Parameters		
Betatron function at IP-vertical [β_y]	m	0.0012
Betatron function at IP-horizontal [β_x]	m	0.8
Transverse size [σx]	μm	69.97
Transverse size [σy]	μm	0.15
Beam-beam parameter [ξ_x]		0.118
Beam-beam parameter [ξ_y]		0.083
Hourglass factor	Fh	0.680
Lifetime due to Beamstrahlung-Telnov [τ_{BS}]	min	1005
Lifetime due to Beamstrahlung [simulation]	min	47
RF Parameters		
RF voltage [V_{rf}]	GV	6.87
RF frequency [f_{rf}]	GHz	0.65
Harmonic number [h]		118800
Synchrotron oscillation tune ［ν_s］		0.180
Energy acceptance RF［η］	%	5.99
Synchrotron Radiation		
SR loss/turn [U_0]	GeV	3.11
Damping partition number [Jx]		1

Damping partition number [Jy]		1
Damping partition number［Jε]		2
Energy spread SR［$\sigma_{\delta.SR}$]	%	0.1317
Energy spread BS［$\sigma_{\delta.BS}$]	%	0.0960
Energy spread total［$\sigma_{\delta.tot}$]	%	0.1629
Average number of photons emited per electron during the collision［nγ]		0.23
Transverse damping time [n_x]	turns	77.05
Longitudinal damping time [n_ε]	turns	38.52
Ring parameter		
Circumference [C]	km	54.374
Revolution period [T_0]	s	1.83E-04
Revolution frequency [f_0]	Hz	5475.46
Horizontal tune		201.08
Vertical tune		201.22
Number of arcs		8
Number of interaction regions		2
Number of short straight sections		4
Number of long straight sections		2
Number of straight sections with RF		8
Total number of dipoles[w/o FFS]		1952
Total number of quadrupoles[QF/D][w/o FFS]		2224
Total number of sextupoles[SF/D][w/o FFS]		1920
Total number of horizontal correctors[w/o FFS]		2224
Total number of vertical correctors[w/o FFS]		2224
Regular lattice period parameters		
Lattice type		FODO
Phase advance(horizontal/vertical)		60◦ /60◦
Cell length	m	47.2
Dipole type in regular lattice		MB

Number of dipoles[MB]		2
Dipole length	m	19.6
Strength of diplole	T	0.066
Quadrupole type in regular lattice		MQF/D
Number of quadrupoles[MQF/D]		2
Quadrupole length	m	2
Strength of quadrupole	m^{-2}	0.0218
Sextupole type in regular lattice		MSF/D
Number of sextupoles[MSF/D]		2
Sextupole length	m	0.4
Strength of MSF	m^{-3}	0.377
Strength of MSD	m^{-3}	0.596
Correcting dipole type		MBH/V
Number of MBHs		2
Number of MBVs		2
Strength of MBH[maximum]	urad	14
Strength of MBV[maximum]	urad	11
Maximum β value	m	82.8
Minimum β value	m	27.8
Maximum β value	m	82.8
Minimum β value	m	27.8
Maximum dispersion	m	0.38
largest horizontal size [σ_x]	mm	0.9435
largest vertical size [σ_y]	mm	0.0390
Dispersion suppressors		
Length	m	94.4
Horizontal phase advance/2π		0.333
vertical phase advance/2π		0.333
Dipole type		MB
Number of dipoles		2
Dipole length	m	19.6

Strength of dipole	T	0.066	
Quadrupole type		MQF/D	
Number of quadrupoles		4	
Quadrupole length	m	2	
Strength of quadrupole	m^{-2}	0.022	
Number of horizontal correctors		4	
Number of vertical correctors		4	
Strength of horizontal corrector[maximum]	urad	14	
Strength of vertical corrector[minimum]	urad	11	
Arcs			
Length	m	5852.8	
Number of cells per ARC		120	
Number of dispersion suppresors per arc		2	
Horizontal phase advance/2π		20.6667	
vertical phase advance/2π		20.6667	
Type	**Length[m]**	**Strength**	**Number**
MB	19.6	0.066[T]	244
MQF/D	2	0.022[m^{-2}]	248
MSF	0.4	0.377[m^{-3}]	120
MSD	0.4	0.596[m^{-3}]	120
BH[maximum]	0	14[urad]	248
BV[maximum]	0	11[urad]	248
Short Straight section			
Length	m	849.6	
Horizontal phase advance/2π		2.968	
vertical phase advance/2π		2.986	
Type	**Length[m]**	Strength	**Number**
SSQF/D	2	0.0218[m^{-2}]	36
SSBH[maximum]	0	43[urad]	36
SSBV[maximum]	0	16[urad]	36
Long Straight section			

Length	m	1132.4	
Horizontal phase advance/2π		3.968	
vertical phase advance/2π		3.986	
Type	**Length[m]**	**Strength**	**Number**
SSQF/D	2	0.0218[m^{-2}]	48
SSBH[maximum]	0	43[urad]	48
SSBV[maximum]	0	16[urad]	48
Interaction section			
Length	m	1132.4	
Horizontal phase advance/2π		6	
vertical phase advance/2π		6	
Maximum β value	m	5925	
Maximum dispersion	m	0.15	
The main RF system parameter			
Frequency	GHz	0.65	
Harmonic number		118800	
Cavity type		5-cell cavity	
Cavity operating voltage	MV	17.9	
Cavity operating gradient	MV/m	15.5	
Number of cavities per cryomodule		4	
Cavity active length(five-cells)	m	1.154	
Cryomodule length	m	10	
Number of Cryomodules per section		12	
Number of cavities per section		48	
Total number of cryomodules		96	
Total number of cavities		384	

A1.2 Booster

Accelerator Parameters		Unit	Injection	Extraction
Beam energy [E]		GeV	6	120
Circumference [C]		km	54.374	54.374
Revolution frequency [f_0]		kHz	5.4755	5.4755
SR power / beam [P]		MW	1.62E-05	2.4584
Bending radius [ρ]		m	6518.986	6518.986
n_B / beam			50	50
Lorentz factor [γ]			11741.9	234838.0
Magnetic rigidity [$B\rho$]		T·m	20.01	400.28
Beam current / beam [I]		mA	0.9197	0.8737
Bunch population [N_e]			2.10E+10	1.99E+10
emittance-horizontal [ε_x]	in equilibrium	m·rad	5.13E-11	2.05E-08
	injected from linac	m·rad	1.00E-07	
emittance-vertical [ε_y]	in equilibrium	m·rad	5.13E-13	2.05E-10
	injected from linac	m·rad	1.00E-07	
RF voltage [V_{rf}]		GV	0.213867	5.12
RF frequency [f_{rf}]		GHz	1.3	1.3
Harmonic number [h]			237423	237423
Synchrotron oscillation tune [ν_s]			0.32076	0.32076
Energy acceptance RF [η]		%	17.307	2.091
SR loss / turn [U_0]		GeV	1.7586E-05	2.814
Energy spread [σ_δ]	in equilibrium	%	0.00637	0.127
	injected from linac		0.1	
Bunch length [σ_δ]	in equilibrium	mm	0.13	2.66
	injected from linac	mm	~1.5	
Transverse damping time [τ_x]		ms	124577.9	15.56
		turns	682122	85.2
Longitudinal damping time [τ_ε]		ms	62317.8	7.789
		turns	341219	42.7
Circumference [C]		km	54.752	

Accelerator Parameters	Unit	Injection	Extraction
Horizontal tune		127.18	
Vertical tune		127.28	
Momentum compaction factor [αp]		7.69E-05	
Number of arcs		8	
Number of short straight sections		4	
Number of long straight sections		4	
Number of straight sections with RF		8	
Total number of dipoles		5248	
Total number of quadrupoles[QF/D]		1560	
Total number of sextupoles[SF/D]		1280	
Regular lattice period parameters			
Lattice type		FODO	
Phase advance(horizontal/vertical)		60°/60°	
Cell length	m	71.665	
Number of dipoles in a cell		8	
Dipole length	m	8.0	
Defection angle of dipole	mrad	1.2272	
Magnetic field of the diplole at injection	T	0.00307	
Magnetic field of the diplole at ejection	T	0.06140	
Number of quadrupoles		2	
Quadrupole length	m	1.0	
Strength of QF	m^{-2}	0.0281707	
Strength of QD	m^{-2}	-0.0281700	
Number of sextupoles		2	
Sextupole length	m	0.2	
Strength of SF	m^{-3}	0.20175	
Strength of SD	m^{-3}	-0.33382	
Length of BH/BV	m	0.3	
Strength of BH	T	0.1	
Strength of BV	T	0.1	

Accelerator Parameters	Unit	Injection	Extraction
Maximum horizontal β value	m	123.84	
Minimum horizontal β value	m	41.472	
Maximum Vertical β value	m	122.97	
Minimum Vertical β value	m	41.472	
Maximum dispersion	m	0.879	
Maximum horizontal size [σ_x]	mm	1.948	
Maximum vertical size [σ_y]	mm	0.159	
Dispersion suppressors			
Length	m	143.330	
Horizontal phase advance/2π		0.333	
vertical phase advance/2π		0.333	
Dipole type		C-Type rectangular	
Number of dipoles		8	
Dipole length	m	8.0	
Strength of dipole at injecton	T	3.070E-03	
Strength of dipole at ejecton	T	6.140E-02	
Number of quadrupoles		4	
Quadrupole length	m	1.0	
Strength of SF	m^{-3}	0.2018	
Strength of SD	m^{-3}	-0.3338	
Arcs	Unit	Value	
Length	m	5876.520	
Number of cells per ARC		80	
Number of dispersion suppresors per arc		2	
Horizontal phase advance/2π		13.67	
vertical phase advance/2π		13.67	
Type	**Length[m]**	**Strength**	
MB	8	0.00307~0.0614[T]	
MQF/D	1	0.028[m^{-2}]	

Accelerator Parameters	Unit	Injection	Extraction
MSF	0.2	0.20175[m^{-3}]	
MSD	0.2	0.3338[m^{-3}]	
Short Straight section			
Length	m	859.979	
Horizontal phase advance/2π		2	
vertical phase advance/2π		2	
Type	**Length[m]**	**Strength**	
SSQF/D	1	0.028[m^{-2}]	
Long Straight section			
Length	m	1074.974	
Horizontal phase advance/2π		2.5	
vertical phase advance/2π		2.5	
Type	**Length[m]**	**Strength**	
SSQF/D	1	0.028[m^{-2}]	
The main RF system parameter			
Frequency	GHz	1.3	
Harmonic number		237423	
Cavity type		9-cell cavity	
Cavity operating volage	MV	20	
Cavity operating gradient	MV/m	19.3	
Number of cavities per cryomodule		8	
Cavity active length(nine-cells)	m	1.038	
Cryomodule length	m	12.0	
Number of RF cryomodules per section		4	
Number of cavities per section		32	
Total number of cryomodules		32	
Total number of cavities		256	
Total RF Voltage at 120GeV	GV	5.12	
Length	m	1074.974	

Accelerator Parameters	Unit	Injection	Extraction
Number of bypasses		2	
Number of FODO cells in a bypass		15	
Number of bending magnets in a bypass		48	
Number of quadropole magnets in a bypass		30	
Width of bypass	m	13.16	

A1.3 Linac

Main parameter of linac	Unit	Value
E^- beam energy[E_{e-}]	GeV	6
E^+ beam energy[E_{e+}]	GeV	6
Repetition rate[f_{rep}]	Hz	50
E^- bunch population[N_{e-}]		2×10^{10}
E^+ bunch population[N_{e+}]		2×10^{10}
Energy spread (E^+/E^-)[σ_E]		$<1\times10^{-3}$
Emitance (E^-)		0.1 mm× mrad
Emitance (E^+)		0.1 mm× mrad

Electron Gun			
Gun type	Thermionic Triode Gun		
Cathode	Y824 (Eimac) Dispenser		
Beam Current (max.)		A	15
High Voltage of Anode		kV	150-200
Bias Voltage of Grid		V	0 ~ -200
Pulse duration （FWHM）		ns	1
Repetition Rate		Hz	50
Electron operation	Bunch charge	nC	3.2
Positron operation	Bunch charge	nC	11nC

Main parameter of linac	Unit	Value	
Positron source			
E- beam energy on the target		GeV	4
E- bunch charge on the target		nC	10
Target material		W	
Target thickness		mm	14
Focus device	Flux Concentrator		6 T
E+ bunch charge after capture		nC	3.2
E+ Energy after capture section		MeV	200
Accelerating structure parameters			
Operation frequency	MHz	2856.75	
Operation temperature	°C	40.0 ± 0.1	
Number of cells		84 +2 coupler cells	
Section length	mm	3048	
Phase advance per cell		2p/3 - mode	
Cell length	mm	35.0012	
Shunt impedance (r0)	MW/m	54.6 ~ 63.9	
Q factor		13990 ~ 13836	
Group velocity (vg/c)		0.0208 ~ 0.0070	
Filling time	ns	830	
Attenuation factor	Neper	0.57	

Appendix 2 Alternative Designs

A2.1 50-km Ring vs. 100-km Ring

In order to control the construction cost, the baseline design of the CEPC is a 54-km ring as described in Chapter 3. However, a cost estimate for a 100-km ring has also been done. This is based on the consideration that if additional funding sources can be identified to complement the government funds, the ring size can be increased. This is desired especially for the future SPPC in order to reach 100 TeV center-of- mass energy instead of 70 TeV as in the baseline.

For a Higgs factory, doubling the ring size will reduce the synchrotron radiation power by half for the same bunch intensity and same number of bunches. But the luminosity will also be reduced by 50% because the collision frequency is reduced by half. To keep the same luminosity, the number of bunches will have to be doubled, which leads to the same RF power as in a 50-km ring.

Most other systems in a 100-km ring will be doubled, such as the magnets, power supplies, vacuum, instrumentation, mechanical systems, etc. The tunnel length is also doubled.

With all these factors taken into account, the estimate is a 40% increase in cost for a 100-km ring relative to a 50-km ring.

A2.2 Two-Beam Pipes vs. One-Beam Pipe

In order to make the ring size as large as possible within the budget constraint, the baseline design of the CEPC uses one-beam pipe, i.e. both the electron and positron beams share the same beam pipe, similar to the BEPC-I, LEP and the CESR. An alternative design, which is preferred for beam physics considerations and machine operation, is to use two beam pipes, one each for the electron and positron beams, as in the BEPC-II, PEP-II, KEKB and DAFNE. Two-beam pipes could give higher luminosity because a larger number of bunches are allowed.

However, the cost increase for two-beam pipes is significant. The number of magnets, power supplies, vacuum, instrumentation, control, mechanical systems, and survey and alignment will be doubled, although the magnet aperture could be made smaller to offset some of the cost increase. The number of RF cavities may also need to be doubled in order to avoid multiple cross-overs of the two beams, which would lead to a significant increase in synchrotron radiation. But the cost of the RF power source and cryogenics will remain the same.

A rough estimate gives a 30% increase in accelerator cost if a two-beam pipe design is adopted.

A2.3 Pretzel Orbit vs. Bunch Train

Because the synchrotron radiation power is limited to 50 MW per beam in the CEPC, the number of bunches is limited to 50. In the baseline design, these 50 bunches are equally spaced, and the collisions are head-on. This design requires a pretzel orbit in order to avoid parasitic collisions in the arcs. From the experience of LEP and CESR, the pretzel orbit is difficult to operate and control, and is also difficult for injection.

An alternative, as suggested by Mike Koratzinos [1], is to use a bunch train, namely, to put the 50 bunches close to each other as if it is a "macro" bunch. The two macro bunches, one each for electrons and positrons, circulating in the ring will only collide at the two interaction points (IPs) without any parasitic collision in the arcs. Therefore, a pretzel orbit is not needed. This is shown in Figure A2.1. The length of the interaction regions will need to be made longer (~2 km each).

.

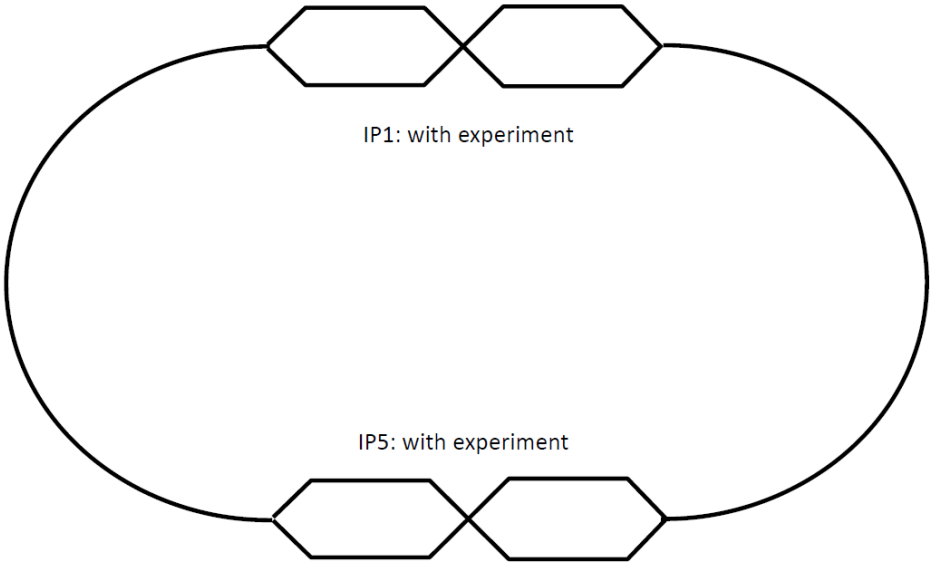

Figure A2.1: Illustration of using a bunch train in the CEPC to avoid the pretzel orbit.

However, the head-on collision has to be replaced by a collision angle, which would make the machine-detector interface (MDI) design more complicated.

The RF loading due to unevenly distributed bunches does not seem to be a problem [2].

This alternative design has certain merits and will be studied further.

References:

1. Mike Koratzinos, private communication.
2. Carlo Pagani, private communication.

Appendix 3 Operation for Super Z

There is significant physics interest in a high-luminosity run at the Z-pole, 45 GeV energy per beam. At this beam energy, much higher beam current can be supported due to the reduced synchrotron-radiation power. At the same time the beam emittance shrinks with the square of the energy ratio, which has to be mitigated to avoid exceeding the beam-beam limit. Furthermore, the rate of radiation damping is reduced thus reducing the beam-beam limit (albeit this relation is of a rather soft nature).

To assess the potential luminosity for Z-energy running, the following formula can be used:

$$\mathcal{L} = 2.07 \times 10^{39} \frac{P_0 L\left(\beta_x^* \xi_y + \beta_y^* \xi_x\right)}{\gamma^3 \beta_x^* \beta_y^*} \qquad (A3.1)$$

We use the same β_y^* at the IP and a slightly lowered value of β_x^* compared to CEPC at Higgs energy. The beam-beam parameters ξ_x and ξ_y are derated by the energy ratio since the damping time increases by the 3rd power of the energy ratio, but the dependence of the beam-beam limit is closer to the 3rd root of the damping time. We also derate the bunch current by the energy ratio from that of CEPC at Higgs energy to maintain the same stability margin as Higgs operation. Using the above equation and the parameters in Table A3.2 we calculate a luminosity of 2.27×10^{34} /cm^2/s.

In order to achieve this luminosity, the number of bunches will be increased beyond the 50 used for running at the Higgs energy. To fit the larger number of bunches into the machine without major global changes to the design, we will separate the beams about 24 m upstream of the interaction point using electrostatic separators of 0.332 mrad angle per beam. Both beams pass off-center through the insertion doublet (QF1 and QD0) and cross at the IP with a 0.8 mrad crossing angle. The geometry is determined to separate the beams at the first parasitic crossing, 0.692 m away from the IP, by 7.5 σ_x. This allows us to put 64 trains of up to 28 bunches spaced by 3 RF periods apart from each other into the machine. With the chosen number of bunches per train, no parasitic crossing in the IR is separated by less than 7.5 σ_x. Both beams are centered throughout the critical CCX and CCY sections of the interaction region optics. Beam separation in other regions of the machine remains the same as for Higgs running.

A non-zero crossing angle at the IP and an increase in beam horizontal emittance both make getting the beams in and out of the final focus doublets more difficult. For Z running we use the parameters found in Table A3.2. The Beam-Stay-Clear (BSC) for the IR we define to be 12 uncoupled σs+0.5 mm COD for X and 5 fully coupled σs+0.5mm COD for Y. The 1.6 mrad total crossing angle shifts the X orbit away from the nominal beam axis and closer to the beam pipe walls. The larger emittance (16.0×10^{-9} nm-rad) increases the BSC envelope and further reduces the space between the beams and the vacuum chamber walls. In addition, the off-axis orbits in the final doublet significantly increases the synchrotron radiation (SR) generated by these magnets. Figure A3.1 shows a plan view of the IR with the final focus magnets. Note that the vertical scale in the figure is greatly increased in this anamorphic view.

The magnet apertures and beam pipe have been increased to accommodate the larger beam with the crossing angle. Table A3.1 below summarizes the changes to the final focus doublet and the cold bore beam pipe inside these magnets.

The arrows in Figure A3.1 indicate the trajectories of the SR fans for beam particles at the edge of the BSC. The incoming BSC boundary produces some SR that strikes a surface between the QF1 and QD0 magnets. The beam pipe between the magnets is warm in order to absorb this SR energy. This means the QDO and QF1 are in separate cryostats.

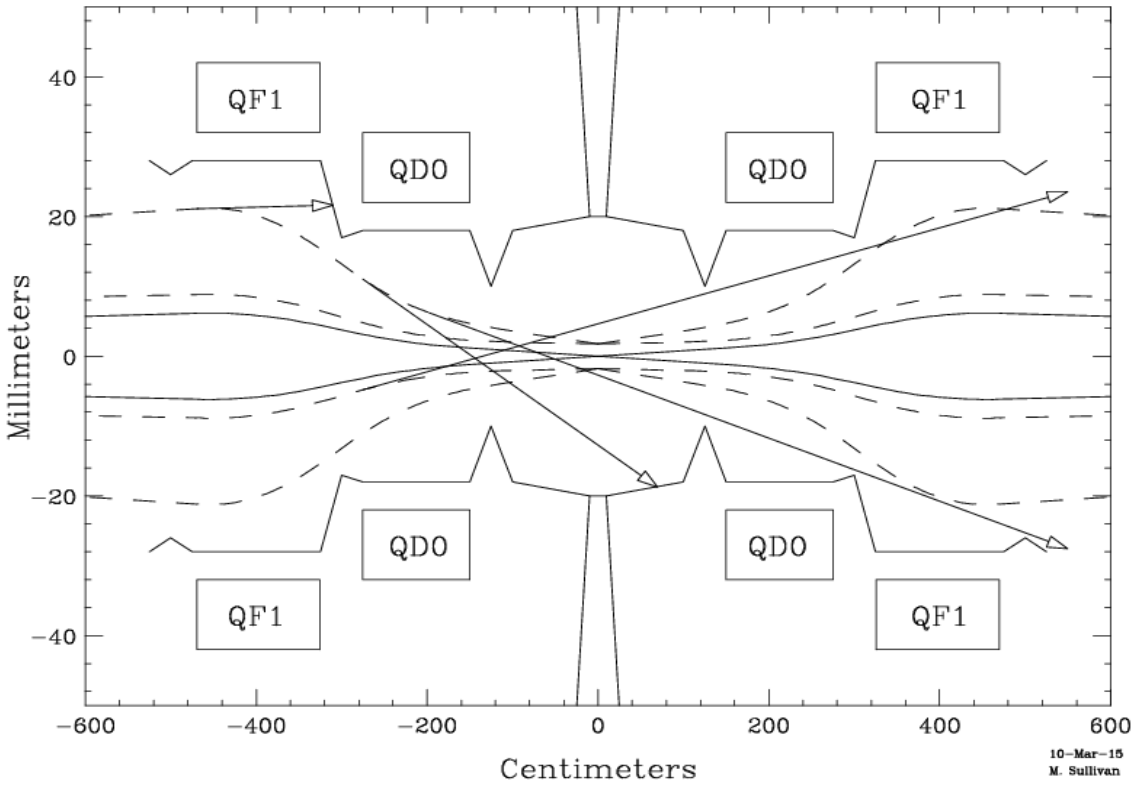

Figure A3.1: Layout of the IP region with the final focus doublets. The solid curved lines are the beam centroid orbits. The dashed lines are the BSC envelopes for each incoming and outgoing beam. The arrows indicate synchrotron radiation trajectories from particles at the BSC boundary. In this case, this is from 12σ beam particles. The beam particle density at 12σ should be quite low. Therefore we do not expect there to be very many photons striking these surfaces near the cold bore of the magnets. In general, most of the produced radiation escapes the local area.

Table A3.1: Summary of the final doublet changes needed to accommodate the Z running. Note the scaled up gradients do not exceed the Higgs running design gradients. We also include SR power numbers in this table. Part of the large SR power increase comes from the increase in beam current (from 223 mA when compared to Higgs running at 17 mA).

Magnet	Z (m)	L (m)	G (T/m)	Inner rad. of beam pipe (mm)	Inner rad. of coil (mm)	SR power per beam (kW)	Total SR power (kW)
QD0	1.5	1.25	107.45	18	22	35.3	141
QD1	3.25	1.44	53.76	28	32	75.8	307

The electrostatic separators needed to separate the beams and recombine the beams are located ±24 m outboard of the IP. Table A3.2 lists some of the separator parameters. The separators will have to be shielded from SR from the last bend magnet of the

chromaticity correction block as well as SR coming out of the interaction region. We chose a separator gap of 30 mm which should be large enough to allow SR masks to fully shield the plates. A more thorough study of the SR around the separator and the IR in general is needed to confirm these initial conclusions.

The natural emittance of the CEPC lattice is below 1 nm-rad. In order to increase this value to the 16 nm-rad required for operation at the Z-pole, the average value of the curly-H function, $<\mathcal{H}>$, needs to be increased. This can be done by either increasing the average value of the dispersion function, $<\eta>$ or by introducing a modulation of η. Since the momentum compaction depends on $<\eta>$ and its value should not increase to maintain short bunches, we opt for a combination of the two. It turns out that doubling the cell length and introducing a dispersion modulation allow us to reach the desired beam emittance while keeping momentum compaction at an absolute value of about 3×10^{-5}. Figure A3.2 shows the lattice functions of such a super period, Figure A3.3 the beam envelopes. This modification would require a change in powering of the arc quadrupoles, incl. turning half of them off and reversing the polarity of others, but avoids any mechanical modification of the arc structure of the machine. Also, the arc quadrupoles do not require more power or aperture than for Higgs operation. While this arc period is not fully optimized it provides a proof that the required beam parameters are achievable. The powering requirements can be designed into the machine thus ensuring the flexibility needed for both operational modes.

While we believe there are no fundamental design issues, there are a number of areas requiring further study. With about 1800 bunches in the machine, there are an equal number of parasitic crossings separated by the pretzel orbit. A careful analysis of the residual tune shift from these crossings has to be carried out to determine the required separation. This has potential impact on the aperture requirement for the vacuum system. The total beam current of 2×223 mA reduces the tolerance against impedance esp. from the low-lying modes of the multi-cell cavities, possibly limiting the number of cells that can make up one RF structure. It also raises the HOM power although the reduced bunch current will partially mitigate the increase in total current. Lattice and IR require further optimization and scrutiny to ensure the projected performance can be achieved.

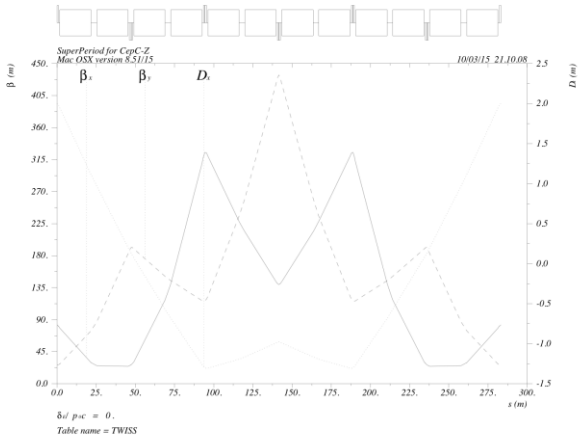

Figure A3.2: Lattice functions of an arc super period for the CepC collider running at Z energy.

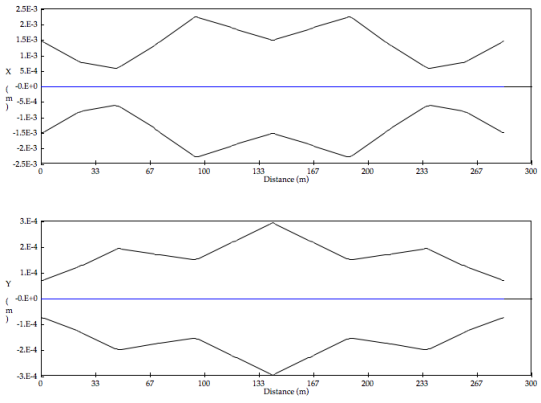

Figure A3.3: Beam envelope (1σ) in an arc super period for the CepC collider running at Z energy. Top frame is the horizontal envelope, bottom frame is the vertical envelope.

Table A3.2: CEPC collider parameters for running at Z energy

Parameter	Unit	Value
Beam energy [E]	GeV	45
No. of bunch trains		64
No. of bunches per train		28
Spacing of bunches in train	m	1.384
Luminosity	$cm^{-2}s^{-1}$	2.27×10^{34}
Beam current	mA	223
S.R. power per beam	MW	13.4
Particles per bunch		1.4×10^{10}
Beta function at IP, horizontal	m	0.692
Beta function at IP, vertical	m	0.003
Beam emittance, horizontal	m-rad	16×10^{-9}
Beam emittance, vertical	m-rad	1.4×10^{-10}
Beam size at IP, horizontal	μm	105
Beam size at IP, vertical	μm	0.65
Energy spread dE/E		0.5×10^{-3}
Crossing angle at IP (per beam)	mrad	0.8
Beam-beam parameter, horizontal		0.044
Beam-beam parameter, vertical		0.031
Momentum compaction (arc super period)		-3.34×10^{-5}
Energy loss per turn	MeV	59.55
Length of arc cell	m	94.4
Field of electrostatic separator	MV/m	35
Length of electrostatic separator	m	5
DC voltage of separator	kV	110

Appendix 4 Operation for High Intensity γ Ray Sources

A4.1 Features of the CEPC γ Ray Sources

A4.1.1 High Flux and Brightness

A4.1.1.1 From Bending Magnets

These are the assumed conditions: electron energy 120 GeV, current 16.6 mA, emittance 6.8 nm·rad, coupling degree 0.3%. Then these are the properties of the resulting synchrotron light: characteristic energy about 600 keV, brightness more than 10^{16} phs/s/mm^2/mrad^2/0.1% B.W., and flux more than 10^{12} phs/s/0.1%B.W. When the radiation energy is higher (lower) than 100 keV, the radiation brightness and flux from the CEPC bending magnets are higher (lower) than the radiation from 3rd generation synchrotron light sources in the world. Refer to Figures A4.1 and A4.2 for details.

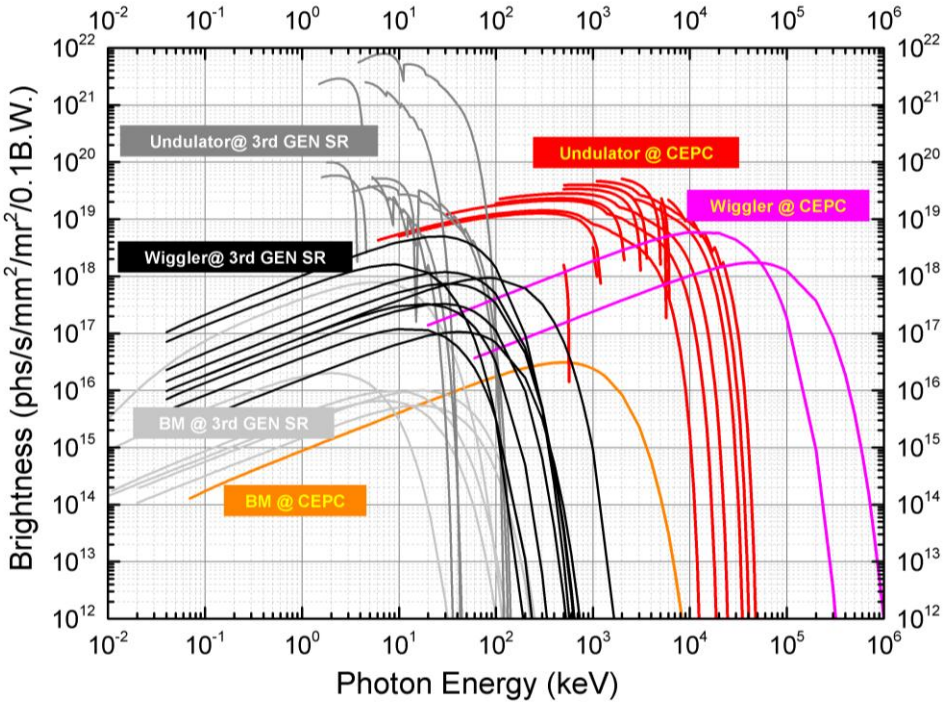

Figure A4.1: The brightness of bending magnet, wiggler, undulator and Low K undulator of a γ-ray beam at CEPC.

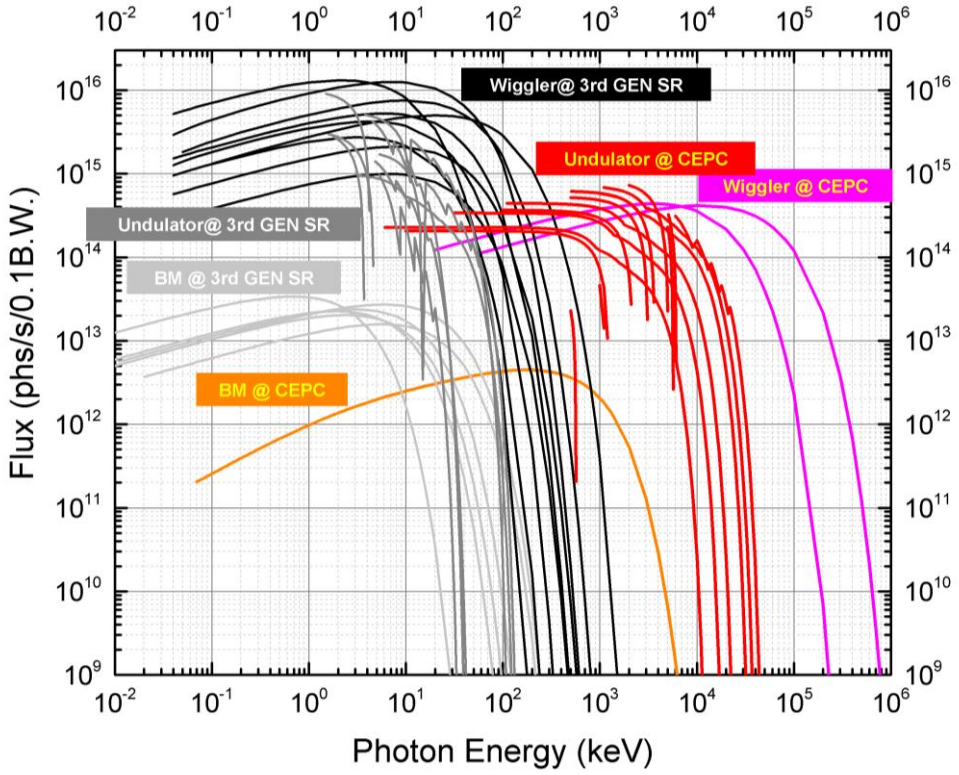

Figure A4.2: The flux of bending magnet, wiggler, undulator and Low K undulator of a γ-ray beam at CEPC.

A4.1.1.2 From Wiggler

Under the same conditions as above, the characteristic energy with a wiggler in the CEPC ring is 17.2 MeV; its brightness is more than 10^{18} phs/s/mm^2/mrad^2/0.1% B.W., and its flux more than 10^{14} phs/s/0.1% B.W. High flux radiation can reach 300 MeV. When the radiation energy is higher (lower) than 0.5 MeV, the radiation brightness and flux are higher (lower) than the radiation from the wigglers of 3rd generation synchrotron light source in the world. Refer to Figures A4.1 and A4.2 for details.

A4.1.1.3 From Undulator

Under the same conditions as above, the undulator of CEPC can provide higher brightness gamma radiation than the wiggler. Its brightness is more than 10^{19} phs/s/mm^2/mrad^2/0.1% B.W., and its flux is more than 10^{14} phs/s/0.1% B.W. Radiation with high flux can reach 20 MeV. When the radiation energy is higher (lower) than 0.1 MeV, the brightness and flux from a CEPC undulator are higher (lower) than the radiation from the undulators of 3rd generation synchrotron light sources in the world. Refer to Figures A4.1 and A4.2 for details.

A4.1.2 Advantages

Compared with the radiation from other 3rd generation synchrotron light sources, gamma rays from CEPS has three advantages:

1) From 0.1 MeV to 100 MeV CEPC can provide radiation with much higher brightness and flux than that from other 3rd generation synchrotron light sources.
2) The divergence angle of gamma rays from CEPC is very small, from 0.1 mrad to 0.01 mrad.
3) The energy range of the gamma rays from CEPC is very wide compared with 3rd generation synchrotron sources, from 0.1 MeV up to 300 MeV.

A4.2 Comparison with Laser γ Ray Source

Today the state of the art gamma ray source is a gamma ray facility based on Laser-electron Thomson scattering. It is called a laser gamma source. The performance of the main laser gamma sources in the world are listed in Table 1 and compared with what is possible from CEPC. The flux of CEPC gamma rays is much higher than the flux of all other laser gamma sources in the world.

Based on the results in A4.1 and A4.2, we can say that the CEPC gamma sources would have the highest brightness and highest flux of all kinds of gamma ray sources in the world.

Table A4.1. Performance comparison between the CEPC gamma source and the main Laser gamma sources in the world.

Source	CEPC BM	CEPC Undulator	CEPC Wiggler	SSRF (China)	TUNL-HIGS (USA)	TERAS (Japan)	ALBL (Spain)
Gamma energy rang (MeV)	0.1~5	0.1~20	0.1~100	0.4-20 330-550	2-100	1-40	0.5-16 16-110 250-530
Energy resolution (deltaE / E)	continuous	~1%	continuous	5%	0.8~10%		
Flux (phs/s)	$>10^{12}$ @0.1%	$>10^{14}$	$>10^{14}$ @0.1%	10^{6}	10^{8}	10^{4}~10^{5}	10^{5}~10^{7}

A4.3 Applications of CEPC γ Ray Source

- Nuclear physics research, including nuclear astrophysics, nuclear structure, multi-quark states, hadron physics, gamma ray spectroscopy.
- Applied research, including national security, engineering materials, medical applications, aviation and aerospace.

A4.4 Key Technologies for Applications of CEPC γ Ray Source

A4.4.1 Insertion Device

This component in modern synchrotron light sources stimulates highly brilliant, forward-directed synchrotron radiation emission by forcing a stored charged particle

beam to perform wiggles, or undulations. With an insertion device one can have a quasi-monochromatic beam when an undulator is operated in its fundamental mode. The benefits are to reduce the energy loss rate of electrons and to decrease the heat load by at least 3 orders of magnitude, and at the same time increase the flux and brightness by several orders of magnitude for experiments that don't need very good energy resolution.

There are 3 type of fundamental wave undulator. The low K undulator is a good candidate for the CEPC. It produces 0.5 MeV to 10 MeV gamma rays with 1% energy resolution and is adjustable in energy. Compared to the normal undulator, its flux is lower by as much as one order of magnitude. Details are in Figures A4.1 and A4.2

A4.4.2 Transport and Modulation

Both the total radiation power and the power density of CEPC gamma rays are very high. The total radiation power of CEPC is 100 - 1000 times that of 3rd generation synchrotron sources. So the very high heat load is a big challenge in using the gamma rays. The techniques include multistage slow-release heat load and optimizing the beam split and the materials.

The gamma ray modulation technique is another key technique to use the CEPC gamma rays. This includes gamma ray crystal based monochromatization, gamma ray focusing based on a refraction lens, and gamma ray slits and BPM.

Achievable gain using a refraction lens focusing system at 0.5 – 1 MeV is a few times ten.

A4.4.3 Detection

The gamma rays from the CEPC have high brightness, a small spot and good collimation. Experiments require a detector with high resolution (0.1^{o} angular resolution, 1 micron spatial resolution) and high efficiency, much higher than the level of today's gamma ray detectors. We need to resolve the contradictory requirements between high resolution and detector efficiency. We also need to try and combine the detection of gammas, neutrons, and charged particle at the same time.

It is very important to consider both the new experimental method and the special sample environment for using the high brightness gamma ray.

Careful consideration is needed in the layout of the frontend, the beamline and the experiment station taking into account CEPC facility features, such as large deflection radius, small lead angle, long distance between the branch pipe and the gamma source, and all of this underground.

A4.5 Summary

CEPC gamma sources have the highest brightness and flux compared to all kinds of gamma ray sources in the world. There are many technical challenges to fully realize all of its advantages.

Appendix 5 Option for XFEL

A5.1 The Requirements for an XFEL Driven by the CEPC Linac

In order to realize an XFEL based on the CEPC Linac, one key parameter is the peak electron beam current before entering the undulators. The peak current should reach a few thousands of Amperes, otherwise the saturation length of the radiation will become too long or the peak brilliance of the XFEL will be too low. The peak current depends on the bunch population and compressed bunch length. A typical value of bunch population in the Linac for an XFEL is in the range of 20 - 200 pC, while the bunch length is on the order of 10 fs.

Additionally, it is required that the Linac should furnish an electron beam with high energy (6 GeV or more), low emittance (normalized emittance lower than 1 mm.mrad), low rms energy spread (on the scale of 10^{-4}). Such requirements are also of benefit for the CEPC injector.

The electron energy of presently existing or under construction XFELs range from 5.8 GeV (SwissFEL) to 17.5 GeV (EXFEL). Therefore, the 6 GeV beam energy our Linac is fine.

The normalized emittance for an XFEL is typically required to be lower than 1 mm.mrad. At the SwissFEL, of similar energy, the normalized emittance is 0.65 mm.mrad (long pulse mode) or 0.25 mm.mrad (short pulse mode). Therefore a photocathode RF gun instead of a thermal cathode electron gun is required. Considering the fact that the technology related to a photocathode RF gun is more advanced than for a thermal cathode gun, it is reasonable to initially construct the Linac based on a thermal cathode. At the same time R&D can begin for another injector based on a photocathode RF gun.

The energy spread needs to be about 10^{-4}. To reach this value, a photocathode RF gun and laser heater are required.

To obtain high peak current, the bunch length of the SwissFEL is 6 μm or 20 fs. On the other hand, the nominal value of the electron bunch in our linac is 10 ps. To reduce the bunch length while at the same time realizing a flat top in the beam current profile, bunch compressors are necessary, and start-to-end global optimization of the beam quality is essential.

To sum up, an injector with a photocathode RF gun is required, and space for a laser heater and bunch compressors should be reserved in the main linac, so as to reach the beam quality requirement of an XFEL.

A5.2 Possible XFEL Options

It is possible to realize an XFEL based on our linac, if the bunch length can be reduced, and a peak current of ~3kA achieved at the entrance of the undulator sections.

The advantage of this option is the low cost. The most expensive part of the XFEL is the linac. The following beamline, including undulators, phase shifters and end-station, are relatively low cost.

In the case there is 3kA peak current, 50-m long undulators are enough for lasing. The total cost for beamline and end-station is about 40-50M RMB.

The operational disadvantage may be the frequent alternation of modes between ring-injection to lasing-injection. Thus, the time for XFEL is limited.

LLRF is essential for timing and synchronization of the XFEL, and also required for the experiments. This requires an extremely high precision LLRF system. (for the XFEL but not for injection into CEPC).

A5.3 R&D Issues

1) To construct a hard X-ray FEL of 1 angstrom, the undulator should be of the SwissFEL-type (with short undulator period, <20 mm). We only have experience in EXFEL-types (undulator period of about 30 mm). Therefore the design and especially the engineering of the SwissFEL-type undulators is required.
2) The design of bunch compressor should be optimized.
3) We have no experience with a laser heater. R&D, especially engineering will be necessary.
4) The precision of the LLRF need to be on the order of fs. This requires R&D and engineering.
5) A photocathode RF gun can be provided by Tsinghua University, but some engineering is needed. Or we can develop the XFEL gun in house.
6) For the end-station, R&D on experimental instruments and methods, including sample manipulations, data collections and analysis, ultrafast timing techniques and ultrafast X-ray detectors is required.

Appendix 6 International Review

There was a review of this CEPC-SPPC Preliminary Conceptual Design Report (Pre-CDR) by an International Committee chaired by Prof. Katsunobu Oide (KEK, Japan) from February 14 to 16, 2015 at the IHEP in Beijing, China. The Committee issued a report on March 2, 2015 and gave permission to publish the executive summary of the report as an appendix of the Pre-CDR.

A6.1 Executive Summary of the International Review Committee's Report

Accelerator

CEPC-SPPC is the most ambitious accelerator project ever proposed in China. It will be housed in a 54 km circular tunnel (current baseline). The first phase is an electron-positron Higgs factory at a center-of-mass energy of 240 GeV (CEPC) for precise measurements of the newly discovered Higgs boson. The experiment is planned to start in 2028 and run though the 2030's. Experiments at the Z pole and the WW production threshold will be also possible. Then the tunnel will be filled by a proton-proton collider with a 70 TeV center-of-mass energy (SPPC) with a next-generation superconducting magnets, to explore the energy frontier. **The merit of this proposal is that the e+e- experiment starts as early as possible and will run concurrently with the HiLumi LHC. The construction of CEPC will not wait for the completion of the R&D for SPPC, relying on its progress during the CEPC construction and running period.**

It is highly likely that if CEPC-SPPC gets the go-ahead, it will be the dominant machine for high energy physics in the world for the next 50 years, and no other machine will be built in a similar energy range considering the limited resources given to HEP worldwide. **Thus this machine cannot be a second rate project, and must satisfy the physics goals and the aspirations of the majority of the high energy physicists in the world.**

The design work of CEPC has started just about a year ago. Tremendous effort has been made to prepare the *Preliminary Conceptual Design Report*, which is now nearly ready, and covers the entire project comprehensively. **The Committee has been very impressed with the progress during such a short period of time, as well as the work and presentations shown, mostly done by the young generation, who are the ones that can devote their careers to this project through the coming decades.**

The CEPC design is based firmly on the experience and lessons learned with past and current e+e- colliders, in particular the BEPC-I&II at IHEP, the Large Electron Positron collider (LEP1/2) at CERN (the highest energy e+e- machine to date) and the high luminosity B factories (KEKB at KEK and PEP-II at SLAC). The Committee applauds the CEPC design team for this achievement.

The Committee believes that the CEPC project and the required R&D will strengthen China's technological capacities in several areas, for example high-efficiency solid-state amplifiers, high-temperature superconducting materials and

superconducting RF technology. Important spin-offs for industrial applications can be expected.

The Committee appreciates the efforts to maximize the synergy with possible worldwide collaborators for an eventual CEPC consortium. This approach is applauded and the committee thinks that a strong international consortium can form around this approach, involving the leading accelerator laboratories of the world.

The current baseline of CEPC assumes a single-ring collider with a pretzel orbit to accommodate the necessary number of bunches. It is the cheapest option at least regarding construction, but also has several limitations and complexity. **The Committee encourages to complete a consistent design with the pretzel scheme, taking beam orbit/optics in the arcs and the interaction region (IR), dynamic aperture, beam-beam, beam injection, etc. into account. Then compare the pretzel scheme with other possibilities such as full double ring or partially separated single ring, in terms of performance, risk, construction and running costs, and achieving the physics goals for the Higgs, Z, and WW.** Since the project proposes a 5-year R&D before the start of construction, the choice of scheme does not necessarily need to be determined at this moment, and the decision can be made during the R&D period.

The baseline of the size of the ring, 54 km, has been chosen as the minimum to achieve the goal for a Higgs factory considering the construction cost. No fundamental limitation has been found for a larger ring of order 100 km from beam dynamics and accelerator technology points of view.

Science

The Committee understands that the goal of an integrated luminosity of 250 /fb per year at the ZH is competitive compared to other proposals with regard to achieving the desired accuracies in the Higgs physics study. The goal luminosities at Z and WW, however, have not been stated clearly, but they may have a big impact on the accelerator design.

Recommendation: Define clear physics goals at the Z-pole and WW threshold with the requirements on beam polarization if needed.

Response to the Charge Letter

We wish to summarize our response to the charge (see A6.2) we were given by making the following statements, supported by our report:

1. The Committee considers the CEPC-SPPC to be well aligned with the future of China's HEP program, and in fact the future of the global HEP program.
2. The design goals are well defined and comprehensive. We provided remarks and recommendations to improve the design, but we definitely consider this design to be credible and with sufficiently conservative assumptions.
3. The great majority of the accelerator physics issues are adequately addressed, and after addressing our recommendations, we expect that all the accelerator physics issues would be adequately addressed.
4. The designs of the technical systems and conventional facilities are effective for achieving the performance goals.
5. We find the CEPC design compatible with the future upgrade to the SPPC.

6. Technical risks and their potential impact were presented together with mitigation measures, while in some cases more study and R&D are needed.
7. The R&D program is clearly defined, and while we recommended a few additional R&D items, the program is adequate. We further believe that this R&D program will be highly beneficial to the science and technology infrastructure in China and will contribute to its economy.
8. We made a few suggestions for improvements of the design.

A6.2 Charge Letter to the Committee

Review of the CEPC-SPPC Preliminary Conceptual Design Report

February 14-16, 2015, IHEP, Beijing, China

Charge

The Institute of High Energy Physics (IHEP) in collaboration with a number of other institutions, domestic and international, has completed a Preliminary Conceptual Design Report (Pre-CDR) for the CEPC-SPPC. This is a proposal for the design and construction of a major new facility for the medium- and long-term future of China's HEP program. This proposal will be submitted to the Chinese government for approval, first as an R&D program (~5 years), followed by a construction project (~7 years).

The International Review Committee chaired by Prof. Katsunobu Oide (KEK) is asked to review this report before its formal release. The Committee is specifically asked to review and comment on the following aspects:

1. Does the committee view the CEPC-SPPC to be well aligned with the future of China's HEP program?
2. Are the design goals well defined and credible?
3. Are the accelerator physics issues adequately addressed?
4. Are the designs of the technical systems and conventional facilities effective for achieving the performance goals?
5. Is the CEPC design compatible with the future upgrade to the SPPC?
6. What are the primary technical risks and potential impacts? What mitigation measures should be taken?
7. Is the R&D program adequate and is it clearly defined?
8. How can the design be improved?

The site description and the cost are primarily informative. No specific comments on these topics are requested at this time.

A draft of the Pre-CDR will be made available to the Committee during the review. The Review Committee is invited to make comments or suggestions on any aspect of the Pre-CDR beyond those specifically included in this charge.

It is requested that a Committee report responding to this charge be forwarded to the IHEP Director by March 2nd, 2015.

International Review Committee Members:

Ralph Assmann, DESY (Germany)
Ilan Ben-Zvi, BNL (USA)
Marica Biagini, INFN (Italy)
Mike Koratzinos, CERN/Univ. of Geneva (Switzerland)
Eugene Levichev, BINP (Russia)
Katsunobu Oide (Chair), KEK (Japan)
Bob Rimmer, JLab (USA)
John Seeman, SLAC (USA)
Zhentang Zhao, SSRC (China)